THE UNIVERSITY OF CHICAGO

A CHARACTERIZATION OF THE MORPHOLOGY, FUNCTION, AND EVOLUTION OF

PURKINJE CELLS WITH MULTIPLE PRIMARY DENDRITES

A DISSERTATION SUBMITTED TO

THE FACULTY OF THE DIVISION OF THE BIOLOGICAL SCIENCES

AND THE PRITZKER SCHOOL OF MEDICINE

IN CANDIDACY FOR THE DEGREE OF

DOCTOR OF PHILOSOPHY

COMMITTEE ON NEUROBIOLOGY

BY

SILAS EDWARD BUSCH

CHICAGO, ILLINOIS

DECEMBER 2024

Abstract

Canonically, each Purkinje cell (PC) in the adult cerebellum receives only one climbing fiber (CF) from the inferior olive. Underlying current theories of cerebellar function is the notion that the equally unusual singularity of the CF input and numerousness of excitatory parallel fiber (PF) inputs renders PC dendrites into a single computational compartment. In this thesis, I outline my use of several anatomical and physiological methods both *in vitro* and *in vivo* to determine that PC morphology is diverse and impacts CF-PC connectivity and dendritic signaling in the mouse cerebellum. I also describe my expanded anatomical findings that PC morphology varies substantially across cerebellar regions and across species, with a focus on the primate lineage in relation to humans. First, I demonstrate that PCs with multiple primary dendrites can receive non-canonical CF multi-innervation in mice, rejecting a textbook dogma of cerebellar physiology that has existed since the 1960's. This may be a specific phenomenon permitting CF-PF receptive field matching for PCs with separated primary dendrite compartments. This is further supported by a second set of findings that 'enhanced' CF-PC signaling is not always beneficial and can be pathological in some disease states. Third, my analysis of human PCs, remarkably uncharacterized since their original illustration at the end of the 19th century, reveals that they exceed allometric constraint in their expanded size, compartmentalization, and spine structure. Finally, I have found that PC morphology is surprisingly diverse across species such that the cerebellum—classically considered a conserved and stereotypical brain region—may be a brain area for which evolutionary adaptation is detectable at the level of cellular morphology and physiology. Morphological variation is better predicted by phylogeny than allometry, adding further support for the hypothesis that PC morphology dictates function and that PC demographics may thus be recruited depending on a regional or species-specific functional need.

For those who shaped me and those I will shape in the mold of a scientist and artist

Contents

Appendices

List of Figures

Acknowledgments

I would not be where I am today if not for my teachers and mentors; I am lucky to have been inspired, encouraged, and guided by many. My deep gratitude for their guidance as I began to grow into my current interests and proclivities goes to many of my high school (Rondout Valley) teachers, some of whom are very tragically no longer with us: Doug Serson, Madame Christine Berg, Carol Sturm, Kevin Storrs, Elissa Jury. Likewise, I thank my college (Bard) biology and philosophy professors who helped me hone my intellectual and career goals: Drs. Mike Tibbetts (Bio), Felicia Keesing (Bio), Brooke Jude (Bio), William Mullen (Classics), Daniel Berthold (Phil). I also thank Dr. Vanessa Ruta and (now Dr.) Raphael Cohn; almost exactly a decade ago, they gave me a second chance and truly inspired my passion for neuroscience.

My indebtedness deepens for my college advisors, who are two of the most important people shaping my early growth as a thinker and a scientist. Arseny Khakhalin (Bio) and Kritika Yegnashankaran (Phil), I am most grateful that you shared with me your seemingly endless wisdom, eccentricities, and friendship; I am not sure if I could repay you.

Many of the most important lessons that have shaped me have come from outside of academia. My soccer coach Emmanual Nneji has always exuded leadership and loyalty, grit and grace, integrity and bravery; I can only hope that I have developed some of his quality.

I thank Drs. Maria Medalla and Jennifer Luebke (Boston University), who gave me broad experience as a technician in their labs before I started graduate school. Their knowledge and training were the biggest factors that allowed me to hit the ground running and incorporate experimental approaches for which the current Hansel lab configuration had little expertise.

I thank the members of my thesis committee, Drs. Ruth Anne Eatock, Wei Wei, and Mark Sheffield, who have played many roles in my graduate education: teachers, rotation hosts, research

and career advisors, and manuscript readers. Thank you for helping me to land the plane. I thank also the numerous other faculty who have contributed—in ways small or large but all significant—to my education here at UChicago: Drs. Daniel McGehee, Xiaoxi Zhuang, Pascalis Kratsios, John Maunsell, Daniel Margoliash, Matthew Kaufman, and Christopher Gomez. Equally important has been the guidance and judiciousness of Elena Rizzo (the best graduate program administrator of any department or university in my and many others' opinion).

It is funny how some mentors are chosen and others pop out of left field. I cannot express sufficiently here how grateful I am to Dr. Peggy Mason with whom I developed and taught a neuroethics course. Going well beyond that in your effort and friendship, you have made me a better and more confident teacher, mentor, communicator, and scientist.

I thank everyone in the Hansel lab who has supported me over the years. Thank you (Drs.!!!) Dana Simmons, Daniel Gill, and Gabrielle Watkins for showing me the ropes. Thank you, Tuan Pham, for easing my entry into using some computational methods and for always bringing joy, humor, and sharp intellect to the lab. The way that I think and communicate about science has been profoundly shaped by the many, many conversations and deep dives with Aurora Ferrell, Abby Silbaugh, Dr. Donald Huang. Thank you for being my friends and colleagues (and partners in the daily Hansel lab coffee expeditions)!

I must reserve a special thank you for Dr. Ting-Feng Lin, who started in the Hansel lab when I did in 2019. Ting was always the first person I went to… for everything. He was always there when I had a new result, wanted to share a paper I found, if I was stuck on something, needed career advice, wanted feedback on new analyses or writing, needed a coffee break, the list goes on. I have worked more closely with him over these six years than with anyone else, ever. I simply

could not have asked for a better lab partner and guide. Ting, thank you thank you thank you. I cannot express how much better you have made me and my science.

Dr. Christian Hansel made it all happen. I cannot thank him enough for giving me the opportunity to work in his lab and for giving me the runway to explore a new research direction. Christian always pushed me and taught me how to improve, whether I was running an experiment, presenting or interpreting a result, or trying to take a wider perspective in my thinking and writing. It could only be fully recognized in retrospect that Christian was perfectly blending the hands-on and -off approaches. He fostered me to learn and grow and do science in a way that I can call my own, while also always being available to guide me and shape the direction from his position of perspective and wisdom. Christian was always there if I had a question, gave quick and insightful feedback on every draft of anything I sent him. Some of the greatest lessons he taught are inarticulable; they are developments of intuition that can only come from a subtle shaping of perspective over time and proximity.

If I do not focus this section on my academic acknowledgements, I fear it may never end. However, I cannot leave out my dearest families. Endless gratitude goes to my parents Barbara and Stephen, who raised me to be creative, just, and hard-working. The more I have developed as a scientist, the more I have realized that I am following in your footsteps and becoming an artist. I wouldn't have it any other way. I am deeply grateful to have grown up alongside my sister Nora; though much younger, she was always ready for a rip-roaring time building and exploring with me. I also thank my pets, who can't read (obviously) but will get a nice treat later: Brynn, the smartest, fastest, and most earnest dog; Beamer and Dusty, the cutest furballs ever.

Finally: You have been everything. Through the trials, my rock; through the joys, my effervescence; and through the in-betweens, my partner. Thank you, Ariella.

CHAPTER 1

GENERAL INTRODUCTION

<u>Opening comments</u>

The principal neurons of the cerebellar cortex received their name from Jan Purkinje but their face from Camillo Golgi and Santiago Ramón y Cajal. As the 19th century was giving rise to the 20th, both anatomists introduced Golgi's mercurial silver dye to brain tissue and selectively revealed isolated 'perikaryon' structures, as they were called then. This allowed Ramón y Cajal and other anatomists to concretize an idea that was eventually termed the 'neuron doctrine', which held that brain cells are not a fused syncytium but are instead discrete entities that must therefore propagate signals in a directed way and through external signaling. Possibly the most iconic representation of this concept that brain cells are independent and unfused entities is Ramón y Cajal's illustration of a lone, spine-dense human Purkinje cell in 1899 (Figure 1A).

The human Purkinje cell (PC) is manifestly complex in morphology. Mouse PCs stand in stark relief (Figure 1B). This distinction between the model system we most commonly study today and the enigmatic human cell drove much of the beginning of our inquiry. For one thing, it is understood that while Ramón y Cajal distinguished himself as an anatomist through his dedication to detail, he described his own process as amalgamating scenes he would observe over the course of hours and days at the microscope. Since this time, human PCs have gone remarkably unexplored. Only a handful of studies have been undertaken on small numbers of cells and with seemingly incomplete characterization. We were left to wonder: is this truly how a human PC looks? The extreme difference between human and rodent also made us, as physiologists, curious about the consequences of dendritic complexity. Do the morphological differences confer distinct functional capacities?
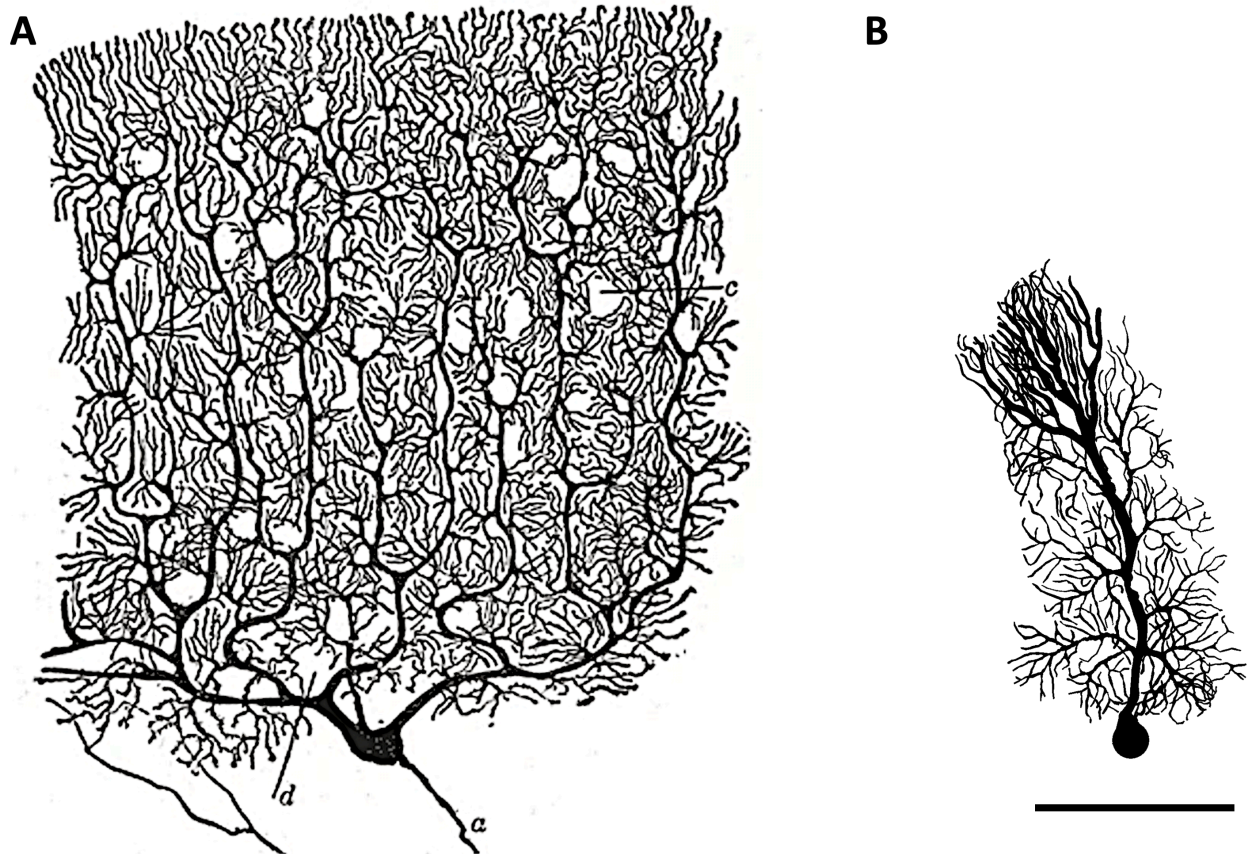
Figure 1. Cerebellar Purkinje cell morphology. A) Illustration of a human Purkinje cell by Santiago Ramón y Cajal in 1899. **B)** Digital reconstruction of a mouse Purkinje cell on approximately the same scale (scale bar is 100µm).

No previous studies had distinguished PCs by their dendritic morphology in mammals. Similarly, no previous studies had distinguished PCs by their functional properties in mammals, aside from observing a difference in spontaneous firing rates based on zebrin identity, a striped molecular pattern in the cerebellum the purpose of which is not yet fully clear. A lack of focus on these topics was certainly jarring, but it was not terribly surprising.

The technology to address these questions is recent and theories of cerebellar anatomy and function have, in the meantime, congealed into a highly dogmatic sense that cerebellar anatomy, being highly conserved across vertebrates, is geometrical and stereotypical in equal measure. Consequently, PC morphology, their input arrangement, and their physiological capacity are all

generally taken to be stereotypical. The fractal-like regularity of their dendritic branching gives the impression that the dendritic tree is a single arborizing compartment, but this belies what can be profound complexity and diversity in their shape. Studies of PC computation have largely considered the dendritic tree a continuous functional compartment due to the equally unusual singularity and numerousness of excitatory input from climbing fibers and parallel fibers, respectively.

We observed that human PCs are often 'multi-branched', having either numerous trunks emerging from the soma or a proximal bifurcation of a single trunk. This feature was particularly notable when compared to the mouse, where the notion that PCs have a single primary dendrite is borne out consistently. The multi-branched motif produces highly segregated dendritic compartments. Does this structure confer functional properties that have gone unreported? While the multi-branched motif stood out at the morphological level, it also drew our attention for a strategic, physiological reason. The thick primary dendrites provide a) the target for translocation from the soma to the growing dendritic compartment of one 'winning' climbing fiber among many competing for synaptic territory early in development and b) the scaffolding on which, in adult, the canonical lone climbing fiber grows and entwines. Could the existence of several primary dendrites enable multiple climbing fibers to be retained (and compartmentalized) in the adult cerebellum?

In my first experiment, I combined whole cell patch clamp and electrical climbing fiber stimulation in acute cerebellar slices with dye loading and confocal imaging of recorded PC morphology. This allowed me to reveal that there is modest climbing fiber multi-innervation in adult mice—this was present in previous data but not described as a phenomenon—and demonstrate that this non-canonical innervation pattern happened almost exclusively to PCs with

multiple primary dendrites. My finding defied textbook wisdom about the climbing fiber to PC relationship and uncovered morphological and functional diversity in what was classically considered a clearly defined and stereotypical cell, circuit, and brain region. Thus began the hunt to characterize the morphology, function, and evolution of PCs with multiple primary dendrites as a novel sub-population and a likely source of yet undescribed anatomical and functional diversity.

Cerebellar anatomy is conserved and stereotypical

The cerebellum is one of the most evolutionarily conserved brain structures; all vertebrates have a cerebellum or a 'cerebellum-like' structure with similar anatomy and function (Devor, 2000). Analogous structures can even be found in invertebrates. For example, the fruit fly mushroom body bears a striking resemblance to the cerebellar cortical circuit in both its anatomy—having a dense array of calyx cells (granule cells) converging onto the arbor of the mushroom body output neurons (Purkinje cells) to be integrated with a 'corrective' signal from dopaminergic neurons (climbing fibers)—and its function as a site of robust expansion recoding, associative plasticity, and supervised learning (Farris, 2011; Litwin-Kumar et al., 2017). Weathering changes over millennia in body shape and size, ecological niche, and nervous system complexity, the cerebellum has served as many ethological functions as there are species in possession of a cerebellar structure. Among only those species-specific functions that have been experimentally tested, the cerebellar circuit enables such a wide set of behaviors as corollary charge subtraction for proprioception in electric fish (Sawtell, 2017); vocalization precision and learning in song birds (Pidoux et al., 2018); undulating, rectilinear, or legged movement among squamates (Larsell, 1926; Macrì et al., 2019); and language and higher order cognitive performance in humans (King et al., 2019; LeBel et al., 2021). For other species, such as those featuring later in this thesis, we

can only yet imagine their cerebellar specialization for: trunk representation in elephants, arboreal brachiation in gibbons, prehensile tail climbing by spider monkeys (who also lack thumbs), and poly-dexterous limb use particularly among the non-human great apes.

As the cerebellum optimizes these diverse motor and non-motor behaviors, vast information arrays representing sensory, internal, and cognitive states arrive in the cerebellar cortex from across the entire brain and must undergo complex integration. Being the sole cortical output, PCs reside at the core of this integration and thus of cerebellar function. The dendritic arbor of each PC is the primary target of two excitatory input pathways (Figure 2). First, the most spine-dense and largely distal dendritic branches are contacted typically by a single synapse each from thousands of parallel fibers (PFs) that run for long distances (3mm in the mouse) orthogonal to the flat parasagittal planes of the PC dendritic arbors. PFs are the axons of the most numerous neuron in the brain—cerebellar granule cells—and provide an expansion recoding of contextual input from mossy fiber (MF) inputs to the cerebellum (Albus, 1971; Marr, 1969). Second, the thicker caliber primary dendrites of PCs receive what are classically thought to be prediction-error signals carried by one climbing fiber (CF) axon from the inferior olive (Ito & Kano, 1982).

Taken together, a single mouse PC will receive approximately 50,000 synaptic contacts from roughly the same number of granule cells (each receiving 3-5 MF inputs) and several hundred synapses from one CF. To compare with the principal neuron type of another cortical structure, a single pyramidal cell in the mouse neocortex receives roughly 5,000 synapses, an order of magnitude fewer than the cerebellar PC. Thus, PCs must be (and are) adapted to receive the most numerous input array on one of the largest dendritic arbors of the central nervous system.
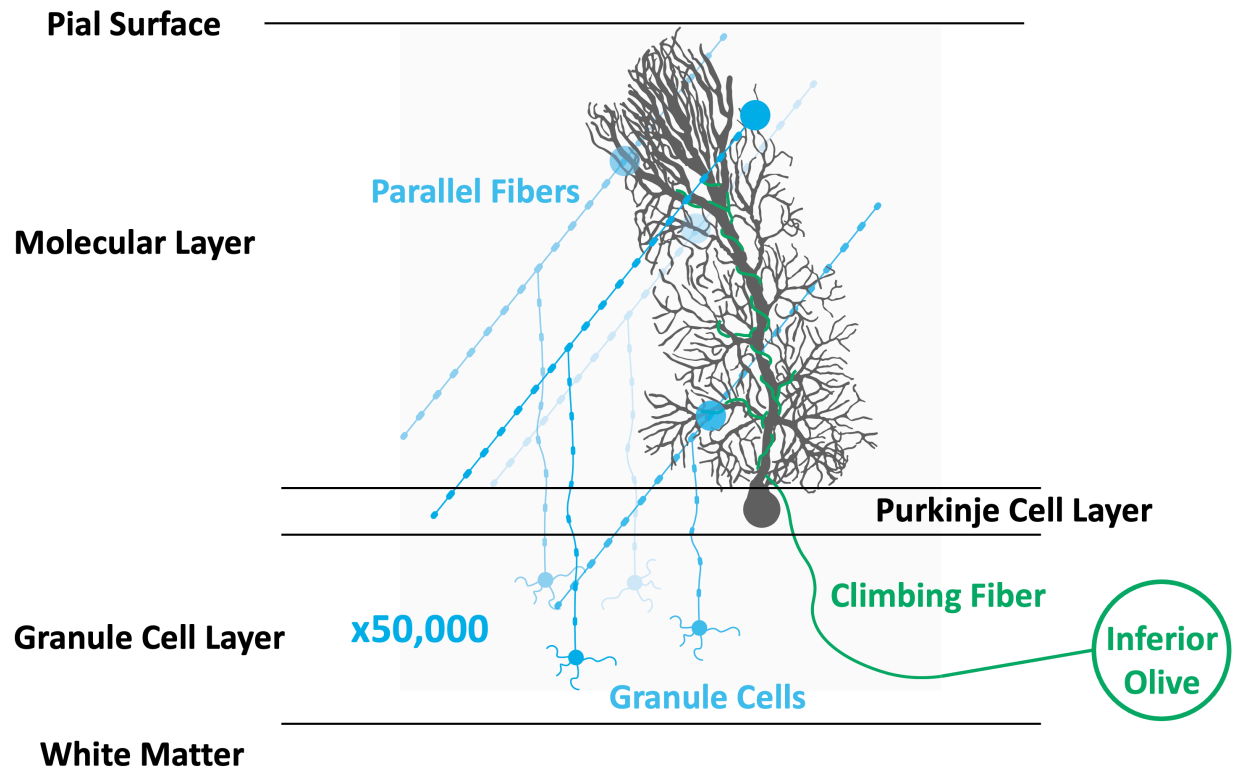
Figure 2. The canonical cerebellar cortical circuit motif.

CF role as error signal and PF teacher

What does this massive input array achieve? The standard characterization of PC function is as a perceptron (Brunel et al., 2004), a feed-forward neural network with a readout (response) unit (e.g. the PC) whose input weights (PF synaptic input strength and influence on PC somatic output) are shaped by supervised learning through the corrective "teaching" signal of the CF. CF activity activates NMDARs in adult animals (Piochon et al., 2007; Renzi et al., 2007) and P/Q-type voltage gated calcium channels to produce a robust calcium signal that is distributed throughout the dendrites evenly by the equal distribution of CF terminals across the arbor (Miyakawa et al., 1992). CF-dependent calcium concentration also triggers αCaMKII and PKC-meditated AMPAR GluR2 phosphorylation and endocytosis (Piochon, Titley, et al., 2016). All PF synapses are thus exposed to this calcium signal that selectively permits synaptic long-term depression (LTD) at coincidently

active PF synapses where locally elevated depolarization drives further calcium influx through P/Q-type channels and mGluR1 activation drives IP$_3$-mediated calcium release from the endoplasmic reticulum (Takechi et al., 1998; Tempia et al., 1998; S. S.-H. Wang, Denk, et al., 2000).

While PF LTD can also be induced by strong, repetitive PF stimulation (Eilers et al., 1997; Hartell, 1996) or current injection induced PC depolarization (Linden et al., 1991), it is suspected that cerebellar learning that depends on PF-LTD proceeds through PF and CF coincidence (Jörntell & Ekerot, 2002). The critical prerequisite for the accurate plasticity of this process, therefore, is the accurate matching of receptive fields (RFs) between the CF and the PF array (and thus the PF subset co-active with the CF). If the RF of the PFs (representing contextual information about the state of, say, a patch of skin or a light in a particular location) does not match the receptive field of the CF providing the supervisory signal, then the coincident PF weights will be adjusted inappropriately.

In anatomical terms, this means that the PF inputs to each PC should derive their contextual RFs from a relatively similar subset of mossy fiber signals that can thus be related consistently with the RF of the CF for that PC. This connectivity pattern is plausible when we assume the PC forms a dendritic arbor that is narrow and joined as a singular, albeit densely packed, compartment. Then a single PC can receive a restricted set of PF inputs, which are demonstrated to exhibit spatio-functional clustering (Wilms & Häusser, 2015), from a narrow medio-lateral band that might plausibly receive clustered MF inputs (Nguyen et al., 2023). It has also been postulated that the strongest GC input comes from the ascending fibers of granule cells immediately sub-adjacent to the dendritic arbor rather than the PFs of medio-laterally distant GCs (Sims & Hartell, 2006). Thus, the PC may be most impacted by GC input with an even tighter RF defined by somewhat spatially

clustered MF inputs to the GCL. In this scheme, the developmental selection of a single CF can produce a tightly matched RF between the GC inputs and the CF.

<u>Newfound diversity in a classically conserved and stereotypical circuit</u>

We took note of the fact, however, that some PCs in the rodent have multiple primary dendrite compartments (Nedelescu et al., 2018; Nedelescu & Abdelhack, 2013) that often exhibit a substantial spatial gap and thus have a wider dendritic profile in the parasagittal plane. We reasoned that, in a circuit with such stereotypical and geometrical arrangement, the horizontal axis may be a critical determinant of function. Thus, the morphological diversity was surprising and gave rise to the first question this thesis asks: **Does PC morphology influence input arrangement?** In the scheme above, the presence of segregated dendritic compartments could make PCs vulnerable to receiving more disparately located GC PFs that may receive and represent more distinct MF RFs. While this has never been tested, this eventuality is clear from purely geometrical considerations. In this event, a single CF RF may only accurately match the RF of a subset of GC inputs to the PC. This would be problematic for the perceptron model that requires the RFs to match. Those GC inputs whose RF doesn't match the CF may be inappropriately corrected by the CF such that the strengthening or weakening of their inputs might be meaningless and contribute noise to the PC representation.

We postulated that the maintenance of multiple CFs into adulthood could solve for multi-compartment vulnerability to mismatch by providing additional CF RFs that could isolate to the dendrite with the appropriate GC input sub-population (see Appendix Figure S11). Though this defied the half-century old dogma that PCs are universally mono-innervated in the adult brain (Eccles et al., 1966), there were hints in the literature that a small, but not insignificant, number of

PCs maintain multiple CFs in the adult rodent. Starting with the pioneering and field-defining work of Masanobu Kano to describe the process of CF pruning and cerebellar cortical circuit development, slice electrophysiology methods were designed to detect the completion of CF pruning across mouse postnatal development (Kano et al., 1997). This method, the same used today by myself and others, consistently revealed the rapid postnatal CF pruning that reduced the multi-innervation frequency from universal to absent.

But not completely absent. Consistently, the data of Dr. Kano and others, including members of the Hansel lab, held evidence that roughly 10-20% of adult PCs retain multiple CFs (Kano et al., 1997; Nishiyama & Linden, 2004; Piochon et al., 2014). But this was never reported as a finding in a formalized way. That is, the result was present in figures from these papers, but it was not commented upon. Whether the experimenters took note of this to themselves I cannot say, but nonetheless the dogma of universal mono-innervation—always strictly and specifically defined as a one-to-one connectivity phenomenon whose universality is total, not merely a preponderance— has held through decades of consistent, albeit tangential, results to the contrary (Najafi & Medina, 2013; Schutter & Maex, 1996; Simpson et al., 1996). My early experiments applied the same slice electrophysiological methods to confirm that ~15% of adult PCs are multi-innervated. However, by dye loading and recording morphological characteristics of every patched PC, I expanded this observation to demonstrate that the multi-innervation phenomenon is exclusive to PCs with multiple primary dendrite compartments.

In a circuit whose theoretical function relies on the universal singularity of the CF error signal, the presence of multi-innervation was surprising and gave rise to the second question this thesis asks: **Does CF multi-innervation produce distinct compartment signaling *in vivo*?** Retained CF multi-innervation would likely occur through the translocation of multiple CFs to distinct

dendrites, as this would provide the means for multiple CFs to mitigate competitive pressure and avoid eliminative synaptic pruning. The presence of CF-PC signals that are both non-unitary and spatially segregated, combined with the introduction of more distinct contextual information from GC RFs on a broader dendritic arbor, would diversify cerebellar cortical computation. CF multi-innervation may thus be a feature, not a bug, and may shape the information content of the PC output. As such, each multi-innervated PC would represent more than one olivary signal and more than one CF-induced shift in PF plasticity and thus PF-induced modulation of the PC simple spike rate. These cells may then play a role as generalists with a broader range of state-dependent activation that may contribute to associative learning in the cerebellar cortex.

Beyond the level of dendritic input, morphology could also plausibly influence post-synaptic integration. The physical separation and clustering of dendritic branches might produce different combinations of signaling relationships across dendritic branches at different scales. Extensive work has documented the scales of calcium compartment signaling by distinct patterns of PF, CF, or PF+CF input in slice (Canepari & Vogt, 2008; Midtgaard et al., 1993; Miyakawa et al., 1992; Ouares et al., 2019; Ouares & Canepari, 2020; Rudolph et al., 2015; Santamaria et al., 2011; S. S.-H. Wang, Denk, et al., 2000) and *in silico* (Anwar et al., 2013, 2014; Cirtala & De Schutter, 2024; Zang et al., 2018; Zang & De Schutter, 2019, 2021). However, we do not know how different sub-cellular signaling pathways operate in the awake, intact brain. This led to the third question of my thesis: **Are there distinct spatial scales of sub-cellular dendritic computation *in vivo*?**

Cerebellar evolution and disease

The sense that cerebellar circuits are stereotypical truly penetrates the cerebellar field. Our suggestion, based primarily on observations in the rodent, that distinct dendritic morphologies may

produce non-canonical connectivity and signaling properties thus has numerous ramifications throughout the field. The sense that the cerebellar circuit is highly evolutionarily conserved—that is, also in a stereotyped way—similarly penetrates the field. Yet, we observed that PC morphology diverges significantly in the human relative to the mouse. Thus arose the fourth question of this thesis: **How does the human diverge from the mouse anatomically?** Additionally, preliminary assessment of PCs from non-human primates and other non-primate mammalian species indicates that PC morphological properties are not only diverse within a species but assume highly distinct profiles across species. Even among a clade we could observe substantial variation. This led to the fifth question of this thesis: **How might variable PC morphology produce species-specific functions?**

Increased dendritic complexity and the likely consequences for PF RF sampling and CF multi-innervation have so far been framed as an expansion in the diversity of dendritic computation and therefore the diversity of PC input/output processing. However, it should also be noted that expansion of CF signaling on PC dendrites is not necessarily a net positive for the system. Multi-innervation may be advantageous under certain circumstances, such as to match segregated GC RFs on multi-dendritic PCs, and otherwise disadvantageous. Aberrant CF multi-innervation has been reported in several mouse models of cerebellar disease, such as syndromic autism (Piochon et al., 2014) and spinocerebellar ataxia (Du et al., 2013, 2019). What constitutes the difference between advantageous and disadvantageous CF multi-innervation? To answer this question, we would first need to complement our documentation of normally occurring, putatively advantageous CF multi-innervation with a clarification of aberrant CF signaling in a disease model. The sixth and final question of this thesis is therefore: **How is expanded olivo-cerebellar signaling pathological in autism model mice?**

The origin of the question and development of a morphological framework

The answer to the first question of the thesis (Chapter 2) is the first description of a structure-function relationship that can impact cell-wide computation in Purkinje cells. This finding depended on our simple but critical initial observation: PC dendrite morphology is quite diverse. Our project then depended on the development of a novel framework for categorizing PC morphological type based on the gross structure of the primary dendrite(s). I categorized cells as having either one ("Normative") or multiple primary dendrite compartments ("Split" when compartments arise from one proximally bifurcated dendrite, or "Poly" when multiple dendrites emerge directly from the soma). In retrospect, the Normative label may have been a mistake borne out of our own biased knowledge of the rodent cerebellum. Normative for whom? Indeed, the Normative label accurately describes a significant plurality of cells in mouse. However, when we turned to human cerebellar tissue, and eventually that of other primates, we came to discover that 'Normative' is a notable misnomer. Almost no human PCs are 'Normative'.

In the following chapters, I will present my use of anatomical and physiological methods *in vitro* and *in vivo* to determine that PC morphology is diverse within and across species and impacts CF-PC connectivity and dendritic signaling. In Chapter 2, I demonstrate that multi-branched PC structure is uncommon in mouse but nearly universal in human and can permit non-canonical CF-PC multi-innervation and heterogeneous dendritic calcium signaling. In Chapter 3, I detail how human PCs exceed allometric constraint in size, compartmentalization, and spine structure. Chapters 2 and 3 also collectively find that regional PC demographics, the prevalence of distinct PC morphological sub-types in the population, co-vary with functional rather than anatomical boundaries. In Chapter 4, I show preliminary results that PC morphology is diverse across species

and better predicted by phylogeny than allometry—especially surprising for a brain region classically considered conserved and stereotypical. This provides further support for the hypothesis that PC morphology dictates function and that PC demographics may be differentially recruited for regional or species-specific functional needs. In Chapter 5, I show that 'enhanced' CF-PC signaling is not always beneficial such as in pathological olivo-cerebellar signaling in autism. Finally, in Chapter 6, I demonstrate that molecular factors underlying plasticity and learning operate across different spatial scales. Their contribution to dendritic computation may thus be differentially reshaped by PC dendrite morphology.

CHAPTER 2

CLIMBING FIBER MULTI-INNERVATION OF MOUSE PURKINJE DENDRITES WITH

ARBORIZATION COMMON TO HUMAN

This chapter is a full reprint of: Busch SE and Hansel C. (2023) Climbing fiber multi-innervation of mouse Purkinje dendrites with arborization common to human. *Science*, 381: 420-427. https://doi.org/10.1126/science.adi1024. This work is included with permission from the publisher. An open-access preprint version of the manuscript can be found on *bioRxiv:* https://doi.org/10.1101/2023.03.27.534425

Abstract: Canonically, each Purkinje cell in the adult cerebellum receives only one climbing fiber from the inferior olive. Underlying current theories of cerebellar function is the notion that this highly conserved one-to-one relationship renders Purkinje dendrites into a single computational compartment. However, we discovered that multiple primary dendrites are a near-universal morphological feature in human. Using tract-tracing, immunolabeling, and *in vitro* electrophysiology, we found in mice that ~25% of mature multi-branched cells receive more than one climbing fiber input. Two-photon calcium imaging *in vivo* revealed that separate dendrites can exhibit distinct response properties to sensory stimulation, indicating some multi-branched cells integrate functionally independent climbing fiber receptive fields. These findings indicate that Purkinje cells are morphologically and functionally more diverse than previously thought.

One Sentence Summary: Multi-branched dendrites common in human drive novel input patterns and signal complexity in a mouse Purkinje cell population.

Main Text

Inputs to the cerebellar cortex are integrated by the dendrites of Purkinje cells (PCs), its sole cortical output neuron. Despite their well-characterized position in what is considered a conserved and stereotypical circuit (Apps & Hawkes, 2009), PCs exhibit remarkably diverse dendritic morphology in the rodent (Nedelescu et al., 2018) and it is not known how specific features of dendritic arborization may affect their function.

Human PC morphology remains even more elusive. Studies of human PC morphology – dating back over 120 years to the iconic illustrations of Golgi and Ramón y Cajal (Golgi, 1874; Ramón y Cajal, 1909) – investigate small numbers of cells (Eccles et al., 1967; Kato et al., 1985; Louis et al., 2014). While no quantitative information on frequency and distribution of morphological types is available, it can be observed that human PCs are often 'multi-branched', having either numerous trunks emerging from the soma or a proximal bifurcation of a single trunk. These features produce highly segregated dendritic compartments, raising the question whether this confers functional properties that have gone unreported.

We specifically asked whether the existence of several primary dendrites enables multiple climbing fiber (CF) innervation in the adult cerebellum. During development, the early growth of a primary dendrite provides structural support for the ramification of a 'winner' CF amidst competitive elimination of surplus CFs (Hashimoto et al., 2009; Hashimoto & Kano, 2003; Wilson et al., 2019). Weaker CF inputs fail to translocate to the dendrite, possibly as a result of competitive processes resembling adult bidirectional synaptic plasticity (Bosman et al., 2008; Hansel & Linden, 2000; Ohtsuki & Hirano, 2008; Piochon, Kano, et al., 2016). In PCs where multiple primary dendrites conceivably offer a means to evade competition from other CFs, is the

elimination pressure reduced enough to allow multiple CFs to be maintained? Would multi-innervation provide functionally independent receptive fields to distinct dendritic compartments?

A majority of human, but not murine, PCs have multiple primary dendrites

We used fluorescent calbindin immunolabeling to visualize PCs in post-mortem human tissue (Fig. 3A). Based on proximal primary dendrite structure, which articulates the contours of the entire arbor, we define one standard structural category, *Normative* – one primary dendrite that may have a distant bifurcation (beyond a two somatic diameter threshold of 40μm in mouse and 50-70μm in human), and two multi-branched categories: *Split* – one trunk that bifurcates into multiple primary dendrites proximal to the soma (below the somatic diameter threshold); and *Poly* – multiple trunks emerging directly from the soma (Fig. 3A and Appendix Figure S1; see Appendix 1: Methodology and Statistics). While these categories translate to the mouse (Fig. 3D), we found that mice diverged significantly from humans in that they had fewer Split PCs (35.9 vs. 44.8%) and far fewer Poly PCs (16.6 vs. 51.2%; Fig. 3G and Appendix Figure S2A). Instead, in mice Normative PCs constituted the largest PC category (47.5%) in contrast to humans (4.0%).

We manually marked the distribution of dendritic morphologies in collectively ~8,000 cells across whole, reconstructed parasagittal slices of mid-hemisphere in human and mouse (Fig. 3B,E and Appendix Figure S2B-C). In posterior lobules of human, there is a higher percentage of Poly PCs (53.8 vs. 40.9%) and a lower percentage of Normative PCs (3.5 vs. 6.1%) than in anterior lobules (Fig. 3C and Appendix Figure S2A and table S1). While the total rate is far lower, Poly PCs are relatively more prevalent in posterior lobules of the mouse as well (10.3 vs. 21.2%, Fig. 3F-G and Appendix Figure S2A and table S2).

The broad morphological distributions were consistent across non-pathological human and mouse individuals (Appendix Figure S2B-C and tables S1-2) and did not depend on zonal patterning by zebrin II expression (Cerminara et al., 2015) (Appendix Figure S3). Physical constraints, however, might play a role in the spatial distribution of PC dendrite morphologies by foliar sub-region (Eccles et al., 1967) . Indeed, the multiple dendrites of Split and Poly PCs predominantly ramified in a horizontal orientation (80%; defined by <30° angle deviation from the PC layer) in the sulcus of human folia while this occurred much less frequently in the bank and gyrus (23 and 25%; Appendix Figure S4D). This effect was not present in mouse (Appendix Figure S4C-D). In human PCs – where dendritic size expands strongly (Fig. 3A+D) – the horizontal orientation follows the inward curvature of the sulcus, possibly indicating a developmental response to physical constraints on growth. Because the physiological implications cannot be readily studied in human, we turn to the corresponding mouse cells for further characterization.

Figure 3. Comparative morphology and regional variability in human and mouse cerebellar Purkinje cells. (**A**) Immunolabeling of Purkinje cells in human reveals a range of dendritic morphologies, categorized by primary dendrite geometry as Normative, Split, or Poly. (**B**) Human mid-hemisphere reconstruction demonstrating the spatial distributions of each morphological type. Due to variable preservation of the tissue, some anterior lobules and intervening posterior sublobules had a lower density of labeled PCs. (**C**) Morphology demographics across lobules (n = 3 individuals >86yo, 6,640 cells; see table S1). (**D**) Purkinje cells filled with dye during a patch experiment in the mouse, to scale with human cells, also exhibit Normative, Split, and Poly morphology. (**E-F**) As in (**B-C**), but in mouse. (n = 3 mice >P50, 1,350 cells; see table S2). (**G**) Morphological category distribution counted by lobule (top) in human (n = 20, 21, and 21 lobules) and mouse (n = 30, 30, 29) reveals a consistent increase in the number of Split and Poly PCs in human matching the rates of the whole cell population (bottom). Average lines depict median lobule value. *P < 0.05, **P < 0.01, ***P < 0.001.

Multiple climbing fibers may innervate separate primary dendrites

CF activity causes complex spike firing in Purkinje cells (Eccles et al., 1966; Simpson et al., 1996), which is reciprocally related to simple spike firing (Badura et al., 2013; Simpson et al., 1996) and exerts powerful control over dendritic integration and PF plasticity (Ito et al., 1982; S. S.-H. Wang, Denk, et al., 2000; Lev-Ram et al., 2002; Medina et al., 2002; Coesmans et al., 2004; Piochon, Titley, et al., 2016; Streng et al., 2017; Titley et al., 2019). Though many studies cite the critical importance of one-to-one CF to PC connectivity in cerebellar function – and abnormal connectivity in dysfunction – some work has shown CF multi-innervation in ~15% of PCs in adult rodents (Kano et al., 1997; Nishiyama & Linden, 2004; Piochon et al., 2014).

To test whether multiple CF innervation can be found in mature PCs, we combined a sparse dextran tracer (DA-594) labeling of inferior olivary (IO) neurons (Fig. 4A) with immunolabeling of CF terminal boutons (VGluT2) and PCs (calbindin). Because all CF terminals are marked by VGluT2, but only some will express DA-594, this method allows for the identification of multiple CF inputs from distinct IO neurons onto single Purkinje cells (Hashimoto et al., 2009; Miyazaki & Watanabe, 2011). Fig. 4B shows a Poly PC (P87) that was indeed innervated by two CFs on its separate primary dendrites.

Quantification of CF multi-innervation in mature PCs

We obtained a quantitative measure of CF multi-innervation across the PC population by using whole-cell patch-clamp recordings in murine cerebellar slices (Fig. 4C). We adjusted current intensity and stimulus electrode position in the granule cell layer – sub-adjacent to each patched PC – to identify any ascending CF inputs and their stimulus thresholds. Mono-innervated PCs had a single, discrete EPSC while multi-innervated PCs exhibited two or more discrete EPSC

amplitudes selectively evoked by distinct stimulus intensities (Fig. 4C bottom and Appendix Figure S5A-B). About 15% of all PCs in mature animals (P20-66) received multiple CFs (Fig. 4D). CF competition for survival is complete by P20 (Kano et al., 1997; Hashimoto & Kano, 2003; Hashimoto et al., 2009; Kano et al., 2018). In keeping with this, we did not find an effect of age on the rate of multi-innervation (Appendix Figure S6L).

Combining this technique with fluorescent dye loading and confocal imaging revealed that multi-innervation was largely restricted to PCs with multi-branched structures (23/24 PCs) and occurred in ~25% of cells in this group (1/64 Normative, 15/61 Split, and 8/34 Poly PCs, Fig. 4D). The summed CF EPSC of multi-innervated PCs was larger, on average, than the amplitude of individual CF inputs to mono-innervated PCs. The amplitude of the smaller CF (at -30 to -10mV holding potential) was typically >200pA (Fig. 4E). This indicates that, under physiological membrane potentials, even the weakest of multiple CFs will likely deliver sufficient current to the soma to influence output (Llano et al., 1991). The amplitude of weaker CFs increased with age (Appendix Figure S5M), which may denote a delayed or elongated maturation period of these inputs relative to the completed development of single CF inputs or the more dominant of multiple CFs (Appendix Figure S5N). The relative EPSC amplitude ratio between dominant and smaller CFs varied widely, but smaller CFs most often had >25% the relative amplitude of the dominant CF (Appendix Figure S5O). This ratio differed across foliar sub-areas (Appendix Figure S5P) and correlated with the angle between Poly PC trunks (Appendix Figure S5Q), further emphasizing the relationship between morphology and CF input properties.

Figure 4. Climbing fiber multi-innervation of mature multi-branched Purkinje cells. (**A**) Schematic of tracer (DA-594) injection. (**B**) A Poly PC after immunolabeling for PCs (calbindin) and CF terminals (VGluT2). Tracer label distinguishes CFs with distinct olivary origin on the left and right trunks. (**C**) Scheme of whole-cell patch-clamp in cerebellar slices and CF EPSCs recorded from either a mono- or multi-innervated PC. (**D**) Number of mono- vs. multi-innervated PCs as a combined population (*left*). Categorizing by morphology reveals that effectively all multi-innervation occurs in multi-branched PCs (n = 50 animals, 159 cells). (**E**) Summed multi-CF EPSCs are larger than mono-CF EPSCs (n = 135 and 24 cells). The weaker of multiple CFs typically provides >200pA signals. Holding potential: -10 to -30mV (n = 24 cells). (**F**) Multi-innervated PCs have earlier dendrite bifurcations (n = 135 and 24 cells). (**G**) Among PCs with a bifurcated primary dendrite, multi-innervated cells have a wider distance between compartments (n = 85 and 9 cells). (**H**) Multi-innervated Poly PCs have a wider angle between emerging trunks (n = 26 and 8 cells). Summary points indicate mean ± SEM. *P < 0.05, **P < 0.01, ***P < 0.001.
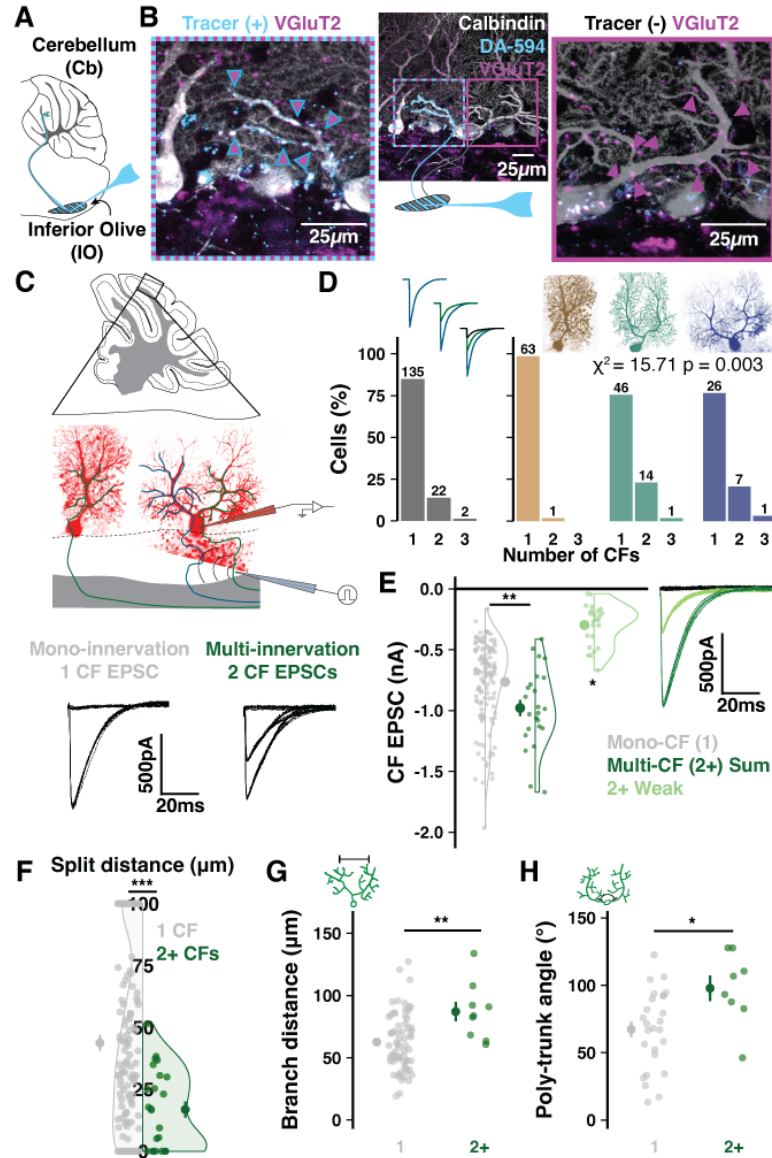
The prevalence of multi-innervation was correlated with proximity of bifurcation and angle of separation between emerging trunks in Split and Poly PCs, respectively (Fig. 4F and H and Appendix Figure S5D-F). Multi-CF PCs also had wider dendritic arbors in the parasagittal plane

(Fig 2G and Appendix Figure S5G), while not differing in the angle of bifurcation (Appendix Figure S2E) or soma size (Appendix Figure S5H).

CF multi-innervation was present across cerebellar regions and foliar sub-areas (Appendix Figure S6A-I). Posterior lobules had a higher frequency of multi-innervation (Appendix Figure S6I), possibly due to increased prevalence of Poly-PCs (Appendix Figure S6H and J), matching our finding in immunolabeled tissue (Fig. 3F-G). We did not observe a preferential rate of multi-innervation within the sulcus as a general pattern (but see (Nishiyama & Linden, 2004) for more detailed analysis within vermis).

CF multi-innervation produces heterogeneous Ca^{2+} signals across dendrites *in vivo*

Do multiple converging CFs provide functionally distinct inputs to a single Purkinje cell? How would this impact dendritic signaling *in vivo*? To answer this, we examined whether CF multi-innervation produces heterogeneous Ca^{2+} signals across separate dendritic branches. CF input triggers massive Ca^{2+} entry into PC dendrites via voltage-gated Ca^{2+} channels (Schmolesky et al., 2002), NMDA receptors (Piochon et al., 2010), and release from internal stores (Takechi et al., 1998), which can be locally modulated by ion conductance plasticity (Ohtsuki et al., 2012; Schmolesky et al., 2002) and interneuron inhibition (Callaway et al., 1995; Rowan et al., 2018). These mechanisms contribute to the calcium events that we monitor here *in vivo* and to their modulation (Kitamura & Häusser, 2011; Roome & Kuhn, 2018; Zang et al., 2018).
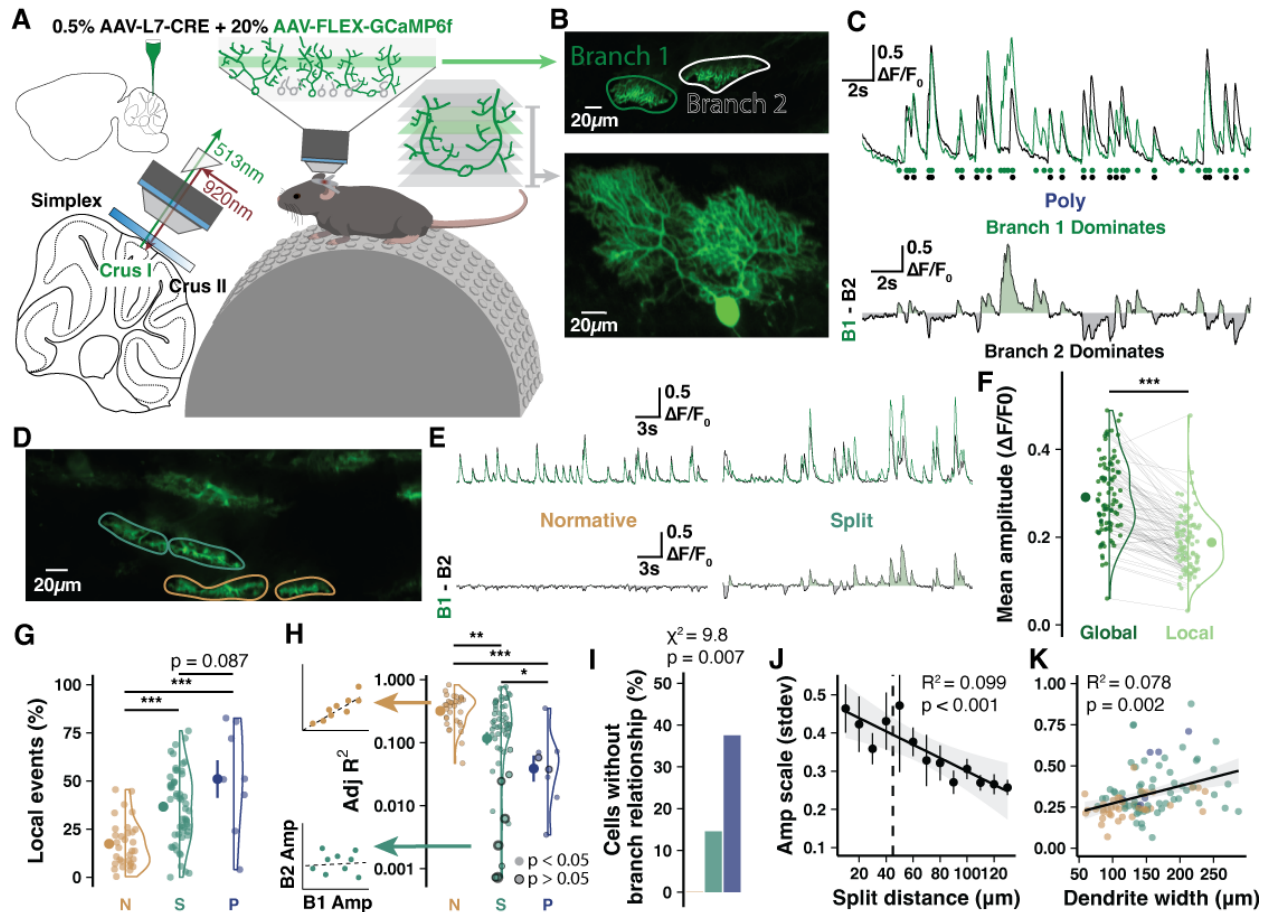
Figure 5. Two-photon imaging *in vivo* reveals Ca^{2+} signal heterogeneity across Purkinje cell dendrites. (**A**) Schematic of experimental preparation. (**B**) Example imaging plane and 3D-reconstruction of a Poly PC. (**C**) Spontaneous signal and deconvolved events (circles) by branch with difference trace below demonstrates heterogeneous global event amplitude scale and branch-specific events. (**D-F**) Another recording from a Normative and Split PC highlights homogeneous vs. heterogeneous signaling. (**F**) Local events are moderately smaller than global events (n = 15 animals, 95 cells). (**G**) Branch-specific local events as a percentage of total events in each cell by morphology (n = 15 animals; n = 32, 55, and 8 cells). (**H**) Linear regressions on branch cross-correlation quantifies branch similarity (*left*). Model fit R^2 values (*right*) reveals that cells with low branch signal similarity are predominantly Split and Poly PCs (n = 32, 55, and 8 cells). Bordered points indicate non-significant covariance. (**I**) Cells lacking detectable relationship using regression on inter-branch amplitudes are all Split or Poly PCs. (**J-K**) Interbranch amplitude variation by split distance (n = 105 cells) and total parasagittal width of the dendrites (n = 109 cells). Summary points indicate mean ± SEM. *P < 0.05, **P < 0.01, ***P < 0.001.

We obtained a sparse PC expression of the Ca^{2+} indicator GCaMP6f and used two-photon imaging of mice in a state of quiet wakefulness (awake; no detected motion) to record non-evoked

'spontaneous' Ca^{2+} signals from primary dendrite compartments in small populations of <10 cells (Fig. 5A-B; see Appendix 1: Methodology and Statistics). Volumetric scans visualized cellular morphology and permitted manual tracing of compartment ROIs (Fig. 5B,D and Fig. 6A and Fig. 7A) so fluorescence signals were extracted and deconvolved separately to contrast event amplitude and frequency across branches (Fig. 5C-E). In this configuration, non-evoked Ca^{2+} signals beyond the micro-compartment scale are almost entirely CF-dependent (Gaffield et al., 2019; Najafi et al., 2014b) and Ca^{2+} event amplitude reflects the number of spikes in the presynaptic CF burst (Roh et al., 2020). This is confirmed by our observed ~1.2Hz spontaneous Ca^{2+} event frequency (Appendix Figure S7D) that matches an expected CF input frequency moderately greater than 1Hz (Simpson et al., 1996).

We first identified local Ca^{2+} peaks detected in only one branch of each cell (Fig. 5C, F-G and Movie 1), which were moderately smaller than globally expressed events (Fig. 5F). We also compared the inter-event cross-correlation of Ca^{2+} events across branches, for which the fit and significance of a linear regression describes the inter-branch covariation (Fig. 5H-I).

Most PCs had homogenous Ca^{2+} signals with linear inter-event covariance relationships across branches (Adj R^2 > 0.1) and low numbers of local events (Fig. 5G-H). However, some PCs exhibited Ca^{2+} signal heterogeneity characterized by a linear regression of inter-event covariation with low Adj R^2 < 0.1 that was not significant (0, 15, and 38% of Normative, Split, and Poly PCs, respectively; Fig. 5H-I) or a higher ratio of local events (17.4, 36.6, and 51%; Fig. 5G). High variability of inter-event amplitude scale between branches, another measure of heterogeneity, correlated with the bifurcation distance and total parasagittal dendritic width (Fig. 5J-K and Appendix Figure S7C). This further links heterogeneity to underlying morphological contours defined by primary dendrite geometry. Confirming that local events are the product of additional

CF input, PCs with high local event rates had higher mean (Appendix Figure S7G-H and P) and maximum total event rates (Appendix Figure S7L-M), producing a larger dynamic range (Appendix Figure S7N-O). Our observations link the occurrence of local CF events to underlying morphological contours defined by primary dendrite geometry, although other factors, such as inhibition by molecular layer interneurons (MLIs), are likely to contribute as well (Callaway et al., 1995; Najafi et al., 2014b).

Climbing fibers convey distinct whisker receptive fields to separate primary dendrites

To identify CF receptive fields (RFs) and their localization on PC dendrites, we took advantage of the discrete organization of whiskers as a sensory input array (Bosman et al., 2010; Ju et al., 2019). We anaesthetized animals to stimulate untrimmed individual whiskers at 2Hz for 50s periods while recording Ca^{2+} activity of PCs in medial Crus I (Fig. 6A and Appendix Figure S8A; see Appendix 1: Methodology and Statistics). Most PCs had only global events identically represented across primary dendrites (Appendix Figure S8A2-A3). However, some PCs had high numbers of local events in response windows during the stimulus period (Fig. 6B-C and Appendix Figure S8A4) that varied in magnitude between distinct whisker stimuli (Fig. 6D), indicating RF selectivity.
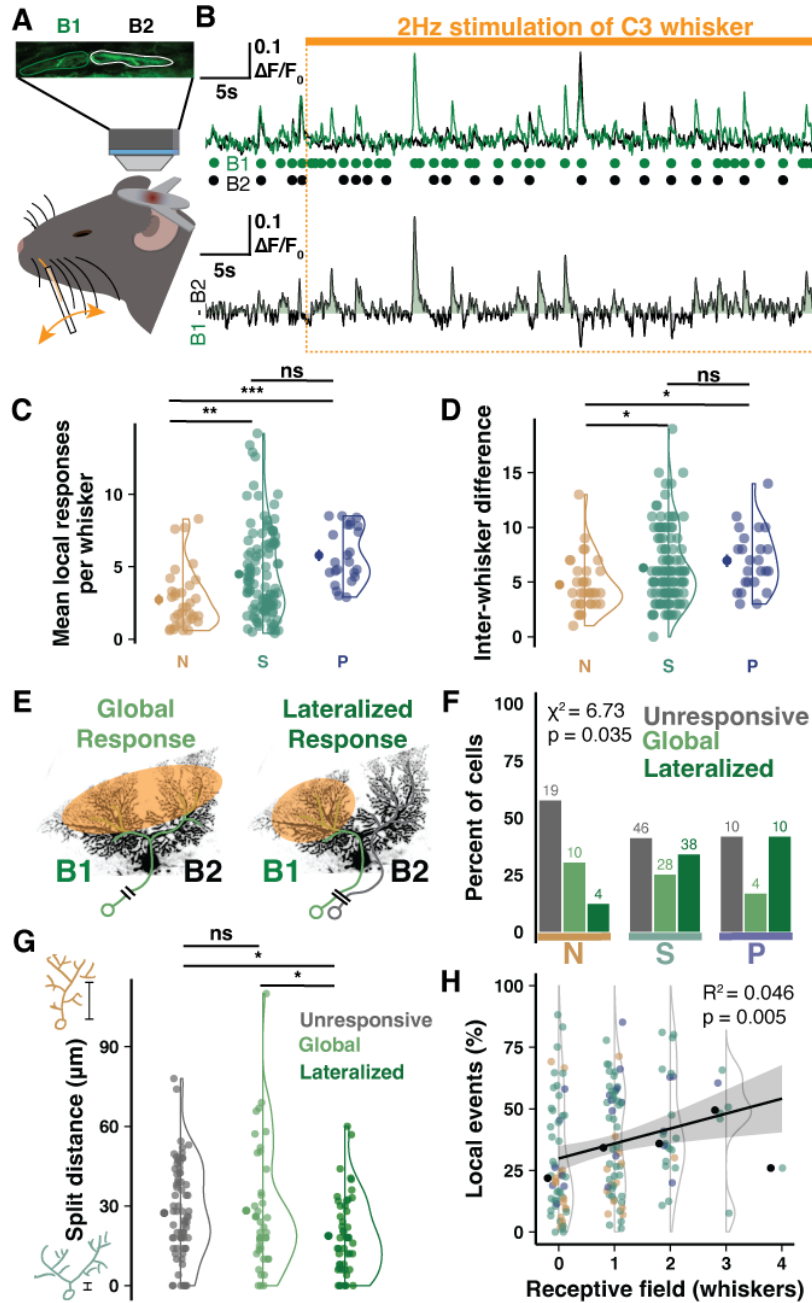
Figure 6. Branch-specific whisker receptive fields produced by climbing fiber multi-innervation of multi-branched Purkinje cells. (**A**) Schematic of the imaging configuration and whisker stimulation under anesthesia. (**B**) Sample traces and deconvolved events by branch during 50s whisker stimulation. Each whisker is tested twice; data from both periods are combined. Responsiveness of one branch and not the other drives an enhanced local event rate in B1 during the stimulus period. (**C**) Mean number of local branch events in response windows during stimulus periods of each tested whisker (n = 13 animals P95-120, n = 33, 112, and 24 cells). (**D**) Difference in local event number between whiskers eliciting maximum and minimum local responses (n = 33, 112, and 24 cells). (**E**) Schematic of global vs. lateralized responses. (**F**) Percentage of PCs by dendritic response profile and morphological category. Fewer Normative PCs have lateralized responses than multi-branched PCs (n = 169 cells). (**G**) Cells with lateralized responses have shorter split distances (n = 75, 42, and 52 cells). (**H**) Cells with more spontaneous local events respond to a higher number of whiskers (n = 151 cells). Summary points indicate mean ± SEM. *P < 0.05, **P < 0.01, ***P < 0.001.

Anaesthetized activity is sparsened, so responses were determined using the z-scored response probability during the experimentally bootstrapped high-frequency stimulus (Appendix Figure

S8B-D). Comparing the z-scored response probability of each dendrite, we observed a 'lateralized' response in some PCs, in which local events of one branch constituted a whisker response not observed in the other branch (Fig. 6E-F). Nearly all lateralized responses arose in Split and Poly PCs (48/52 cells, 92%; Fig. 6F) and in PCs with more signal heterogeneity, which map to Split and Poly PCs as in previous experiments (Appendix Figure S8F). Furthermore, PCs with lateralized responses had more proximal dendrite bifurcations than PCs with only global responses (18.73 μm vs. 28.24 μm; Fig. 6G). Importantly, PCs with higher rates of branch-specific spontaneous events also exhibited responses to more whiskers, denoting an integration of more whiskers into their RFs (Fig. 6H). This supports the hypothesis that heterogeneous signals represent distinct, converging RFs such that heterogenous PCs are sampling more upstream RFs carried by functionally independent CF inputs.

Climbing fiber induced branch-specific representations of stimulus modality in awake mice

While anesthesia provided excellent control and precision for single whisker stimulation, even subanesthetic ketamine alters network activity (Cichon et al., 2022). To confirm that PC primary dendrites can differentially represent CF RFs in a more naturalistic state, we exposed awake animals to uni- and multisensory stimuli (Fig. 7A). As a major hub for sensory integration during associative learning, PC dendrites are an important model for how converging input profiles are represented across dendrites. The amplitude and duration of CF-induced dendritic Ca^{2+} spikes depend on stimulus strength (Gaffield et al., 2019; Najafi et al., 2014a), which is reflected in CF burst behavior (Roh et al., 2020), and also on synaptic connectivity and weight of the CF input itself (Simmons et al., 2022).
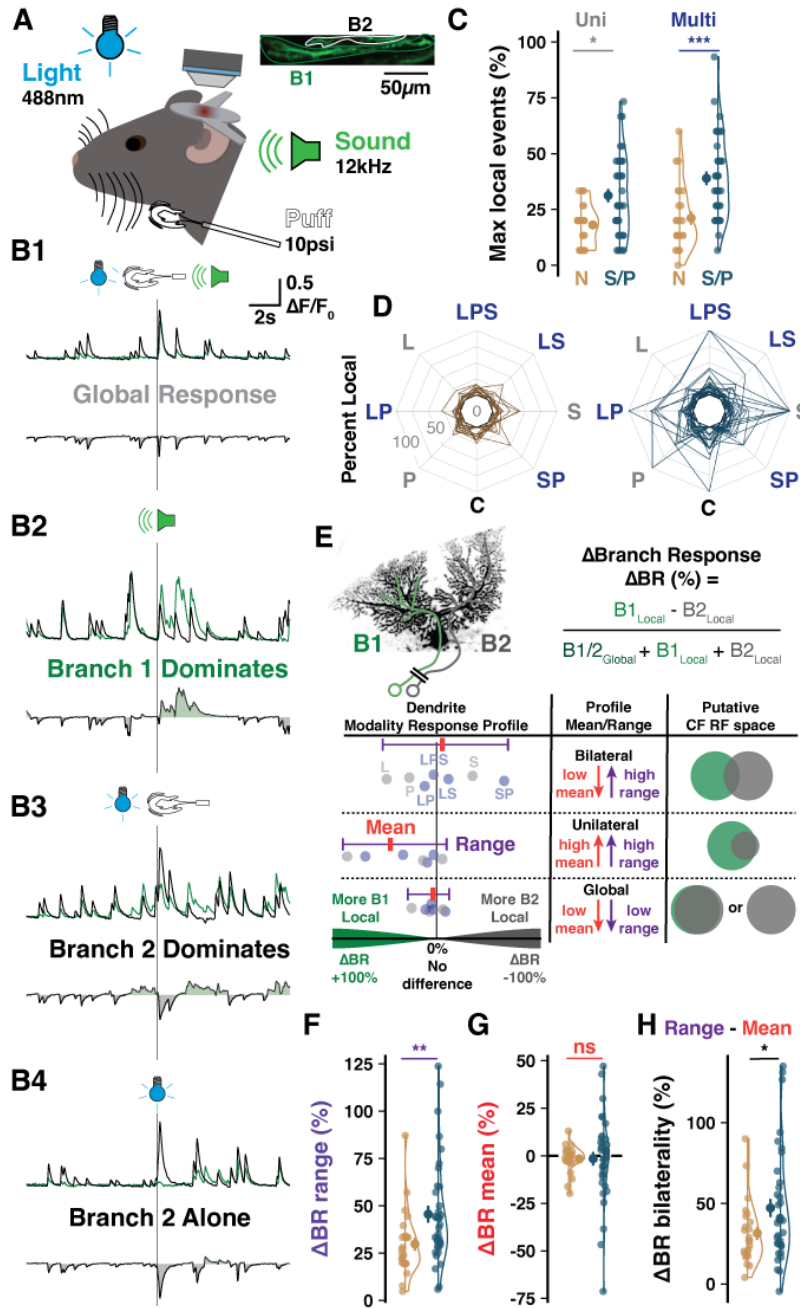
Figure 7. Branch-specific multisensory receptive fields. (**A**) Scheme of imaging and sensory stimulation of awake animals. (**B**) Sample traces showing combinations of inter-branch responses to different stimulus modalities. (**C**) The maximum number of local events observed for a stimulus of any category in Normative vs Split and Poly (S/P) PCs (here and below: n = 12 animals, n = 24 and 38 cells). (**D**) The percentage of responses having a local component, regardless of branch identity, across control (C), uni-, or multisensory trials. Lines connect values for each PC. (**E**) Calculation of ΔBranch Response (ΔBR, *top*) between the stimulus types most favoring opposite branches. ΔBR values of each modality are calculated for each cell (*bottom, schematic points*) to map the ΔBR profile across stimuli and identify the mean and range. (**F**) The range is more pronounced in S/P cells (n = 24, 38). (**G**) No group difference in ΔBR mean (n = 24, 38). (**H**) Response profile bilaterality is the subtraction of ΔBR mean from the range. S/P PCs exhibit more bilaterality due to high ranges and low means (n = 24, 38). Summary points indicate mean ± SEM. *P < 0.05, **P < 0.01, ***P < 0.001.

We stimulated awake animals with light (488nm, ipsilateral), sound (12kHz tone, bilateral), and peri-oral air puff (10psi, ipsilateral) stimuli either alone or in multi-modal combinations while recording response properties in PC primary dendrites. Sensory evoked events – more than

spontaneous – typically produced a global dendritic signal with consistent inter-trial amplitude ratio between branches (Fig. 7B1). Yet, we also observed complex sensory-evoked bursts of CF input with heterogeneous amplitudes between branches (Fig. 7B2-3) and either branch-specific responses alone (Fig. 7B4) or combined with a global response (Fig. 7B2). While PCs with multiple primary dendrites (Split and Poly, or S/P) had similar total response probabilities as Normative PCs (Appendix Figure S9C), a larger share of responses were branch-specific in S/P PCs across stimulus modalities (Fig. 7C-D and Appendix Figure S9A-B). To assess the relationship between uni- and multi-modal stimuli, we identified the maximum branch-specific responses to stimuli of each category (Appendix Figure S9D), obtained the difference between uni- and multi-sensory maxima, and found an enhanced rate of local responses in S/P but not Normative PCs (Appendix Figure S9F). This revealed that multisensory stimuli could enhance the differential representation of CF RFs across primary dendrites in putatively multi-innervated PCs while failing to influence mono-innervated Normative PCs.

While the previous analyses were blind to branch identity, we next asked how much the differential representation of each stimulus could favor one branch over the other (Appendix Figure S9E). We generated a ΔBranch Response (ΔBR) index for each stimulus modality by calculating the difference in branch-specific, local responses as a fraction of total responses (Fig. 7E, *top*). Absolute ΔBR indicates the reliability of local responses on either branch while the sign of the ΔBR indicates which branch over-represented the modality. This allowed us to generate a profile of branch-specific representation across all stimulus modalities, which could be quantified by the ΔBR mean and range for each cell (Fig. 7E, *bottom*). In this way, PCs could be distinguished as having one of three classes of multisensory response profile: *global*, with identical representation across branches in all cases; *unilateral*, with one branch exhibiting a larger RF

representation than the other; and *bilateral*, with both branches capable of differentially representing unique stimulus modalities.

On average, S/P cells had a wider range, denoting branch-specific (e.g., unilateral or bilateral) representations that were more distinct across modalities (Fig. 7F and Appendix Figure S9G-I). Cells for which only one branch exhibits local responses – unilateral – would have both a large ΔBR range but also a ΔBR mean that deviates from zero to favor that branch. To better characterize whether some PCs had bilateral representation profiles, we calculated the bilaterality of the RF profile by subtracting the ΔBR mean from the range. The local responses of S/P cells, more than Normative, produced RF profiles wherein a larger percentage of local signaling produced bilateral representations across sensory modalities (Fig. 7H and Appendix Figure S9G-H and K). Collectively, this shows that PCs with multiple primary dendrites can differentially represent RFs of distinct CF inputs across their separate dendrites in the awake, mature mouse (for a summary of heterogeneous signaling observed in our two-photon recordings across the three dendrite morphologies in mouse PCs, see Appendix Figure S10).

Discussion

We found that non-canonical CF multi-innervation of PCs does occur in the mature murine cerebellum and is dependent on primary dendrite morphology. Nearly all observed multi-innervation occurred in neurons with multiple primary dendrites. Based on a quantitative categorization of >6,000 PCs from three human brains, we report that this type of PC dendritic structure is predominant in the human cerebellum. In contrast, we detected that only a minority of murine PCs fall into the Split or Poly category. Within these morphological groups, about 25% of PCs were innervated by two or more CFs in the mouse.

Our two-photon recordings suggest that most multi-innervated PCs have the capacity for branch-specific CF signaling and have distinct CF RFs. Our data do not allow us to conclude that the same results would be found in human PCs if such recordings were possible. However, they do describe a new motif in PC dendritic compartmentalization: separate dendritic subfields with their own assigned CF inputs may emerge when early branching forms a multi-branched architecture. Variable CF burst frequency and modulation of CF input amplitude by MLIs may further contribute to compartmentalization (Callaway et al., 1995; Najafi et al., 2014b).

CFs provide instructive signals in cerebellar function and plasticity (Simpson et al., 1996) by encoding signals related to error (Ito et al., 1982; Yang & Lisberger, 2014), sensory omission (Ohmae & Medina, 2015), as well as reward or reward-prediction (Heffley & Hull, 2019; Kostadinov et al., 2019). Our findings constitute a substantial shift from the currently held belief that one CF innervates each PC. Instead, our observations suggest that one CF innervates each primary dendrite.

The consequences for dendritic integration and, ultimately, the activation of target cells in the cerebellar nuclei (Person & Raman, 2012) are potentially multifold. Here, we discuss those that

immediately result from geometric considerations. Multi-branched structure often increases dendritic length in the sagittal plane (Fig. 5K), in some cases even opening a cleft between compartments (see Figs. 3A+D, 5B, 6E, S1B-C, S4B). This configuration inevitably leads to a wider physical gap between innervating PF bundles and thus to a potential functional separation of the contextual information they provide (Nguyen et al., 2023; Wilms & Häusser, 2015). It is therefore conceivable that PCs drive spike output from a multitude of contextual input combinations that expand with increased dendrite size and complexity. Multiple CF innervation that – as we describe here – occurs at an elevated rate in multi-branched PCs may serve several critical purposes. First, it may enhance PC function as a supervised associative learning perceptron that optimizes synaptic weights (Brunel et al., 2004) by providing RF-matched CF inputs – and thus relevant error / instructive signals – to the different PF inputs that convey specific contextual information (Appendix Figure S11A). In this way, the perceptron orchestrates synaptic weight optimization based on compartmentalized rather than all-dendritic instructive signals. Thus, in receiving multiple CF inputs, some PCs are permitted to fully capitalize on diverse context representations surveyed by their multi-branched architecture. Second, multiple CF innervation may enable more complex PC computations, such as multiplexing and conveying input from a wider array of sensory modalities (Appendix Figure S11B). In this scenario, individual multi-branched PCs may pair different contexts presented by their PF inputs with instructive information collected from a multimodal environment.

In both the human and mouse cerebellum, multi-branched PCs are more prevalent in the posterior cerebellar hemisphere, a region linked to cognitive and affective roles (Stoodley & Schmahmann, 2010; Badura et al., 2018; LeBel et al., 2021). Whether or not the multi-branched

architecture enables such complex functions through the gained computational power that is postulated here needs to be investigated in future studies.

On the other hand, excessive CF-PC strength resulting from disrupted synaptic pruning and ectopic innervation of distal PC dendrites is linked to pathological dysfunction in autism model mice (Piochon et al., 2014; Simmons et al., 2022) and in mouse and human essential tremor (Pan et al., 2020). The preferential targeting of distinct primary dendrites by multiple CFs (Fig. 4B) may bring computational advantages, while avoiding disruptive enhancement of CF inputs to individual dendritic compartments.

CHAPTER 3

NON-ALLOMETRIC EXPANSION AND ENHANCED COMPARTMENTALIZATION OF

PURKINJE CELL DENDRITES IN THE HUMAN CEREBELLUM

This chapter is a full reprint of: Busch SE and Hansel C. Non-allometric expansion and enhanced

compartmentalization of Purkinje cell dendrites in the human cerebellum. It has been under peer

review at Cell Reports since 09/13/2024. An open-access preprint version of the manuscript can

be found on *bioRxiv*: https://doi.org/10.1101/2024.09.09.612113

Abstract

Purkinje cell (PC) dendrites are optimized to integrate the vast cerebellar input array and drive the

sole cortical output. Classically, PCs are stereotypical computational units. Yet, mouse PCs are

morphologically diverse and those with multi-dendritic structure can receive non-canonical

climbing fiber (CF) multi-innervation that confers independent compartment-specific signaling.

This morphological motif is universal among human PCs, but their morphology is otherwise

uncharacterized. Do human PCs exceed allometry to achieve enhanced integrative capacities

relative to mouse? To answer this, we used comparative histology in human and mouse to analyze

cellular morphology, parallel fiber (PF) and CF input arrangement, and regional PC demographics.

Quantitatively and qualitatively distinct, human PCs: are substantially larger than predicted by

cortical thickness, have increased spine density and size, commonly host multiple CFs, and exhibit

previously unreported 'spine clusters'. They harness a horizontally oriented multi-dendritic motif

to multiplex broad PF/CF arrays, which may subserve computations requiring multi-modal

association.

Highlights

- Human PC size and compartmentalization as a multidendritic motif exceeds allometry

- Spine structure, type may underlie human adaptation to size, associative complexity

- Peripherin CF labeling reveals non-canonical multi-innervation is common in human

- PC demography covaries with functional regions and exhibits patchy local clustering

Introduction

"In our parks are there any trees more elegant and luxurious than the Purkinje cell from the cerebellum. . .?"
-*Santiago Ramón y Cajal* (Ramón y Cajal, 1917)

As the cerebellum optimizes motor and non-motor behavior, vast information arrays representing sensory, internal, and cognitive states arrive in the cerebellar cortex from across the entire brain and undergo a complex integration. Being the sole cortical output, Purkinje cells (PCs) reside at the core of cerebellar function. The dendritic arbor of each PC is the target of thousands of granule cell parallel fiber (PF) axons, which deliver an expansion recoding of mossy fiber contextual input (Albus, 1971; Marr, 1969), and prediction-error signals carried by one—*or several*—climbing fiber (CF) axons from the inferior olive (Busch & Hansel, 2023; Ito & Kano, 1982). PCs are thus adapted to receive the most numerous input array on one of the largest dendritic arbors of the central nervous system.

Yet, PC dendrites are often considered a single, simple computational unit. Cerebellar anatomy and function is most often characterized in such a way that PC output represents a summation of a vast, unsorted PF array modulating the simple spike rate (Herzfeld et al., 2015; Jörntell & Ekerot, 2002) and a single CF inducing complex spikes (Eccles et al., 1966) that reciprocally influence simple spikes (Badura et al., 2013; Simpson et al., 1996). These properties underlie the

computational description of PCs as perceptrons matching (CF) error signals to adjust coincident (PF) contextual input (Brunel et al., 2004). This echoes most descriptions of PC dendritic arborization as space-filling tertiary branches emerging from a singular, core primary dendrite (Berry & Bradley, 1976; X. R. Chen et al., 2013; Fujishima et al., 2012; Sotelo & Dusart, 2009; Tanaka, 2015), as modeled and described in guinea pigs (De Schutter & Bower, 1994; Llinás & Sugimori, 1980; Rapp et al., 1994), rats (Masoli et al., 2015; Shelton, 1985; Zang et al., 2018), and mice (Masoli et al., 2024).

Challenging this perspective, recent studies show that rodent PC morphology is heterogeneous (Busch & Hansel, 2023; Kaneko et al., 2011; Nedelescu et al., 2018) and physiological excitability is heterogeneous across sub-branches (Cirtala & De Schutter, 2024; Midtgaard, 1995; Ohtsuki, 2020; Ohtsuki et al., 2012; Roome & Kuhn, 2018; Zang et al., 2018; Zang & De Schutter, 2021). Dendritic compartments can undergo independent plasticity *in vitro* (Ohtsuki et al., 2012) and recent work demonstrated *in vivo* that intrinsic and synaptic plasticity mechanisms operate on distinct, compartment-level spatial scales to tune dendritic signaling and gate its impact on axosomatic output (T.-F. Lin et al., 2024). Furthermore, CF multi-innervation in adult mice— revising the prevailing view that mono-innervation is universal—correlates with primary dendrite morphology to produce independent signaling across compartments *in vivo* (Busch & Hansel, 2023). These findings come largely from the use of the rodent cerebellum as a model system. Human PCs are far more enigmatic; very little is known about the nature of their dendrite morphology, input arrangement, or physiology.

Since their iconic illustration by Camillo Golgi (Golgi, 1874) and Santiago Ramón y Cajal (Ramón y Cajal, 1909), human PC dendrites have only been analyzed occasionally and in small numbers (Eccles et al., 1967; Kato et al., 1985; Louis et al., 2014). Their morphology thus eluded

systematic quantification until our recent comparative analysis of thousands of cells using a new framework for morphological categorization in human and mouse (Busch & Hansel, 2023). We defined PCs as having either one ("Normative") or multiple primary dendrite compartments ("Split" when compartments arise from one proximally bifurcated dendrite, or "Poly" when multiple dendrites emerge directly from the soma). This approach revealed that humans have almost universally multi-dendritic PCs with half being Poly, whereas half of mouse PCs are Normative and <20% are Poly. A quarter of multi-dendritic PCs received multiple functionally distinct CFs while Normative cells did not, indicating a link between primary dendrite morphology and cellular physiology in mice. Human PC physiology, on the other hand, remains largely inaccessible, but recent work indicates the value of a comparative approach with the experimentally accessible rodent (Masoli et al., 2024). While these studies represent significant steps forward in our understanding of human cerebellar anatomy and function, we are still limited to broad or incomplete data and know nothing about the arrangement of input on human PCs.

Here, we provide a comprehensive quantification and comparative analysis of human PC morphology, excitatory input arrangement, and regional distribution. Our reconstructions reveal that—with dendritic lengths of 6-7cm—Purkinje cells far exceed pyramidal cells as the largest neuron in the human brain. They also exceed allometric scaling relative to mouse; they are more compartmentalized and ramify horizontally to produce an expanded multi-dendrite structural motif. We hypothesized that this motif would permit more input multiplexing and association. In support of human-specific expansions of PF input association and local amplification, we found that human cells have increased spine size (~0.36 vs 0.29μm diameter) and density (6.9 vs 4.9 spines/μm)—receiving upwards of 1 million inputs compared with 30-40,000 in mouse—and host a previously unreported 'spine cluster' class not found in mouse. Rejecting the textbook wisdom,

our co-labeling of PCs and CFs—the first in adult human—reveals that non-canonical CF multi-innervation is present and likely more common than in mouse. The regional prevalence of multi-dendrite motifs among PC populations covaries with human functional boundaries and exhibits sub-regional patches of clustered morphologies, indicating that enhanced input multiplexing of multi-dendritic PCs may subserve complex multi-modal association and learning.

Results

Human PCs are not an allometrically scaled mouse PC

We used fluorescent calbindin immunohistochemistry in fixed, unembalmed post-mortem cerebellar tissue to achieve specific and complete labeling of human PCs for cellular reconstruction (Fig. 8A; Appendix 1: Methodology and Statistics). Calbindin density in mouse tissue precludes individual cell separation, so we acheived sparse labeling via viral expression of Cre-dependent GCaMP6f (Fig. 8B; Appendix 1: Methodology and Statistics). High resolution confocal scans permitted manual reconstruction and analysis of dendritic morphology (n = 5,5 cells; Appendix Figure S12). Human PCs were selected for completeness of the arbor but minor truncation (approximately <5%) was unavoidable.

Human PCs were substantially (~11x) longer than in mouse, more than was previously appreciated (Y. Gao et al., 2011; Joo et al., 2014; Kaneko et al., 2011; Louis et al., 2014; Masoli et al., 2024; Mavroudis et al., 2017, 2022; Ruela et al., 1980; Takeo et al., 2021) (Fig. 8C), having total dendritic lengths of 63,645±4572μm and 6,004±831um, respectively (Fig. 8D). Human PCs had 3.9x the number of total and terminal branch segments (2,750±247 vs 707±118 and 1,377±125 vs 355±59; Fig. 8E and Appendix Figure S13A), which were produced by branching that reached nearly double the maximum and average branch order (50±5.4 vs 28±5.3 and 25±2.5 vs 14±2.6;

Fig. 8F and Appendix Figure S13B). Despite considerable morphological variation, a trend emerged wherein human primary dendrites commonly ramified parallel with the PC layer and bore numerous, often 7-8 (Appendix Figure S13C), compartments that projected vertically toward the pial surface. This alignment rendered their arbor ~4.5x wider than in mouse (644±126μm vs 143±31μm; Fig. 8G), while their molecular layer thickness—a crucial allometric variable— defined the maximal arbor height only 2.3x taller (366±58μm vs 158±22μm; Fig. 8H). Thus, human PCs attained a horizontal dimensionality with 79±42% greater width than height while mouse PCs had 6.3±31% greater height than width (Fig. 8I). Horizontal orientation was not limited to the primary dendrites. Across branching orders and somatic distances, human branches ramified at more horizontal eccentricities than in mouse (~37±24° vs 45±24°; Fig. 8J). Both human and mouse dendrite eccentricities turned upward with increased distance from the soma (~29±23°, 39±24°,42±23° among branches in proximal, intermediate, and distal compartments vs 41±24°, 43±25°, and 51±23°; Fig. 8J), a trend conserved across cells (Appendix Figure S13D).

Emerging from a somatic compartment that is 2x the diameter (7.7x the volume) of mouse (32.8±3.07μm vs 16.5±0.78μm; Appendix Figure S13E), human primary dendrites were 2.1x thicker (6.49±2.43μm vs 3.12±1.17μm; Fig. 8K). Human dendrites narrow nearly ten-fold as they branch (Fig. 8L) such that the spiny dendrites of both species converge on an apparently conserved thickness (~0.6-1μm; Fig. 8M and Appendix Figure S13F). As a result, most branching orders have only ~15% the diameter of the primary dendrite in human compared with ~25% in mouse (Fig. 8N). Relatedly, 95% of human dendritic length is devoted to thin, spiny dendrites with <1.3μm diameter (the log-normal mean + 1SD of dendrite diameter across species) while that figure is 89% in the mouse (Fig. 8O).

Both species shared patterns of near-symmetric fractal branching over similar relative orders (17/50, 34% vs 10/28, 36%; Appendix Figure S13G) and evenly distributed length (Appendix Figure S13H). Individual branch segments were 2.3x longer on average in human and varied more in their length (24.53±18.78μm vs 9.23±5.7μm; Fig. 8P). The species difference was even greater (3x) among terminal dendritic segments (33.14±19.59μm vs 10.9±5.81μm; Appendix Figure S13J). Also reflecting more heterogeneity in the human arbor, the rate of branch emergence in human peaked at precisely half the dendritic height while mouse PC branch segments emerged at a constant rate through roughly the middle 60% of their arbor (Appendix Figure S13J). This pattern was also observed in the distributions of relative total dendritic length (Fig. 8Q-R) and branch number (Appendix Figure S13L-M) across Sholl radii.
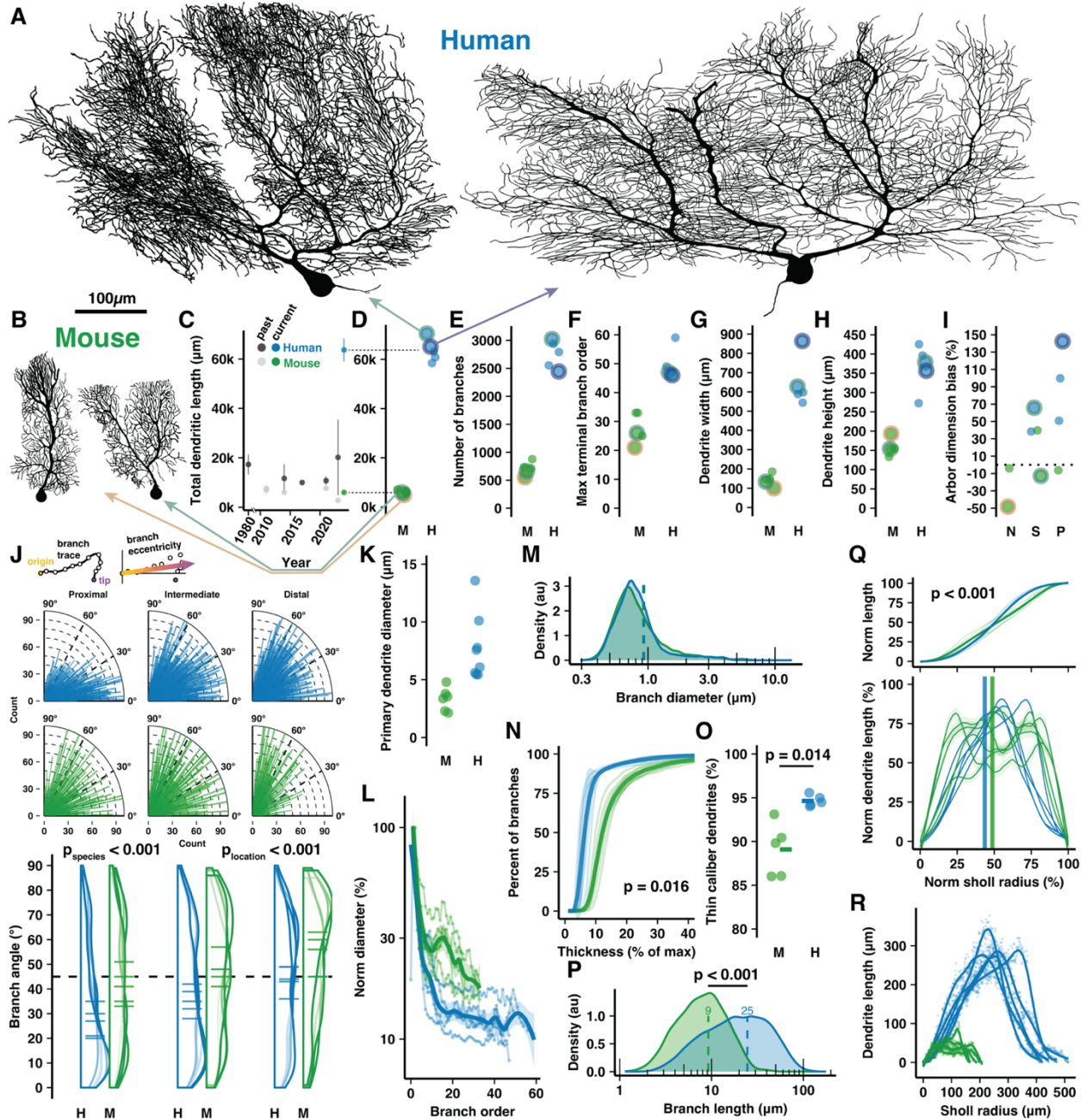
Figure 8. Cell reconstructions reveal expanded dendritic size and compartmentalization of human PCs. A-B) Manually reconstructed human and mouse PCs (same scale). **C)** Meta-analysis of historical measures of mean±sd total dendritic length in human (dark grey) and mouse (light grey) compared with that reported here (blue/green; mean±sd of values in D). **D-I)** Total dendritic length, number of branches, maximum terminal branch order, maximum width and height of the dendritic arbor, and numerical index for the shape of the dendritic area by morphological category (N—Normative, S—Split, P—Poly; positive values indicate arbors with greater width than height; n = 5,5 cells, 3,2 individuals; cells pictured in A-B are highlighted). **J)** Schematic calulation of branch segment eccentricity with data on quarter-radial plots (top) and as distributions with cell

averages (bottom) by categories of distance from the soma in human and mouse (ANOVA, Tukey's HSD post-hoc; n = 2749,7595,2541 and 877,1247,1056 branches). **K)** Maximum diameter of the primary dendrite (or dendrites for Poly PCs). **L)** Dendrite diameter normalized to the thickest primary dendrite by order. **M)** Distribution of all branch diameters. **N)** Cumulative distribution of branch segments by their diameter relative to the thickest dendrite. (Kolmogorov-Smirnov test; n = 5,5 cells). **O)** Percent of the total dendritic length classified as thin caliber using a 1.31um threshold (log-normal mean + 1sd of all branch thicknesses across species (Student's t-test; n = 5,5 cells). **P)** Branch segment lengths (Mann-Whitney U test; n = 12885,3180 branches). **Q)** Cumulative (top) and non-cumulative (bottom) normalized distributions of dendritic length by centrifugal Sholl distance from the soma (Kolmogorov-Smirnov test, n = 5,5 cells). **R)** Total dendritic length at each 1μm Sholl radius without normalization.

Human-specific adaptations for size and associative complexity in spine structure and number

As predominantly the sites of excitatory PF input and plasticity, dendritic spines and their morphology contribute to PC physiology. To assess this input pathway, we manually reconstructed ~4,000 spines from high resolution confocal images of spiny dendrite segments across molecular layer compartments (Fig. 9A). Human PCs exhibited higher spine density than mouse PCs (6.81±0.77 vs 5.1±0.61spines/μm; Fig. 9B). Both species had higher densities on distal dendrites (6.32±0.62 to 7.1±0.77/μm in proximal vs distal compartments of human; 4.55±0.55 to 5.48±0.35/μm in mouse; Fig. 9C), suggesting that increased PF input density on distal compartments may be a conserved mammalian trait (Kano et al., 2018). Combining measures of total dendritic length and spine density, we can extrapolate that a mouse PC has roughly 30-40,000 spines, consistent with recent findings (Nguyen et al., 2023), while a human PC has roughly 400-600,000 spines.

The elevation in human spine density was largely attributable to thin-head spines (5.37±0.82 vs 4.56±0.56/μm) and large mushroom spines (0.49±0.44 vs 0.13±0.14/μm). Thin spine density increased in distal branches of mouse (4.09±0.64 to 4.86±0.28/μm) while mushroom spine density increased in distal branches of human (0.39±0.45 to 0.7±0.59/μm). Both species had similar

densities of branched spines (Harris & Stevens, 1988; Lee et al., 2004, 2005; Loschky et al., 2022) (0.42±0.18 vs 0.49±0.13/μm) that were elevated on distal branches (0.38±0.19 to 0.45±0.18/μm in human and 0.37±0.11 to 0.6±0.08/μm in mouse).

Among spines with standard head and neck structure (thin and mushroom), head diameters were larger in human (0.36±0.1μm vs 0.29±0.08μm; Fig. 9D). As in our cell reconstructions (Appendix Figure S13N-O), spiny dendrite thicknesses were equivalent in both species (0.68±0.1μm vs 0.73±0.1μm; Appendix Figure S14C), leading us to hypothesize that human spine necks may be longer to maintain a similar volume ratio between spines and the space surrounding the dendrite (see Appendix 1: Methodology and Statistics). Spine necks were indeed longer on average in human (0.83±0.48μm vs 0.7±0.31μm; Fig. 9E), but the ratio of spine to surrounding volume nearly doubled from mouse to human (1.96±0.5% vs 3.73±0.92%; Fig. 9F), such that elongated necks did not compensate for elevated spine density and size in the human. Increased spine neck length and head diameters made human spines protrude further from the dendrite than in mouse (1.41±0.57μm vs 1.13±0.41μm) and with an elevated distance distally (1.34±0.51μm to 1.47±0.58μm), while in mice this value was stable (1.16±0.44μm to 1.13±0.38μm; Appendix Figure S14F).

In mouse, spines were smaller in distal compartments than proximal (0.28±0.08 vs 0.31±0.08μm), but in human we observed the opposite effect where distal spine heads were larger than proximal ones (0.43±0.21 vs 0.4±0.17; Fig. 9G). As a result, the total spine volume fraction around the dendrite remains stable in mouse (1.87±0.24 vs 2.1±0.55%; Fig. 9H) while in human there is a trend toward higher spine volume on distal branches (4.44±1.36%) than proximal branches (3.52±0.44%). This may indicate that distal compartments amplify synaptic strength through larger spine structure to compensate for increased distance from the somatic compartment.
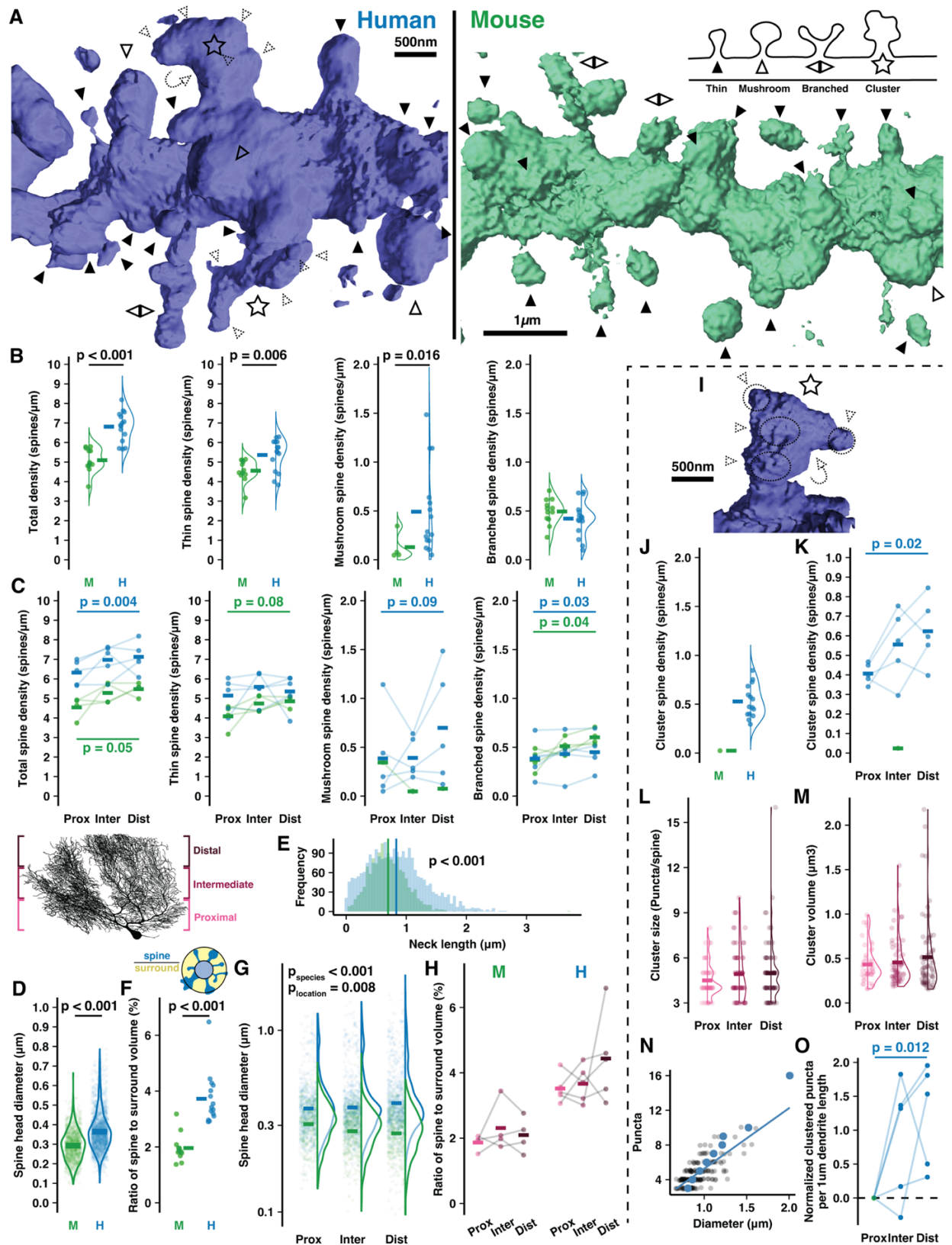
Figure 9. Human PCs host an expanded input array on spines with complex morphology. A) Example 3D reconstructions of human and mouse spiny dendrites (background removed for

clarity) with inset schematic of spine types: thin (solid arrowhead), mushroom (open arrowhead), branched (back-to-back arrowheads), cluster (star) with puncta (dashed arrowhead). **B)** Density of all spines (left) and by spine type in human and mouse (n = 15,12 branches). **C)** Spine densities by branch location relative to the soma (Student's paired one way t-test for promixal vs distal compartments; n = 5,4 cells) **D)** Spine head diameters of thin and mushroom spines (Student's t-test; n = 2066,1246 spines). **E)** Spine neck length by species (Student's t-test; n = 2323,1376 spines). **F)** Ratio of spine head volume to volume surrounding the dendrite (Student's t-test; n = 15,12 branches). **G)** Spine head diameter by branch location (ANOVA, Tukey's HSD post-hoc; n = 345,478,424 spines in human, 676,767,812 in mouse). **H)** Spine to surround ratios by branch location (n = 4,4 branches). **I)** Example spine cluster with enlarged neck diameter and expanded spine head matrix supporting multiple puncta. **J)** Spine cluster density, included in the total density in (**B**, left). **K)** Spine cluster density by branch location, included in the total density in (**C**, left) (Student's one way t-test for promixal vs distal compartments; n=5 individuals). **L)** Number of puncta per cluster by branch location (n = 46,67,76 spines). **M)** Spine cluster head volume by branch location (n = 46,67,76 spines). **N)** Spine cluster diameter as a function of puncta number (n = 189 spines). Blue points are means by puncta number. **O)** Total puncta across spine clusters on each branch segment by location and normalized to the proximal branch (Student's one way t-test for promixal vs distal compartments; n = 5 individuals).

Human-specific 'spine cluster' structures throughout the dendritic arbor

The most notable difference between the species was the presence in humans of a previously unreported spine structure we term a "spine cluster". Unlike branched spines, spine clusters have one large head serving as a ground matrix structure for the partial emergence of multiple spiny prominences, or puncta. Individual puncta diameters are typically 0.1-0.4μm and could putatively host a synaptic density like thin spine heads with the same dimensions (Fig. 9A,I and Appendix Figure S14B). While only one of 1,380 mouse spines met the criteria, spine clusters were present across all human branches, cells, and specimens. The following analyses focus on the phenomenon in human.

Spine clusters were present at an average density of 0.52±0.16/μm (Fig. 9J; included in the total of Fig. 9B) that increased distally from 0.41±0.05 to 0.62±0.17/μm (Fig. 9K; included in the total of Fig. 9C). Spine clusters typically had 4-6 puncta (4.84±1.75; Fig. 9L) and a spherical

volume of $0.49\pm0.42\mu m^3$ such that the average puncta volume was $0.1\mu m^3$ (Fig. 9M)—approximately that of thin spines with 0.3-0.5μm head diameters. Spine clusters had larger diameters than thin and mushroom spines (0.93 ± 0.19 vs 0.34 ± 0.07 and $0.58\pm0.07\mu m$; Appendix Figure S14G-H). The number of puncta (Fig. 9L), puncta volumes (Fig. 9N), and size (Appendix Figure S14H) were constant across compartments. Diameter and puncta number scale linearly (Fig. 9N), suggesting that spine clusters vary in size largely through the gain or loss of discrete, stereotypically sized puncta and not through growth or shrinkage of the puncta. The increased number and trend toward increased size of spine clusters in distal compartments contributed to almost double the density of putative clustered inputs per dendritic length in proximal vs distal compartments (1.85 ± 0.37 to $3.07\pm0.81/\mu m$; Fig. 9O).

Climbing fiber multi-innervation may be more common in human than mouse cerebellum

While PFs are the predominant source of input onto the spines of thin dendrites, the dendritic shaft and primary dendrite are the sites of a second excitatory projection from CF axons of the inferior olive. CF innervation has been explored extensively in cat (Eccles et al., 1966) and rodent models (Ito & Kano, 1982; Maekawa & Simpson, 1972; Simpson et al., 1996) and was recently updated to appreciate multi-innervation of multi-dendritic PCs in adult mice (Busch & Hansel, 2023). During development numerous CF-PC inputs undergo a competitive pruning (Hashimoto et al., 2009; Hashimoto & Kano, 2003; Wilson et al., 2019) that may resemble adult bidirectional synaptic plasticity (Bosman et al., 2008; Hansel & Linden, 2000; Ohtsuki & Hirano, 2008; Piochon, Kano, et al., 2016) and determines which CFs translocate to the dendrite. We previously hypothesized that multi-dendritic structure offers independent territories for CFs to evade competitive pressure. Ostensibly, being almost exclusively multi-dendritic may permit a higher

prevalence of CF multi-innervation in humans, but we lack physiological or tract-tracing methods to test this, so only a small number of studies (C.-Y. Lin et al., 2014; Y.-C. Wu et al., 2021) have addressed adult human CFs after their first depiction by Ramón y Cajal in 1890.

To access this vital input pathway, we immunolabeled CF axonal fibers with the intermediate neurofilament protein peripherin (Errante et al., 1998). Though extremely sparse, we identified 44 PCs with co-labeled peripherin fibers that could be classified as: "putative mono-innervation" (Fig. 10A), incompletely labeled multi-innervation we term either "absence" and "putative" multi-innervation (absence: having one fiber that is conspicuously absent from some primary dendrites, Fig. 10B; putative: having multiple truncated fibers, Fig. 10C), or "fully labeled multi-innervation" (Fig. 10D-E; see Appendix 1: Methodology and Statistics). The sparsity precluded analysis of regional or foliar variation; but, taken as an average of posterior hemisphere (L6-8), the cases were classified as: putative mono-innervation (22/44), absence (11/44) or putative multi-innervation (6/44), or fully labeled multi-innervation (5/44). Thus, at least 11%, and possibly up to half of human PCs receive multiple CFs, setting the minimum likelihood to the same rate (~15%) of multi-innervation observed in mouse (Busch & Hansel, 2023). Variable fiber thickness and arrangement may reflect diverse CF strengths and distributions on the dendritic arbor (Fig. 10E).

This method naturally underestimates multi-innervation by distant or unlabeled CFs. However, the underlying PC morphology offers a modestly more concrete range. In mouse, multi-dendritic structure and wider dendrite separation distances elevate the rate of multi-innervation (Busch & Hansel, 2023). Overall, our peripherin co-labeled PCs have typical rates of multi-dendritic structure for human posterior hemisphere (2.3% Normative, 36.4% Split, 61.3% Poly). Mono-innervated cells, however, are less multi-dendritic (4.5% Normative, 41% Split, 54.5% Poly; Fig. 10F) and horizontally oriented (31.8% vertical, 68.2% horizontal; Fig. 10G) while fully labeled

multi-innervated cells are more multi-dendritic (0% Normative, 20% Split, 80% Poly) and horizontal (20% vertical, 80% horizontal). Factors shaping the relationship between multi-dendritic structure and CF multi-innervation may thus be conserved across mice and humans. The demographics of intermediate classifications diverge: absence multi-innervation PCs (0% Normative, 45.5% Split, 54.5% Poly) closely align with mono-innervated PCs while putative multi-innervation PCs (0% Normative, 16.7% Split, 83.3% Poly) resemble fully labeled multi-innervated PCs (Fig. 10F). Thus, putative and fully labeled cases may in fact demarcate the same phenomenon, multi-innervation, and set the population rate to at least 25% in human.

Beyond climbing fibers, our staining reveals that segregated primary dendrite compartments can be the recipient (Appendix Figure S15A) of narrowly branching recurrent PC axon terminals (Ramón y Cajal, 1909). In mouse, recurrent PC axons target interneurons, PC somata (Witter et al., 2016), and superficial granule cells (Guo et al., 2016); on rare occasion a diminutive branch will ascend into the molecular layer. We also found that primary dendrites sometimes host the axon, thereby differentiating the axon initiation site exposure to the distinct primary dendrite signals (Appendix Figure S15B). This has not been shown in cerebellum of any species and complements our finding that PC output may be disproportionately driven by subsets of input.
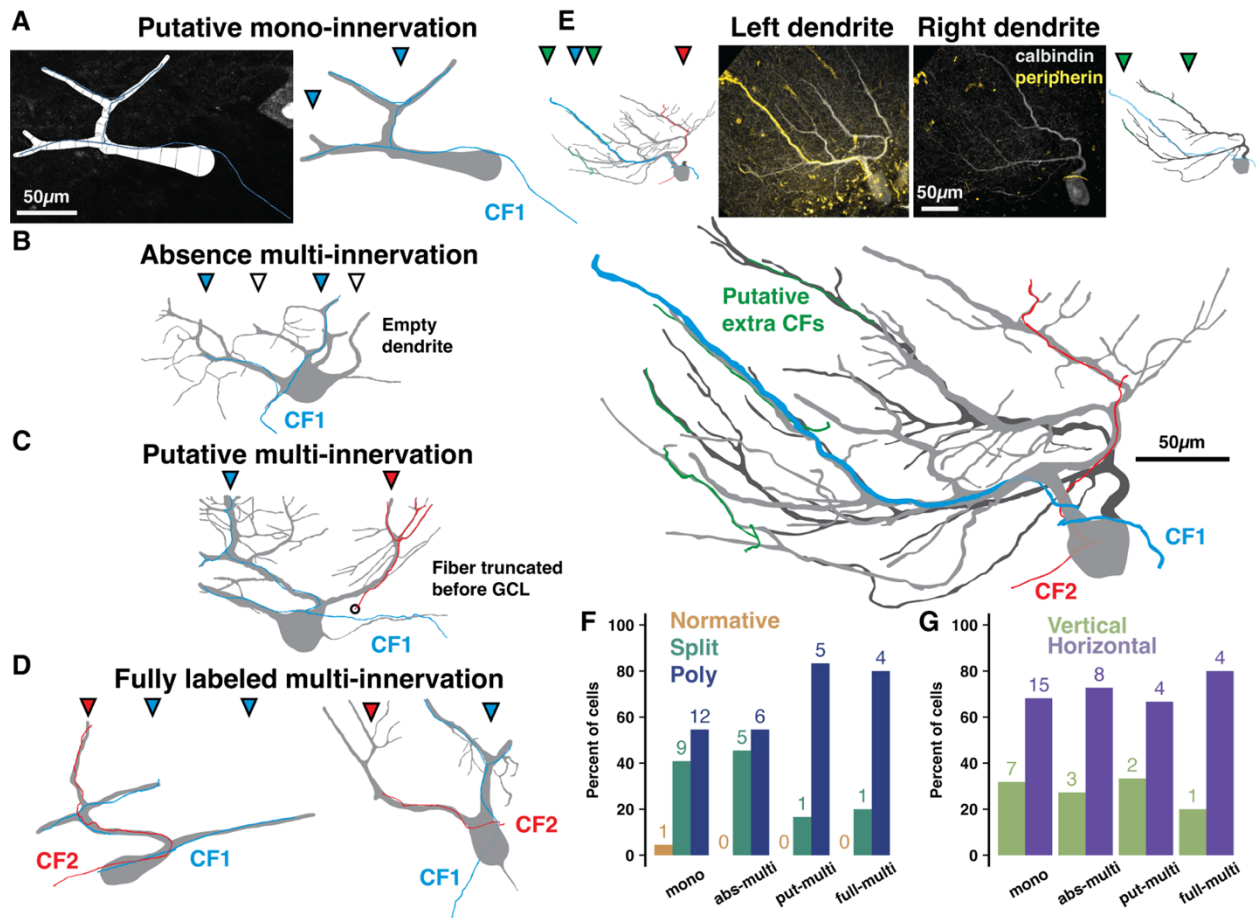
Figure 10. Peripherin and calbindin dual-labeling reveals non-canonical CF multi-innervation of adult human PCs. A) Example reconstruction from human of a PC and peripherin-labeled fiber as originally traced (left) and with masks drawn for visualization (right) to exemplify putative mono-innervation. **B)** Example PC and peripherin-fiber masks to exemplify absence multi-innervation. **C)** Example of putative multi-innervation. **D)** Examples of fully labeled multi-innervation. **E)** A Poly PC with multiple peripherin fibers of varying thickness approaching separate dendrite compartments from distinct locations in the granule cell layer. Untraced composite PC and peripherin-fiber images (top, center) with separate (top, outside) and combined (bottom) masks of each primary dendrite. **F-G)** Distribution of cell types **(F)** and orientations **(G)** by peripherin fiber classification (n = 2 individuals, 44 cells). Numbers above bars indicate absolute counts.

Regional distributions of PC demographics in vermis are distinct from hemisphere and align

with human functional boundaries

Because PC dendritic computation and input arrangement is likely shaped by morphology, we

next asked whether PC morphology demographics vary across cerebellar regions in alignment with

local task-specific demands. The prevalence of multi-dendritic PCs increases in more posterior hemisphere lobules of both species, forming an anterior-posterior gradient (Busch & Hansel, 2023). This may reflect that multi-dendrite morphology—and the input multiplexing and independent branch signaling this confers—is needed for multi-modal associative tasks performed by posterior hemisphere. If PC demographics indeed align with functional demands, we hypothesized that the cerebellar vermis, having more evolutionarily conserved somatosensory and motor functions like anterior hemisphere (Buckner et al., 2011; Nettekoven et al., 2024; Saadon-Grosman et al., 2022), would lack this gradient and demographically resemble the anterior hemisphere.

To test this, we used our previous morphological framework to categorize PCs in the vermis of human and mouse, which could be done exhaustively due to embalmed human tissue quality or the smaller size of the mouse (Fig. 11A and Appendix Figure S16A-B). The specimens used were the same as in our previous work (Busch & Hansel, 2023), so all regions can be directly compared within individuals. Indeed, vermis lobules lacked a clear anterior-posterior gradient and largely resembled anterior hemisphere with an elevated rate of normative PCs and more Split than Poly PCs (Fig. 11B, bottom), though vermis PC orientations (Fig. 11B, top) better resembled posterior hemisphere (Appendix Figure S19A-C). These regional trends were similar in the mouse (Fig. 11C-D). In human, the anterior- and posterior-most lobules (L1-2 and L9-10) diverged from the general trend by having higher rates of Poly, Normative, and vertically oriented PCs. A similar divergence was observed in the anterior-most but not posterior-most regions of the mouse. Instead, mouse L7-9 appeared distinct in having a higher rate of Poly PCs.

Figure 11. Regional and locally clustered PC demographics in the vermis of human and mouse. A) Parasagittal exhaustive reconstruction of PC morphological distributions in human vermis. **B)** Morphological orientation (top) and type (bottom) demographics across lobules (Chi-squared test; n = 3 individuals, 6346 cells). **C)** Parasagittal exhaustive reconstruction of mouse vermis. **D)** Morphological type (top) and orientation (bottom) demographics across lobules in mouse (Chi-squared test; n = 3 individuals, 2284 cells). **E)** Observed and shuffled rates of adjacent PC clustering in human and mouse (within species ANOVA, Tukey's HSD post-hoc; n = 3 individuals and 20 shuffles of each).

Local cell type clustering produces 'patchy' heterogenous processing zones within regions

Human fMRI studies demonstrate that functional boundaries do not align with the anatomical boundaries of lobules. Particularly given the size and foliation of human cerebellum, it is not clear at what spatial scale PC

51
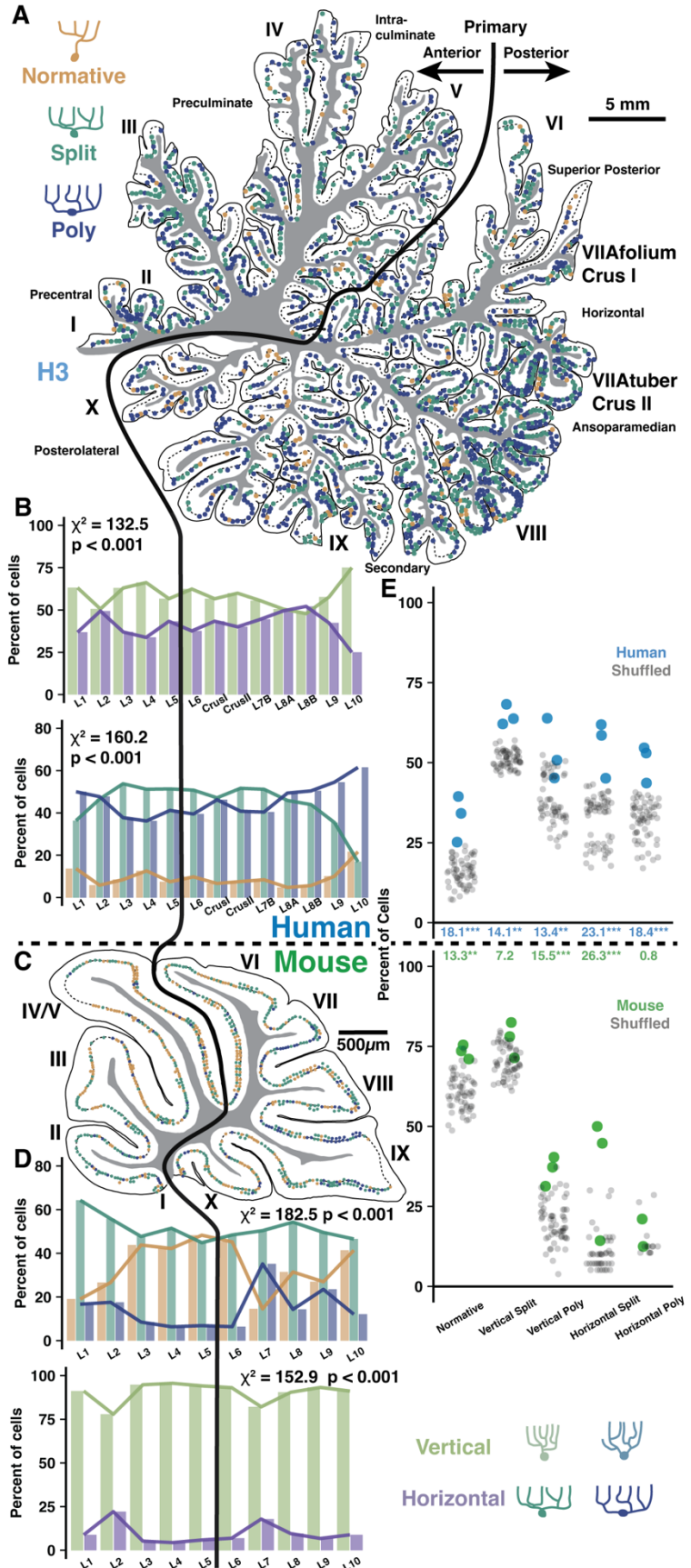
demographics are compiled to serve computational needs. We asked whether task-specific computational demands act on PC populations at the level of whole regions, individual folia, or smaller circuits of neighboring cells with overlapping dendrites. The distribution of PC morphologies would thus sort randomly throughout a region, be homogeneous in each folium, or exhibit 'patches' of homogeneous morphologies among neighboring PCs.

To assess demographic sorting, we first tested cell type clustering at the scale of adjacent PCs close enough to partially overlap their dendrites (Fig. 12). Each cell received a score between 0-2 to reflect how many adjacent cells matched their morphological type (Normative, Split, or Poly) and orientation (Vertical or Horizontal) along the parasagittal line of the PC layer (Fig. 12A). The rate of non-zero cluster scores was compared to a shuffled dataset (see Appendix 1: Methodology and Statistics), revealing that adjacent cells with possible dendritic overlap were more likely than chance to share morphological categories (Fig. 11E). The non-random clustering rate was modestly more robust in human than mouse (17.4 vs 12.6%). Clustering was only apparent when requiring a complete match of morphological type and orientation (Fig. 12B-C), not for partial matches (Appendix Figure S17C-D), in both vermis and hemisphere (Appendix Figure S16F-G and S19F-G). Conceivably, clustering may produce even more precise morphological similarity among adjacent cells than surmised via broad categories. This analysis also revealed that uninterrupted clusters have on average 2.6 cells forming an inter-somatic length of 537μm in human vermis (Fig. 12B-C). In mouse, uninterrupted clusters have 3.1 cells forming a 71μm length. Compared with clusters in the vermis, clusters in the hemisphere were longer in human (2.7 cells and 838μm length; Appendix Figure S17E-F) but identical in mouse (3 cells with 70μm length).

PC shapes are often congruent with the expansion of the molecular layer in the gyral lip or the compression in the base of the sulcus (Eccles et al., 1967; Friede, 1955). While this suggests that

clustering may be mechanically driven by tissue foliation, we find little variation in PC demographics across foliar location (gyrus, bank, or sulcus) in human and mouse (Appendix Figure S16C), though there were more horizontally oriented PCs in human sulcus (Appendix Figure S16D). The same patterns were observed in hemisphere (Busch & Hansel, 2023). To control for foliation, we performed the same clustering analyses with shuffled data where foliar location was held constant (see Appendix 1: Methodology and Statistics). Non-random clustering was still observed (Appendix Figure S16E), particularly in human vermis, but also in mouse and human hemisphere (Appendix Figure S19D-E). Separating by foliar sub-area, clustering was present within bank regions—lacking bias from mechanical force—as well as the gyrus and sulcus of both vermis (Appendix Figure S16F-G) and hemisphere (Appendix Figure S19F-G).

It is also possible that clustering occurs among a broad population where most, but not all, cells are the same. The previous analysis could not resolve this, so we measured how well the morphology of each cell was matched by the demographics of all surrounding cells within variable distances (Fig. 12D). Non-random clustering provided an increased chance that surrounding cells had a matching morphology by ~13-14% in human and ~9-10% in mouse. Non-matching cells, inversely, had diminished likelihoods. The elevated prevalence fell below 5% within 2mm and 500μm in human and mouse, respectively, and dropped to near zero at scales roughly over 1cm and 2mm. Clustering within the core of a measured area could artificially inflate the rate of drop-off, so we next sampled only cells surrounding variably sized core regions (Fig. 12E). This revealed that clustering was largely restricted to a 2mm and 400μm range in human and mouse, respectively. The scale of non-random clustering in the hemisphere extended to 3mm in human and held at 400μm in mouse (Appendix Figure S18).
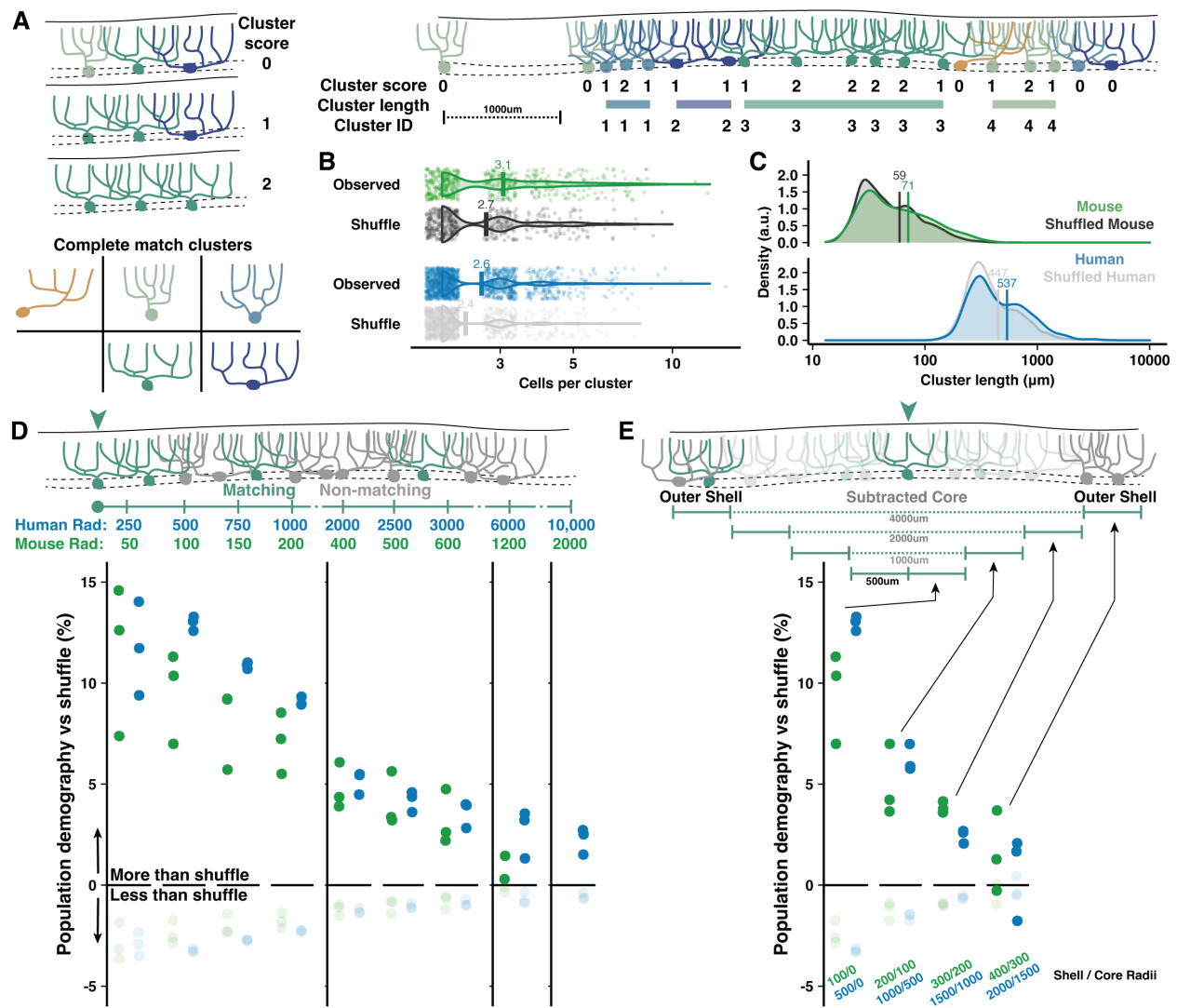
Figure 12. Adjacent and local non-random cell type clustering in human and mouse vermis.
A) Schematic of cluster score assignment based on complete morphological match (left) and score use to identify the number of cells and parasagittal length of clusters (right). **B-C)** Number of cells **(B)** and length **(C)** of PC clusters in mouse and human compared to shuffled data (Mann-Whitney U test; n = 288,1295 observed clusters; n = 263,1122 shuffled clusters). **D)** Schematic of local population demographics measured over variable distances (top). Radii in mouse are 20% the length in human, matching the difference in dendritic width. Rates of matching (dark points) and non-matching (light points) morphologies in a shuffled population are subtracted from unshuffled data to measure the percent elevation of clustering in human and mouse. Points mark the average demographic difference between observed and shuffled rates across all five cell groups (i.e. one dark point represents the average for matching cell rates of Normative to Normative, Split to Split, etc.). **E)** To measure the absolute spatial scale of elevated PC clustering, we measure the observed vs shuffled rate for 500μm increments of a shell region around a growing core. By ignoring the

morphologies of the core region, we exclude local clustering from measurements of distant clustering.

Inter-hemisphere PC demographic similarity covaries with functional symmetry

As some lobules have higher functional asymmetry across hemispheres in human (Nettekoven et al., 2024; O'Reilly et al., 2010; Stoodley & Schmahmann, 2009; D. Wang et al., 2013, 2014), we hypothesized that inter-hemisphere PC demography might reflect these patterns if it is related to function. Functionally symmetric regions (e.g. L5-L6) may then exhibit more similar PC demographics than highly asymmetric regions (eg. Crus I-II). To test this, we compared PC demographics in lobules 5-Crus II of the opposing hemisphere of specimens from which we previously examined one hemisphere (Busch & Hansel, 2023) (Fig. 13A-B and Appendix Figure S19A-B). We now show that the previously described anterior-posterior gradient is a *bilateral* phenomenon, as Poly PCs were universally more prevalent in Crus I/II than L5-6 (Fig. 13C). The inter-hemisphere rate of PC sub-types varied more in Crus I/II than L5 and especially L6 (Fig. 13D). Averaging the difference across morphologies (Fig. 13E), the mean inter-hemisphere demographic variation of each lobule confirmed that L5 and 6 exhibited less variation (2.9±1.63 and 2.17±1.35%) than Crus I and II (5.03±2.88 and 4.21±2.26%). Due to high inter-individual variation, we normalized the rate of variation in L5, Crus I, and Crus II to that of L6 within individuals. This revealed that all lobules had more variation.
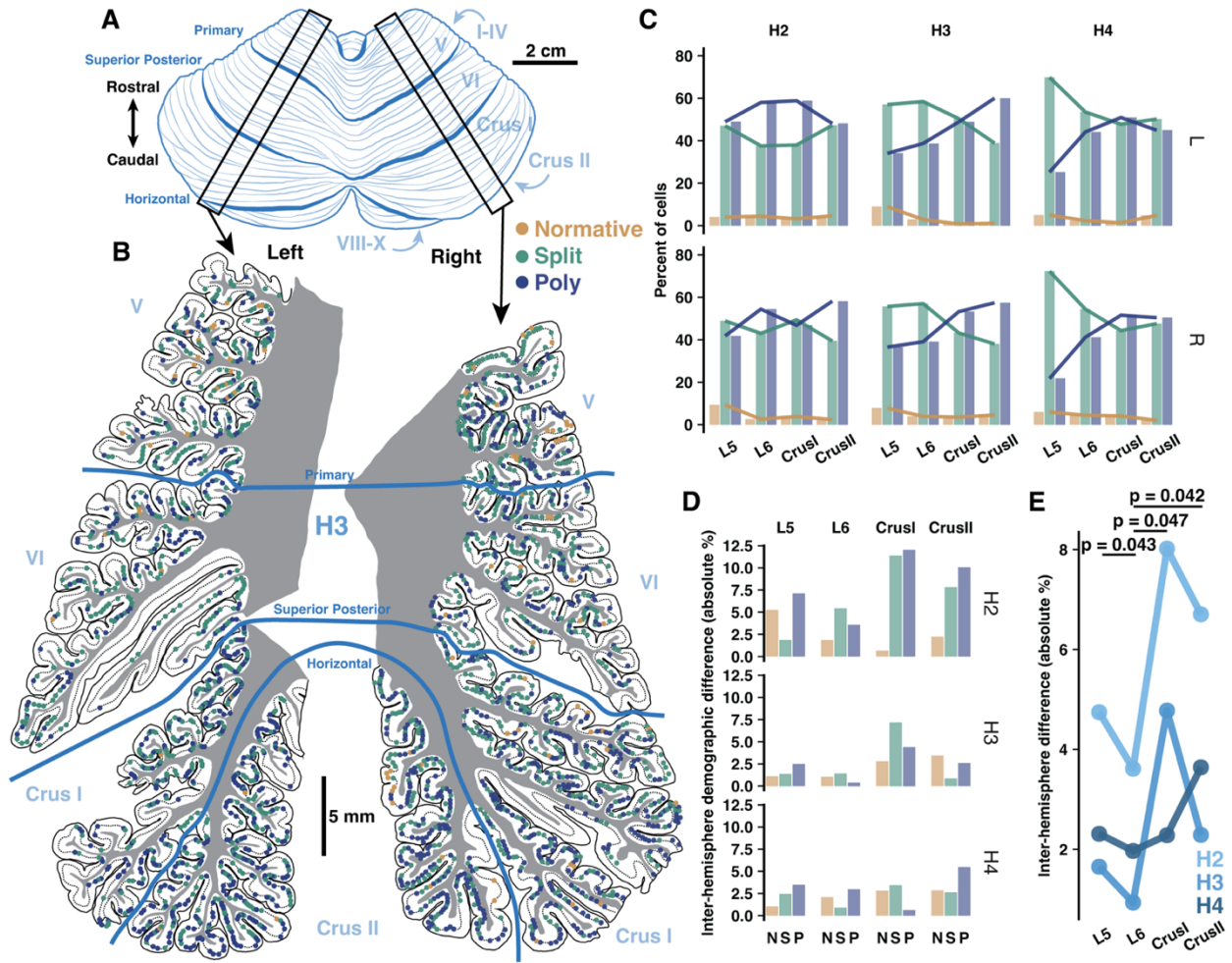
Figure 13. Inter-hemisphere similarity of PC demographics is congruent with functional lateralization. A) Schematic of human cerebellum. **B)** Parasagittal reconstructions of PC morphological distributions in left and right mid-hemisphere lobules L5-Crus II within the same individual. **C)** Morphological demographics across lobules in left (top) and right (bottom) hemispheres by individual. **D)** Absolute differences of morphological demographics across hemispheres by lobule and individual. **E)** Normalized mean inter-hemisphere demographic difference from L6 by lobule and individual (Student's one-way t-test; n = 3 individuals).

Discussion

Our histological interrogation of Purkinje cells in post-mortem human and mouse tissue defines human PC morphology, input arrangement, and likely physiology as both *quantitatively* and *qualitatively* distinct from the rodent model. In clarifying how the species diverge, this work highlights the importance of further anatomical study in human but also strengthens the interpretability of disease studies that must by necessity be pursued in animal and *in silico* models (Masoli et al., 2024). Dendrite morphology may factor into cerebellar disease etiology. In mouse, PC morphology and CF signaling is altered in disease models such as spinocerebellar ataxia (Du et al., 2013, 2019) and syndromic autism (Busch et al., 2023; Piochon et al., 2014; Simmons et al., 2022). On the only occasions that human PC morphology has been measured with respect to cerebellar disease, it was disrupted in Essential Tremor (Louis et al., 2014; Mavroudis et al., 2022) and Friedrichs Ataxia (Kemp et al., 2016).

Are human PCs an allometrically scaled mouse PC?

Human PCs are substantially larger than those of the mouse. But are they *just* allometrically scaled mouse PCs? The answer is likely no. Only some features appear to be either invariant or proportionally scaled with molecular layer thickness. We observed similar fractal branching patterns and relative average distances of peak branch number and dendritic length from the soma, suggesting a possible shared dependence on cell autonomous factors governing the branching pattern. The diameter of thin caliber dendrites is identical, indicating a shared constraint on dendritic thickness perhaps by limits of physiological conduction.

The dimensions of the cerebellar cortex are a plausible allometric constraint on cellular growth. Yet, human PCs expand their size well beyond the relative difference in molecular layer

57

thickness— reflected by PC height—by multiplying and extending their primary dendrites outward in the parasagittal axis to articulate an expanded horizontal profile. The horizontal eccentricities of non-primary dendrites further drive the extended width of human PCs and permit spiny branches to double back, overlap in distinct mediolateral planes, and possibly resurvey the PF axons projecting through the arbor. The latter feature could expand combinatorial coding by human PC dendritic branches without requiring increased granule cell or PF densities. The horizontal structure of human PCs may also allow them to defy allometric constraint by producing a more circular emminance from the soma. As a result, human PCs feature a rapid rise and decline in branch location, total length, and branching order relative to the position of the soma. The complexity of this distribution is quite distinct from that of mouse PCs that maintain homogeneous morphological properties through most of their structure.

These non-allometric features indicate that human PC physiology diverges from the rodent not only as a matter of scale (Masoli et al., 2024) but as a matter of kind. For example, conserved dendrite thickness may similarly expose synaptic contacts to synaptic maintenance factors, electrical resistance, and membrane capacitance. Yet, with greater length, human spiny branches may be more electrotonically compartmentalized and capable of more independent signaling. More variable branch lengths may further diversify independent signaling capacity across the arbor.

Enhanced and human-specific features of input amplification and association by dendritic spines

Qualitative, unlike *quantitative*, species differences are uncommon, rendering our discovery of human-specific spine clusters potentially fertile ground to explore new modes of synaptic and

dendritic signaling. Some spine clusters features—larger size and possibly more postsynaptic densities—represent quantitative expansion, but others represent novel physiological phenomena. First, unlike branched or calyx spines (Lee et al., 2005; Loschky et al., 2022), several synaptic contacts would be exposed to membrane potentials and cytosolic plasticity factors in common. Second, while not quantified here, clustered inputs may operate in variable isolation from the dendrite and other local synapses as the neck diameter varies widely from the conserved value of 0.1-0.3μm (Harris & Stevens, 1988; Ofer et al., 2021) to 0.5-0.7μm (Fig. 9A,I). The latter would have low electrical resistance, more contiguity with the dendritic shaft, and therefore behave like a small dendritic sub-branchlet. Indeed, spine clusters protrude ~1.5-3μm, echoing the 2-4μm length of the smallest terminal dendritic branchlets in the mouse. These two features may combine to produce both an associative structure, like proposed for branched spines (Loschky et al., 2022), and a new form of amplifying structure providing the substrate to initiate dendritic calcium spikes (Eilers et al., 1995; Hartell, 1996; Roome & Kuhn, 2018).

In addition to spine clusters, human PCs are more spine dense and thus receive disproportionately more inputs than rodent PCs. The spine density we observe in mouse differs from studies reporting 1-2/μm—or the frequently cited work in rat reporting, by extrapolation, ~17/μm (Napper & Harvey, 1988)—but are in perfect agreement with recent confocal (O'Brien & Unwin, 2006) and EM reconstructions (Hillman & Chen, 1984; Ichikawa et al., 2016; Loschky et al., 2022; Lu et al., 2009; Nguyen et al., 2023; Špaček & Hartmann, 1983). Our data reveal elevated spine density in distal compartments, which comports with the knowledge that distal compartments receive denser PF innervation (Eccles et al., 1967). We also show that branched spine density increases distally, possibly supporting their proposed role in associative PF plasticity, a critical feature of the perceptron model (Brunel et al., 2004; Loschky et al., 2022). Larger spine heads in

human may strengthen post-synaptic signaling so a higher percentage of inputs can influence PC output than in mouse. Alternatively, this amplification may simply compensate for human PC size, an idea supported by the fact that in human, unlike mouse, the spines are larger in distal compartments. Possibly reflecting shared factors of increased computational complexity and compensation for size or compartmentalization (Beaulieu-Laroche et al., 2018), pyramidal cells have similarly greater spine density (pyramidal: 1.3x vs Purkinje: 1.41x) and size (1.27x vs 1.41x) (Benavides-Piccione et al., 2002, 2013).

Human Purkinje dendrite size and input numerosity

The previously reported average human PC dendritic length was 10-20,000μm, varying with methodology (Golgi impregnation (Louis et al., 2014; Ruela et al., 1980) vs post-fix dye electroporation (Masoli et al., 2024)). Our current knowledge, then, would conclude that human PCs are the same size as pyramidal cells (L2/3 are ~14,500μm, <22,000μm (Mohan et al., 2015); thick tufted L5/6 are ~1-2000μm longer (Mohan et al., 2015); hippocampal CA1 are ~18,600μm, <27,000μm (Mertens et al., 2024)). While one might naturally expect the 2D radiations of PCs to make them larger in human than 1D radiating pyramidal cells, the previous data would suggest instead that there is a ceiling for maximal neuronal size and that, in human, both cell types met that limit before diverging. On the contrary, we demonstrate for the first time that PCs are substantially bigger than pyramidal cells and boast the largest dendritic arbor of any recorded neuron in the human brain. Intriguingly, our findings also indicate that pyramidal and Purkinje cells scale differently in mouse (~5,500 vs ~6,000μm) than human (~15,000 vs ~65,000μm).

With higher spine density and longer spiny dendrites, we can extrapolate that human PCs likely host half a million spines compared to ~30,000 in mouse. Branched spines (~7% of spines in both

species) can host synapses with two PF axons while spine clusters (~10% in human) may host over four. As such, the human may receive ~750,000 synaptic inputs on spines. It is not only staggering to consider a single neuron receiving ~1 million inputs, but it highlights that the species' dendritic length ratio (11:1) belies an input ratio around 30:1.

Human PCs multiplex CFs and other inputs

We previously found more multi-innervated PCs in posterior lobules of mouse (Busch & Hansel, 2023), likely due to the heightened prevalence of multi-dendritic PCs. This was recently replicated, albeit tangentially (Nakayama et al., 2024). We predicted that multi-dendritic structure permits CF multi-innervation by providing segregated synaptic territories where multiple CFs could avoid the competitive pruning that would have prevented their translocation from soma to dendrite. This prediction was also supported by our finding that surplus CFs had greater synaptic strength in older animals (Busch & Hansel, 2023), possibly reflecting a delayed or elongated maturation process following distinct developmental trajectories of presynaptic plasticity at weak versus strong CF inputs before P21 (Pätz et al., 2019).

Human PC dendrites commonly ramify in more horizontal eccentricities than in mouse. This produces a distinct multi-dendritic motif with primary dendrites ramifying outward and giving rise to numerous (around 7-8) sub-compartments, each ~5-10,000μm in length — roughly an entire rodent cell. Dendrite width complements multi-dendritic structure to further enable CF multi-innervation in mouse (Busch & Hansel, 2023). Here, co-immunolabeling of calbindin and peripherin (Errante et al., 1998) provides the first demonstration of CF multi-innervation in adult human. It also extends to humans the hypothesis that multi-branched structure supports CF

competition avoidance. Finally, our co-labeling supports a likely higher prevalence of multi-innervation than in mouse.

Cerebellar cortical geometry allows us to speculate that a horizontally aligned dendritic arbor—often almost a millimeter wide (Fig. 8A,G)—would allow human PCs to receive input from highly segregated excitatory PFs from distant granule cells. If conserved, spatial-functional PF clustering reported in mouse (Wilms & Häusser, 2015) would make their functional similarity diminish with distance. Thus, the disproportionate width of human PCs may sample more distinct PF representations. Similarly, this dendritic width may engender more compartment-specific inhibition by molecular layer interneurons (Lackey et al., 2024) and oversampling of modulatory influence by vertically ascending cholinergic beaded fibers (Barmack et al., 1992) and Bergmann glia (De Zeeuw & Hoogland, 2015). Taken together, human PCs likely perform highly complex input multiplexing and dendritic computations that are unlike what is commonly reported in mouse. This would, in turn, distinguish human PC dendritic plasticity and output information content as distinct from mouse PCs.

Studies of PC computation have largely considered the dendritic arbor a continuous functional compartment due to the equally unusual singularity and numerousness of CF and PF input, respectively. More recently, experimental and modeling studies demonstrate that Purkinje dendrite compartments exhibit heterogeneous ion channel density and plasticity (Ohtsuki, 2020; Ohtsuki et al., 2012), localized calcium signals (Kitamura & Häusser, 2011; Roome & Kuhn, 2018), PF input clustering (Wilms & Häusser, 2015), and variable calcium signaling due to branch shape in a homogeneous channel model (Cirtala & De Schutter, 2024; Zang et al., 2018; Zang & De Schutter, 2021). Combined with the finding that some PC dendrites are innervated by multiple CFs that

confer branch-specific signaling (Busch & Hansel, 2023), the potential for dendritic input multiplexing is becoming more widely appreciated (Zang & De Schutter, 2021).

We previously suggested that CF multi-innervation may be an adaptation to maintain receptive field matching in multi-dendritic PCs with more disparate PF representations across segregated dendritic compartments (Busch & Hansel, 2023). This would preserve perceptron function among mouse PCs with expanded dendritic arbors. Our findings extend this concept to human PCs where there is likely a greater demand to match distinct receptive fields. As a possible consequence, human PC output may convey more features of sensory, internal, or cognitive state. Individual CFs convey a variety of signals (Gaffield et al., 2019; Ju et al., 2019; Kostadinov et al., 2019). PF-dependent simple spike modulation reflects unidimensional movement kinematics in oculomotor L6-7 (Pi et al., 2024), but can represent multiple proprioceptive features in anterior vermis during passive vestibular stimulation (Zobeiri & Cullen, 2022) and reinforcement learning error and learning state during a visuomotor association task among Crus1-2 PCs (Sendhilnathan et al., 2022) where multi-dendritic structure is more common. Thus, multi-dendritic PC computation may resemble mixed selectivity encoding by pyramidal cells involved in complex decision-making (Tye et al., 2024). Importantly, expansion of input numerosity or strength does not necessarily improve computational capacity. Excess CF innervation is linked to sensory over-responsiveness in mouse autism models (Busch et al., 2023; Simmons et al., 2022). Human essential tremor is characterized in part by excess CF innervation from ectopic lateral crossings (Y.-C. Wu et al., 2021) and thin dendrite translocation (Pan et al., 2020).

Human cerebellum may harness regional PC demographics and sub-regional clustering to generate task-specific computation

We previously described a parasagittal gradient of PC morphological demographics in human and mouse mid-hemisphere (Busch & Hansel, 2023). Here, we control for a possible role of parasagittal developmental gradients (Beekhof et al., 2021) both through comparison with the vermis—with a distinct demographic gradient despite shared parasagittal development—and by showing that inter-hemisphere demographic similarity covaries with functional symmetry (Buckner et al., 2011; Krienen & Buckner, 2009; Nettekoven et al., 2024; Stoodley & Schmahmann, 2009; D. Wang et al., 2013, 2014). In mouse, posterior hemisphere processes multisensory information from mossy fibers (Huang et al., 2013; Ishikawa et al., 2015; Shimuta et al., 2020) and CFs (Bosman et al., 2010; Busch et al., 2023; De Zeeuw et al., 1998; Gaffield et al., 2019; Ju et al., 2019; Ohmae & Medina, 2015; Rondi-Reig et al., 2014; Simmons et al., 2022) and receive stronger somatosensory feedback from neocortex than the vermis (Pisano et al., 2021). In human, lateral and posterior regions are more responsive to cognitive, affective, and socio-linguistic information (LeBel et al., 2021; LeBel & D'Mello, 2023; Stoodley & Schmahmann, 2009; Van Overwalle et al., 2015) and, intriguingly, are the main culprit of expanded human cerebellar volume that—more than neocortex—largely defines increased human brain volume relative to non-human primates (Magielse et al., 2023).

We propose that the relative proportions of multidendritic structure and horizontal orientation act as complementary toggles to generate four classes of morphological demography (Appendix Figure S20A). Surprisingly, the regional borders of each class align with four functional classes from a new consensus atlas of human cerebellum (Nettekoven et al., 2024). Furthermore, regions with more complex morphology (increased multi-dendritic and horizontal orientation) roughly

64

match regions processing information that is more cognitive (co-active with non-primary sensory neocortical regions) and associative (requiring integration and association of multi-modal inputs) in nature (Appendix Figure S20B).

Sub-regional clustering is more prevalent in human and only partly reflective of developmental tissue foliation. The spatial scale of clustering and the comparative scale ratio (~5-7x longer in human; enhanced clustering in core regions of 2mm vs 400μm) are congruent with the absolute and relative widths of the dendritic arbor. Both properties support the idea that neighboring cells' primary dendrites may reciprocally influence each other during development. Notably, the clustering scale ratio exceeds the comparative PC height ratio (a proxy for allometric constraint). This comports with observations that segregated branches of multidendritic mouse PCs often stagger in interweaving dendrite arrays with lower medio-lateral overlap (Nedelescu et al., 2018). This suggests that cerebellar cortex, especially in human, may employ heterogeneous "patches" of PCs circuits within each region that use distinct morphological niches for specific computations. Non-random spatial clustering of neuronal cells by morphological sub-type has not previously been described in other brain areas, potentially making this a cerebellum-specific means to boost functional diversity.

CHAPTER 4

COMPARATIVE MORPHOLOGY OF CEREBELLAR PURKINJE CELLS REVEALS AN

EVOLUTIONARY TRAJECTORY OF ENHANCED DENDRITIC COMPLEXITY IN

HUMANS

This chapter contains rough draft text and preliminary data for a manuscript to be co-authored by myself and Aurora Ferrell (University of Chicago undergraduate) under the supervision of Dr. Christian Hansel. My contribution was to the original conceptualization with Dr. Hansel, initial data collection and study design, and data analysis. Aurora Ferrell co-designed parts of the study, collected most of the data, and conducted some of the analysis. The work will also be co-authored by our collaborators who provided the primate tissue: Madison Hillegas and Drs. Chet C. Sherwood and William D. Hopkins. This work will be submitted for publication and as a preprint in early 2025 and has been provided here with the permission of all authors.

Abstract

Cerebellar Purkinje cell (PC) dendrites conduct robust supervised learning that is highly conserved across vertebrates but also serves numerous species-specific behaviors. PC morphology is classically considered stereotypical, yet it was recently observed that primary dendrite structure varies considerably within and across mice and humans and that this variation can influence PC integrative capacity. Regional gradients of PC structure in mice provided early support of the hypothesis that morphology-dependent cellular function may underlie task-specific regional computations. Our finding that human PC demographics also vary by region, are almost universally multi-dendritic, and have more proximal branching may supply added support.

However, allometric or foliation factors are plausible confounds as it is unclear if these traits are unique to humans, present across primates, or depend on brain size. We immunolabeled PCs (calbindin) in crus 1-2 of adult primates (monkeys, lesser and great apes, human) and non-primates (mouse, elephant) to comprehensively analyze PC morphology with respect to phylogeny, allometry, and foliation. In primates, the rate and complexity of multi-branched structure increase with phylogenetic proximity to human. While human PCs largely represent a peak in a linear primate trajectory (macaque < gibbon < gorilla < chimpanzee < bonobo < human) they also stand out as distinct in the extremity of their multi-branched structure. The elephant demographic profile is distinct from the primate trend, with more frequent—but less complex—multi-branched structure than human. Thus, phylogenetic proximity to humans—more than allometry—predicts more proximal and segregated multi-branched structure. This work unveils extensive anatomical diversity in a brain region considered evolutionarily stereotypical and supports the hypothesis that PC morphology underlies functional specificity by region and species.

Introduction

The cerebellum is one of the most evolutionarily conserved brain structures; all vertebrates have cerebella or cerebellum-like structures with similar anatomy and function (Devor, 2000). With varying body structure, ethological niche, and nervous system complexity, the cerebellum has served numerous species-specific functions, such as corollary charge subtraction for proprioception in electric fish (Sawtell, 2017), vocalization learning and precision in song birds (Pidoux et al., 2018), and language and higher order cognitive performance in humans (King et al., 2019; LeBel et al., 2021). To perform these varied functions the cerebellum integrates information from many areas of the brain to coordinate movement, motor learning, and cognitive tasks. At the center of this integration is the Purkinje cell (PC), whose elaborate dendritic arbor receives converging contextual inputs from granule cell parallel fibers and corrective error signals either from olivary climbing fibers or directly from primary sensory areas in cerebellum-like structures.

Theories of mammalian cerebellar function are largely based on studies in the rodent, an experimentally accessible model system. Seminal anatomical work defined the cerebellar cortical circuitry as precisely geometrical in arrangement and highly regular across cerebellar regions and across species (Eccles et al., 1967). Since the first anatomically-informed theories of cerebellar function in the 1960-80's (Albus, 1971; Ito, 1993; Marr, 1969), PCs have been presumed to be stereotypical in structure and function within molecularly defined modules of the cerebellum (Cerminara et al., 2015). Yet, recent reports demonstrated that rodent PCs have diverse dendritic structures within and between region (Nedelescu et al., 2018). Does PC morphology influence their function in this geometrically organized circuit?

In the first report to demonstrate a PC structure-function relationship, we found that some features of PC morphology among a sub-set of cells in mice enable new computations that produce expanded receptive fields and more complex associative integrations (Busch & Hansel, 2023). Additionally, we have shown that mouse and human PC morphology vary substantially across levels: spine and dendrite micro-structure, arrangement of excitatory input from PFs and CFs, broad contours of the dendritic arbor, and PC morphological demographic profiles in regional and sub-regional populations (Busch & Hansel, 2024). The presence of morphological variation both across cerebellar regions within each species and across these two species supports the hypothesis that some functional variability based on morphological diversity may be crucial for the cerebellum to perform the tasks necessary for species-specific cognitive, sensorimotor, and social demands.

However, morphological diversity may alternatively be simply the products of allometric factors such as body size or cortical folding mechanics (Herculano-Houzel, 2009; Herculano-Houzel et al., 2014; Mota & Herculano-Houzel, 2015) and not the product of functional demands. We begin to address whether PC morphological diversity derives from allometry, phylogeny, or functional demands through a broad comparative anatomical analysis. We immunolabeled PCs of adult primates—marmoset, spider monkey, macaque, baboon, gibbon, siamang, orangutan, gorilla, chimpanzee, bonobo, and human—as well as mouse and elephant. Focusing on Crus 1 PCs, we characterized >200 cells per species according to previously defined categories (Normative, Split, and Poly; Busch and Hansel 2023, 2024) and designed a panel of morphological properties that were systematically measured in >120 cells per species. Despite being considered a stereotypical and rigidly conserved brain structure, we observed a wealth of interspecies morphological variation. Morphological variation often eludes allometric constraint to exhibit a phylogenetic

relationships such as being: constant across primates, increasingly complex with proximity to human, or distinct in humans. Amid considerable morphological variability across primate PCs, we observed a progressive increase in multi-branched and horizontally oriented PC morphological categories with phylogenetic proximity to human. A shrinking primary dendrite bifurcation distance coincides with increased prevalence of Poly PCs, placing the dendrite categories along an axis of primary dendrite separation and introducing this as a species-specific mechanism to shape dendrite growth toward functional demands.

Results

We have previously shown that human Purkinje cell (PC) morphology has more frequent (Busch & Hansel, 2023) and more complex (Busch & Hansel, 2024) multi-branched morphology than mouse. Is enhanced multi-branched structure a human-specific trait or does it result primarily from continuous phylogenetic or allometric factors? To test this, we immunolabeled PCs of post-mortem fixed tissue from adult primates–including two platyrrhine monkeys (marmoset and black-handed spider monkey), two cercopithecid monkeys (rhesus macaque and olive baboon), a platyrrhine (marmoset), hylobates (northern white cheeked gibbon and siamang), and hominids (orangutan, gorilla, chimpanzee, bonobo, and human)—and non-primates (mouse and elephant). Using confocal images of hemisphere lobules simplex, crus I, and crus II from 2-3 individuals per species (Fig. 14A-B; see Table S11 for individual demographics), we performed cell type categorization as previously described (Busch and Hansel 2023, 2024) for >2000 cells (>200/species) and designed a panel of dendrite morphology parameters that were manually assayed from >1450 cells (>120/species). For cell categories, we defined PCs as having either one

("Normative") or multiple primary dendrite compartments ("Split" when compartments arise from one proximally bifurcated dendrite, or "Poly" when multiple dendrites emerge directly from the soma) and these primary dendrite types could be sub-classified according to whether they project directly toward the pial surface ("Vertical") or ramify parallel with the PC layer at <30degrees ("Horizontal") (see Appendix 1: Methodology and Statistics).

In addition to cell type categories, we delineated 13 cerebellar and PC morphology parameters. These included factors defining cortical dimensions (ML and GCL thickness, measured at the location of each cell), cell size (Soma area/circumference, thickness of all primary dendrites), axon projection (Arc distance of the GCL-facing somatic surface vs to axon), and dendritic shape (Split distance, split angle, poly-dendrite angle, arbor width, outward angles of the primary dendrite compartments) and compartmentalization (Distance to and angles of secondary branches) (see Table S12 and Appendix 1: Methodology and Statistics). As many measurements were recorded for every cell as was possible given variable tissue quality.

Human dendritic complexity both continues and interrupts the primate phylogenetic trend

Cell type categorization revealed a linear increase in the frequency of Poly (Fig. 14C) and Horizontal PCs (Fig. 14D) through primate phylogeny. There were some notable divergences such as the low number of Poly PCs in gorilla and a high number of Vertical PCs in chimpanzee. Combined with a lower prevalence of Poly PCs than bonobo, the lack of Horizontal orientation in the chimpanzee renders their PC morphology more distinct from human not only than bonobo but most hominids. Outside the great apes, the Poly PC rate in all monkeys was particularly notable for being much lower even than in mouse, though they do have more Split, generally fewer Normative, and more Horizontal PCs than mice, all indicative of increased dendritic complexity.

71
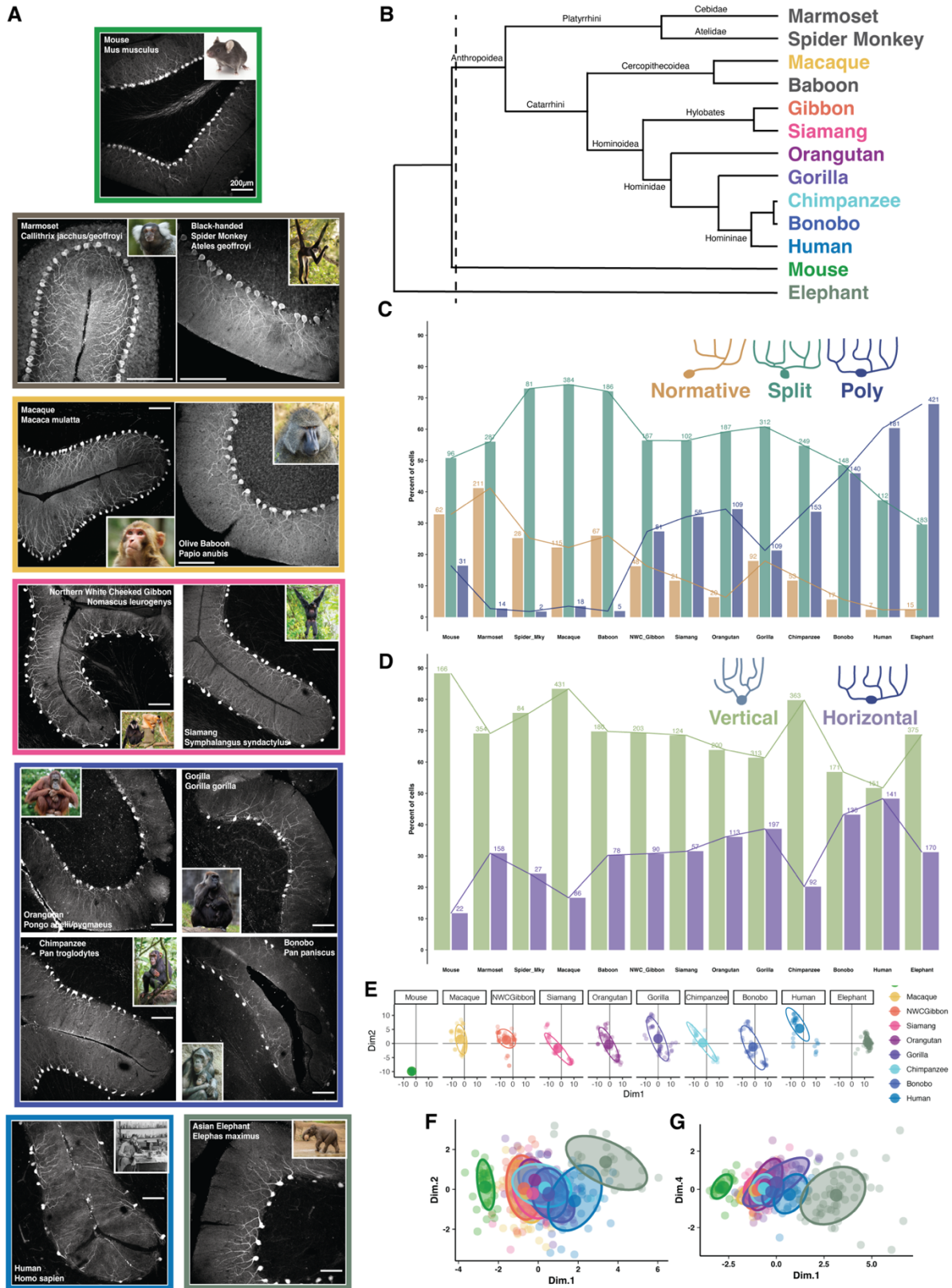
Figure 14. Comparative morphological demographics exhibit a phylogenetic trend toward greater complexity in humans that belie human-specific features in the total dataset. A)

Example images of hemisphere lobules simplex, crus I, or crus II (scale bars are 200um) with image borders separating clades (rodentia, platyrrhines, cercopithecids, hylobates, non-human hominoids, human, and elephantidae). **B)** Phylogenetic relationships with approximate relative distance to common ancestors among primates. **C)** PC morphological type demographics across species. **D)** PC morphological orientation demographics across species. **E)** t-SNE visualization of manually measured dendritic parameters producing species-specific cell clusters. **F-G)** PCA analysis of manually measured dendritic parameters.

Turning to our panel of morphology parameters, we assessed whether their combined, multi-dimensional relationships would define cell clusters by species, family, or broader clade. Here we do not yet have data for marmoset, spider monkey, and baboon. We first used t-distributed stochastic neighbor embedding (t-SNE) to visualize cell distributions while preserving species information to group post-hoc (Fig. 14E; see Appendix 1: Methodology and Statistics). This technique revealed a continuous separation of most human cells from the typical arrangement of primate cell clustering along reduced parameter dimensions. We additionally performed linear dimensionality reduction via principal component analysis (PCA), which similarly revealed a typical relationship among primate cells that excluded the human (Fig. 14F-G). The distance between human and non-human primate cells was almost that separating the anatomically and phylogenetically distant non-primate mouse and elephant. Unlike the t-SNE method, we performed separate PCAs for sub-sets of variables representing broader classes of anatomical or physiological traits. Scree analysis of the PCA variable loadings revealed roughly even distributions of explained variance across input variables, suggesting that the parameters we selected define a rich and complex interplay of structural traits and belie a highly diverse range of cerebellar and PC morphology.

Dropping split distance across primate evolution increased multi-branched complexity and compartmentalization

We next sought to clarify which morphological parameters distinguish or are shared across species. To start, we aimed to explain the cross-species pattern of PC demographics we observed with decreasing Normative and increasing Poly PCs (Fig. 14C). The relationship between cell type categories can be summarized along an axis defined by the location of the bifurcation point where the primary dendrite compartments separate relative to the soma. In this scheme, Normative PCs have a more distal, if any, bifurcation of the primary dendrite than Split PCs and Split PCs have a more distal bifurcation than Poly PCs where the 'bifurcation' distance is subsumed by the soma. We hypothesized that the pattern of PC demographics revealed by those categories may be produced by a species-specific pattern of dendrite growth that dictates a median bifurcation distance. Thus, lower rates of Normative PCs and higher rates of Poly PCs could be an effect of a dendrite growth mechanism that produces a dropping bifurcation distance.

Indeed, we observed that the median bifurcation distance, normalized to cell size by setting it as a function of total molecular layer thickness, dropped progressively across primates (e.g. Cercopithecidae > Lesser Ape > Great Ape > Human) and was notably highest in the rodent and low, but above the human, in elephant (Fig. 15A). Here, the median split distance was calculated using the measured distance among Split PCs and Normative PCs if one was present. A similar trend is observed if Poly PCs are included and their bifurcation distance set to 0 (Fig. 15B). The dropping median bifurcation distance is directly related to Poly PC prevalence (Fig. 15C, *right*).

Beyond dropping bifurcation distance, another feature of the PC demographic transition from mostly Normative and Split PCs to mostly Poly PCs might be the symmetry of primary dendrite compartments. The hypothesis that Poly PCs occupy an extreme position along a continuous axis

of dendrite compartmentalization predicts that some PCs might exhibit intermediate or transitional dendritic morphologies. Extremely short bifurcation distance among Split PCs may be one example of a 'transitional' cell type, especially when presenting with a thick proximal trunk compartment (Fig. 15C, *left*). Another example may be asymmetric growth of multiple dendrites among Poly PCs (Fig. 15D, *left*). By measuring the disparity of trunk thicknesses, we observed that the degree of trunk disparity correlated with the prevalence of Poly PCs in most species (Fig. 15D, *right*). Macaques conspicuously lack Poly PCs and diverge significantly from the inter-species trend in Poly PC trunk disparity, suggesting that macaque PCs may undergo a distinct dendrite growth paradigm.

Figure 15. Compartmentalization of primary dendrites is congruent with increasing prevalence of polydendritic PCs. A) Primary dendrite bifurcation distance from the soma as a function of molecular layer thickness across species. **B)** As in (A), including Poly PCs as 0 values. **C)** Cross-species median bifurcation distance normalized to ML thickness (among Normative and Split PCs) by the prevalence of Poly PCs. **D)** Example cells showing the range from symmetrical to asymmetrical dendrite thicknesses among Poly PCs (*left*). Cross-species median disparity between trunk thickness (smallest as a percentage of the largest; among Poly PCs) by the prevalence of Poly PCs (*right*). Yellow trend line includes all species while black trend line excludes the macaque outlier. **E)** Split angle across species. **F)** Polydendritic trunk angle across species.
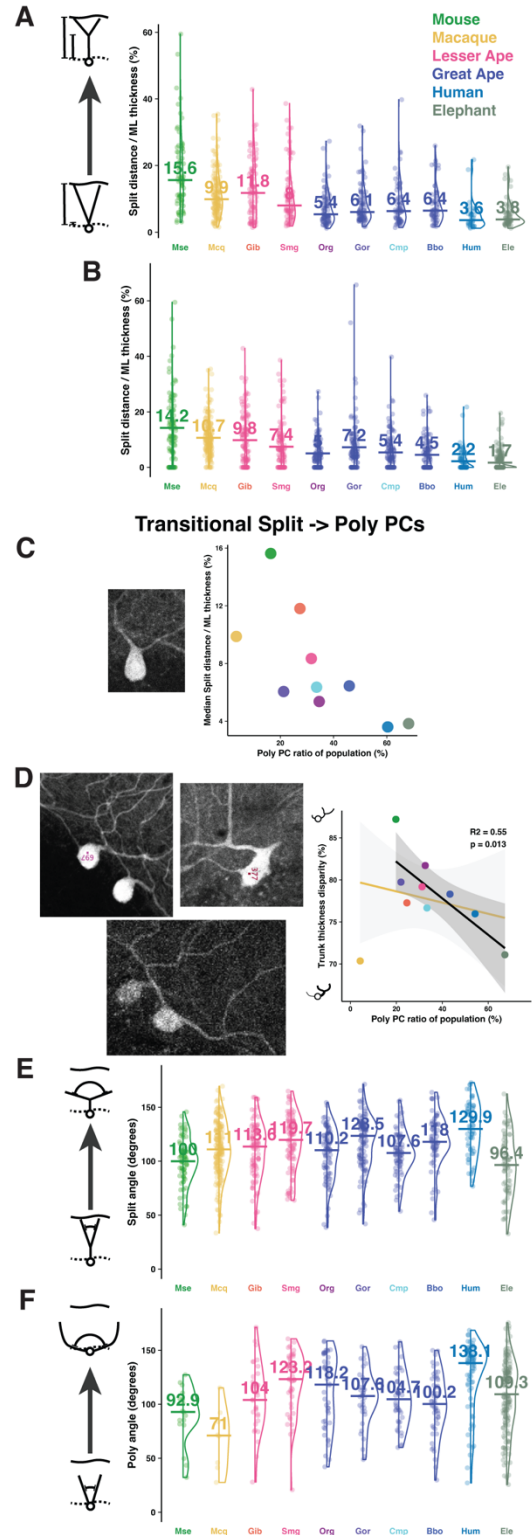
We next analyzed how segregated in space the primary dendrite compartments become across species. The bifurcation distance sets the floor for compartmentalization by dictating the earliest point at which compartment segregation can occur during the trajectory of dendrite development. Many additional factors, however, combine to articulate the final contours of compartmentalization. Chief among these factors is the angle of primary dendrite separation either at the bifurcation (Fig. 15E) or as they emerge directly from the soma (Fig. 15F). Unlike the largely progressive inter-species decrease in bifurcation distance, split and poly angles both exhibited substantial inter-species variation amid a broad, modest trend of increasing angles across primate clades. Most notably, while the human exhibits a shorter split distance than Great Apes, the difference is consistent with the trajectory across primate clades. On the other hand, the median and distribution of split and poly angles in human stands apart from and exceeds the primate trend.

Human dendritic area exceeds the primate phylogenetic trend to expand the input field beyond expectation

Having observed that human PC compartmentalization exceeds expectation based on the primate trajectory, we next asked how this might impact their input. PC dendrites are flat and expand laterally in the parasagittal axis. They integrate thousands of orthogonally projecting parallel fiber inputs passing through their arbor. Given the geometrical organization of the cerebellar cortical circuit (and consistent spine density), the parasagittal dimensions of the PC dendritic arbor indicate the size of their GC input array. The height of the dendritic arbor is defined by the thickness of the molecular layer (ML), which is not simply defined by allometry (see below; Fig. 18A). For a subset of cells with more complete dendrites, we measured the distance between dendritic compartment centroids (see Appendix 1: Methodology and Statistics) as a proxy for the

degree of horizontal parasagittal ramification of the dendrites. To control for differences in cell size, we normalized this trunk separation measure by the somatic diameter. This revealed not only a general trend of increasing dendritic width with phylogenetic proximity to human, but an unexpectedly large increase in dendritic width among human PCs (Fig. 16A). The relative width of PC dendrites vs their origin somatic compartment in human exceeds even that of the elephant, whose substantially larger somas overcompensate for their larger dendrites even more than most Great Apes.

In most species, trunk separation distance has a modest positive relationship with split angle (Fig. 16B) and polydendrite angle (Fig. 16C). Human split cells are the exception as their trunk separation distance is, invariably, wider than those of every other species, except those elephant cells with the widest split angles. It is worth noting, however, that these relationships are modest specifically among the primates. This indicates that other variables are involved in dictating dendritic width and thus, there are a wide variety of dendritic structures present in primates while dendritic shape is more readily predicted by fewer variables in the non-primate species in our study (mouse and elephant).
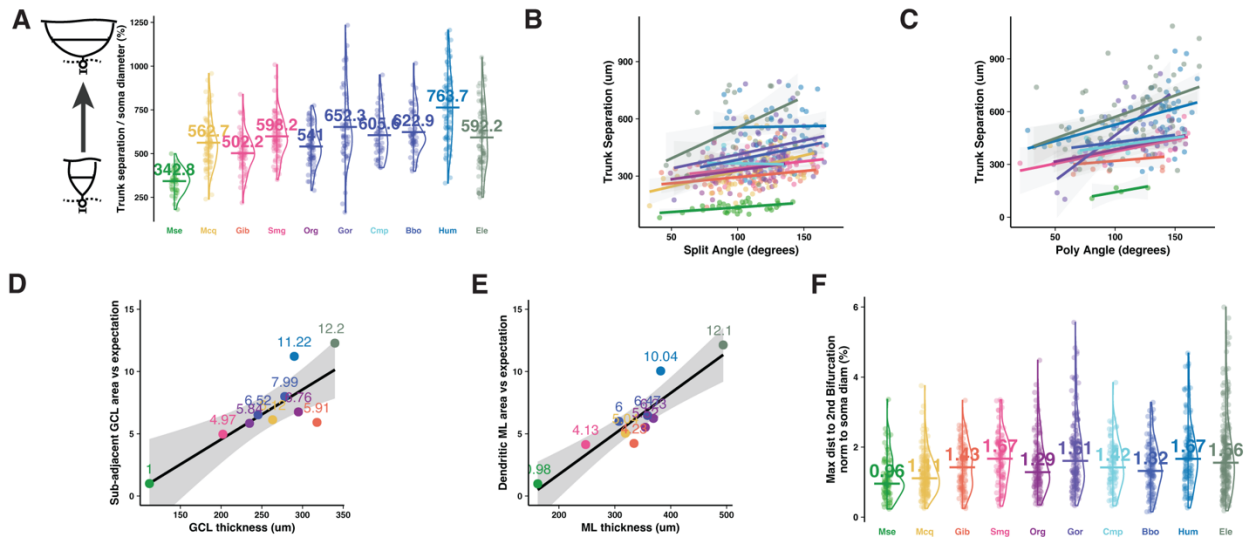
Figure 16. Human dendritic area exceeds the primate phylogenetic trend to expand the input field beyond expectation. A) Distance between primary dendrite compartment centroids across

species. **B)** Relationship between split angle and distance between primary dendrite compartment centroids. **C)** Relationship between polydendritic trunk angle and distance between primary dendrite compartment centroids. **D)** Relationship between GCL thickness and the fraction by which the sub-adjacent GCL area exceeds the expectation set in mouse. **E)** Relationship between ML thickness and the fraction by which the dendritic area within the ML exceeds the expectation set in mouse.

We next asked whether we could determine the approximate relative GC input array size across species based on the measurements we collected and previously reported features of the circuit anatomy. GC PFs project orthogonally with the dendritic arbor, allowing us to start with the assumption that all GC inputs are located in an area of the GCL that is sub-adjacent to the PC in question and extends in the mediolateral plane by variable distances. Using our knowledge of circuit anatomy in the rodent, we calculated that the dendritic area within the ML (ML thickness * (2 * Trunk separation)) precisely matched the area (Fig. 16E) expected based on: a) the expected number of PF contacted PC spines (~40,000; (Busch & Hansel, 2024)), b) the percent of ML area containing PFs (42%), c) PF thickness (0.15um; (Wyatt et al., 2005)), and d) PF-PC connection probability (49%; (Nguyen et al., 2023)) (see Appendix 1: Methodology and Statistics). As we also have a recent approximation of total PF inputs to a human PC (~600,000; (Busch & Hansel, 2024)), so we next compared the expected (in rodent) and actual (human) dendritic ML area and observed that the human dendritic area was 10x that expected. This roughly matches both the difference in total dendritic length in the human vs mouse and, considering increased medio-lateral thickness of the dendrites and increased length of the PFs (~3x, thus permitting more distal GCs to contact a PC), the extrapolated difference in the total number of inputs. Observing how this matched the expectation in both species, the same comparison was then performed for the remaining species. We also performed the analogous calculation for the size of the sub-adjacent GCL in each species,

this time based on GC soma area and packing density in the GCL and observed a similar trend across species (Fig. 16D).

Decreased split distance gives access to a wider range of primary dendrite thicknesses

We next asked whether very proximal primary trunk bifurcations provide an advantage over more distant bifurcations beyond the opportunity to have a wider separation between primary dendrite compartments. We found that PCs with shorter split distances exhibited more variable trunk thickness (Fig. 17A-C). The average thickness of primary dendrites with the shortest split distances best represents species divergence in trunk thickness from ~4um in mouse to ~22um in elephant, whereas dendrites with longer split distances strongly converge on a thickness of ~5um, seemingly a conserved value across primates that further resembles the thickness of dendrites from species with such variable sizes as mouse (~4um) and elephant (~8um). Thus, not only does a dendrite growth program favoring short split distances permit higher Poly PC prevalence, but also permits a wider variation in contiguity between the somatic compartment at the convergence point for separated primary dendrite compartments.
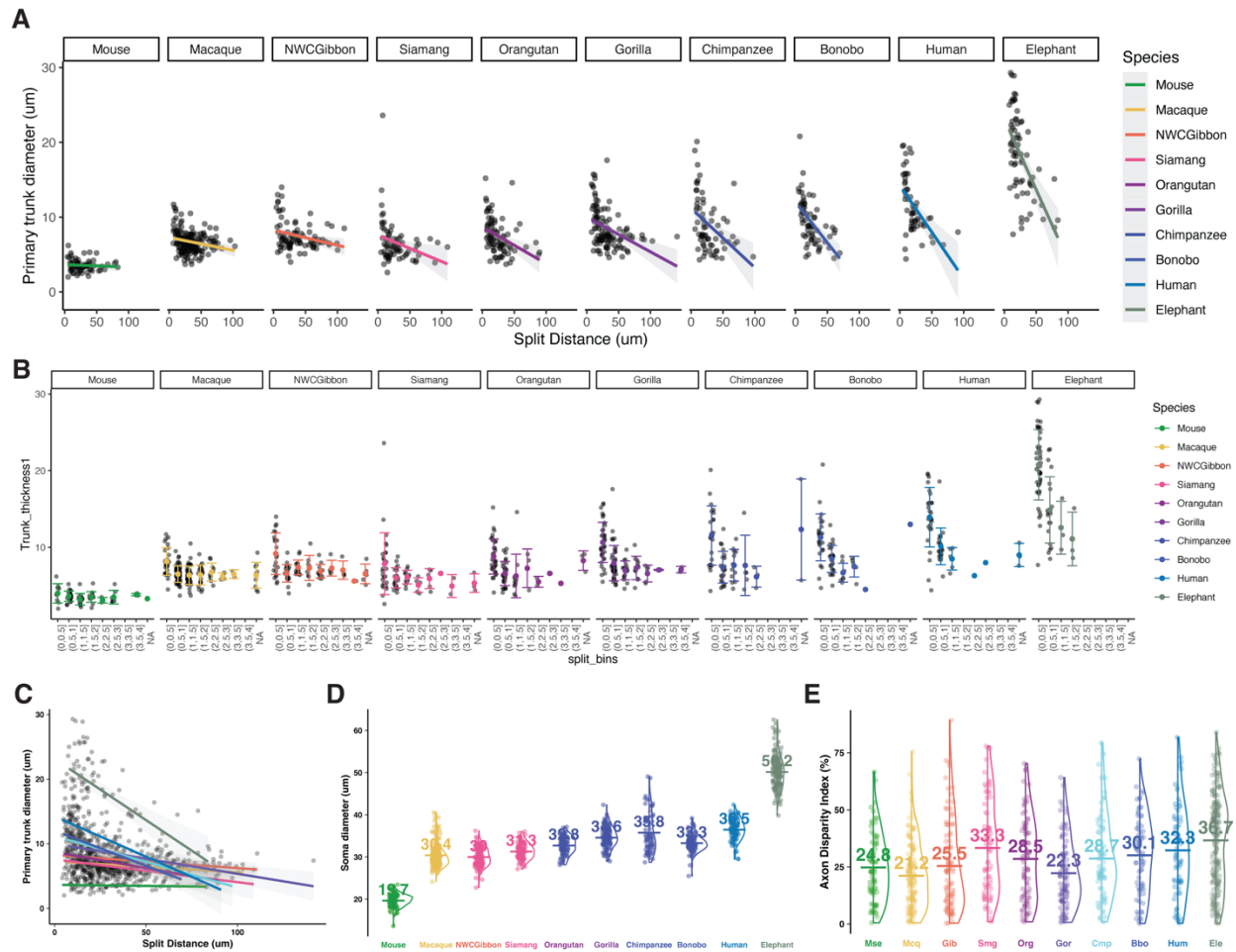
Figure 17. PCs with decreased split distance access a wider range of primary dendrite thicknesses. A) Primary dendrite diameter as a factor of split distance separated by species. **B)** As in (A), but cells are sorted into bins of split distance relative to somatic diameter. **C)** As in (A-B) collapsed across species to highlight the convergence of trunk size with longer split distaces. **D)** Somatic diameter by species. **E)** Axon offset index from perfectly polar to the primary dendrite.

Human PC arbor dimensions exceed allometric constraint

Human PC trunk separation exceeds the primate trend with respect to phylogenetic proximity. Is this due merely to allometric factors? It is conceivable that with a larger brain size, there might be increased cortical thickness and thus greater space for the human PC to grow. Indeed, the thickness of the molecular and granule cell layers roughly increase in conjunction with the log-scaled average size of each species' body (Fig. 18A-B) and brain size (Fig. 18C-D). The mean PC

trunk separation of each species roughly obtains to allometry, except in the case of humans (Fig. 18E).

In many ways, PC morphology does not conform to those allometric constraints, particularly in the human. Human trunk separation exceeds the trends predicted by phylogenetic distance, calculated as the distance to the latest common ancestor (Fig. 18F), or intra-individual allometric relationships such as the relative mass of the cerebellum compared with the size of the body (Fig. 18G) or the size of the neocortex (Fig. 18H). The exceptional position of human represents a confluence between the unusually large PC dendritic arbor and brain (Fig. 18G). Neocortical mass grows substantially among primates specifically, keeping the relative mass of cerebellum low compared with Elephant. The cerebellum is enriched by granule cells, which may expand cell number and possibly signal representation to match or even exceed the relative change in neocortex. Thus, the exceptional position of human in Fig. 18H may indicate that human PCs expand their input field and signaling capacity to match neocortical expansion. These data thus favor the interpretation that PC morphology varies according to functional needs, not due simply to brain size.
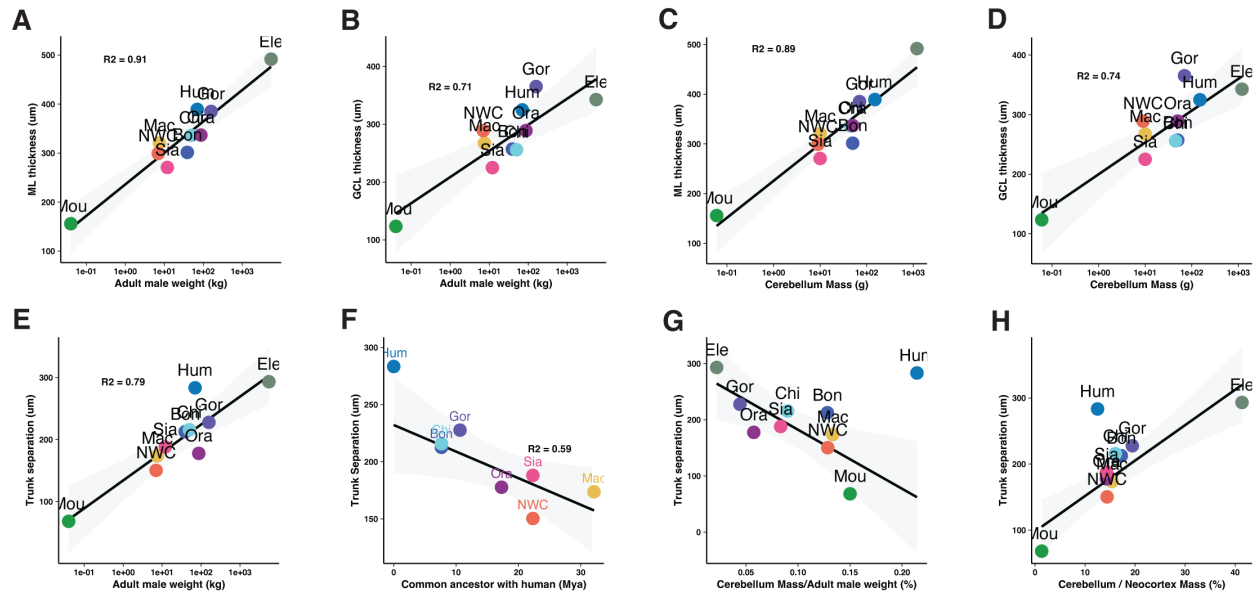
Figure 18. Human PC size exceeds the allometric constraints of cerebellar cortical thickness and body size. A-B) Thickness of either the molecular layer or the granule cell layer as a factor of the average weight of an adult male of each species. **C-D)** As in (A-B), with cortical thicknesses as a factor of cerebellar mass of each species. **E-H)** Parasagittal distance between primary dendrite compartments as a factor of adult male weight (E), distance to the common ancestor with human (F), relative cerebellar to total body mass (G), relative cerebellar to neocortical mass (H). Regression lines in F-H exclude human.

Foliation only loosely and variably explains PC morphology across species

PC morphology may also plausibly be largely dependent on cerebellar foliation. To test this, PCs were assigned location identities either in the gyrus, bank, or sulcus or in additional categories for intermediate versions of a gyral or sulcal region (see Appendix 1: Methodology and Statistics). Intriguingly, foliation appears to modestly influence factors construed to be allometric and invariable within species, such as soma diameter (Fig. 19A). Foliation appears to exert variable degrees of influence on soma diameter across species (Fig. 19B).

Foliation does appear to influence some features of PC dendrite morphology, such as Poly dendrite trunk angle (Fig. 19C). Again, foliation appears to influence poly angle by variable extents across species and is thus not a universally shared phenomenon of tissue folding mechanics. It is

also notable that there is substantial variation—more than for soma diameter— in the poly angle across foliar subdivisions. This suggests that while foliation plays some role, it is not total and that a wide variation of PC morphologies can be present anywhere in the cortex.

A

B

C

Figure 19. Cerebellar foliation influences some morphological features but does so differentially across species. A) Somatic diameter of cells across foliar sub-regions by species. **B)** Breakdown of somatic diameter distribution across foliar sub-regions in some example species. **C)** The angle between trunks emerging directly from the soma (Poly PCs) across foliar sub-regions by species.

Specifying the role of compartmentalization on signal processing

How does PC dendrite compartmentalization influence signal processing? While the primate species used in this study are largely, if not entirely, inaccessible to physiological experiments, we can attempt to address this question using single cell modeling. We performed the first reported

manual reconstruction of a complete macaque PC (Fig. 20A), used customized NEURON modeling software to segment dendrite compartments (Fig. 20B), and simulated PC spiking behavior. Whole cell patch clamp recordings of macaque PCs *in vivo*, as a ground truth for the target model behavior, do not yet exist. Thus, we adjusted ionic conductances within the model from a starting parameter space derived from established models of guinea pig neurons (Cirtala & De Schutter, 2024; Zang et al., 2018) to achieve approximately regular spiking properties and shape in the new model (Fig. 20C). The same procedure was applied to a manually reconstructed human PC.

We then compared dendrite and spine morphological differences between macaque and human PCs. Using high resolution confocal imaging, we estimated spine densities across numerous dendritic segments of distinct branching orders relative to the soma (>3 segments per branching order, n = 3 macaque PCs and 1 human PC). This revealed that spine density per linear dendritic length is low and modestly increases with branching among the classically thick 'smooth' primary dendrites (orders 0-2; Fig. 20D). Spine density is much higher on classically thin 'spiny' dendrites (order 4), particularly on the terminal segments of the thin branches (order 5). These traits were shared in both species, but with a higher spine density across orders after the second branching level in the human than the macaque. Regardless of branching order, spine density increased in a roughly exponential manner with decreasing diameter (Fig. 20E), further highlighted when presented on a log-scale (Fig. 20F).
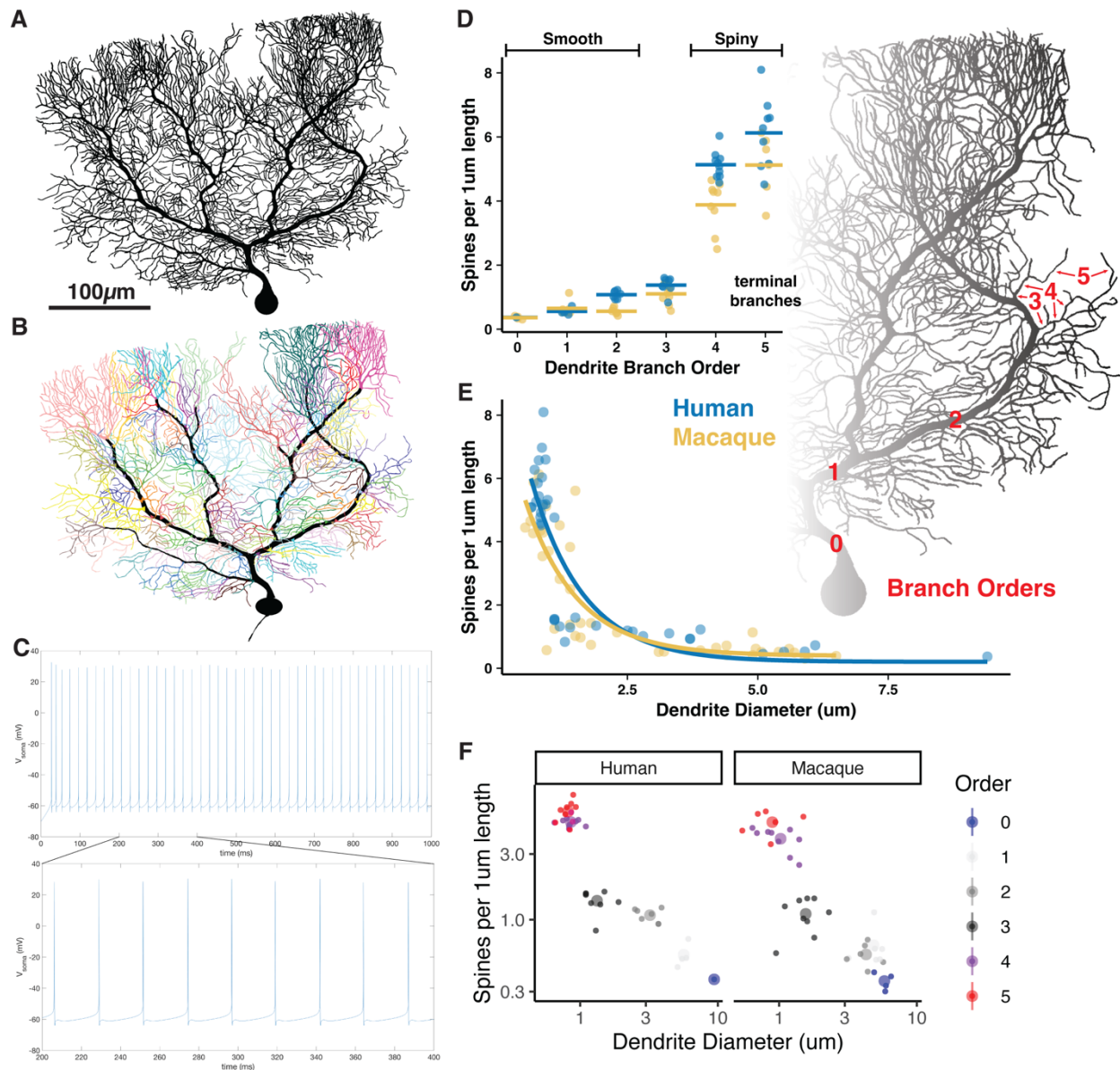
Figure 20. Single cell modeling of manually reconstructed macaque PC and comparative macaque vs human spine density. A) Full manual reconstruction of a macaque PC. **B)** Dendrite sub-section segmentation in the NEURON model of the cell in (A). **C)** Preliminary spike train (*top*) with physiologically relevant firing rate and spike shape (zoomed trace, *bottom*). **D)** Spine density along dendritic segments by branching order across human and macaque. **E)** Spine density by dendrite segment mean diameter. **F)** As in (E) but separated by species and plotted on a log-scale to highlight the exponential relationship.

Discussion

We used comparative histology across a wide array of species to map the evolutionary trajectory of Purkinje cell dendritic morphology profiles. Using our recent morphology categorization framework in human and mouse, we revealed that the prevalence of multi-branched (Split and Poly) and horizontally oriented PCs varied along phylogenetic boundaries with some regularity. The high prevalence of Poly PCs in human is thus partly a feature of Hominoidea (apes) that distinguishes them from Cercopithecidae monkeys (their fellow Catarrhines) and Platyrrhine monkeys (a separate branch within Anthropoidea), and partly a result of continued evolution that distinguishes them from the rest of the Hominoidea lineage. By measuring a panel of anatomical and morphological parameters in >120 cells per species, we provide a rich characterization of dendrite growth that reveals distinct evolutionary trajectories of each factor. Dendritic morphology is diverse, resulting in a wide variation of each parameter and its relationships with other parameters. Yet, some patterns stood out, such as the linear drop in the median distance from the somatic compartment to the bifurcation of primary dendrite compartments. A dropping bifurcation distance explains the heightened prevalence of Poly PCs in human. Alongside other parameters (e.g. bifurcation angle and parasagittal compartment distance), this trend reveals a tendency for highly segregated compartmentalization of the dendritic arbor that arises both as a gradual trend through primate evolution, but also as a distinct, human-specific jump in morphological complexity.

Though cerebellar cortical circuit anatomy is often considered simplistic—or at least straightforward—and stereotypical, the picture is becoming more clearly complicated. Some features are constant across cerebellar regions and species: granule cell size and morphology, PF density and orthogonal (mediolateral) projection relative to flat parasagittal PCs, and PCs

generating the sole output of the cerebellar cortex. That evolution left those features untouched makes it more intriguing that it generated substantial diversity in PC dendritic morphology.

Amid a conserved circuit architecture, the morphological parameters we describe may influence PC physiology. We have previously shown that the presence and spatial segregation of multiple primary dendrites in PCs can strongly impact CF-PC connectivity, permitting non-canonical CF multi-innervation and heterogeneous CF RF signaling across primary dendrite compartments (Busch & Hansel, 2023). Despite limited experimental access to human, we are beginning to demonstrate a similar effect of dendrite morphology on CF multi-innervation in human (Busch & Hansel, 2024). In this study, we present high variation—within and across species—in dendritic parameters that may influence CF input connectivity (multi-branched motif prevalence, Split distance, poly angle, trunk separation), the PF and MLI input field size (dendritic width and height), the compartmentalization of synaptic input and dendritic signaling (split distance and angle, poly angle, secondary bifurcation distances and angles, primary dendrite compartment symmetry), and electrotonic conductance (trunk thickness, somatic diameter, axon disparity).

Neither allometry nor foliation mechanics are sufficient to predict these results, particularly in humans. Though this study focused on PCs in the Crus 1 region of the hemisphere, the data may support the hypothesis that PC morphology underlies functional specificity by cerebellar region and species. Recent comparative studies of neocortical pyramidal cells have revealed a similar expansion of morphological and physiological complexity in the primate lineage and particularly in human (Beaulieu-Laroche et al., 2018, 2021; Benavides-Piccione et al., 2002; Mohan et al., 2015). Similar morphological observations have also been made in the hippocampus (Benavides-Piccione et al., 2020). Taken together, our data reveal a startling diversity and complexity of

dendritic morphology both within and across species in a highly conserved brain region that is classically considered stereotypical in structure. Thus, the cerebellum joins the set of brain structures for which evolutionary adaptation is detectable at the level of cellular morphology and physiology.

CHAPTER 5

ABERRANT CLIMBING FIBER INNERVATION DISRUPTS SENSORY

RESPONSIVENESS IN PURKINJE DENDRITE SIGNALING AND BEHAVIOR IN TWO

MOUSE MODELS OF AUTISM

This chapter contains two manuscripts to which I contributed as second and first author, respectively. For simplicity, the manuscripts are reprinted here in full with permission from the publishers and the other authors. I clarify my role in each below. In the General Discussion (Chapter 7), I direct the reader to the portions I completed and how it pertains to my dissertation.

My contributions to the first paper were conducting the investigation to generate Figures 1+3 (here Figures 21+23), retrieving all stored data to compile the manuscript after the first author graduated, co-writing the manuscript with Dr. Hansel, and addressing reviewer comments with experiments generating Supplementary Figures 1-5 (here Appendix Figures 21-25). My contributions to the second paper were conducting the investigation to generate Figures 2+4-5 (here Figures 28+30-31), coordinating and in part assisting collaborators to collect the data for Figure 1 (here Figure 27), retrieving all stored data to compile the manuscript, co-writing the manuscript with Dr. Hansel, and addressing reviewer comments with experiments generating Supplementary Figures 1-5 (here Appendix Figures 28-32).

1. Simmons, DH, Busch SE, Titley, HK, Grasselli, G, Shih, J, Du, X, Wei, C, Gomez, CM, Piochon, C and Hansel C. (2022) Sensory over-responsivity and aberrant plasticity in cerebellar cortex in a mouse model of syndromic autism. *Biological Psychiatry: Global Open Science*, 2: 450-459. https://doi.org/10.1016/j.bpsgos.2021.09.004

2. Busch SE, Simmons, DH, Gama, E, Du, X, Longo, F, Gomez, CM, Klann, E and Hansel C. (2022) Overexpression of the autism candidate gene Cyfip1 pathologically enhances olivo-cerebellar signaling in mice. *Frontiers in Cellular Neuroscience*, 17: 1219270. https://doi.org/10.3389/fncel.2023.1219270

PART 1
Sensory Over-responsivity and Aberrant Plasticity in Cerebellar Cortex in a Mouse Model of Syndromic Autism

Abstract

BACKGROUND: Patients with autism spectrum disorder often show altered responses to sensory stimuli as well as motor deficits, including an impairment of delay eyeblink conditioning, which involves integration of sensory signals in the cerebellum. Here, we identify abnormalities in parallel fiber (PF) and climbing fiber (CF) signaling in the mouse cerebellar cortex that may contribute to these pathologies.

METHODS: We used a mouse model for the human 15q11-13 duplication (patDp/+) and studied responses to sensory stimuli in Purkinje cells from awake mice using two-photon imaging of GCaMP6f signals. Moreover, we examined synaptic transmission and plasticity using in vitro electrophysiological, immunohistochemical, and confocal microscopic techniques.

RESULTS: We found that spontaneous and sensory-evoked CF-calcium transients are enhanced in patDp/+ Purkinje cells, and aversive movements are more severe across sensory modalities. We observed increased expression of the synaptic organizer NRXN1 at CF synapses and ectopic spread of these synapses to fine dendrites. CF–excitatory postsynaptic currents recorded from Purkinje cells are enlarged in patDp/+ mice, while responses to PF stimulation are reduced. Confocal measurements show reduced PF+CF-evoked spine calcium transients, a key trigger for

PF long-term depression, one of several plasticity types required for eyeblink conditioning learning. Long-term depression is impaired in patDp/+ mice but is rescued on pharmacological enhancement of calcium signaling.

CONCLUSIONS: Our findings suggest that this genetic abnormality causes a pathological inflation of CF signaling, possibly resulting from enhanced NRXN1 expression, with consequences for the representation of sensory stimuli by the CF input and for PF synaptic organization and plasticity.

Introduction

Synaptopathies play a dominant role in autism (Grant, 2012; Zoghbi, 2003; Zoghbi & Bear, 2012). However, it is difficult to directly relate synaptic to social abnormalities (Simmons et al., 2020). A promising complementary approach is to study simple motor behaviors—more easily linked to their underlying circuits—in the cerebellum (Kloth et al., 2015; Piochon et al., 2014). Impaired motor coordination is a common feature of autism spectrum disorder (ASD); a majority of children with ASD show motor problems (Fournier et al., 2010; Green et al., 2009), including difficulties with eye movement control (Johnson et al., 2013; Mosconi et al., 2013) and impaired delay eyeblink conditioning (EBC) (Oristaglio et al., 2013; Sears et al., 1994), a form of associative learning that requires the cerebellum (McCormick & Thompson, 1984). These findings place the cerebellum aside other brain structures that contribute to ASD-related behavioral abnormalities (S. S.-H. Wang et al., 2014). The advantages for circuit approaches are obvious: the cerebellum and its circuit architecture are conserved throughout vertebrate evolution, and results from EBC studies can be compared between humans and mice (Fanselow & Poulos, 2005).

In previous work, we have shown that EBC is impaired in a mouse model for the human 15q11-13 duplication (Piochon et al., 2014), a copy number variation that is one of the most frequent and penetrant genetic ASD causes (Cook et al., 1997) and is associated with motor problems (Bolton et al., 2001). In this model, mice inheriting the duplication paternally (patDp/+) show ASD-resembling deficits in social behaviors (Nakatani et al., 2009). In patDp/+ mice, we observed not only impaired delay EBC but also impaired long-term depression (LTD) at parallel fiber (PF)–Purkinje cell (PC) synapses (Hansel, 2019; Piochon et al., 2014). LTD is one of several plasticity mechanisms that contribute to this type of associative learning (Z. Gao et al., 2012; Hansel et al., 2001). In addition, blockade of long-term potentiation (LTP) at PF synapses (Schonewille et al., 2010), plasticity of inhibitory synapses (Boele et al., 2018), and intrinsic plasticity in PCs (Grasselli et al., 2020) have been found to reduce delay EBC performance. LTD is triggered by repetitive coactivation of PF and climbing fiber (CF) inputs (Ito et al., 1982; Ito & Kano, 1982) and is controlled by spine calcium signaling, because LTD has a higher calcium threshold than LTP (Coesmans et al., 2004; Piochon, Titley, et al., 2016; Titley et al., 2019). The olivocerebellar system plays a key role in this type of plasticity; the CF input conveys an error signal, for example in response to an airpuff directed to the eye in EBC (unconditioned stimulus). The contribution of CF signaling to LTD induction consists of an enhancement of the calcium signal in PF-contacted spines. Here, we focus on the characterization of physiological abnormalities that cause the deregulation of LTD, with a particular focus on aberrant CF signaling.

We found that the two types of excitatory input to PCs are altered in patDp/+ mice: PF synapses are weakened, whereas CF synapses are strengthened. Two-photon recordings reveal that CF-evoked calcium transients in response to sensory input are enhanced in awake patDp/+ mice, which also show stronger aversive motor responses, including faster eyelid closure when corneal airpuffs

are applied. We found ectopic CF synapses on fine dendritic branches, together with increased expression of NRXN1. PF-evoked spine calcium transients are reduced. LTD is blocked in patDp/+ mice but is rescued on pharmacological enhancement of calcium signaling with the ampakine CX546 (van Beugen et al., 2014). Thus, the 15q11-13 duplication results in pathologically enhanced CF signaling with consequences for PF input organization and plasticity and for the representation of sensory stimuli.

Results

To assess whether olivocerebellar signaling is altered in patDp/+ mice, we performed two-photon imaging from crus I in awake mice that express the genetically encoded calcium indicator GCaMP6f under control of the PC-specific promoter L7-cre (dual viral injection of GCaMP6f and L7-Cre AAV). PCs located in crus I are responsive to a wide range of sensory modalities (Bosman et al., 2010). In these recordings, dendritic arbors of 15 to 25 PCs viewed from the top appear as thin stripes (Fig. 21A). Calcium transients were calculated as ΔF/F values. Under spontaneous firing conditions, the calcium event rate was not significantly different between PCs from wild-type (WT) and patDp/+ mice (WT: 1.17 ± 0.03 Hz, n = 55 cells, 3 mice; patDp/+: 1.24 ± 0.02 Hz, n = 87 cells, 3 mice; p = 0.068) (Fig. 21B, C). However, both the calcium transient amplitude and its variability (standard error of event amplitudes for each cell) were significantly enhanced in patDp/+ mice (amplitude: WT: 0.22 ± 0.006 ΔF/F, patDp/+: 0.28 ± 0.005 ΔF/F, p = 3.387×10^{14}; variability: WT: 0.0331 ± 0.0013 SEM, patDp/+: 0.0467 ± 0.0011 SEM, p = 3.054×10^{13}) (Fig. 21B, C).

The amplitudes of calcium transients evoked by application of sensory stimuli were also significantly larger in PCs from patDp/+ mice than WT mice (stimuli were applied in random order using interstimulus intervals $\geq$30 s). This holds true when light pulses (488-nm light-emitting diode, 30 ms) were directed to the ipsilateral eye (WT: 0.56 ± 0.03 ΔF/F; patDp/+: 0.96 ± 0.05 ΔF/F; p = 1.36 x 10^{13}), airpuffs (10 psi, 30 ms) were directed to the ipsilateral whisker field (WT: 0.35 ± 0.04 ΔF/F; patDp/+: 0.56 ± 0.03 ΔF/F; p = 0.005), auditory stimuli (12 kHz pure tone, 70–80 dB; 30 ms) were presented (WT: 0.22 ± 0.01 ΔF/F; patDp/+: 0.54 ± 0.03 ΔF/F; p = 2.86 x 10^8), or all three stimuli were applied together (WT: 0.49 ± 0.03 ΔF/F; patDp/+: 0.99 ± 0.03 ΔF/F; p =< 1 x 10^{15}; for all stimulus conditions: WT: n = 55 cells, 3 mice; patDp/+: n = 87 cells, 3 mice) (Fig. 21D, E). Under control conditions (no stimulus), the largest calcium events within the same time window were 0.15 ± 0.01 ΔF/F (WT) and 0.22 ± 0.01 ΔF/F (patDp/+). Finally, as a reference measure, we applied airpuffs (10 psi, 30 ms) to the ipsilateral eye. This stimulus is used as the unconditioned stimulus in EBC and is known to evoke complex spikes. The resulting response amplitude in WT mice was 0.28 ± 0.02 ΔF/F, while in patDp/+ mice, it was 0.54 ± 0.03 ΔF/F (p = 0.001). These findings confirm previous observations that evoked calcium events are larger than spontaneous ones (Najafi et al., 2014b, 2014a) and show that the amplitudes of spontaneous and evoked calcium events are significantly larger in PCs from patDp/+ than WT mice. While it is known that evoked calcium events can result from a mixture of both CF and PF signals (Najafi et al., 2014b, 2014a), the enhanced amplitude of sensory-evoked calcium transients observed in patDp/+ mice at least partially reflects a change in CF signal. This is concluded because the amplitude of spontaneous calcium events—which occur at a frequency around 1 Hz that is characteristic of spontaneous CF firing (Simpson et al., 1996)—is similarly enhanced.
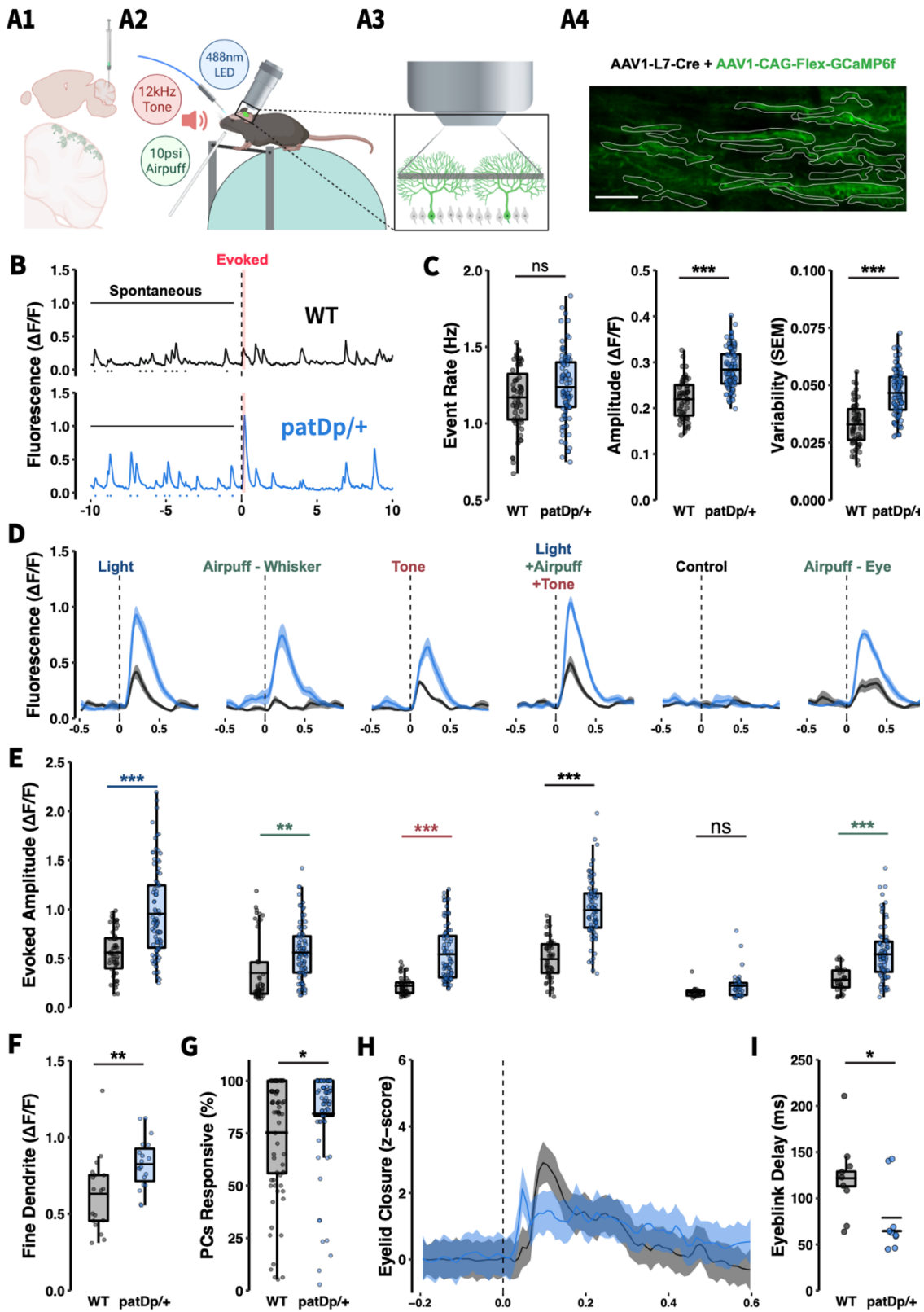
Figure 21. Spontaneous and sensory-evoked climbing fiber–mediated calcium events in PC dendrites are enhanced in awake patDp/+ mice. (A1) Dual viral injection of 2% AAV1-L7-Cre

and 10% AAV1-CAG-Flex-GCaMP6f produces strong expression in sparse PC populations in cerebellar crus 1. (**A2**) Schematic of the in vivo recording condition with light, airpuff, and sound stimuli administered while a mouse is head-fixed over a treadmill. (**A3**) Two-photon scanning of intermediate dendrites yielded clear, cell-wide dendritic calcium influx events. (A4) Sample imaging field of view with the dendrites of 19 healthy, active PCs. Scale bar = 50 μm. (**B**) Sample fluorescence traces extracted from individual cell regions of interest during a 20- second recording session with a light stimulus after 10 seconds. Spontaneous events were measured during the 0–9 seconds time frame before stimulus in each trial while evoked responses were measured during the 240-ms post-stimulus window (red). (**C**) Quantification of spontaneous event rates, amplitudes, and amplitude variability for each cell by genotype (WT, n = 55; patDp/+, n = 87). (**D**) Example traces from 1 WT and 1 patDp/+ cell highlighting trial-averaged evoked responses to sensory stimuli and control conditions (30-ms stimuli, 10 trials each). Light and airpuff stimuli were targeted to the ipsilateral eye or whisker pad. Tone stimuli were delivered through bilateral speakers. (**E**) Quantification of evoked response amplitudes for all cells in all animals by genotype (WT, n = 55; patDp/+, n = 87). (**F**) Quantification of evoked responses to light stimulus exclusively in fine dendrites in a subset of cells where large-caliber and fine dendrites were easily distinguished (WT, n = 19; patDp/+, n = 19). (**G**) Percentage of cells in a field of view producing an evoked response in the 240-ms window during each trial (three trials of eight stimulus types each for 3 animals per genotype; WT, n = 72; patDp/+, n = 72). The dashed line indicates the prediction that 25% of independently active cells with an average event rate of ~1 Hz are expected to be active at baseline during a 240-ms time window. (**H**) Genotype average z-score traces of the pixel intensity change in a region of interest encompassing the ipsilateral eye. Traces normalized to the mean z score value during 1.5 seconds before stimulus (WT, n = 9; patDp/+, n = 9). (**I**) Quantification of the delay to peak change in intensity by genotype (WT, n = 9; patDp/+, n = 9). $*p < 0.05$, $**p < 0.01$, $***p < 0.005$. Boxplots show mean line with interquartile range. Boxplot error bars show the least extreme of either the highest and lowest values or mean $\pm$ (1.5 x interquartile range). All traces show mean $\pm$ SEM. All data are noted in the text and legends as mean $\pm$ SEM. LED, light-emitting diode; ns, not significant; PC, Purkinje cell; WT, wild-type.

The recordings described earlier were performed from PC dendrites, roughly at equal distance from the soma and the pial surface. This measure includes dendritic compartments of various calibers. When analysis was restricted to calcium transients from fine dendrites [the PF input territory; see below (Strata & Rossi, 1998)], we still observed larger calcium transients in patDp/+ PCs (0.83 ± 0.04 $\Delta F/F$; n = 19; 2 mice; analyzed for the light stimulus) than in WT PCs (0.63 ± 0.06 $\Delta F/F$; n = 19; 2 mice; p = 0.008) (Fig. 21F). These findings show that the CF-evoked calcium

transients within the PF input zone are significantly enhanced in the ASD mouse model. The number of PCs showing an above-threshold calcium response was also enhanced in patDp/+ mice. Of the 15 to 25 PCs that we recorded from in each experiment, in WT mice, $75.2 \pm 3.3\%$ responded, while in patDp/+ mice, $85.5 \pm 2.6\%$ responded within a time window of 240 ms after stimulus onset ($p = 0.000248$; analyzed for all stimulus types combined; 3 trials per each of 8 stimulus types; 3 mice per genotype) (Fig. 21G; Appendix Figure S21).

Sensory stimulation also caused enhanced motor responses in patDp/+ mice. For example, corneal airpuff stimulation initiated eyelid closure that occurred with shorter delays in patDp/+ mice (WT: 121.86 ± 14.5 ms; patDp/+: 78.85 ± 12.74 ms; both genotypes: $n = 9$; $p = 0.0408$) (Fig. 21H, I) and longer persisting closure (Appendix Figure S22). Similarly, we observed enhanced movement of the front ipsilateral paw, facial structures (nose and ear), and chest in patDp/+ mice (Appendix Figures S23-25). Together, these findings point toward an increased sensitivity to sensory stimuli.

Differences in the amplitude of CF-evoked calcium transients may arise from changes in postsynaptic responsiveness but can also result from changes in presynaptic CF activity (Gaffield et al., 2019; Roh et al., 2020). To obtain an independent confirmation that CF signaling is enhanced in patDp/+ mice and that this effect can be a consequence of postsynaptic alterations, we applied single CF stimuli in vitro and examined CF–excitatory postsynaptic currents (EPSCs) in patch-clamp recordings from PCs. In WT mice, the amplitude of CF-EPSCs recorded at a -30 mV holding potential was 1.36 ± 0.12 nA ($n = 16$). CF-EPSC amplitudes recorded in patDp/+ mice were significantly higher (3.19 ± 0.41 nA; $n = 10$; $p = 0.0005$; Mann-Whitney U test) (Fig. 22A, B). At -70 mV holding potential, the CF-EPSC amplitudes recorded in WT PCs amounted to 3.09 ± 0.31 nA ($n = 7$), while those recorded from patDp/+ PCs reached 6.27 ± 0.78 nA ($n = 6$; $p = 0.008$) (Fig.

22C, D). The paired-pulse depression ratio (EPSC2/EPSC1) did not differ between the genotypes at either holding potential (-30 mV: WT: 0.79 ± 0.02, n = 16; patDp/+: 0.75 ± 0.02, n = 10; p = 0.1615; -70 mV: WT: 0.72 ± 0.05; n = 7; patDp/+: 0.66 ± 0.04, n = 6; p = 0.432) (Fig. 22B, D). These observations suggest that CF signaling is postsynaptically enhanced in patDp/+ mice, but they do not exclude the possibility of an additional change in CF burst firing.

The observed differences in CF response amplitudes may be associated with altered CF innervation. Developmental elimination of surplus CFs is delayed but reaches completion in patDp/+ mice (Piochon et al., 2014). In the adult cerebellum, CF synapses contact spines on the primary dendrite and first-degree branches, while PF synapses contact spines on higher-order branches (we use here the terms "large-caliber dendrites" and "fine dendrites") (Strata & Rossi, 1998). We used co-immunolabeling of cerebellar sections for the PC-specific marker calbindin and the CF terminal marker VGluT2 and segregated dendrites in the molecular layer into large-caliber (>2μm diameter) and fine dendrites to assess the distribution and density of CF terminals. We observed that the density of VGluT2-stained terminals on proximal, large-caliber dendrites was enhanced in patDp/+ mice (24.18 ± 1.17 VGluT2 spots/100 μm; n = 49 sections, 6 mice) as compared with WT mice (19.23 ± 0.9 VGluT2 spots/100 μm; n = 45 sections, 7 mice; p = 0.0014) (Fig. 22E, F). Similarly, we observed a higher density of VGluT2 terminals on fine dendrites of patDp/+ mice (7.52 ± 0.68 VGluT2 spots/100 μm; n = 28 sections, 6 mice) than WT mice (4.59 ± 0.5 VGluT2 spots/100 μm; n = 34 sections, 7 mice; p = 0.0019) (Fig. 22E, G). These findings show that in patDp/+ mice, the CF input forms ectopic synapses on fine dendrites.
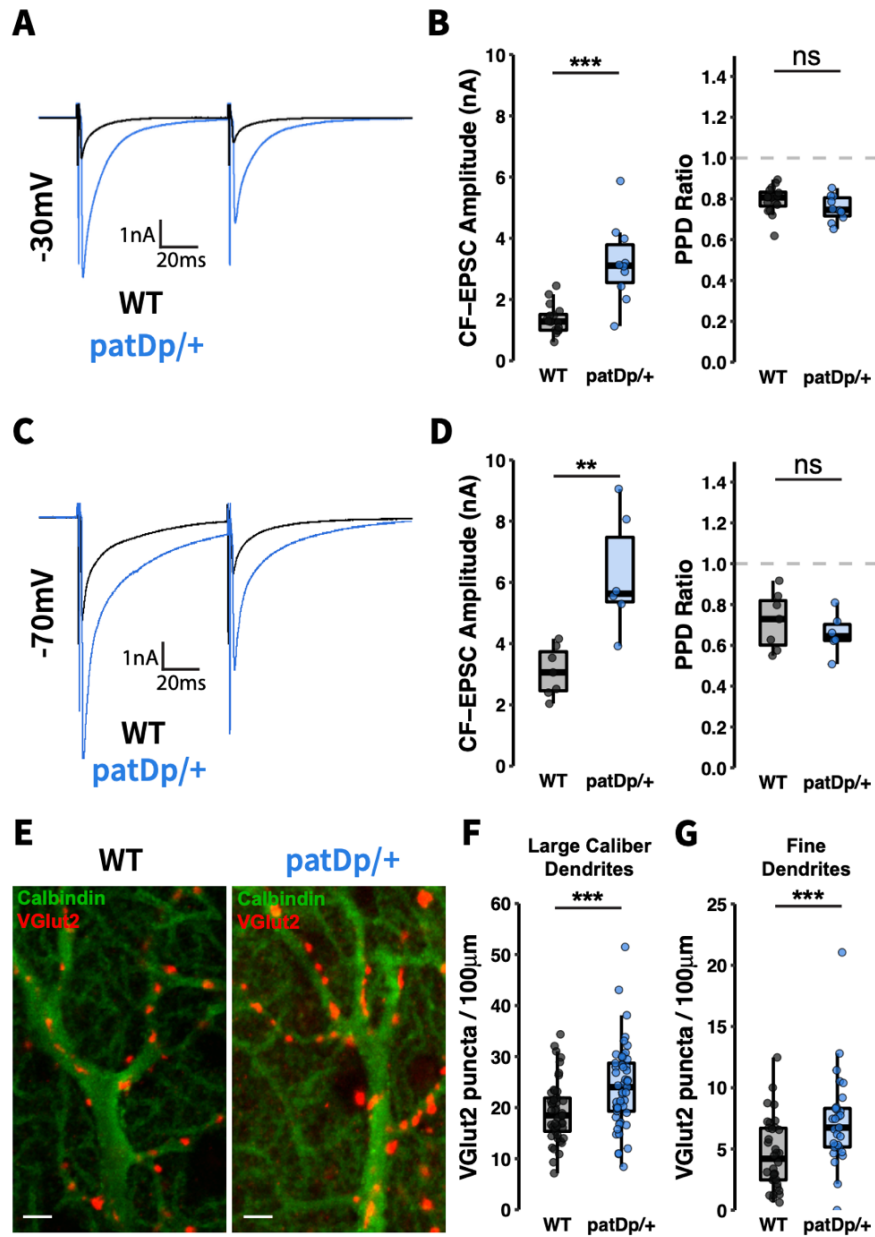
Figure 22. CF-PC synaptic transmission is enhanced in patDp/+ mice. (**A**) Typical CF-EPSCs recorded in WT and patDp/+ PCs at a holding potential of -30 mV. (**B**) Paired CF stimulations with a 100-ms interval show enhanced CF-EPSC amplitudes but equivalent paired-pulse depression in patDp/+ PCs compared with WT PCs (patDp/+, n = 10; WT, n = 16). (**C**) Typical CF-EPSCs recorded at a holding potential of -70 mV. (**D**) Again, paired CF stimulations show enhanced CF-EPSC amplitudes and equivalent paired-pulse depression in patDp/+ PCs compared with WT PCs (patDp/+, n = 6; WT, n = 7, respectively). (**E–G**) Dual label immunohistochemistry stains for calbindin (PCs) and VGlut2 (CF presynaptic terminals) in WT and patDp/+ cerebellar tissue reveals CF terminal arrangement on PC dendrites. Quantifying the number of VGlut2 puncta per 100-μm lengths of dendrite shows increased density of CF inputs to both (F) large-caliber (>2 μm)

primary dendrites (patDp/+, n = 49; WT, n = 45) and (G) fine dendritic branches (patDp/+, n = 28; WT, n = 34). Scale bar = 2 μm. *p < 0.05, **p < 0.01, ***p < 0.005. Boxplots show mean line with interquartile range. Boxplot error bars show the least extreme of either the highest and lowest values or mean ± (1.5 x interquartile range). All data are shown as median ± SEM. CF, climbing fiber; EPSC, excitatory postsynaptic current; ns, not significant; PC, Purkinje cell; PPD, paired-pulse depression; WT, wild-type.

The mouse model for the human 15q11-13 duplication is based on an interstitial duplication of the conserved linkage group on mouse chromosome 7, which is composed of about 23 genes (Nakatani et al., 2009). This group includes the ubiquitin protein ligase gene Ube3a, which is upregulated in patDp/+ mice (Piochon et al., 2014). To assess transcription profiles, we performed laser capture microdissection of PCs and quantified messenger RNA (mRNA) content by quantitative reverse transcriptase polymerase chain reaction for selected candidate genes. The laser microdissection led to the collection of PC somata (Fig. 23A), likely including proximal dendritic stumps, axon initial segments, and attached (mostly CF) synaptic terminals. In our selection of candidate mRNAs to be tested, we focused (Fig. 23B) on the synaptic organizer molecules neuroligin 1-3 (Nlgn1, Nlgn2, Nlgn3), cerebellin 1 (Cbln1), and neurexin 1 (Nrxn1); Ube3a; the translation control factors CYFIP1 (Cyfip1), eIF4E (Eif4e), and eIF4G (Eif4g); mGlu1 receptors (Grm1); and SK2-type K1 channels (Kcnn2). (For information on these genes, see Mouse Genome Database; http:// www.informatics.jax.org.) Several of these mRNAs showed significant changes in expression levels (Fig. 23B), but we focused on Nrxn1 because its change in mRNA levels was the most pronounced (increase over WT: 1487.3 ± 46.0%; p = 3.7822 x 10^{11}).
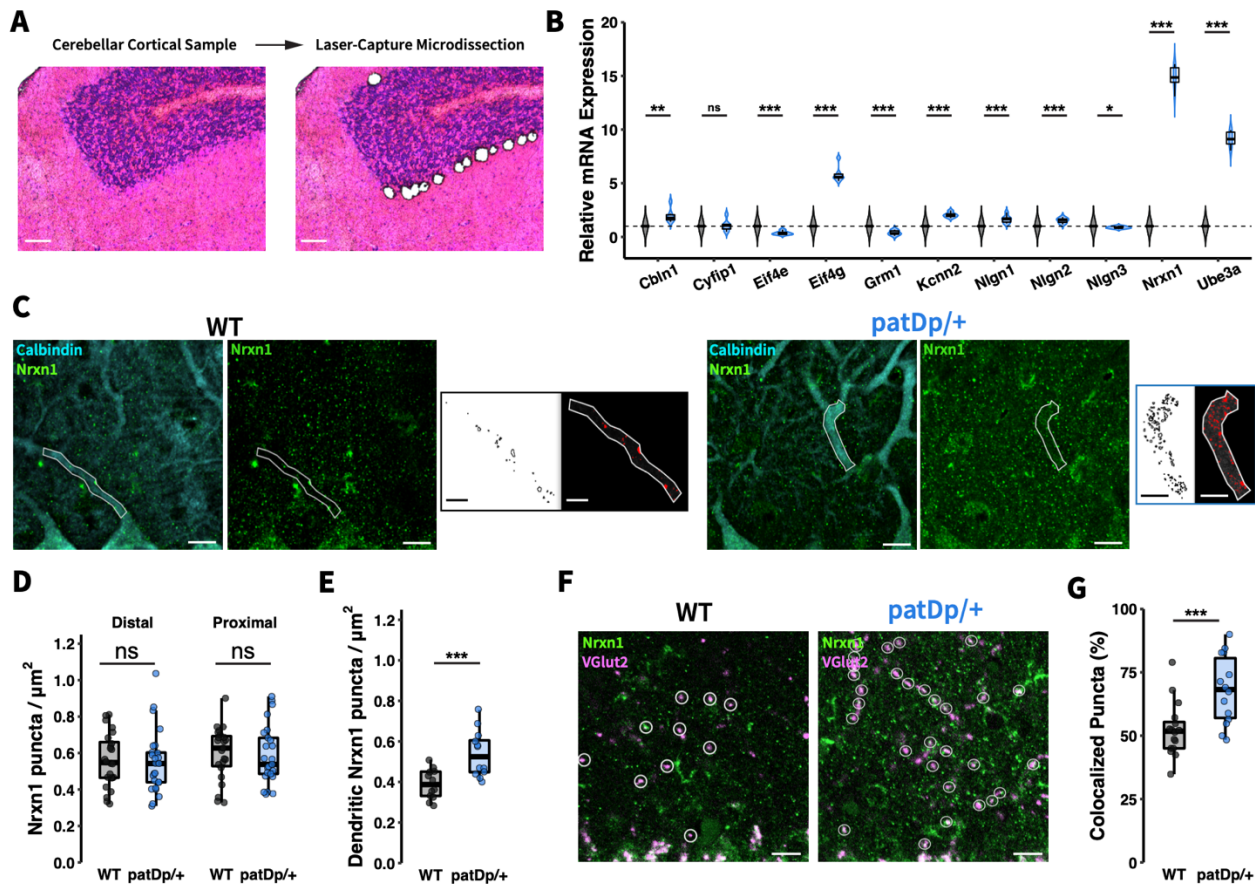
Figure 23. Altered expression and localization of the presynaptic organizer NRXN1. (**A**) Sample cerebellar cortical tissue before and after laser capture microdissection of Purkinje cell somatic regions for mRNA isolation and quantitative reverse transcriptase–polymerase chain reaction quantification. Scale bars = 50 μm. (**B**) Relative mRNA expression of genes of interest (n = 6, 6). (**C**) Triple label immunohistochemistry stains for calbindin (Purkinje cells), NRXN1, and VGlut2 (hidden for clarity) in WT and patDp/+ cerebellar tissue reveals NRXN1 localization patterns across the broad molecular layer and within sections of primary dendritic branches. Scale bars = 10 μm. NRXN1 channel thresholding highlights signal and objects detected in dendritic regions. Scale bars = 5 μm. (**D**) Quantifying the number of NRXN1 puncta across broad sections of the molecular layer does not reveal altered NRXN1 expression (WT, n = 24 sections; patDp/+, n = 25 sections). (**E**) Examining NRXN1 expression specifically in primary dendritic sections reveals enhanced NRXN1 puncta in patDp/+ tissue (n = 12) compared with WT (n = 12). (**F**) Manually counting and labeling VGlut2 puncta as NRXN1^{+} or NRXN1^{-} further defines the role of NRXN1 in enhanced CF–Purkinje cell transmission. Scale bars = 10 μm. (**G**) Colocalization analysis shows increased NRXN1 expression on climbing fiber terminals in patDp/+ tissue (n = 14) compared with WT (n = 16). *$p < 0.05$, **$p < 0.01$, ***$p < 0.005$. Boxplots show mean line with interquartile range. Boxplot error bars show the least extreme of either the highest and lowest values or mean ± (1.5 x interquartile range). All data are shown as median ± SEM. mRNA, messenger RNA; ns, not significant; WT, wild-type.

NRXN1 acts as a presynaptic organizer at both PF [with cerebellin 1 as binding partner (Matsuda et al., 2010; Uemura et al., 2010)] and CF synapses [with neuroligins 1 and 3 as binding partners (L. Y. Chen et al., 2017; Zhang et al., 2015)]. We performed immunohistochemical analysis using antibodies against calbindin and NRXN1 to assess whether NRXN1 levels are enhanced at these synapses. We did not find a difference in expression levels between WT and patDp/+ mice in either distal or proximal molecular layer compartments (Fig. 23C, D). We did note, however, a large range in NRXN1 counts, even in WT mice, which suggests that this measure may be affected by unspecific background stains and/or fluorescence from different focus planes. To overcome this problem, we next restricted analysis to fluorescent punctae that are colocalized with large-caliber, proximal dendritic compartments (calbindin staining), a measure that biases the count toward NRXN1 molecules located at CF terminals (CF input zone) (Strata & Rossi, 1998). In this measure, we observed an increase in the NRXN1 count in patDp/+ mice (0.54 ± 0.11 punctae/μm^2; n = 12 sections; 6 mice) as compared with WT littermates (0.39 ± 0.07 punctae/μm^2; n = 12 sections; 6 mice; p = 0.0035) (Fig. 23C, E). To examine whether NRXN1 is expressed at enhanced rates specifically at CF terminals, we analyzed the percentage of VGluT2-labeled CF terminals that showed costaining with NRXN1. Indeed, we found that a higher proportion of CF terminals across the molecular layer showed NRXN1 costaining in patDp/+ mice ($68.1 \pm 13.5\%$; n = 14 sections; 4 mice) compared with WT mice ($52.4 \pm 10.7\%$; n = 16 sections; 4 mice; p = 0.0022) (Fig. 23F, G). Together with the Nrxn1 mRNA increase that we observed after laser capture microdissection of PC somata (including CF terminals located on the soma and proximal dendrite), these findings suggest that the observed strengthening of CF input at least partially results from enhanced NRXN1 expression.

To assess whether PF synaptic transmission was similarly strengthened, we recorded responses to PF stimulation in PCs in vitro. In a previous study (Piochon et al., 2014), we have shown that isolated, single PF-EPSCs are unaffected in patDp/+ mice. We now looked at more dynamic response properties and applied a train of 5 PF stimuli at 10 Hz. In WT mice, we observed a buildup of response amplitudes over the course of the stimulus train (Fig. 24A), which was not seen in recordings from patDp/+ mice. Because there is no difference in the paired-pulse facilitation ratio at PF synapses between the two genotypes (Piochon et al., 2014), this buildup seems to be of largely postsynaptic origin. While no significant difference was observed with regard to excitatory postsynaptic potentials 1–4, significance emerged when comparing the amplitude of excitatory postsynaptic potential 5 (WT: 17.4 ± 3.9 mV; n = 12; patDp/+: 8.3 ± 1.7 mV; n = 8; p = 0.03) (Fig. 24B). Moreover, the number of evoked spikes (excitatory postsynaptic potential 5) was significantly lower than in WT mice (WT: 1.02 ± 0.23; patDp/+: 0.18 ± 0.10; p = 0.0093) (Fig. 24C). A particular signaling pathway that is required at PF synapses for the induction of LTD (Alba et al., 1994; Conquet et al., 1994) but not LTP (Belmeguenai et al., 2008) is the activation of mGluR1s. However, we did not find alterations in mGluR1 expression levels using western blotting analysis, nor did we find differences in an electrophysiological correlate of mGluR1 activation at PF to PC synapses—slow mGluR1-EPSCs (Tempia et al., 1998) (Appendix Figure S27).
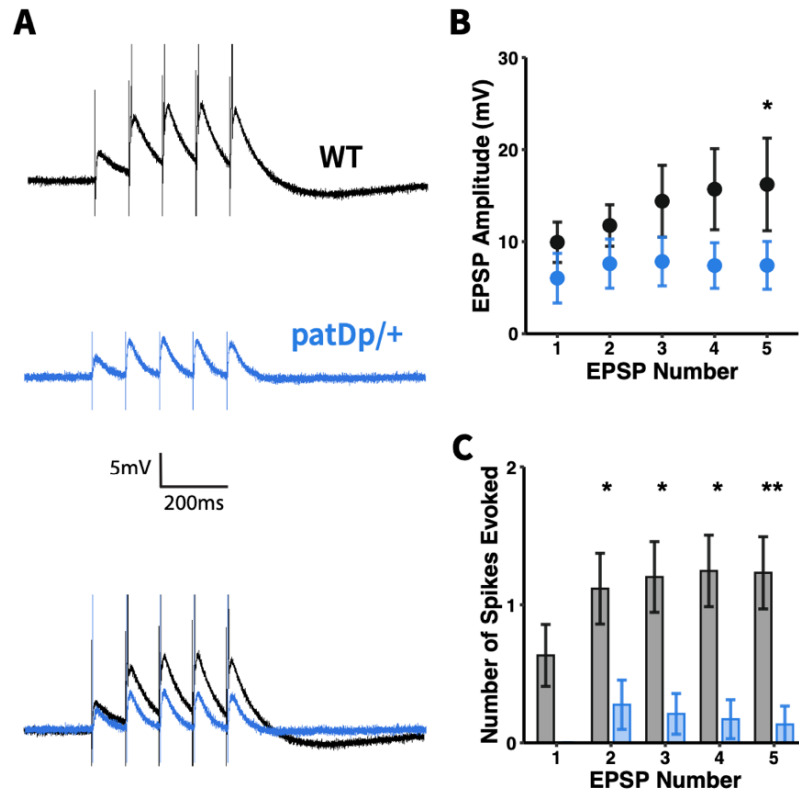
Figure 24. PF–Purkinje cell synaptic transmission is weakened in patDp/+ mice. (**A**) Typical PF–EPSPs recorded in WT and patDp/+ Purkinje cells. PF stimulation at 10 Hz for 5 pulses reveals weakened PF-EPSP synaptic transmission in patDp/+ Purkinje cells, indicated by panel (**B**) a reduced EPSP amplitude and (**C**) failure to reach a potential threshold necessary to evoke spikes (WT, n = 12; patDp/+, n = 8). $*p < 0.05$, $**p < 0.01$, $***p < 0.005$. Plots show mean ± SEM. All data are noted in the text and legends as mean ± SEM. EPSP, excitatory postsynaptic potential; PF, parallel fiber; WT, wild type.

Does the altered synaptic connectivity observed result in abnormal spine calcium transients? We performed confocal recordings of calcium transients in spines on fine dendritic branches to assess whether these signals are changed in patDp/+ PCs. We began with measures of resting calcium levels using the high-affinity ($K_d = 485$ nM) calcium indicator Oregon Green BAPTA-2 (200 μM) that was added to the patch pipette saline together with the calcium-insensitive fluorescent dye Alexa 633 (30 μM). Calcium levels were calculated based on the measurements of G/R ratios, where G is the calcium-sensitive fluorescence of Oregon Green BAPTA-2 and R is the

calcium-insensitive fluorescence of Alexa 633 (Piochon, Titley, et al., 2016). Resting calcium levels $[Ca^{2+}]_i$ were not significantly different between PCs from WT (132.1 ± 17.6 nM; n = 21) and patDp/+ mice (104.8 ± 24.9 nM; n = 11; p = 0.1527) (Fig. 25A, B). For the measurement of synaptically evoked spine calcium transients, we changed our approach slightly. First, expecting larger calcium transients than at resting state, we replaced the high-affinity calcium indicator Oregon Green BAPTA-2 with the low-affinity (K_d = 1.8 mM) indicator Fluo-5F (300 μM). Second, we switched from the calculation of absolute calcium levels $[Ca^{2+}]_i$ to normalized calcium transients ΔG/R, which are more accurate and still allow for quantitative comparisons of calcium signals. The calcium affinity of Fluo-5F is low, and CF-evoked calcium transients in the proximal dendrite, which have low amplitudes (Appendix Figure S27), may not reliably measure amplitude differences. We therefore only provide genotype comparisons between calcium transients evoked by PF bursts (8 PF stimuli at 100 Hz) paired or not paired with a single CF stimulus (LTD stimulus, 120 ms after PF stimulus onset). We observed that application of PF bursts alone caused reduced calcium transients in spines from patDp/+ PCs (WT: 0.43 ± 0.07 ΔG/R; n = 14; patDp/+: 0.14 ± 0.04 ΔG/R; n = 14; p = 0.0024). PF bursts followed by a CF stimulus also caused lower calcium transients in spines from patDp/+ PCs (0.29 ± 0.06 ΔG/R; n = 14) compared with WT PCs (0.65 ± 0.1 ΔG/R; n = 14; p = 0.0127) (Fig. 25D–G).
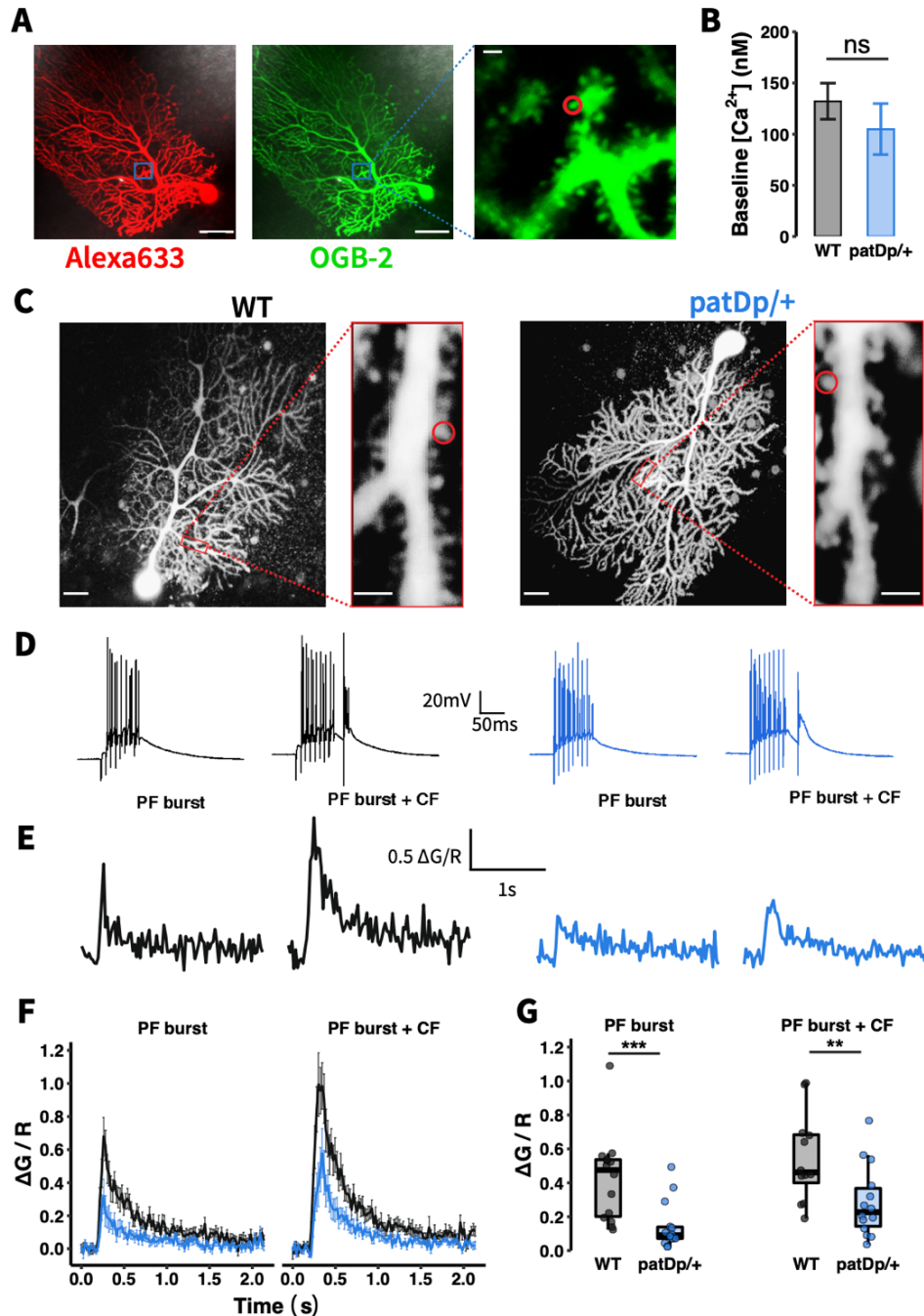
Figure 25. PF-evoked calcium transients are decreased in patDp/+ Purkinje cell spines. (**A**) Representative images of a patDp/+ Purkinje cell filled with OGB-2 Ca^{2+} indicator (green) and Alexa 633 dye (red) and visualized spines from that cell. Scale bars = left, 50 μm; right, 2 μm. (**B**) No difference between resting concentrations of Ca^{2+} between WT and patDp/+ spines (WT, n = 21; patDp/+, n = 11). (**C**) Representative images of WT (left) and patDp/+ (right) Purkinje cells filled with Fluo-5F Ca^{2+} indicator and Alexa 633 dye. Red box indicates the dendrite with the maximally responding spine. Scale bars = 20 μm (cell images) and 2 μm (dendrite/spine images). (**D**) Electrophysiological responses from somatic whole-cell patch clamp to two stimulus types:

100-Hz PF burst of 8 pulses alone (PF burst), and a 100-Hz PF burst of 8 pulses + 1 CF pulse (PF burst + CF). (**E**) Typical traces of simultaneously recorded spine Ca^{2+} transients during each stimulus type. (**F**) Mean ± SEM traces of Ca^{2+} transients for each stimulus type between WT and patDp/+ spines (WT, n = 14; patDp/+, n = 14). (**G**) Quantification of Ca^{2+} signal peak amplitudes during a 200-ms window after stimulus onset reveals diminished PF signaling (PF burst and PF burst + CF). *p < 0.05, **p < 0.01, ***p < 0.005. Boxplots show mean line with interquartile range. Boxplot error bars show the least extreme of either the highest and lowest values or mean ± (1.5 x interquartile range). Bar plots and average traces show mean ± SEM. All data are shown as median ± SEM. CF, climbing fiber; ns, not significant. OGB, Oregon Green BAPTA; PF, parallel fiber; WT, wild-type.

Finally, we tested whether LTD impairment resulted from reduced calcium signaling. PF-EPSCs were recorded in the test periods before and after application of the LTD protocol (tetanization), which consisted of a train of eight stimuli (100 Hz), followed 120 ms after stimulus onset by a single CF stimulus. This protocol was applied at 1 Hz for 5 minutes. In WT mice, tetanization resulted in LTD (72.2 ± 2.6%; t = 41-45 min; n = 5; p = 0.0004) (Fig. 26). In contrast, EPSC potentiation was seen in patDp/+ mice (149.7 ± 10.5%; t = 41-45 min; n = 7; p = 0.003; group comparison: p = 0.0058) (Fig. 26). The reduced calcium signal on PF+CF coactivation suggests that in patDp/+ mice, the calcium signal did not reach LTD threshold (Coesmans et al., 2004). If true, experimental manipulation of the calcium signal amplitude should restore LTD. We bath-applied the ampakine drug CX546 (300 μM), an allosteric modulator of AMPA receptors that enhances synaptic transmission by slowing receptor desensitization (Lynch, 2002) and in PCs enlarges dendritic calcium transients (van Beugen et al., 2014). In the presence of CX546, LTD was restored in patDp/+ mice (73.7 ± 5.7%, n = 6; p = 0.006) (Fig. 26); the LTD amplitude was not different from that observed in WT mice (72.2 ± 2.6%, n = 5; p = 0.0004; comparison: p = 0.65). This observation demonstrates that the impairment of LTD in patDp/+ mice resulted from a reduction in spine calcium transients (Fig. 25).
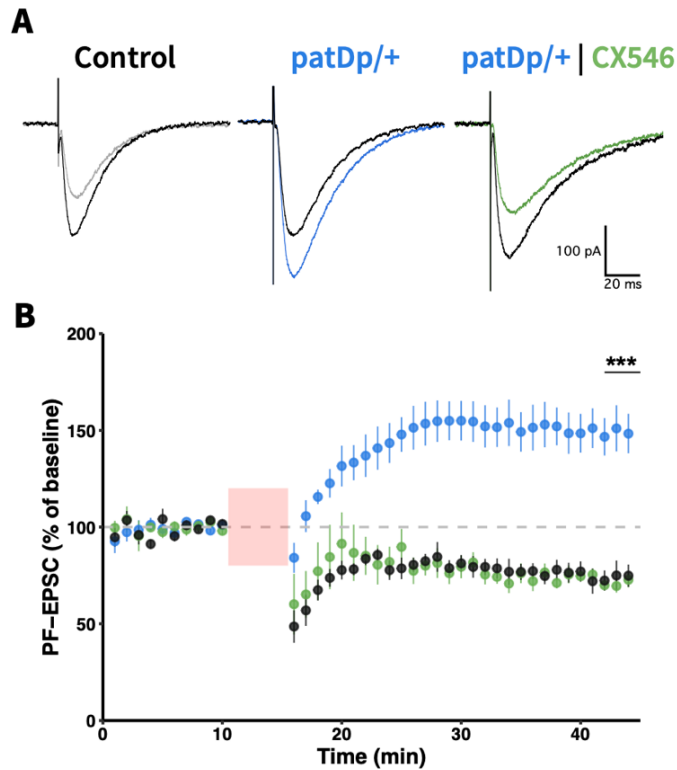
Figure 26. PF–Purkinje cell LTD is impaired in patDp/+ mice. (**A**) Typical PF-induced EPSCs in wild-type and patDp/+ Purkinje cells recorded before (black traces) and 30 minutes after (colored traces) tetanization using a LTD protocol, a 1-Hz train of stimuli over 5 minutes where each stimulus consists of a PF burst of 8 pulses at 100 Hz followed by 1 climbing fiber stimulation 120 ms after the first PF pulse. Scales = 100 pA, 20 ms. (**B**) Time graph showing PF-EPSC mean ± SEM amplitudes monitored during baseline (0–10 min) and post-tetanization (15–45 min) periods in wild-type (n = 5) and patDp/+ (n = 7) cells. Relative to wild-type, PF-LTD was impaired in patDp/+ cells, which instead underwent long-term potentiation. In the presence of CX546, an allosteric AMPA receptor modulator, patDp/+ cells show a rescued PF- LTD (n = 6). *p < 0.05, **p < 0.01, ***p < 0.005. Average traces show mean ± SEM. All data are noted in the text and legends as mean ± SEM. EPSC, excitatory postsynaptic current; LTD, long-term depression; PF, parallel fiber.

Discussion

A key observation is that CF signals recorded from PCs are stronger in patDp/+ mice than in WT mice. This increase is seen in CF-EPSC amplitudes, spontaneous CF-evoked calcium events, and responses of individual PCs and PC populations to sensory stimuli. CF responses in PCs are

compartmentalized: the complex spike is generated in the soma and is driven by the dendritic potential, but the latter is independently regulated (Davie et al., 2008; Ohtsuki et al., 2012). We will therefore consider enhanced CF signaling separately for 1) local dendritic phenotypes (LTD impairment) and 2) phenotypes that may result from an altered spike firing (Badura et al., 2013).

What is the origin of enhanced CF signaling? Mutations in genes encoding synaptic cell adhesion molecules, including neurexins, have been implicated in nonsyndromic ASD (Südhof, 2008). The finding that NRXN1 expression is altered in patDp/+ mice, a syndromic mouse model of ASD, therefore points toward a convergence in synaptopathies that may lead to ASD-related phenotypes. NRXN1 is a synaptic organizer at CF synapses; thus, enhanced NRXN1 expression may lead to an expansion of CF input territory and the increase in CF response amplitudes (Zhang et al., 2015). We did not observe an upregulation of NRXN1 protein in the molecular layer at large, a measure that would reflect changes in expression levels at PF synapses. However, a weakening of the PF input was evident from the reduction in synaptic weights and in calcium transients. An explanation for this PF signaling reduction can be found in the competitive relationship between CF and PF inputs. In the developmental competition for dendritic territory, the winner CF outcompetes weaker CF and PF inputs in a calcium-dependent manner (Ichikawa et al., 2016). In adult rodents, a similar phenomenon was observed after lesioning the inferior olive, which causes PC denervation from the CF input and a spread of PF synapses to former CF input sites. CFs surviving incomplete lesions sprout and reinnervate PCs, pushing PF synapses out from the proximal dendrite (Rossi et al., 1991). An underlying mechanism was identified in culture: δ2 glutamate receptors, which stabilize PF synapses, are internalized on calcium influx (Hirai, 2001). It is thus possible that the emergence of strong CF synapses diminishes the PF input territory by means of enhanced calcium signaling (Strata & Rossi, 1998).

In patDp/+ mice, we do observe an impairment of LTD [but not LTP (Piochon et al., 2014)]. Our confocal calcium imaging experiments show that the LTD deficit results from reduced calcium signaling at PF synapses. Thus, LTD is not saturated, as we previously concluded (Piochon et al., 2014). CX546 acts as an allosteric AMPA receptor modulator at CF and PF synapses, but here it is compensating for the deficit in PF signaling. One of the motor problems observed in patDp/+ mice is impaired EBC, which may be related to LTD deregulation. LTD is only one of several plasticity types involved in the proper execution of EBC (Z. Gao et al., 2012; Hansel et al., 2001). However, its deregulation alone removes one of the mechanisms underlying proper EBC execution. While not tested here, a prediction for future experiments is that pharmacological rescue of LTD will restore EBC in patDp/+ mice. This prediction is based on the observation that genetic rescue of LTD in mGluR12/2 mice results in normal EBC (Ichise et al., 2000; Kishimoto et al., 2002). Are there nonmotor consequences of LTD deregulation (Piochon, Kano, et al., 2016)? Previous mouse model work could not establish a link between LTD deregulation and impaired performance in nonmotor tasks (Galliano et al., 2013). An alternative view was suggested by Masao Ito in the early 1990s: cerebellar associative learning may be equally important for the construction of social behavior, thought, and language as it is for the construction of movement (Ito, 1993, 2008).

The enhanced presentation of sensory information to PC dendrites by CF synapses raises the question of whether this effect could have behavioral consequences related to CF's error signal function. There is no change in the complex spike waveform in patDp/+ mice (Piochon et al., 2014), but the observed increase in population response might well change the activation of target neurons in the cerebellar nuclei (Person & Raman, 2012). Note that in patDp/+ mice, there is no PC loss (Piochon et al., 2014), which could outbalance or hamper the enlarged population

response. The suggestion of a cerebellar contribution to nonmotor phenotypes in ASD is not new (Schmahmann & Sherman, 1998; Tsai, 2016; S. S.-H. Wang et al., 2014). Our findings allow us to specifically address one phenotype, sensory defensiveness, which does not constitute a diagnostic criterion but is frequently observed in ASD. This phenomenon describes negative reactions to sensory stimuli, including avoidance behaviors (Markram et al., 2007), and is also observed in children diagnosed with Dup15q syndrome (documented by the Dup15q Alliance: http://dup15q.org/care/sensory/). The sensory over-responsivity that we observed in CF signaling in patDp/+ mice may cause a faulty representation of error signals, e.g., in response to corneal airpuff stimulation. Whether or not such change in cerebellar output affects cognitive processes related to sensory defensiveness we cannot conclude from our findings. However, there are reasons that make this a plausible scenario. First, manipulation of cerebellar output has been shown to impair cognitive and social behaviors (Badura et al., 2018; Stoodley et al., 2017; Tsai et al., 2012). Second, in our experiments, patDp/+ mice show enhanced aversive movements on sensory stimulation, which places the observed sensory over-responsivity in context of startle-resembling behaviors. Third, clinical observations show that cerebellar diseases can lead to tactile defensiveness and sensory overload (Schmahmann et al., 2007), establishing a link between cerebellar dysfunction and abnormal sensory processing.

PART 2
Overexpression of the autism candidate gene *Cyfip1* pathologically enhances olivo-cerebellar signaling in mice

Abstract

Cyfip1, the gene encoding cytoplasmic FMR1 interacting protein 1, has been of interest as an autism candidate gene for years. A potential role in autism spectrum disorder (ASD) is suggested by its location on human chromosome 15q11-13, an instable region that gives rise to a variety of copy number variations associated with syndromic autism. In addition, the CYFIP1 protein acts as a binding partner to Fragile X Messenger Ribonucleoprotein (FMRP) in the regulation of translation initiation. Mutation of *FMR1*, the gene encoding FMRP, causes Fragile X syndrome, another form of syndromic autism. Here, in mice overexpressing CYFIP1, we study response properties of cerebellar Purkinje cells to activity of the climbing fiber input that originates from the inferior olive and provides an instructive signal in sensorimotor input analysis and plasticity. We find that CYFIP1 overexpression results in enhanced localization of the synaptic organizer neurexin 1 (NRXN1) at climbing fiber synaptic input sites on Purkinje cell primary dendrites and concomitant enhanced climbing fiber synaptic transmission (CF-EPSCs) measured using whole-cell patch-clamp recordings from Purkinje cells *in vitro*. Moreover, using two-photon measurements of GCaMP6f-encoded climbing fiber signals in Purkinje cells of intact mice, we observe enhanced responses to air puff stimuli applied to the whisker field. These findings resemble our previous phenotypic observations in a mouse model for the human 15q11-13 duplication, which does not extend to the *Cyfip1* locus. Thus, our study demonstrates that CYFIP1 overexpression shares a limited set of olivo-cerebellar phenotypes as those resulting from an increased number of copies of non-overlapping genes located on chromosome 15q11-13.

Introduction

The proximal long arm of human chromosome 15 is a frequent hot spot for copy number variations due to the local existence of multiple chromosomal breakpoints (BPs). The Prader-Willi / Angelman syndrome deletion region (PWACR; 15q11.2-13.1) is flanked by BP1 or BP2 proximally and BP3 distally, with more severe symptoms resulting from a larger deletion(Butler et al., 2004; Hartley et al., 2005). Duplication of the PWACR region results in dup15q syndrome, which is also frequently associated with autism spectrum disorder (ASD) (Cook et al., 1997; Cook Jr & Scherer, 2008). The BP1-BP2 region houses four genes (*Nipa1*, *Nipa2*, *Cyfip1*, and *Tubgcp5*; Fig. 27A) (Chai et al., 2003). Microdeletion of this region (Burnside-Butler syndrome) as well as its microduplication can result in autism and developmental delays, including motor and language delays (Burnside et al., 2011). In a Dutch family study, it was found that of three individuals with a BP1-BP2 microduplication in a seven-member family, all exhibited autism symptoms (van der Zwaag et al., 2010), which highlights the need to study phenotypes related to enhanced dosages of the four genes located in this region – in particular *Nipa1/2 and Cyfip1*, which are highly expressed in the brain.

In mouse models of autism, CYFIP1, as a binding partner of the Fragile X Messenger Ribonucleoprotein (FMRP) (Schenck et al., 2001), has been studied in some detail. Notably, in *Cyfip1* heterozygous knockout mice some phenotypes related to hippocampal plasticity were observed that mimicked the phenotypic profile described in *Fmr1* knockout mice (Bozdagi et al., 2012). *Cyfip1* overexpression has also been shown to alter spine density and maturation in cultured mouse hippocampal neurons (Davenport et al., 2019; Pathania et al., 2014) and neocortical pyramidal neurons (Oguro-Ando et al., 2015). CYFIP1 is enriched at excitatory (Pathania et al., 2014) and inhibitory synapses and alterations of Cyfip1 dosage produce bi-directional changes in

the balance of excitation and inhibition, with Cyfip1 overexpression enhancing excitatory and diminishing inhibitory synapses (Davenport et al., 2019). Moreover, an exaggerated and generalized fear response has been observed in fear conditioning in these mice, while no abnormalities were found in behavioral test batteries assessing ASD-typical social or repetitive behaviors (Fricano-Kugler et al., 2019). This is different from observations made in a mouse model for the human 15q11-13 duplication (patdp/+), in which a conserved linkage group of mouse chromosome 7 – corresponding to the BP2-BP3 region on human chromosome 15q11-13 – was duplicated using chromosomal engineering. These mice show abnormalities in social interactions, behavioral inflexibility and increased anxiety (Nakatani et al., 2009).

Cerebellar involvement in cognitive function has been suggested for decades (Cerebellar cognitive affective syndrome; (Schmahmann & Sherman, 1998)) and it has more recently been suggested that cerebellar dysfunction during a critical postnatal period may be one of the strongest predictive factors in ASD (S. S.-H. Wang et al., 2014). With these developments in mind, we have previously analyzed cerebellar function and sensorimotor behaviors in the patdp/+ mouse model for the human 15q11-13 duplication described above (Nakatani et al., 2009). We found abnormalities in locomotion and associative learning in these mice (Piochon et al., 2014) as well as enhanced climbing fiber-mediated responses to sensory input in Purkinje cell dendrites that were associated with aversive behaviors (Simmons et al., 2022). Localization of the synaptic organizer molecule neurexin 1 (NRXN1) was heightened at climbing fiber input sites on the Purkinje cell primary dendrite and we found that climbing fiber excitatory postsynaptic currents (EPSCs) – recorded from Purkinje cells in cerebellar slices using the whole-cell patch-clamp technique – were increased in amplitude (Simmons et al., 2022).

In the present work, we examined cerebellar climbing fiber signaling in CYFIP1 overexpressing (CYFIP1 OE) mice (originally described in (Oguro-Ando et al., 2015)). We make the same key observations of enhanced climbing fiber signaling that we made in patdp/+ mice with normal *Cyfip1* gene dosage: a) increased NRXN1 localization *to* climbing fiber terminals onto Purkinje cell dendrites, b) increased amplitudes of CF-EPSCs, and c) larger responses to sensory stimulation as measured using two-photon imaging of dendritic calcium signals in intact mice. Although only reported for the better studied deletions, and not the duplications, symptoms in human patients are more severe when the longer area BP1-BP3, rather than just BP2-BP3, undergoes a change in copy number. The phenotypic resemblance of CYFIP1 overexpression to the BP2-BP3 duplication demonstrates a potential pathway for an increase in symptom severity with the longer BP1-BP3 duplication.

Results

Transgenic mice harboring a bacterial artificial chromosome (BAC) spanning the *Cyfip1* locus and previously shown to over-express CYFIP1 protein in frontal cortex (Oguro-Ando et al., 2015), also exhibited enhanced CYFIP1 protein in the cerebellum at a level that is significantly higher than that of wild-type littermates (Fig. 27B; Cytoplasmic fraction at 1.32 ± 0.024, p = 0.0538; Nuclear fraction at 1.38 ± 0.055, n = 6 CYFIP1 OE and 6 WT mice). This observation validates CYFIP1 OE mice as a model for enhanced expression of CYFIP1 protein in the cerebellum.

To assess the potential effects of enhanced *Cyfip1* dosage on other molecular pathways, we used a targeted approach to determine Purkinje cell specific transcription profiles by performing

laser capture microdissection (LCM) exclusively on the somata and proximal dendrites of Purkinje cells. The content of messenger RNA (mRNA) was quantified using real time PCR (qRT-PCR) after reverse transcription for selected candidate genes that we previously assessed in the patdp/+ mouse model of the human 15q11-13 duplication (Simmons et al., 2022). In our quantification, we focused on the synaptic organizer molecules neuroligin 1-3 (*Nlgn1*, *Nlgn2*, *Nlgn3*), cerebellin 1 (*Cbln1*), and neurexin 1 (*Nrxn1*); Ube3a (*Ube3a*); the translation control factors eIF4E (*Eif4e*), eIF4G (*Eif4g*) and CYFIP1 itself (*Cyfip1*), as well as SK2-type K^+ channels (*Kcnn2*) and type 1 metabotropic glutamate receptors (mGluR1, *Grm1*). We observed alterations in many of these candidates (Fig. 27C) but will highlight a few notable findings. First, *Cyfip1* mRNA is upregulated in CYFIP1 OE mice (22.17 ± 0.33 fold above WT; here and below, $p < 0.001$, n = 6 and 6 animals), consistent with the desired genotype. The discrepancy between mRNA and protein upregulation that we observe (2217 vs 30-40%, respectively) is similar to that described in human patients with 15q11-13 duplications (~2400 vs ~250%, respectively; (Oguro-Ando et al., 2015)). Note that those results were found in homogenized superior frontal gyrus tissue, which could explain the remaining difference in protein upregulation in homogenized cerebellar tissue that we present here. Second, *Eif4g* mRNA is upregulated (14.58 ± 0.08 fold above WT), which may constitute a homeostatic regulation in response to enhanced CYFIP1 expression. Third, *Nrxn1* mRNA is upregulated (15.7 ± 0.22 fold above WT). The latter observation is of interest as it recapitulates a finding that we previously made in patdp/+ mice, which led to our investigation of enhanced NRXN1 localization at climbing fiber-Purkinje cell synapses and enhanced climbing fiber transmission (Simmons et al., 2022).
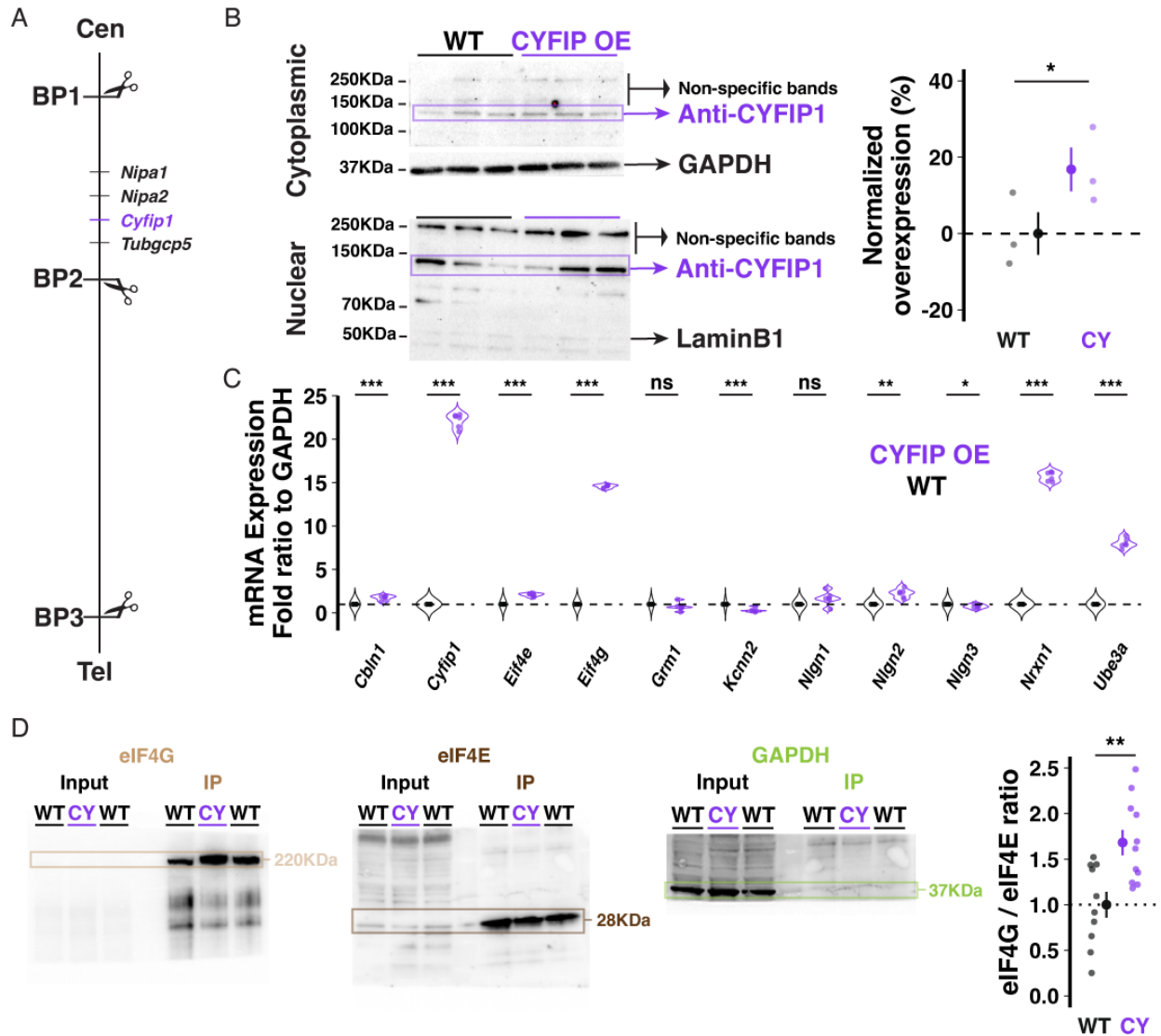
Figure 27. Genetic and molecular description of the CYFIP1 OE model. (A) Schematic of the location of the *Cyfip1* gene between BP1 and 2 of the murine chromosome 7. Cen: centromere; Tel: telomere. **(B)** Western blot demonstrates increased CYFIP1 protein in cerebellum of adult CYFIP1 OE mice in cytoplasmic (left, top) and nuclear fractions (left, bottom). Relative overexpression to WT mean across cytoplasmic and nuclear fractions (right). **(C)** The mRNA expression profiles of several candidate genes in CYFIPOE mice normalized to WT. **(D)** CYFIP1 OE mice have an elevated eIF4G/eIF4E binding ratio as determined by co-immunoprecipitation via m^7GTP bead pull-down assay and western blot quantification. For each sample, eIF4E and eIF4G were probed on the same membrane that was then cut at ~70 KDa for visualization. GAPDH expression was measured in input and pull-down to confirm specificity of the assay. The protein ratios are normalized to the WT group average. For B and D, large inset points indicate mean ± SEM while smaller points depict individual values.

As the FMRP/CYFIP1 complex regulates mRNA translation via its control of the formation of the eIF4G/eIF4E complex (Napoli et al., 2008; Santini et al., 2017), we used an m^7GTP bead pull-down assay of translation complexes followed by western blot analysis to measure the eIF4G/eIF4E binding ratio in the cerebellum of CYFIP1 OE mice and wild-type littermates. Unexpectedly, we observed a significant increase in the eIF4G/eIF4E binding ratio in CYFIP1 OE mice (Fig. 27D; 1.68 ± 0.14, p = 0.003, n = 11 CYFIP1 OE and 10 WT mice), likely due to the increase in eIF4G expression. Regardless, this finding indicates changes in translation profiles for proteins of interest in the CYFIP1 OE mice. In the following, we will focus on localization properties of the cell adhesion protein NRXN1.

At climbing fiber synapses to both soma and primary dendrite compartments, NRXN1 acts as a synaptic organizer, strengthening connectivity by forming trans-synaptic cell adhesion complexes with neuroligins 1 or 3 (L. Y. Chen et al., 2017; Zhang et al., 2015). To test whether NRXN1 localization to climbing fiber synapses is enhanced in CYFIP1 OE mice, we performed immunohistochemical staining using antibodies against NRXN1 and calbindin, a calcium binding protein expressed densely and specifically throughout the dendritic and somatic compartments of Purkinje cells. We restricted our analysis of NRXN1 localization to proximal branches of the primary dendrite (Fig. 28A-B), which are most selectively contacted by the climbing fiber input (Rossi et al., 1991). In this measure, we observed an increase in the number of NRXN1 puncta in CYFIP1 OE mice as compared to WT littermates (Fig. 28C; 0.63 ± 0.06 vs 0.39 ± 0.02 puncta/μm^2, p = 0.003, n = 8 and 12 dendrites, 4 and 4 mice). We did not observe a genotype difference in the average size of NRXN1 puncta (Fig. 28D; 0.081 ± 0.005 vs 0.084 ± 0.006 μm^2, p = 0.714), suggesting that CYFIP1 over-expression selectively influences the maintenance of surplus synapses but not the gross size of the synapse to an extent that could be measured with this

technique. It is not clear if the combined findings of increased *Nrxn1* transcripts and NRXN1 localization to primary dendrite synapses also relates to increased NRXN1 protein expression overall.
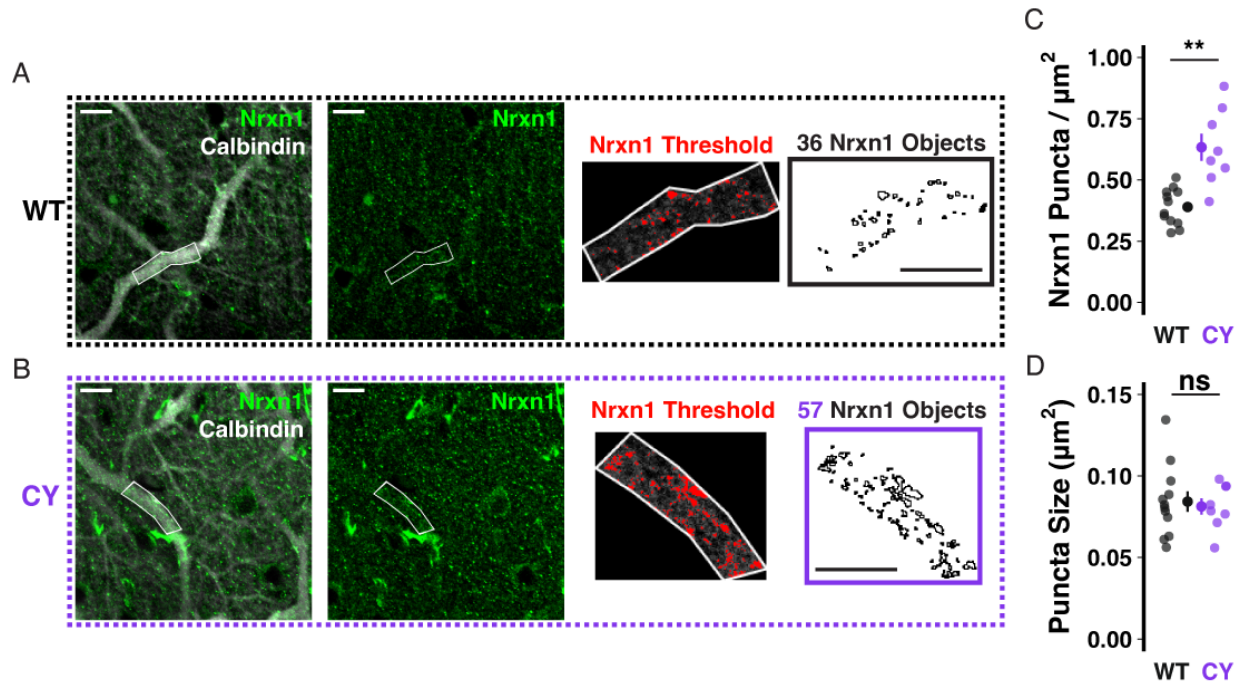
Figure 28. Enhanced NRXN1 localization at putative CF terminals in CYFIP1 OE mice. (A-B) Immunohistochemical labeling reveals increased NRXN1 puncta along primary dendrites of calbindin-labeled Purkinje cells in CYFIP1 OE mice. The right two panels show the threshold applied to extract NRXN1 specific objects exclusively within the dendritic ROI. **(C)** Quantification of NRXN1 puncta per square micron area of primary dendrite ROIs. **(D)** Quantification of the average size of NRXN1 puncta within dendrite ROIs. For C-D, large inset points indicate mean ± SEM while smaller points depict individual values. Scale bars are each 10μm.

In patdp/+ mice, enhanced NRXN1 localization at climbing fiber synapses may result in strengthened synaptic transmission (Simmons et al., 2022). To test whether the same relationship would be observed in CYFIP1 OE mice, we performed *in vitro* whole-cell patch-clamp recordings of climbing fiber-evoked excitatory postsynaptic currents (CF-EPSCs) in Purkinje cells filled with Cesium-based internal solution, to reduce space-clamp error, and kept at a -30mV holding potential. Indeed, we found that CF-EPSC amplitudes were significantly larger when recorded

from Purkinje cells in CYFIP1 OE mice than from Purkinje cells in WT littermates (Fig. 29C; 1.71 ± 0.12 vs 1.36 ± 0.12 nA, p = 0.048, n = 17 and 12 cells, 7 and 6 mice). On the other hand, CF-EPSC paired pulse depression (the ratio of EPSC2 / EPSC1 during paired stimuli) was unaffected (Fig. 29D; 0.72 ± 0.03 vs 0.75 ± 0.01, p = 0.36, n = 17 and 12 cells, 7 and 6 mice), indicating that there is no genotype difference in pre-synaptic release probability.
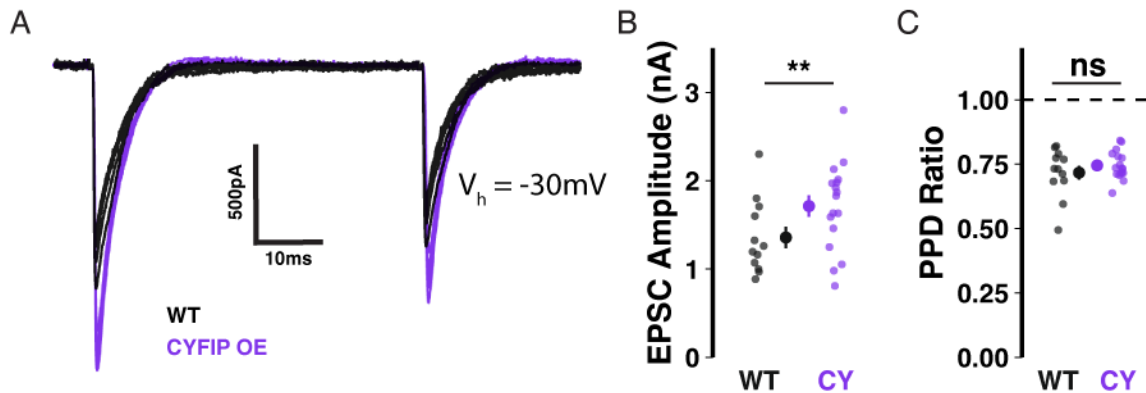
Figure 29. Enhanced CF-EPSCs in Purkinje cells of CYFIP1 OE mice. (A) Sample traces of stimulated CF-EPSCs recorded from WT and CYFIP1 OE Purkinje cells. Holding potential: -30mV. **(B)** Quantification of CF-EPSC amplitudes. **(C)** Quantification of CF-EPSC paired pulse depression (EPSC2 / EPSC1) with a 100ms inter-stimulus interval. For B-C, large inset points indicate mean ± SEM while smaller points depict individual values.

We next asked whether the abnormally strong climbing fiber input observed *in vitro* would translate into enhanced olivocerebellar signaling in the intact brain. To answer this, we dual injected adenovirus constructs encoding cre-recombinase on the Purkinje cell-specific L7 promoter (0.2 x 10^{12} GC/mL) and cre-dependent GCaMP6f (1 x 10^{12} GC/mL), a genetically-encoded calcium indicator, to obtain specific expression in Purkinje cell dendrites of lateral crus 1 (Fig. 30A-B). Lateral crus 1 is a region of the cerebellar hemisphere that is sensitive to multiple sensory modalities (Bosman et al., 2010; Ju et al., 2019) and which exhibits enhanced responsiveness to sensory stimuli in patdp/+ mice (Simmons et al., 2022). As GCaMP6f expression stabilized, mice were partially habituated to head-restraint over a treadmill (Fig. 30C) and exposure

to 30ms sensory stimuli administered ipsilateral to the injected hemisphere, which receives climbing fiber input encoding ipsilateral receptive fields from the contralateral inferior olive. Stimuli included a 488nm light and a 10psi airpuff to the whisker pad (Fig. 30D). As a benchmark, we also tested airpuffs delivered to the eye, a common unconditioned stimulus used for eye-blink conditioning and known to evoke climbing fiber-dependent complex spikes in Purkinje cells.

Sensory stimuli consistently evoked dendritic calcium events in GCaMP6f-expressing crus 1 Purkinje cell dendrites (Appendix Figure S28). The maximum amplitude of sensory responses was larger in Purkinje dendrites of CYFIP1 OE mice than in those from WT littermates (Fig. 30E-F). We observed elevated responses to Light (0.89 ± 0.04 vs 0.74 ± 0.03 dF/F0, $p = 0.005$, n = 75 and 66 cells; here and below, cells are from 5 CYFIP1 OE and 5 WT animals; see Appendix Figure S29), Whisker puff (0.65 ± 0.03 vs 0.54 ± 0.02 dF/F0, $p = 0.006$, n = 73 and 65 cells), and Eye puff (0.58 ± 0.03 vs 0.41 ± 0.02 dF/F0, $p < 0.001$, n = 74 and 65 cells), resembling the heightened over-responsivity across sensory modalities of patdp/+ mice (Simmons et al., 2022). Occasional non-evoked events during the response window of control trials – absent any stimulation – had lower maximum amplitudes than when a stimulus was presented and were equivalent between genotypes (Fig. 30E; 0.41 ± 0.03 vs 0.36 ± 0.02 dF/F0, $p = 0.163$, n = 54 and 49 cells).
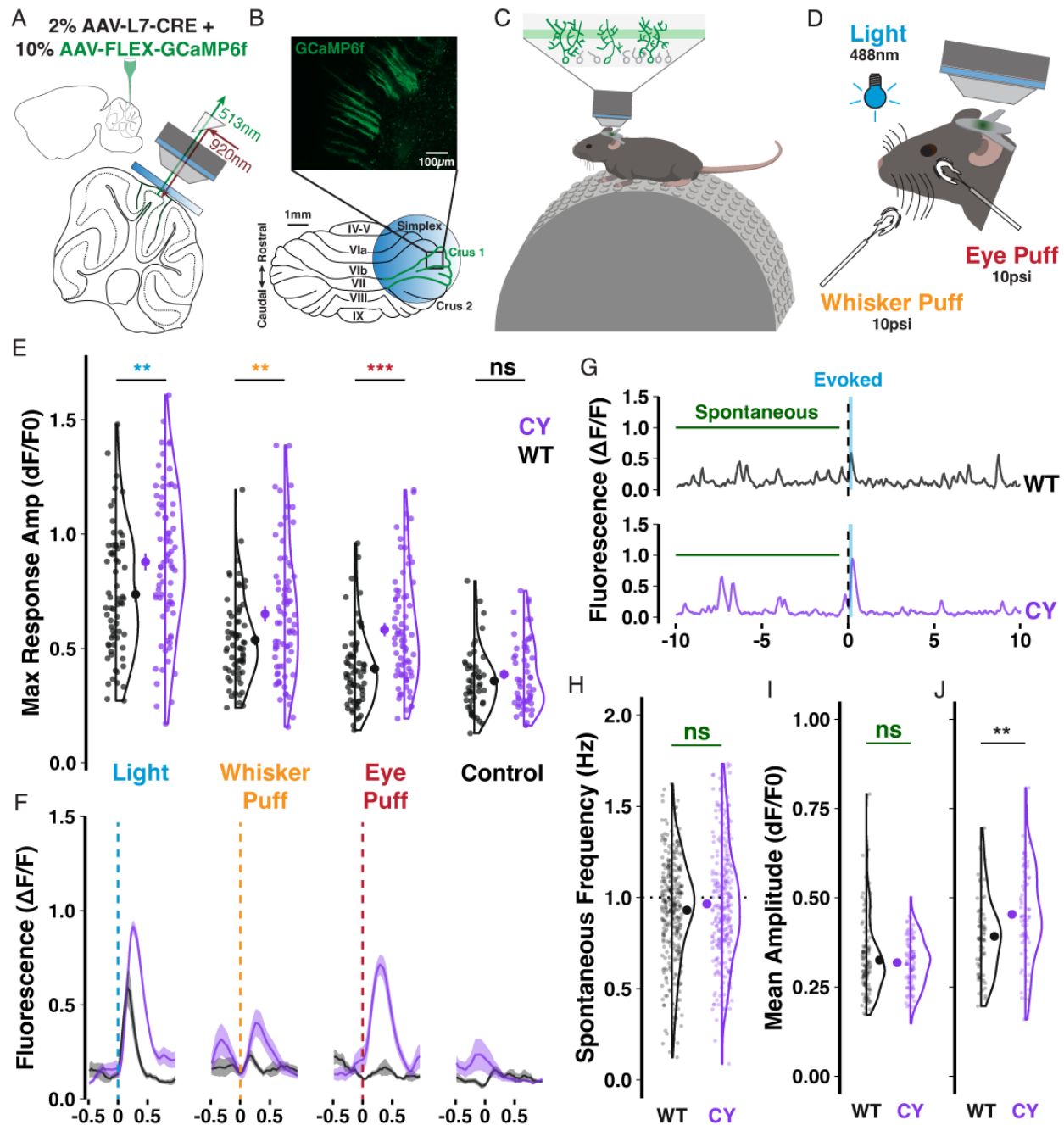
Figure 30. Enhanced sensory responsiveness of CYFIP1 OE crus 1 Purkinje cells *in vivo*. (A-D) Schematics of **(A)** the dual injection of viral constructs and placement of an implanted cranial window; **(B)** the imaging configuration over lateral crus 1 and a sample field of view showing the sparse cellular label enabling calcium events from individual Purkinje cells to be separately deconvolved for analysis; **(C)** the experimental arrangement with mice head-restraining and resting on a treadmill during imaging of the intermediate Purkinje dendrites; and **(D)** the multisensory stimuli. **(E)** Purkinje cells of CYFIP1 OE mice exhibit larger calcium responses on average across sensory stimuli, but not during control trials without stimulus where any events during the response window are spontaneous (non-evoked) events. **(F)** Inter-trial calcium traces

(mean with shaded SEM) of two individual cells, each exemplifying average WT and CYFIP1 OE responses. Given the mixed multi-sensory responsiveness of these cells, not all cells respond to every stimulus type equally, resulting in the heterogeneity of response size. **(G)** Sample traces from a 20s trial of light stimulation exemplifying typical light-evoked responses and spontaneous events. Spontaneous events taken for quantification were sampled from the pre-stimulus period of each trial. **(H)** No difference in the spontaneous calcium event frequency between Purkinje cells of CYFIP1 OE and WT mice. **(I)** The mean amplitude of spontaneous calcium events is not different between genotypes. **(J)** The mean evoked calcium response – averaged over all sensory modalities – is larger in Purkinje cells of CYFIP1 OE mice. For E and H-J, large inset points indicate mean ± SEM while smaller points depict individual values.

Comparing pre-stimulus spontaneous events to evoked responses (Fig. 30G), we did not observe a difference in the frequency of spontaneous events during the pre-stimulus periods of each trial (Fig. 30H; 0.96 ± 0.02 vs 0.93 ± 0.02 Hz, p = 0.171, n = 275 and 322 cells), but the typical 1Hz frequency of both genotypes identifies these events as calcium transients caused by climbing fiber-evoked complex spikes (Simpson et al., 1996). Consistent with previous reports, the mean amplitude of spontaneous events is smaller than that of sensory-evoked ones (Fig. 30I-J; (Najafi et al., 2014b)). While the mean evoked amplitude is enhanced in CYFIP1 OE animals (Fig. 30J; 0.45 ± 0.02 vs 0.39 ± 0.01 dF/F0, p = 0.003, n = 75 and 66 cells), we did not observe a difference in the mean amplitude of spontaneous events between CYFIP1 OE and WT animals (Fig. 30I; 0.32 ± 0.01 vs 0.33 ± 0.01 dF/F0, p = 0.554, n = 96 and 109 cells).

Repeated stimulus presentation may have an impact on response amplitudes. In case of the climbing fiber mediated responses studied here, we observed in WT animals that repeated exposure to a whisker puff (1 Hz for 5min) reduced the amplitude (-13.72 ± 5.04%, p = 0.028, n = 42 cells from 5 animals) and probability (-0.53 ± 0.21 responses out of 5 trials per stimulus type during the first 20min of exposure, p = 0.016, n = 45 cells) of responses to subsequent test pulses of whisker puff (raw and normalized changes shown in Appendix Figure S30A,C and Fig. 31A,C respectively). In contrast, Purkinje cells of CYFIP OE mice exhibited enhanced response

amplitude (15.41 ± 5.05%, p = 0.005, n = 106 cells from 5 mice) and probability (0.41 ± 0.12 responses, p = 0.002, n = 106 cells) to whisker puff following repeated exposure (Fig. 31A,C). As a control, repeated exposure to whisker puffs did not have a genotype specific effect on Purkinje cell responsiveness to light stimuli in *either* WT and CYFIP1 OE animals, though the response probability decreased modestly in cells from CYFIP1 OE mice (Appendix Figure S30B,D and Fig. 31B,D -0.31 ± 0.1 responses, p = 0.003, n = 106 cells). Genotype differences in untrained multisensory responses are easily obscured at the level of the averaged population response in each animal (Appendix Figure S29); however, a consistent repeated exposure protocol and the subsequent analysis of normalized change instead of absolute response amplitude, can provide a better assessment of genotype differences at the level of mice as well as cells. Indeed, the effects of repeated exposure could also be observed when averaging cells in each mouse (Appendix Figure S31).
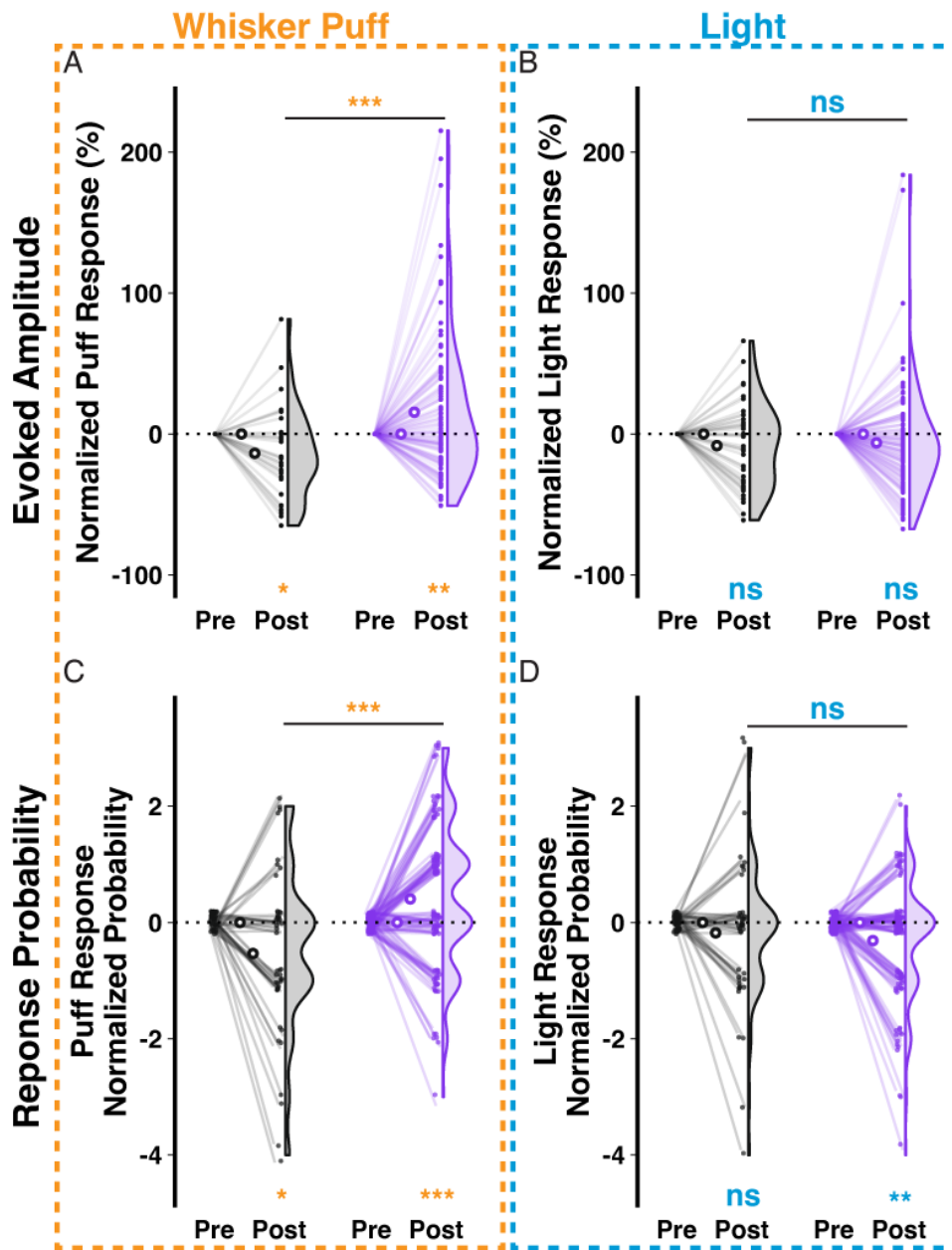
Figure 31. Repeated sensory exposure decreases responsiveness of WT cells but enhances that of CYFIP1 OE cells *in vivo*. (A) A repeated exposure paradigm (1Hz whisker puffs for 5min) induces opposite changes in response amplitude to subsequent whisker puff trials in Purkinje cells of WT vs CYFIP1 OE mice. Here and below, normalized response is calculated as (Post – Pre) / Pre of either the dF/F0 of response amplitude or the probability of response. **(B)** The same repeated whisker puff exposure paradigm has no effect on subsequent responses to light stimuli. **(C-D)** As in A-B, but for the calcium response probability. **(C)** There is a decrease in the whisker puff response probability of WT cells and an increase in the response probability of CYFIP1 OE cells following repeated exposure to whisker puff. **(D)** The same repeated whisker puff exposure has no effect on subsequent response probability to light stimuli. For A-D, large inset, hollow points indicate mean ± SEM while smaller points depict individual values.

125

Cerebellar lateral crus 1 is responsive to multiple stimulus modalities, and many –but not all– individual cells are themselves responsive to all modalities (Ju et al., 2019). While the previous analysis identified trends in the whole population of WT and CYFIP1 OE cells, we next analyzed subsets of cells based on their stimulus responsiveness to assess the contributions of different subgroups to the trends in the population (Appendix Figure S32). We observed that changes in population responsiveness were a factor both of changes in the number of cells with at least moderate response frequency (a decrease among WT cells and an increase among CYFIP OE cells; Appendix Figure S32A-B,D-E) and changes in response frequency among cells that were consistently at least moderately responsive before and after the repeated exposure (Appendix Figure S32C,F).

Discussion

The main finding presented here is that phenotypes in olivocerebellar signaling are similar between CYFIP1 OE mice and the mouse model for the human 15q11-13 duplication. This notion holds for enhanced NRXN1 localization on the primary dendrite, enhanced CF-EPSC amplitudes as well as enhanced climbing fiber-mediated calcium events recorded from Purkinje cells in awake mice. All of these phenotypes were previously reported in the mouse model for the human 15q11-13 duplication (Simmons et al., 2022) and are in keeping with findings, albeit in hippocampus, that increased Cyfip1 dosage enhances excitatory synapses (Davenport et al., 2019). Intriguingly, increased excitatory synaptic density and size is particularly pronounced on the dendritic shaft of pyramidal neurons, where greater space may permit more expansion of synaptic area, which is the

same region of Purkinje cell dendrites that is predominantly innervated by CF terminals with variable sizes of synaptic densities (Xu-Friedman et al., 2001).

The molecular reason for the phenotypic resemblance of patdp/+ and CYFIP1OE mice is currently not known. However, our finding speaks to the observation that clinical symptoms in patients with a long BP1-BP3 copy number variation are often more severe than symptoms in patients with a shorter BP2-BP3 one (Butler et al., 2004; Hartley et al., 2005). Although reported for deletions, the phenotype resemblance demonstrated here provides a proof-of-principle example how the same phenotypes might have their origin in BP1-BP2 as well as BP2-BP3, providing a basis for the added severity effect in BP1-3 alterations.

The consequences of pathologically enhanced signaling in the olivocerebellar system for patients with ASD are potentially manifold. One is that climbing fiber responses function as error signals in sensory-motor signaling (Marr-Albus-Ito models; see (Ito, 2001)). Abnormally strong climbing fiber responses to sensory stimuli might contribute to sensory defensiveness in autistic children, which includes avoidance behaviors to touch and other sensory stimuli (Markram et al., 2007). Moreover, climbing fiber co-activation promotes associative plasticity at parallel fiber to Purkinje cell synapses (Ito et al., 1982; Titley et al., 2019) and thus, ultimately, associative behavioral learning. Thus, too strong climbing fiber activity may abnormally promote associative plasticity, but it may also hinder it when preventing the proper development of parallel fiber input (as observed in patdp/+ mice; (Piochon et al., 2014)). In either case, pathologically enhanced climbing fiber activity will interfere with appropriate learning of associative relationships (Hansel, 2019).

An interesting observation made here is that repeated whisker stimulation at 1Hz for 5min causes a reduction in sensory-evoked calcium events in awake mice. A reminiscent effect has been

described in the visual system and is known as 'repetition suppression' (Desimone, 1996; Henson & Rugg, 2003). The reduction observed here outlasts the whisker stimulation and therefore includes a plasticity component. As this effect appears modality-specific – responses to whisker, but not light stimuli are significantly reduced – it is possible that it reflects long-term depression (LTD) of a parallel fiber component that is co-activated with the climbing fiber (Najafi et al., 2014b). An interesting, alternative possibility is that this reduction reflects LTD at the climbing fiber input itself (Carta et al., 2006; Hansel & Linden, 2000), which can be monitored as a depression of widespread, dendritic calcium transients (Weber et al., 2003) and might show at different efficiencies when test responses are differently measured (same climbing fiber, but response to different sensory stimuli). CF-LTD as well as a transient reduction in climbing fiber transmission is promoted by the release of the neuropeptide corticotropin-releasing factor (CRF) from climbing fiber terminals and subsequent PKA / PKC activation in Purkinje cells (Schmolesky et al., 2002). Whatever the mechanism, the fact that in CYFIP1 OE mice repeated climbing fiber activation does not lead to any transient or lasting response reduction adds to the list of abnormalities in the olivocerebellar system described here.

Abnormal climbing fiber connectivity and/or transmission strength has also been found in motor diseases that involve the cerebellum, such as essential tremor and spino-cerebellar ataxia type 6 (Du et al., 2019; C.-Y. Lin et al., 2014). This observation shows how sensitive proper cerebellar function is to alterations in climbing fiber signal strength. The particular phenotypes resulting from these alterations will depend on variations in cerebellar regions affected as well as on a host of accompanying abnormalities.

CHAPTER 6

INTRINSIC AND SYNAPTIC DETERMINANTS OF RECEPTIVE FIELD PLASTICITY IN

PURKINJE CELLS OF THE MOUSE CEREBELLUM

This chapter contains a manuscript to which I contributed as second author. For simplicity, the

manuscript is reprinted here in full while in the General Discussion (Chapter 7) I direct the

reader to the portions I completed and how it pertains to my dissertation. My contributions

included assisting to troubleshoot and perform a portion of the *in vivo* 2-photon imaging

experiments that often required multiple experimenters present as they involved direct

electrophysiological or logistically challenging sensory stimulation. I also made specific

recommendations to assist in the analysis of spatial calcium signals contributing to Fig. 4 (here

Figure 35) and co-wrote the manuscript with Drs. Lin and Hansel.

Lin, TF, Busch SE, and Hansel C. (2024) Intrinsic and synaptic determinants of receptive field

plasticity in Purkinje cells of the mouse cerebellum. *Nature Communications*, 15, 4645.

https://doi.org/10.1038/s41467-024-48373-3.

This work is included with permission from the publisher. An open-access preprint version of the

manuscript can be found on *bioRxiv:* https://doi.org/10.1101/2023.07.19.549760

Abstract

Non-synaptic (intrinsic) plasticity of membrane excitability contributes to aspects of memory formation, but it remains unclear whether it merely facilitates synaptic long-term potentiation or plays a permissive role in determining the impact of synaptic weight increase. We use tactile stimulation and electrical activation of parallel fibers to probe intrinsic and synaptic contributions to receptive field plasticity in awake mice during two-photon calcium imaging of cerebellar Purkinje cells. Repetitive activation of both stimuli induced response potentiation that is impaired in mice with selective deficits in either synaptic or intrinsic plasticity. Spatial analysis of calcium signals demonstrated that intrinsic, but not synaptic plasticity, enhances the spread of dendritic parallel fiber response potentiation. Simultaneous dendrite and axon initial segment recordings confirm these dendritic events affect axonal output. Our findings support the hypothesis that intrinsic plasticity provides an amplification mechanism that exerts a permissive control over the impact of long-term potentiation on neuronal responsiveness.

Introduction

Synaptic plasticity shapes connectivity maps by selectively regulating synaptic weights, a mechanism long considered the core determinant of memory formation. However, membrane excitability, across neuron types and cellular compartments (Belmeguenai et al., 2010; Gill & Hansel, 2020; Grasselli et al., 2020; Losonczy et al., 2008; Ohtsuki et al., 2012; Shim et al., 2017), predicts spike output better than synaptic strength (Larkum et al., 2001; Ohtsuki & Hansel, 2018), and may also play a role in memory representation (Titley et al., 2017). Nevertheless, it remains unclear whether intrinsic plasticity, which tunes excitability, provides computational capacities beyond that achieved by synaptic plasticity alone, and whether this capacity is necessary or sufficient for memory formation. We have previously predicted that synaptic plasticity controls synapse stabilization and connectivity, while intrinsic plasticity 'sets an amplification factor that enhances or lowers *synaptic penetrance*' (Titley et al., 2017). Synaptic penetrance describes to what degree synaptic weights control spike output. Therefore, in this theory intrinsic plasticity assumes the role of a permissive gate that may prevent or allow efficient EPSP-spike coupling. As synaptic penetrance can be set to zero levels, intrinsic plasticity is not merely facilitatory, but it is permissive.

Here, we study the isolated role of each plasticity mechanism in memory formation using cerebellar Purkinje cells (PCs) as a model and by leveraging transgenic mice with selective plasticity impairments. In order to optimize motor and non-motor learning (Popa & Ebner, 2019), cerebellar PC dendrites maintain numerous synaptic connections carrying information that gets selectively integrated into a unitary axonal signal. Peripheral inputs traverse through mossy fibers to cerebellar granule cells, which provide an expansion recoding of sensory information through parallel fibers (PFs) (Cayco-Gajic et al., 2017; Litwin-Kumar et al., 2017; Nguyen et al., 2023).

The receptive fields (RFs) of PCs are defined by the RFs of their synaptic inputs as well as the gain at these synapses (Bosman et al., 2010; Bower, 1997; Bower & Woolston, 1983; Eccles et al., 1972; Ekerot & Jörntell, 2001; Shambes et al., 1978; Shimuta et al., 2020; Thach, 1967) – determined by synaptic weight and intrinsic amplification-controlled synaptic penetrance. To adapt in a dynamic world, PCs need to continually update their RFs through neural plasticity (Jörntell & Ekerot, 2003, 2011; Márquez-Ruiz & Cheron, 2012; Ramakrishnan et al., 2016; Roggeri et al., 2008), allowing the cerebellum to learn and process information based on experience (Jörntell & Ekerot, 2002, 2011; Márquez-Ruiz & Cheron, 2012; Ramakrishnan et al., 2016). As synaptic connectivity, synaptic weight, and synaptic penetrance ultimately contribute to EPSP-spike coupling and therefore the functional definition of a PC's RF, both synaptic and intrinsic plasticity constitute candidate mechanisms that may contribute to efficient RF plasticity.

In brain slices, repetitive PF stimulation induces synaptic long-term potentiation (LTP) at PF-PC synapses (Coesmans et al., 2004; Crepel & Jaillard, 1991; Hirano, 1990; Sakurai, 1987; Shibuki & Okada, 1992), thereby increasing PF-evoked PC firing (Lev-Ram et al., 2003). Tetanus of PFs carrying somatosensory information in the intact circuit (Bengtsson & Jörntell, 2009; Bower & Woolston, 1983; Shimuta et al., 2020; Thach, 1967) modifies the sensory-evoked simple-spike (SS) rate thus changing the PC somatosensory RF (Jörntell & Ekerot, 2002). Furthermore, tetanization-induced SS potentiation has also been demonstrated with indirect PF activation by peripheral cutaneous stimulation (Jörntell & Ekerot, 2011; Márquez-Ruiz & Cheron, 2012; Ramakrishnan et al., 2016). PF tetanization co-induces intrinsic plasticity in PCs (Belmeguenai et al., 2010). While EPSP amplitude alone is a poor predictor of spike output, intrinsic excitability is a better predictor (Ohtsuki & Hansel, 2018). Based on these *in vitro* observations, we therefore hypothesized that intrinsic plasticity acts as a permissive gate mechanism that regulates the

propagation of distal EPSPs to the soma (Larkum et al., 2001) and therefore determines how well LTP may control spike output. Here, we ask whether *in vivo* recordings from intact mice support this scenario.

To investigate the distinctive roles of these plasticity mechanisms, we conducted RF plasticity experiments in two transgenic mouse models with selective plasticity impairments: CaMKII-TT305/6VA (Piochon, Titley, et al., 2016), wherein a specific mutation blocking the inhibitory autophosphorylation of the postsynaptic protein CaMKII promotes synaptic long-term depression (LTD) at PF-PC synapses and prevents LTP induction (Piochon, Titley, et al., 2016), and SK2-KO (Belmeguenai et al., 2010; Grasselli et al., 2020), wherein the absence of small conductance Ca^{2+} activated K^+ (SK2) channels impairs intrinsic plasticity. Instead of recording SS frequency, we used two-photon microscopy to monitor calcium responses in PC dendrites as a readout of PF-mediated RFs. Consistent with earlier experiments documenting SS potentiation (Jörntell & Ekerot, 2011; Márquez-Ruiz & Cheron, 2012; Ramakrishnan et al., 2016), we observed an increase in dendritic calcium responses to either airpuff stimulation of the paw or direct electrical stimulation of PFs following an induction protocol in awake wild-type mice. This potentiation was impaired in both CaMKII-TT305/6VA and SK2-KO mice, suggesting that synaptic plasticity alone –without the contributions of intrinsic plasticity– is insufficient for proper RF plasticity. PF tetanization also resulted in a potentiation of test responses to airpuff stimulation, including responses that remained below the defined event detection threshold during the baseline and thus constitute no or low-amplitude responses. This observation of an emergence of new tactile inputs that are able to evoke dendritic calcium responses classifies the phenomenon described here as plasticity of the RF itself. Furthermore, PF tetanization resulted in distinct spatial patterns of calcium response on PC dendrites among different genotypes, highlighting the unique roles of

synaptic versus intrinsic plasticity. By simultaneously monitoring PF-evoked responses across the dendrite, soma and axonal initial segment (AIS) of individual PCs, we identified correlated dendritic and AIS calcium responses, demonstrating that the dendritic events observed here do influence axonal calcium signals that likely accompany changes in spike output.

Results

PF stimulation elicits local calcium responses

To establish compatibility with conventional *in vitro* experiments, we developed a platform that allows us to apply direct electrical stimulation to a bundle of PFs (Roome & Kuhn, 2014), which project >2mm in the medio-lateral axis orthogonal to the parasagittal alignment of PC dendrites (W. Gao et al., 2006; Reinert et al., 2004; X. Wang et al., 2009), while simultaneously monitoring the corresponding single cell response properties using two-photon imaging of GCaMP6f-encoded calcium events in the cerebellum of awake mice. To generate mice expressing GCaMP6f specifically in a sparse population of PCs, we co-injected AAV vectors encoding Cre-recombinase under the Purkinje cell protein 2 (Pcp2)/L7 promoter and Cre-dependent GCaMP6f (Fig. 32a) in Crus I, a region where somatosensory information is processed (Bower, 1997; Cramer et al., 2013; Eccles et al., 1972; Edge et al., 2003; Ishikawa et al., 2015; Ju et al., 2019; Romano et al., 2018; Thach, 1967). To minimize motor-related signals from obscuring those of evoked PFs, mice were trained to stay motionless on the experimental apparatus and position their forelimbs on a horizontal bar to maintain comfort and keep any cerebellar activation by posture consistent across experimental designs (see Appendix 1: Methodology and Statistics and later experiments

below). This training also maximized preparation stability, which was especially critical to ensure consistent stimulation of the same PF bundle throughout the experiment.

During the experiment, a glass pipette filled with artificial cerebrospinal fluid (ACSF) was inserted through a transparent silicone access port in the center of a 5mm glass cranial window to provide extracellular stimulation of PF axon bundles (Fig. 32b-c). A stimulus train of 8 pulses applied at 100Hz successfully evoked calcium responses within a local region of each PC dendrite (Roome & Kuhn, 2018) reflecting the parasagittal width of the stimulated PF bundle (Fig. 32d). This stimulus protocol, resembling test pulse protocols *in vitro* (Belmeguenai et al., 2010; Piochon, Titley, et al., 2016), was selected because stronger (more pulses or longer pulse duration) or weaker (fewer pulses) stimulations of PF bundles either oversaturated and damaged PFs or evoked diminutive PF inputs that fail to produce a detectable post-synaptic calcium signal. Previous *in vivo* recordings from cat cerebellar lobule V have shown that local PF stimulation elicits dendritic spikes (Nilsson & Jörntell, 2021), which likely underlie the calcium transients that we measure here.
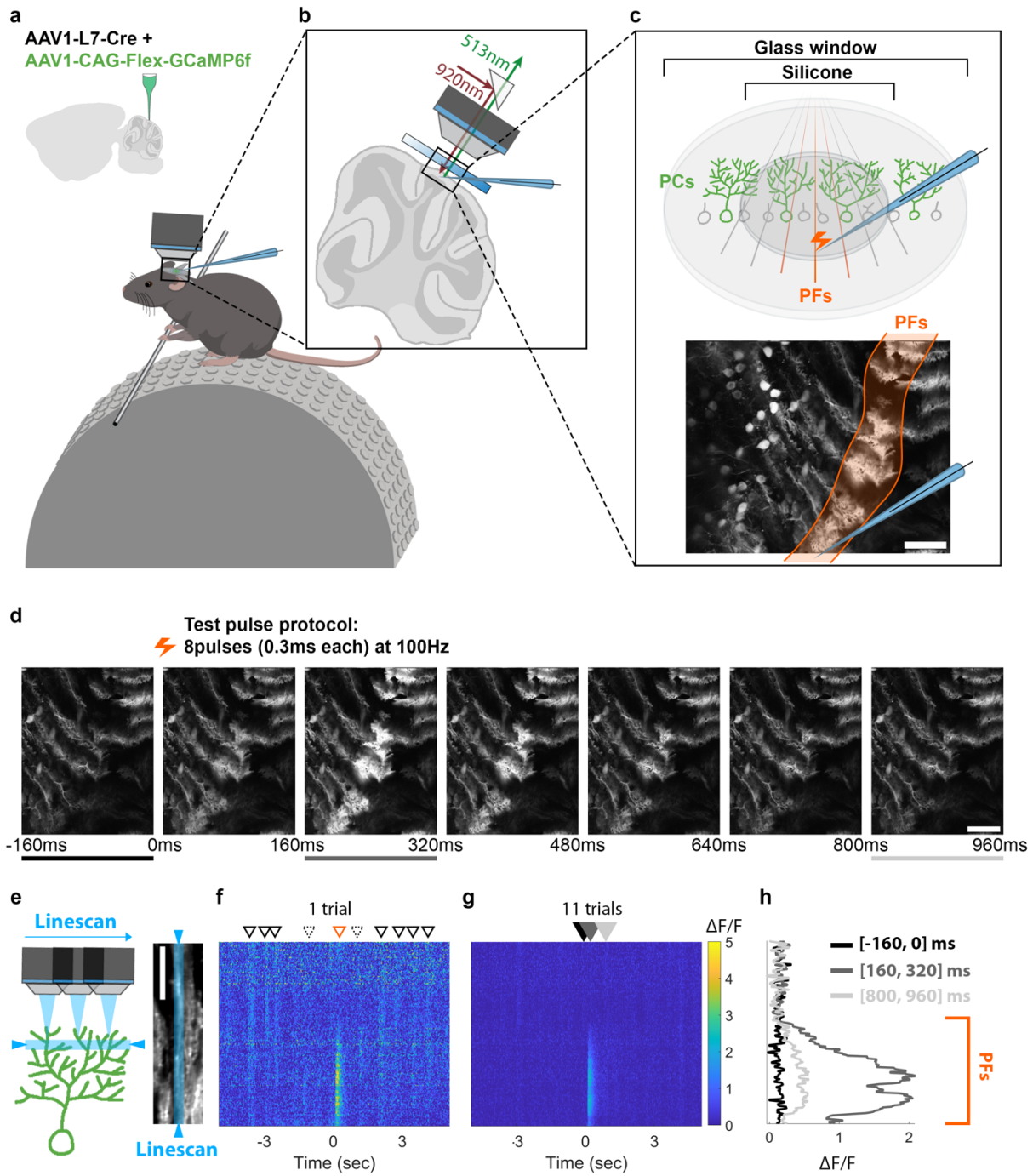
Figure 32. Electrical PF stimulation produces a localized calcium response in PC dendrites of awake mice.

a. AAV vectors were injected into Crus I of cerebellar cortex to express Cre-dependent GCaMP6f specifically in PCs.

b-c. Schematic illustrations of the experimental setup of PF stimulation and calcium recording. A microelectrode was used to apply electrical stimuli to a bundle of PFs in Crus I while calcium responses in PC dendrites were recorded using a two-photon microscope. The bottom panel of **c**

shows a representative field of view during cerebellar recording and the resulting calcium response in PCs to the PF stimulus. Calcium images were obtained with a 31 Hz frame rate, 3-4x digital zoom, and dimensions of 380-669μm width and 306-539μm height. Images were collected during periods without animal movement.

d. Two-photon images demonstrating calcium signals in PCs over time. Test pulses were applied at 0ms.

e. Schematic of imaging approach with a linescan plane of focus (*left*, in blue), which forms a cross-section field of view (FOV) of a single representative PC (*right*).

f-h. Calcium signals of the example cell in **e** are shown as a spatiotemporal calcium map with the y-axis indicating the pixel locations along the linescan in the right panel of **e**. Calcium distribution of a single trial (**f**) and the average of 11 trials (**g**) during a 10sec recording period. (**f**) The triangles with solid black line denote global calcium responses, while the triangles with dashed line denote local calcium responses. The orange triangle indicates the PF stimulus. (**h**) The quantified fluorescence signals in different time windows, which are color-coded to correspond with lines and filled arrows shown in **d** and **g**, respectively. Scale bars are 100μm (**c-d**) and 50μm (**e**).

Linescans of individual PC dendrites (Fig. 32e) and the corresponding local calcium activity reveal a spatiotemporal map that contrasts spontaneous from evoked signals (Fig. 32f-g). Although spontaneous calcium signals exhibited a dynamic range of spatial distribution (Busch & Hansel, 2023; Roome & Kuhn, 2018, 2020), most events were relatively homogeneous across the entire dendrite. In contrast, evoked PF responses were clearly restricted to a local area representing the boundaries of the stimulated PF bundle (Fig. 32f). Quantified calcium signals before, during the peak, and at the end of the PF response (Fig. 32h) further demonstrate a time-locked local fluorescence peak with a clear drop-off at the edge of the stimulated PF-bundle input area. Our recordings reproduced the previously reported medio-lateral stripe-like PF response in PCs (W. Gao et al., 2006; Reinert et al., 2004; X. Wang et al., 2009), and at a subcellular scale revealed sub-compartmental calcium responses to PF stimuli, affirming previous observations *in vitro* (Canepari & Vogt, 2008; Eilers et al., 1995, 1997; Finch & Augustine, 1998; Hartell, 1996; Hildebrand et al., 2009; S. S.-H. Wang, Khiroug, et al., 2000).

PF stimulation elicits analog calcium signals in PC dendrites

To investigate how intrinsic and synaptic plasticity may underlie various forms of cerebellar learning as has been suggested previously (Jörntell & Hansel, 2006; Titley et al., 2017), we used two established loss-of-function models, SK2-KO (Grasselli et al., 2020) and CaMKII-TT305/6VA (Piochon, Titley, et al., 2016) mice, to assess their respective contributions. In SK2-KO mice, cellular specificity is achieved through L7 promotor-dependent Cre expression, selectively excising translation initiation sites for the *Kcnn2* (SK2) gene in PCs. CaMKII-TT305/6VA mice carry a global mutation; however, synaptic specificity is conferred by the unique function of CaMKII at PF-PC synapses. At these synapses, CaMKII promotes LTD (Augustine et al., 2003; Coesmans et al., 2004; Hansel et al., 2006; Hirano, 1990; Konnerth et al., 1992; Sakurai, 1987, 1990; Titley et al., 2019), in contrast to LTP induction at most other types of glutamatergic synapses (Elgersma et al., 2002; Jörntell & Hansel, 2006).The TT305/6VA mutation blocks the inhibitory autophosphorylation of CaMKII, thus preventing the proper induction of LTP (Piochon, Titley, et al., 2016).

First, to determine whether PF-PC innervation follows well-established rules from *in vitro* studies during our *in vivo* stimulation and across our transgenic models, we characterized the calcium signal response to increasing PF stimulus amplitudes in all genotypes. Echoing the classic result, average calcium signals showed a linear stimulus intensity-dependent increase in amplitude across genotypes (Fig. 33a). In these and the following plasticity experiments (Fig. 34), we selected a response time window of 0-200ms that captures calcium responses during the stimulus train (0-70ms) and leaves sufficient time for response build-up. When separating the average signals of responsive and non-responsive trials (Fig. 33b), we observed that both probability (Fig. 33c) and amplitude (Fig. 33d) are stimulus intensity-dependent. Correlation coefficients of

138

normalized data across stimulus intensities, allowed the categorization of PCs into stimulus intensity-dependent or -independent groups (Appendix Figure S33). Across genotypes, over 93% of PCs were categorized as stimulus intensity-dependent, further confirming that our transgenic models retain the standard physiological characteristics of PF-PC innervation. Overall, the stimulus-intensity dependence of our observed calcium signals *in vivo* are highly consistent with previous studies both *in vitro* (Canepari & Vogt, 2008; Hartell, 1996) as well as *in vivo* (Najafi et al., 2014a; Roome & Kuhn, 2020). In the following experiments, we use these PF-mediated responses to characterize PF-PC synaptic plasticity (Bengtsson & Jörntell, 2009; Bower & Woolston, 1983; Jörntell & Ekerot, 2002, 2011; Márquez-Ruiz & Cheron, 2012; Ramakrishnan et al., 2016; Shimuta et al., 2020; Thach, 1967).
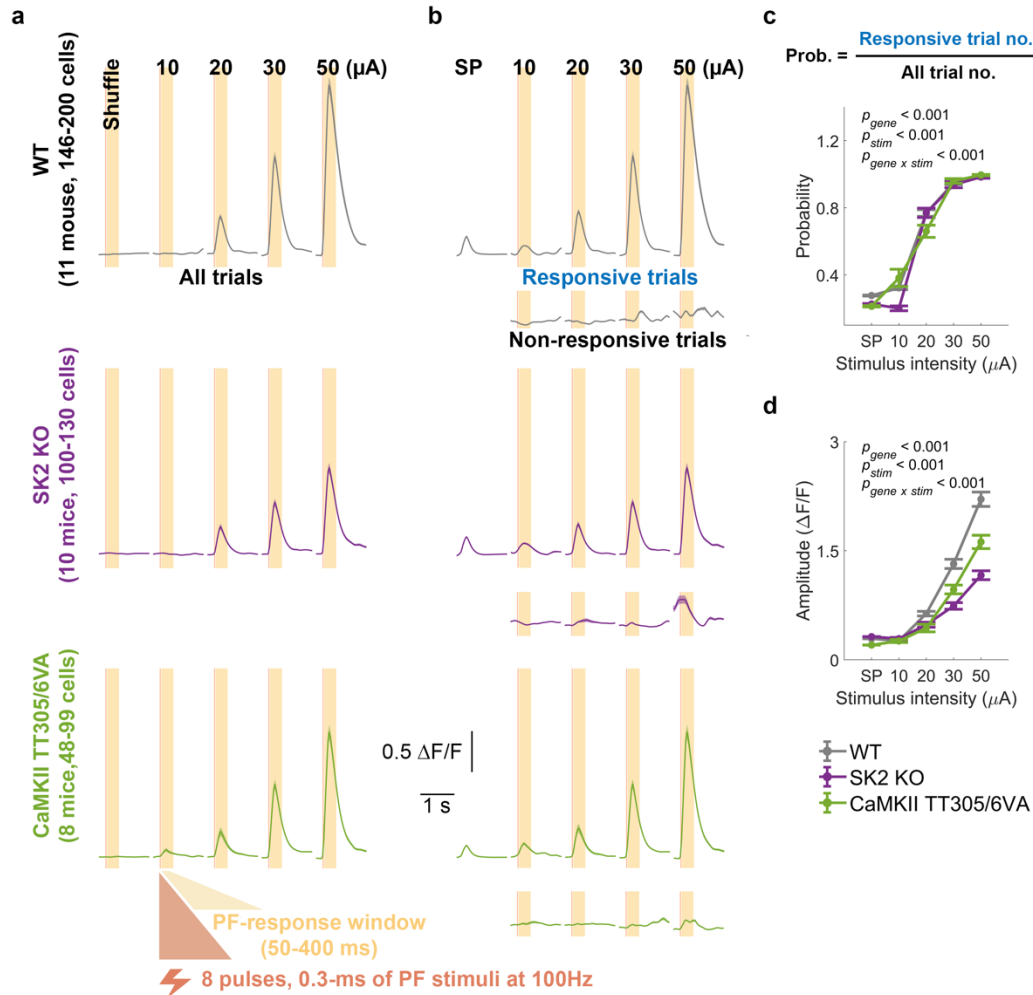
Figure 33. Linear stimulus intensity-dependence of PC responses to PF stimuli *in vivo* indicates intact PF response characteristics across genotypes.

a-b. Average calcium signals ± SEM in response to PF stimuli with varying intensities (10, 20, 30, and 50µA) for all trials (**a**) and responsive trials (**b**). The light orange area represents either a 200ms shuffling window (**a**) or a response window (0-200ms) for evoked events (**a-b**). Trials with detected events within the response window are categorized as responsive trials, whereas those without are considered non-responsive trials (not shown). Spontaneous calcium events (SP) are shown for comparison (**b**).

c. Probability (mean ± SEM) of detecting a calcium event within the defined time windows for spontaneous or responsive conditions. (Two-way ANOVA: $F_{gene}[2,2939] = 2.3$, $p = 0.101$; $F_{stim}[4,2939] = 2975.5$, $p < 0.001$; $F_{stim \times gene}[8,2939] = 13.35$, $p < 0.001$, n = 2954).

d. Maximum values (mean ± SEM) within the 200ms shuffled time window or after the initiation of stimulus for evoked calcium transients shown in **a**. (Two-way ANOVA: $F_{gene}[2,2939] = 129.60$, $p < 0.001$; $F_{stim}[4, 2939] = 799.20$, $p < 0.001$; genotype, $F_{stim \times gene}[8,2939] = 42.07$, $p < 0.001$, n = 2954).

SP, spontaneous calcium events. Sh, shuffled traces.

Intrinsic and synaptic plasticity contribute to PF-RF plasticity

To validate the potentiation of PC responses to PF stimulation *in vivo*, and its dependence on synaptic and intrinsic plasticity, we employed direct electrical PF tetanization to induce potentiation of PC calcium responses. We selected the stimulus intensity that produced a reliable and intermediate response level in each session (usually around 30μA) after testing the calcium response to a broad range of stimulus strengths (Fig. 33). The experimental procedure began with establishing a baseline by recording responses to a test stimulus (8 pulses, 0.3ms duration, 100Hz) for 10-12 trials over a 20min period. Next, to potentiate the calcium response, we applied PF tetanization (1Hz, 0.2ms pulses for 5min) and then recorded responses to test stimuli for 40min post-tetanus (Fig. 34a). The average calcium signals were separated into those immediately after the tetanus (early post-tetanus) or 20 minutes later (late post-tetanus) and are shown in Figure 34b. We observed an enhanced amplitude of calcium responses after PF tetanization in wild-type mice and either no enhancement or a substantially lower effect in non-tetanized wild-type controls and both mutants (Fig. 34c-d). Specifically, although wild-type mice exhibited significantly higher potentiation than CaMKII-TT305/6VA mutants, the deficient LTP resulting from the mutation did not completely abolish the potentiation. Instead, CaMKII-TT305/6VA mutants showed a modest but significant calcium potentiation, while this is absent from SK2-KO mutants (bottom two panels of Fig. 34d), suggesting the existence of a contributor to this potentiation other than LTP. Non-responsive trials were excluded from this amplitude analysis.
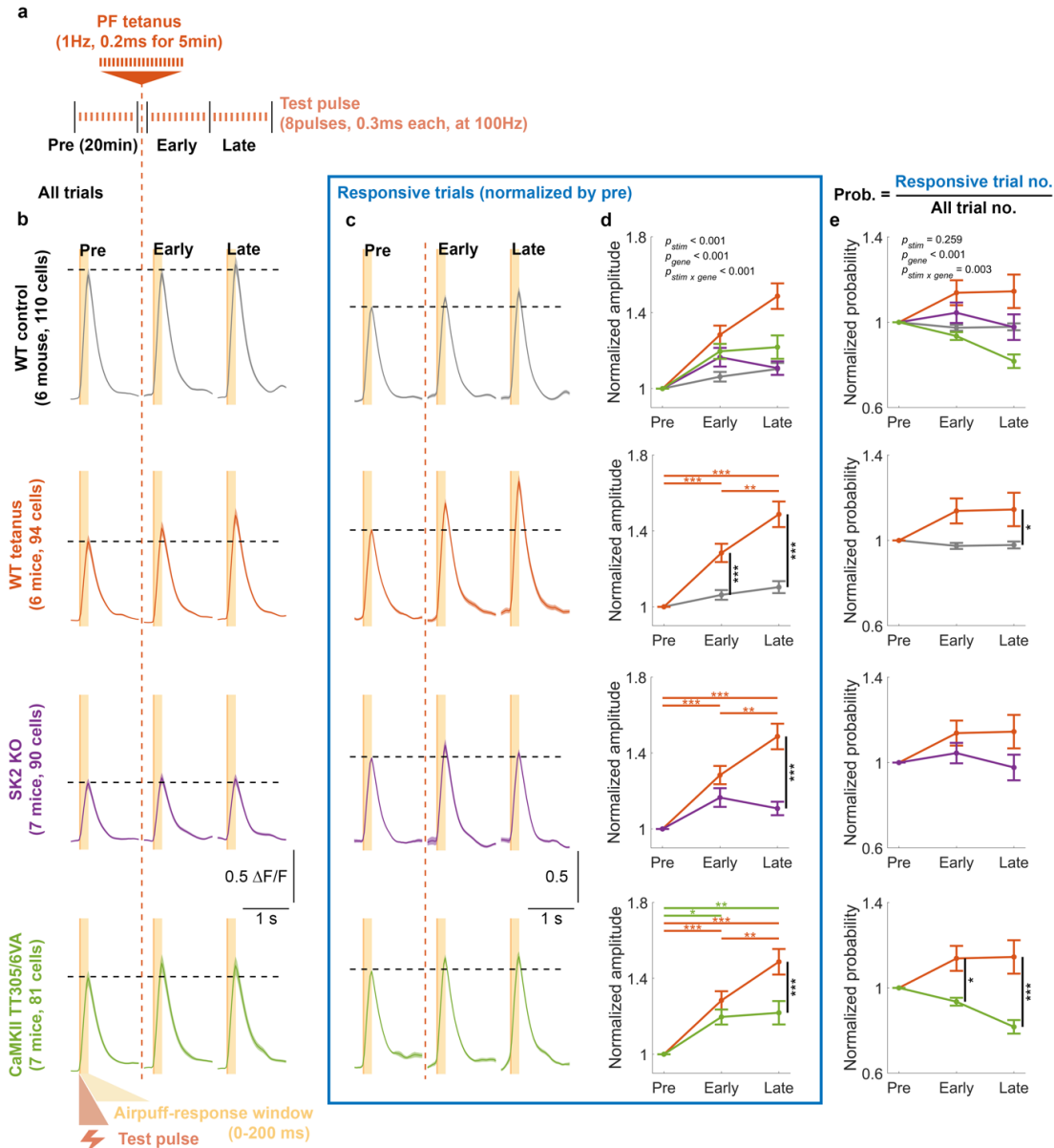
Figure 34. Electrically evoked PF plasticity on PC dendrites requires both synaptic and intrinsic plasticity in awake mice.

a. Schematic illustration of the experimental protocol *in vivo*. The recording began with a 20min baseline recording consisting of 10-12 trials, followed by a PF tetanus to potentiate the calcium response. The recording concluded with early and late post-tetanus recording periods, each consisting of 10-12 trials and lasting 20min. Post-tetanus trials began immediately (<2min) after cessation of the tetanus.

b. Average calcium signals ± SEM of different genotypes for all trials.

c. Normalized average calcium signals ± SEM for responsive trials of each genotype. The signals are normalized by the average amplitude of pre-tetanus calcium transients (y-axis scale denotes normalized value units). Only trials with detected events within the response window (0-200ms) were included.

d. Mean ± SEM of the normalized amplitudes of calcium transients for responsive trials shown in **c**. (Two-way ANOVA: $F_{stim}[2,1108] = 41.29$, $p < 0.001$; $F_{gene}[3,1108] = 17.52$, $p < 0.001$; $F_{stim \times gene}[6,1108] = 6.51$, $p < 0.001$, n = 1125).

e. Mean ± SEM of the normalized probability of detecting a calcium event within the defined time windows. Data are normalized by the probability of pre-tetanus value. (Two-way ANOVA: $F_{stim}[2,1113] = 1.35$, $p = 0.259$; $F_{gene}[3,1113] = 10.88$, $p < 0.001$; $F_{stim \times gene}[6,1113] = 3.35$, $p = 0.003$, n = 1125).

Asterisks denote the significance levels of post hoc comparisons using Tukey's HSD (*, $p < 0.05$; **, $p < 0.01$; ***, $p < 0.001$).

In these recordings, PF stimulation leads to well-timed responses that occur at high pre-tetanus probability (Appendix Figure S34), which remain unchanged after tetanization (Fig. 34e). Our *in vivo* observation of PF-RF potentiation aligns with previous studies of PF-induced potentiation conducted *in vitro* (Crepel & Jaillard, 1991; Hirano, 1990; Lev-Ram et al., 2003; Sakurai, 1987; Shibuki & Okada, 1992; Steuber et al., 2007), as well as in decerebrated (Jörntell & Ekerot, 2002) and anesthetized (W. Gao et al., 2006; Ramakrishnan et al., 2016; Reinert et al., 2004; X. Wang et al., 2009) animals. Furthermore, we find that both synaptic and intrinsic potentiation play important roles in enhancing the postsynaptic calcium response as mutant mice lacking one or the other mechanism failed to exhibit the same degree of potentiation as wild-type mice.

Synaptic and intrinsic mechanisms show distinct spatial patterns of plasticity

Though dendritic signals of individual PCs are often analyzed as a whole *in vivo*, local calcium dynamics in dendritic sub-compartments can play a critical role in PC function (Busch & Hansel, 2023; Roome & Kuhn, 2018, 2020) and may reflect input structure and distinct plasticity types. Intrinsic plasticity is hypothesized to provide a widespread amplification function necessary to increase cellular gain and compliment the role of synaptic plasticity to locally tune the weight of individual inputs (Titley et al., 2017). This hypothesis predicts that the unique mechanisms of each

plasticity type would produce distinct spatial patterns of dendritic potentiation *in vivo*, reflecting the spatial differences between tuning synaptic weights versus cellular gain. To elucidate whether intrinsic and synaptic mechanisms of PF-RF plasticity operate with distinct spatial properties, we took advantage of the high spatial resolution afforded by our two-photon imaging approach to conduct a subcellular-level investigation.

While PCs from the two mutants displayed significantly lower potentiation compared to PCs in wild-type mice, the enhanced calcium response was not completely abolished, particularly in CaMKII-TT305/6VA mice. We propose that, unlike wild-type mice with intact plasticity, SK2-KO PCs will show a particularly strong deficit in the spatial spread of potentiation since they lack a global amplifier mechanism in dendrite-wide SK2 channel expression, whereas CaMKII-TT305/6VA PCs will maintain this plasticity component more strongly (Fig. 35a-d).

To investigate the spatial pattern of PF-induced potentiation, we compared pre-tetanus calcium signals with those during early post-tetanus recordings, as this time period showed a more pronounced calcium enhancement than the late period in both mutants (Fig. 34; more example cells presented in Appendix Figure S35). Linescan imaging along a representative wild-type PC dendrite demonstrates that the potentiation of the calcium response (dendritic pixels >0.9 Normalized ΔF/F) consisted of a robust signal enhancement both within and around the responsive hotspot (Fig. 35e shows a representative PC). In SK2-KO PCs, we observed only a modest potentiation exclusively within the hotspot, and in a subpopulation (16 out of 61 cells) the surrounding area was even depressed relative to pre-tetanus values (Fig. 35f). In PCs from CaMKII-TT305/6VA mice, with intact intrinsic plasticity but impaired PF-LTP, potentiation of regions around hotspot was preserved, though the effect was less robust compared to wild types (Fig. 35g).
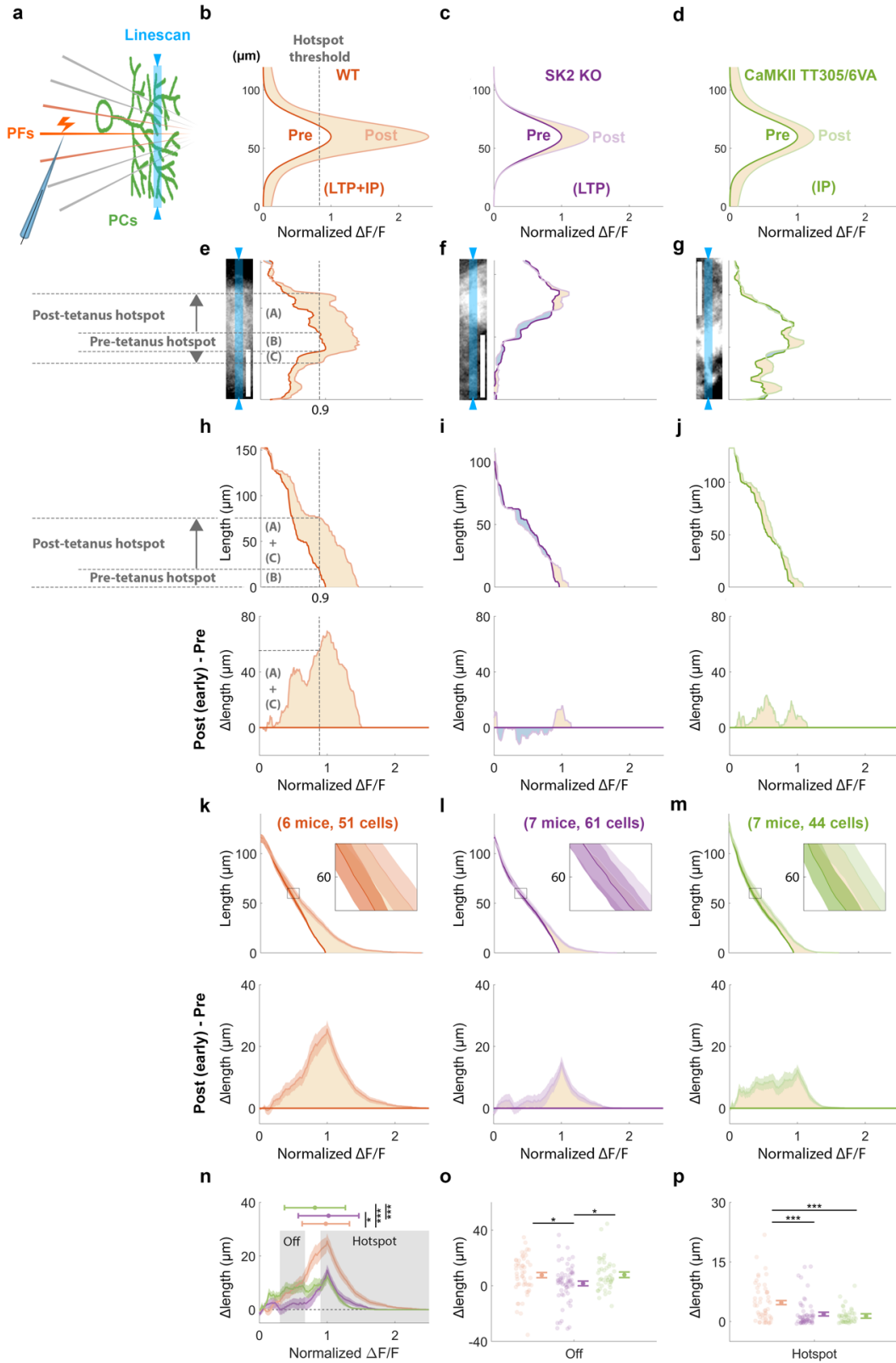
Figure 35. Selective loss of off-hotspot calcium potentiation in SK2 KO but not CaMKII TT305/6VA mice underlines the spatial role of intrinsic plasticity in global amplification.

a. Schematic diagram illustrating the linescan of PC dendrite calcium signals (blue) in response to PF stimulation.

b-d. Conceptual models depicting hypothesized fluorescence signals along the PC dendrites of **a**. Dark and light traces showing pre- and (early) post-tetanus data, respectively. The X-axis represents the ΔF/F normalized by the maximum value of pre-tetanus data.

e-g. Representative two-photon images of individual PCs from each genotype are shown in the left panels, with corresponding linescan fluorescence signals in the right panels. Blue shaded areas depict the linescan recording site. The dark and light traces represent pre- and post-tetanus data. The hotspot area (pixels with >0.9 normalized pre-tetanus ΔF/F) expanded from a length of (B) during the pre-tetanus period to a combined length of (A)+(B)+(C) during the post-tetanus period, thus the (A)+(C) represents Δlengths.

h-j. The top panel displays the cumulative lengths as a function of fluorescence level, while the bottom panel displays the corresponding Δlengths of the representative data shown in **e-g**. Cumulative lengths were obtained by summing up the dendritic length exhibiting the given fluorescence level, depicted as the dashed lines in **e** and the top panel of **h**. Δlengths were calculated by subtracting post-tetanus from pre-tetanus cumulative length, as indicated by the dashed lines in **h**.

k-m. For all cells from all mice in each group, mean ± SEM of cumulative lengths (top panel) and Δlengths (bottom panel) as in **h-j**.

n. Superimposed genotype Δlengths obtained from the bottom panel of **k-m**. The horizontal bar represents the median ± median absolute deviation of the distribution. Asterisks denote significance in distribution shift using Dunn & Sidák's approach (*, $p < 0.05$; **, $p < 0.01$; ***, $p < 0.001$) following Kruskal-Wallis test ($H[2] = 161.17$, $p < 0.001$, $n = 3929$).

o-p. Mean ± SEM of Δlengths, calculated from the off-hotspot (**o**) and hotspot (**p**) grey shaded areas shown in **n**, with individual cell values alongside. (One-way ANOVA: off-hotspot, $F[2,153] = 3.9$, $p = 0.022$; hotspot, $F[2,153] = 12.45$, $p < 0.001$, $n = 624$).

Asterisks denote the significance levels of post hoc comparisons using Tukey's HSD (*, $p < 0.05$; **, $p < 0.01$; ***, $p < 0.001$). LTP, long-term potentiation. IP, intrinsic plasticity.

To quantify the differences in spatial patterns across genotypes, we sorted linescan pixels by their fluorescence intensity to plot the cumulative length of those pixels as a function of fluorescence level (top panels of Fig. 35h-j; derived from the individual PCs of Fig. 35e-g). This provided the total dendritic length above a given fluorescence threshold (e.g., the hotspot threshold of 0.9, Fig. 35e-h section 'B'), regardless of location along the dendrite. The cumulative length could then be compared between pre- and post-tetanus to obtain a tetanus-induced Δlength value.

Genotype differences in Δlength revealed that the calcium signal expanded in wild-type and, to a lesser degree, CaMKII-TT305/6VA mice at all fluorescence levels (Fig. 35h and 35j). In contrast, while SK2-KO mice also exhibited a diminished potentiation, this effect was limited to the PF-responsive hotspot and the off-hotspot region (0.3-0.67 normalized ΔF/F) such that intermediate fluorescence became more narrow (Fig. 35i).

Upon averaging the cumulative length and Δlength of all recorded PCs by genotype (Fig. 35k-m), we observed a similar pattern to that exemplified by the representative individual data. However, as only a subset of SK2-KO PCs exhibited the hyper-localized 'narrowing' of the off-hotspot region, the effect was less pronounced in the broader cell population across animals (Fig. 35l). Nonetheless, the reduced expansion remained evident compared to the other two genotypes (Fig. 35n-o). Across cells, the off-hotspot region was centered around 60μm cumulative length from the peak intensity of the hotspot (insets in Fig. 35k, 35l, and 35m), which represents the dendritic area ~30μm on either side of responsive peak in the PC cross section. As such, impairment of SK2-KO, but not CaMKII-TT305/6VA, plasticity in this region indicates the spatial influence of intrinsic mechanisms. Furthermore, the hotspot of both mutants showed less potentiation effect compared to wild types (Fig. 35p). As a result, the population Δlength distribution (Fig. 35n) revealed a leftward shift in CaMKII-TT305/6VA PCs (reduced hotspot expansion) and a rightward shift in SK2-KO PCs (reduced off-hotspot expansion) compared to wild types. These differences were transient, as the difference in spatial patterns faded during the late post-tetanus period (Appendix Figure S36), primarily attributed to the transient potentiation of the off-hotspot area in CaMKII-TT305/6VA PCs (Appendix Figure S36l).

Taken together, these results demonstrate the spatial patterns of different plasticity mechanisms. Synaptic mechanisms alone (SK2 KO) sharpen the response area through local

potentiation, while intrinsic mechanisms alone (CaMKII TT305/6VA) permit a widespread potentiation along the dendrite.

Dendritic calcium events relate to PC axonal output

Thus far, we have treated the measured dendritic calcium events as a read-out of PC activity without asking the question whether these events remain locally isolated or influence axonal spike output. Although the correlation between PF input and the SS output has been studied extensively in the past (Lev-Ram et al., 2003; Nilsson & Jörntell, 2021; Steuber et al., 2007), it remains undetermined whether dendritic calcium events – the measure used in our two-photon recordings from intact animals – reflect this input-output relationship as well. Of note here, we have previously shown that dendrite-soma coupling is modulated by SK2-channel-dependent intrinsic plasticity (Ohtsuki & Hansel, 2018).

In previous studies, somatic and AIS calcium signals have been correlated with neural firing in PCs (Gründemann & Clark, 2015; Ramirez & Stell, 2016). To identify corresponding calcium activity across dendrites, soma, and AIS, we stimulated PF bundles and recorded PCs located in the bank of lobule Crus I sulcus (Fig. 36a), as opposed to the superficial gyrus, where PCs lie perpendicular to the imaging plane. This strategy allowed us to record all three cellular compartments simultaneously and draw ROIs separately based on their morphology (Fig. 36b). Figure 36c-d show the average signals of spontaneous and PF-evoked calcium transients, respectively, alongside the morphological structures shown in Fig. 36b. We observed that calcium activity in the dendrites is often accompanied by calcium transients in the soma and AIS, regardless of whether it is generated spontaneously (Fig. 36c and Appendix Figure S37a-c) or evoked by PF stimuli (Fig. 36d and Appendix Figure S37d-f). To further examine their relationships, we

conducted correlation analyses between calcium amplitude in the dendrites and either the soma or AIS (Fig. 36e-h). We observed a significant correlation between AIS and dendrites in response to PF electrical stimuli (Fig. 36h), indicating the impact of dendritic PF input on axonal activity. As discussed previously, our PF-induced dendritic calcium events likely reflect dendritic voltage spikes shown to result from PF stimulation *in vivo* (Nilsson & Jörntell, 2021). Additionally, we observed a suppression of calcium signal following the positive calcium transient (bottom panel of Fig. 36d), though the suppression level is not correlated with the amplitude of dendritic calcium transients (Appendix Figure S37d and f). This suppression might correlate with a pause in spike firing that has been described following PF bursts (Steuber et al., 2007). In conclusion, our data show that the PF-evoked dendritic calcium signals do indeed impact the somatic and axonal compartments in a manner that is likely to shape PC output.
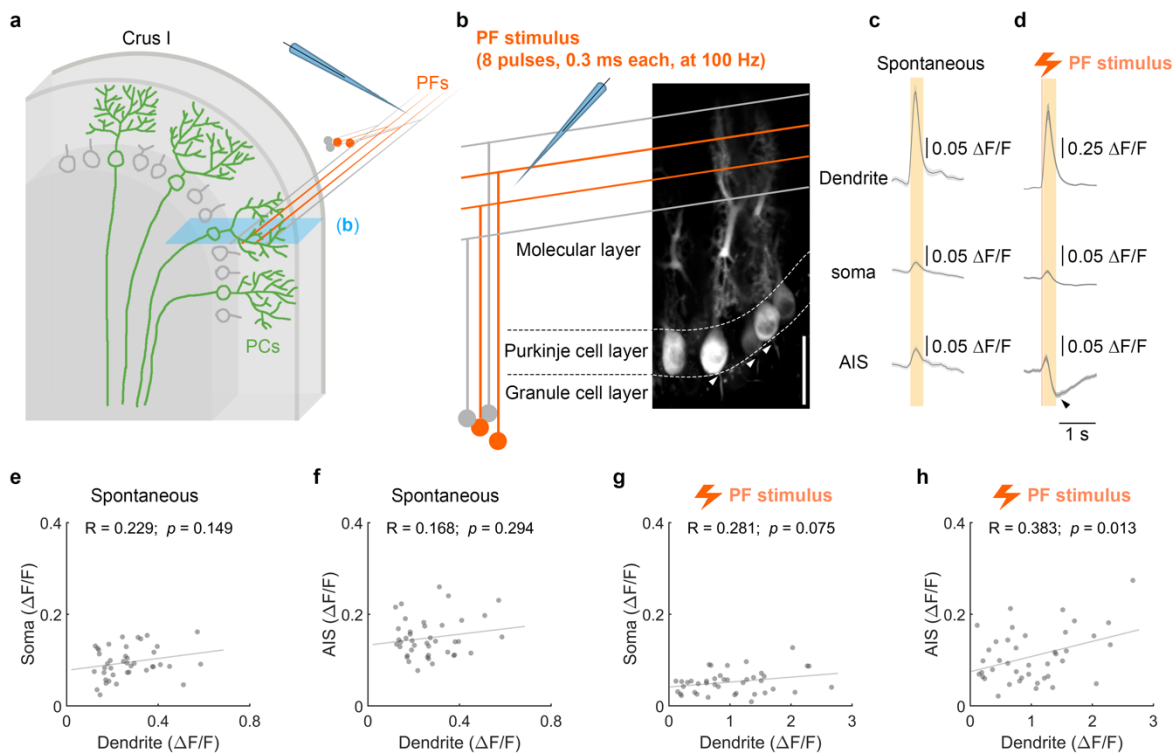
Figure 36. Simultaneously recorded calcium response amplitudes in PC dendrites and AIS are correlated during PF stimulation.

a. Schematic of microelectrode placement to apply electrical stimuli to a bundle of PFs while two-photon imaging was performed in the sulcus of lobule Crus I, where PCs lie horizontal to the imaging plane. This allowed the dendrite, soma and AIS of each PC to be captured within a single field of view. The blue shaded area represents the two-photon image plane, which yields a calcium image such as that shown in **b**.

b. Representative two-photon images of the dendrites, soma, and AIS of each PC captured by a single field of view. Arrowheads point to the AIS. The schematic diagram shows PF stimulation using a microelectrode to generate a calcium response. Calcium imaging followed the same protocol as for PF-RF experiments (Fig. 32). Scale bar is 50μm.

c-d. Mean ± SEM of spontaneous calcium events (**c**) and evoked responses (**d**) of 41 cells from 5 mice. The black arrowhead in **d** indicates a suppression of AIS calcium signals following the initial response.

e-h. Maximum values of somatic and axonal calcium transients plotted against the maximum values of dendritic signals within the time window of 0-200ms after the initiation of the rising phase and stimulus for spontaneous events (**e-f**) and evoked events (**g-h**). Lines represent the linear regression fit, with R indicating the Pearson correlation coefficient and *p* indicating its significance.

Tactile stimulation elicits analog calcium signals in PC dendrites

While extensive research has explored phenomenological attributes of cerebellar tactile-RF plasticity through electrophysiological experiments (Jörntell & Ekerot, 2011; Márquez-Ruiz & Cheron, 2012; Ramakrishnan et al., 2016), the underlying mechanisms of cellular plasticity remain unclear. To obtain a highly reproducible readout of tactile-RFs in physiological conditions, we delivered airpuffs to the finger or wrist on the ipsilateral forelimb using a glass capillary tube (see Appendix 1: Methodology and Statistics; Fig. 37a-b) while recording the corresponding calcium response in PCs of awake mice (Fig. 37c). Trials with motion were removed and a gentle airpuff stimulus (4-10psi) was used to avoid aversive responses and reduce the probability for the activation of an olivary climbing fiber (CF) pathway which is generally sensitive to tactile and nociceptive input (Ekerot et al., 1991b, 1991a; Ekerot & Jörntell, 2001). At the start of each experiment, we identified the region of lateral Crus I responsive to tactile stimulation of the paw

and then focused our recording on the medial edge. Recording at the border of this tactile response area provided a higher ceiling for potentiation of tactile responsiveness while still minimizing the likelihood of failing to observe paw responsiveness.

To characterize calcium responses to tactile stimulation of the forelimb, we compared spontaneous calcium events, randomly sampled from a 200ms time window before the airpuff stimulus, with time-locked responses during 0-200ms after stimulus onset. As in earlier experiments with direct PF stimulation, we tested responses to a range of stimulus strengths using a step increment of only 2psi (4, 6, 8, and 10psi; Fig. 37d-e) and observed an intensity-dependent increase in responsive trials (Fig. 37e), also reflected by the linear increase of response probability from 0.25 to 0.37, compared with 0.22, the spontaneous probability within shuffled windows before the stimulus (reflecting a 1.25 to 1.85Hz evoked rate, and 1.1Hz spontaneous rate, within the 200ms windows; Fig. 37f). By plotting the average calcium signal of all trials, we also observed a stimulus intensity-dependent increase in the size of calcium transients (Fig. 37d) though this could be attributable to a change in either the amplitude, probability, or both. Therefore, we separately analyzed the average signals of only responsive trials and observed a modest increase in amplitude (Fig. 37g), consistent with *in vitro* studies of PF responses in PCs (Canepari & Vogt, 2008; Hartell, 1996), and our result *in vivo* (Fig. 33).
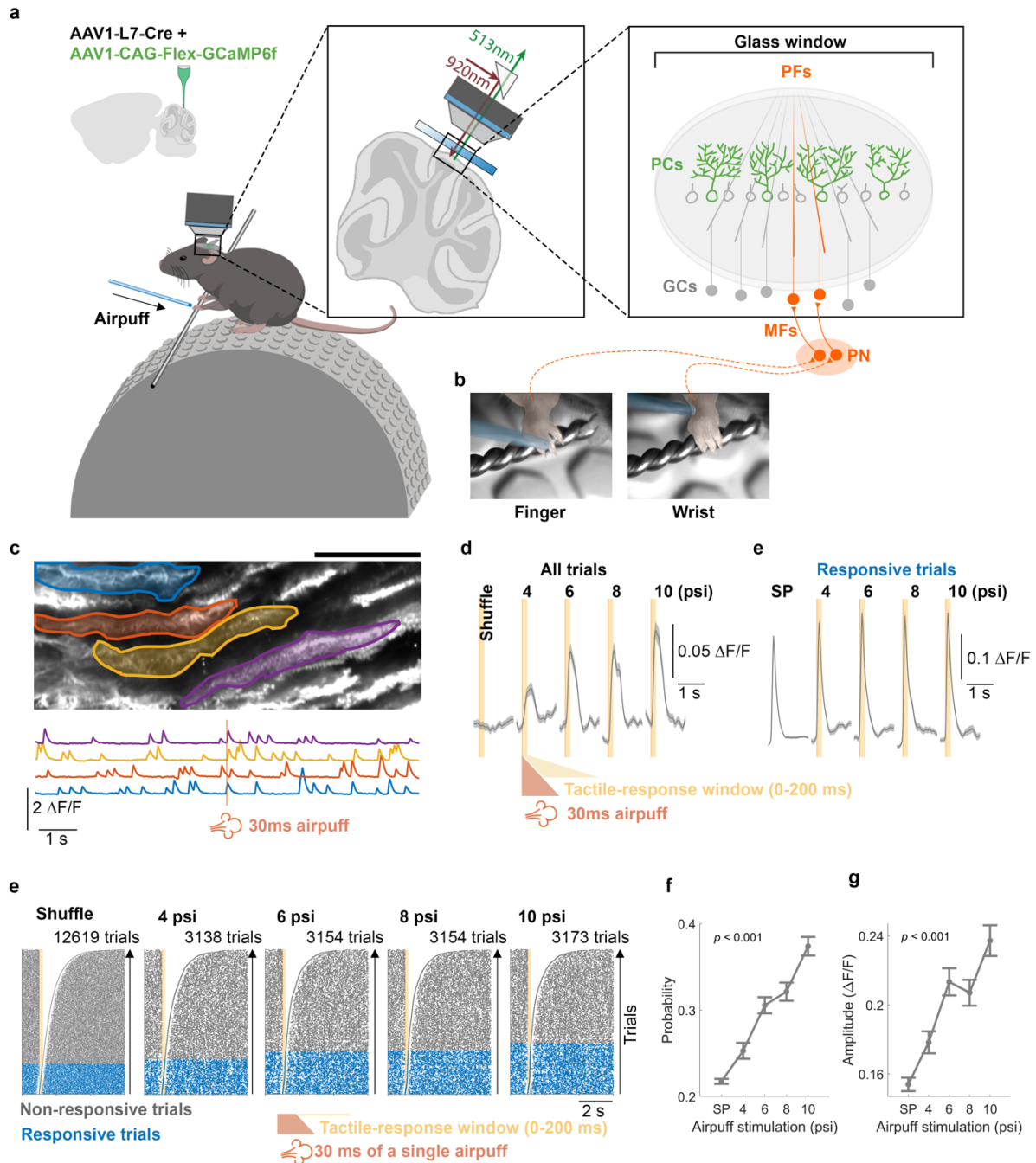
Figure 37. PC dendritic calcium responses to tactile stimuli exhibit a linear stimulus-intensity dependence.

a-b. AAV vectors were injected into Crus I of cerebellar cortex to express Cre-dependent GCaMP6f specifically in PCs. Cutaneous airpuff stimuli were applied to the finger or wrist of the forelimb while calcium responses in PC dendrites were recorded in ipsilateral Crus I under the two-photon microscope. Trials with movement of the limb or body were discarded.

c. Example field of view with a subset of manually drawn dendritic ROIs and corresponding deconvolved calcium traces below from one 20s trial with an airpuff delivered to the wrist at 10ms. Calcium images were obtained with a 62 Hz frame rate, 3-4x digital zoom, and dimensions of 380-669μm width and 153-270μm height.

d-e. Average calcium signals ± SEM for all trials (**d**) and responsive trials (**e**).

f. Raster plots depict trials with both spontaneous and evoked responses to airpuff stimuli with varying pressures (4, 6, 8, and 10psi). To estimate a spontaneous event rate, 200ms time windows were randomly selected from the period before the stimulus and aligned to compare with evoked trials that are aligned by stimulus onset. The light orange area represents a 200ms shuffling window for spontaneous events or a response window (0-200ms) for evoked events. Trials with detected events within the response window are categorized as responsive trials (blue), whereas those without are considered non-responsive trials (gray). Trials are sorted based on the timing of the first event following the initiation of either time window.

g. Probability (mean ± SEM) of detecting a calcium event within the defined time windows for spontaneous or responsive conditions. (One-way ANOVA: $F[4,1225] = 45.14$, $p < 0.001$, n = 1230).

h. Maximum values (mean ± SEM) within the 200ms shuffled time window or after the initiation of stimulus for evoked calcium transients shown in **d**. (One-way ANOVA: $F[4,1225] = 20.62$, $p < 0.001$, n = 1230).

GCs, granule cells. MFs, mossy fibers. PN, pontine nuclei. SP, spontaneous calcium events. Sh, shuffled traces. (246 cells from 18 mice for all analyses).

Based on the correlation coefficients of either probability or amplitude across stimulus conditions and normalized by spontaneous events, we categorized PCs into stimulus intensity-dependent or -independent groups (Appendix Figure S38). Approximately 52% and 56% of PCs were categorized as the stimulus intensity-dependent group based on their probability and amplitude parameters, respectively. Initially, it was believed that *in vivo* dendritic calcium responses were exclusively due to CF input (Gaffield et al., 2019; Kitamura & Häusser, 2011), but subsequent studies showed that these responses may also contain non-CF components (Najafi et al., 2014a, 2014b; Roome & Kuhn, 2018, 2020). In the current study, the dependence of evoked calcium transients on the small step change in stimulus intensity resembles the stereotypical PF response. Therefore, we conducted further examinations to determine whether calcium signals in

awake mice exhibit tactile-RF plasticity that is achieved through plasticity within the PF-PC pathway (Ramakrishnan et al., 2016).

Intrinsic and synaptic plasticity contribute to tactile-RF plasticity

To investigate plasticity of RFs to tactile stimulation (tactile-RFs) in PCs, we recorded changes in calcium responses to tactile stimuli (specifically airpuffs to the wrist; see Appendix 1: Methodology and Statistics) before and after application of a repetitive tactile induction protocol. To estimate the pre-tetanus baseline calcium response to an airpuff stimulus (8psi, 30ms), we performed 10-12 trials over 20min. Airpuff tetanization (8psi, 30ms) was then applied at 4Hz for 5min, reproducing a tactile-RF plasticity protocol described in previous studies (Jörntell & Ekerot, 2011; Márquez-Ruiz & Cheron, 2012; Ramakrishnan et al., 2016). We then recorded the conditioned calcium response for 40min post-tetanization and divided the responses into 20min early and late post-tetanus periods (Fig. 38a). While intrinsic and synaptic potentiation have been suggested to underlie various forms of cerebellar learning (Jörntell & Hansel, 2006; Titley et al., 2017), their role in tactile-RF plasticity in an intact, awake animal has not been tested before.
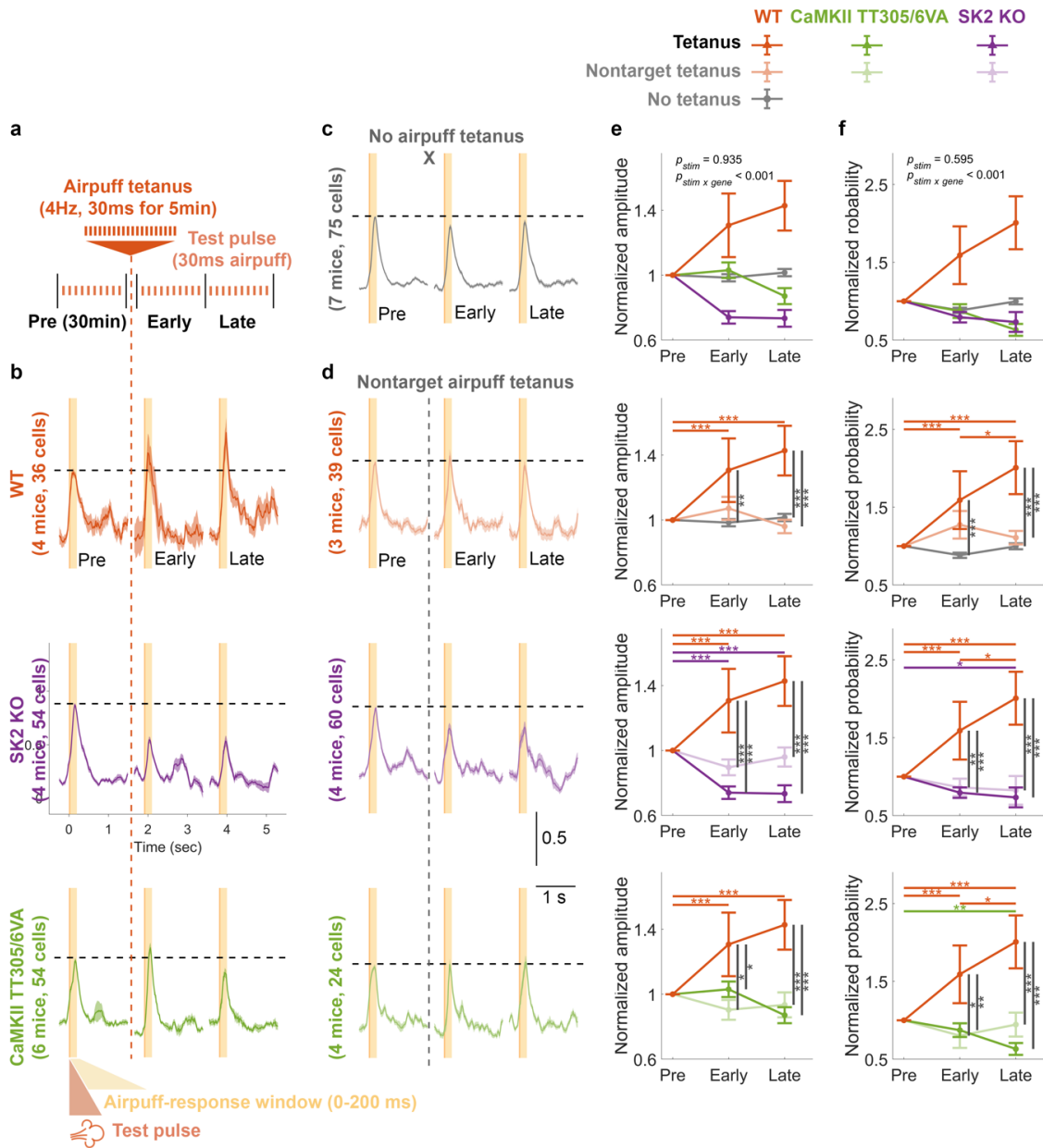
Figure 38. Physiological tactile-RF plasticity on PC dendrites requires both synaptic and intrinsic plasticity.

a. Schematic illustration of the experimental protocol for wrist airpuff tetanization. The recording began with a 20min baseline recording consisting of 10-12 trials, followed by a wrist airpuff tetanus to potentiate the calcium response. The recording concluded with another 20min early and late post-tetanus recordings, each consisting of 10-12 trials. Post-tetanus trials began immediately (<2min) after cessation of the tetanus.

b. Normalized average calcium signals ± SEM across trials from different genotypes.

c. Normalized average calcium signals ± SEM across trials of the control condition in WTs where no tetanization protocol was applied.

d. Normalized average calcium signals ± SEM across trials from control conditions across genotypes where airpuff tetanization was applied to the finger and thus was unmatched to the test location (wrist). The signals shown in **b-d** are normalized by the average amplitude of pre-tetanus calcium transients (y-axis scale denotes normalized value units). Only trials with detected events within the response window (0-200ms) were included.

e. Mean ± SEM of the normalized calcium-event amplitudes, calculated as the maximum value within the 0-200ms time window of individual trials. The data were normalized by the pre-tetanus amplitude. (Two-way repeated measure ANOVA: $F_{stim}[2,1144] = 0.068$, $p = 0.935$; $F_{stim\ x\ gene}[24,1144] = 4.126$, $p < 0.001$, n = 2073).

f. Mean ± SEM of the normalized probability of detecting a calcium event within the 0-200ms time windows. The data were normalized by the pre-tetanus probability. (Two-way repeated ANOVA: $F_{stim}[2,1356] = 0.520$, $p = 0.595$; $F_{stim\ x\ gene}[24,1356] = 5.274$, $p < 0.001$, n = 2067). Asterisks denote the significance levels of post hoc comparisons using Tukey's HSD (*, $p < 0.05$; **, $p < 0.01$; ***, $p < 0.001$).

To investigate this, we asked whether tetanization would enhance the calcium response probability or amplitude within the 0-200ms time window. Here we consider both measures – response probability and amplitude– to be relevant parameters in describing a neuronal RF as both identity and strength dictate the cellular representation. The time window was selected to capture the early response that encodes peripheral inputs (Shimuta et al., 2020). (Note that the overall calcium response may peak after 200ms, Fig. 38b; our analysis nevertheless focuses on early response amplitudes that better reflect immediate responses to sensory input.) The analysis of evoked calcium responses (Fig. 38b), compared with control experiments wherein airpuff stimuli during tetanus were absent (Fig. 38c) or directed to the unmatched location on the paw (i.e. to finger during wrist response testing; Fig. 38d), showed that both calcium amplitude (Fig. 38e) and probability (Fig. 38f) were significantly potentiated after the induction protocol in wild-type mice. We also found that these changes were absent in SK2-KO and CaMKII-TT305/6VA mice as in wild-type mice under control conditions (see Appendix 1: Methodology and Statistics). Here, the amplitude was measured as the maximum value within the time window because PF-evoked

responses in a naturalistic condition are not expected to exhibit a sharp spike shape (Roome &

Kuhn, 2018, 2020) that can be reliably detected using defined criteria (Najafi et al., 2014a). The

absolute values of pre-tetanus baseline are provided in Appendix Figure S39. We also performed

airpuff finger tetanization experiments but did not observe potentiation (Appendix Figure S40).

Tetanization of the underlying white matter –which includes CFs– does not result in potentiation

The responses to tactile stimulation reported here likely include both PF- and CF-mediated

components. Recently, numerous challenges have been posed to classically used parameters to

identify CF (all-dendrite signal) and PF responses (linear increase in response amplitude upon

increase in stimulus intensity). PF inputs may cause all-dendritic signals *in vivo* as granule cells

project a dense input representation to PCs (Giovannucci et al., 2017). CF input participation

cannot be fully excluded by a linear stimulus-intensity dependence (Fig. 37) as CF input also

displays graded responses, e.g. as a result of changes in the CF burst waveform (Gaffield et al.,

2019; Roh et al., 2020; Roome & Kuhn, 2020). To assess whether the CF input is even able to

undergo potentiation under the tetanization protocols used here, we performed the following

control experiment. Using the same approach as for PF stimulation but with deeper penetration of

the stimulating electrode (Appendix Figure S41a-b; see Appendix 1: Methodology and Statistics),

we electrically stimulated the white matter (WM) below and leading to the PCs of interest to record

test responses (Appendix Figure S42) and apply tetanic stimulation. WM stimulation in this

location will activate the CF input, among other input structures, and cause a massive CF response

in the downstream PCs (Eccles et al., 1964). Application of the test stimulus (4 pulses at 333 Hz,

mimicking a typical CF burst waveform (Maruta et al., 2007)) at 4Hz for 5min (Appendix Figure

S41c), to reproduce the tactile tetanic protocol, caused a significant reduction in calcium response amplitudes in the early phase (Appendix Figure S41d-e), without a significant change observed in the late phase. The response probability was reduced during the early and late phases (Appendix Figure S41f). Thus, we observed response depression that, at least in the early phase, resembled CF-LTD (Hansel & Linden, 2000). No cells exhibited response potentiation, strongly suggesting that non-CF components evoked by tactile stimulation are responsible for the tactile response potentiation described in Figure 38.

Direct PF tetanization mimics tactile tetanization to induce tactile-RF plasticity

Having found that the CF component of the tactile response is unlikely to potentiate under our tactile tetanization protocol, we next asked whether we could directly show that the PF component of a tactile response could induce tactile-RF expansion. To test this, we monitored PC responses to both electrical (PF) and wrist (tactile) stimulation before and after PF tetanization (Fig. 39a). We hypothesized that if PF potentiation was responsible for tactile-RF expansion, then PCs with formerly little to no tactile response may develop a sensitivity to the paw stimulus after tetanization. Indeed, we observed that PCs exhibiting a potentiated PF response after tetanization also displayed a strengthening of their tactile response (Fig. 39b, *top*). Furthermore, when we selectively analyzed the subset of PCs with undetectable tactile responses during the pre-tetanus baseline (having an averaged maximum response amplitude less than 1.8 ΔF/F, double our calcium event inclusion criterion; Fig. 39b, *bottom*; see Appendix 1: Methodology and Statistics), we found that all cells but one increased in amplitude (Fig. 39c-d). Notably, many cells exhibited such a large potentiation that their average response amplitude grew to exceed the detection threshold in the post-tetanization period (values in the upper left quadrant of the vertical and horizontal dotted

threshold lines; Fig. 39e). Thus, it is likely that the PF stimulus included a subset of PF inputs encoding sensory information from the wrist and that the tetanization protocol was sufficient to potentiate those inputs and strengthen the total PC dendritic representation of the tactile stimulus.
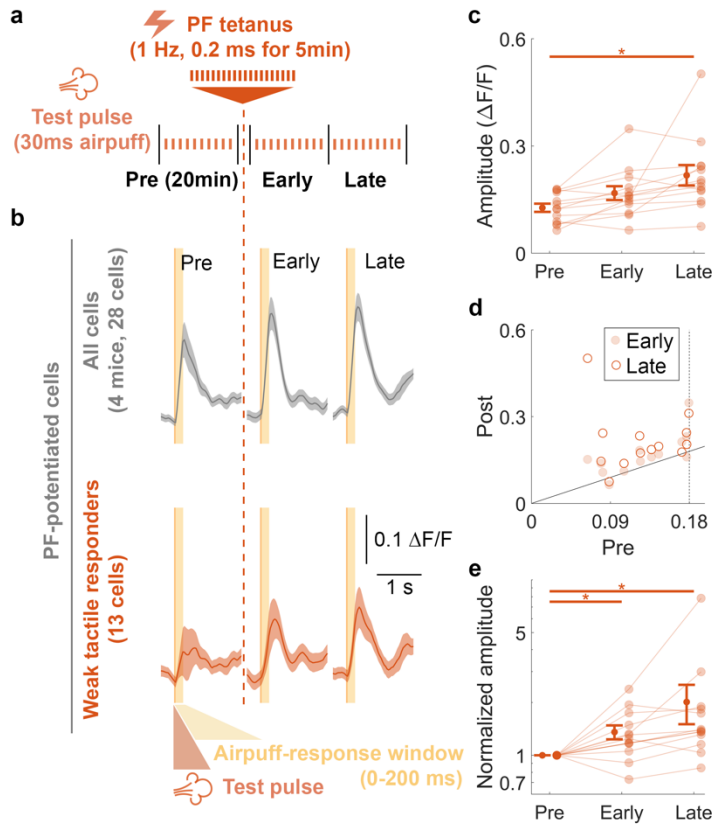
Figure 39. PF tetanization induces tactile-RF plasticity and adds new inputs to the tactile stimulus representation of PCs.
a. Schematic illustration of the experimental protocol *in vivo*. Calcium imaging followed the same protocol as for PF-RF experiments (Fig. 32). The recording began with a 20min baseline recording consisting of 10-12 trials each of PF and tactile responses, followed by a PF tetanus using the PF tetanus protocol of 1Hz for 5min. The recording concluded with early and late post-tetanus recording periods, each consisting of 10-12 trials of both PF and tactile responses and lasting 20min. Post-tetanus trials began immediately (<2min) after cessation of the tetanus.
b. Average calcium signals ± SEM for all cells exhibiting PF potentiation (*top*, All cells) and the subset with below-threshold responses during baseline (*bottom*, Weak tactile responders).
c. Mean ± SEM of the raw calcium-event amplitudes for the subpopulation of non-responding cells, calculated as the maximum value within the 0-200ms time window of individual trials. (One-way ANOVA: $F_{[2,52]} = 7.486$, $p = 0.001$, $n = 84$).

d. Mean ± SEM of the normalized calcium-event amplitudes, calculated as the maximum value within the 0-200ms time window of individual trials. The data were normalized by the pre-tetanus amplitude. (One-way ANOVA: $F[2,52] = 5.509$, $p = 0.007$, $n = 84$).

e. Mean raw calcium-event amplitudes after tetanization (Post) plotted as a function of baseline amplitude (Pre). Values for early (solid dot) and late (empty dots) post-tetanus periods are plotted separately for each cell. Dotted lines indicate 2x the individual calcium event amplitude detection threshold. Points falling above the solid unity line exhibited potentiation. Points in the upper left quadrant of the dotted lines exhibited potentiation from below to above detection threshold. Asterisks denote the significance levels of post hoc comparisons using Tukey's HSD (*, $p < 0.05$; **, $p < 0.01$; ***, $p < 0.001$).

Discussion

Our study demonstrates that both direct PF tetanization and tetanic application of naturalistic tactile stimuli can potentiate dendritic calcium responses in PCs of awake mice (Fig. 40). These effects are abolished in genetically modified mice with selective deficits in either synaptic (Fig. 40b) or intrinsic plasticity (Fig. 40c), demonstrating that both are necessary cellular determinants of the overall intact plasticity phenomenon (for effects on baseline response parameters, see Appendix Figures S34 and S39). The role of synaptic plasticity in information storage and memory is established (Nabavi et al., 2014). Here, we asked whether intrinsic plasticity would add a qualitatively distinct function to LTP. The response parameter measured in our recordings – the dendritic calcium signal – is linked to an output signal in the soma/AIS (Fig. 36; discussed further below). Our finding that in the absence of SK2-mediated intrinsic plasticity synaptic LTP is unable to enhance this dendritic calcium response demonstrates that there are two cellular plasticity mechanisms that need to take place to couple enhanced synaptic input to enhanced signal propagation in the dendrite of target neurons: 1) LTP and 2) intrinsic potentiation that – by downregulating K^+ channels – opens a permissive gate for propagation and, ultimately, spike

output. The two-photon-monitored dendritic calcium signal is a measure of synaptic drive and intrinsic amplification, and thus captures the critical driving parameters involved well.
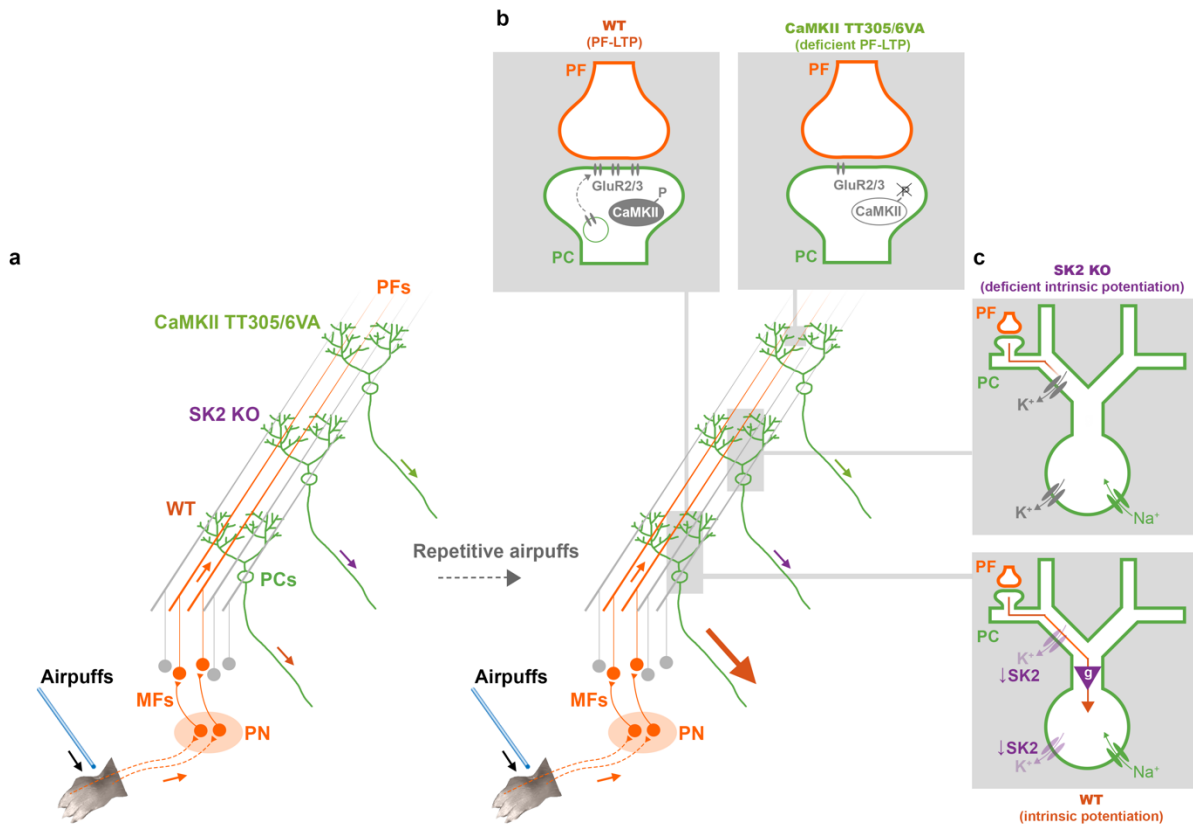
Figure 40. RF potentiation requires both local PF-LTP and an SK2 gate control.
a. Potentiation of tactile response in PCs can be evoked by a repetitive PF stimulation. However, this potentiation is impaired without either PF-LTP (**b**) or intrinsic potentiation (**c**).
b. Blockade of CaMKII inhibitory autophosphorylation enhances the probability that CaMKII is in an active state, which at these synapses, in turn, lowers the probability for LTP.
c. SK2 regulation in dendrite and soma serve as a tunable gain operator (purple triangle) that gates the propagation of dendritic EPSPs towards the soma, and thus the effect of local PF-PC synaptic plasticity. PF-LTP without a coherent downregulation of SK2 channels is not sufficient to reveal the dynamic change in activity of PC dendrites, soma, or axon. Note that in SK2-KO mice, the baseline calcium responses are equally large or smaller than in WT mice (Appendix Figures S34 and S39), pointing to a compensatory mechanism (potentially through upregulating different types of K+ channels as depicted with grey color in the top panel) that stabilizes excitability without enabling its plasticity. Thus, dendritic gating is not expected to be different under baseline conditions in SK2-KO mice. MFs, mossy fibers. PN, pontine nuclei. LTP, long-term potentiation.

161

Previous studies have reported that LTP and LTD can increase or decrease the SS frequency in response to PF or tactile stimuli, both *in vitro* and *in vivo* (Jörntell & Ekerot, 2002, 2011; Lev-Ram et al., 2003; Márquez-Ruiz & Cheron, 2012; Ramakrishnan et al., 2016; Steuber et al., 2007). However, the mechanisms that regulate input integration and signal propagation in the dendrite remain unclear. To investigate synaptic and intrinsic components of plasticity, we selected two approaches: a) measurement of calcium responses to direct electric stimulation of PF bundles and b) measurement of calcium responses to tactile stimuli, which were previously thought to only reflect CF input *in vivo* (Gaffield et al., 2019; Kitamura & Häusser, 2011), but which have recently been shown to also contain non-CF input components (Najafi et al., 2014a, 2014b; Roome & Kuhn, 2018, 2020). In both recording scenarios, input tetanization resulted in a potentiation of calcium responses. Before discussing the intrinsic plasticity contribution, the synaptic players involved deserve consideration.

Perhaps the most simplistic interpretation is that PF tetanization causes PF-LTP. This scenario is supported by the observation from patch-clamp recordings in cerebellar slices that the same 1Hz, 5min stimulation of PF synapses (GABA$_A$ receptors blocked) indeed causes LTP (Coesmans et al., 2004). In this simplistic interpretation, tactile stimulation would similarly activate PFs, producing PF-LTP that then mediates potentiation of the overall response. A challenge to this simplistic scenario comes from the likely participation, or even dominance, of CF components in the response to tactile stimulation (Gaffield et al., 2019; Kitamura & Häusser, 2011). Although not demonstrated as a plasticity phenomenon in adult rodents yet, LTP might occur at CF synapses and this effect could mediate tactile response potentiation. Our control experiments exclude this possibility, as CF inputs (activated with a WM stimulation protocol) failed to potentiate, and actually depressed, following tetanization with the same temporal pattern applied during tactile

experiments (Appendix Figure S41). Finally, it is possible that depression of molecular layer interneurons (MLIs) causes a disinhibition of CF responses (Gaffield et al., 2018). CFs may drive MLI activation (Mathews et al., 2012) and potentially trigger MLI plasticity, but our CF stimulation experiments also make this scenario unlikely as we would expect to see an MLI-mediated potentiation of CF responses. This leaves PF-driven feedforward inhibition via MLIs as a potential scenario (Mittmann et al., 2005; ten Brinke et al., 2015).

Plasticity of MLI inhibition may indeed contribute to the response potentiation observed here. As noted above, our CF stimulation experiment indicates that this plasticity must be triggered by PF activation, both in the recordings of PF responses and tactile responses, suggesting even in the latter a substantial PF response component. Moreover, the fact that PF-LTP results from 1Hz, 5min PF stimulation in slices when inhibition is blocked (Canepari & Vogt, 2008) and various low- and high-frequency protocols when inhibition is intact (Titley et al., 2019) suggests this is a robust phenomenon that occurs at activated PF synapses under these conditions. Thus, it is reasonable to conclude that PF-LTP contributes to the response potentiation seen in the PF stimulation experiments (Fig. 3). However, MLI plasticity – causing a disinhibitory effect – cannot be excluded as a factor that adds to the overall potentiation. For the larger question that this study addresses – whether intrinsic plasticity plays a critical role in the gating of dendritic potentials – we focus on a dendritic potential that in its sum is depolarizing, subject to potentiation, and that is gated by intrinsic plasticity, regardless of whether this potential and its potentiation was in some way shaped by inhibition.

What do our findings tell us about intrinsic amplification and gating? The absence of intrinsic plasticity in SK2-KO mice prevented almost all calcium potentiation, while CaMKII-TT305/6VA mice lacking synaptic potentiation exhibited a partially impaired yet significant residual

potentiation effect (Fig. 3; in light of the observed plasticity impairment in these mutants, no further control experiments were performed to observe response fate in the absence of tetanization; see, however, off-tetanization site controls shown in Fig. 38d-f). These observations demonstrate that intrinsic plasticity does not merely enhance the effects of LTP, but instead exerts a permissive gating function (Fig. 40). Without intrinsic gate regulation (opening), the amplitude of distal EPSPs remains poorly correlated with spike output (Larkum et al., 2001; Ohtsuki & Hansel, 2018), likely because intrinsic conductances across the dendrite attenuate the dendritic potential while it propagates towards the soma.

By analyzing the spatial patterns of calcium amplification, we observed distinct forms of potentiation (Fig. 35): local potentiation in the synaptic plasticity model (SK2 KO) and global potentiation in the intrinsic plasticity model (CaMKII-TT305/6VA). These observations provide insights into how different plasticity mechanisms modulate PF responses at different distances relative to the stimuli. Notably, only SK2 KO showed a limited expansion of the off-hotspot area (Fig. 35o), while both mutants displayed impaired amplitude potentiation of the hotspot compared to wild types (Fig. 35p). These observations suggest that only intrinsic plasticity exerts long-distance effects (~30μm relative to the center of PF stimuli in the image plane), while both mechanisms contribute to potentiation on the hotspot. Through their complementary roles, the interplay between synaptic and intrinsic plasticity enables the expansion of the RF without compromising input selectivity.

PF tetanization causes a potentiation of tactile test responses (Fig. 39). This finding allows for two conclusions. First, potentiation of these responses may result from plasticity of PF synapses and perhaps inhibitory synapses, but it does not require plasticity at CF synapses, thus confirming what we learned from the control experiments, in which no potentiation resulted when the CF input

was directly tetanized (Appendix Figure S41). Second, detectable tactile responses evolve from signals below the defined detection threshold (thus including no responses and very low responses). This observation shows that RF plasticity is taking place, which shows as not only an increase in the response amplitude, but as a true expansion of the RF (Fig. 39e). It should be noted that the response to tactile stimulation evolved from an input that previously did not evoke a calcium response, while there were baseline responses to PF stimulation. Thus, the observed phenomenon likely constitutes RF plasticity in PCs that is based on enhanced synaptic weight and permissive gating by intrinsic plasticity. Without this plasticity, the dendritic potential may remain inconsequential as it does not sufficiently propagate through the dendrite.

Local PF input does not always lead to faithful modulation of spike output. Instead, the summation of multiple inputs, whether temporal (Ohtsuki & Hansel, 2018) or spatial (Ohtsuki, 2020), is required to exert an influence on spike output. Only then would the preceding PF inputs be considered physiologically significant. By up-regulating the excitability of compartmental or entire dendrites, the likelihood of inducing spiking activity can be enhanced (Ohtsuki & Hansel, 2018). In our investigation, we examined calcium signals in various regions of the PCs, including dendrites, soma, and AIS, simultaneously (Fig. 36). Obtaining calcium signals from the soma and AIS has been challenging primarily due to the high firing frequency. However, through adjustments in the experimental configuration and by averaging signals from multiple trials, we were able to obtain clear calcium responses time-locked to the stimulus. The significant correlation between dendritic and axonal responses confirmed the impact of dendritic input on axonal output. This finding legitimates the optical plasticity measure used here and suggests that potentiation in the dendritic calcium response is predictive of a higher probability for neuronal spike firing.

Nevertheless, to gain a deeper understanding of the specific components contributing to calcium transients in the soma and axon, further electrophysiological recordings are necessary.

Our observations explain why delay eyeblink conditioning is impaired in SK2-KO mice where synaptic plasticity is intact (Schreurs et al., 1998; Titley et al., 2020). In dentate gyrus, suppressing synaptic plasticity impairs fear learning, but conditioned responses can be rescued by photoactivating engram cells (Ryan et al., 2015). This finding demonstrates that memory representation requires the conveyance of synaptic input to neuronal output (for a review, see (Titley et al., 2017)). As we show here, this may be achieved through modulation of intrinsic excitability that selectively gates the influence of synaptic strength on somatic activation (Fig. 40a). Thus, as a general rule across neuron types, intrinsic plasticity may exert permissive control over the coupling of LTP to spike output, and thus the integration of neurons into engrams (Hansel & Disterhoft, 2020; Titley et al., 2017). This control would outlast transient roles assigned to intrinsic excitability, for example in the memory allocation hypothesis. There, allocation of neurons to a memory engram occurs when these neurons show high excitability at the time of learning, facilitating subsequent integration via LTP (Rogerson et al., 2014; Yiu et al., 2014). It is conceivable that intrinsic plasticity has such facilitatory function in addition to a permissive gate function, without which, however, LTP remains without impact on spike output.

CHAPTER 7

GENERAL DISCUSSION

In the introduction I defined six core questions which this thesis sought to address. Below I summarize the findings of each chapter as they pertain to these questions:

Does Purkinje cell morphology influence input arrangement? (Chapter 2)

Does climbing fiber multi-innervation produce distinct compartment signaling *in vivo*? (2)

Are there distinct spatial scales of sub-cellular dendritic computation *in vivo*? (6)

How does the human diverge from the mouse anatomically? (3)

How might variable Purkinje cell morphology produce species-specific functions? (4)

How is expanded olivo-cerebellar signaling pathological in autism model mice? (5)

Chapter Summaries

In Chapter 2, I demonstrated that Purkinje cell (PC) morphology impacts dendritic input arrangement and signaling in mice. I first developed a novel framework to categorize PC morphology as either Normative, Split, or Poly. An exhaustive comparative analysis of PC morphology across mouse and human cerebellum revealed that the Normative category, so named because it describes the stereotypical idea of a rodent PC, was almost entirely absent from human. Instead, human PCs were almost universally multi-branched (Split or Poly). Whole cell patch clamp in acute mouse cerebellar slices revealed that 1) some PCs (~15%) receive multiple climbing fiber (CF) inputs in adult animals, rejecting the textbook wisdom, and 2) CF multi-innervation is maintained exclusively by PCs with multi-branched morphology. Among that population, up to

25% can receive multiple CFs. To test whether CF multi-innervation could influence dendritic computation *in vivo*, I used 2-photon imaging of sparse, PC-specific expression of GCaMP6f to discover that some PCs, particularly those with multi-branched morphology, exhibited heterogeneous, compartment-specific calcium signals in the form of either cell-wide calcium spikes with highly variable amplitude across compartments or calcium events that were entirely restricted to one compartment. Broad calcium signals at this scale are largely CF-dependent, indicating that independent calcium signaling is likely driven by the integration of CFs with distinct receptive fields (RFs). As a proof of principle that the RFs could be distinct, I stimulated individual whiskers in sedated animals to selectively evoke individual CFs, whose RFs are often restricted to one or a small number of whiskers. I observed branch-specific responses to individual whiskers, supporting the hypothesis that multiple CFs innervating one PC can have distinct RFs. Finally, I demonstrated that distinct CF RFs are heterogeneously expressed across dendritic compartments in the awake animal by applying multi-sensory stimuli and observing distinct, branch-specific profiles of maximal responsiveness across modalities. Taken together, this study revealed that PCs are more structurally diverse that previously thought and may thus exhibit a wide range of computational capacities across the population. Given that human PCs almost universally exhibit the morphological motif that gives rise to these new computational capacities in the mouse, it is thus likely that the human cerebellum is much more functionally rich than previously appreciated.

Chapter 3

Human PCs have been remarkably uncharacterized since their original illustration by Camillo Golgi and Santiago Ramón y Cajal at the end of the 19th century. Chapter 2 painted a very broad

picture of them as they compare to mouse PCs. Human cells remain largely physiologically inaccessible, but, in Chapter 3 I presented a paper that is currently in review where I used comparative histology to reveal human anatomical properties that relate to cellular physiology. Most of these properties are either the first of their kind or rewrite our current understanding. First, co-immunolabeled peripherin (climbing fibers) and calbindin (PCs) provides the first demonstration of non-canonical climbing fiber multi-innervation in adult human. I found that multi-innervation is common and related to the underlying dendrite morphology (complementing our findings in mouse), further rewriting textbook wisdom that PCs are universally mono-innervated, a core dogma among modern theories of cerebellar function. I also provide the most complete reconstructions of human PC dendrites and spines—predominantly innervated by parallel fibers (PFs)—currently reported, which demonstrate *quantitative* and *qualitative* species differences. High resolution imaging of spiny dendrites revealed not only a higher spine density and size in human, but the presence of human-specific 'spine clusters' not previously described in any cell type or species to our knowledge. Spine clusters have an enlarged head with typically 3-7 partially emerging spines that could plausibly host independent synapses. This may confer several new physiological properties such as input amplification, calcium spike initiation, and complex synaptic association. I also show that human cells have 6-7cm total dendritic length. This eclipses mouse (0.6cm) and previous reports for human (averaging 1-2cm), shows that human cells exceed allometric constraint, and distinguishes Purkinje cells from the roughly allometric pyramidal cell anatomy (~0.55cm in mouse and ~1.5-2cm in human). This is also the first demonstration that Purkinje cells are the largest neuron in the human brain. Finally, I systematically characterized PC morphology in whole sections of cerebellar vermis, showing that variable cell type ratios are better predicted by human functional regions than anatomical segmentation by lobules. This supports our

hypothesis that morphology influences cellular computational capacity so cerebellar regions may produce distinct functions by recruiting distinct PC populations. I also found that cells clustered into heterogeneous arrays of locally homogeneous PCs that may be selectively recruited to diversify regional computation.

Chapter 4

Are these species differences specific to human? Chapter 4 presented preliminary results of a broad comparative histology project that seeks to 'connect the dots' between these mouse and human, with a particular focus on primate phylogeny. Through new collaborations with the Anatomical Gift Association of Illinois (AGAI), the Bensmaia and Hatsopoulos labs at UChicago, Dr. Chet Sherwood at George Washington University, and Dr. Michael Brecht at Humboldt University of Berlin, I obtained post-mortem cerebellar tissue from platyrrhine (Marmoset and Spider Monkey) and cercopithecid (Macaque and Baboon) monkeys, lesser apes (Northern White Cheeked Gibbon and Siamang), great apes (Orangutan, Gorilla, Chimpanzee, and Bonobo), human, and elephant. UChicago undergraduate, Aurora Ferrell, and I designed a panel of morphological properties which she then systematically measured from confocal images of calbindin stained tissue. The properties address features of PC morphology that relate to their input field, compartmentalization, electrotonic conductance, and allometry. We observe a rich variety of interspecies morphological variation, further emphasizing that the cerebellum exhibits substantial anatomical diversity—within and across species—despite being considered a stereotypical and rigidly conserved brain structure. Some morphological variation coincides with allometric scaling, but many properties diverge from allometric constraint to exhibit a range of phylogenetic relationships such as being: constant across primates, increasingly complex with proximity to

170

human, specifically distinct in the human case, etc. Taken together, non-human primates do connect the dots between mouse and human species differences observed in previous chapters, but a significant evolutionary divergence from the primate lineage also appears to drive some of the enhanced complexity of human PCs.

Chapter 5

The previous chapters outline my findings that PC dendritic morphology is diverse—within and across species—and may shape multiple features of input arrangement and dendritic computation. Most notably, I have shown that multi-branched structure can permit non-canonical olivo-cerebellar CF-PC multi-innervation. This may provide more complex combinatorial dendritic computation, but it is important to note that 'enhanced' CF-PC signaling is not always beneficial and may, as we predict, be a specific phenomenon to allow proper receptive field matching between PF and CF inputs to maintain perceptron function in cells with expanded size and segregation of dendritic compartments. Chapter 5 provides my contributions to collaborative projects within and outside the lab which explored pathologically enhanced olivo-cerebellar CF signaling in two mouse models of autism. Previous work in the Hansel lab found that both patdp/+ mice (carrying a similar chromosomal duplication as in the human 15q13dup syndrome) and mice overexpressing CYFIP1, a putative autism gene, had ectopically enhanced CF-PC signaling (via stronger CF-ESPC amplitudes and, in the case of patdp/+ mice, larger VGluT2-labeled CF terminal territories along thin caliber dendrites) and reduced PF-PC signaling such that CF-dependent PF-LTD, a bedrock for cerebellar learning, was disrupted. Building on those findings, I discovered that both mouse models had increased localization of NRXN1, a synaptic maintenance molecule that has been implicated in autism, on PC primary dendrites. More specifically, I found that

NRXN1 was more colocalized with VGlut2 in patdp/+ mice, suggesting that enhanced CF-PC signaling may rely on increased NRXN1 trafficking at CF-PC synapses. I then showed that PC dendrites in both models exhibited enhanced responsiveness (higher amplitude CF-dependent GCaMP6f Ca^{2+} events) to multi-sensory stimuli in awake mice. Furthermore, I discovered that patdp/+ mice exhibit behavioral sensory over-responsivity (longer lasting blinks following corneal airpuff and larger startle responses) and that PC dendrites in CYFIP1-OE mice fail to match the WT tendency for habituation following repeated sensory stimuli, instead exhibiting larger responses specifically to repeatedly presented sensory modalities and not to others. These final tests revealed that pathologically enhanced olivo-cerebellar signaling may play a role in sensory defensiveness, a common trait in autism.

Chapter 6

This chapter builds on the *in vivo* imaging studies of chapters 2 and 5. While this and the other studies recorded calcium activity in PC dendrites, the previous studies used the PC dendritic signal strictly as a readout of CF pre-synaptic input properties (Chapter 2) or sensory encoding (Chapter 5). Instead, Chapter 6 provides the first use of PC dendritic calcium as a measure of a) PF inputs, and b) post-synaptic dendritic computation and its potential influence on PC output. Here, I assisted in developing and running experiments to provide either tactile stimulation to the paw or direct electrophysiological stimulation of PFs during 2-photon calcium imaging in awake mice. The goal of the study was to identify the differential contributions of either intrinsic or synaptic plasticity to reshaping the PF-PC RF. To test each mechanism's role in RF plasticity following either tactile or direct electrical stimulation, we compared PC signaling in WT animals to that of mice lacking SK2 channels (SK2-KO) or with blocked inhibitory autophosphorylation of CaMKII

(CaMKII-TT305/6VA). These mutants exhibit disrupted intrinsic or synaptic plasticity, respectively. Beyond experimental assistance, my discovery of calcium signal heterogeneity across the arbor (Chapter 2) inspired us to analyze the spatial distribution of the PF calcium signal. We uncovered a physical manifestation of our hypothesized contributions of synaptic and intrinsic plasticity as mechanisms either, respectively, of input selectivity or gating control of the translation of synaptic potentiation to cellular output. Specifically, we observed that tetanic stimulation of a PF bundle produced an enhanced dendritic signal both within the area of the stimulated PF bundle, which can be clearly defined along a subset of the PC arbor, and in areas surrounding the PF bundle. SK2-KO PCs lacked the *surrounding* potentiation while CaMKII-TT305/6VA PCs lacked the *local* potentiation. These findings relate to the core argument of this thesis by highlighting how the wealth of molecular factors controlling dendritic computation and plasticity often work independently or in conjunction on dynamic spatial scales within the dendritic arbor. Diversity in PC dendritic morphology may then provide a scaffolding not only for distinct excitatory input arrangements but for distinct patterns of compartmentalization and integration of dendritic signals during computation.

Below are additional observations not already described in the chapter discussion sections.

Delayed maturation of surplus CFs on multi-innervated adult PCs

In my slice patch recordings, I observed that neither the dominant CF on multi-CF PCs (n = 24 cells) nor the lone CFs of mono-innervated PCs (n = 135 cells) exhibited a relationship between age and EPSC amplitude (Appendix Figure S5N; note that this is with Cesium-based internal and with V_{hold} = -30 to -10). This is expected given that these recordings were conducted entirely on >P20 mice and CF pruning is canonically complete by P18-P20. On the other hand, I observed a

significant—and positive—age dependent increase in surplus (weaker) CF EPSC amplitude in multi-CF PCs (n = 24 cells; Appendix Figure S5M). This may indicate a continued or delayed development of fiber arrangement or synaptic strength following circuit maturation (Fig. 41). I did not observe any effect of age (within the sample range of 21-65) on multi-innervation probability such that older animals were no more or less likely to have multi-CF PCs (Appendix Figure S6L), which supports the idea that CF pruning—as a binary phenomenon dictating whether a CF is maintained or not, regardless of the final arrangement—is complete by P20. Relatedly, multi-innervation is additive as summed multi-CF EPSCs are as much larger than mono-CF EPSCs as the size of weaker CFs (Fig. 4E).
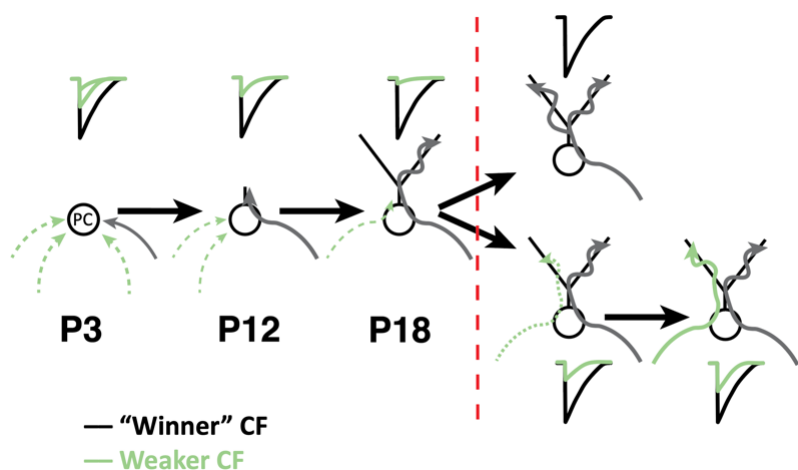
Figure 41. Hypothesized extension of CF-PC developmental timeline beyond canonical completion at P20 with universal mono-innervation. Increasing EPSC amplitude of 'weak' but not 'winner'/mono-CFs (Appendix Figure S5N-M) is congruent with delayed maturation to near parity shown in the lower right section.

I also observed that the ratio of EPSC amplitude between strong and weak CF inputs to multi-innervated PCs varied widely across cell morphologies. While the effect was not significant with the number of cells recorded here, it is likely that Poly PCs have a greater parity in their ratio (the strong and weak CFs are closer to having the same strength; Appendix Figure S5O), which would fit with our hypothesis that increased morphological/spatial compartmentalization can increase the effect of a single PC soma having effectively two PCs-worth of CF input. Building on that notion, a wider dendrite separation angle correlates with greater EPSC amplitude parity between multiple

CFs on Poly PCs (n = 8 cells; Appendix Figure S5Q). A similar effect was not observed for the split angle (Appendix Figure S5R), though the distance to the split correlated with the prevalence of multi-innervation (Appendix Figure S5C). Among all multi-innervated PCs, there is no variation in the rate of multi-innervation between foliar locations (Appendix Figure S6G), but the EPSC amplitude ratio is smaller in the gyrus (28%) than the sulcus (56%; n = 6, 11, 7 cells; Appendix Figure S5P), which builds on the finding that multi-innervation is enhanced in sulcus of the vermis (Nishiyama & Linden, 2004).

PC morphology is not zebrin dependent

Until now, cerebellar anatomy has only been characterized as containing diverse cell and circuit anatomy through the description of molecular patterning factors such as Aldolase-C (zebrin+ or zebrin-) or parvalbumin (low or high). Aldolase-C is a glycolytic enzyme that confers protection against excitotoxicity (Slemmer et al., 2007) and is expressed in a pattern of parasagittal stripes in transverse zones that correlates with different average simple spike firing rates (Zhou et al., 2014). Parvalbumin, a Ca^{2+} binding protein, has differential expression density across foliar sub-areas and strong expression correlates with a faster, burst-like simple spike rate, likely due to its Ca^{2+} buffering qualities (Brandenburg et al., 2021). While I did not test for a possible role of PV expression on PC morphology, the variation of PC morphology across foliar structures that I observe in my data does not appear to covary with the reported pattern of PV expression—albeit currently only reported in the rodent. I did however test whether PC morphology varied by Aldolase-C (zebrin) expression and observed no effect of zebrin expression in either mouse and human (Appendix Figure S3B,E).

PC morphology varies regionally and sub-regionally as an additional dimension of cerebellar functional specification beyond zebrin patterning

Non-random morphological clustering such as described in Chapter 3 has not previously been described in laminar brain structures aside from the stratification of pyramidal cell morphological types across layers. It is possible that the cerebellum—a three-layered cortex with a PC monolayer—may harness non-random clustering, alongside medio-lateral molecular patterning by zebrin, as a 'horizontal' means to boost functional diversity while the neocortex does so 'vertically' through layered, columnar circuits. Naturally, the neocortical circuit is entirely different from the cerebellar cortical circuit, but the broader point is that the brain can add computational complexity into a cortical structure either through a vertical stack of layers with distinct cell types and positions within a sequence of processing or by generating patches of distinct computational capacities that are distributed horizontally in a flat cortex. The higher degree of foliation, and therefore increased surface area, of the cerebellum is ideal for the latter while the neocortex is ideal for the prior.

CF-dependence of *in vivo* Ca^{2+} signal heterogeneity

There are a few conceivable alternative explanations for the Ca^{2+} heterogeneity I observe: branch-specific PF beam input, inhibition by MLIs, or expression of channels controlling Ca^{2+} conductance. While we speculate that these factors may contribute to additional branch independence than that described here (Cirtala & De Schutter, 2024; Roome & Kuhn, 2018; Zang & De Schutter, 2021), they are unlikely to be observable in this configuration. We are recording large Ca^{2+} events averaged across multiple fine dendrite sub-compartments, which would obscure PF inputs. If local events were caused by a lone barrage of PF input from a PF beam, we would expect a notable elevation of spontaneous event rate, but we observe spontaneous rates that match

documented CF rates (~0.8-1.3Hz, citation). If MLI inhibition was the primary cause, particularly of local events, we would expect heterogeneity to be observed more universally in PCs with wide dendritic arbors. Instead, we only observe heterogeneity in a subset of PCs more closely matching the rate of CF multi-innervation observed *in vitro*. The absence of heterogeneity in many PCs with wide dendritic arbors, particularly those with distant bifurcations, acts as an internal control. Being naturally subtractive, MLI inhibition should also produce a lower average event rate in heterogeneous PCs than adjacent homogenous PCs. Finally, we would not expect to see dynamic switching of signal dominance across branches at the rapid time scale of seconds if intrinsic ion channel expression was the primary culprit as it would take longer time scales on the order of minutes for such a shift in branch-specific ion channel expression.

Heterogeneous calcium signals across dendrites tend to represent a minority of cellular activity. That is, most events are globally expressed across the dendrites. This would suggest that the multiple CFs innervating a single PC have partly overlapping activity profiles. Single cell tracing studies by Sugihara and others demonstrated that nearby IO neurons tend to project their CF terminals to similar regions of the cerebellar cortex (Sugihara, 2006; Sugihara et al., 1999, 2001). Combined with demonstrated gap junction coupling of IO neurons (De Zeeuw et al., 1998) this provides support for the scheme whereby modular olivo-cerebellar loops form with local regions of IO innervating spatially compact sub-populations of PCs, which then project to compact regions of the DCN that project out to the rest of the brain and provide feedback to the same upstream IO neurons (De Zeeuw, 2020). This scheme would thus predict that multi-innervated PCs must be receiving CF terminals from two neighboring, coupled IO neurons that are completely synchronized and have little functional effect. Yet, the anatomical and physiological compactness of each stage of this olivo-cerebellar loop is not as tight as typically presumed; small (~100um

diameter) IO sub-regions project broadly to many cerebellar lobules (Sugihara, 2006; Sugihara et al., 1999, 2001) and the coupling strength of neighboring IO neurons is quite weak in most pairs within 50um (Hoang et al., 2020; Hoge et al., 2010). It is also worth noting that the IO, as well as DCN, expands not only in size but structural complexity in the human compared with the mouse (Baizer, 2014). These nuclei obtain a highly foliated structure in human brainstem and cerebellar white matter, respectively, instead of maintaining the spherical shape observed in rodents. This could plausibly decrease the likelihood of neighboring CFs deriving from strongly coupled, adjacent IO neurons and increase the odds of heterogeneous signaling even over distances in the cerebellar cortex of a single dendritic arbor (Schultz et al., 2009).

While we do not have tracing data to confirm this anatomically, we may plausibly expect that multiple CF inputs will have partly non-overlapping activity, and therefore provide some degree of heterogeneous activity and thus a moderate elevation of the combined CF input rate. Consistent with this expectation, when normalized to the rate of adjacent homogenous PCs (to control for different event rates across fields of view that could have different zebrin identity and therefore different average PC and CF event rates), heterogeneous PCs have, on average, ~25% higher total event rates (Appendix Figure S7J). Altogether, our observed heterogeneity is most consistent with the expectation that these PCs are receiving multiple partly non-overlapping CF inputs.

Elevated whisker responses when segregating responses by branch

When measuring whisker responses in the averaged signal across branches of each PC, we observe the same ratio of cell responses to the tested whiskers (~40% with a response to one or more whiskers) as reported previously in medial Crus 1(Bosman et al., 2010; Ju et al., 2019). When we analyze the responsiveness of the signal from each PC branch separately, instead of averaged

178

together as a cell-wide ROI, we observe a slight elevation in the number of cells with a response (94/169; 56%). Ostensibly, in a PC receiving multiple CF inputs with partly non-overlapping activity and receptive fields, the responses of one CF input may be obscured by the spontaneous activity of an additional CF if the signal in all branches is averaged together for analysis. This could explain the slight rise in responsiveness observed with our technique (~16% more cells). It is also of note that this matches the expectation that 10-20% of PCs might be multiply innervated and, in those cells, the conflicting signal from partly non-overlapping CF inputs could create enough noise to obscure the observation of a response under these conditions. This also predicts our observation of a subset of PCs with whisker responses in one branch and not the other.

Putative roles of morphological variation on compartmentalization and combinatorial computation

Diversity of PC computation may not be restricted only to the presence of CF multi-innervation among some PCs. There are many possible relationships between the presence and lack of CF multi-innervation and the presence or lack of segregated dendritic compartments (which may otherwise influence PC connectivity and physiology). For example, many multi-branched PCs are mono-innervated. This might also provide a distinct combinatorial operation whereby multiple PF RFs are exposed to only one corrective signal and may thus exert some form of competitive influence by contextual information streams on PC output. Alternatively, some PCs may not have enough segregation between primary dendrite compartments for multiple distinct PF RFs to be realized on the arbor yet retain multiple CFs. This conformation would recruit a wider profile of CF RFs, which could produce a more generalizing corrective signaling process. This will need to be explored further as my results do not allow me to make a claim in any direction besides noting that the axes of functional diversity may be multi-fold.

Spatial segregation of primary dendrite compartments may provide additional combinatorial complexity both at the cell and circuit level. At the cellular level, I have observed a few cases in human where an individual primary dendrite compartments will be either the recipient of a recurrent (projecting back into the ML) PC axon (Appendix Figure S4A) or host the axon of the cell instead of the soma (Appendix Figure S4B). The prior feature may allow PCs to selectively, recurrently inhibit individual primary dendrite compartments of neighboring PCs both at baseline, since PCs spike spontaneously at ~40-50Hz, and especially when they are strongly modulated either by PFs or CFs. I only observed axon-carrying dendrites—so termed in pyramidal cells, the only cortical neuron where the phenomenon has been described (Thome et al., 2014; Triarhou, 2014)—among PCs with multiple trunks emerging directly from the soma with wide angles of separation. The isolation of the axon and thus the spike initiation zone, onto one primary dendrite may render PC output modulation differentially sensitive to inputs based on their location either on or off the axon-carrying dendrite.

During the same stages of post-natal development as the CF pruning process, P1-18, mouse PC dendrites undergo a dendritic planarity remodeling whereby the early monoplanar growth of the nascent dendrites undergoes an expansion in the medio-lateral plane briefly before refining back, most often, to the classically thin monoplanar structure with ~20um maximal thickness (Kaneko et al., 2011). In my slice and in vivo calcium imaging experiments, I observed that multi-planar structure was also predictive of CF multi-innervation, but less so than the primary dendrite separation in the parasagittal plane (Appendix Figure S6J). That is, having multiple primary dendrite compartments appeared more determinative of CF multi-innervation than multi-planarity, particularly because many multi-CF PCs were mono-planar whereas all PCs with multiple CFs and a multi-planar structure had a severity of multi-planar structure that was only possible through

the spatial segregation of the arbor into multiple primary dendrite compartments. Whether planar remodeling also occurs in human is unknown, as is the prevalence of PCs retaining multi-planar structure. My data do not provide sufficient evidence either way. However, I do observe that among human PCs with what appears to be most analogous to rodent monoplanar structure, there is significant expansion of the total medio-lateral thickness of the arborization to ~50um.

PC dendrite growth exhibits robust self-avoidance through molecular recognition factors like protocadherins (Ing-Esteves et al., 2018; Lefebvre et al., 2012). In the dense but medio-laterally restricted arbor of rodent PCs, this produces a maximally space filling structure whereby fine dendrites precisely interdigitate without overlap. In the human, however, the expanded medio-lateral range appears to allow the fine dendrites to overlap in the parasagittal axis while properly self-avoiding into distinct medio-lateral positions. This distinct structural motif—having extensively overlapping fine dendrites—may be permitted specifically by the remarkably conserved thickness (~0.7-1.2um diameter) of the fine dendrites across rodents and humans. If this thickness had instead increased proportionally in human, the dendrites may have been unable to overlap while sufficiently self-avoiding, even with the expanded medio-lateral range. The overlapping motif may permit spiny branches in the human to resurvey the PF axons projecting through the arbor. This could expand combinatorial coding of PF inputs by individual branches without requiring increased granule cell or PF densities.

A remarkable and under-appreciated feature of CF signaling was recently demonstrated to be the CFs ability to so strongly depolarize the PC dendrite that it can induce a hyperpolarization of adjacent PC dendrites through ephaptic coupling (Han et al., 2020). Ephaptic coupling of adjacent dendrites during CF signaling thus provides route by which PCs with multiple, spatially segregated

primary dendrites—with or without multiple CFs—could differentially influence, and be influenced by, multiple PC sub-populations.

The expression of logic gates in PC output representation of olivo-cerebellar signals

Discrete CF receptive fields across primary dendrites could produce undescribed PC computational capacities such as combinatorial coding and the expression of logic gates. Multi-CF PCs may be performing functions of either discrimination across branches or generalization summed at the axon. Upon somatic convergence, these two or more dendritic signals could assume different logic gate functions (e.g. AND, OR, XOR), depending on activation demands of target cells in the deep cerebellar nuclei (DCN). Thus, the *presence and timing of output*, as a binary function, may be a generalizing OR operation on multiple CF→PC circuits, while the *strength of PC output*–relayed to deep cerebellar nucleus by CS waveform, burst number, and SS pause duration–or the *locations of PF→PC synaptic plasticity* could differentiate and encode input modality to shape the immediate response and long-term learning.

Increased PC-DCN contrast by individual PCs integrating more CF RFs

Given the high baseline firing rate of PCs carrying an inhibitory signal to the deep cerebellar nuclei (>40 of which converge on each DCN cell in rodents), it is a curiosity that nucleus cells should fire at all. Many studies have described the features of DCN input pathways and intrinsic properties of the nucleus cells that enable activity in the midst—and indeed because—of the high rate of PC inhibition (Person & Raman, 2012; Y. Wu & Raman, 2017). As CF EPSPs consistently provoke a CS, multi-CF PCs with higher event rates would thus exhibit more CS output that has a higher likelihood of being asynchronous with the timings of the other PCs converging on each

DCN cell. This could elevate DCN suppression during low salience conditions, rest, or smooth performance of a movement or cognitive task as CFs would be spontaneously active and uncorrelated, producing a constant, low level inhibitory drive from the PC population on the DCN cell. Then, during a sensory or motor condition where wide-scale CS synchrony erupts, this asynchronous inhibitory drive would alleviate and instead the converging PCs would provide time-locked spiking. While this would seem to further increase inhibitory drive, it has been shown that synchronous hyperpolarization of DCN cells by converging PCs produces rebound excitation in a narrow time window that can allow DCN excitability to be paradoxically entrained to synchronous PC inhibition up to 100Hz (Person & Raman, 2012; Y. Wu & Raman, 2017). Thus, during synchronized PC activity, the DCN is switched to a high activity state relative to the baseline period. In this theory, complex PC morphology and CF multi-innervation could act as a feature, not a bug, to expand the dynamic range of PC activity and thus increase contrast between baseline activity and feature representation in the DCN.

Clustering motif across levels of morphological organization

Taken together, human cerebellar anatomy commonly favors a 'clustering' of PC morphological features into heterogeneous groups instead of a homogenous distribution. Morphological clustering occurs across levels of computation: spine clusters and compartmentalized dendritic branches produce more distinct input combinations than if synaptic inputs were evenly distributed; the multiplication and segregation of primary dendrite compartments multiplexes CF and PF population signaling; structural similarity among local PC clusters may allow cerebellar regions to recruit functionally distinct PC circuits. Collectively, this

clustering motif may give rise to more complex combinatorial computations at the level of synaptic input, dendritic signals, and population activity.

Non-random spatial clustering of neuronal cells by morphological sub-type has not previously been described in other brain areas, potentially making this a cerebellum-specific means to boost functional diversity. Combined with our findings at the cellular level, the human cerebellum presents a proclivity for "clustering" morphological properties to achieve heterogeneous, combinatorial functions. Non-random spatial clustering of neuronal cells by morphological sub-type has not previously been described in other brain areas, potentially making this—in addition to molecular patterning by zebrin—a cerebellum-specific means to boost functional diversity. This is evident across scales: synaptic input (cluster spines); dendritic branches (multi-branched structure, compartmentalization); local cells (non-random morphological clustering), and broad populations (covarying regional demographics with function).

Future Directions

Having updated our anatomical and physiological understanding of PC morphology and CF-PC signaling—fundamental features of the cerebellar circuit—there are numerous new directions to pursue. In the lab we have already begun follow up studies seeking to explore the molecular profile of PC morphological sub-types. While the morphological continuum is likely determined by a milieu of countless signaling pathways, as well as external forces and circuit activity, it's possible that a small number of factors play an oversized role in the somewhat discrete determination of number and ramification polarity of PC primary dendrites. It would thus be useful to assess transcription profiles of morphologically identified PCs for dendrite selection and growth factors such as: dendritic self-avoidance factors like clustered protocadherins (Ing-Esteves et al.,

2018; Lefebvre et al., 2012), upstream transcription factor CTCF (Hirayama et al., 2022), *RORα*, or Slit2/Robo2 (Fujishima et al., 2018); axon and dendrite polarity regulators (Liver Kinase B1, upstream of Slit2) (Kuwako & Okano, 2018); golgi apparatus localization control factor atypical proteinase C (aPKC) (Fujishima et al., 2012; Kapfhammer, 2004); pro-survival apoptosis factor bcl-w which interacts with downstream autophagy factor beclin-2 that forms a complex with the intracellular domain of GluD2 (Liu & Shio, 2008); and cerebellar patterning molecules (parvalbumin, aldolase-C). If a molecular marker were identified, it would not only provide vital information about cerebellar dendritic development, but also provide a target for transgenic perturbations that can allow future research to scale up a causal analysis of the role of dendrite morphology on circuit connectivity and function.

As was recently demonstrated (Masoli et al., 2024), full reconstructions of human and non-human primate PCs can permit single cell modeling of cellular physiology. A cell modeling approach may be one of the best tools currently available to advance our understanding of human and non-human primate physiology. It is currently more difficult to get acutely resected cerebellar tissue for *ex vivo* electrophysiology than neocortical tissue (we tried) and we do not yet have non-invasive techniques to overcome this problem. Computational modeling allows a wide range of synaptic, morphological, and intrinsic factors to be altered so a wide parameter space can be tested that would regardless have been precluded by a limited *in vivo* or *ex vivo* recording modality.

I observed spine cluster structures on the fine dendrites of human PCs using high resolution confocal imaging of calbindin stained tissue. Their morphology suggests that these structures could permit a new physiological phenomenon whereby multiple synaptic connections are exposed to shared post-synaptic ionic conductances, plasticity factors, and excitability states. These were almost but not completely absent from the mouse. I also observed similar structures in the

macaque. Thus, it is possible that the physiology of spine clusters could be experimentally assayed in a non-human animal model. Doing so would also clarify whether these structures are, on the other hand, merely an artifact of human post-mortem treatment spanning several days and imperfect perfusion in mice and macaques.

I have shown that CF multi-innervation can produce distinct branch signaling *in vivo* and that this signaling relates to the integration by segregated dendritic compartments of distinct CF RFs. However, we do not know what additional forms of computation might be occurring across PC dendrites, how these signals are combined into cellular output, and how during behavior this signaling encodes information and shapes organismal responses. This could all be investigated by employing newer generations of calcium indicator, voltage indicators, and glutamate sensors, all sparsely expressed to permit single cell analysis, and imaging distinct regions of the dendrites or soma, or possibly combining visualization of PC dendrite signaling with presynaptic activity of CFs (Roh et al., 2020), MLIs (Gaffield et al., 2018; Gaffield & Christie, 2017), or GCs (Garcia-Garcia et al., 2024; Wagner et al., 2017).

Dendrite morphology may factor into cerebellar disease etiology. In mouse, PC morphology and CF signaling is altered in disease models of spinocerebellar ataxia (Du et al., 2013, 2019) and syndromic autism (Busch et al., 2023; Piochon et al., 2014; Simmons et al., 2022). On the only occasions that human PC morphology has been measured with respect to cerebellar disease, it was disrupted in Essential Tremor (Louis et al., 2014; Mavroudis et al., 2022) and Friedrichs Ataxia (Kemp et al., 2016). Having an established frameworks for categorizing (Busch and Hansel 2023, 2024) and parameterizing (unpublished; Chapter 4) PC morphology across species, post-mortem tissue from cerebellar disease patients may be assessed for morphological aberrations. Possibly,

mouse models could then also be harnessed to determine the mechanisms for anatomical and physiological pathologies observed in human (Pan et al., 2020).

Regarding development, it may be revealing to test the role of activity during early post-natal development on PC morphology and CF multi-innervation. As a first step, this could be tested through sensory deprivation or enrichment during this early post-natal period (P3-20) and analysis of PC morphological variation and CF multi-innervation frequency. Increased sensory association through exposure may drive more complex CF-PC arrangements.

Conclusion

Broadly speaking, this work demonstrates an underappreciated degree of diversity in cerebellar anatomy and physiology. The cerebellar cortical circuit is classically considered a uniform array of stereotypical functional modules. At the cellular level, the principal cortical neuron, the Purkinje cell, is likewise considered a stereotypically unitary processing compartment. Nuances of cerebellar function during behavior are tacitly thought to emerge only at the scale of cell populations organized into microzones—containing thousands of PCs presumed to be redundant. The cerebellar field has undergone a significant shift in focus with recent progress in describing the cerebellum's substantial contributions to non-motor behavior. No longer just a region for the coordination of smooth movement and posture, there is a new focus on how the cerebellum may exert considerable control over a host of brain regions and behaviors, particularly in species such as humans and non-human primates where there is considerable cognitive, social, and linguistic complexity. My findings in this dissertation begin to suggest a substrate for cerebellar roles in such diverse functions both within and across species. From the anatomical, physiological, and evolutionary perspectives, perhaps the cerebellum is far more diverse than we imagined.

APPENDIX 1: METHODOLOGY AND STATISTICS

CHAPTER 2: CLIMBING FIBER MULTI-INNERVATION OF MOUSE PURKINJE

DENDRITES WITH ARBORIZATION COMMON TO HUMAN

Materials and Methods

Subjects

Human cerebellar tissue was collected from three embalmed donor bodies provided to the University of Chicago Pritzker School of Medicine Anatomy Lab by the Anatomical Gift Association of Illinois (AGAI). Individuals were 92 (F), 95 (F), and 86 (M) years old, died of causes unrelated to cerebellar morphology (e.g. 'failure to thrive', likely 'failure to thrive', and colon cancer, respectively), and tissue was stored for 2, 6, and 2 months, respectively. During life, all study subjects signed an informed consent approved by the AGAI.

For experiments involving mice, both *in vitro* and *in vivo*, all experimental and surgical procedures were in accordance with the University of Chicago Animal Care and Use Committee guidelines. We used wildtype C57BL/6J mice housed on a 12hr light/dark cycle. Animals of either sex were used in all experiments and no sex differences were observed in any reported measures.

Immunohistochemistry

Embalmed human tissue. Due to incomplete fixation during the embalming process, we immediately submerged whole cerebella in 4% paraformaldehyde (PFA) for one week after they were obtained. Following this fixation period, each specimen was sectioned by hand in the sagittal axis to obtain 2-5mm blocks from the mid-hemisphere of each individual. Given the anterior curvature of folia in the hemisphere, blocks were cut at varying angles relative to the midline.

Tissue blocks with incomplete fixation of deep structures were further fixed for 2-4 days. Depending on their size, blocks were cut transversely into dorsal and ventral sections, typically through the horizontal fissure, such that Lobules III through VIIAf/Crus I were in the dorsal block and VIIAt/Crus II through VIIIB in the ventral block. Occasionally, we also needed to cut the dorsal block into rostral and caudal sections. Next, each block was rinsed in 0.01M Phosphate buffer saline (PBS), dried on one side, mounted with super glue into the slicing chamber of a vibratome (Leica VT-1000S), and sliced at 35µm in the parasagittal plane.

Slices selected for immunolabeling were transferred to a clear tray, placed over a broad-spectrum LED array, covered with a reflective aluminum foil lid, and photobleached at 4℃ for 3-4 days. This reduced the strong autofluorescence in the green channel. Then tissue was washed in 50mM Glycine in 0.01M PBS for 2hrs at 4℃ and incubated in 20mM Sodium Citrate in 0.01M PBS at 50-60℃ using a heated water bath for 30min. After cooling to room temperature (RT), tissue was washed in 20mM Sodium Citrate for 5min then rinsed 2x30sec in dH20. Next, slices were permeabilized at RT in 0.01M PBS containing 0.025% Triton-X (PBS-TX) for 1hr. Blocking was done with PBS-TX containing 5% normal donkey serum (NDS) and 5% bovine serum albumin (BSA) for 1hr at RT followed by incubation in guinea pig anti-calbindin primary antibody (1:1000; Synaptic Systems Cat# 214 004, RRID:AB_10550535) solution overnight (18-20hrs) at 4℃ with 1% normal donkey serum in PBS-TX. After 3x10min washes in PBS-TX at RT, slices were incubated in donkey anti-guinea pig AF488 secondary antibody (1:200; Jackson ImmunoResearch Labs Cat# 706-545-148, RRID:AB_2340472) for 2hrs at 4℃ with 1% NDS in PBS-TX. Finally, slices were washed in PBS-TX for 3x10min, mounted and coverslipped with Vectashield (Vector Laboratories, Inc.), and allowed to set overnight before visualization.

Slice reconstruction and cell counting. Slides were visualized under 10x or 20x magnification (Zeiss Achroplan 0.25NA, air; Olympus UMPlanFL N 0.5NA, water) and illuminated with an epi-fluorescent light source (LEJ HBO-100) cast through a 450nm-pass filter cube. This allowed us to manually scan through the cerebellar cortex and classify Purkinje cells (PCs) by their dendritic morphology and their location by foliar sub-region (e.g. gyrus, bank, and sulcus), both based on criteria listed below. Post-mortem storage, embalming, and subsequent short-term submersion in ethanol, which renders many antigen sites inaccessible, diminished the tissue quality; however, this provided some advantage for our purposes. The condition of the tissue resulted in a sparse labeling of PCs that we expect to be random and without morphological bias. The sparsity provided a clearer visualization of each cell's individual morphology and decreased the total number of cells so that an exhaustive count for each region was feasible and unbiased without the use of stereology.

To mark the morphology and cell location accurately in both human and mouse tissue, we initially traced the outlines of the pial surface, white matter tracts, and PC layer over low magnification images of the entire section. Cells were only included for categorization if the soma and at least 200µm lengths of primary dendritic trunks were clearly labeled such that all features of Normative, Split, and Poly categories were unambiguously present or absent (Fig. 3A and Appendix Figure S1; see criteria below). We marked the location and morphological type of each cell in the slice map and scanned these notes as an input image to a custom Matlab GUI where each point could be digitized. This allowed us to generate a .csv table output with a cell ID, XY coordinates, morphological category, foliar sub-region, and lobule of each marked cell (Fig. 3B and Appendix Figure S2). These data were imported to R for downstream analysis and plotting.

Purkinje cell morphological category definitions and criteria. In human, PCs were deemed Normative if they had the following features: 1) a single trunk emerging from the soma, and 2) either no bifurcation of the primary trunk within two soma distances (2x the diameter of the soma, 25-35µm per soma) or a highly asymmetrical bifurcation where the smaller branch did not project in the parasagittal axis more than 200µm from the main dendritic compartment. PCs were defined as Split if they had the following features: 1) a single trunk emerging from the soma, and 2) either symmetrical bifurcation of the primary trunk within two soma distances or an asymmetrical bifurcation within two soma distances where the smaller branch projected more than 200µm from the main dendritic compartment and thus reached prominence by its overall length and sub-branching. PCs were defined as Poly if they had more than one trunk emerging from the soma regardless of relative size.

In mouse, PC categories were defined the same way, except that the bifurcation threshold of two soma distances (each soma diameter is 18-22µm) was set at 40µm, and the smaller branch of an asymmetrical bifurcation had to project only 100µm away from the main dendritic compartment.

In mouse and human, Split and Poly PCs were further subdivided into Vertical or Horizontal ramification patterns (Appendix Figure S4B). Split and Poly PCs were defined as Horizontal if one of two primary dendrites ramified parallel with the PC layer for >300µm in human (>150µm in mouse), or both primary dendrites ramified in opposing directions parallel with the PC layer for >150µm each in human (>75µm in mouse). Dendrites were considered parallel if dendrite, at 300 or 150µm from the soma respectively, ramified at <30º from the top of the PC layer. Otherwise, the cell was defined as Vertical.

Foliar sub-region category definitions and criteria. Purkinje cell locations were defined as either Gyrus, Bank, or Sulcus based on the relative expansion/compression of the granule cell/molecular layers in the parasagittal axis (Appendix Figure S4A). *Gyrus* was defined as a region where the total parasagittal length of the pial surface exceeded that of the border between the granule cell layer and the white matter. *Bank* was defined as regions where those two lengths were equal, such that neither layer of the cortex was compressed or expanded relative to the other. Finally, *Sulcus* was defined as regions where the total parasagittal length of the pial surface was less than that of the border between the granule cell layer and the white matter. Both intermediate sulci, embedded within a continuous Bank region, and full sulci were combined for these analyses.

Climbing fiber tracer immunohistochemistry. Tracer injections in the inferior olive (Fig. 4A) were performed on mice aged 13-15 weeks under ketamine/xylazine anesthesia (100 and 10mg/kg, respectively, 0.1mL/10g weight, Covetrus) with subcutaneous injections of meloxicam (0.06mL, 1-2 mg/kg), buprenorphine (0.05mL, 0.1 mg/kg, Covetrus), and sterile saline (0.5-1mL). Body temperature was maintained at 35-37°C with a feedback dependent heating pad. Mice were positioned in an upright, sitting position with the head clamped such that the line described by the maxilla and the ear bars in the acoustic foramen was parallel with ground. In this configuration, the atlanto-occipital joint membrane was exposed when skin above the posterior skull and posterior muscles attaching to the occipital bone were removed. Cutting open the membrane, approximately 1uL of 25% Alexa 594 conjugated dextran amine tracer (10,000 MW, Invitrogen) in saline was injected 1.8mm deep and 0.5mm lateral from midline into the medulla at a 59º angle (30). After 4-5 days of recovery, mice were anesthetized with ketamine/xylazine (100 and 10mg/kg) and perfused with 4% PFA. Cerebella were removed and incubated for 2hrs in 4% PFA at 4°C and then

overnight in 30% sucrose in 0.1M PB at 4°C (until the tissue sank from the surface). The tissue was then rinsed briefly in 0.1M PB, dried and blocked, submerged in OCT medium, flash frozen, and then sliced (50μm, parasagittal plane) using a cryostat microtome (CM 3050S, Leica).

After slicing, tissue was immunolabeled as described above with several changes: glycine incubation for 1hr instead of 2hrs and heated Sodium Citrate incubation for 20min instead of 30min. Slices were incubated in primary antibody solution with rabbit anti-VGluT2 (1:500; Thermo Fisher Scientific Cat# 42-7800, RRID:AB_2533537) and guinea pig anti-calbindin (1:1000), then in secondary antibodies with donkey anti-rabbit AF647 (Jackson ImmunoResearch Labs Cat# 711-605-152, RRID:AB_2492288) and donkey anti-guinea pig AF488 (both 1:200). Slices were imaged at 40x (Zeiss EC Plan-Neofluar 1.3NA, oil immersion) and z-stacks of the molecular layer were obtained with a confocal microscope (Fig. 4B; Zeiss LSM 5 Exciter, Axioskop 2).

Aldolase-C/Zebrin II immunohistochemistry and quantification. Human and mouse tissue was immunolabeled as described above for each respective species. For double immunolabeling in human, unembalmed tissue was obtained after storage at 4°C for two days post-mortem, fixed in 4% PFA for 5 days, and sliced as described above for embalmed tissue. Slices were incubated first in primary antibody solution with mouse anti-Aldolase-C (i.e. zebrin II; 1:500; Santa Cruz Biotechnology Cat# sc-271593, RRID:AB_10659113) and guinea pig anti-calbindin (1:500), then in secondary antibodies with donkey anti-mouse AF488 (Jackson ImmunoResearch Labs Cat# 715-545-150, RRID:AB_2340846) and donkey anti-guinea pig AFCy3 (both 1:200; Jackson ImmunoResearch Labs Cat# 706-165-148, RRID:AB_2340460). Within each species, imaging

parameters were consistent across images to allow comparison of expression intensity (Appendix Figure S3A and D).

In mouse, a series of z-stack images were collected at 40x (Zeiss EC Plan-Neofluar 1.3NA, oil immersion) in representative regions of dorsal anterior and posterior lobules with a confocal microscope (Zeiss LSM 900, Examiner.Z1). Cells were classified as either Zebrin+ or Zebrin- (Appendix Figure S3A) and the location and cellular morphology was noted (Appendix Figure S3B and C). In human, a series of images were collected at 10x (Zeiss Achroplan 0.25NA, air) in representative regions of lobules VII and VII in the hemisphere and lobules III-VIII in the vermis. Each image had ~15-20 visible somas, of which typically half of the cells were complete enough to allow morphological categorization. Somatic compartment ROIs were drawn manually in ImageJ and the mean intensity of both calbindin and zebrin II as well as cellular morphology was noted for each cell. Due to more variable cell quality in human compared to mouse tissue, we used the expression of calbindin, a universally expressed protein in Purkinje cells, as a baseline to normalize zebrin II intensity by subtracting calbindin intensity from zebrin II intensity and dividing by calbindin intensity. We then categorized cells in either the top or bottom 25th percentiles as Zebrin+ or Zebrin- (Appendix Figure S3E).

Slice Electrophysiology

To quantify the frequency of functional climbing fiber (CF) multi-innervation, we used whole cell patch clamp and electrical stimulation in acute cerebellar slices with a cesium internal solution. Mice (P20-65) were anesthetized with isoflurane and decapitated. The cerebellum was immediately dissected in ice cold artificial cerebrospinal fluid (ACSF) containing (in mM): 124 NaCl, 5 KCl, 1.25 Na_2HPO_4, 2 $CaCl_2$, 2 $MgSO_4$, 26 $NaHCO_3$, and 10 D-glucose, bubbled with

95% O_2 and 5% CO_2. Sagittal slices of the cerebellum (250μm thick, including medial hemisphere, paravermis, and vermis) were prepared with ice cold ACSF in a chilled slicing chamber using a vibratome (Leica VT-1000S), and allowed to recover for 1hr at room temperature in oxygenated ACSF. During recordings, the slices were continuously perfused with oxygenated ACSF containing 100μM picrotoxin to block $GABA_A$ receptors.

Whole cell patch-clamp recordings from the PC somata were performed at room temperature using an EPC-10 amplifier (Fig. 4C and S3A; HEKA Electronics). The workstation was also equipped with a confocal microscope (Fig. 4C; LSM 5 Exciter and Axioskop 2, Zeiss) for the identification and morphological characterization of patched and dye-filled cells. Currents were filtered at 3kHz, digitized at 25kHz, and acquired using Patchmaster software (HEKA Electronics). For recordings of CF-EPSCs (Fig. 4C and S3A-B), the pipette solution was Cesium based to improve space clamp of inputs to distal dendrites and contained (in mM): 60 CsCl, 10 Cs D-Gluconate, 20 TEA-Cl, 20 BAPTA, 4 $MgCl_2$, 4 Na_2ATP, 0.4 Na_3GTP, 30 HEPES (osmolarity: 295-305mmol/kg; pH 7.3, adjusted with CsOH). Alexa-633 dye (30μM) was added to the pipette solution to allow visualization of the dendritic arbor. Pipette solution was kept on ice and shielded from light during the experiment to prevent degradation of the dye or ATP and GTP salts. Patch pipettes had a tip resistance of 4-6MOhm and were mounted in a motorized manipulator (Luigs & Neumann). Liquid junction potential was not corrected. Fast and slow capacitances were compensated, and series resistance was partially compensated (50-80%). Cell health was monitored through the consistency of input current and by calculating series and input resistances with test pulses throughout the recording (Appendix Figure S5B). Cells were rejected if any value deviated ±20% of baseline for more than 1min.

CF inputs were stimulated with 0.2ms step pulses using an electrode connected to an isolated current source (SIU91A, Cygnus Technology) and immersed in a glass pipette filled with ACSF. The cell was held in voltage clamp at -10 to -30mV. The stimulus intensity (0-150nA) and location (2-4 sites in the granule cell layer, 50-150μm from the PC soma, spanning the space sub-adjacent to the dendritic arbor) were systematically varied to search for multiple CF inputs. CF excitatory post-synaptic currents (EPSCs), particularly of reduced amplitude in some multi-innervated cells, were distinguished from parallel fiber (PF)-EPSCs by their paired pulse depression (400ms interval) and stable amplitude with small changes in stimulus intensity. PF-EPSCs exhibit paired pulse facilitation and linear amplitude relationship with even small stimulus intensity changes due to the recruitment of additional fibers.

CF-EPSCs were recorded after 20min post-patch to allow sufficient perfusion of cesium and dye. CF multi-innervation was only determined with multiple, discrete and consistent EPSC amplitude steps during both increasing and then decreasing stimulus intensity. After each recording, confocal z-stack images of each cell were obtained with a 63x objective (EC Plan-Neofluar 1.3NA, water immersion, Zeiss) using Zen software.

Two-Photon Ca^{2+} Imaging

Cranial window and GCaMP injection surgeries. Surgeries were performed on animals aged 10-12 weeks under ketamine/xylazine anesthesia (100 and 10mg/kg) with subcutaneous injections of meloxicam (1-2 mg/kg), buprenorphine (0.1 mg/kg), and sterile saline (0.5-1mL) as above. Body temperature was maintained at 35-37°C with a feedback dependent heating pad. The skin above the posterior skull was excised and the bone cleaned to implant a metal headframe over the interparietal bone via dental cement. After 3-4 days of recovery, mice were anesthetized and a

4mm craniotomy and durectomy was made at 2.5mm lateral from midline and 2.5mm caudal from lambda, exposing cerebellar simplex, crus I, and anterior crus II. A glass microelectrode with ~300μm tip diameter was used to inject a viral cocktail with low titer PC-specific L7-Cre (0.5%, AAV1.sL7.Cre.HA.WPRE.hGH.pA; Princeton Neuroscience Institute (PNI) Viral Core Facility; acquired from the lab of Dr. Samuel Wang, Princeton University) and high titer Cre-dependent GCaMP6f (20%, AAV.CAG.Flex.GCaMP6f.WPRE.SV40; Addgene, #100835) was injected ~300μm below the pial surface of medial and/or lateral crus I (~900nL per site, 5min wait before needle retraction) and a two-layer cranial window (4mm inner window, Tower Optical; 5mm outer window, Warner Instruments) was implanted over the craniotomy and sealed with dental cement (Metabond).

Habituation. The mice recovered for 7 days before habituation began. During the first week, habituation sessions were conducted every other day and consisted of exposure to handling and then to the imaging apparatus and head fixation on the treadmill. In the last 3 days before the experiment (6-10 days after habituation began), mice were habituated every day to head fixation, noises and activity typical during an experimental session, and occasional exposure to multisensory stimuli. Habituation allowed animals to exhibit relative comfort and reduced running behavior.

Imaging protocols. Imaging experiments were performed when the GCaMP6f indicator reached stable expression in a sparse cell population (11-20 days post-injection). PC dendrites were imaged at either 61.8 or 30.9Hz using a laser scanning two-photon microscope (Mai Tai DeepSee, Spectra-Physics) with an 8KHz resonant scanning module (Thorlabs) and 16x water immersion objective

(Nikon LWD 0.8NA, 3mm WD) controlled with Scanbox (Neurolabware). A digital 4x magnification was used for imaging lateral crus I during spontaneous and multisensory experiments and 2x for imaging medial crus I during whisker stimulation experiments. GCaMP6f was excited using a 920nm femtosecond-pulsed two-photon laser (~30mW laser power at sample; Spectra-Physics) and fluorescence emission collected by a GaAsP PMT (Hamamatsu). Interlocking light shields were fit around the headframe and objective to block ambient light from increasing background noise and to prevent an artifact from blue light stimuli directed at the eye. The microscope is custom designed with a rotating objective turret such that the angle of imaging could be adjusted to capture a perpendicular cross-section of PC dendritic arbors, thus reducing each cell's imaging profile to reduce the chance of contamination.

In order to increase the imaging rate for spontaneous and multisensory experiments to 62Hz, a narrow field of view was used (656 x 256 pixels scanned instead of 656 x 512 lines for whisker experiments). To image the complete arbor of several PCs when the short axis of the field of view was only ~153μm, we installed the treadmill, camera, and stimulus apparatuses on a large rotating platform (Thorlabs) such that the animal and all experimental components could be rotated under the objective until the parasagittal plane of PC dendrites aligned with the long axis (~392μm) of the image. Having the entire width of the dendrites aligned with the scanning direction also provided the benefit of technically optimizing the scanning time for each cell, thus reducing the chance for movement artifacts to appear as a branch-specific signal.

Volumetric imaging to confirm morphology. At the end of each imaging session, a volumetric scan was performed over the field of view at the maximum z-resolution of 2μm per step. For each scan, the laser power was turned up to 4-15%, the PMT gain down to 0.7-0.85, and 20-30 images

were collected and averaged per step for optimal spatial resolution and morphological detail. Cells were only accepted for use if the somatic and dendritic compartments were entirely visible and major branch points of the primary dendrite were differentiable. These rules restricted our analyses to cells wherein the following parameters were unambiguous: 1) distance from the soma to primary dendrite split, 2) presence or absence of multiple primary trunks emerging from the soma, 3) rostral-caudal distance between branch centroids, and 4) maximal rostral-caudal spread of the whole dendritic arbor. For high-magnification recordings at 4x zoom, where multiple regions of interest (ROIs) were drawn for each major dendritic branch (spontaneous and multisensory experiments), we additionally required the unambiguous distinction of lesser branch points generating sub-compartments. Each cell's dendritic measurements and morphological category were noted at this time.

Stimulus Conditions

Multisensory stimuli. During each experiment, calcium activity was monitored in ~1-10 cells per animal during 20s imaging sessions. One of eight stimulus types (1. Light, 2. Air Puff, 3. Sound, 4. Light + Puff, 5. Light + Sound, 6. Puff + Sound, 7. Light + Puff + Sound, and 8. Control without stimulus) was triggered 10s after scanning initiation and lasted for 30ms. Light stimulus was a 488nm LED light (Prizmatix) targeted to the ipsilateral eye, Air Puff was delivered at 10psi (Picospritzer III, Parker Hannifin) via a 0.86mm diameter capillary tube positioned 2-3mm from the center of the ipsilateral whisker pad, and Sound stimulus was a 12kHz pure tone produced by speakers (Harman/Kardon) positioned bilaterally at ~70-80dB. The stimuli were applied with inter-stimulus intervals ≥ 30s. An Arduino Uno microcontroller triggered by the imaging software provided distinct stimulus type triggering output to the light, puff, and tone instruments. The

microcontroller was programmed to cycle through stimulus types randomly until 15 trials were acquired of each type (120 trials total).

Spontaneous activity. Spontaneous activity was obtained either on a day without sensory stimulation, or from the 10s pre-stimulus baseline period of multisensory imaging sessions. Trials were only used if the animal was resting such that there was no active running and/or whisking (Lanore et al., 2021).

Single whisker stimulation. We obtained a sparse expression of GCaMP6f in PC dendrites and habituated mice to head fixation as described above. In some cases, we used the same mice for this experiment after spontaneous recordings were collected. Before the experiment began, we identified whisker responsive areas of medial Crus I by gently brushing varying numbers of whiskers and observing cellular activity in real time. We then sedated the animals with a minimal dose of ketamine/xylazine (80 and 8mg/kg, respectively) before headfixing them at the two-photon microscope. We strived to conduct the experiment during the 40-60min that the animal was in a stable level of sedation, so whisker responses and spontaneous activity were as close to comparable across whiskers and animals as possible. In a few cases a supplemental dose was required; the experiment was paused while the animal was waking, receiving the supplement, and returning to an equivalent state of sedation.

When the animal reached a state of anesthesia where it stopped actively whisking, a glass capillary tube attached to a rotating motor (SG92R Micro servo, Tower Pro) was manually manipulated to capture a single whisker. Previous work has shown that CF-dependent complex spike responses to whisker stimulation are most commonly tuned to dorsal, caudal, and dorso-

caudal directions of whisker displacement (Bosman et al., 2010), so the rotating servo was oriented such that rotation moved the whisker at 135º in the dorsal-caudal direction (Appendix Figure S8A).

It is important to note that these experiments are meant as a proof of principle which cannot be construed to represent naturalistic behavior in the awake animal. As previously reported (Ju et al., 2019), responses to whisker stimulation, particularly of a single whisker, are very sparse in the anesthetized animal (~10% of trials). Several approaches could be used to compensate for this. Most obviously, experiments could be conducted in the awake animal when responsiveness is elevated. This approach did not work for us as it is virtually impossible to isolate a single whisker in a capillary tube while the mouse is awake (even if all but some whiskers are trimmed, which we prefer to avoid), and it would be extremely challenging to segregate active whisking from experimental passive whisker deflection. Second, while the animal is under anesthesia numerous individual trials (perhaps 50) with distant stimulus times could be conducted on a single whisker to confidently identify a response that is distinct from spontaneous CF activity. While this approach is more attractive for several reasons, it poses a substantial logistical problem as it would require a long time (>30min) to test a single whisker. This substantially limits how many whiskers could be tested under a consistent state of anesthesia, which massively reduces the chances of identifying whisker responses. Given the limitations of these approaches, we designed an experimentally bootstrapped stimulus wherein each whisker was stimulated many times at a high rate. At the expense of a possible change in responsiveness with repeated stimuli, this allowed many attempts to produce a response while accelerating our recordings so we could test a large set of whiskers in each animal.

The servo was controlled by an Arduino Uno microcontroller programed to execute a sine function (7º maximal rotation forming an arc circumference of ~1.5cm at the tip of the capillary

tube) at a rate of 2Hz for 50s (100 total stimulations of the whisker with 500ms intervals between starting movement initiations). The microcontroller was triggered by the imaging software with a 10s delay-to-start so spontaneous activity was recorded of ahead of each whisker stimulation. Images were thus 60s in duration (10s spontaneous activity and a 50s stimulation epoch), and two trials were conducted per whisker (200 total stimulations with 20s of spontaneous recording). After two trials, the capillary tube was manually withdrawn and moved to another whisker. Across animals, seven whiskers were stimulated in random order (β, γ, C1, C2, C3, B2, D2; occasionally D1 if D2 was inaccessible).

To sample a wider population of cells and increase the chance of observing whisker responses, imaging was conducted at 2x digital magnification and 31Hz, rather than 4x and 62Hz as above. As in previous 2-photon experiments, a z-stack was obtained at the end of recording to measure morphological properties of each cell and allow ROIs to be drawn manually across dendrites.

Two-photon image processing

Images were converted to tiffs and motion corrected using custom MATLAB scripts. Cellular ROIs were drawn manually in ImageJ based on volumetric cell reconstructions. The plane of focus for each experiment was selected to maximize the dendritic area of each branch of each target PC present in the scan while remaining within the intermediate region of the molecular layer. As a result, most interbranch ROIs were reasonably similar in size (representative example ROIs can be observed in Fig. 5B and D, Fig. 6A, and Fig. 7A), and there was no systematic difference in the ratio of interbranch ROI areas by morphological type. In unusual cases where there were substantial differences (>10:1) in size or profile of branches within the imaging plane, the cell was removed from consideration if the smaller ROI exhibited a higher baseline noise level. Another

MATLAB script measured the pixel intensity of each ROI across frames and videos and saved the data as a .mat file. An interactive MATLAB GUI was used to manually confirm detection quality and consistency across imaging sessions to either include or exclude each cell for downstream analysis. Analyses were performed using MATLAB scripts and output for final data shaping, plotting, and statistics in R.

Manual event curation. In preliminary experiments, an interactive MATLAB GUI was used to manually curate a findpeaks autodetection of events. Curation involved adjusting rise and peak times as needed and, in cases of a branch-specific event, marking trace locations where a peak was missing. Thus, missed events could be tallied to obtain the number of local events (Appendix Figure S7A).

Calcium peak detection and comparing inter-branch signals. Raw signal from all ROIs was imported to a custom MATLAB script that performed a five-frame moving window smoothing function and a background correction function. Then, ROI traces were input to the MATLAB version of OASIS deconvolution to obtain times and amplitudes of calcium peaks exceeding 3SD of the baseline. We decided not to distinguish between multiple tightly clustered events producing a single, accumulated large amplitude peak. While accumulated peaks from clustered inputs often retain multiple peaks (a partial peak within the rising phase of the larger event), the slow time constant of the GCaMP6f indicator and the natural variability between small, branch ROIs can alter the appearance of multiple peaks and produce varying spike deconvolutions. This reduces our confidence in the ability to appropriately determine if there is a branch-specific event within a cluster of global events. As such, we identified peak times <4 frames apart – having only 1-2

frames (16-32ms) between detected peaks, which is below the ~50ms rise time constant of GCaMP6f (T.-W. Chen et al., 2013) – and took only the second and highest peak or the last in a sequence of >2 events all of which are <4 frames apart.

To compare the deconvolved signal of each branch within a cell, we segregated the data for each trace into five groups: all signal in branch 1, all signal in branch 2, only global events, only local events in branch 1, and only local events in branch 2. Branch number assignment was arbitrary. Subsequent analyses were then performed on each subset of detected peaks individually.

Whisker movement traces and timing. First, whisker stimulation times were obtained from 30Hz video recordings (Genie Dalsa, Phase 1 Technology) of the mouse face where the stimulated whisker and the capillary tube moving the whisker were clearly visible. An ROI was drawn in ImageJ at the location in the capillary tube's movement trajectory where the whisker started to be bent or translated. Thus, when the whisker was moved, the bright capillary tube passed through the ROI and created a time locked peak in light intensity. The entire trace for each video (1min) was extracted in ImageJ for downstream analyses in a custom MATLAB script.

The first derivative of pixel intensity across frames was calculated for each trace, a baseline was measured during the 10s spontaneous period where there was no whisker movement, and whisker stimulus onset times were thus identified as the n-1 frame where a peak in the first derivative exceeded 3SD of the baseline. This also captured the return movement of the capillary tube that returned the whisker to its natural position.

Whisker experiment calcium signal. The same methods as described above were used to obtain calcium signal traces from two-photon recordings. Raw signal from all ROIs was imported to a

custom MATLAB script that performed the same smoothing and background correction as described above. Then, ROI signals for each cell were analyzed two ways: averaged into a whole cell signal trace or kept separate to independently assess each branch. We input either whole cell or branch traces into OASIS deconvolution to obtain times and amplitudes of calcium peaks exceeding 2SD of the baseline and >10% the amplitude of the largest detected peak. These parameters allowed the initial detection of smaller and less typically shaped events and the post-hoc elimination of excessively small events that could be noise during a period of elevated baseline or a highly irregular peak possibly due to a PF burst.

As above, when comparing branches within a cell, we segregated deconvolved calcium events into the same five groups. The next step, determining if the events constituted a response to the stimulated whisker, was then performed on each subset of detected peaks individually.

As two 1min trials were conducted for each whisker, we concatenated the event amplitude and timing data from each trial of the same whisker. We then compared the event rise times (when the rising phase began) with the whisker stimulus times to assess how many peaks occurred during 150ms (5 frame) time windows after each whisker movement, as opposed to non-response windows of 150ms before each whisker movement or the 10s spontaneous time window when there was no whisker stimulation. Probabilities and amplitudes of response and non-response events were thus calculated for each ROI-averaged whole cell and individual branch ROIs. Since whisker responses are known to be very sparse under anesthesia, we stimulated each whisker 100 times per trial (for a total of 200 trials over 2min) to experimentally bootstrap response probabilities. The repetition allowed us to calculate not only the absolute probability of response, but the variability of the response and non-response probabilities across frames relative to whisker

movement time such that we could obtain a Z-score of the response probability using the following formula:

$$Z_{response} = \frac{Prob_{response} - Prob_{spontaneous}}{StDev_{spontaneous}}$$

For each set of input event times, if the $Z_{response} > 1.96$ (2SD) – high enough to reject H_0 with $\alpha < 0.05$ – then we considered this a response to the whisker.

Statistics and Quantifications

Statistical analysis was carried out using R (v4.2.1). Data following a normal distribution was tested with unpaired two-tailed Student's t-tests to compare two groups or ANOVA followed by a Tukey post-hoc correction for repeated measures to compare more than two groups and/or multiple factors. We used a one sample Student's t-test to compare individual groups with a specific, benchmark value where appropriate. Otherwise, for non-parameteric data, a Wilcoxon rank sum test was used for two group comparisons. We used a Pearson's Chi-squared test for independence to assess contingency tables from data with two non-continuous variables. Post-hoc comparisons of contingency tables from mouse and human cell count data were assessed with pairwise Z-tests of proportion with Bonferroni correction as the total numbers of cells differed greatly by species or sub-region, distorting the comparative strength of a standard chi-squared comparison of frequency. P-values and effect sizes (φ) of pairwise Z-tests are reported. To assess a relationship between two continuous variables, we used a linear regression and report the adjusted R^2 value and significance. For all analyses, $\alpha = 0.05$ was used to determine significance and figure panels refer to the significance of comparisons in the following way: ns $p > 0.05$, * $p \leq 0.05$, ** $p \leq 0.01$, *** $p \leq 0.001$.

Data and materials availability: All data are available in the manuscript or the supplementary materials in Appendix 2: Supplementary Figures S1-42 and Tables S1-12. Data and post-processing analysis code are publicly available in a Dryad archive: S. Busch, Climbing fiber multi-innervation of mouse Purkinje dendrites with arborization common to human, Dryad (2023); https://doi.org/10.5061/dryad.kh18932c1.

Main Figures

Fig 3C: Pearson's Chi-squared, Ratio of cell morphologies ~ Lobule; n = 6,646 cells, p < 0.001, $\chi^2 = 170.18$.

Fig 3F: Pearson's Chi-squared, Ratio of cell morphologies ~ Lobule; n = 1,350 cells, p < 0.001, $\chi^2 = 106.83$.

Fig 3G: Morphology and Species: Pearson's Chi-squared, p < 0.001, $\chi^2 = 55.27$; Post-hoc pairwise Z-tests of proportion with Bonferonni correction: Normative, n = 598 and 268 cells, representing a mean ± SEM of 46.53 ± 2.2 and 5.82 ± 1.42 Percent of cells (%) in 30 and 20 lobules (mouse vs human); Split, n = 447 and 2977 cells in 30 and 21 lobules, 36.6 ± 2.04 and 47.7 ± 2.4 Percent of cells (%); Poly, n = 212 and 3401 cells in 29 and 21 lobules, 17.46 ± 2.45 and 46.76 ± 2.97 Percent of cells (%). All comparisons presented in table S3.

Fig 4D: Pearson's Chi-squared, Number of climbing fibers ~ Morphology; n = 159 cells, p = 0.003, $\chi^2 = 15.71$.

Fig 4E: 1 vs. 2+ CFs: n = 135 and 24 cells, -763.65 ± 2.51 and -978.75 ± 13.45 CF EPSC amplitude (pA), p = 0.006, Two-tailed Student's t-test; Weak CFs: n = 24 cells, -389.13 ± 10.3 CF EPSC amplitude (pA), p < 0.001, One-way Student's t-test, μ = 0.

Fig 4F: 1 vs. 2+ CFs, all PCs: n = 135 and 24 cells, 43.74 ± 3.13 and 16.86 ± 3.28 Split distance (µm), $p < 0.001$, Two-tailed Student's t-test.

Fig 4G: 1 vs. 2+ CFs, mono-planar PCs: n = 85 and 9 cells, 54.48 ± 3.26 and 87.09 ± 7.73 Branch distance (µm), $p = 0.002$, Two-tailed Student's t-test.

Fig 4H: 1 vs. 2+ CFs, Poly PCs: n = 26 and 8 cells, 67.32 ± 5.7 and 95.91 ± 10 Trunk angle (°), $p = 0.029$, Two-tailed Student's t-test.

Fig 5F: Global vs. Local events: n = 95 cells, 0.29 ± 0.009 and 0.19 ± 0.007 Mean amplitude (ΔF/F0), $p < 0.001$, Two-tailed Student's t-test.

Fig 5G: Normative, Split, Poly: One-way ANOVA, $p < 0.001$; Tukey's HSD post-hoc, n = 32, 55, 8 cells, 17.36 ± 2.12, 36.62 ± 2.54, and 51.01 ± 9.76 Local events (%); Normative vs. Split, $p < 0.001$; Normative vs. Poly, $p < 0.001$; Split vs. Poly, $p = 0.087$.

Fig 5H: Normative, Split, Poly: Kruskal-Wallis test, $p < 0.001$; Pairwise Wilcoxon rank sum test, n = 32, 55, 8 cells, 0.37 ± 0.03, 0.24 ± 0.03, and 0.079 ± 0.04 Adjusted R^2; Normative vs. Split, $p = 0.002$; Normative vs. Poly, $p < 0.001$; Split vs. Poly, $p = 0.016$.

Fig 5I: Pearson's Chi-squared, Rate of significant branch covariation ~ Morphology; n = 95 cells, $p = 0.007$, $\chi^2 = 9.8$.

Fig 5J: Linear Regression, Inter-branch amplitude scale (sd) ~ Split distance (µm); n = 105 cells, $p < 0.001$, $R^2 = 0.099$.

Fig 5K: Linear Regression, excluding multi-planar cells, Inter-branch amplitude scale (sd) ~ Dendrite width (µm); n = 109 cells, $p = 0.002$, $R^2 = 0.078$.

Fig 6C: Normative, Split, Poly: One-way ANOVA, $p < 0.001$; Tukey's HSD post-hoc, n = 33, 112, 24 cells, 2.72 ± 0.36, 4.48 ± 0.29, and 5.78 ± 0.39 Mean local responses (#); Normative vs. Split, $p = 0.004$; Normative vs. Poly, $p < 0.001$; Split vs. Poly, $p = 0.089$.

Fig 6D: Normative, Split, Poly: One-way ANOVA, p = 0.02; Tukey's HSD post-hoc, n = 33, 112, 24 cells, 4.76 ± 0.42, 6.29 ± 0.33, and 6.96 ± 0.56 Inter-whisker difference (#); Normative vs. Split, p = 0.041; Normative vs. Poly, p = 0.029; Split vs. Poly, p = 0.623.

Fig 6F: Pearson's Chi-squared, Response category ~ Morphology; n = 169 cells, p = 0.035, χ^2 = 6.73.

Fig 6G: Unresponsive, Global, and Lateral: One-way ANOVA, p = 0.02; Tukey's HSD post-hoc, n = 75, 42, 52 cells, 27.35 ± 2.06, 28.24 ± 3.58, and 18.73 ± 2.05 Split distance (μm); Unresponsive vs. Global, p = 0.967; Unresponsive vs. Lateral, p = 0.034; Global vs. Lateral, p = 0.043.

Fig 6H: Linear Regression, Local events (%) ~ Receptive field (whiskers); n = 151 cells, p = 0.005, R^2 = 0.046.

Fig 7C: Morphology and Stimulus Category: Two-way ANOVA, Morphology p < 0.001, Stimulus Category p = 0.047; Tukey's HSD post-hoc: Uni-modal, n = 24 and 38 cells, 18.06 ± 1.94 and 31.23 ± 2.98 Maximum local events (%), $Uni_{Normative}$ vs. $Uni_{Split+Poly}$, p = 0.014; Multi-modal, n = 24 and 38 cells, 21.11 ± 3.02 and 38.95 ± 3.01 Maximum local events (%), $Multi_{Normative}$ vs. $Multi_{Split+Poly}$, p < 0.001; $Uni_{Normative}$ vs. $Multi_{Normative}$, p = 0.917; $Uni_{Split+Poly}$ vs. $Multi_{Split+Poly}$, p = 0.176.

Fig 7F: Normative vs. Split+Poly PCs: n = 24 and 38 cells, 29.84 ± 3.51 and 45.58 ± 4.43 ΔBranch response range (%), p = 0.008, Two-tailed Student's t-test.

Fig 7G: Normative vs. Split+Poly PCs: n = 24 and 38 cells, -1.64 ± 1.44 and -1.57 ± 3.57 ΔBranch response mean (%), p = 0.986, Two-tailed Student's t-test.

Fig 7H: Normative vs. Split+Poly PCs: n = 24 and 38 cells, 31.47 ± 4.02 and 47.14 ± 5.55 ΔBranch response bilaterality (%), p = 0.027, Two-tailed Student's t-test.

Supplementary Figures

Appendix Figure S3B: Pearson's Chi-squared, Morphology ~ Zebrin expression; n = 150 cells, p = 0.078, χ^2 = 5.09. All comparisons presented in table S5.

Appendix Figure S3E: Pearson's Chi-squared, Morphology ~ Zebrin expression; n = 162 cells, p = 0.014, χ^2 = 8.47. All comparisons presented in table S6.

Appendix Figure S4C: Pearson's Chi-squared, Morphology ~ Foliar sub-region.

Mouse: n = 1350 cells, p = 0.027, χ^2 = 10.96. All comparisons presented in table S7.

Human: n = 6645 cells, p < 0.001, χ^2 = 65.17. All comparisons presented in table S8.

Appendix Figure S4D: Pearson's Chi-squared, Dendrite orientation ~ Foliar sub-region.

Mouse: n = 1350 cells, p = 0.002, χ^2 = 17.41. All comparisons presented in table S9.

Human: n = 6645 cells, p < 0.001, χ^2 = 1876.9. All comparisons presented in table S10.

Appendix Figure S5C: Pearson's Chi-squared, Multi-CF rate (%) ~ Split distance (μm); n = 159 cells, p = 0.025, χ^2 = 18.65.

Appendix Figure S5D: 1 vs. 2+ CFs, non-Poly PCs excluding Normative PCs with no split: n = 79 and 16 cells, 36.77 ± 2.17 and 25.29 ± 3.25 Split distance (μm), p = 0.006, Two-tailed Student's t-test

Appendix Figure S5E: 1 vs. 2+ CFs, non-Poly PCs: n = 79 and 16 cells, 96.97 ± 2.61 and 105.44 ± 4.95 Split angle (°), p = 0.16, Two-tailed Student's t-test.

Appendix Figure S5F: 1 vs. 2+ CFs, Poly PCs: n = 26 and 8 cells, 67.32 ± 5.7 and 95.91 ± 10 Trunk angle (°), p = 0.029, Two-tailed Student's t-test.

Appendix Figure S5G: 1 vs. 2+ CFs, all PCs excluding Normative PCs with no split: n = 104 and 24 cells, 66.85 ± 2.41 and 83.19 ± 6.05 Arbor separation (μm), p = 0.018, Two-tailed Student's t-test

Appendix Figure S5H: 1 vs. 2+ CFs, Poly PCs: n = 26 and 8 cells, 21.23 ± 0.35 and 21.2 ± 0.49

Soma diameter (μm), p = 0.97, Two-tailed Student's t-test.

Appendix Figure S5M: Linear Regression, CF EPSC amplitude (nA) ~ Age (days); n = 24 cells,

p < 0.001, R^2 = 0.445.

Appendix Figure S5N: Dominant CF to multi-CF PCs: Linear Regression, CF EPSC amplitude

(nA) ~ Age (days); n = 24 cells, p = 0.235, R^2 = 0.021; Single CF to mono-CF PCs: Linear

Regression, CF EPSC amplitude (nA) ~ Age (days); n = 126 cells, p = 0.383, R^2 = -0.002.

Appendix Figure S5O: Normative, Split, and Poly: Kruskal-Wallis rank sum test, p = 0.21; Split

vs. Poly PCs: n = 15 and 8 cells, 36.48 ± 1.23 and 53.96 ± 3.16 Small CF : big CF EPSC amplitude

(%), p = 0.112, Two-tailed Student's t-test (p = 0.056, One-tailed Student's t-test).

Appendix Figure S5P: Gyrus, Bank, and Sulcus: One-way ANOVA, p = 0.058; Tukey's HSD

post-hoc, n = 6, 11, 7 cells, 27.91 ± 9.32, 40.69 ± 5.78, and 56.16 ± 7.04 Small CF : big CF EPSC

amplitude (%); Gyrus vs. Bank, p = 0.431; Gyrus vs. Sulcus, p = 0.048; Bank vs. Sulcus, p = 0.27.

Appendix Figure S5Q: Linear Regression, Small CF : big CF EPSC amplitude (%) ~ Trunk angle

(°); n = 8 cells, p = 0.007, R^2 = 0.687.

Appendix Figure S5R: Linear Regression, Small CF : big CF EPSC amplitude (%) ~ Split

distance (μm); n = 23 cells, p = 0.138, R^2 = 0.059.

Appendix Figure S6L: 1 vs. 2+ CFs, all PCs: n = 135 and 24 cells, 37.48 ± 0.79 and 42.58 ± 2.54

Age (days), p = 0.065, Two-tailed Student's t-test.

Appendix Figure S7A: Normative, Split, Poly: One-way ANOVA, p = 0.028; Tukey's HSD post-

hoc, n = 25, 29, 5 cells, 5.27 ± 1.18, 12.7 ± 2.58, and 16.74 ± 7.25 Local events (%); Normative

vs. Split, p = 0.05; Normative vs. Poly, p = 0.11; Split vs. Poly, p = 0.75.

Appendix Figure S7B: Normative, Split, Poly: One-way ANOVA, p = 0.01; Tukey's HSD post-hoc, n = 25, 29, 5 cells, 0.006 ± 0.07, 0.351 ± 0.08, and 0.19 ± 0.17 Ca^{2+} amplitude coefficient of variation between vs. within branches (CV); Normative vs. Split, p = 0.006; Normative vs. Poly, p = 0.71; Split vs. Poly, p = 0.77.

Appendix Figure S7C: Linear Regression, Amplitude scale (sd) ~ Compartment separation (µm); n = 95 cells, p = 0.017, R^2 = 0.05.

Appendix Figure S7D: Normative, Split, Poly: One-way ANOVA, p = 0.389; Tukey's HSD post-hoc, n = 32, 55, 8 cells, 1.26 ± 0.04, 1.38 ± 0.06, and 1.37 ± 0.17 Event rate (Hz); Normative vs. Split, p = 0.366; Normative vs. Poly, p = 0.757; Split vs. Poly, p = 0.998.

Appendix Figure S7E: Split vs. Normative PCs: n = 13 animals, 102.72 ± 5.76 Split / Normative Rate (%), p = 0.645, One-way Student's t-test, µ = 100.

Appendix Figure S7F: Linear Regression, Split / Normative Rate (%) ~ Local gap (%); n = 13 animals, p = 0.813, R^2 = -0.085.

Appendix Figure S7G: Linear Regression, Rate above minimum (Hz) ~ Local events (%); n = 94 cells, p = 0.001, R^2 = 0.1.

Appendix Figure S7H: Linear Regression, Event rate (Hz) ~ Local events (%); n = 95 cells, p = 0.008, R^2 = 0.06.

Appendix Figure S7I: Normative, Split, Poly: One-way ANOVA, p = 0.043; Tukey's HSD post-hoc, n = 32, 55, 8 cells, 2.23± 0.09, 2.74 ± 0.14, and 2.71 ± 0.46 Event rate (Hz); Normative vs. Split, p = 0.036; Normative vs. Poly, p = 0.387; Split vs. Poly, p = 0.995.

Appendix Figure S7J: Split vs. Normative PCs: n = 13 animals, 126.25 ± 8.29 Split / Normative Rate (%), p = 0.008, One-way Student's t-test, µ = 100.

Appendix Figure S7K: Linear Regression, Split / Normative Rate (%) ~ Local gap (%); n = 13 animals, p = 0.005, R^2 = 0.48.

Appendix Figure S7L: Linear Regression, Rate above minimum (Hz) ~ Local events (%); n = 94 cells, p < 0.001, R^2 = 0.14.

Appendix Figure S7M: Linear Regression, Event rate (Hz) ~ Local events (%); n = 95 cells, p < 0.001, R^2 = 0.26.

Appendix Figure S7N: Normative, Split, Poly: One-way ANOVA, p = 0.019; Tukey's HSD post-hoc, n = 13, 16, 6 animals, 2.12 ± 0.23, 3.36 ± 0.47, and 2.85 ± 0.31 Event rate gap (Hz); Normative vs. Split, p = 0.014; Normative vs. Poly, p = 0.384; Split vs. Poly, p = 0.607.

Appendix Figure S7O: Linear Regression, Event rate gap (Hz) ~ Local events (%); n = 95 cells, p < 0.001, R^2 = 0.2.

Appendix Figure S7P: Minimum vs. non-minimum cells: n = 16 and 78 cells, 13.39 ± 4.93 and 22.21 ± 2.11 Local events (%), p = 0.032, Wilcoxon rank sum test.

Appendix Figure S8E: Normative, Split, Poly: One-way ANOVA, p = 0.002; Tukey's HSD post-hoc, n = 28, 99, 22 cells, 22.32 ± 3.58, 36.88 ± 2.34, and 43.36 ± 4.29 Local events (%); Normative vs. Split, p = 0.007; Normative vs. Poly, p = 0.003; Split vs. Poly, p = 0.428.

Appendix Figure S8F: Unresponsive, Global, and Lateral: One-way ANOVA, p < 0.001; Tukey's HSD post-hoc, n = 75, 42, 52 cells, 32.13 ± 2.62, 32.72 ± 3.24, and 46.76 ± 2.51 Local events (%); Unresponsive vs. Global, p = 0.988; Unresponsive vs. Lateral, p < 0.001; Global vs. Lateral, p = 0.004.

Appendix Figure S9B: Pearson's Chi-squared, Response Type ~ Morphology; n = 2,520 and 3,990 events, 24 and 38 cells, p < 0.001, χ^2 = 169.13.

Appendix Figure S9C: Morphology and Stimulus Category: Two-way ANOVA, Morphology $p = 0.88$, Stimulus Category $p = 0.002$; Tukey's HSD post-hoc: Uni-modal, $n = 24$ and 38 cells, 70.37 ± 4.29 and 70.12 ± 4.03 Response probability (%), $Uni_{Normative}$ vs. $Uni_{Split+Poly}$, $p = 0.999$; Multi-modal, $n = 24$ and 38 cells, 82.22 ± 4.83 and 83.73 ± 3.53 Response probability (%), $Multi_{Normative}$ vs. $Multi_{Split+Poly}$, $p = 0.994$; $Uni_{Normative}$ vs. $Multi_{Normative}$, $p = 0.285$; $Uni_{Split+Poly}$ vs. $Multi_{Split+Poly}$, $p = 0.053$.

Appendix Figure S9D: Morphology and Stimulus Category: Two-way ANOVA, Morphology $p < 0.001$, Stimulus Category $p < 0.001$; Tukey's HSD post-hoc: Control, $n = 24$ and 38 cells, 5 ± 1.15 and 7.54 ± 1.38 Maximum local events (%), $Ctrl_{Normative}$ vs. $Ctrl_{Split+Poly}$, $p = 0.983$; Uni-modal, $n = 24$ and 38 cells, 18.06 ± 1.94 and 31.23 ± 2.98 Maximum local events (%), $Uni_{Normative}$ vs. $Uni_{Split+Poly}$, $p = 0.014$; Multi-modal, $n = 24$ and 38 cells, 21.11 ± 3.02 and 38.95 ± 3.01 Maximum local events (%), $Multi_{Normative}$ vs. $Multi_{Split+Poly}$, $p < 0.001$; $Ctrl_{Normative}$ vs. $Uni_{Normative}$, $p = 0.019$; $Ctrl_{Split+Poly}$ vs. $Uni_{Split+Poly}$, $p < 0.001$; $Uni_{Normative}$ vs. $Multi_{Normative}$, $p = 0.975$; $Uni_{Split+Poly}$ vs. $Multi_{Split+Poly}$, $p = 0.166$.

Appendix Figure S9E: Morphology and Stimulus Category: Two-way ANOVA, Morphology $p < 0.001$, Stimulus Category $p < 0.001$; Tukey's HSD post-hoc: Control, $n = 24$ and 38 cells, 3.33 ± 0.8 and 4.74 ± 0.9 Directional maximum local events (%), $Ctrl_{Normative}$ vs. $Ctrl_{Split+Poly}$, $p = 0.997$; Uni-modal, $n = 24$ and 38 cells, 13.61 ± 1.73 and 23.33 ± 2.84 Directional maximum local events (%), $Uni_{Normative}$ vs. $Uni_{Split+Poly}$, $p = 0.029$; Multi-modal, $n = 24$ and 38 cells, 13.61 ± 1.77 and 26.14 ± 2.7 Directional maximum local events (%), $Multi_{Normative}$ vs. $Multi_{Split+Poly}$, $p = 0.001$; $Ctrl_{Normative}$ vs. $Uni_{Normative}$, $p = 0.043$; $Ctrl_{Split+Poly}$ vs. $Uni_{Split+Poly}$, $p < 0.001$; $Uni_{Normative}$ vs. $Multi_{Normative}$, $p = 1.0$; $Uni_{Split+Poly}$ vs. $Multi_{Split+Poly}$, $p = 0.914$.

Appendix Figure S9F: Normative PCs: n = 24 cells, 3.06 ± 0.44 Uni vs. Multi-modal difference in maximum local events, p = 0.171, One-way Student's t-test, μ = 0; Split+Poly PCs: n = 38 cells, 7.72 ± 0.34 Uni vs. Multi-modal difference in maximum local events, p < 0.001, One-way Student's t-test, μ = 0.

Appendix Figure S9I: Unimodal Normative vs. Split+Poly PCs: n = 24 and 38 cells, 21.41 ± 3.66 and 32.71 ± 4.41 ΔBranch response range (%), p = 0.053, Two-tailed Student's t-test; Multimodal Normative vs. Split+Poly PCs: n = 24 and 38 cells, 17.29 ± 2.14 and 27.44 ± 3.12 ΔBranch response range (%), p = 0.01, Two-tailed Student's t-test.

Appendix Figure S9J: Unimodal Normative vs. Split+Poly PCs: n = 24 and 38 cells, -3.18 ± 2.11 and 3.73 ± 4.51 ΔBranch response mean (%), p = 0.172, Two-tailed Student's t-test; Multimodal Normative vs. Split+Poly PCs: n = 24 and 38 cells, -0.48 ± 1.43 and -4.11 ± 3.35 ΔBranch response mean (%), p = 0.329, Two-tailed Student's t-test.

Appendix Figure S9K: Unimodal Normative vs. Split+Poly PCs: n = 24 and 38 cells, 24.59 ± 0.44 and 28.98 ± 6.63 ΔBranch response bilaterality (%), p = 0.602, Two-tailed Student's t-test; Multimodal Normative vs. Split+Poly PCs: n = 24 and 38 cells, 17.78 ± 2.52 and 31.56 ± 4.65 ΔBranch response bilaterality (%), p = 0.013, Two-tailed Student's t-test.

Appendix Figure S10A: Pearson's Chi-squared, Morphology ~ Cells above threshold (%); n = 95 cells, p < 0.001, χ^2 = 19.33.

Appendix Figure S10B: Pearson's Chi-squared, Morphology ~ Cells above threshold (%); n = 169 cells, p = 0.03, χ^2 = 7.02.

Appendix Figure S10C: Pearson's Chi-squared without Yates' continuity correction, Morphology ~ Cells above threshold (%); n = 61 cells, p = 0.095, χ^2 = 2.78.

CHAPTER 3: NON-ALLOMETRIC EXPANSION AND ENHANCED
COMPARTMENTALIZATION OF PURKINJE CELL DENDRITES IN THE HUMAN
CEREBELLUM

Methods

Subjects

Human cerebellar tissue was collected from three embalmed donor bodies provided to the University of Chicago Pritzker School of Medicine Anatomy Lab by the Anatomical Gift Association of Illinois (AGAI) and two unembalmed donor bodies provided directly by the AGAI. Embalmed individuals were 92 (F), 95 (F), and 86 (M) years old, died of causes unrelated to cerebellar morphology (e.g. 'failure to thrive', likely 'failure to thrive', and colon cancer, respectively), and cadavers were stored for 2, 6, and 2 months, respectively. Unembalmed individuals were 93 (F) and 71 (M), died of causes unrelated to cerebellar morphology (e.g. chronic obstructive pulmonary disease and bile duct cancer, respectively), and cadavers were stored for 6 and 7 days, respectively. During life, all study subjects signed an informed consent approved by the AGAI.

For experiments involving mice, all experimental and surgical procedures were in accordance with the University of Chicago Animal Care and Use Committee guidelines. We used wildtype C57BL/6J mice housed on a 12hr light/dark cycle. Animals of either sex were used in all experiments and no sex-dependent differences were observed in any reported measures.

Human tissue preparation. One hemisphere from each of the embalmed specimens was used previously (Busch & Hansel, 2023). Preparation of the vermis and opposing hemisphere from the embalmed specimens and of one hemisphere from the unembalmed specimens followed the same

procedure as previously reported. In brief, whole cerebellums were fixed in 4% paraformaldehyde (PFA) for one week after being obtained. Specimens were sectioned by hand in the parasagittal axis to obtain 3-5mm blocks that were sometimes cut transversely and further fixed for 2-4 days. Blocks were rinsed in 0.01M phosphate buffer saline (PBS) and sliced at 50µm in the parasagittal plane with a vibratome (Leica VT-1000S). Slices selected for immunolabeling were photobleached at 4°C for 3-4 days to reduce autofluorescence.

Mouse tissue preparation. To obtain sparse PC labeling for single cell dendrite and spine reconstruction in mice, we used tissue from animals expressing PC-specific GCaMP6f label for unrelated imaging studies. Surgeries were performed as described previously (Busch & Hansel, 2023) on animals aged 10-12 weeks under ketamine/xylazine anesthesia (100 and 10mg/kg) with subcutaneous injections of meloxicam (1-2 mg/kg), buprenorphine (0.1 mg/kg), and sterile saline (0.5-1mL) as above. Body temperature was maintained at 35-37°C with a feedback dependent heating pad. The skin above the posterior skull was excised and the bone cleaned to implant a metal headframe over the interparietal bone via dental cement. After 3-4 days of recovery, mice were anesthetized and a 4mm craniotomy and durectomy was made at 2.5mm lateral from midline and 2.5mm caudal from lambda, exposing cerebellar simplex, crus I, and anterior crus II. A glass microelectrode with ~300µm tip diameter was used to inject a viral cocktail with low titer PC-specific L7-Cre (0.5%, AAV1.sL7.Cre.HA.WPRE.hGH.pA; Princeton Neuroscience Institute (PNI) Viral Core Facility; acquired from the lab of Dr. Samuel Wang, Princeton University) and high titer Cre-dependent GCaMP6f (20%, AAV.CAG.Flex.GCaMP6f.WPRE.SV40; Addgene, #100835) at a depth of ~300µm below the pial surface of lateral crus I (~900nL per site, 5min wait before needle retraction). A two-layer cranial window (4mm inner window, Tower Optical; 5mm

outer window, Warner Instruments) was implanted over the craniotomy and sealed with dental cement (Metabond).

Imaging experiments were performed 2-3 weeks later, after which mice were anesthetized with ketamine/xylazine (100 and 10mg/kg) and perfused with 4% PFA. Sleep/wake periods may influence spine densities (Loschky et al., 2022), but we controlled for this in part by collecting mouse tissue during their sleep cycle, which may compare well with our human cases that passed away either during sleep or a period of decreased metabolism. Cerebellums were removed and incubated for 2hrs in 4% PFA at 4°C and then overnight in 30% sucrose in 0.1M PB at 4°C (until the tissue sank from the surface). The tissue was then rinsed briefly in 0.1M PB, dried and blocked, submerged in OCT medium, flash frozen, and then sliced (50μm, parasagittal plane) using a cryostat microtome (CM 3050S, Leica). Sparseness was not required to quantify cell morphology demographics across the vermis, so tissue was obtained from wildtype C57BL/6J mice without previous surgery and were anesthetized, perfused, and sliced as above.

Calbindin immunohistochemistry. Tissue was washed in 50mM Glycine in 0.01M PBS for 2hrs at 4°C and incubated in 20mM Sodium Citrate in 0.01M PBS at 50-60°C using a heated water bath for 30min. After cooling to room temperature (RT), tissue was washed in 20mM Sodium Citrate for 5min then rinsed 2x30sec in dH20. Next, slices were permeabilized at RT in 0.01M PBS containing 0.025% Triton-X (PBS-TX) for 1hr. Blocking was done with PBS-TX containing 5% normal donkey serum (NDS) and 5% bovine serum albumin (BSA) for 1hr at RT followed by incubation in guinea pig anti-calbindin primary antibody (1:1000; Synaptic Systems Cat# 214 004, RRID:AB_10550535) solution overnight (18-20hrs) at 4°C with 1% normal donkey serum in PBS-TX. After 3x10min washes in PBS-TX at RT, slices were incubated in donkey anti-guinea pig Cy3

secondary antibody (1:200; Jackson ImmunoResearch Labs Cat# 706-165-148, RRID:AB_2340460) for 2hrs at 4°C with 1% NDS in PBS-TX. Finally, slices were washed in PBS-TX for 3x10min, mounted and coverslipped with Vectashield (Vector Laboratories, Inc.), and allowed to set overnight before visualization.

For calbindin based labeling of PCs in mouse tissue without GCaMP6f, the same procedure was used as above with some small changes: glycine incubation for 1hr instead of 2hrs and heated Sodium Citrate incubation for 20min instead of 30min. Slices were incubated in primary antibody solution with guinea pig anti-calbindin (1:1000), then in secondary antibodies with donkey anti-guinea pig Cy3 (both 1:200).

Dual calbindin and peripherin immunohistochemistry. VGluT2 and Cocaine- and Amphetamine-Regulated Transcript (CART) (Press & Wall, 2008; Reeber & Sillitoe, 2011) label CFs in human (C.-Y. Lin et al., 2014; Y.-C. Wu et al., 2021), but are restricted to terminal boutons and minor processes in the molecular layer, precluding disambiguation of mono- and multi-innervation without an olivary tracer (Busch & Hansel, 2023; Miyazaki & Watanabe, 2011). Some reports used Golgi impregnation to visualize human CFs(Marin-Padilla, 1985; Ramón y Cajal, 1909) but this technique cannot visualize CF-PC pairs in reliably beyond the molecular layer in post-natal tissue due to myelination. To distinguish fiber sources, we instead labeled CF axonal fibers with the intermediate neurofilament protein peripherin (Errante et al., 1998). Unembalmed human tissue was washed in 200mM Glycine in 0.01M PBS for 2hrs at RT and incubated in 10mM Sodium Citrate in 0.01M PBS at 80-90°C using a heated water bath for 30min. After cooling to RT, tissue was washed in 0.5% Tween-20 in 0.01M PBS (PBS-Tween) for 3x5min. Next, slices were permeabilized at RT in 0.01M PBS containing 2.5% Triton-X (PBS-TX) for 1hr and then

incubated in 200mM Glycine in PBS-Tween for 15min. Blocking was done with PBS-Tween containing 10% normal donkey serum (NDS) and 5% bovine serum albumin (BSA) for 2hr at RT followed by incubation in polyclonal guinea pig anti-calbindin (1:500; Synaptic Systems Cat# 214 004, RRID:AB_10550535) and polyclonal rabbit anti-peripherin (1:500; EnCor Biotechnology Cat# RCPA-Peri, RRID: AB_2572375) primary antibody solution overnight (18-20hrs) at 4°C and then at RT for 3-4hrs with 1% normal donkey serum in PBS-Tween. After 3x10min washes in PBS-Tween at RT, slices were incubated in donkey anti-guinea pig AF488 (1:200; Jackson ImmunoResearch Labs Cat# 706-545-148, RRID:AB_2340472) and donkey anti-rabbit Cy3 (1:200; Jackson ImmunoResearch Labs Cat# 706-165-152, RRID:AB_2307443) secondary antibody solution for 2hrs at RT with 1% NDS in PBS-Tween. Finally, slices were washed in PBS-Tween for 3x10min, mounted and coverslipped with Vectashield (Vector Laboratories, Inc.) and allowed to set overnight before visualization.

Confocal imaging for cell, spine, and peripherin fiber reconstruction. Following immunolabeling of unembalmed human tissue and perfusion of GCaMP6f labeled mouse tissue, we selected PCs within L6-8 of the midhemisphere for their lack of truncation of their dendritic arbor and isolation from adjacent cells to minimize the chance of misattributing a branch from another cell. We collected z-stack tile scans of individual PCs at 40x (Zeiss EC Plan-Neofluar 1.3NA, oil immersion) with a confocal microscope (Zeiss LSM 900, Examiner.Z1) with 1x digital zoom, 2x line averaging, and 0.2079μm x 0.2079μm x 0.5μm voxel resolution. Multi-channel z-stack images of PCs and peripherin fibers were collected at 40x (Zeiss EC Plan-Neofluar 1.3NA, oil immersion; Zeiss LSM 900, Examiner.Z1) with 0.72x digital zoom, 2x line averaging, and 0.289um x 0.289um x 1um voxel resolution. Single z-stack images of branch segments from distal,

intermediate, and proximal compartments for spine reconstruction were collected at 63x (Leica HC PL APO 1.4 UV, oil immersion; Leica Stellaris 8 laser scanning confocal microscope; University of Chicago Integrated Light Microscopy Core RRID: SCR_019197) with 7x digital zoom, 4x line averaging, and 25.76nm x 25.76nm x 0.15μm voxel resolution. Cells and spines were then manually reconstructed using NeuronStudio (Rodriguez et al., 2003). No shrinkage factor or z-correction was applied.

Branch eccentricity was calculated by translating the origin of every branch to (0,0) in the coordinate plane and taking the slope of the best fit line for all branch trace vertices. The slope was mirrored over the x-axis for branches projecting downward toward the Purkinje cell layer (in quadrants 3 and 4 of the coordinate plane). As it made no difference whether the branch projected to the left or right, all branches projecting leftward (in the second quadrant of the coordinate plane) were mirrored over the y-axis for simplicity. Thus, the eccentricity of every branch relative to the horizontal plane of the Purkinje cell layer was maintained while the direction was reversed.

Each instance of an intact co-labeled PC and peripherin fiber allowed us to make one of four observations: "putative mono-innervation", in which a single fiber approaches the target PC and branches to run in apposition to all major primary dendrites (Fig. 10A); "absence multi-innervation", in which a single fiber approaches and runs in apposition with some primary dendrites but is conspicuously absent from others (Fig. 10B); "putative multi-innervation", in which the primary dendritic branches receive multiple unconnected fibers that are truncated so we could not observe their independence in the GCL (Fig. 10C); and "fully labeled multi-innervation", in which multiple labeled fibers approach the PC from the GCL and travel to distinct primary dendrites either entirely separately, or following a brief distance of shared apposition to a primary dendrite before diverging to different dendrites (Fig. 10D-E).

Slice reconstruction and cell counting. Parasagittal slices were traced and cells were mapped as described previously (Busch & Hansel, 2023). Briefly, slides were visualized under 10x or 20x magnification (Zeiss Achroplan 0.25NA, air; Olympus UMPlanFL N 0.5NA, water) and illuminated with an epi-fluorescent light source (LEJ HBO-100). We manually scanned through the cerebellar cortex and classified Purkinje cells (PCs) by their dendritic morphology and their location by foliar sub-region (e.g. gyrus, bank, and sulcus), both based on criteria listed below. To mark the morphology and cell location accurately in both human and mouse tissue, we initially traced the outlines of the pial surface, white matter tracts, and PC layer of the whole parasagittal section. Cells were only included for categorization if the soma and at least 200μm lengths of primary dendritic trunks were clearly labeled such that all features of Normative, Split, and Poly and vertical or horizontal categories were unambiguously present or absent (see criteria below). We marked the location and morphological type of each cell in the slice map and scanned this map as an input image to a custom Matlab GUI where each point's X,Y coordinate, foliar location, and morphological category could be digitized. The output data were imported to R for downstream analysis and plotting.

Purkinje cell morphological category definitions and criteria. Criteria for morphology category definitions were the same as previously (Busch & Hansel, 2023) but we reiterate the full description here for clarity. In human, PCs were deemed Normative if they had the following features: 1) a single trunk emerging from the soma, and 2) either no bifurcation of the primary trunk within two soma distances (2x the diameter of the soma, 25-35μm per soma) or a highly asymmetrical bifurcation where the smaller branch did not project in the parasagittal axis more

than 200µm from the main dendritic compartment. PCs were defined as Split if they had the following features: 1) a single trunk emerging from the soma, and 2) either symmetrical bifurcation of the primary trunk within two soma distances or an asymmetrical bifurcation within two soma distances where the smaller branch projected more than 200µm from the main dendritic compartment and thus reached prominence by its overall length and sub-branching. PCs were defined as Poly if they had more than one trunk emerging from the soma regardless of relative size.

In mouse, PC categories were defined the same way, except that the bifurcation threshold of two soma distances (each soma diameter is 18-22µm) was set at 40µm, and the smaller branch of an asymmetrical bifurcation had to project only 100µm away from the main dendritic compartment.

In mouse and human, Split and Poly PCs were further subdivided into Vertical or Horizontal ramification patterns. Split and Poly PCs were defined as Horizontal if one of two primary dendrites ramified parallel with the PC layer for >300µm in human (>150µm in mouse), or both primary dendrites ramified in opposing directions parallel with the PC layer for >150µm each in human (>75µm in mouse). Dendrites were considered parallel if the dendrite, at 300 or 150µm from the soma respectively, ramified at <30° from the top of the PC layer. Otherwise, the cell was defined as Vertical.

Foliar sub-region category definitions and criteria. Criteria for foliar category definitions were the same as previously (Busch & Hansel, 2023) but we reiterate the full description here for clarity. Purkinje cell locations were defined as either Gyrus, Bank, or Sulcus based on the relative expansion/compression of the granule cell/molecular layers in the parasagittal axis. Gyrus was

defined as a region where the total parasagittal length of the pial surface exceeded that of the border between the granule cell layer and the white matter. Bank was defined as regions where those two lengths were equal, such that neither layer of the cortex was compressed or expanded relative to the other. Finally, Sulcus was defined as regions where the total parasagittal length of the pial surface was less than that of the border between the granule cell layer and the white matter. Both intermediate sulci, embedded within a continuous Bank region, and full sulci were combined for these analyses.

Spine morphology criteria, and volume calculations. Manual reconstruction of spines was performed using NeuronStudio and by scanning through a z-stack image of a spiny branch to better visualize the relations between contiguous and sometimes non-contiguous structures surrounding the dendrite. Spines were categorized as either thin or mushroom spines if they had a classical head and neck structure with a head that had either a less than or greater than 500nm diameter, respectively. Spines were categorized as branched if two heads emerged from a shared neck emerging from the dendrite. Spines were categorized as 'spine clusters' if they had a single head with discontinuous and/or bumpy structure that produced three or more puncta with distinct prominences from the core head matrix.

Spine volume as a fraction of volume surrounding the dendrite was calculated by taking the sum of the spine head volumes for each branch segment and dividing it by the volume of the surrounding cylindrical space, which in turn was the subtraction of the cylindrical volume of the dendrite (using the mean dendritic radius) from the larger cylindrical volume with a radius combining the mean dendrite radius and the mean spine head protrusion distance.

Cell morphology clustering analysis. The output dataset from slice reconstruction and cell counting contained cell ID information paired with X,Y coordinates in the slice. To calculate cell type clustering, we wrote a custom R script to measure cluster scores for each cell based on either immediately adjacent cells or cell populations.

Adjacency clustering: First, for each dataset (one slice each from vermis and the mid-hemisphere for each individual), the Euclidean distance was calculated between each consecutive pair of cells along the PC monolayer from anterior to posterior. Second, an initial cluster score of -1 was assigned to each cell. Third, the final cluster score was assessed for each cell based on whether the leading or following immediately adjacent cell matched the morphology of that cell. If there were adjacent cells within the threshold distance (1000μm for human, 200μm for mouse), then the cluster score was set at 0. Leading or following adjacent cells with matching morphologies each added (+1) to the cluster score, producing either a final score of 1 if one of two adjacent cells match or 2 if both are matching. The morphology match was determined one of several different ways, requiring either a complete match (e.g. both the morphological type of Normative, Split, or Poly and the orientation of vertical or horizontal are the same; thus, cells fall into five total categories of Normative, vertical Split, horizontal Split, vertical Poly, and horizontal Poly, wherein a vertical Split cell does not match with a horizontal Split cell or a vertical Poly cell), or a more liberal match by only morphological type (e.g. Normative, Split, or Poly; thus, a vertical Split cell matches with a horizontal Split cell but not a vertical Poly cell) or orientation (e.g. vertical or horizontal; thus, a vertical Split cell does not match with a horizontal Split cell but does match a vertical Poly cell). Once cluster scores were calculated, consecutive IDs were assigned to each cluster such that the number of cells and total parasagittal inter-somatic distance could be determined. The identical operation was performed for a shuffled version of each dataset to

compare the observed effect of clustering with chance based on cell type ratios. All aspects of cell information were held constant (e.g. X,Y coordinate, location by foliar sub-division) and the morphology was shuffled without replacement (i.e. the same ratio of cell types was maintained). To assess the specific effect of foliar location on clustering, the same analysis was performed but using a shuffled dataset in which the possible shuffled cell type identities for each cell was only drawn from the cells within the same foliar sub-division (e.g. gyrus, bank, or sulcus).

Population clustering: Here, the number of cells of every type was tallied among the whole population of cells within a defined distance of each cell in question. This threshold varied from 250µm and 50µm in human and mouse, respectively, to 10mm and 2mm, respectively. Thus, this analysis is more lenient to interruptions in an otherwise relatively homogeneous population by assessing multiple cells and not just the single most adjacent leading and following cells. The frequency of observing each cell type in the population around each cell type was determined. From that was subtracted the same calculation for a version of each dataset that was shuffled as described above without considering foliar location (e.g. new shuffled identities were drawn from the whole population, not just from those cells in the same foliar sub-division). This subtraction gave us a percent relative increase in the rate of observing either the one complete matching morphology, or any of all four non-matching morphologies, versus the rate expected by chance. Then, across all cell types, we averaged the rates of all matches (e.g. combining the rate of vertical Splits near a vertical Split with the rate of horizontal Polys near horizontal Polys, etc.) and non-matches (e.g. combining the rate of vertical Splits near a horizontal Polys with the rate of vertical Polys near Normative, etc.).

When measuring wider populations with larger radius thresholds, we controlled for the effect of local clustering on the rate of clustering among distant cells by instead assessing cell populations

selectively in 500μm leading and following shell regions around each cell while ignoring the most immediately local cells within the core region (from the soma location to the inner edge of the shell analysis region) around the cell in question. For example, to analyze clustering in a 500-1000μm shell region, we only included cells that were at least 500μm away but no more than 1000μm away on either side (leading and following the cell in question), and thus ignored more local cells within a core 1000μm (500um on either side) of the cell in question. Similarly, to analyze clustering in a 1500-2000μm shell region, we only included cells that were at least 1500μm away but no more than 2000μm away on either side (leading and following), and thus ignored more local cells within a 3000μm core region around the cell. By calculating the elevation of clustering over chance for equivalently sized shell regions with variable distances running step-wise in 500μm increments while ignoring a growing core region, we could selectively isolate distant populations and observe the true drop-off distance for clustering.

Statistics. Standard parametric statistics such as the Students' T-test or ANOVA with Tukey post-hoc and Bonferroni correction were used to assess individual and multi-group comparisons except in cases where the data were non-normally distributed, in which case we used single or multiple comparisons Mann-Whitney U tests. In cases of a paired comparison where the underlying inter-individual variability was uninformative, we performed a one-way Students' T-test on within-individual normalized data. A Kolmogorov-Smirnov test was used to assess differences between cumulative distributions. A Chi-squared test for independence was used to distinguish the ratios of categorical data by group. Co-variation of each measure by sex was assessed but no significant differences were observed.

CHAPTER 4: COMPARATIVE MORPHOLOGY OF CEREBELLAR PURKINJE CELLS

REVEALS AN EVOLUTIONARY TRAJECTORY OF ENHANCED DENDRITIC COMPLEXITY

IN HUMANS

Methods

Subjects

Human cerebellar tissue was collected from two unembalmed donor bodies, one provided by the Anatomical Gift Association of Illinois (AGAI) and one by the New York Brain Bank via Dr. Phyllis Faust of Columbia University. During life, all study subjects signed informed consents. Chimpanzee cerebellar tissue was obtained from the National Chimpanzee Brain Resource in partnership with the George Washington University and the University of Texas MD Anderson Cancer Center. One macaque specimen was kindly provided by Dr. Sliman Bensmaia and one marmoset specimen was kindly provided by Dr. Nicho Hatsopoulos at the University of Chicago. The remaining non-human primate tissue was provided by Dr. Chet Sherwood at the Center for Advanced Study of Human Paleobiology at George Washington University. Elephant tissue was provided Dr. Michael Brecht at the Humboldt-Universität zu Berlin. Wildtype C57BL/6J mouse tissue was harvested in accordance with all procedures outlined by the University of Chicago Animal Care and Use Committee guidelines. Appendix Table S11 provides additional demographic information about all specimens.

Immunohistochemistry

Human tissue preparation. Preparation of one hemisphere from the unembalmed specimens followed the same procedure as previously reported (Busch & Hansel, 2023). In brief, whole cerebellums were fixed in 4% paraformaldehyde (PFA) for one week after being obtained.

Specimens were sectioned by hand in the parasagittal axis to obtain 3-5mm blocks that were sometimes cut transversely and further fixed for 2-4 days. Blocks were rinsed in 0.01M phosphate buffer saline (PBS) and sliced at 50µm in the parasagittal plane with a vibratome (Leica VT-1000S).

Mouse tissue preparation. Mice were anesthetized with ketamine/xylazine (100 and 10mg/kg) and perfused with 4% PFA. Cerebella were removed and incubated for 2hrs in 4% PFA at 4°C and then overnight in 30% sucrose in 0.1M PB at 4°C (until the tissue sank from the surface). The tissue was then rinsed briefly in 0.1M PB, dried and blocked, submerged in OCT medium, flash frozen, and then sliced (50µm, parasagittal plane) using a cryostat microtome (CM 3050S, Leica).

Perfused primate tissue preparation. Some individuals (all macaques, all marmosets, one baboon) were anesthetized and perfused with 4% PFA. Brains were then stored in 0.01M PBS with 0.5% Sodium Azide. Cerebellar specimens were sectioned by hand in the parasagittal axis to obtain 3-5mm blocks that were sometimes cut transversely. Blocks were rinsed in 0.01M PBS and sliced at 50µm in the parasagittal plane with a vibratome (Leica VT-1000S).

Un-perfused primate and elephant tissue preparation. Brain tissue from the remaining primate individuals (all apes, etc) and the elephant were removed post-mortem and immersion fixed with 4% PFA and stored in 0.01M PBS with 0.5% Sodium Azide. As above, cerebellar specimens were sectioned by hand, rinsed in PBS and sliced at 50µm in the parasagittal plane with a vibratome (Leica VT-1000S).

Calbindin immunohistochemistry. Tissue was washed in 50mM Glycine in 0.01M PBS for 2hrs at 4°C and incubated in 20mM Sodium Citrate in 0.01M PBS at 80-90°C using a heated water bath for 40min. After cooling to room temperature (RT), tissue was washed in PBS with 0.5% Tween-20 (PBS-Tween) for 3x15min. Next, slices were permeabilized at RT in 0.01M PBS containing 0.025% Triton-X (PBS-TX) for 1hr and then in PBS-Tween and 200um Glycine for 15 min. Blocking was done with PBS-Tween containing 10% normal donkey serum (NDS) and 5% bovine serum albumin (BSA) for 1hr at RT followed by incubation in guinea pig anti-calbindin primary antibody (1:1000; Synaptic Systems Cat# 214 004, RRID:AB_10550535) solution overnight (18-20hrs) at 4°C with 1% normal donkey serum in PBS-Tween. After 3x10min washes in PBS-Tween at RT, slices were incubated in donkey anti-guinea pig Cy3 secondary antibody (1:200; Jackson ImmunoResearch Labs Cat# 706-165-148, RRID:AB_2340460) for 2hrs at 4°C with 1% NDS in PBS-Tween. Finally, slices were washed in PBS-Tween for 3x10min, mounted and coverslipped with Vectashield (Vector Laboratories, Inc.), and allowed to set overnight before visualization. For labeling in mouse tissue, the same procedure was used as above with: glycine incubation for 1hr and heated Sodium Citrate incubation for 20min.

Confocal Imaging

Confocal Imaging for Population measurements. Following immunolabeling, we identified 10-15 representative regions across gyrus bank and sulcus sub-regions of Crus 1 that contained as many PCs as possible. We then collected z-stack images throught he whole section thickness at 20x (Olympus UMPlanFL N 0.5NA, water) in mouse, 10x (Zeiss Achroplan 0.25NA, air) in all primates, and 4x (Zeiss… , air) in elephant. Images were then marked for cell type categories using

the ObjectJ package in ImageJ and measured for the below described morphological parameters using standard measurement tools in ImageJ.

Confocal Imaging for Human and Macaque Cell Reconstruction. Following immunolabeling, we identified representative PCs whose dendrites were complete and relatively isolated from adjacent PCs. We then collected multiple z-stack scans to capture the whole PC at 40x (Zeiss EC Plan-Neofluar 1.3NA, oil immersion) with a confocal microscope (Zeiss LSM 900, Examiner.Z1) with 1x digital zoom, 2x line averaging, and 0.2079μm x 0.2079μm x 0.5μm voxel resolution. We stitched the images using VIAS software and then manually reconstructed using NeuronStudio (Rodriguez et al. 2003). No shrinkage factor or z-correction was applied.

Cell Classification and Measurement Definitions.

Purkinje cell morphological category definitions and criteria. Criteria for morphology category definitions were the same as previously (Busch and Hansel 2023, 2024) but we reiterate the full description here for clarity. PCs were deemed Normative if they had the following features: 1) a single trunk emerging from the soma, and 2) either no bifurcation of the primary trunk within two soma distances (2x the diameter of the soma) or a highly asymmetrical bifurcation where the smaller branch did not project in the parasagittal axis more than ~5x the somatic diameter from the main dendritic compartment. PCs were defined as Split if they had the following features: 1) a single trunk emerging from the soma, and 2) either symmetrical bifurcation of the primary trunk within two soma distances or an asymmetrical bifurcation within two soma distances where the smaller branch projected more than ~5x the somatic diameter from the main dendritic compartment and thus reached prominence by its overall length and sub-branching. PCs were defined as Poly if

they had more than one trunk emerging from the soma regardless of relative size. All PCs were further subdivided into Vertical or Horizontal ramification patterns. PCs were defined as Horizontal if one primary dendrite ramified parallel (within 30 degrees) with the PC layer for ~7x the somatic diameter or both primary dendrites ramified in opposing directions parallel with the PC layer for 4x the somatic diameter. Otherwise, the cell was defined as Vertical.

Foliar sub-region category definitions and measurement criteria. Criteria for foliar category definitions were the same as previously (Busch and Hansel 2023, 2024) but we reiterate the full description here for clarity. Purkinje cell locations were defined as either Gyrus, intermediate Gyrus, Bank, intermediate Sulcus or Sulcus based on the relative expansion/compression of the granule cell (GCL)/molecular layers (ML) in the parasagittal axis. Gyrus was defined as a region where the total parasagittal length of the pial surface exceeded that of the border between the GCL and the white matter. Intermediate Gyrus was defined as a region where the pial surface expanded relative to the GCL, but there was no obvious extension of white matter into the structure. Bank was defined as regions where those two lengths were approximately equal, such that neither layer of the cortex was compressed or expanded relative to the other. Intermediate sulcus was defined as regions where the ML contracted, but without gyrus structures around it. Finally, Sulcus was defined as regions where the total parasagittal length of the pial surface was less than that of the border between the GCL and the white matter.

GCL thickness was measured using the shortest line from where the PC soma abuts the GCL to where the GCL abuts the white matter. ML thickness was measured using the shortest line from where the PC soma abuts the ML to the pial surface.

Population Measurement Definitions. Measurement parameters are defined and illustrated in Appendix Table S12. Measurements were taken only if the relevant parameter was intact and visible for a given PC. All measurements were performed in ImageJ.

CHAPTER 5: ABERRANT OLIVO-CEREBELLAR SIGNALING IN TWO MOUSE MODELS OF

AUTISM

PART 1: Sensory Over-responsivity and Aberrant Plasticity in Cerebellar Cortex in a Mouse Model of Syndromic Autism

Methods

In vivo two-photon imaging from awake mice

Surgeries were performed on animals aged 11-13 weeks under ketamine/xylazine anesthesia (100 and 10mg/kg, respectively, 0.1mL/10g weight; Henry Schein) with subcutaneous injections of meloxicam (0.06mL, 1-2 mg/kg), buprenorphine (0.1mL, 0.05-0.1 mg/kg), and sterile saline (1mL). Body temperature was maintained at 35-37°C with a feedback dependent heating pad. The skin above the posterior skull was excised and the bone cleaned to implant a metal headframe over the interparietal bone via dental cement. After 1-4 days of recovery, mice were anesthetized and a 4mm craniotomy and durectomy was made at 2.5mm lateral from midline and 2.5mm caudal from lambda, exposing cerebellar simplex, crus 1, and anterior crus 2. Combined low titer PC-specific L7-Cre (2%, AAV1.sL7.Cre.HA.WPRE.hGH.pA; Addgene) and high titer Cre-dependent GCaMP6f (10%, pAAV.CAG.Flex.GCaMP6f.WPRE.SV40; Addgene) was injected ~750μm below the pial surface of central simplex and crus 1 (~900nL per site, 5min wait before needle retraction) and a cranial window was implanted over the craniotomy.

The mice recovered for 5 days before daily habituation to the imaging apparatus, head fixation on the treadmill, and multisensory stimulus application (6-10 days). To encourage resting behavior to reduce the conflation of running motor programs on cerebellar activity, animals were fixed on the treadmill such that their rear legs were centered on the treadmill apex and the front paws rested on a horizontal bar (~2mm diameter). Animals were habituated in this position until they exhibited

relative comfort and reduced running behavior. Imaging experiments were performed when the GCaMP6f indicator reached stable expression in a sparse cell population (11-20 days post-injection). PC dendrites were imaged at 61.8Hz using a laser scanning two-photon microscope (Neurolabware) and 16x water immersion objective (0.8NA, 3mm WD; Nikon). GCaMP6f was excited at 920 nm with a femtosecond-pulsed two- photon laser (~30mW laser power; Spectra-Physics) and fluorescence collected by a GaAsP PMT (Hamamatsu).

During each experiment, calcium activity was monitored in ~15-25 cells per animal during 20s imaging sessions. One of eight stimulus types (1. Light, 2. Airpuff (whisker), 3. Tone, 4-6. Combinations of two modalities, 7. Light + Puff + Tone combined, and –to include a stimulus that is well-known to evoke complex spikes– 8. Airpuff to the eye) was triggered 10s after scanning initiation and lasted for 30ms. Light stimulus was a 488nm LED light targeted to the ipsilateral eye, Airpuff was delivered at 10psi via a 0.86mm diameter pipette positioned 2-3mm from the center of the ipsilateral whisker pad or ipsilateral eye, and Tone stimulus was a 12KHz pure tone produced by speakers positioned bilaterally at ~70-80dB.

The stimuli were applied with inter-stimulus intervals $\geq$ 30s. Stimulus order was randomized, included control sessions–imaging under identical conditions but without any stimulus delivered–and was repeated until 10 trials were acquired of each type. Images were processed and motion corrected using custom Matlab scripts and cellular ROIs were drawn manually in ImageJ based on volumetric cell reconstructions. Custom Matlab scripts were written to extract calcium signals for each ROI and automatically detect and measure calcium events based on thresholds for amplitude and temporal qualities that were kept the same across animals and genotypes. An interactive GUI

was used to manually confirm detection quality and consistency. Finally, analyses were performed using both Matlab and R scripts.

In vivo behavioral analysis in awake mice

During *in vivo* imaging and multisensory stimulation experiments, mouse behavior was recorded using an infrared camera (Dalsa M640 CCD, 61.8Hz sampling rate) that was triggered by the imaging software and positioned in front of the animals to capture the head, body, and paws. To measure sensory evoked responses, we used three distinct methods:

1. To measure temporally precise eyeblink onset, we captured ROIs surrounding exclusively the ipsilateral eye and measured the average pixel intensity of each frame and then used the absolute value of the first derivative to assess the timing of changes in the eye.

2. To better assess eyelid position during eyepuff stimulation, we used the DeepLabCut toolbox to train a deep neural network to identify the top and bottom eyelid of the ipsilateral eye. We also used this method to track the position of the nose and several points on the chest to quantify startle responses to non-eye puff sensory stimuli.

3. In order to track rapid and sometimes partly obscured paw movements, we used a real-time object detection algorithm, You Only Look Once (YOLOv5), that relies on a convolutional neural network to predict object presence and location. We built a training set to identify paws in numerous positions and levels of obscurity, ran YOLOv5 object inference, and then applied the deepSORT tracking algorithm to obtain continuous tracking of paw objects across whole videos. We also used this pipeline to track the location of each animal's eartag, which was highly visible, easily distinguished, and an effective proxy for movement of the ears.

A custom R script was then used to combine, pre-process, and analyze the output of each pipeline to quantify startle responses to sensory stimulation. We also converted marker and object position output of DeepLabCut and YOLOv5+deepSORT to instantaneous velocity by calculating the first derivative of position from one frame to another and applying a multiplication factor to convert change in pixel coordinates per frame into the more intuitive velocity unit of mm/s. Analysis was performed on early trials pooled across stimulus types to characterize generalized sensory responsiveness rather than distinguish modality-specific response profiles.

Slice preparation and electrophysiology

Mice (P35-80) were anesthetized with isoflurane and decapitated. The cerebellar vermis was removed and cooled in artificial cerebrospinal fluid (ACSF) containing (in mM): 124 NaCl, 5 KCl, 1.25 Na_2HPO_4, 2 $CaCl_2$, 2 $MgSO_4$, 26 $NaHCO_3$, and 10 D-glucose, bubbled with 95% O_2 and 5% CO_2. Sagittal slices of the cerebellar vermis (200µm thick) were prepared using a Leica VT-1000S vibratome, and were subsequently kept for at least 1h at room temperature in oxygenated ACSF. For recordings, the slices were perfused with ACSF that was supplemented with picrotoxin (100µM) to block $GABA_A$ receptors.

Patch-clamp recordings from the Purkinje cell soma were performed at room temperature using an EPC-10 amplifier (HEKA Electronics). Room temperature was selected rather than more physiological temperatures to reduce noise in image acquisition in the confocal recordings from dendritic spines (Fig. 25). Currents were filtered at 3kHz, digitized at 25kHz, and acquired using Patchmaster software (HEKA Electronics). Patch pipettes (2-5MΩ) were filled with a solution containing (in mM): 9 KCl, 10 KOH, 120 K-gluconate, 3.48 $MgCl_2$, 10 HEPES, 4 NaCl, 4 Na_2ATP, 0.4 Na_3GTP, and 17.5 sucrose (osmolarity: 295-305mmol/kg, pH 7.25). For recordings

of CF- EPSCs, the pipette solution contained (in mM): 128 CsOH, 111 gluconic acid, 4 NaOH, 10 CsCl, 2 $MgCl_2$, 10 HEPES, 4 Na_2ATP, 0.4 Na_3GTP, and 30 sucrose (osmolarity: 295-305mmol/kg, pH 7.25). PF and CF inputs were activated using glass pipettes filled with ACSF (200μs stimulus duration). Liquid junction potentials were not corrected. Fast and slow capacitances were compensated and series resistance was partially compensated (50-80%). In the CF-EPSC recordings, the stimulus intensity and location were not systematically varied to search for multiple CF inputs. A caveat of this approach is that in case of persisting multiple innervation (in < 30% of cells in adults from both genotypes; see (Piochon et al., 2014)), there will be a bias toward measurements of EPSCs resulting from activity of the larger CF input. In the LTD experiments, test responses were recorded at 0.05Hz in voltage-clamp mode before and after tetanization, which was applied in current-clamp mode. Series and input resistances were monitored by applying a hyperpolarizing voltage step (-10mV) at the end of each sweep. Recordings were excluded if the series or input resistance varied by >15% over the course of the experiments. For the recording of mGluR1-EPSCs, we used a holding potential of -70mV. NBQX (10μM) and D-APV (10μM) were added to the ACSF to block AMPA and NMDA receptors, respectively. The pipette saline was adjusted to contain 144mM K-gluconate and 6 mM KCl; the calcium chelator EGTA was added (1mM) to increase the stability of the recordings. The currents were evoked by stimulating the PF input with eight pulses delivered at 100 Hz. At the end of the recordings, the group I/II antagonist MCPG was bath-applied (100μM) to confirm that these currents were triggered by the activation of metabotropic glutamate receptors.

Confocal calcium imaging

Calcium signals were measured from PCs in 4-7 week-old mice using a Zeiss LSM 5 Exciter confocal microscope equipped with a 63x Apochromat objective (Carl Zeiss Microimaging).

Calcium signals were calculated as $\Delta G/R = (G(t) - G_0)/R$, where G is the calcium-sensitive fluorescence (G_0 = baseline signal) of either OGB-2 (200µM) or Fluo-5F (300µM), and R is the calcium-insensitive fluorescence of Alexa 633 (30µM). For the calculation of resting $[Ca^{2+}]_i$ concentrations with OGB-2, the G/R values were used as follows:

$$[Ca^{2+}]_i = K_d \, (G/R - G/R_{min}) \, / \, (G/R_{max} - G/R)$$

where K_d is the dissociation constant of OGB-2 (485nM), and G/R_{max} and G/R_{min} are the maximal and minimal G/R values at the extreme ends of the calcium range (see (Piochon, Titley, et al., 2016)). The green fluorescence G resulted from excitation at 488nm using an argon laser. The red fluorescence R resulted from excitation at 633nm using a HeNe laser (both from Lasos Lasertechnik). PCs were loaded with the dyes through diffusion from the patch pipette.

Laser-capture microdissection (LCM) of PCs, mRNA isolation, and Quantitative Real-Time PCR

LCM and mRNA isolation were performed as previously reported (Du et al., 2019). Each 25µL reaction solution contained 2µL primers, 12.5µL SYBR green Supermix (BioRad, CA, USA), and was run under the following conditions: 50°C 2 min; 95°C 10min; 95°C 15s, 60°C 1min for 40 cycles, followed by a melting curve. As a relative quantification, fold changes were measured using the ∆∆Ct method, with *Gapdh* as an internal control.

Immunohistochemistry

Frozen cerebellar sections (10 µm thick; ~P100 mice) were cut on a Cryostat NX50 (Leica, Milton Keynes, UK). Sections were attached to RNase free PEN-membrane slides (Leica, Milton Keynes, UK) and were stained with fast HE staining (ScyTek Labs, UT, USA). 30 PCs were isolated from each side of the cerebellum in three slices per animal, for each group (360 Purkinje cells and six

RNA samples per genotype; two mice per group), and collected in the tube using Leica LMD 6500 for subsequent RNA isolation. Total RNAs were extracted using Arcturus Picopure RNA isolation Kit (Thermo Fisher, VA, USA). All samples passed Bioanalyzer RNA QC analysis (Agilent, CA, USA), with a RNA integrity Number (RIN) of at least 7.

Calbindin + VGlut2 double immunolabeling

Experiments were performed on patDp/+ and WT mice aged 10-13 weeks. Mice were anesthetized with sterile deionized water containing 10% ketamine (Henry Schein) and 5% xylazine (Akorn), then perfused with 4% paraformaldehyde (PFA). Cerebella were removed, incubated overnight in 4% PFA at 4°C, incubated for 24 hours in 30% sucrose solution at 4°C, and then sliced (50 μm, sagittal) using a microtome. Permeabilization was done in deionized water containing 0.025% triton (TX) and 10% phosphate buffered saline (PBS) for 1hr at room temperature (RT). Blocking was done with PBS-TX containing 10% normal donkey serum for 2 hrs at RT. The primary antibody incubation took place overnight at 4°C with a 1% normal donkey serum in PBS-TX solution containing: rabbit anti-VGluT2 at 1:500 (Synaptic Systems) and mouse anti-calbindin at 1:500 (Swant). After 3x10min washes in PBS-TX at RT, the secondary antibody incubation lasted for 2hrs at 4°C in a 1% normal donkey serum in PBS-TX solution containing: (donkey anti-rabbit, CY3, 1:200, Jackson ImmunoResearch, and donkey anti-mouse, AF488, 1:200, Jackson ImmunoResearch). Following antibody binding, slices were washed PBS- TX for 3x10min, mounted and coverslipped with Vectashield (Vector Laboratories, Inc.), and allowed to dry overnight before visualization. Slices were imaged at 40x (Apochromat 1.3NA, oil immersion) and z-stacks of the molecular layer were obtained (6 images with a 0.431μm z-step for a total height of 2.586μm) with a confocal microscope (Zeiss LSM 5 Exciter, Axioskop 2).

Immunohistochemical data analysis was performed using Excel (Microsoft) and ImageJ (NIH). Dendrites with a diameter > 2µm or < 2µm were considered either large caliber (Fig. 22F) or fine dendrites (Fig. 22G), respectively. Co-localization of VGluT2 with calbindin was confirmed with z-stacks. VGluT2 was quantified and normalized to the measured length of large caliber and fine dendrites. Lengths between 40µm and 85µm were measured for primary dendrites. Data are expressed as mean ± standard error of the mean (SEM).

Calbindin + VGlut2 + Nrxn1 triple-immunolabeling

Experiments were performed on patDp/+ and WT mice aged 13-15 weeks. Tissue was prepared as above and sliced (50µm, sagittal) using a cryostat microtome (CM 3050S, Leica). After slicing, tissue was washed in 50mM Glycine in 0.01M phosphate buffered saline (PBS) for 1hr at 4°C (aldehyde linking), and then incubated in 20mM Sodium Citrate in 0.01M PBS at 50- 60°C using a heated water bath for 20min (antigen retrieval). After cooling to room temperature (RT), tissue was washed in 10mM Sodium Citrate for 5min then 2x30sec in dH_2O, and then permeabilized at RT in dH_2O containing 0.025% triton (TX) and 10% PBS for 1h. Blocking was done with PBS-TX containing 5% normal donkey serum and 5% bovine serum albumin for 1hr at RT. Primary antibody incubation occurred overnight at 4°C with a 1% normal donkey serum in PBS-TX solution containing: rabbit anti-VGluT2 at 1:500 (Invitrogen), guinea pig anti-calbindin at 1:1000 (Synaptic Systems), and mouse anti-Nrxn1 at 1:200 (Millipore). After 3x10min washes in PBS-TX at RT, the secondary antibody incubation lasted for 2hrs at 4°C with the 1% normal donkey serum in PBS-TX solution containing: donkey anti-rabbit AF647, donkey anti-guinea pig Cy3, and donkey anti-mouse AF488, all at 1:200 (Jackson ImmunoResearch). Following antibody binding, slices were washed in PBS-TX for 3x10min, mounted and coverslipped with Vectashield (Vector Laboratories, Inc.), and allowed to dry overnight before visualization. Slices were imaged

at 40x (Apochromat 1.3NA, oil immersion) and z-stacks of the molecular layer were obtained (11 images with a 0.431μm z-step for a total height of 4.89μm) with a confocal microscope (Zeiss LSM 5 Exciter, Axioskop 2). Separate images, 75μm x 75μm x 4.89μm, were collected from distal and proximal portions of the molecular layer in Lobules 3-5 of 4 stained sections per animal.

Image processing was performed using ImageJ (NIH) on blinded images. Given variable background intensities across images and the sensitivity of a small-object count to the image background, we applied a Triangle threshold operation (Fig. 23c, (Zack et al., 1977), which a) calculates the drop off point in the pixel intensity distribution that separates signal from noise, b) applies a small offset as a buffer, and c) determines an image-specific threshold point on that basis. We confirmed with blinded data that there was no detectable difference in the range of image backgrounds or applied thresholds between genotypes before proceeding (data not shown). Counting Nrxn1 punctae in the whole molecular layer (Fig. 23D) was done using 3D Object Detection (Size constraint: 1-250pixels, ImageJ) on the thresholded Nrxn1 channel of distal and proximal molecular layer images. To count Nrxn1 punctae on proximal dendritic segments (Fig. 23E), a 100μm^2 ROI was traced over large caliber dendrites visible in the central plane (image 6 of 11) of the calbindin channel z- stack. This ROI was used as a mask to obtain counts using the 2D Analyze Particles function (ImageJ) in the central plane of the Nrxn1 channel. VGlut2 punctae were marked and counted manually using the ObjectJ plugin for ImageJ in the central plane of z-stack composite images of Vglut2 and Nrxn1 channels (Fig. 23F+G). During manual counting, VGlut2 punctae were labeled as Nrxn1+ or Nrxn1- based on presence or absence of visible colocalization between VGlut2 and Nrxn1 channels. Blinded image data was compiled in an excel database and a custom R script decoded animal ID, section number, and genotype from image

numbers and analyzed the data. Measurements are expressed as mean ± standard error of the mean (SEM).

Western Blots

Western blot analysis was performed as previously described (Piochon et al., 2014): mouse cerebellar tissue was collected after isoflurane anesthesia and was snap-frozen in dry ice. Whole protein extract was obtained by homogenization in ice-cold tissue lysis buffer (50mM Tris pH 7.5, 150mM NaCl, 0.5% Na-Deoxicholate, 1% Nonidet P-40, 10% Glycerol, 2% EDTA, 1% Sigma-Aldrich protease inhibitor cocktail). The homogenate was centrifuged at 16000xg for 15min at 4°C and the supernatant collected. The protein extracts were quantified for protein concentration by Pierce BCA protein assay kit (ThermoFisher), divided into aliquots and stored at -80°C. An equal amount of 60μg protein extract for each animal was denatured at 95°C for 5min and loaded on 10% SDS-polyacrylamide precast gel (BioRad). Gels were blotted on PVDF membranes (BioRad). Immunodetection was performed by anti-mGluR1 (mouse, 1:500, overnight; BD Pharmigen Cat. N. 556331), anti-GAPDH (rabbit, 1:2000, overnight, AbCam Ab9485), horseradish peroxidase conjugated secondary antibodies (goat anti-mouse and goat anti-rabbit, 1:10,000, Millipore) and ECL-Plus (Amersham) by Chemigenius bioimaging system (Syngene). Exported images were analyzed for densitometric quantification of bands by ImageJ. Values normalized to GAPDH levels were reported as expression level relative to the WT average. Differences between groups were assessed by unpaired Student's t-test.

Methods

Animals

All animal experiments were approved and carried out in accordance with the regulations and guidelines for the care and use of experimental animals from the Institutional Animal Care and Use Committee of the University of Chicago (according to National Institute of Health guidelines).

Statistics and Quantifications

Animals of both sexes were used across experiments and no differences were observed. Statistical analysis was carried out using R (v4.2.1). Data following a normal distribution was tested with unpaired two-tailed Student's t-tests to compare two groups. A one sample Student's t-test was used to compare individual groups with a specific, benchmark value where appropriate. For all analyses, $\alpha = 0.05$ was used to determine significance and figure panels refer to the significance of comparisons in the following way: ns $p > 0.05$, * $p \leq 0.05$, ** $p \leq 0.01$, *** $p \leq 0.001$.

Western Blots

Western blot analysis was performed as previously described (Du et al., 2019): cerebellar tissue was collected from 2 to 4 months old mice. Nuclear and cytoplasmic protein fractions were then extracted by homogenization in NE-PER Nuclear and Cytoplasmic Extraction Reagents (Thermofisher, Cat# 78833). The lysates were quantified for protein concentration using the Bio-Rad Protein Assay Dye Reagent Concentrate (Cat# 5000006). Lysates were then diluted to

normalize protein concentration and denatured in boiling water for 5min. Then, 60µg of protein was loaded on 8% SDS-Polyacrylamid gels in Tris-Glycine buffer. Gels were blotted on PVΔF membranes (Millipore Sigma, Cat# IPVH00010) and blocked for 1 hour in TBST containing 5% nonfat milk. Membranes were then incubated with primary antibodies (rabbit anti-PIR121/Sra-1 (CYFIP1, 1:500; Millipore, Cat# 07-531) and either mouse anti-GAPDH (1:20000; Thermofisher, Cat# AM4300) or mouse anti-LaminB1 (1:500; Santa Cruz, Cat# SC-374015) overnight at 4°C in TBST containing 5% nonfat milk. Membranes were then probed with HRP conjugated mouse IgG binding protein (1:20,000 and 1:2,000, for GAPDH and LaminB1 respectively; Santa Cruz, Cat# SC-516102) and mouse anti-rabbit (1:2,000; Santa Cruz, Cat# SC-2357) for 1hr at room temperature. Membranes were washed in TBST three times and then visualized with chemiluminescent detection using Clarity Western ECL Substrate (Bio-Rad, Cat# 170-5061). Images were captured using autoradiography or a ChemiDoc MP imaging system (Bio-Rad). Exported images were analyzed for densitometric quantification of bands by ImageJ (NIH). The CYFIP1/GAPDH and CYFIP1/LaminB1 values for each animal were normalized to the WT mean.

Pull down co-immunoprecipitation and western blot analysis

Pull-down assay was performed as previously described (Santini et al., 2017). Mouse cerebellar tissue was collected after carbon dioxide anesthesia and was snap-frozen in dry ice. Tissues were sonicated in cold lysis buffer containing 150 mM NaCl, 10 mM $MgCl_2$, 30 mM tris buffer (pH 8.0), 1 mM DTT, 1.5% Triton X-100, protease and ribonuclease inhibitors (10 µl/ml). 500 µg of lysate were incubated with 30 µl of m^7GTP beads (#AC155; Jena Bioscience) for 1 hour at 4°C. The beads were centrifuged for 1min at 6000 rpm, and the supernatant was collected. The beads were then washed three times in wash buffer containing 100 mM KCl, 50 mM tris buffer

(pH 7.4), 5 mM MgCl$_2$, 0.5%Triton X-100. Finally, the beads were eluted with 5X Laemmli buffer and analyzed using western blotting. The following antibodies were used in the western blotting analysis: rabbit anti-eIF4E (1:1000; Bethyl Laboratories; Cat# A301-153A) and rabbit anti-eIF4G (1:1000; Cell Signaling Technology; #C45A4). eIF4E and eIF4G were probed on the same membrane for each sample and the gel was then cut ~70 KDa for visualization. Quantification is expressed as a ratio of eIF4G/eIF4E in each sample normalized to the average across WT controls such that the WT mean binding ratio is 1 and that of CYFIPOE animals is 1.68 times higher. Protein quantification was carried out before pull-down and loaded in equal volume for western blotting analysis. The assay was checked for specificity by measuring GAPDH expression with rabbit monoclonal antibodies (1:1,000; Cell Signaling Technology; Cat# 2118) in the input and pull-down

Samples were prepared with 5X sample buffer (0.25M Tris-HCl pH6.8, 10% SDS, 0.05% bromophenol blue, 50% glycerol and 25% -β mercaptoethanol) and heat denatured at 95 °C for 5 min. 40 µg protein per lane was run in pre-cast 4–12% Bis1053 Tris gels (Invitrogen) and subjected to SDSPAGE followed by wet gel transfer to polyvinylidene difluoride (PVΔF; Immobilon-Psq, Millipore Corporation, Billerica, USA) membranes. Membranes were blocked for 90 min with 5% milk in Tris-buffered saline supplemented with 0.1% Tween-20 (TBST) and then were probed overnight at 4 °C using rabbit anti-eIF4E (1:1000; Bethyl Laboratories; Cat# A301-153A) and rabbit anti-eIF4G (1:1000; Cell Signaling Technology; #C45A4). Membranes were probed with horseradish peroxidase-conjugated secondary IgG (1:7000; Promega) for 1 h at room temperature. Signals from membranes were detected with ECL chemiluminescence (GE Healthcare Amersham™) using Alpha Imager 3.4 software and the FluorChem Protein Simple instrument and quantified via densitometry using ImageJ software (NIH, USA).

Laser-capture microdissection (LCM) of PCs, mRNA isolation, and Quantitative Real-Time PCR

LCM and mRNA isolation were performed as previously reported (Du et al., 2019). Frozen cerebellar sections (10 μm thick; ~P100 mice) were cut on a Cryostat NX50 (Leica, Milton Keynes, UK). Sections were attached to RNase free PEN-membrane slides (Leica, Milton Keynes, UK) and stained with fast HE staining (ScyTek Labs, UT, USA). 30 Purkinje cells (somatic and proximal dendritic tissue) were isolated from each side of the cerebellum in three slices per animal, for each group (360 Purkinje cells and six RNA samples per genotype; two mice per group) and collected in the tube using Leica LMD 6500 for subsequent RNA isolation. Total RNAs were extracted using Arcturus Picopure RNA isolation Kit (Thermo Fisher, VA, USA). All samples passed Bioanalyzer RNA QC analysis (Agilent, CA, USA), with a RNA integrity Number (RIN) of at least 7. Each 25μL reaction solution contained 2μL primers, 12.5μL SYBR green Supermix (BioRad, CA, USA) and was run under the following conditions: 50°C 2 min; 95°C 10min; 95°C 15s, 60°C 1min for 40 cycles, followed by a melting curve. As a relative quantification, fold changes were measured using the ΔΔCt method, with *Gapdh* as an internal control.

Immunohistochemistry

Experiments were performed on CYFIP OE and WT mice aged 13-15 weeks. Mice were anesthetized with sterile deionized water containing 10% ketamine (Henry Schein) and 5% xylazine (Akorn), then perfused with 4% paraformaldehyde (PFA). Cerebella were removed, incubated overnight in 4% PFA at 4°C, incubated for 24 hours in 30% sucrose solution at 4°C, and then sliced (50 μm, sagittal) using a microtome. Permeabilization was done in deionized water containing 0.025% triton (TX) and 10% phosphate buffered saline (PBS) for 1hr at room

temperature (RT). Blocking was done with PBS-TX containing 10% normal donkey serum for 2 hrs at RT. The primary antibody incubation took place overnight at 4°C with a 1% normal donkey serum in PBS-TX solution containing: mouse anti-NRXN1 (1:200; Millipore; Cat# MABN607) and guinea pig anti-calbindin (1:1000; Synaptic Systems; Cat# 214 004; RRID:AB_10550535). After 3x10min washes in PBS-TX at RT, the secondary antibody incubation lasted for 2hrs at 4°C in a 1% normal donkey serum in PBS-TX solution containing: donkey anti-guinea pig, CY3 (1:200, Jackson ImmunoResearch; Cat# 711-165-152; RRID:AB_2307443), and donkey anti-mouse, AF488 (1:200, Jackson ImmunoResearch; Cat# 715-545-150; RRID:AB_2340846). Following antibody binding, slices were washed PBS-TX for 3x10min, mounted and coverslipped with Vectashield (Vector Laboratories, Inc.), and allowed to dry overnight before visualization.

Slices were imaged at 40x (Apochromat 1.3NA, oil immersion) and z-stacks of the molecular layer were obtained (11 images with a 0.431µm z-step for a total height of 4.89µm) with a confocal microscope (Zeiss LSM 5 Exciter, Axioskop 2). Separate images, 75µm x 75µm x 4.89µm, were collected from proximal portions of the molecular layer in Lobules 3-5 of 4 stained sections per animal.

Image processing was performed using ImageJ (NIH) on blinded images. Image channels used for analyses were separated and thresholded using the Triangle threshold operation (Zack et al., 1977). To count NRXN1 punctae on proximal dendritic segments (Fig. 28), a 100µm^2 ROI was traced over large caliber dendrites visible in the central plane (image 6 of 11) of the calbindin channel z-stack. This ROI was used as a mask to obtain counts using the 2D Analyze Particles function (ImageJ) in the central plane of the NRXN1 channel. This method was repeated to get two 100µm^2 dendritic ROIs per animal from different images. Blinded image data was compiled in an excel database and subsequently a custom R script decoded animal ID, section number, and

genotype from image numbers. Measurements are expressed as mean ± standard error of the mean (SEM).

Slice preparation and electrophysiology

Young adult mice (P23-50) were anesthetized with isoflurane and decapitated. The cerebellar vermis was removed and cooled in artificial cerebrospinal fluid (ACSF) containing (in mM): 124 NaCl, 5 KCl, 1.25 Na2HPO4, 2 CaCl2, 2 MgSO4, 26 NaHCO3, and 10 D-glucose, bubbled with 95% O2 and 5% CO2. Sagittal slices of the cerebellar vermis (200μm thick) were prepared using a Leica VT-1000S vibratome and were subsequently kept for at least 1h at room temperature in oxygenated ACSF. For recordings, the slices were perfused with ACSF that was supplemented with picrotoxin (100μM) to block GABA$_A$ receptors.

Patch-clamp recordings from the Purkinje cell soma were performed at room temperature using an EPC-10 amplifier (HEKA Electronics). Currents were filtered at 3kHz, digitized at 25kHz, and acquired using Patchmaster software (HEKA Electronics). Patch pipettes (2-5MΩ) were filled with a solution containing (in mM): 128 CsOH, 111 gluconic acid, 4 NaOH, 10 CsCl, 2 MgCl2, 10 HEPES, 4 Na2ATP, 0.4 Na3GTP, and 30 sucrose (osmolarity: 295-305mmol/kg, pH 7.25). Cells were held at -30mV holding potential. CF inputs were activated using glass pipettes filled with ACSF (0.2ms stimulus duration with intensities ranging from 1-150nA). Liquid junction potentials were not corrected. Fast and slow capacitances were compensated and series resistance was partially compensated (50-80%). Stimulus intensity and location were not systematically varied to search for multiple CF inputs. CF excitatory post-synaptic currents (EPSCs), particularly of reduced amplitude in some multi-innervated cells, were distinguished from parallel fiber (PF)-EPSCs by their paired pulse depression (100ms interval, EPSC2 / EPSC1) and stable amplitude

with small changes in stimulus intensity. PF-EPSCs exhibit paired pulse facilitation and linear amplitude relationship with even small stimulus intensity changes.

In vivo two-photon imaging from awake mice

Surgeries were performed as described previously (Simmons et al., 2022) on animals aged 11-13 weeks under ketamine/xylazine anesthesia (100 and 10mg/kg, respectively, 0.1mL/10g weight; Henry Schein) with subcutaneous injections of meloxicam (0.06mL, 1-2 mg/kg), buprenorphine (0.1mL, 0.05-0.1 mg/kg), and sterile saline (1mL). Body temperature was maintained at 35-37°C with a feedback dependent heating pad. The skin above the posterior skull was excised and the bone cleaned to implant a metal headframe over the interparietal bone via dental cement. After 1-4 days of recovery, mice were anesthetized and a 4mm craniotomy and durectomy was made at 2.5mm lateral from midline and 2.5mm caudal from lambda, exposing cerebellar simplex, crus 1, and anterior crus 2. Combined low titer PC-specific L7-Cre (0.2×10^{12} GC/mL, AAV1.sL7.Cre.HA.WPRE.hGH.pA; Princeton Neuroscience Institute (PNI) Viral Core Facility; acquired from Dr. Samuel Wang Lab, Princeton University) and high titer Cre-dependent GCaMP6f (1×10^{12} GC/mL, pAAV.CAG.Flex.GCaMP6f.WPRE.SV40; Addgene plasmid # 100835) was injected ~300μm below the pial surface of central simplex and crus 1 (~900nL per site, 5min wait before needle retraction) and a cranial window was implanted over the craniotomy.

The mice recovered for 5 days before daily habituation to the imaging apparatus, head restraint on the treadmill, and multisensory stimulus application (6-10 days) to encourage resting behavior to reduce the conflation of running motor programs on cerebellar activity. Animals were habituated until they exhibited relative comfort and reduced running behavior. Imaging experiments were performed when the GCaMP6f indicator reached stable expression in a sparse

cell population (20-30 days post-injection). PC dendrites were imaged at 31Hz using a laser scanning two-photon microscope (Neurolabware) and 16x water immersion objective (0.8NA, 3mm WD; Nikon). GCaMP6f was excited at 920 nm with a femtosecond-pulsed two-photon laser (~30mW laser power; Spectra-Physics) and fluorescence collected by a GaAsP PMT (Hamamatsu).

During each experiment, calcium activity was monitored in ~15-25 cells per animal during 20s imaging sessions. One of three stimulus types (1. Light, 2. Airpuff (whisker), and –to include a stimulus that is well-known to evoke complex spikes– 3. Airpuff to the eye) was triggered 10s after scanning initiation and lasted for 30ms. Light stimulus was a 488nm LED light (Prizmatix) targeted to the ipsilateral eye, Air Puff was delivered at 10psi (Picospritzer III, Parker Hannifin) via a 0.86mm diameter capillary tube positioned 2-3mm from the center of the ipsilateral whisker pad or ipsilateral eye.

For repeated exposure experiments, stimulus trials were reduced to 10s duration with stimuli delivered after a 5s delay. Ten trials each of either light or whisker airpuff (five of each) and three control trials without stimulus were conducted before and after the repeated exposure paradigm. The repeated exposure paradigm consisted of 30ms whisker airpuff delivered at 1 Hz for 5min without any imaging sessions.

The stimuli were applied with inter-stimulus intervals $\geq$ 30s. An Arduino Uno microcontroller triggered by the imaging software provided distinct stimulus type triggering output to the light and puff instruments. The microcontroller was programmed to cycle through stimulus types randomly and included control sessions–imaging under identical conditions but without any stimulus delivered–and was repeated until 10 trials were acquired of each type.

Images were converted to tiffs and motion corrected using custom MATLAB scripts. Cellular ROIs were drawn manually in ImageJ based on volumetric cell reconstructions. Another MATLAB script measured the pixel intensity of each ROI across frames and videos and saved the data as a .mat file. An interactive MATLAB GUI was used to manually confirm detection quality and consistency across imaging sessions to either include or exclude each cell for downstream analysis. Analyses were performed using MATLAB scripts and output for final data shaping, plotting, and statistics in R.

Raw signal from all ROIs was imported to a custom MATLAB script that performed a five-frame moving window smoothing function and a background correction function. Raw ROI traces were input to the MATLAB version of OASIS deconvolution to obtain rise initiation times of calcium peaks exceeding 3SD of the baseline. Event amplitude was determined as the maximum value of the smoothed within 3 frames of the deconvolved times. Across animals, cells with saturated baseline fluorescence, determined by the baseline value at which spontaneous event amplitudes were consistently diminished, were removed. We did not distinguish between multiple tightly clustered events producing a single, accumulated large amplitude peak. While accumulated peaks from clustered inputs often retain multiple peaks (a partial peak within the rising phase of the larger event), the slow time constant of the GCaMP6f indicator can alter the appearance of multiple peaks and produce variable spike deconvolution. As such, we identified peak times <3 frames apart – having only 1 frame (31ms) between detected peaks, which is below the ~50ms rise time constant of GCaMP6f – and took only the second and highest peak or the last in a sequence of >2 events all of which are <3 frames apart.

While physiological responses to stimulation are expected to start as early as 50ms after the stimulus, the GCaMP6f indicator provides a slower readout of stimulus response. Thus,

calcium events were considered stimulus-evoked if the event rise initiation occurred within a time window of 225ms (7 frames) that started 60ms (2 frames) after the stimulus. For repeated exposure experiments, the trial average of the stimulus-evoked amplitude (measured as dF/F0 of trials including a response) is obtained for trials before (pre) and after (post) the repeated exposure protocol. Normalized change was calculated with the following formula: ((Post – Pre) / Pre) * 100. Response probability is calculated in the same way by taking the rate of evoked responses out of five trials Pre and Post.

CHAPTER 6: INTRINSIC AND SYNAPTIC DETERMINANTS OF RECEPTIVE FIELD

PLASTICITY IN PURKINJE CELLS OF THE MOUSE CEREBELLUM

Methods

Mice

All animal experiments were approved and conducted in accordance with the regulations and guidelines of the Institutional Animal Care and Use Committee of the University of Chicago (IACUC 72496). All mice were bred and maintained on a C57BL/6J background (The Jackson Laboratory, Bar Harbor, ME, USA). SK2 knockout mice (SK2-KO) were generated by crossing transgenic mice expressing CRE recombinase under the Purkinje cell (PC)-specific promoter Pcp2/L7 (JAX#010536) with transgenic mice with LOXP sites flanking the *Kcnn2* locus encoding SK2 protein (see the previous report[1] for detail). Mice with L7-Cre and homozygous SK2-LoxP were used for the experimental mutant group. CaMKII TT305/6VA genetically modified mice, which carry a global mutation[62], were obtained from Dr. Ype Elgersma (Erasmus Medical Center, The Netherlands). Wild-type mice used in the current studies were collected from the litter mates of both mutants confirmed by genotyping. All genotypes were regularly outcrossed with commercial wild-type C57BL/6J mice. P80-P120 adult mice were selected for the two-photon recording performed in this study, and the necessary surgeries were conducted 2-3 weeks prior to the recording. The parallel fiber (PF) stimulus intensity experiments were conducted in 11 wild-type, 10 SK2-KO, and 8 CaMKII-TT305/6VA mice. PF receptive field (RF) plasticity experiments were conducted in 12 wild-type, 7 SK2-KO, and 7 CaMKII-TT305/6VA mice, all largely the same animals as used for the stimulus intensity experiments. Spatial dendrite analysis was performed on a subset of PF-RF experimental recordings. Simultaneous recordings of dendrite, soma, and axon

initial segment (AIS) were conducted in 5 wild-type mice. The tactile-RF plasticity experiments (finger vs wrist tetanization combined) were conducted in 14 wild-type, 8 SK2-KO, and 10 CaMKII-TT305/6VA mice. Climbing fiber (CF) RF plasticity experiments were conducted in 4 wild-type mice. PF tetanization of tactile-RF plasticity experiments were conducted in 4 wild-type mice. Animals of both sexes were used in all experiments. No sex differences were observed in the reported measures.

Cranial window and GCaMP injection surgeries

The surgeries for GCaMP injection and cranial window installation were performed 2-3 weeks prior to each experiment. The complete surgery was separated into two separate episodes: (1) headframe installation, and (2) virus injection along with cranial window installation. The mice were anaesthetized with ketamine/xylazine (100 and 10 mg/kg, respectively) and administered subcutaneous injections of meloxicam (1-2 mg/kg), buprenorphine (0,1 mg/kg), and sterile saline (1 ml). The surgeries were conducted under deep anesthesia, confirmed through a toe-pinch test. Body temperature was maintained at around 35-37°C using a DC Temperature Controller System (FHC, Bowdoin, ME, USA).

During the first surgery episode, the objective was to implant the headframe onto the skull. The fur on top and back of the skull was shaved, and the skin was sterilized using betadine and 70% ethanol. The skin around the occipital bone was excised, and underlying tissues were removed and cleaned. Muscle tendons connected to interparietal and occipital bones were cut to expose the back side of occipital bone. A custom-made titanium headframe (H. E. Parmer Company, Nashville, TN, USA) was installed via dental cement (Stoelting Co., Wood Dale, IL, USA).

After a recovery period of 2-3 days, the mice were prepared for the second surgery episode, following appropriate monitoring of infections and activity. A circular craniotomy with a diameter of 4mm was performed using a dental drill. The craniotomy was centered at 2.5mm laterally from the midline and 2.5mm caudally from lambda. The dura was carefully removed, exposing lobules simplex, Crus I, and anterior Crus II of the cerebellum. A glass pipette with a tip diameter of approximately 300μm was utilized to inject a total volume of 1800 nl of an AAV virus mix into two separate locations, 900 nl each, at a depth of 300μm below the pial surface of the medial and lateral Crus I (1.8mm and 3.2mm laterally from the midline, respectively). To express GCaMP6f in wild-type and CaMKII TT305/6VA mice, the AAV virus mix was prepared with 0.5% of full titer L7-Cre (AAV1.sL7.Cre.HA.WPRE.hGH.pA[89], Princeton Neuroscience Institute (PNI) Viral Core Facility, kindly provided by the lab of Dr. Samuel Wang at Princeton University), and 20% Cre-dependent GCaMP6f (AAV.CAG.Flex.GCaMP6f.WPRE.SV40[90]; Addgene, #100835). For SK2-KO mice, with constant expression of transgenic Cre recombinase under the control of the L7 promoter, the AAV virus mix was prepared with 10% Cre-dependent GCaMP6f. Low concentrations permitted a sparse labeling of PCs. Following injection, the glass pipette carrying the AAV virus was held in place for 5min before withdrawal. Any potential debris and blood clots on the brain surface were carefully removed, and a two-layer glass window was installed using C&B Metabond dental cement (Patterson Dental Company, Saint Paul, MN, USA). The two-layer glass windows consisted of a 5mm glass window (Warner Instruments, Holliston, MA, USA, # CS-5R) and 4mm glass window (Tower Optical Corp, Boynton Beach, FL, # 4540-0495) adhered together using UV glue Norland Optical Adhesive 71 (Norland Products Inc., Jamesburg, NJ). In preparation for PF- and CF-electrical stimulation experiments, a customized glass window with a central silicone access port was specifically created. To construct the access port, a 1.5mm hole

was carefully drilled and subsequently filled with transparent Kik-Sil silicone adhesive (World Precision Instruments, Sarasota, FL, USA) at the center of the two-layer glass window[36].

Habituation

After virus injection, the experimenter visited the mice daily for 5-7 days to provide post-operative care. Once the mice exhibited exploratory behavior in their cage without showing signs of distress such as trembling or vocalization, the habituation training process began with handling of the mice. Typically, any signs of anxiety during handling diminished within two days, allowing the handling period to increase from 15min to 30min. The mice were handled in the vicinity of the recording area, so they could sniff and interact with the recording apparatus. Following two days of handling, the mice were introduced to a free-running treadmill. Their front paws were placed on a horizontal bar while heads were securely restrained via the head plate clamped on the left and right stands. During this process, the mice tended to use their hindlimbs to run while holding onto the frontal bar with their forelimbs. To alleviate anxiety, a partial wall supporting the side of the mouse body was used to enhance comfort. Throughout the training process, the duration of time spent on the treadmill increased gradually, ranging from 10 minutes to 2 hours per day, based on the mouse's comfort level. The objective of this study was to record calcium responses to tactile or PF stimulation while avoiding signals related to behavioral output, which may be encoded by the same region being imaged. To minimize motor signals, the mice were trained to remain still during stimulation. It was observed that training the mice on a locked treadmill significantly reduced their inclination to make movements. As soon as the mice exhibited relaxed behavioral patterns on the freely moving treadmill, the treadmill was periodically locked. A glass capillary tube for airpuff stimulation mounted on a three-axis manipulator was moved around the mice, so

they could become accustomed to it. To habituate mice with airpuff stimulation without influencing the plasticity experiments, multiple airpuffs at 8 psi were delivered at irregular frequency to various areas of the right forelimb. The distance between the tube and the forelimb moved from far to close when the mice became habituated. Both the duration of treadmill locking and the frequency of airpuff delivery increased throughout the habituation process. In total, the mice underwent habituation for a period of 1-2 weeks until they showed no aversive responses to the airpuff (for tactile-RF experiments) and/or remained comfortably on the locked treadmill (for both tactile-RF and PF-RF experiments) for over two-hours.

Two-photon imaging

We conducted calcium imaging of the genetically encoded indicator GCaMP6f in Crus I of the right hemisphere of head-fixed mice using a laser scanning two-photon microscope (Neurolabware, Los Angeles, CA, USA). For tactile-RF experiments, airpuff stimuli were delivered to the finger or wrist of the ipsilateral (right) forelimb. Motor activity of the mice was monitored using a DALSA M640 CCD camera (Teledyne Technologies, Thousand Oaks, CA, USA). Any movement exhibited by the mice during the experiments led to a pause in the recording until the mouse returned to a steady state. As discussed below, trials with movement were discarded to control for contamination of dendritic responses by motion signals. Calcium images were obtained at a frame rate of 62 Hz with a pixel dimension 635x256 for tactile-RF experiments, and at a frame rate of 31 Hz with a pixel dimension of 635x512 for PF-RF and CF experiments, using an 8KHz resonant scanning mirror. Excitation of GCaMP6f was achieved using a 920-nm laser source provided by Mai Tai® DeepSee (Spectra-Physics, Milpitas, CA, USA), and the fluorescence emission was collected through a 16x water immersed objective (Nikon LWD 0.8NA,

3mm WD) using a GaAsP PMT (Hamamatsu Photonics, Shizuoka, Japan). The recording process was controlled by Scanbox software (Scanbox, Los Angeles, CA), which also applied a 3-4x digital zoom during imaging rendering the imaging field of view width between 380-669µm and field of view height between 153-270µm (tactile) and 306-539µm (PF and CF stimulation). This permitted the imagine of 10-30 PCs per session. To minimize background noise originating from ambient light, a custom-made light shield was fitted around the objective and the brain window.

For RF experiments, we obtained a cross-sectional view of PC dendrites from the top of crus I gyrus. For PF stimulation experiments, we sought to keep the dendrite compartments receiving the stimulated PFs in the same plane of focus across the full medio-lateral extent of the PF bundle in the FOV. This allows the dendrites across the field of view to be maximally comparable even when the PF bundle is not perfectly parallel with the pial surface. Thus, to capture different aspects of PC or PF structure in the imaging plane, the location and angle (typically <10°, at most 20° from zenith) of the motorized objective lens were adjusted. In contrast, for the simultaneous recordings of dendrites, soma, and AIS, we acquired a side view of PCs in the Crus I sulcus (Fig. 36a-b). During the RF experiments, the laser power was set to approximately 2% with a PMT gain of 0.95. This configuration allowed for prolonged recording while minimizing phototoxicity. For the simultaneous recording of the three PC structures, the laser power was increased to 10-15%, while the PMT gain was reduced to 0.6-0.7. This adjustment aimed to optimize the signal-to-noise ratio and enhance the detection of somatic and axonal signals, which display a relatively low fluctuation range of signals compared to the dendrite. With higher laser power, the use of a lower PMT gain helps prevent over-saturation in somatic and axonal fluorescence, ensuring accurate and reliable signal measurements.

Tactile stimulation

To deliver airpuffs to the wrist or finger, we designed a horizontal grabbing bar positioned in front of the mice. By precisely adjusting the position of this bar relative to the mouse body, the mice exhibited a natural tendency to extend their forelimbs and comfortably position their front paws on the bar without retracting them in response to the airpuff stimulus. Before conducting any experiments, we assessed and identified the strongly responsive area in Crus I to tactile stimulation. Through a cranial window centered 2.5mm laterally from the midline, we consistently observed a robust calcium response to tactile stimuli in lateral Crus I. Once we defined this tactile response area, we focused our recording on the medial edge, where the calcium response was at an intermediate level. This approach increased the likelihood of observing a calcium response while avoiding saturation of response potentiation. For all tactile stimulation, we used a Picospritzer III (Parker Hannifin, Mayfield Heights, OH, USA) to deliver a single 30ms airpuff triggered at 10th sec of each 20sec trial, based on TTL signals sent from a PG4000A digital stimulator (Cygnus Technology, Delaware Water Gap, PA, USA). The airpuff was delivered through a 0.86mm diameter capillary tube placed approximately 2mm away from the finger or wrist. The PG4000A digital stimulator and two-photon imaging were synchronized via TTL signaling under control of Scanbox software. Stimulus dependency was assessed over a duration of 40-60min, during which we collected data from 10-12 trials in each condition (4, 6, 8 and 10psi). In the plasticity experiments, we consistently used 8psi for both test and tetanus pulses. By employing these gentle stimuli, we aimed to minimize the likelihood of evoking CF signals to the greatest extent possible[18,67,68]. The plasticity experiment consisted of three periods: pre-tetanus, early post-tetanus and late post-tetanus, each lasting 20min and consisting of 10-12trials. The frequency of trials was intentionally kept low, approximately every 1-2min, to minimize the chance

for evoking a potentiation effect during trial periods. We controlled for signal contamination during animal movement by discarding trials when the animal moved just before, during, and within half a second after the airpuff administration. Between the pre-tetanus and post-tetanus periods, airpuff tetanization at 8psi with a 30ms duration at 4Hz for 5min was delivered to elicit tactile-RF plasticity. As control experiments for wild-type mice, either airpuff tetanization was directed at the paw location unmatched to the test location (i.e. tetanizing the finger while testing pre- and post-tetanus responses to airpuffs to the wrist, or vice versa; 7 mice, 39 cells), or no airpuff tetanization at all (7 mice, 75 cells) for over 5min. No difference was observed between these two groups and were thus pooled together for the analysis shown in the Figure 38 and Appendix Figure 40.

Electrical PF and CF stimulation

During PF-RF or CF stimulation experiments, we intended to remain the same experimental setup as the tactile-RF experiments to maximize their comparability. Calcium signals in Crus I were acquired when the mice were positioned on a locked treadmill and their forelimbs were placed on the horizontal grabbing bar. However, instead of using the airpuff stimulation described earlier, electrical stimulation was applied to a bundle of PFs in the molecular layer or to CFs at the base of the granule cell layer or in the white matter. A glass pipette filled with ACSF was inserted through the silicone access port at the center of the glass brain window. Often, a thin layer of transparent scar tissue developed after removal of the dura between the glass window and the surface of the cerebellum. Successfully positioning the glass pipette usually required a slight overshoot of insertion to pierce the scar tissue, followed by retracting the pipette tip back to the surface area of the molecular layer. The position and angle of the glass pipette was controlled by a PatchStar motorized micromanipulator (Scientifica, Uckfield, UK), while the calcium response

was assessed and identified in epifluorescence mode. To evoke calcium responses to PF or CF stimulation, an electrical pulse was generated using a constant current source SIU91A (Cygnus Technology), triggered by an EPC-10 amplifier (HEKA Elektronik, Lambrecht/Pfalz, Germany) under the control of Patchmaster software (HEKA Elektronik). The Patchmaster software operated on a different computer than the Scanbox software, and they were synchronized through TTL signaling between the EPC-10 amplifier and the Scanbox board. A successful PF bundle stimulation could generate a calcium response in PC dendrites cross a medio-lateral distance of more than 2mm, and this was underestimated due to the folding structure of cerebellar cortex and the size of the craniotomy. To record the PF response and avoid artifact from a direct stimulation of PCs, the glass pipettes were placed at least 100μm away, in the medio-lateral axis, from the PCs being recorded. To record the CF response, the pipettes were positioned below the field of view and more sub-adjacent to the PCs being imaged. Once the glass pipette was in place and a reliable calcium response could be detected by epifluorescence, stimulus-dependence assessment, CF, and PF-RF plasticity experiments were conducted using two-photon microscopy.

During each 10sec trials, at the 5sec mark, an electrical stimulus of 8 pulses with 0.3ms duration at 100Hz was delivered to PFs or 4 pulses with 0.3ms duration at 333Hz to CFs. Stimulus dependence was assessed over a duration of 40min, during which we collected data from 10-12 trials in each condition (10, 20, 30 and 50μA). A stimulus intensity evoking an intermediate level of calcium response, around 30μA, was used for the plasticity experiments. The plasticity experiment consisted of three periods: pre-tetanus, early post-tetanus and late post-tetanus, each lasting 20min and consisting of 10-12 trials. The frequency of trials was intentionally kept low, approximately every 1-2min, to minimize the chance for evoking a potentiation effect. Between the pre-tetanus and post-tetanus periods, PF tetanization was introduced by delivering a single

262

pulse with a duration of 0.2ms at 1Hz for 5min using the same stimulus intensity as the test pulse to elicit PF-RF plasticity. CF tetanization used spike trains of four pulses with a duration of 0.3ms and inter-pulse frequency of 333Hz which were delivered at 4Hz for 5min using a stimulus intensity just above the threshold to induce a detectable calcium event (typically 20-50µA).

Image analysis

The time-series frames obtained from the experiments were converted into TIFF files. To ensure consistency among trials after motion correction, all trials were concatenated along the z-axis, representing the time series, into a single file. Subsequently, the concatenated time-series images underwent motion correction using a custom-made MATLAB R2017b script (MathWorks, Natick, MA, USA; see Code Availability) based on whole frame cross-correlation[91] (kindly provided by the lab of Mark Sheffield, University of Chicago). Cellular regions of interests (ROIs) were manually selected in ImageJ based on volumetric cell reconstruction conducted after each experiment. For PF-RF plasticity experiments, the ROIs encompassed the entire PC dendrite, regardless of whether only a portion of the dendrite intersected with stimulated PF bundle, as indicated by a hotspot within a PC dendrite. This approach allowed us to capture the potentiation that transformed silent synapses into active synapses. The calcium intensity of each ROI was measured, and $\Delta F/F$ values were calculated using the following equation: $(F_t-F_0)/F_0$, where F_t represented the raw calcium intensity of the time series, and F_0 was set as the 20th percentile of each fluorescence trace[92], serving as the baseline fluorescence. The resulting $\Delta F/F$ values were then subjected to low-pass filtering using a five-frame moving window smoothing function. For spike detection, a custom interactive MATLAB GUI was utilized, offering automatic detection with a manual correction function. The spike detection thresholds, including the threshold and

prominence threshold, were set at 0.09, which is approximately equivalent to one standard deviation of the pre-stimulus baseline.

In the analysis of the spatial pattern of calcium distribution during PF-RF plasticity experiments, PC populations that displayed calcium response across the entire dendritic cross-section were excluded. This selection methods allow us to differentiate between hotspot and off-hotspot area within each PC. A line was manually drawn along the cross-section of the PC dendrite, and linescan data was obtained using the reslice function in ImageJ. The *output spacing* parameter was set to approximately 15μm, corresponding to the thickness of PC cross-section. The pixel-by-pixel ΔF/F along the scanned line was calculated using the same approach as described earlier for the cellular ROIs.

Statistical analysis

All data analyses and visualizations were conducted using MATLAB R2021b (see Code Availability). To represent calcium signals, the calcium traces from different trials of individual PC were averaged, and then the average ± SEM across PCs was calculated. To show calcium traces without stimulus ('Shuffled'; Fig. 33a and Fig. 37d), calcium signals were obtained from set duration time windows (200ms), randomly sampled within -4.5 to -0.5sec relative to the stimulus onset. Representative spontaneous spikes (Fig. 33b and Fig. 37e) were selected from -4.5 to -0.5sec relative to the stimulus onset, and their peaks were temporally aligned. The calcium-event probability of each PC was calculated as the number of trials that exhibited a detected spike peak within the defined time window, divided by the total number of trials. Throughout the article, calcium-event amplitude generally refers to the amplitude of detected spikes, except in the context of tactile-RF plasticity (Fig. 38e and Appendix Figure S39), as well as the simultaneous recordings

of dendrite, soma and AIS (Fig. 36 and Appendix Figure S37; for detailed discussion see later paragraph), where the amplitude specifically refers to the maximum value within the designated time window (0-200ms). This approach was used in tactile-RF plasticity experiments, taking into account that the slow rising and the low amplitude characteristics of the naturalistic PF-mediated calcium event[45,47] cannot be reliably detected using a defined criteria[63]. Given the variability in spike timing, the calcium event amplitude of each PC was calculated by averaging the amplitudes of individual calcium responses rather than using the peak of the trial-averaged trace.

To evaluate the differences in calcium-event probability or amplitude attributed to the different factors (stimulus intensity, stimulus tetanization, and genotype), we performed statistical analysis using one-way ANOVA, two-way ANOVA, or two-way repeated measure ANOVA. Post hoc pairwise comparisons were then conducted using Tukey's HSD test. Stimulus intensity-dependent and stimulus intensity-independent PCs were classified based on the Pearson correlation coefficient, with a stimulus intensity-dependent threshold set at $R > 0.5$ and $p < 0.5$, calculated using the 5 data points (spontaneous events and 4 stimulus intensities) within each PC.

To quantify the differences in spatial patterns, we calculated the cumulative length by sorting and summing up pixels of dendritic linescans based on their fluorescence level normalized by the maximum value of pre-tetanus response, disregarding the original dendritic location (Fig. 35e and 35h). Through this method, we can estimate the length of PF-responsive area (hotspot). The difference in cumulative length —Δlength— was calculated by subtracting the pre-tetanus value from the post-tetanus value (Fig. 35h, *bottom*). Δlength represents the spatial expansion of hotspot or off-hotspot. To assess the difference in the distribution of Δlength (Fig. 35n and Supplementary Figure 4m), a non-parametric Kruskal-Wallis test was conducted, followed by post hoc pairwise comparison using Dunn & Sidák's approach.

To analyze the simultaneous recording of dendrite, soma, and AIS, we averaged data from different trials without employing our spike detection method. This was necessary because the somatic and AIS signals were relatively noisy compared to dendritic signals and exhibited distinct time constants which could not be compared using the same event deconvolution parameters. The average trace revealed the presence of positive transients, and the maximum values within a time window of 0-200ms were measured for each individual cell compartment. These maximum values were then used for further correlation analysis, as shown in Figure 36e-h. The correlation coefficient was performed using the Pearson correlation coefficient.

CHAPTER 2: CLIMBING FIBER MULTI-INNERVATION OF MOUSE PURKINJE

DENDRITES WITH ARBORIZATION COMMON TO HUMAN
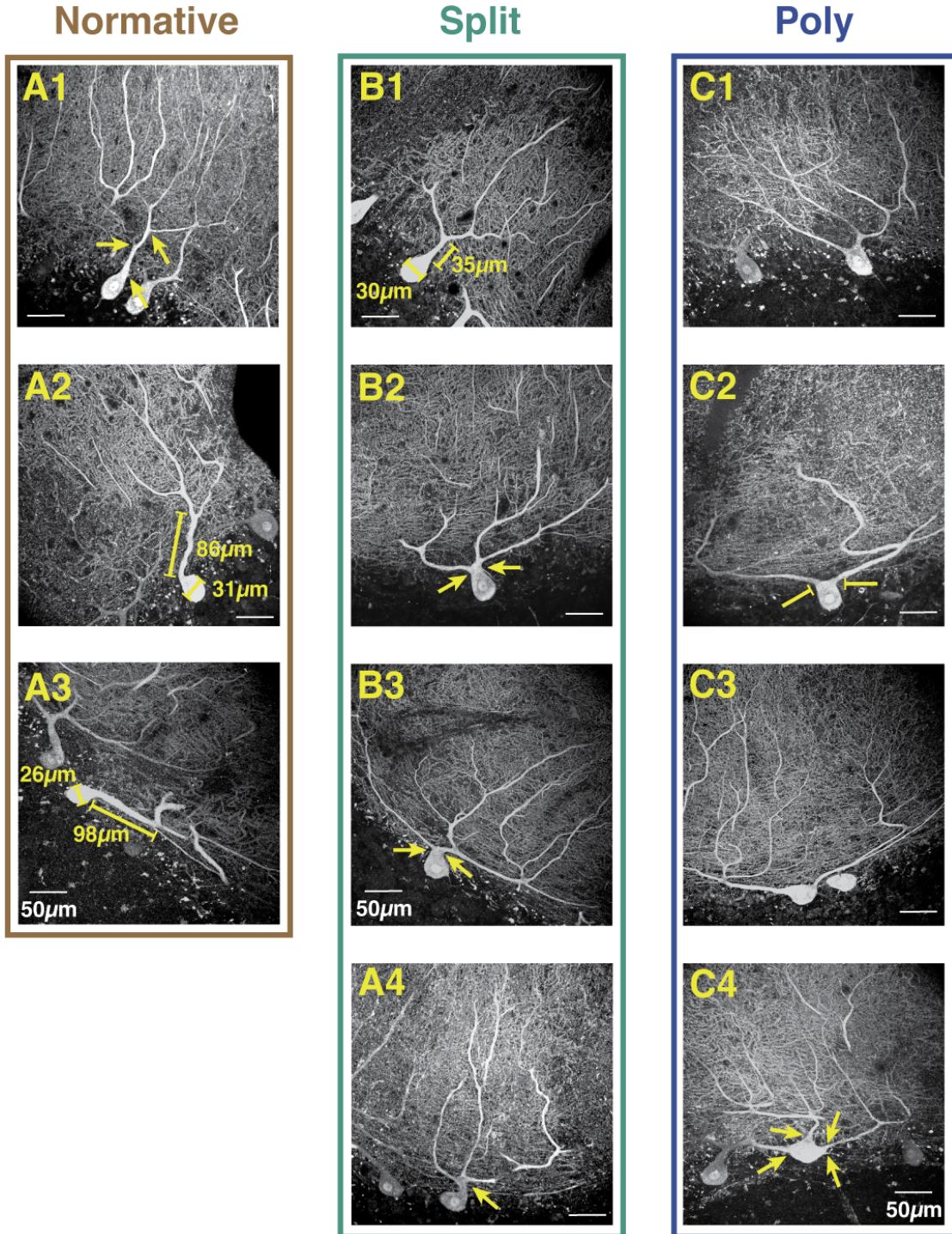
Figure S1. Categorization of human Purkinje cells by proximal primary dendrite geometry

Human PCs were visualized in unembalmed tissue of one individual following immunolabeling for calbindin. (**A1-3**) Normative PCs have one trunk emerging from the soma and either 1) no bifurcation and no proximal minor branches ramifying >200μm laterally (**A1**) or 2) a bifurcation that is >2x the somatic diameter (**A2-3**). We used a threshold bifurcation distance of two somatic diameters measured from the base of the trunk where the circular dimension of the soma ends to the middle of the branch point. As seen in (**A2-3**), the visible bifurcations occur more than 2x the somatic diameter. To accelerate categorization, the distances were only measured when it was not obvious, as it was in most cases, whether the threshold was exceeded. (**B1-3**) Split PCs have one trunk emerging from the soma and either 1) no bifurcation but a large, proximal minor branch ramifying >200μm laterally or 2) a bifurcation that is <2x the somatic diameter (**B1**). Split PCs had spectrums of bifurcation distances and angles. (**B2-3**) The most challenging cases for categorization, which were common, presented with multiple primary dendrites emerging from a compartment which was difficult to define as somatic or dendritic. For our analyses we used the curvature of the space between the branch points and the center of the soma as an indication. As shown in (**B2-3**), there is a minor inward curvature of the superficial somatic compartment, like if the top of the soma was pinched into a single dendritic trunk from which the primary dendrite branches emerge. Compare this with (**C1-2**) where there is no pinching of the superficial soma such that the outer diameter merges directly with the primary dendrites and thus fits a definition of Poly PC. (**B4**) The most challenging cases for categorization, which were rare, presented with proximal bifurcations of the dendrite that were very proximal to the soma, but either asymmetrical or producing more than two primary dendrites. (**C1-4**) Poly PCs have multiple dendritic trunks emerging directly from the somatic compartment. Poly PCs had a spectrum of angles between emerging trunks, from acute (**C1**) or intermediate (**C2**) to emerging from opposite poles of a horizontally oriented somatic compartment. In the latter case, primary dendrites may continue ramifying in opposing directions to form entirely distinct and distant compartments as in (**C3**) or rapidly curve upward to preserve a somewhat compact set of compartments. (**C4**) While less common than two primary dendrites, we also observed many cases where Poly PCs had three or more dendrites emerging at varying relative angles.
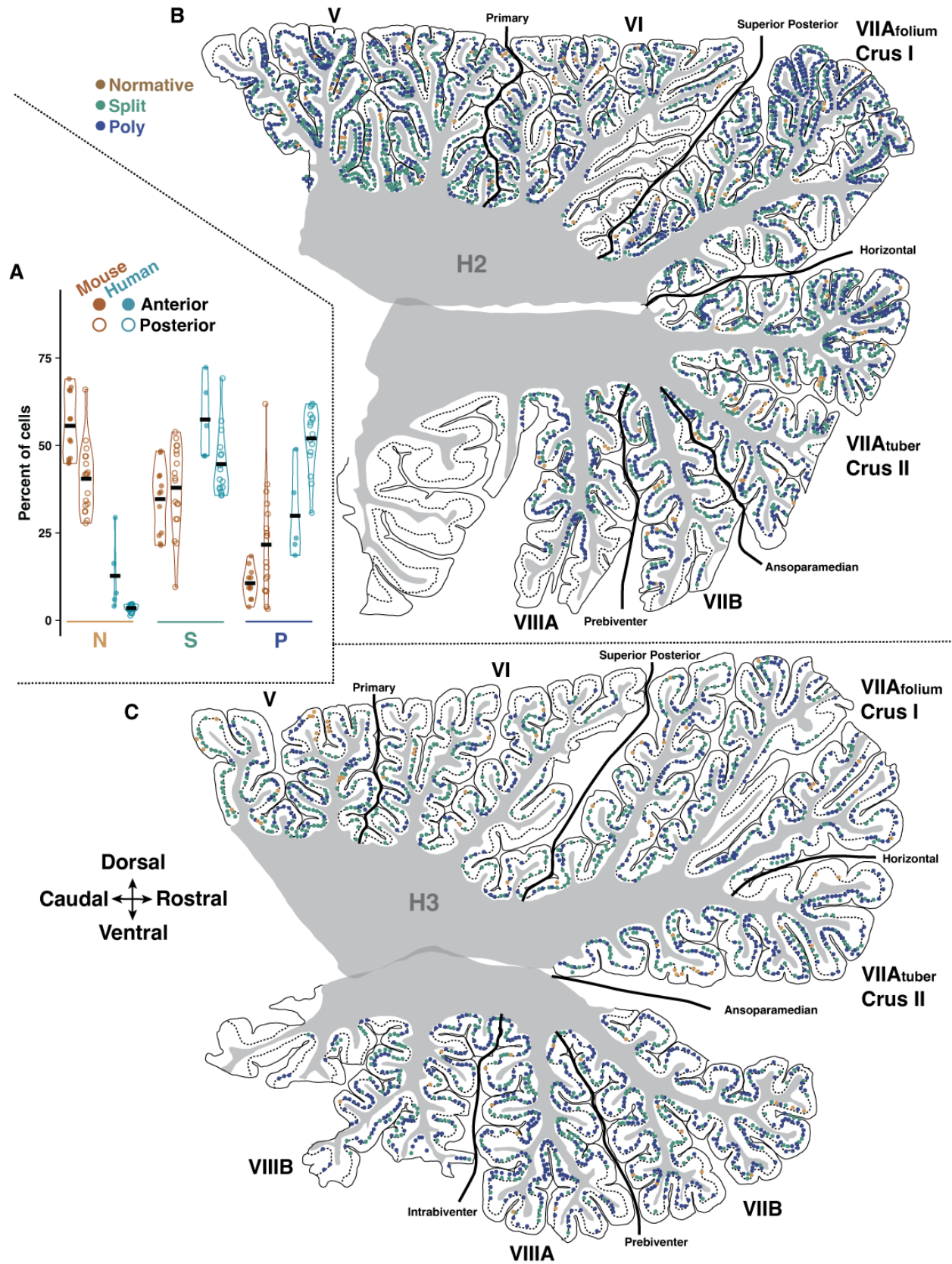
Figure S2. Reconstructed parasagittal sections of human cerebellar hemisphere

(**A**) Summary of relative cell morphology rates across anterior and posterior lobules of human and mouse (see table S4 for statistics). (**B-C**) Cross-section maps of human mid-hemisphere demonstrating the distribution of PC morphological types by region for individual specimens H2 and H3. H4 is presented in (Fig. 3B). See table S1 for quantification.
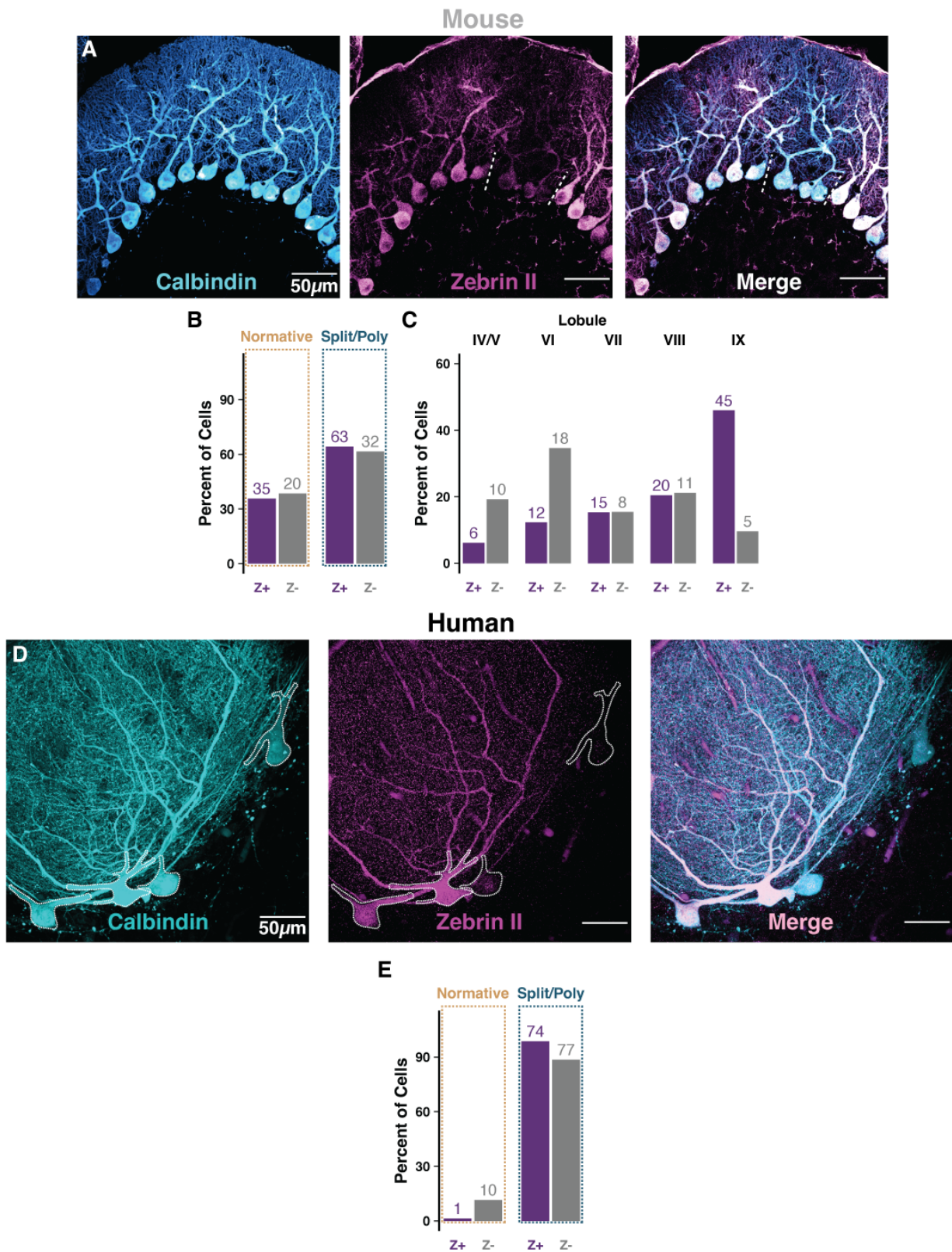
Figure S3. Zebrin expression does not predict Purkinje dendrite morphology in mouse or human. (**A**) Example maximum projection of parasagittally sliced mouse tissue dual labeled for

calbindin (PCs) and aldolase-C (Zebrin II) shows a mixed population of normative and split cells at the borders of a zebrin- zone between zebrin+ zones. (**B**) Quantification of zebrin expression by morphological category shows no relationship (table S5, $\chi^2 = 0.024$ p = 0.88). (**C**) Quantification of zebrin expression by lobule shows the expected elevation of zebrin+ cells in posterior lobules. (**D**) Example maximum projection of parasagittally sliced human tissue dual labeled for calbindin (PCs) and aldolase-C (Zebrin II) shows two cells with distinct zebrin expression intensity despite similar calbindin labeling. (**E**) Quantification of zebrin expression by morphological category shows no relationship (table S6, $\chi^2 = 5.06$ p = 0.024) when PCs are classified as zebrin+ or zebrin- by their ratio of zebrin II to calbindin expression falling in the top or bottom 25th percentiles.
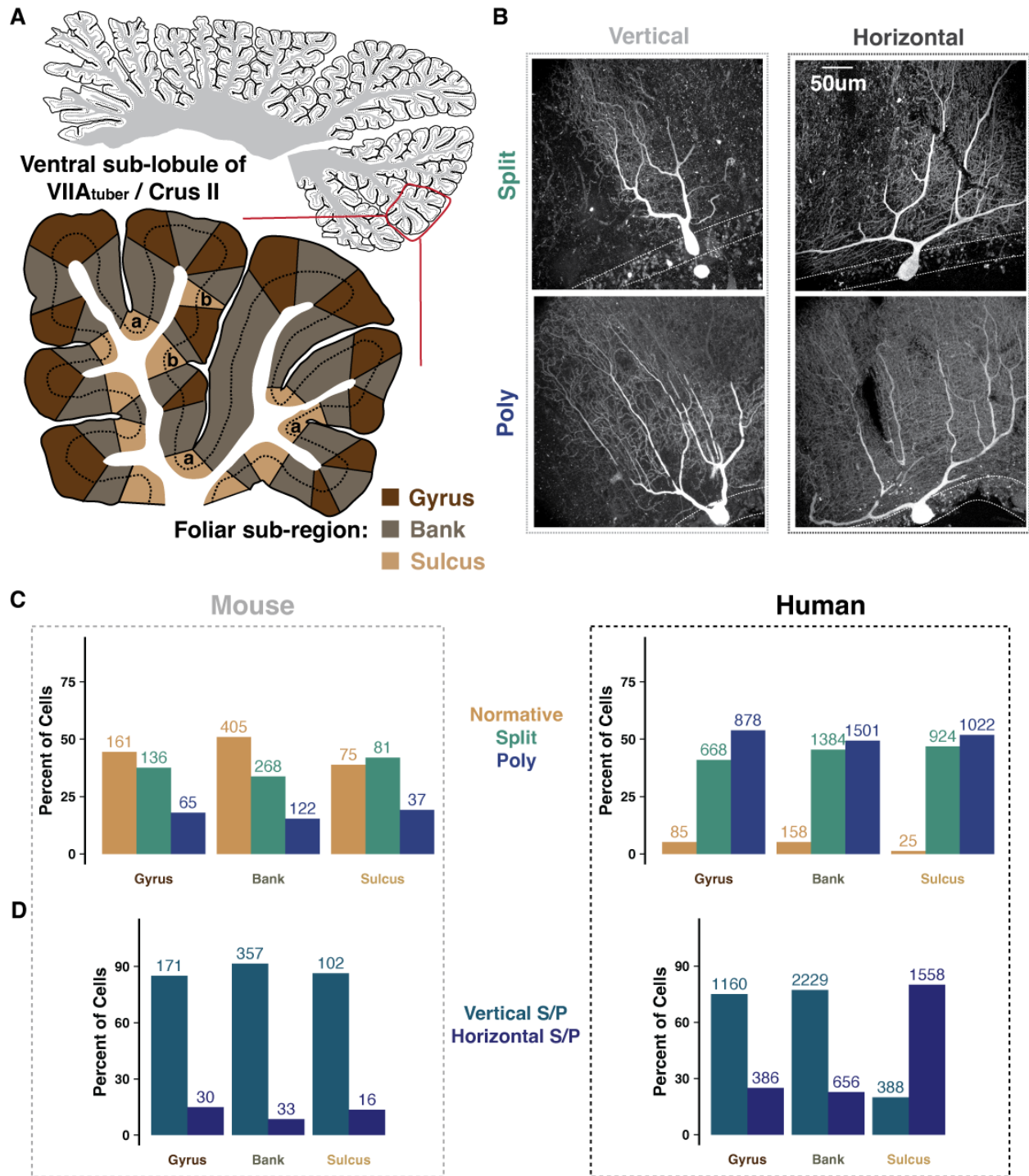
Figure S4. Some features of Purkinje dendrite morphology correlate with foliar sub-region in human. (**A**) Schematic highlighting a ventral sub-lobule of LVIIA$_{tuber}$/Crus II from human specimen H4 and the definition of foliar sub-regions within that area. When marking PCs in the section, their location was denoted as Gyrus, Bank, or Sulcus (see Appendix 1: Methodology and Statistics). Intermediate sulci embedded within a long bank region, indicated by "b", were

combined with full sulci, indicated by "a". (**B**) Example human Purkinje cells belonging to each morphological category and with ramification patterns defined as either Vertical or Horizontal. (**C**) Quantification of the rate of each morphological category (Normative, Split, Poly) by foliar sub-region in mouse (left, table S7, $\chi^2 = 10.96$ p $= 0.027$) and human specimens (right, table S8, $\chi^2 = 65.17$ p < 0.001). While there were limited sub-regional variations in morphology in mice, many morphological features varied by sub-region in human. (**D**) As multi-innervated Split and Poly PCs in the mouse had wider separations in their dendritic arbor or a more obtuse angle between trunks emerging from the soma, we quantified the rate of vertical vs horizontal dendritic ramification (Vertical S/P and Horizontal S/P) in mouse (left, table S9, $\chi^2 = 17.41$ p $= 0.002$) and human specimens (right, table S10, $\chi^2 = 1876.9$ p < 0.001).
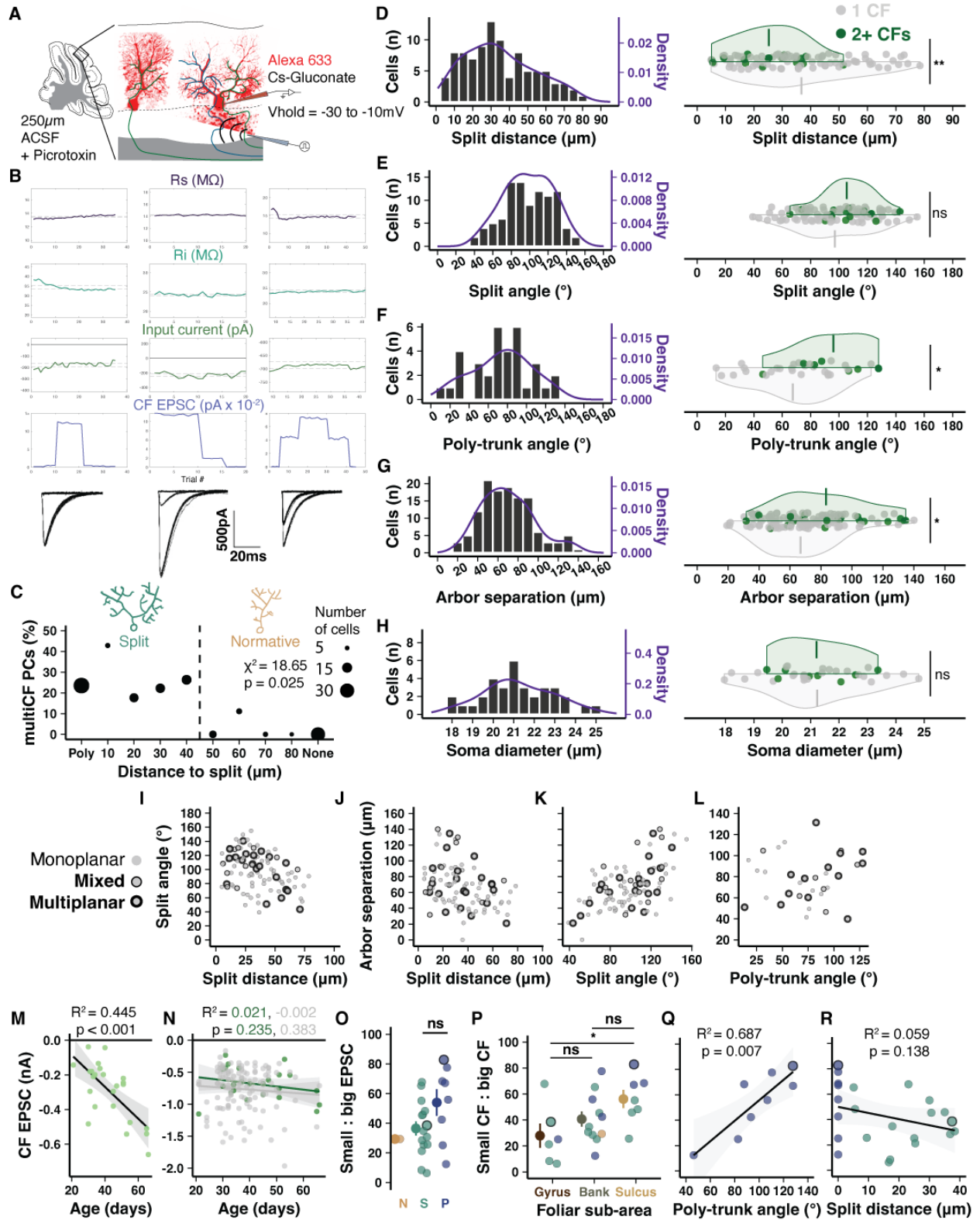
Figure S5. Purkinje dendrite morphology correlates with climbing fiber multi-innervation.

(A) Schematic of PC whole-cell patch-clamp recordings and CF stimulation in acute cerebellar

slices. A cesium internal solution with Alexa 633 dye is used to reduce space clamp error, increase detection of more distant CF inputs, and label the cell for confocal imaging at the end of the experiment. Note, cesium and depolarized holding potentials distort the absolute size of the EPSC. (B) Representative physiology and CF-EPSC traces evoked by increasing and decreasing stimulation intensities. *Left*, a mono-innervated PC exhibits only one CF-EPSC amplitude regardless of stimulation intensity above threshold. *Middle*, a multi-innervated PC with discrete CF-EPSC amplitude steps constituting the stimulation of one small CF (~200pA) and then the summed EPSC amplitude of stimulating two CFs (~1.2nA) at a higher stimulation intensity. *Right*, discrete CF-EPSC steps indicating that this PC receives two CFs of approximately equal size (~400-450pA). (C) Inverse linear relationship between the rate of multi-innervation and distance from soma to primary dendrite split (n = 50 animals, 159 cells). (D-H) Whole population distributions (left) and distributions by CF innervation type (right) of morphological parameters: split distance (n = 79, 16), split angle (n = 79, 16), poly-trunk angle (n = 26, 8), arbor separation (n = 109, 16), and poly PC soma size (n = 26, 8). (I-L) Relationships between morphological parameters and Purkinje dendrite planarity. (M) Age dependency of weaker CF EPSC amplitude to multi-CF PCs indicates a possible continued development following circuit maturation (n = 24). (N) In contrast, neither the dominant CF on multi-CF PCs (green, n = 24) nor lone CFs of mono-innervated PCs (grey, n = 135) show a relationship between age and EPSC amplitude. (O) The ratio of EPSC amplitudes between strong and weak CF inputs to multi-innervated PCs are widely varied across cell morphologies. Bordered points indicate cells with 3 CFs where the smallest of the three inputs is compared with the largest (n = 24 cells). (P) Among all multi-innervated PCs, the ratio of EPSC amplitude between the smaller and larger detected CF is smaller in the gyrus (28%) than the sulcus (56%; n = 6, 11, 7 cells), which builds on the finding that multi-innervation is enhanced in sulcus of the vermis (Nishiyama & Linden, 2004). (Q) Among multi-innervated Poly PCs, a wider dendrite separation angle correlates with greater EPSC amplitude parity between multiple CFs (n = 8 cells). (R) Among multi-innervated PCs, an earlier dendrite split (0 for Poly PCs) does not correlate with greater EPSC amplitude parity (n = 23).
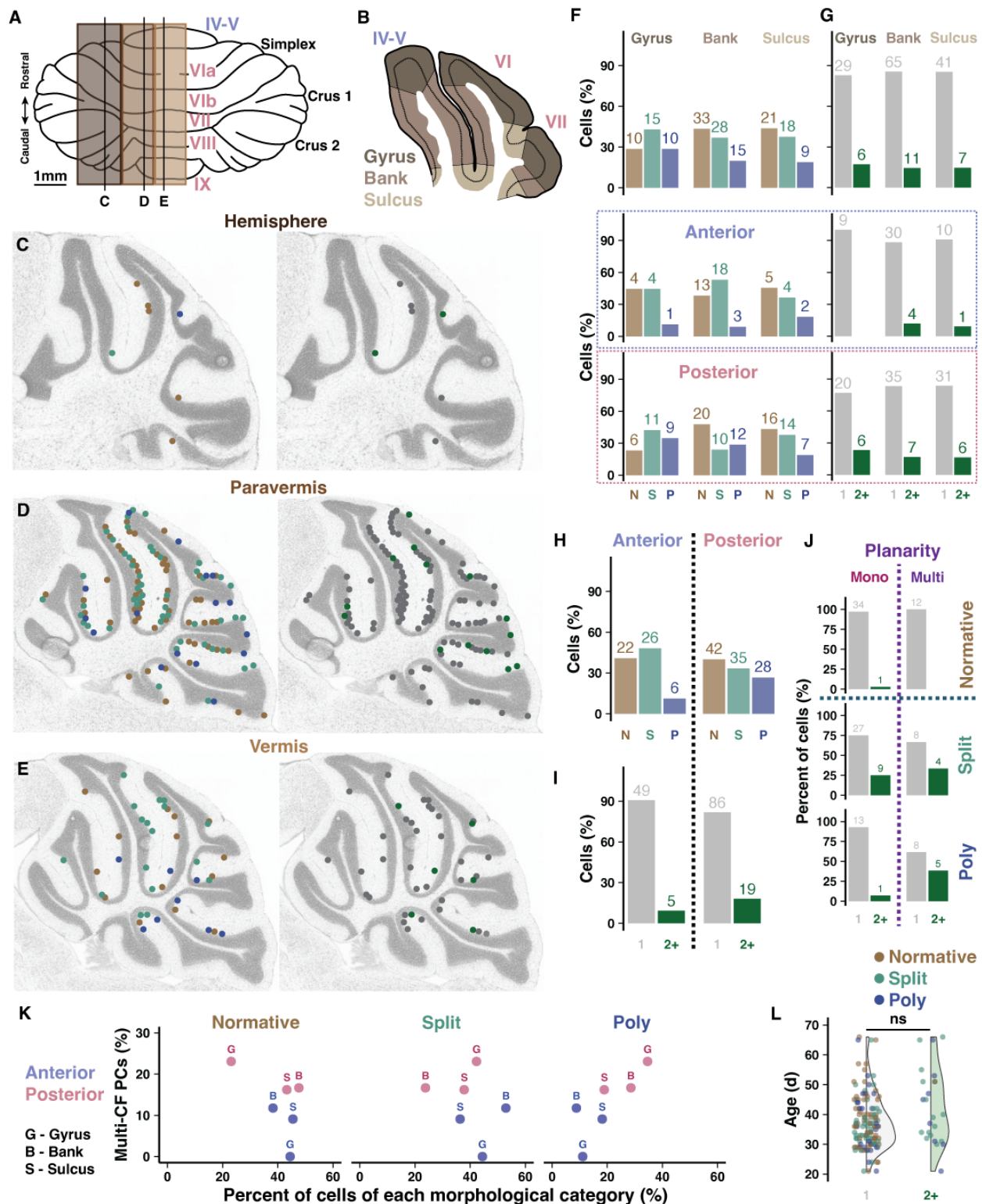
Figure S6. Prevalence of climbing fiber multi-innervation and dendritic morphology across cerebellar regions. (A) Schematic of the mouse cerebellum and the medio-lateral location of acute slices used in whole cell patch clamp recordings. (B) Example of a sagittal section

demonstrating the division of foliar sub-areas. (C-E) Slice maps indicating the location of each recorded PC and its morphology (left) or CF innervation pattern (right, multi-CF PCs are green). (F-G) Distribution of morphological type (left) or CF innervation pattern (right) across foliar sub-areas for all cells (top) or by lobule region (bottom, anterior vs posterior). Numbers above bars are absolute number of cells. (H-I) Distribution of morphological type (H) or CF innervation pattern (I) by lobule region without sub-dividing foliar sub-area. (J) Ratios of multi-innervated PCs by morphology or dendritic planarity. Dendrite planarity has been linked to CF innervation patterns previously (Kaneko et al., 2011), but we find that the presence of multiple primary dendrites – largely requisite to multiplanarity – is slightly more predictive of CF multi-innervation (4 : 96% vs. 55 : 45%). Some PCs could not be clearly identified by planarity, so only a subset of data is presented. (K) Relationship between percent of cells with multi-CF innervation across lobule region (anterior in blue, posterior in pink) and foliar sub-area (G – gyrus, B – bank, S – sulcus) and the percent of cells of either Normative, Split, or Poly structure. (L) No effect of age on the presence of CF multi-innervation (n = 135 and 24 cells).
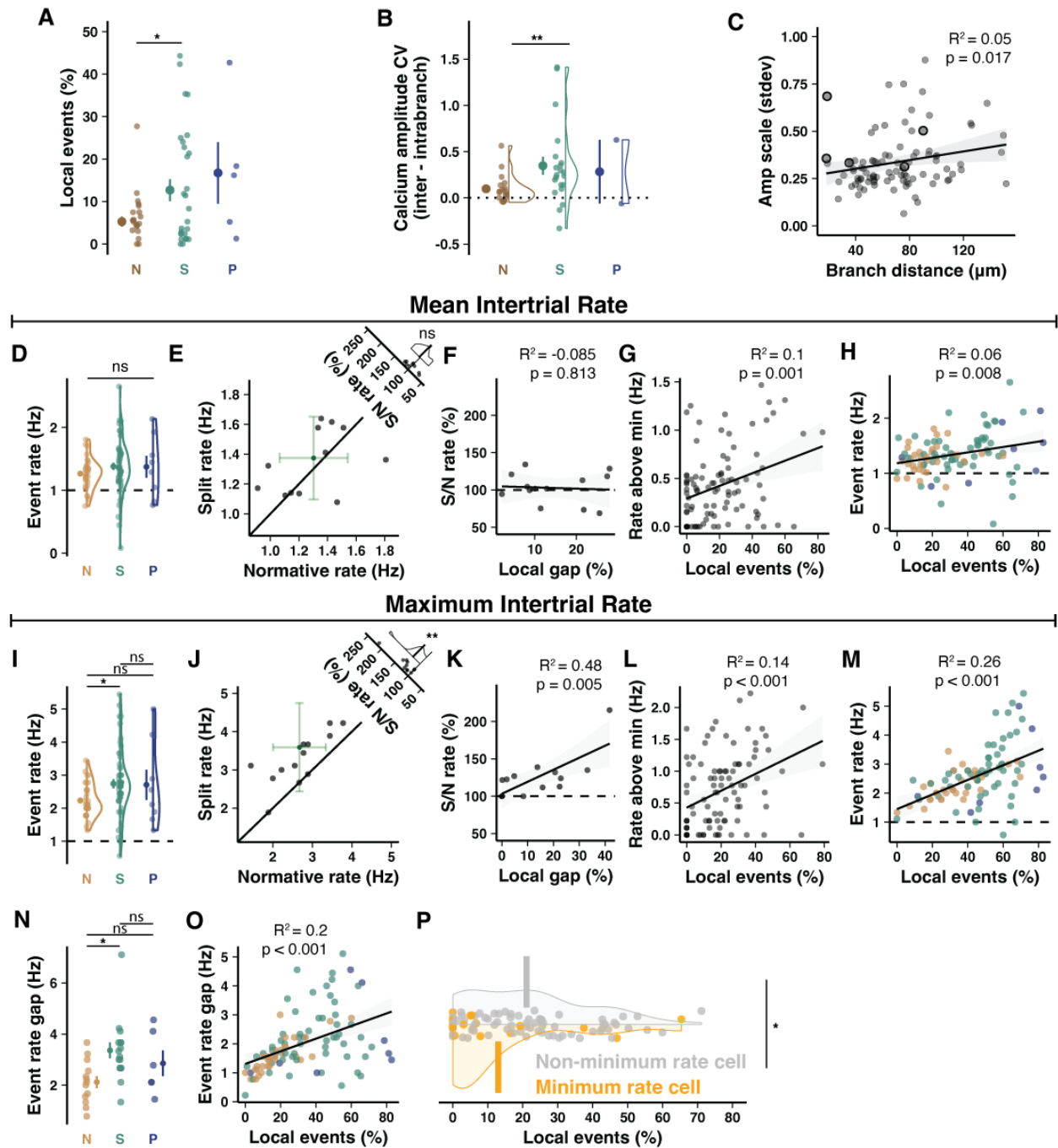
Figure S7. Characterizing calcium signal heterogeneity and subsequent elevation of event rate and total dynamic range. (**A**) Local events identified manually in a subset of data finds a lower baseline frequency of local events but an identical pattern of elevation in Split and Poly PCs (n = 16 animals, n = 25, 29, and 5 cells). (**B**) Analyzing the coefficient of variation of event amplitudes within vs. between branches of each cell shows that, compared to Normative cells, Split PCs have more variability between branches that is not found within branches. This

indicates that heterogeneity is a feature of dendritic macro-compartments instead of small sub-branches within a primary dendrite (n = 16 animals, n = 25, 29, and 5 cells). (**C**) Variability of the inter-event amplitude scale (the mean ratio of event amplitude between branches) as a function of the distance between the centroid of dendritic branches (n = 23 animals, n = 95 cells). (**D-H**) Converging CFs likely originate from neighboring IO cells with local synchrony via gap junction coupling and convergence of IO input pathways. Thus, multiple converging CFs likely exhibit some overlapping activity and supply only modest elevations of input frequency. To test this, we compared total CF-dependent event rates to the quantity of heterogeneity. Lateral crus I PCs are largely zebrin(+), but may still have modest variation in zebrin identity and therefore CF input rate (Zhou et al., 2014). To compensate, we analyzed raw and normalized inter-trial event rates pooled across PCs and animals. When mean spontaneous event rate is measured during control trials, we made several observations. (**D**) There is no difference between mean event rates by morphology (n = 23 animals, n = 32, 55, and 8 cells). (**E**) To control for differences in CF input rates based on PC molecular patterning identities, we can analyze only cells in animals where Split and Normative cells were both present in a local field of view. There is no bias in the Split relative to Normative PC mean rate within each animal (n = 13 animals). (**F**) Relatedly, there is no relationship between the local event ratio difference between Normative and Split PCs (Local ratio gap) and the ratio of Split to Normative PC event rates (n = 13 animals). (**G**) Controlling for event rate differences across animals by normalizing event rates to the local minimum shows an elevation of event rates, regardless of morphology, in PCs with higher local event ratios (n = 23 animals, n = 94 cells). (**H**) As in J, but without normalizing event rate, PCs with higher local event ratios have modestly elevated event rates (n = 23 animals, n = 95 cells). (**I-M**) Numerous variables could be minimizing the effect size observed by using the mean event rate. On the other hand, analyzing the maximum event rate might provide a more direct indication of the elevation of event rate afforded by putative multi-CF innervation. Thus, we performed the same measurements as in (**D-H**) but using the *maximum* rate of spontaneous events during the same control trials. (**I**) A significant difference emerges in event rates by morphology (n = 23 animals, n = 32, 55, and 8 cells). (**J**) Across animals, Split PCs have higher maximum event rates than Normative PCs (n = 13 animals). (**K**) Animals with a larger difference between local event ratios of split PCs relative to Normative PCs also show a higher event rate in Split PCs (n = 13 animals). (**L**) The maximum rate above the minimum local cell rate is higher in

PCs with more local events (n = 23 animals, n = 94 cells). (**M**) PCs with higher local event ratios, particularly Split and Poly, also have elevated event rates (n = 23 animals, n = 95 cells). (**N**) The difference in result between using mean and maximum event rate is partly explained by the fact that Split PCs have wider variability in event rates, with mostly higher maximums and slightly lower minimums, suggesting a larger dynamic range of activity. This is confirmed by computing the gap between minimum and maximum spontaneous event rates during control trials for each cell and comparing Split and Normative PCs (n = 17 animals, n = 13, 16, 6). (**O**) The event rate gap also correlates with the local event ratio (n = 23 animals, n = 95 cells). (**P**) PCs with the minimum spontaneous event rate in each animal (orange) have lower local event rates than the remaining cells (grey, n = 17 animals, n = 17 and 77 cells).
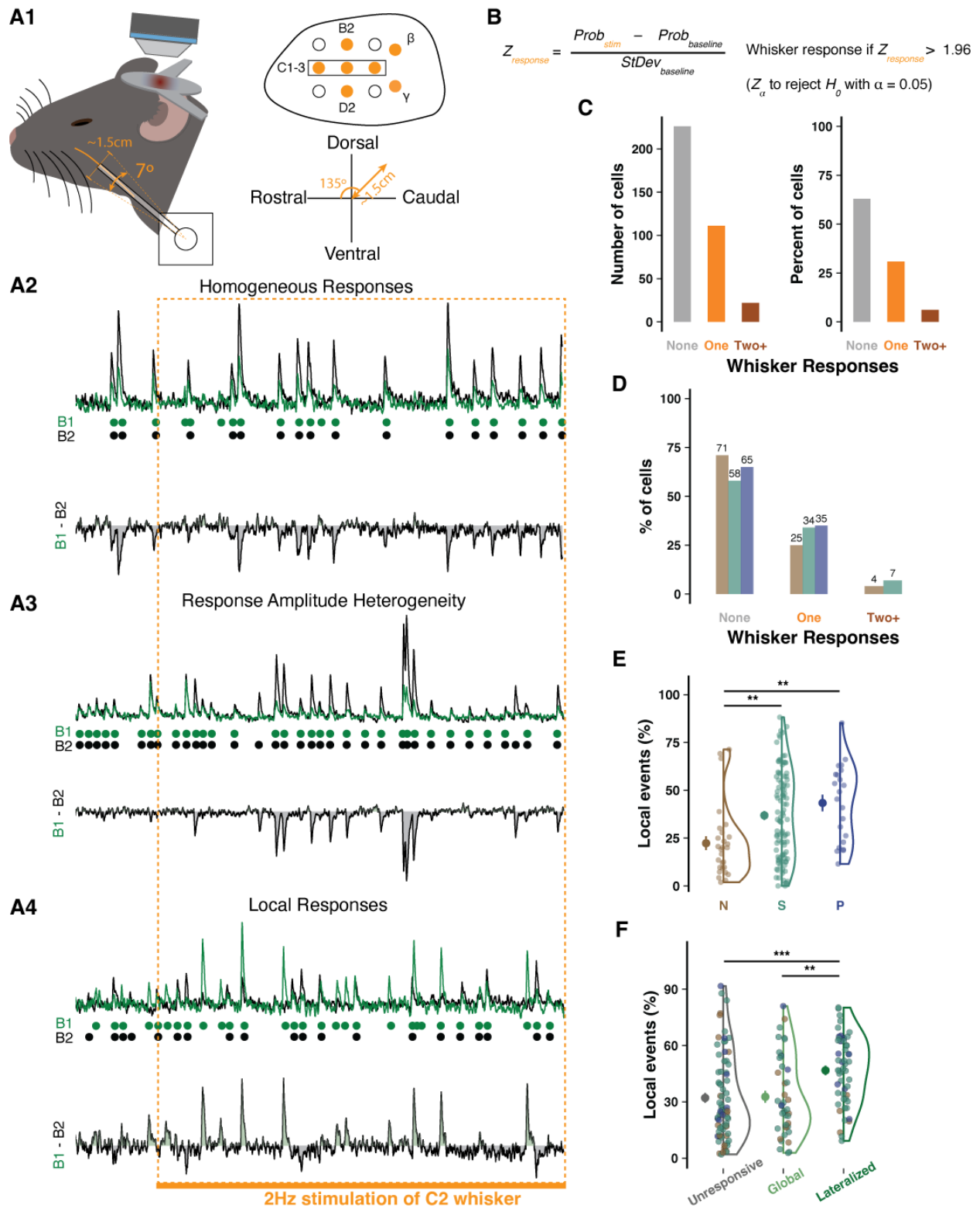
Figure S8. Purkinje cell responses to single whisker stimulation match the literature and branch-specific events match other recording methods. (A) Schematic of rotary servo motor

stimulation of individual whiskers. Whiskers B2, D2, C1-3, β, and γ were stimulated one at a time for two trials each in a random order in each mouse. The servo motor was programmed via an Arduino synchronized to the imaging time to rotate 7° at 2Hz and was positioned to move each whisker in the dorso-caudal direction (135°). (**A2**) Sample traces from a PC with homogeneous activity and responses during the same trial of stimulation of the C2 whisker as shown in different PCs with either largely global responses but dynamic amplitude scaling (**A3**) or with many local responses in addition to dynamic global response amplitude scaling (**A4**). (**B**) The formula used to determine if events in an ROI constitute a response. A z-scored probability of response is obtained by finding the difference between the probability of an event during baseline vs. response time windows and dividing by the deviation of the probability during baseline periods. If the Z-score exceeded two standard deviations, $Z_{response} > 1.96$, we could reject H_0 that there was no response with a confidence of $\alpha = 0.05$). (**C**) Relative rates of non-response (60%) and response to one (25%) or more whiskers (15%) for cells using combined (averaged) branch signal, the typical approach in the field, as opposed to total responses extracted separately from each branch. These values match the expected rate described by Ju and colleagues (46). (**D**) The relative rates as in (**C**) separated by cell morphology. A slight elevation in response rate can be observed in Split and Poly PCs, even when only assessing the averaged dendritic signal. As shown in Fig. 6D, deconvolving events and responses separately for each primary dendrite in the same cell population produced a higher fidelity representation of whisker responses, which revealed more responsiveness than detected with averaged dendritic signal. Crucially, this elevation of detected responsiveness was especially pronounced in Split and Poly PCs, while Normative PC response rates were largely unchanged. (**E**) Rates of spontaneous, branch-specific events by morphological category during recordings in medial Crus I while mice were under anesthesia (n= 13 animals, n = 28, 99, 22 cells). These rates are nearly identical to rates in awake conditions recorded from lateral Crus I. (**F**) PCs with lateralized responses have more branch-specific events (45%) than PCs with global or no response (both 25%, n = 75, 42, 52 cells).
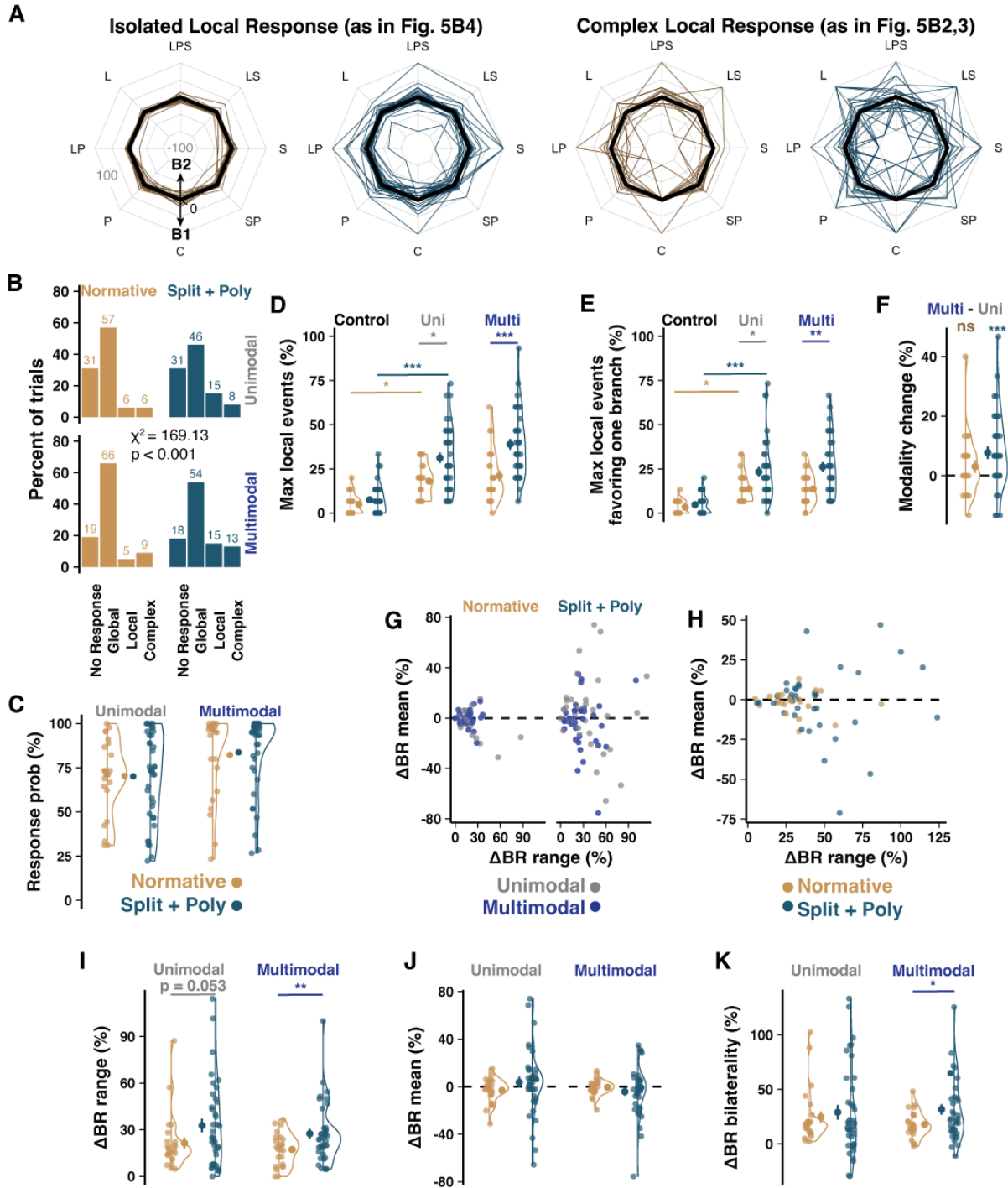
Figure S9. Multisensory CF receptive field representation across Purkinje cell branches.
(**A**) Radar plots of non-absolute (directional) local event rates (in isolation, *top*, or as part of a response with global and local components, *bottom*) favoring arbitrarily designated branch 1 or branch 2 of each PC. Middle back line marks no local responses whereas lines deviating toward the outside or inside of the radar indicate high ratios of local events favoring one or the other

branch. (**B**) Ratios of uni- and multisensory response type by morphology (n = 2,520 and 3,990 events, from 24 and 38 cells). (**C**) Average response probability (here and below: n = 12 animals, n = 24 Normative and 38 Split+Poly cells). (**D**) As in (Fig. 7C), the highest percentage of local events regardless of branch identity, across stimuli for each cell. (**E**) Obtaining the difference between the number of local responses from each branch for each stimulus – if both branches have local responses to a stimulus this determines how many more local responses one branch had over the other – gives the directionality of the local responses as favoring one branch or the other. Taking the maximum absolute value gives the maximum directional rate. (**F**) Relative difference of maximum local events between uni- and multisensory stimuli reveals no change in Normative PCs but a modest increase of local events in SP PCs during multisensory stimulation. (**G-H**) The relationship between range and directional ΔBR mean grouped by sensory modality category (uni vs. multi-sensory) or morphology (Normative vs. Split+Poly). (**I-J**) As in (Fig. 7F-G), the ΔBranch Response (ΔBR) range and mean, but here separated by uni- vs multisensory stimulus types instead of combined (Student's t-test). (**K**) As in (Fig. 7H), subtracting the ΔBR mean from the range distinguishes cells with either unilateral or bilateral profile of modality representations. Unilateral cells (high ΔBR range and mean) have one branch that shows branch-specific responses to some but not all modalities, whereas both branches of bilateral cells (high ΔBR range and low ΔBR mean) show branch-specific responses to different modalities.
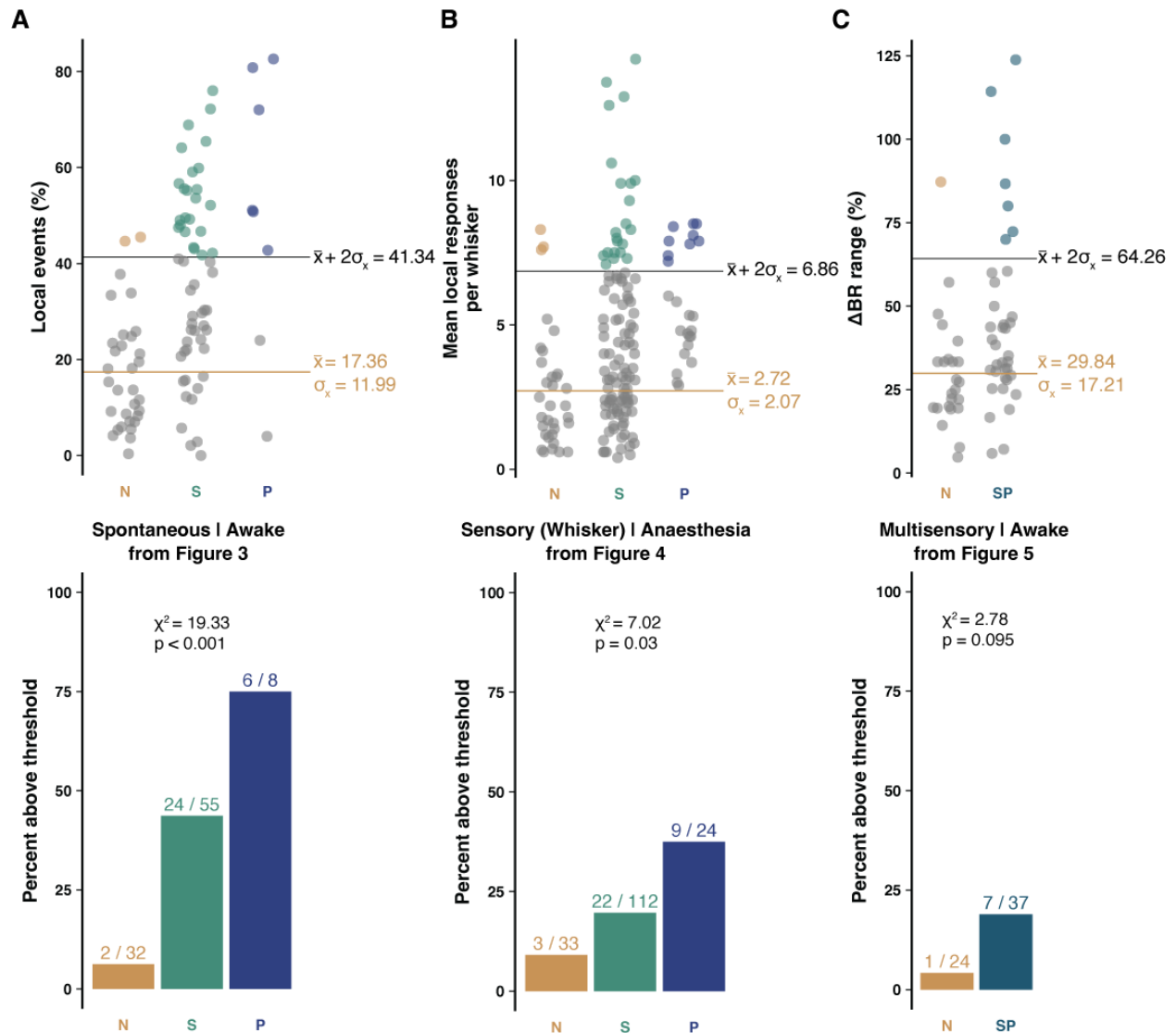
Figure S10. Comparative statistics across Ca²⁺ imaging datasets shows similar absolute and relative rates of enhanced heterogeneity in Split and Poly PCs as of multi-innervation in slice electrophysiology. To obtain an approximate quantification of potential CF multi-innervation from the two-photon imaging data that can be compared to the quantification obtained from the *in vitro* patch-clamp recordings, we extracted percentages of local events from our datasets, comparing Split and Poly PCs to Normative PCs. We obtained the mean ($\bar{x}$) and standard deviation (σ_x) of the Normative population and defined the threshold as values exceeding $\bar{x} + 2\sigma_x$ (e.g. Z-score of 2). We then applied this threshold across different measures of heterogeneity from different datasets. (**A**) Applying the threshold to local event rate data (top) under spontaneous conditions where the mice were awake and resting (data from Fig. 5G), we

observe enhanced heterogeneity in 6%, 43%, and 75% of Normative, Split, and Poly PCs, respectively (bottom). See also the ratios of PCs without significant correlations between branch activity in Fig. 5I. (**B**) Applying the threshold to the number of evoked local whisker responses while the mice were under ketamine anesthesia (data from Fig. 6C), we observe enhanced heterogeneity in 9%, 20%, and 38% of Normative, Split, and Poly PCs, respectively. (**C**) Applying the threshold to the range of the Δbranch response profiles across multi-sensory stimuli while the mice were awake (data from Fig. 7F), we observe enhanced heterogeneity in 4% and 19% of Normative and Split/Poly PCs, respectively. The increased prevalence of cells with enhanced heterogeneity in Split and Poly population relative to Normative is highly consistent across experiments. The absolute ratios vary to some extent, but largely mirror the ratio of multi-innervation observed in slice electrophysiology experiments (Fig. 4D) and reflect an expected relationship in which spontaneous activity, as in A, is more likely to be affected by unsynchronized climbing fiber signaling than sensory evoked conditions, as in B and C. Among evoked conditions, climbing fiber signaling is most likely to be highly synchronized, reducing the ability to observe multi-innervation, during awake responses to multi-sensory stimuli.
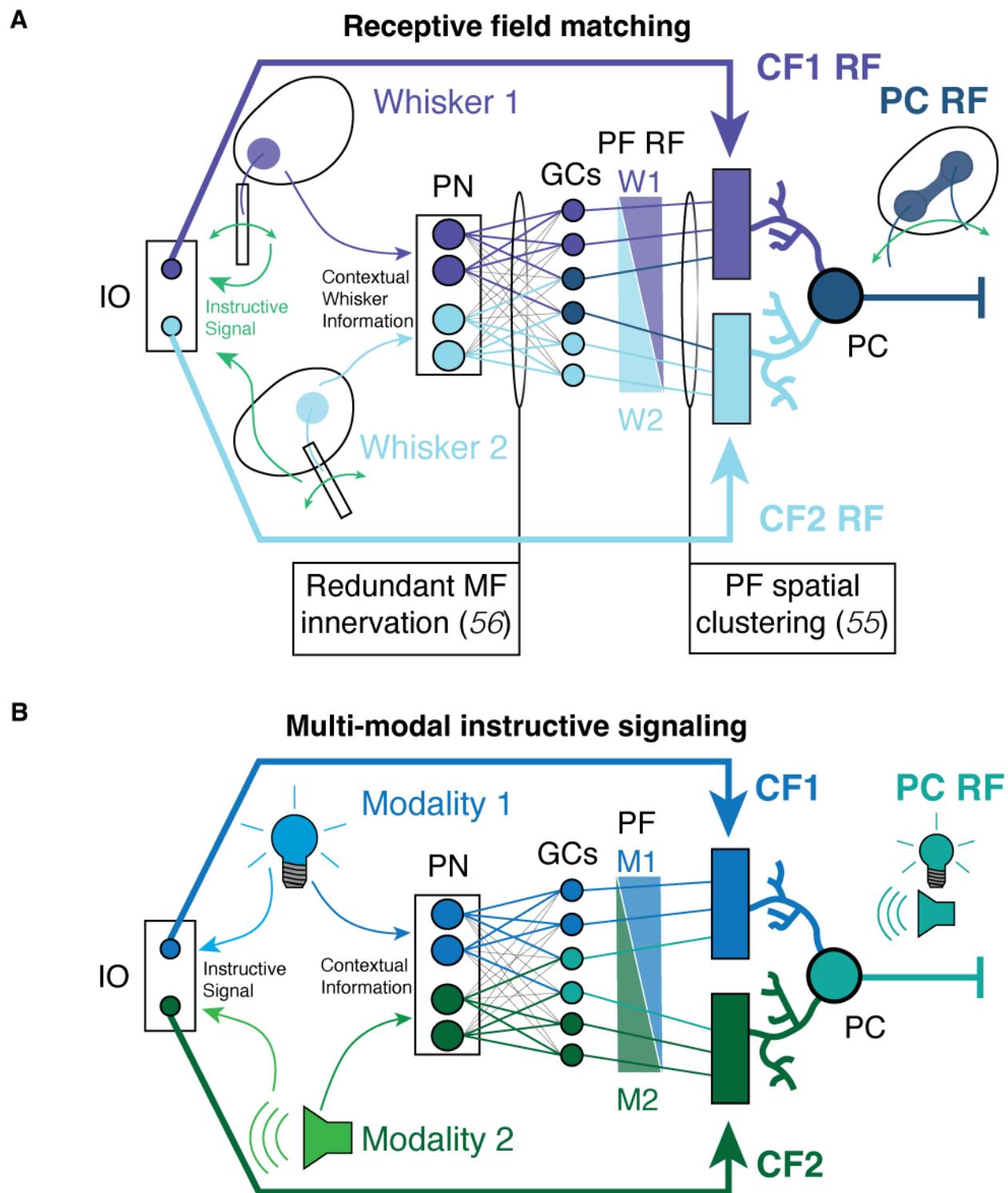
Figure S11. Perceptron circuit diagram highlighting the advantage of climbing fiber multi-innervation for polydendritic Purkinje cells. (A) A cerebellar circuit diagram with a two-layer perceptron network model representing the supervised associative learning function of a Purkinje cell (PC) during exposure to perturbations within the same modality but with distinct receptive

fields. The increased dendritic complexity of Split and Poly Purkinje cells – with the addition of parasagittally segregated primary dendrite compartments – within a cortical architecture with functional clustering of upstream projections (Nguyen et al., 2023; Wilms & Häusser, 2015) – may increase the range of parallel fiber (PF) receptive field (RF) representation across opposing branches. In a classical perceptron model of the Purkinje cell, a hidden layer of granule cell (GC) parallel fibers (PF) has full connectivity with a single PC dendritic compartment. PF synaptic weights are updated during supervised learning by the instructive signal of a single climbing fiber (CF). Avoiding inappropriate correction of weights requires RF matching between instructor and instructee; the CF RF should thus match that of the PF input population. In some cases, the segregation of PF RFs to different primary dendrites may necessitate distinct CF inputs to retain RF-matching. The diagram in A demonstrates RF matching of the CF instructive signal with the propagation of the mossy fiber (MF) input layer RF through the GC hidden layer to a two compartment PC output layer. A consequence of this arrangement is that signals from the output layer generalize across RFs of the PF and CF inputs. (**B**) A second advantage of CF multi-innervation is the potential use for representation of error / instructive signals from multi-modal sensory environments.

IO = inferior olive, PN = pontine nucleus

Lobule*	H2†						H3‡						H4§					
	N		S		P		N		S		P		N		S		P	
	n	%	n	%	n	%	n	%	n	%	n	%	n	%	n	%	n	%
L3													5	29	8	47	4	24
L4													14	16	56	65	16	19
L5	34	4	394	47	410	49	18	8	128	56	84	37	11	6	133	72	40	22
L6	18	4	153	38	236	58	10	4	146	57	100	39	7	4	86	54	65	41
L7Af/Crus1	25	3	297	38	460	59	17	4	207	43	255	53	12	4	129	44	150	52
L7At/Crus2	32	5	326	47	332	48	12	5	100	38	151	57	10	2	236	48	250	50
L7B	9	5	79	40	111	56	11	3	125	36	214	61	7	3	106	50	101	47
L8A	6	3	77	40	108	57	7	2	102	36	175	62						
L8B			9	69	4	31	3	1	80	37	135	62						

*Lobules present in each individual differ with variations in slicing and tissue quality.

†92yo, Female, Cause of Death: 'Failure to Thrive'

‡95yo, Female, Cause of Death: 'Failure to Thrive'

§86yo, Male, Cause of Death: 'Colon Cancer'

Table S1. Distribution of PC morphologies in human.

Lobule specific numbers and percentages (in color) of each morphological type for each individual in the study. Lobule information is empty if the lobule was not present or could not be assessed in sections from that individual. Related to Figure 1B-C, and fig S2.

Lobule	Mse1						Mse2						Mse3					
	N		S		P		N		S		P		N		S		P	
	n	%	n	%	n	%	n	%	n	%	n	%	n	%	n	%	n	%
L2	19	46	17	41	5	12	29	69	9	21	4	10	27	66	9	22	5	12
L3	42	66	16	25	6	9	22	67	8	24	3	9	15	58	10	38	1	4
L4	23	46	24	48	3	6	19	58	12	36	2	6	16	52	15	48	0	0
L5	22	45	18	37	9	18	23	45	21	41	7	14	22	51	14	33	7	16
L6	30	49	29	48	2	3	33	66	11	22	6	12	30	47	26	41	8	12
L7Af/Crus1	5	42	6	50	1	8	5	33	5	33	5	33	5	42	6	50	1	8
L7At/Crus2	15	31	25	52	8	17	12	36	16	48	5	15	9	31	13	45	7	24
L8A	18	51	14	40	3	9	11	42	14	54	1	4	13	34	11	29	14	37
L8B	17	45	11	29	10	26	5	28	6	33	7	39	6	29	2	10	13	62
L9	54	47	26	23	35	30	26	42	21	34	15	24	25	33	32	42	19	25
L10	12	44	13	48	2	7	17	53	10	31	5	16	14	41	15	44	5	15

Table S2. Distribution of PC morphologies in mouse.

Lobule specific numbers and percentages (in color) of each morphological type for each mouse in this experiment. Related to Figure 1E-F.

	Normative M	Normative H	Split M	Split H	Poly M
Normative H	<0.001				
Split M	<0.001	<0.001			
Split H	1	<0.001	<0.001		
Poly M	<0.001	<0.001	<0.001	<0.001	
Poly H	0.218	<0.001	<0.001	<0.001	<0.001

	Normative M	Normative H	Split M	Split H	Poly M
Normative H	0.512				
Split M	0.116	0.408			
Split H	0.020	0.474	0.067		
Poly M	0.330	0.195	0.219	0.215	
Poly H	0.027	0.527	0.114	0.064	0.260

Table S3. Morphology demographics by species.

Quantification of p-values (top) and φ effect size (bottom) after a multiple comparisons Z-test of proportions with post-hoc bonferroni correction of morphological demographics by species. Related to Figure 1G. M = Mouse; H = Human.

	Anterior M Normative	Anterior H Normative	Posterior M Normative	Posterior H Normative	Anterior M Split	Anterior H Split	Posterior M Split	Posterior H Split	Anterior M Poly	Anterior H Poly	Posterior M Poly
Anterior H Normative	<0.001										
Posterior M Normative	<0.001	<0.001									
Posterior H Normative	<0.001	<0.001	<0.001								
Anterior M Split	<0.001	<0.001	0.0002	<0.001							
Anterior H Split	<0.001	<0.001	<0.001	<0.001	<0.001						
Posterior M Split	<0.001	<0.001	1	<0.001	<0.001	<0.001					
Posterior H Split	<0.001	<0.001	<0.001	<0.001	0.022	<0.001	<0.001				
Anterior M Poly	<0.001	1	<0.001	<0.001	<0.001	<0.001	0.0001	<0.001			
Anterior H Poly	<0.001	<0.001	<0.001	<0.001	<0.001	<0.001	<0.001	<0.001	<0.001		
Posterior M Poly	<0.001	1	<0.001	<0.001	<0.001	<0.001	<0.001	<0.001	1	<0.001	
Posterior H Poly	1	<0.001	<0.001	<0.001	<0.001	<0.001	<0.001	<0.001	<0.001	<0.001	<0.001

	Anterior M Normative	Anterior H Normative	Posterior M Normative	Posterior H Normative	Anterior M Split	Anterior H Split	Posterior M Split	Posterior H Split	Anterior M Poly	Anterior H Poly	Posterior M Poly
Anterior H Normative	0.480										
Posterior M Normative	0.301	0.153									
Posterior H Normative	0.537	0.117	0.304								
Anterior M Split	0.209	0.284	0.107	0.359							
Anterior H Split	0.484	0.846	0.689	0.851	0.659						
Posterior M Split	0.340	0.118	0.039	0.264	0.145	0.722					
Posterior H Split	0.071	0.215	0.158	0.464	0.047	0.348	0.186				
Anterior M Poly	0.477	0.006	0.146	0.095	0.286	0.855	0.114	0.186			
Anterior H Poly	0.187	0.633	0.486	0.705	0.388	0.301	0.522	0.204	0.619		
Posterior M Poly	0.454	0.012	0.153	0.150	0.259	0.812	0.114	0.258	0.019	0.624	
Posterior H Poly	0.008	0.283	0.244	0.556	0.109	0.279	0.271	0.111	0.244	0.131	0.340

Table S4. Morphology demographics by cerebellar region and species.

Quantification of p-values (top) and φ effect size (bottom) after a multiple comparisons Z-test of proportions with post-hoc bonferroni correction of morphological demographics by cerebellar

region and species. M = Mouse; H = Human; A = Anterior lobules (L2-L5); P = Posterior lobules (L6-L10). Related to Figure 1G and fig S2A.

	Z+ N	Z+ S/P	Z- N
Z+ S/P	1		
Z- N	0.046	0.004	
Z- S/P	0.004	0.0001	1

	Z+ N	Z+ S/P	Z- N
Z+ S/P	0.013		
Z- N	0.255	0.276	
Z- S/P	0.276	0.316	0.013

Table S5. No relationship between zebrin II expression and Purkinje morphology in the mouse. Quantification of p-values (top) and φ effect size (bottom) after multiple comparisons Z-test of proportions with post-hoc bonferroni correction of morphological demographics by zebrin expression. Related to fig S3B.

	N Z+	N Z-	S/P Z+
N Z-	0.147		
S/P Z+	0	0	
S/P Z-	0	0	0.147

	N Z+	N Z-	S/P Z+
N Z-	0.177		
S/P Z+	0.960	0.858	
S/P Z-	0.858	0.759	0.177

Table S6. No relationship between zebrin II expression and Purkinje morphology in the mouse. Quantification of p-values (top) and φ effect size (bottom) after multiple comparisons Z-test of proportions with post-hoc bonferroni correction of morphological demographics by zebrin expression. Related to fig S3E.

	Normative Gyrus	Normative Bank	Normative Sulcus	Split Gyrus	Split Bank	Split Sulcus	Poly Gyrus	Poly Bank
Normative Bank	1							
Normative Sulcus	1	0.121						
Split Gyrus	1	0.001	1					
Split Bank	0.020	<0.001	1	1				
Split Sulcus	1	1	1	1	1			
Poly Gyrus	<0.001	<0.001	<0.001	<0.001	<0.001	<0.001		
Poly Bank	<0.001	<0.001	<0.001	<0.001	<0.001	<0.001	1	
Poly Sulcus	<0.001	<0.001	0.001	0.0005	0.005	0.0001	1	1

	Normative Gyrus	Normative Bank	Normative Sulcus	Split Gyrus	Split Bank	Split Sulcus	Poly Gyrus	Poly Bank
Normative Bank	0.058							
Normative Sulcus	0.050	0.093						
Split Gyrus	0.067	0.122	0.009					
Split Bank	0.101	0.173	0.040	0.036				
Split Sulcus	0.020	0.069	0.026	0.039	0.066			
Poly Gyrus	0.283	0.310	0.225	0.216	0.159	0.255		
Poly Bank	0.312	0.377	0.230	0.245	0.212	0.258	0.030	
Poly Sulcus	0.248	0.251	0.211	0.185	0.122	0.242	0.010	0.038

Table S7. Morphology demographics by foliar sub-region in the mouse. Quantification of p-values (top) and φ effect size (bottom) after a multiple comparisons Z-test of proportions with post-hoc bonferroni correction of morphological demographics by cerebellar sub-region (e.g. Gyrus, Bank, and Sulcus). Related to fig S4C (left).

	Normative Gyrus	Normative Bank	Normative Sulcus	Split Gyrus	Split Bank	Split Sulcus	Poly Gyrus	Poly Bank
Normative Bank	1							
Normative Sulcus	<0.001	<0.001						
Split Gyrus	<0.001	<0.001	<0.001					
Split Bank	<0.001	<0.001	<0.001	0.118				
Split Sulcus	<0.001	<0.001	<0.001	0.015	1			
Poly Gyrus	<0.001	<0.001	<0.001	<0.001	<0.001	0.001		
Poly Bank	<0.001	<0.001	<0.001	0.00000	0.104	1	0.132	
Poly Sulcus	<0.001	<0.001	<0.001	<0.001	0.0004	0.072	1	1

	Normative Gyrus	Normative Bank	Normative Sulcus	Split Gyrus	Split Bank	Split Sulcus	Poly Gyrus	Poly Bank
Normative Bank	0							
Normative Sulcus	0.112	0.101						
Split Gyrus	0.423	0.446	0.500					
Split Bank	0.413	0.463	0.480	0.043				
Split Sulcus	0.461	0.494	0.533	0.059	0.013			
Poly Gyrus	0.532	0.558	0.603	0.128	0.079	0.069		
Poly Bank	0.444	0.495	0.510	0.080	0.038	0.024	0.043	
Poly Sulcus	0.503	0.537	0.572	0.108	0.062	0.049	0.019	0.024

Table S8. Morphology demographics by foliar sub-region in the human. Quantification of p-values (top) and φ effect size (bottom) after a multiple comparisons Z-test of proportions with post-hoc bonferroni correction of morphological demographics by cerebellar sub-region (e.g. Gyrus, Bank, and Sulcus). Related to fig S4C (right).

	Normative Gyrus	Normative Bank	Normative Sulcus	Vertical S/P Gyrus	Vertical S/P Bank	Vertical S/P Sulcus	Horizontal S/P Gyrus	Horizontal S/P Bank
Normative Bank	1							
Normative Sulcus	1	0.121						
Vertical S/P Gyrus	1	1	1					
Vertical S/P Bank	1	0.659	1	1				
Vertical S/P Sulcus	1	1	0.285	1	1			
Horizontal S/P Gyrus	<0.001	<0.001	<0.001	<0.001	<0.001	<0.001		
Horizontal S/P Bank	<0.001	<0.001	<0.001	<0.001	<0.001	<0.001	0.224	
Horizontal S/P Sulcus	<0.001	<0.001	<0.001	<0.001	<0.001	<0.001	1	1

	Normative Gyrus	Normative Bank	Normative Sulcus	Vertical S/P Gyrus	Vertical S/P Bank	Vertical S/P Sulcus	Horizontal S/P Gyrus	Horizontal S/P Bank
Normative Bank	0.058							
Normative Sulcus	0.050	0.093						
Vertical S/P Gyrus	0.025	0.033	0.077					
Vertical S/P Bank	0.002	0.059	0.046	0.020				
Vertical S/P Sulcus	0.076	0.013	0.135	0.050	0.061			
Horizontal S/P Gyrus	0.407	0.406	0.367	0.432	0.358	0.494		
Horizontal S/P Bank	0.498	0.522	0.437	0.522	0.472	0.558	0.080	
Horizontal S/P Sulcus	0.366	0.339	0.354	0.388	0.297	0.478	0	0.070

Table S9. Dendrite orientation by foliar sub-region in the mouse. Quantification of p-values (top) and φ effect size (bottom) after a multiple comparisons Z-test of proportions with post-hoc bonferroni correction of dendrite orientation demographics (e.g. Vertical v.s. Horizontal) among Split and Poly PCs by cerebellar sub-region (e.g. Gyrus, Bank, and Sulcus). Related to fig S4D (left).

	Normative Gyrus	Normative Bank	Normative Sulcus	Vertical S/P Gyrus	Vertical S/P Bank	Vertical S/P Sulcus	Horizontal S/P Gyrus	Horizontal S/P Bank
Normative Bank	1							
Normative Sulcus	<0.001	<0.001						
Vertical S/P Gyrus	<0.001	<0.001	<0.001					
Vertical S/P Bank	<0.001	<0.001	<0.001	1				
Vertical S/P Sulcus	<0.001	<0.001	<0.001	<0.001	<0.001			
Horizontal S/P Gyrus	<0.001	<0.001	<0.001	<0.001	<0.001	0.155		
Horizontal S/P Bank	<0.001	<0.001	<0.001	<0.001	<0.001	1	1	
Horizontal S/P Sulcus	<0.001	<0.001	<0.001	0.00000	0.0001	<0.001	<0.001	<0.001

	Normative Gyrus	Normative Bank	Normative Sulcus	Vertical S/P Gyrus	Vertical S/P Bank	Vertical S/P Sulcus	Horizontal S/P Gyrus	Horizontal S/P Bank
Normative Bank	0							
Normative Sulcus	0.112	0.101						
Vertical S/P Gyrus	0.678	0.698	0.739					
Vertical S/P Bank	0.648	0.697	0.706	0.022				
Vertical S/P Sulcus	0.212	0.227	0.300	0.517	0.523			
Horizontal S/P Gyrus	0.262	0.274	0.350	0.475	0.476	0.048		
Horizontal S/P Bank	0.213	0.240	0.289	0.484	0.517	0.022	0.024	
Horizontal S/P Sulcus	0.737	0.760	0.793	0.091	0.065	0.593	0.553	0.565

Table S10. Dendrite orientation by foliar sub-region in the human. Quantification of p-values (top) and φ effect size (bottom) after a multiple comparisons Z-test of proportions with post-hoc bonferroni correction of dendrite orientation demographics (e.g. Vertical v.s. Horizontal) among Split and Poly PCs by cerebellar sub-region (e.g. Gyrus, Bank, and Sulcus). Related to fig S4D (right).

Movie S1. Sample video of spontaneous calcium signal heterogeneity.

An example of sparse expression of GCaMP6f yielding a lone Purkinje cell in the mouse. Individual branches exhibit global events as well as events that are local to either one branch or the other. Video playback speed is reduced to 0.5x speed. (File located in supplementary materials for Busch SE and Hansel C. (2023) Climbing fiber multi-innervation of mouse Purkinje dendrites with arborization common to human. *Science*, 381: 420-427 at the following link: https://doi.org/10.1126/science.adi1024).
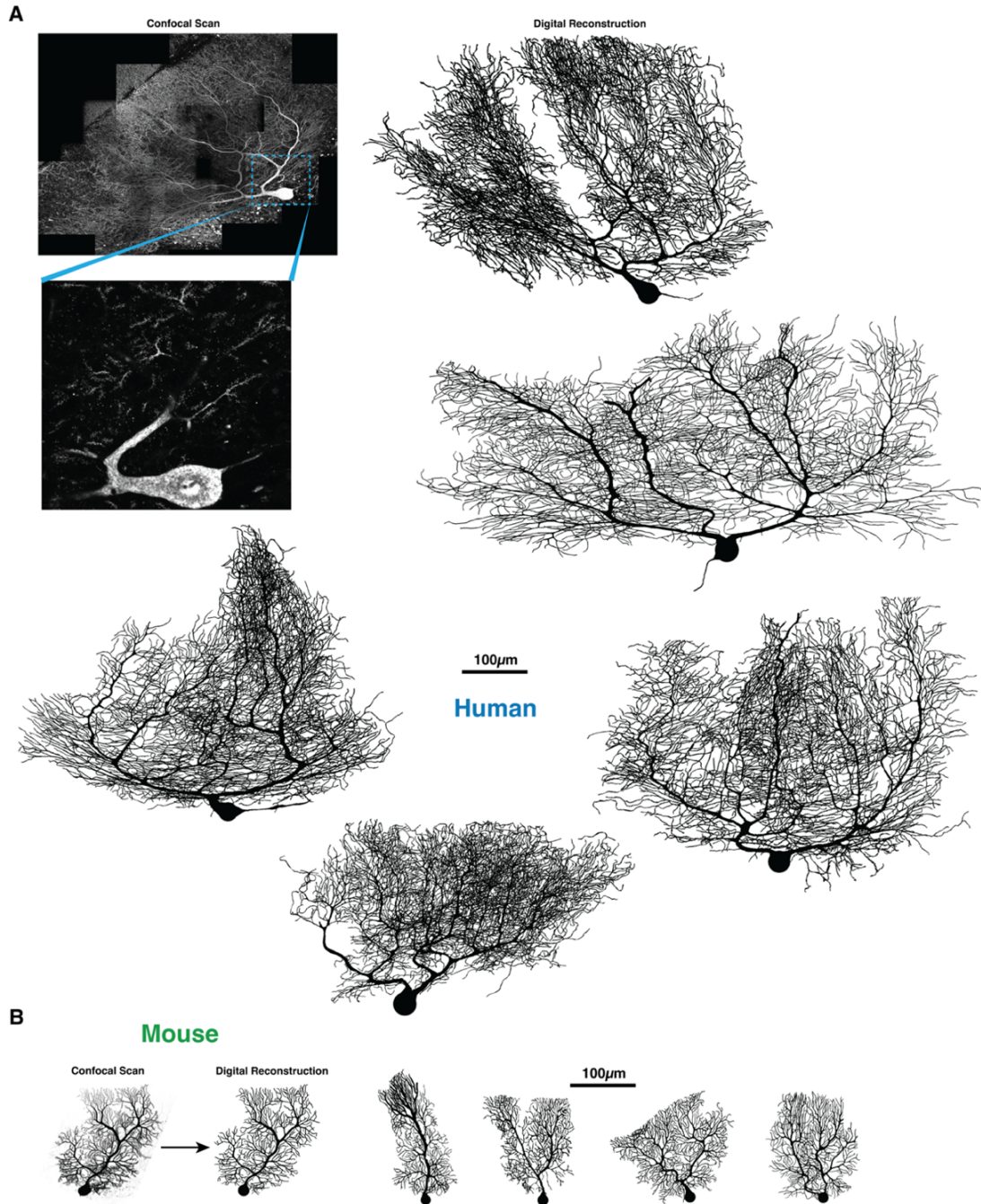
Figure S12. All manual cell reconstructions. A) Example confocal tile scan (top left) and resolution of each individual image (below) with manually reconstructed human PCs. **B)** Manually reconstructed mouse PCs. Cells throughout are at the same scale.
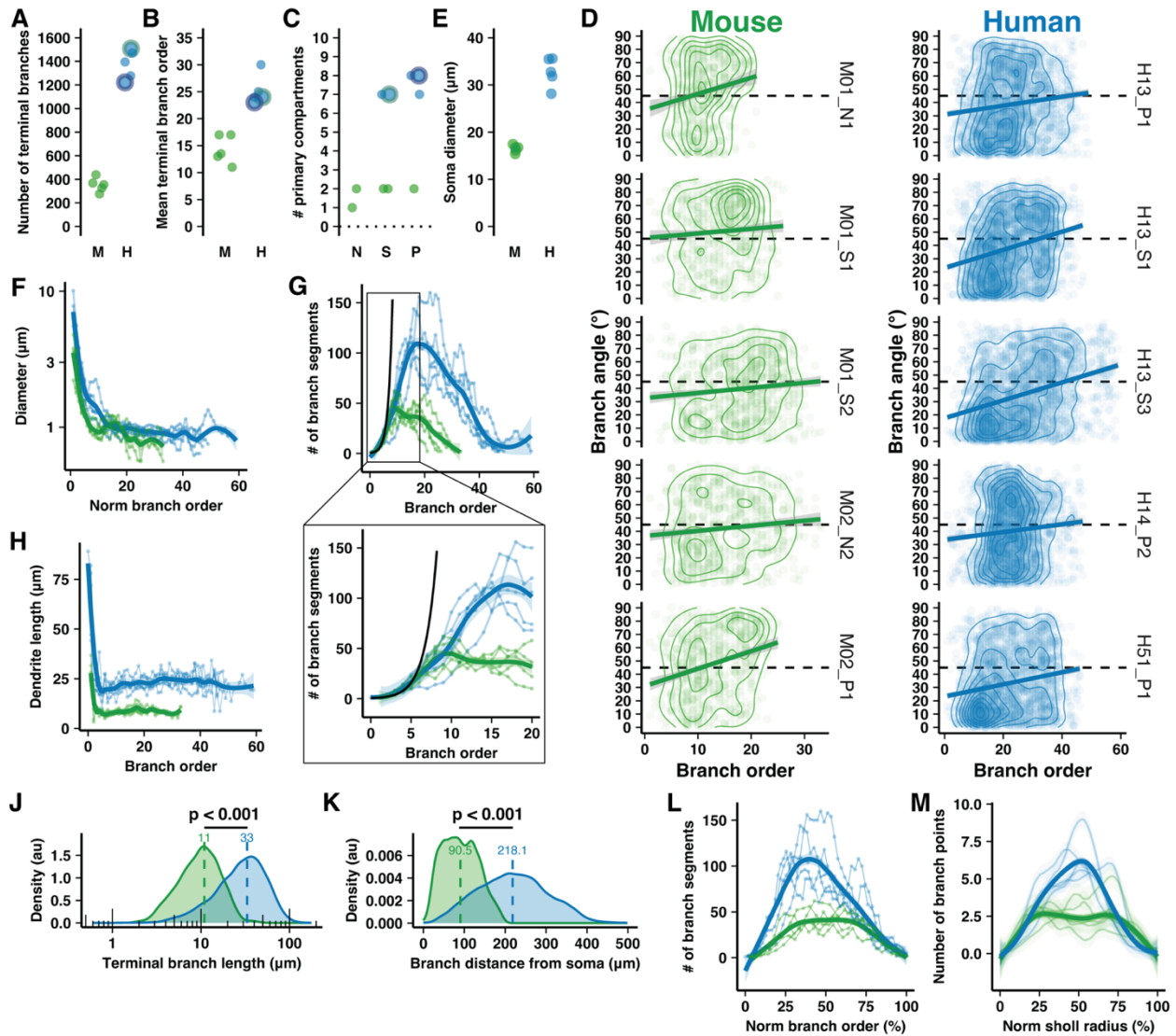
Figure S13. Additional morphological data from digital reconstructions. A) Number of branch points by species. **B)** Maximum number of branch points, regardless of whether the branching is symmetrical or reduces diameter such as would define a change in dendrite caliber, between the terminal segments and the soma. **C)** Number of primary dendrite compartments, defined as the number of thick dendritic sections giving rise to only thin caliber branches, by the morphological category of each reconstructed PC. **D)** Distribution of branch eccentricities as a function of branching order for each reconstructed PC. **E)** Somatic diameters. **F)** Mean branch diameter by order. **G)** Distribution of total branch segments in each branching order. A reference symmetrical fractal pattern is represented by the function $y=2^{x+1}$ (black line). The right panel zooms in on the early branching orders. **H)** Distribution of mean dendritic length across branches of each order. **I)** As in **(F)** but normalizing for maximum branch order. **J)** Distribution of terminal

branch segment lengths (Mann-Whitney U test; n = 6883,1773 branches). **K)** Branch distances from the soma (Mann-Whitney U test; n = 12885,3180 branches). **L)** Distribution of branch segments by branch order as in Fig. 8M but without normalizing segment number across species. **M)** Distribution of branch points by normalized Sholl distance from the soma.
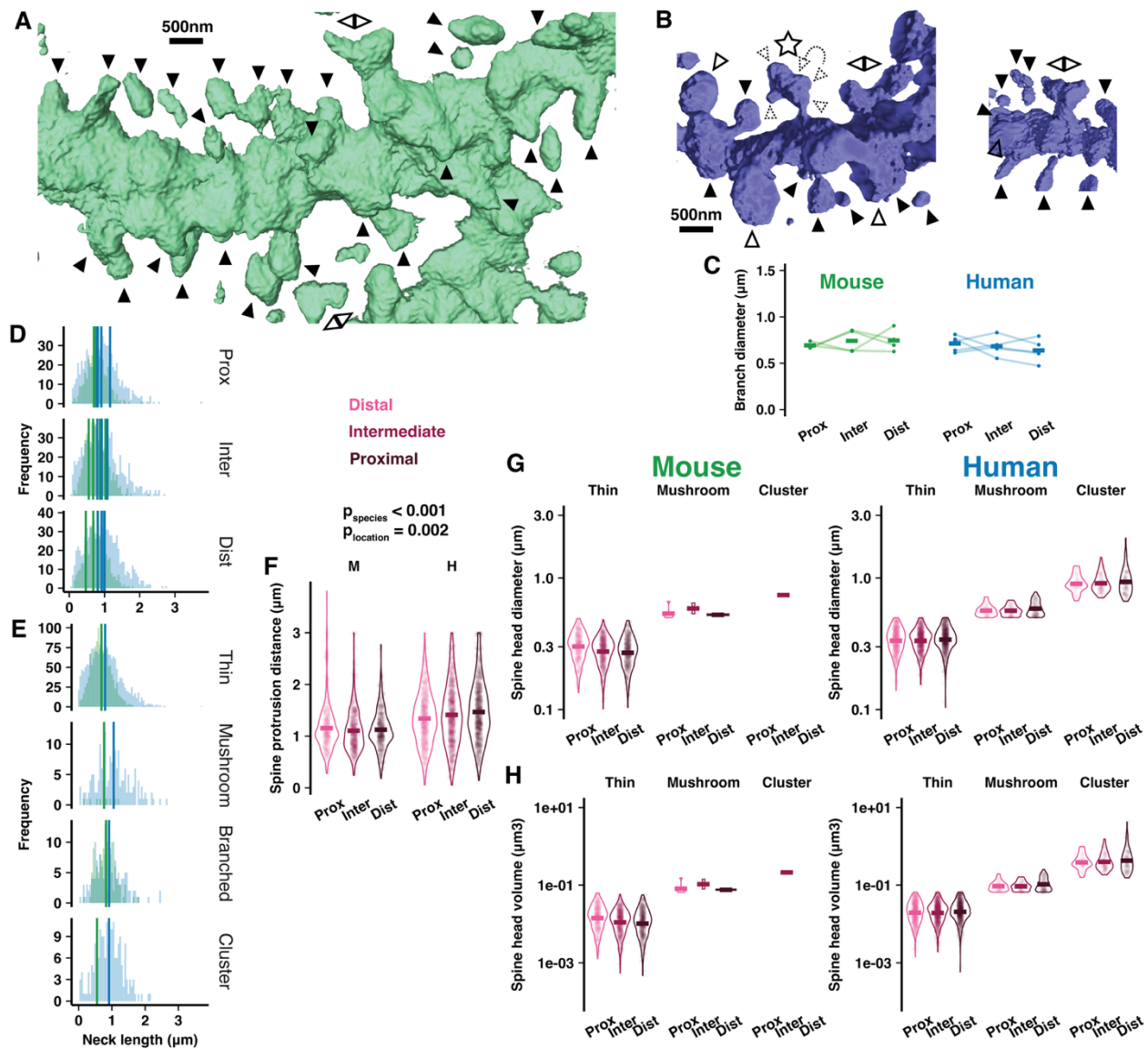
Figure S14. Additional data from digitally reconstructed spines. A) Example slice from a confocal z-stack scan of a spiny dendritic branch and the 3D reconstruction of this branch in the mouse. **B)** Example slice from a confocal z-stack scan of a spiny dendritic branch and the 3D reconstruction of this branch in the mouse. All images on the same scale. **C)** Diameter of all dendritic banches reconstructed in this study. Lines connect the compartments across each cell (n = 4,5 individuals). **D)** Distributions of spine neck lengths by location and species. **E)** Distribution of spine neck lengths by spine type and species. **F)** Spine protrusion distance, measured from the edge of the dendritic shaft to the distal tip of the spine head, in human and mouse (ANOVA, Tukey's HSD; n = 720,818,862 spines, n = 376,528,476 spines). **G)** Spine head diameter by

spine type and location in mouse (top) and human (bottom). **H)** Spine head volume by spine type and location in mouse (top) and human (bottom).
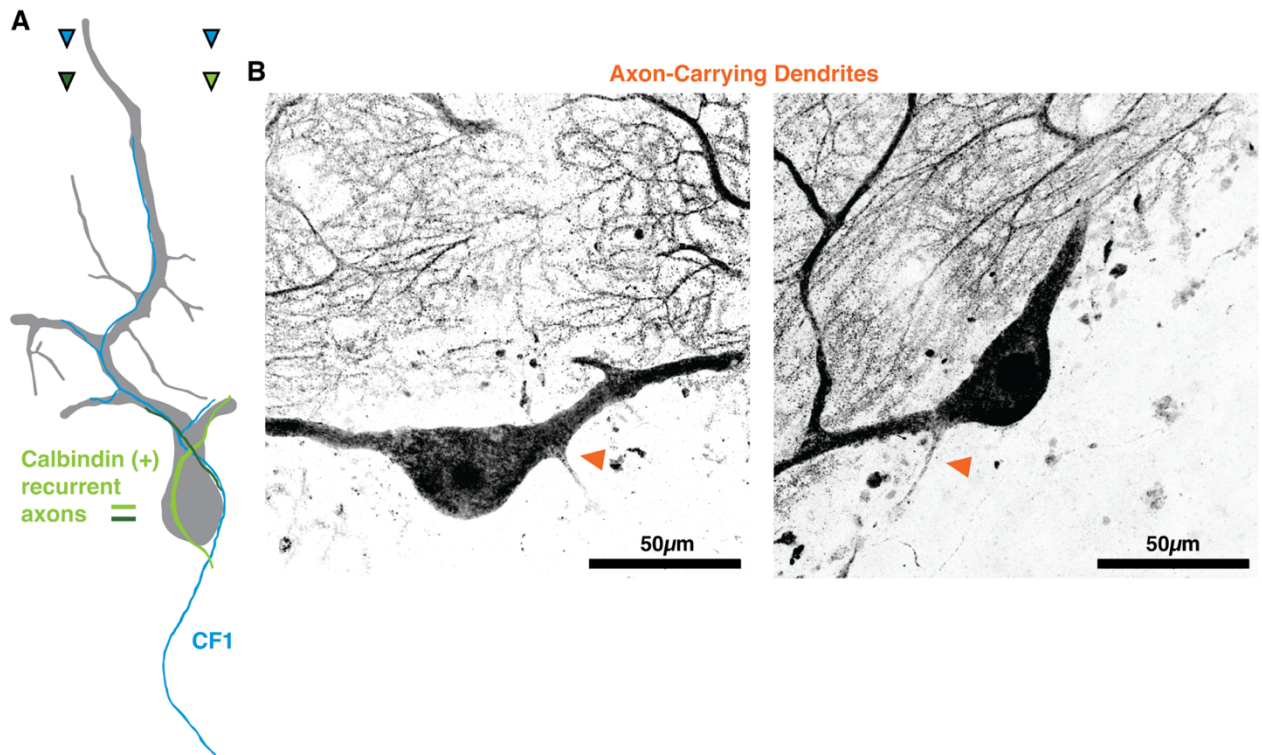
Figure S15. Human PCs with multi-dendritic and horizontally oriented morphology can avail themselves of additional branch specific capacities. A) Example masks from a digitally reconstructed PC (grey) and peripherin fiber (blue) on which two unconnected calbindin(+) PC axons (dark and light green) converge to innervate distinct dendritic compartments. **B)** Example z-projections of two horizontally oriented Poly PCs hosting axons that emerge from the dendrite or an intermediate zone between somatic and dendritic compartments (orange arrowheads).
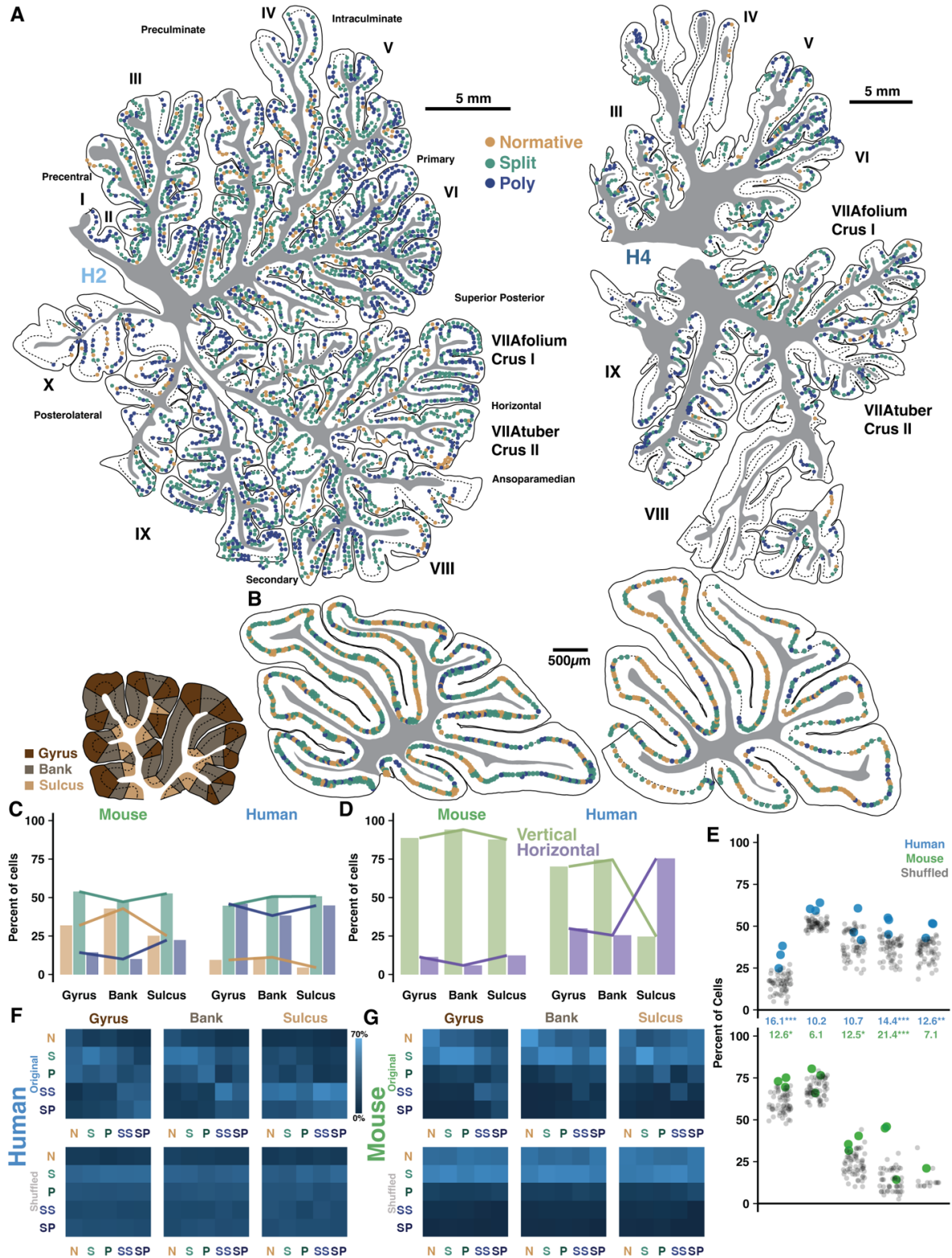
Figure S16. Additional reconstructions and analysis of PC demographics in parasagittal slices of vermis from human and mouse. A-B) Parasagittal human and mouse vermis

reconstructions demonstrating the spatial distributions of each morphological type. **C)** Schematic of foliar subdivisions into gyrus, bank, and sulcus (top) and the demographics of PC types by foliar area (bottom). **D)** Demographics of PC orientations by foliar area. **E)** Observed versus shuffled rate of PCs having the same morphologyical classification by cell type (as if Fig. 11E) when the shuffled data are constrained within foliar subdivision. **F-G)** Matrices of all cell type by cell type clustering likelihoods observed in the original data (top) and in the shuffled dataset (bottom) and separated by foliar area in human and mouse.
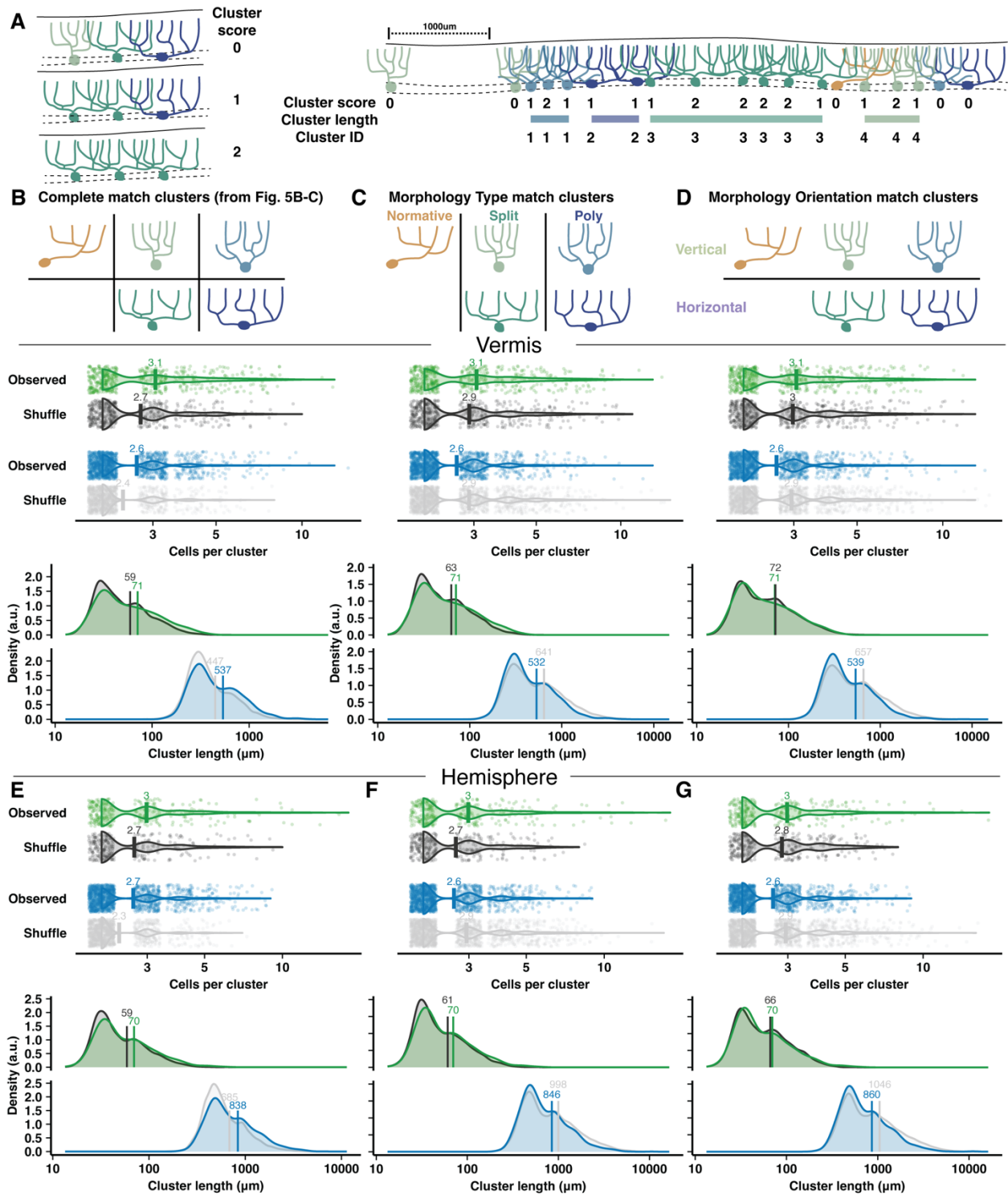
Figure S17. Adjacent PC demographics reveal the spatial scale of non-random morphological clustering among local PCs. A) Schematic of cluster score assignment for each PC based on whether the morphology of adjacent cells (<1000um away) matches (left) and the use of these scores to identify the number of PCs and parasagittal length of clusters of redundant

cell types (right). **B)** Number of cells (top) and length (bottom) of PC clusters with identical morphology (complete match with five cell categories: Normative, vertical Split, vertical Poly, horizontal Split, horizontal Poly) in mouse and human with that of shuffled data in which morphologies are randomly resorted while cell locatiuon is held constant. **C-D)** As in **(B)**, but for PC clusters with only a partial match based on cell type (Normative, Split, or Poly; for example, vertical and horizontal Split PCs are a match) or cell orientation (Vertical or Horizontal; for example, horizontal Split PCs and horizontal Poly PCs are a match). **E-G)** As in **(B-D)** for PCs in slices from mid-hemisphere.
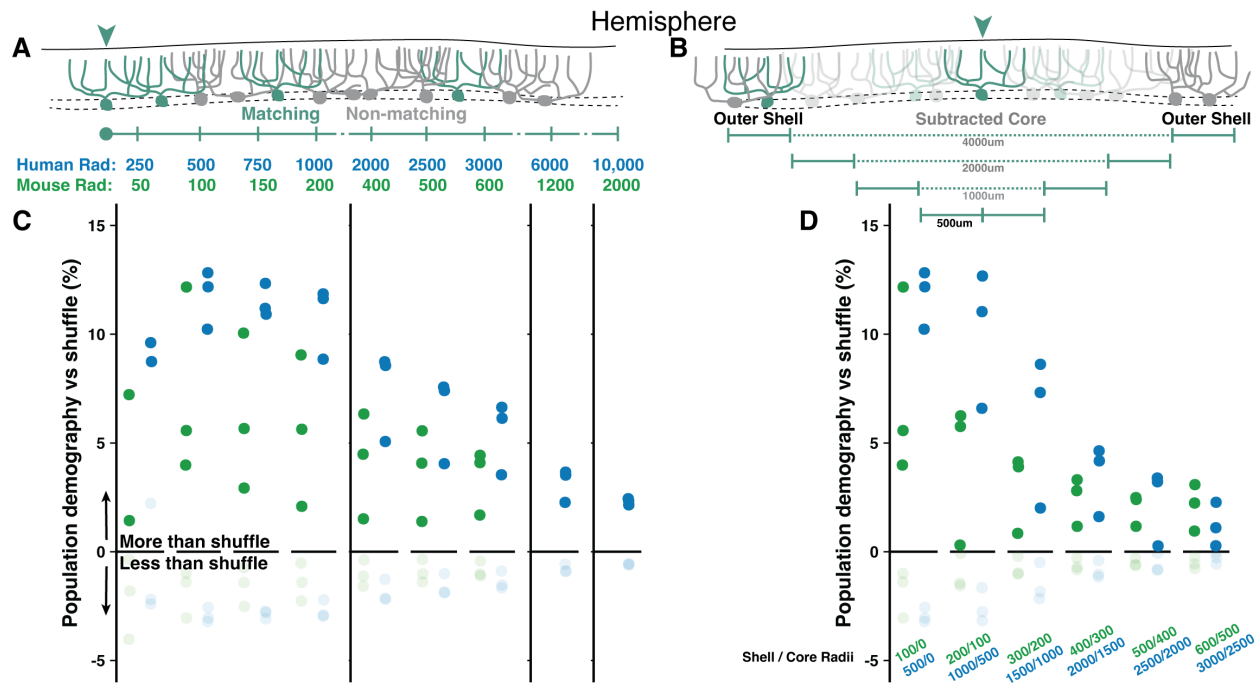
Figure S18. Population PC demographics reveal the spatial scale of non-random morphological clustering among parasagittal PC circuits. A) Schematic of how various radius distances are used to survey the demographics of all cells within a given distance from a PC (top). Radii used in the mouse are set to 20% that of the human, matching the difference in the width of a mouse vs human PC. The rate of PCs with matching morphology (using a complete match across five categories) is compared with the same measurement of shuffled data to generate a difference between the observed vs shuffled percents of cells with a matching morphology (dark points) compared to non-matching morphologies (light points) in human and mouse (bottom). Points mark the average demographic difference between observed and shuffled rates across all five cell groups (i.e. one dark point represents the average for matching cell rates of Normative to Normative, Split to Split, etc.). **B)** To measure the absolute spatial scale of elevated PC clustering, we measure the observed vs shuffled rate for 500um increments of a shell region around a growing core. By ignoring the morphologies of the core region, we control for the effect of highly local clustering on the measurement of more distant PCs. This reveals that non-random morphological clustering appears to drop off at distances of ~1500um and 300um in human and mouse, respectively.
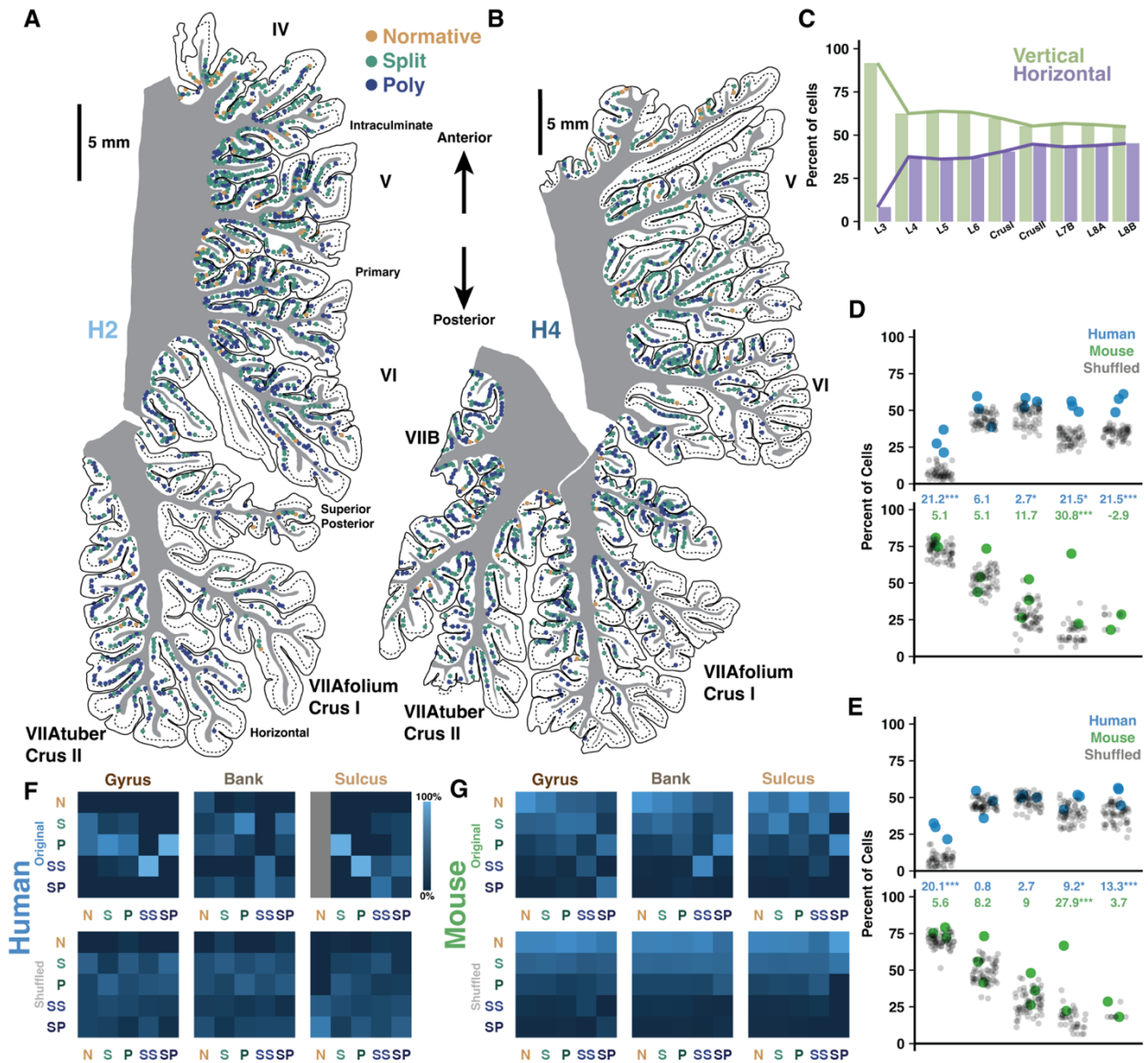
Figure S19. Additional reconstructions and analysis of PC demographics in parasagittal slices of the mid-hemisphere of human. A-B) Parasagittal reconstructions of lobules 5-Crus II of the opposing hemispheres of human specimens used previously, demonstrating the spatial distributions of each morphological type. **C)** Distribution of PCs across lobules of the mid-hemisphere by cell orientation (as in Fig. 11B). **D)** Observed versus shuffled rate of adjacent PCs having the same morphologyical classification by cell type in human (top) and mouse (bottom). **E)** As in **(D)**, but with shuffled morphologies being constrained within foliar subdivision (e.g. PCs in the sulcus are only shuffled among each other, not also with PCs in the bank or gyrus). **F-**

G) Matrices of all cell type by cell type clustering likelihoods observed in the original data (top) and in the shuffled dataset (bottom) and separated by foliar area in human and mouse.

Function	**Motor** Hand and lower body	**Oculomotor Attention** Text, movie, visual search Multiple body movements	**Multiple-Demand** Executive function, working memory load, mental rotation	**Multiple-Demand Social-Linguistic- Spatial**
Cerebellar Region	Hemisphere L1-5	Vermis L3-8	Vermis L1-2,9-10	Hemisphere L6-8
Cell Morphology	Low Poly Low Horizontal	Low Poly High Horizontal	High Poly Low Horizontal	High Poly High Horizontal

Figure S20. Human cerebellar regional borders as defined by morphological demographics or functional imaging. The top and bottom arrays provide four regional sub-divisions according to either involvement in behavioral tasks(Nettekoven et al., 2024) or PC morphological demographics. The middle row indicates the lobules corresponding to both the above functional and below morphological sub-divisions.

CHAPTER 4: COMPARATIVE MORPHOLOGY OF CEREBELLAR PURKINJE CELLS

REVEALS AN EVOLUTIONARY TRAJECTORY OF ENHANCED DENDRITIC COMPLEXITY

IN HUMANS

ID	Species	Common Name	Source	Rearing	Sex	DOB	DOD	Age (yrs)
Lori	Pan paniscus	Bonobo	Jacksonville Zoo	Hand	F	11/4/87	circa 2018	31
Unga	Pan paniscus	Bonobo	Columbus Zoo		F	2/22/93	3/5/21	28
Wanto	Gorilla gorilla	Gorilla	Knoxville Zoo	Hand	M	12/14/76	4/21/21	44.4
Jackie	Gorilla gorilla	Gorilla	Fort Worth Zoo	Hand	F	6/3/90	4/7/21	30.8
Lash	Gorilla gorilla	Gorilla	Jacksonville Zoo	Hand	M	12/25/76	12/01/22	45.9
Gimpy	Pongo pygmaeus	Bornean orangutan	Pittsburgh Zoo	Wild	M	1/1/66	8/16/05	39.6
Melati	Pongo abelii	Sumatran orangutan	Woodland Park Zoo	Captive	F	12/27/71	12/14/21	49.9
Carl	Pan troglodytes	Chimpanzee	Yerkes	Nursery	M	5/21/86	4/22/21	34.9
Binti	Pan troglodytes	Chimpanzee	Knoxville Zoo	Other - Captive Birth	F	11/8/84	6/29/23	38.8
880211	Symphalangus syndactylus	Siamang	Cleveland Metroparks Zoo		F	1/30/83	11/20/09	26.8
Asia	Nomascus leurogenys	Northern white-cheeked gibbon	Virginia Zoo	Wild	F	1/1/77	2/10/22	45.1
Mae	Nomascus leurogenys	Northern white-cheeked gibbon	National Zoo	Wild	F	1/1/70	4/8/13	43.3
23108	Macaca mulatta	Rhesus macaque	Oregon National Primate Center		M			13
25257	Macaca mulatta	Rhesus macaque	Oregon National Primate Center		M	1/15/05	4/1/15	10.2
Brandy	Macaca mulatta	Rhesus macaque	Bensmaia-Uchicago		F			
Oda	Papio anubis	Olive baboon	University of Aix-Marseille		F	4/1/98	2/17/09	10.9
146	Papio anubis	Olive baboon			M			11
31765	Callithrix jacchus	Common marmoset	Trinity College		M	3/30/12	10/1/14	2.5
Pat	Callithrix jacchus	Common marmoset	Hatsopolous-Uchicago					
120901	Callithrix geoffroyi	White-faced marmoset	Cleveland Metroparks Zoo		M	3/12/06	8/18/14	8.43
N98-25 Ag	Ateles geoffroyi	Black-handed spider monkey			F			25
H13	Homo sapiens	Human	AGAI		F			92
T6051	Homo sapiens	Human	NYBB		M			47

Table S11. Specimen demographics.

Measurement Name	Definition	FIJI Tool Used	Example (N,S)	Example (P)
Soma Circumference	Segmented line outlining the edge of the PC soma.	Segmented Polygon (length)		
Soma Area	Area enclosed by segmented outline of the PC soma.	Segmented Polygon (area enclosed)		
Arc to Axon	Segmented line outlining top of the soma from the edge of one side of trunk (N, S) or edge of first trunk (P) to PC axon.	Segmented Line		
Arc Complete	Segmented line outlining top of the soma from the edge of one side of trunk (N,S) or edge of first trunk (P) to other side of trunk (N,S) or edge of second trunk (P).	Segmented Line		
Split Distance	Segmented distance from apex of soma to first dendritic birfucation.	Segmented Line		*n/a*
Second Bifurcation Distance(s)	Segmented distance from first dendritic bifurcation to second dendritic bifurcation.	Segmented Line		
Trunk Thickness(es)	Width of dendritic trunk (N,S) or trunks (P).	Straight Line		
Trunk Separation(s)	Straight line distance between center of mass of primary dendrites.	Straight Line		
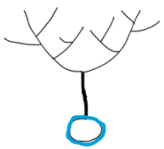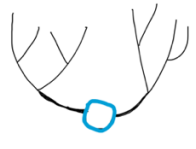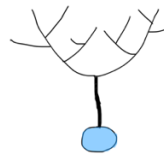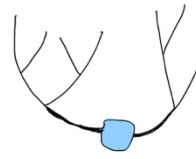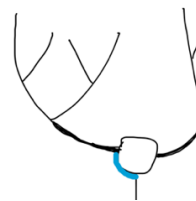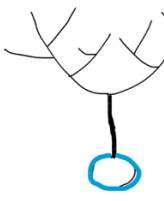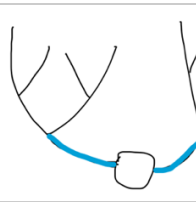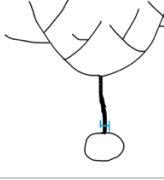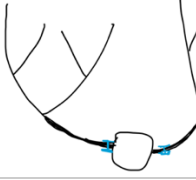
Table S12. PC morphology measurement definitions.

Measurement Name	Definition	FIJI Tool Used	Example (N,S)	Example (P)
Split Angle	Angle of first dendritic bifurcation in N,S PCs.	Angle		*n/a*
Poly Angle	Angle enclosed by outermost poly dendrites in P cells.	Angle	*n/a*	
Secondary Bifurcation Angle(s)	Angle enclosed by second dendritic bifurcation.	Angle		
Secondary Angle(s)	"Goalpost" angle enclosed by the line from base of dendrite to first dendritic bifurcation and line from first dendritic bifurcation to the dendrite's center of mass.	Angle		
Curvy	Cells were classified as curvy if one of more primary dendrite curved over itself in an "S" shape prior to the first dendritic bifurcation.	*n/a*		
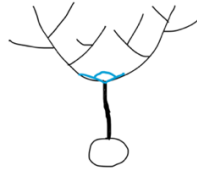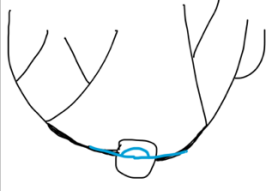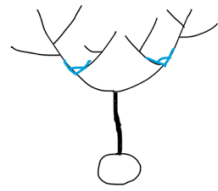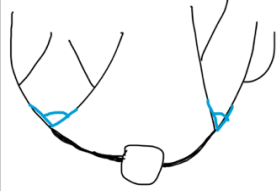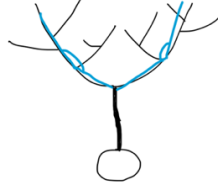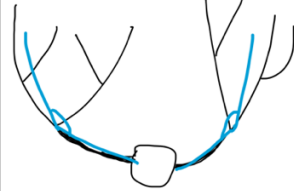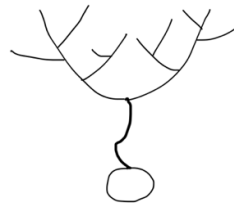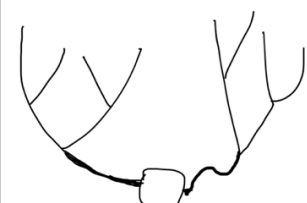
Table S12. PC morphology measurement definitions. (continued)

PART 1: Sensory Over-responsivity and Aberrant Plasticity in Cerebellar Cortex in a Mouse Model of Syndromic Autism
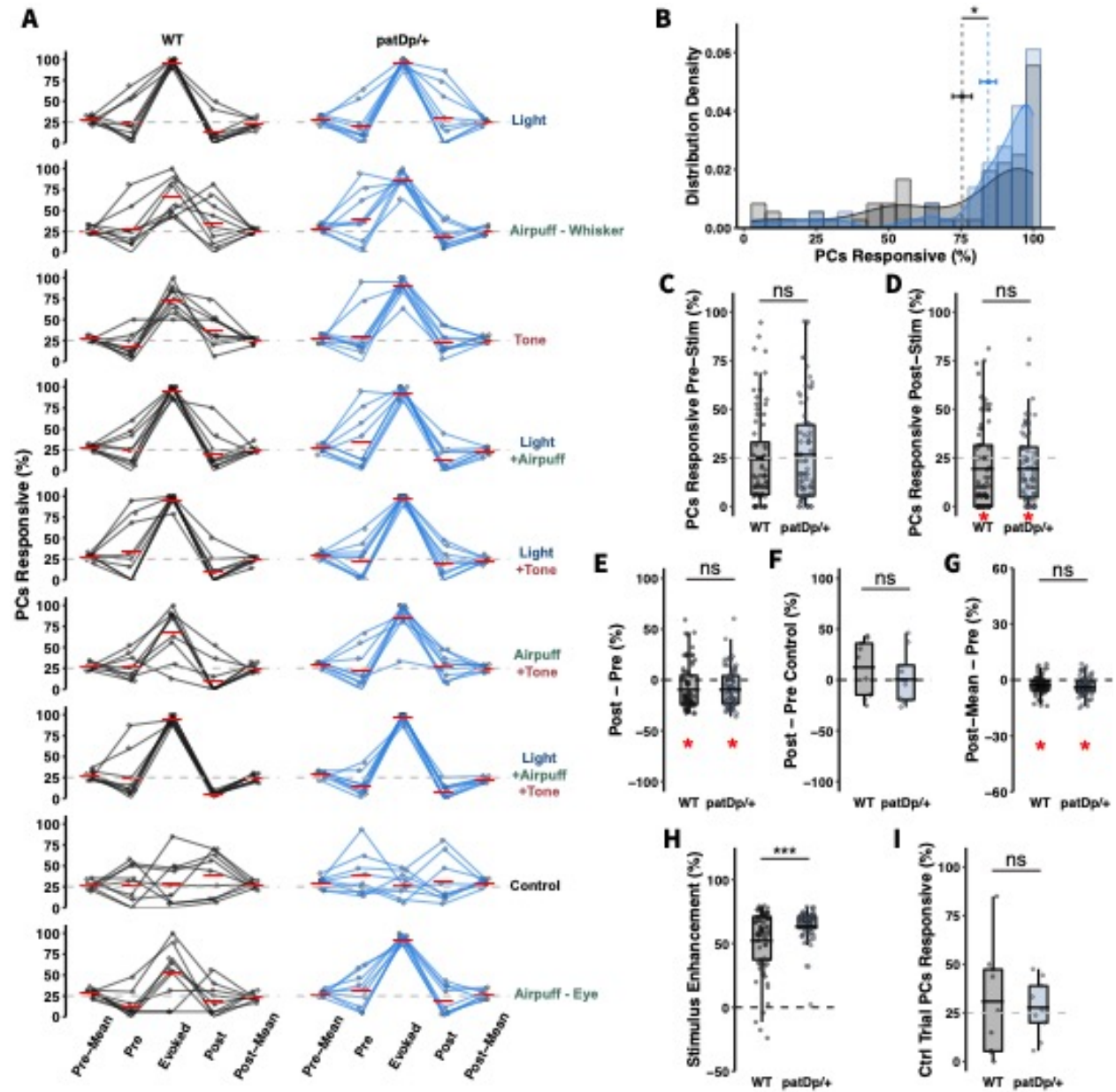
Figure S21. Percent of cells responding to multisensory stimulation. (A) Percent of cells in a field of view producing an evoked response in the 240ms window during early trials of all

stimulus types. Percent responsive is calculated for 240ms time bins across the recording session. "Pre" category indicates the percent of cells active during one time window ending 480ms before the stimulus, while "Post" indicates the percent of cells active during one time window 480ms after the end of the Evoked time window. "Pre-Mean" and "Post-Mean" indicate the average of thirty bins (7.2sec) before and after the stimulus. The grey dashed lines indicate the prediction that 25% of independently active cells with an average event rate of ~1Hz are expected to be active at baseline during a 240ms time window. **(B)** Probability density distribution of percent of cells that are responsive during the evoked time window across stimulus trials (recapitulates data in Fig1g). Vertical dashed lines with point and error bar markers indicate the mean ± SEM in WT vs patDp/+ animals (75.37 ± 3.32% vs 84.38 ± 2.78%, respectively; p = 0.0394). **(C)** Percent of cells active during a Pre-stimulus (spontaneously active) time window. One-sample t-test reveals neither genotype distribution is statistically different from the 25% predicted (24.62 ± 2.8 vs 27.34 ± 3.07%; n = 72, 72; p = 0.891, 0.448), and the genotypes are not different from each other (p = 0.513). **(D)** On the other hand, the percent of cells active during a post-stimulus time window is statistically lower than the predicted value (19.31 ± 2.6 vs 20.16 ± 2.18%; n = 72, 72; p = 0.032, 0.029). The two groups are not different from each other, indicating that this post-stimulus suppression is not genotype dependent (p = 0.802). **(E)** As could be expected from the equivalence of genotypes in FigS1c+d, both groups show a significant, and statistically equivalent, decrease in activity during the early post- stimulus time window (-8.27 ± 2.66% vs -8.24 ± 2.23% relative to pre-stim in WT vs patDp/+ respectively; n = 72, 72; p = 0.0027, 0.00044). **(F)** In control trials, this suppression is not observed in WT or patDp/+ mice (12.84 ± 9.16% vs 1.73 ± 8.92%; n = 9, 9; p = 0.199, 0.851). **(G)** Expanding the analysis past the early post-stimulus period (480-720ms) to the average of time windows for 7.2s post-stimulus, we continue to observe a small, but significant, suppression of activity relative to pre-stimulus (-2.91 ± 0.55% vs -3.38 ± 0.57%; n = 72, 72; p = 1.5×10^{-6}, 8.4×10^{-8}). **(H)** As could be expected from the higher evoked responsiveness of patDp/+ cells in Fig1g, and the equivalence of the pre-stimulus activity in FigS1c, the change in percent of cells responsive from the average pre-stimulus time window to the evoked window shows greater enhancement from baseline due to sensory stimulation in patDp/+ mice than WTs (increase of 64.27 ± 1.35% vs 53.17 ± 2.89%; n = 72, 72; p = 0.00075). **(I)** In control trials, there is no increase in cellular activity during the evoked response time window in WT or patDp/+ mice (30.86 ± 9.34% vs 27.76 ± 4.9%; n = 9, 9;

p = 0.548, 0.589). *p < 0.05, **p < 0.01, ***p < 0.005. Boxplots show mean line with interquartile range (IQR). Boxplot error bars show the least extreme of either the highest and lowest values or mean ± (1.5 x IQR). All data are noted in the text and legends as mean ± SEM.
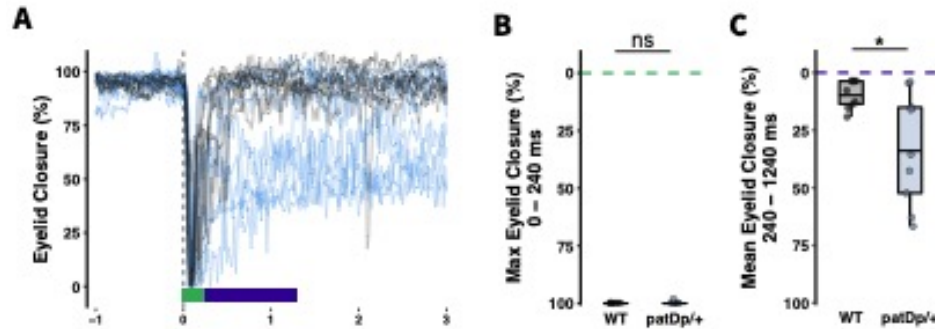
Figure S22. While all mice produce full blinks during each eyepuff trial, patDp/+ mice show a more persistent closure of the eye. (A) Maximum and minimum value normalized distance between the top and bottom eyelid of the ipsilateral eye during eyepuff trials. Green and purple bars below the trace indicate the ranges of evoked response and post-response time windows. **(B)** All mice, regardless of genotype, performed a full blink in every trial, as measured by maximum eyelid closure in the evoked response window 0 - 240ms after stimulus (WT: $100 \pm 0\%$ vs PD: $99.79 \pm 0.21\%$; n = 9, 9; p = 0.35). **(C)** Calculating the mean eye closure for one second after the evoked response window (240-1240ms) reveals a persistent partial eye closure in patDp/+ animals not present in WTs ($90.77 \pm 2.03\%$ vs $66.68 \pm 8.12\%$; n = 9, 9; p = 0.018). *p < 0.05, **p < 0.01, ***p < 0.005. Boxplots show mean line with interquartile range (IQR). Boxplot error bars show the least extreme of either the highest and lowest values or mean $\pm$ (1.5 x IQR). All data are noted in the text and legends as mean $\pm$ SEM.
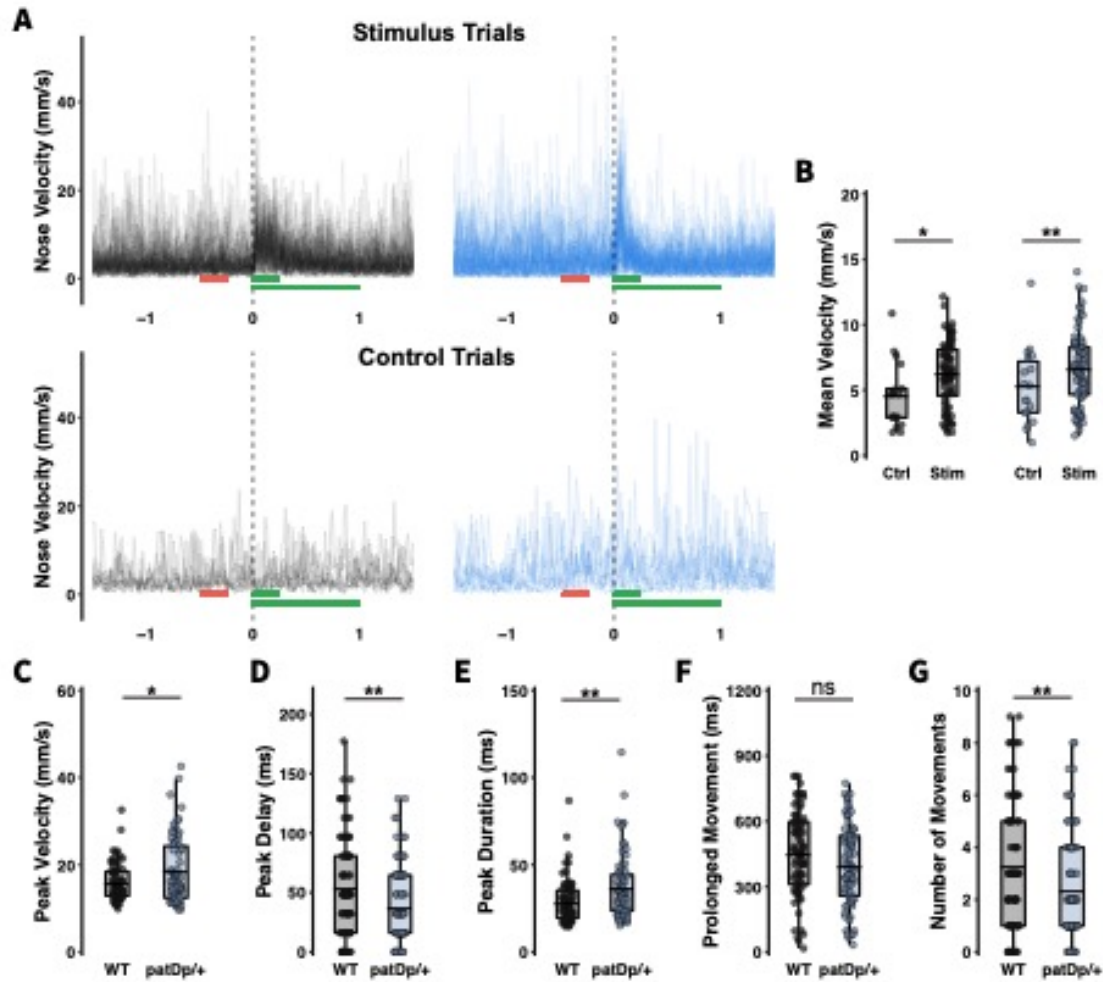
Figure S23. PatDp/+ mice show faster, higher amplitude, and longer duration initial nose movements in response to stimulus. (A) Traces showing the instantaneous velocity of nose movement before and following sensory stimulation. Trials for all stimulus types are pooled in the top traces to demonstrate generalized sensory responses, not modality dependent response profiles. Control trials are shown in the bottom traces. Top red and green bars indicate pre-stimulus and evoked response time windows used for calculations in (B), and bottom green bar indicates the time window used to measure response features in (C-G). **(B)** We calculated change in mean nose velocity from a 240ms time window pre-stimulus to a 240ms evoked response time window and compared between stimulus and control trials to confirm that increased nose movement is dependent on the presence of a stimulus in both genotypes (WT Control vs Stim: p = 0.0204; patDp/+ Control vs Stim: p = 0.0057). **(C)** PatDp/+ mice exhibit a larger magnitude of nose movement, as measured by the peak nose velocity during the 240ms evoked response time

window, than WT animals (18.51 ± 0.85mm/s vs 15.92 ± 0.49mm/s, respectively; n = 81, 78; p = 0.015). **(D)** PatDp/+ mice also perform stimulus response nose movements more rapidly than WTs, as shown by the shorter delay to peak nose velocity (37.44 ± 3.62ms vs 54.38 ± 4.89ms, respectively; n = 81, 78; p = 0.0061). **(E)** In addition to initiating more quickly, patDp/+ nose movements last longer than that of WT mice (37.07 ± 2.08ms vs 28.79 ± 1.47ms, in patDp/+ and WT mice respectively; n = 81, 78; p = 0.003). **(F-G)** PatDp/+ mice exhibit changes in nose position for the same total time (398.25 ± 20.64ms vs 452.65 ± 21.82ms), but over fewer movement events (2.32 ± 0.22 vs 3.371 ± 0.3; n = 81, 78) than WTs over a 1s time window following the initial response (p = 0.072; p = 0.0061). *p < 0.05, **p < 0.01, ***p < 0.005. Boxplots show mean line with interquartile range (IQR). Boxplot error bars show the least extreme of either the highest and lowest values or mean ± (1.5 x IQR). All data are noted in the text and legends as mean ± SEM.
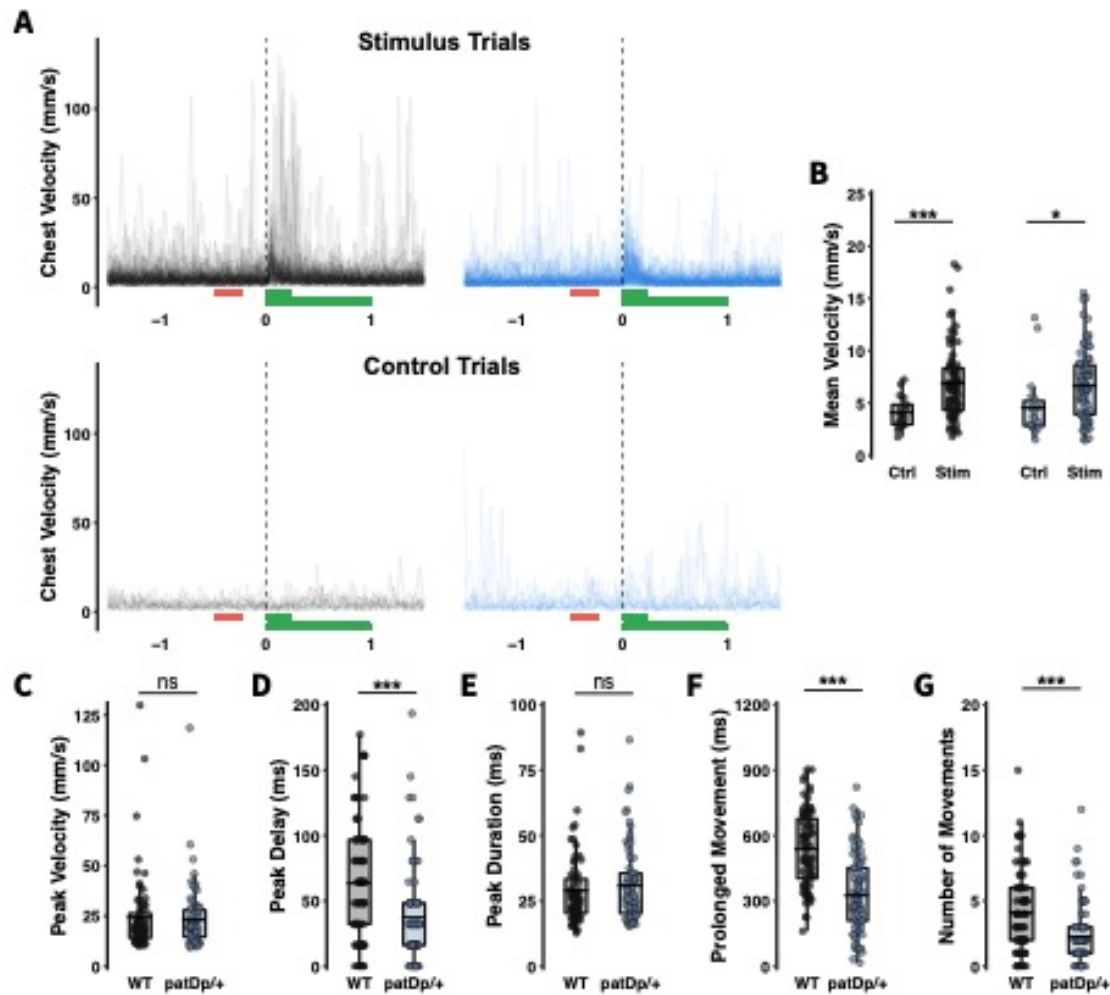
Figure S24. PatDp/+ mice exhibit a similar, but faster, movement of the chest in response to sensory stimulation. (A) Traces showing the instantaneous velocity of chest movement before and following sensory stimulation. Trials for all stimulus types are pooled in the top traces to demonstrate generalized sensory responses, not modality dependent response profiles. Control trials are shown in the bottom traces. Top red and green bars indicate pre-stimulus and evoked response time windows used for calculations in (B), and bottom green bar indicates the time window used to measure response features in (C-G). **(B)** Change in mean chest velocity from 240ms baseline to stimulus time window compared between stimulus and control trials confirm increased chest movement is dependent on the stimulus in both genotypes (WT Control vs Stim: p = 0.0002; patDp/+ Control vs Stim: p = 0.028). **(C)** There is no observed difference in the magnitude of chest movement, as measured by the peak chest velocity during the 240ms stimulus response time window, between patDp/+ and WT animals (23.54 ± 1.77mm/s vs 24.34

± 2.23mm/s, respectively; n = 81, 78; p = 0.792). **(D)** Quantification of the delay to peak chest velocity reveals a more rapid response in patDp/+ animals (37.83 ± 4.09ms vs 66.17 ± 5.73ms, respectively; n = 81, 78; p = 0.000092). **(E)** There is no observed difference in the duration of the initial chest response between genotypes (31.31 ± 1.66ms vs 28.94 ± 1.62ms, in patDp/+ and WT mice respectively; n = 81, 78; p = 0.3449). **(F-G)** PatDp/+ mice exhibit changes in chest position for less time (333.73 ± 19.81ms vs 537.43 ± 19.93ms) and over fewer movement events (2.35 ± 0.25 vs 4.1 ± 0.36; n = 81, 78) than WTs over a 1s time window following the initial response (p = $1.78*10^{-11}$; p = 0.000092). *p < 0.05, **p < 0.01, ***p < 0.005. Boxplots show mean line with interquartile range (IQR). Boxplot error bars show the least extreme of either the highest and lowest values or mean ± (1.5 x IQR). All data are noted in the text and legends as mean ± SEM.
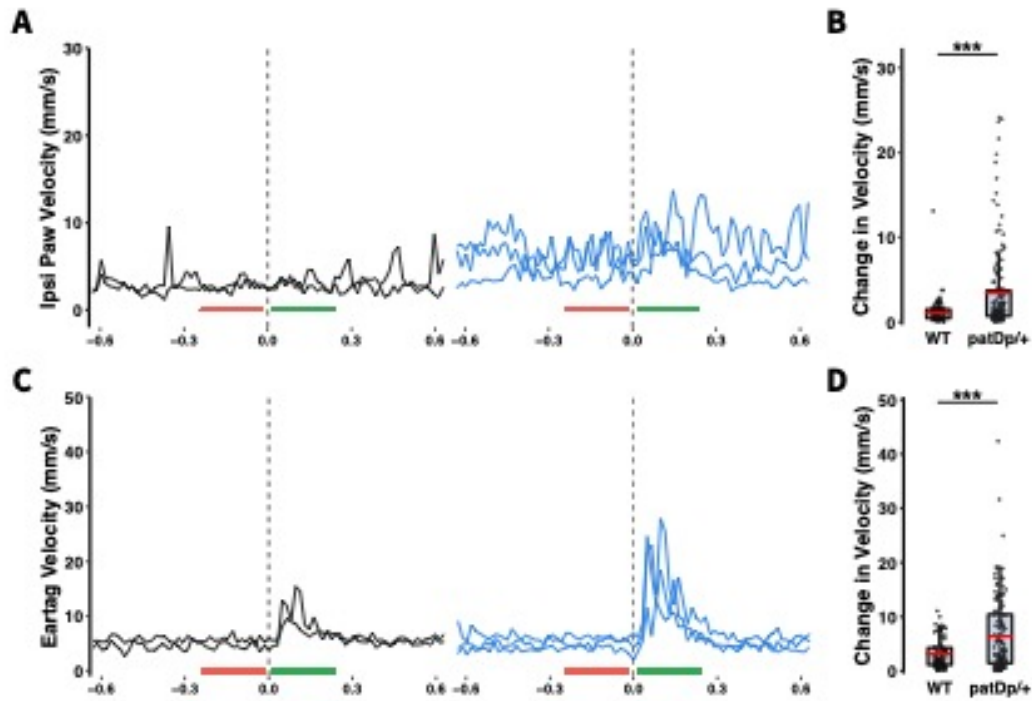
Figure S25. Object detection analysis reveals increased stimulus response movement of ipsilateral paw and eartag markers in patDp/+ mice. (A) Traces showing the instantaneous velocity of the ipsilateral paw before and following sensory stimulation. Trials for all stimulus types are pooled in each animal (n = 3, 3). **(B)** Difference in mean paw velocity between 240ms time windows before and after the stimulus shows a larger increase in mean paw velocity in patDp/+ mice than WTs (3.68 ± 0.48mm/s vs 1.68 ± 0.47mm/s; n = 129, 80; p = 0.003). **(C-D)** Given the posture of the body between the treadmill and paw bar during head fixation, each animals' eartag provided a useful proxy for the presence of movement, though not the nature or magnitude as precisely, in the trunk of the body. This movement could not otherwise be observed by the camera positioned front and center of the animal. Traces and quantification of the eartag velocity show increased movement of the body in patDp/+ animals relative to WTs (6.71 ± 0.61mm/s vs 3.23 ± 0.3mm/s; n = 130, 80; p = 7.3x10^{-7}). While care was taken to create an optimal training set for paw recognition, trials from one WT and one patDp/+ mouse were removed due to errant labeling in some trials. *p < 0.05, **p < 0.01, ***p < 0.005. Boxplots show mean line with interquartile range (IQR). Boxplot error bars show the least extreme of either the highest and lowest values or mean ± (1.5 x IQR). All data are noted in the text and legends as mean ± SEM.
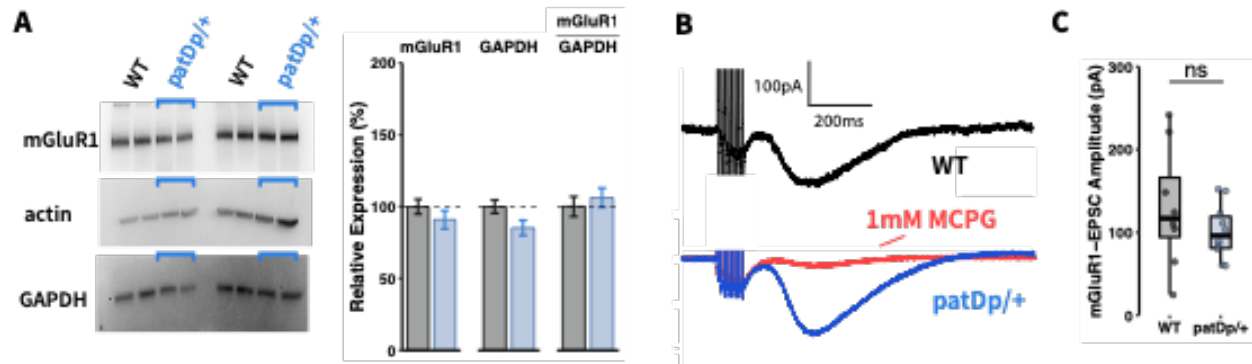
Figure S26. No genotype difference in mGluR1 protein expression or mGluR1 mediated current at PF synapses. (A) To test for alterations in mGluR1 expression levels, we performed western blot analysis. Expression of mGluR1 and GAPDH, relative to actin, shows no genotype differences (WT: $100.0 \pm 6.9\%$ vs patDp/+: $106.2 \pm 6.7\%$; n = 8, 8; p=0.83). **(B-C)**. Likewise, an electrophysiological correlate of mGluR1 activation at PF to Purkinje cell synapses – slow mGluR1-EPSCs following a burst stimulus – does not differ in amplitude in recordings from Purkinje cells obtained from WT (131.6 ± 20.5pA; n=10) and patDp/+ mice (101.2 ± 10.4pA; n=10; p=0.2123). Thus, our findings do not indicate any alteration in mGluR1 expression levels or function. Our western blot data suggest that this notion may extend beyond PF synapses and may also apply to mGluR1 receptors that are activated by CF activity. Application of 1mM MCPG, a non-selective antagonist of group I and II mGluRs, confirms this current is predominantly mediated by mGluRs. $*p < 0.05$, $**p < 0.01$, $***p < 0.005$. Boxplots show mean line with interquartile range (IQR). Boxplot error bars show the least extreme of either the highest and lowest values or mean $\pm$ (1.5 x IQR). Bar plots show mean $\pm$ SEM. All data are noted in the text and legends as mean $\pm$ SEM.
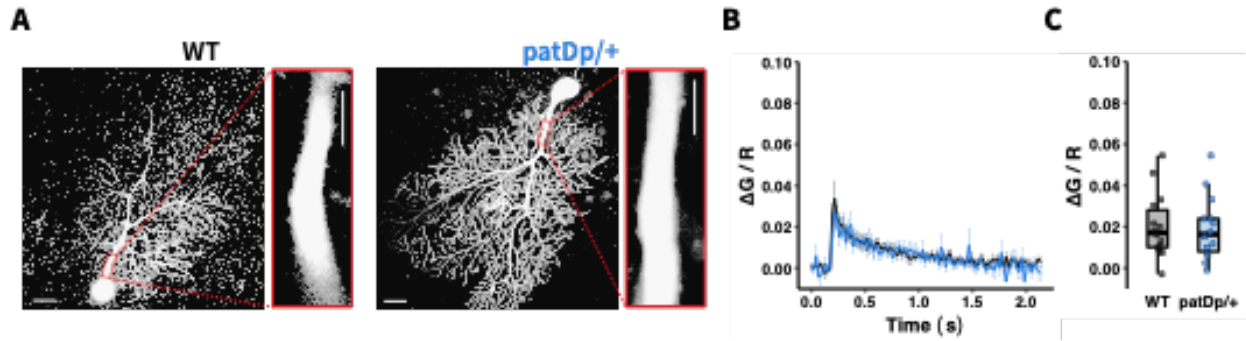
Figure S27. No detected genotype difference in primary dendrite Ca^{2+} amplitude during CF stimulation *in vitro*. (A) Representative images of WT and patDp/+ Purkinje cells filled with Fluo-5F (300µM) Ca^{2+} indicator and Alexa 633 dye. Red box indicates the primary dendritic area used for fluorescence quantification. Scale bars: 20µm (cell images) and 2µm (dendrite images). **(B)** Mean ± SEM traces of Ca^{2+} transients after CF stimulation for WT and patDp/+ primary dendrites (n = 14, 14). **(C)** Quantification of peak amplitude during a 200ms window following stimulus onset shows no difference in CF-induced primary dendrite Ca^{2+} signal in WT and patDp/+ animals in this recording confirmation (WT: 0.0204 ± 0.0042 ΔG/R vs patDp/+: 0.0191 ± 0.0041 ΔG/R; p = 0.8362). Boxplots show median line with interquartile range (IQR). Boxplot error bars show the least extreme of either the highest and lowest values or mean ± (1.5 x IQR). All data are noted in the text and legends as mean ± SEM.
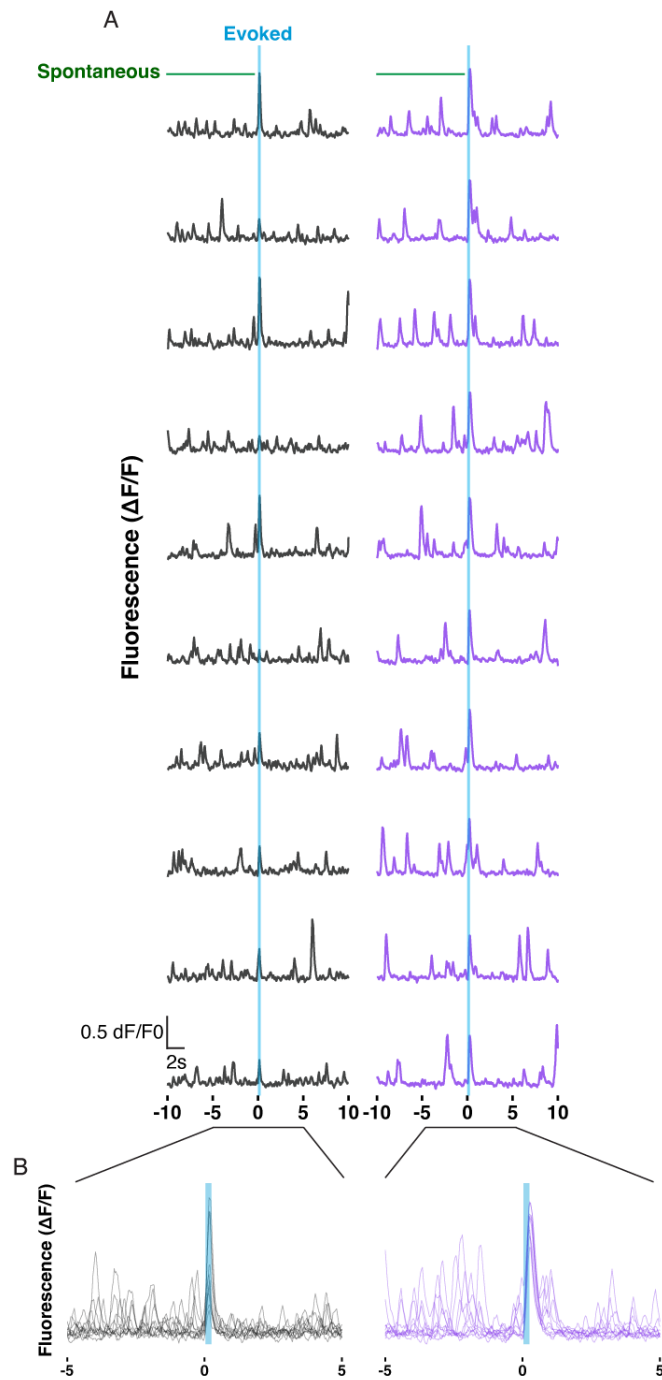
Figure S28. Sample raw traces across trials of light stimulus. (A) Responses to light stimulation presented with a 10s delay during each of ten 20s trials of stimulation from individual example WT and CYFIPOE cells. **(B)** Trial traces are overlaid for each cell in (A) to demonstrate the modest difference in average evoked amplitude.
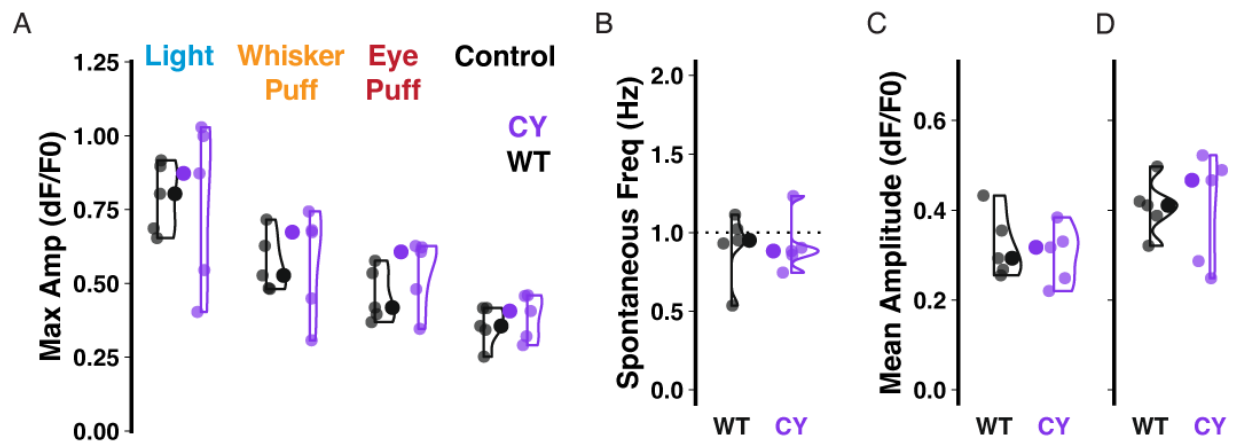
Figure S29. Multisensory responsiveness averaged by animal. (A-D) All cell data from Figure 30E,H,I,J averaged by animal. Large inset, hollow points indicate median while smaller points depict individual values.
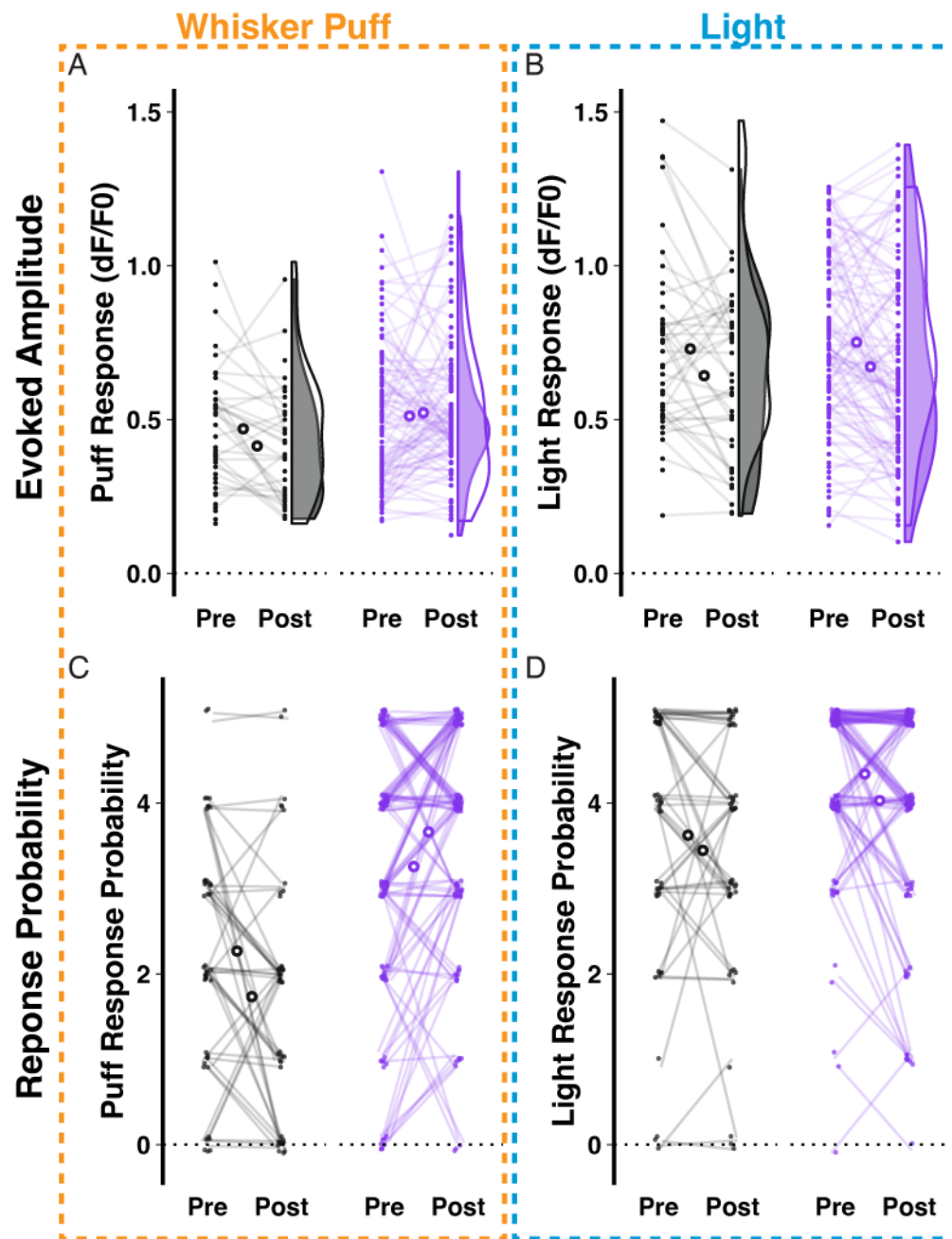
Figure S30. Un-normalized evoked Ca^{2+} amplitude and probability of response reflects the same effect of repeated exposure as observed with normalized data despite variable baseline responsiveness. (A-B) Raw Puff and Light evoked response dF/F0 values for each cell pre vs post. **(C-D)** Raw Puff and Light evoked response probability for each cell out of 5 trials during the first 20min before and after repeated exposure. For A-D, large inset, hollow points indicate mean ± SEM while smaller points depict individual values.
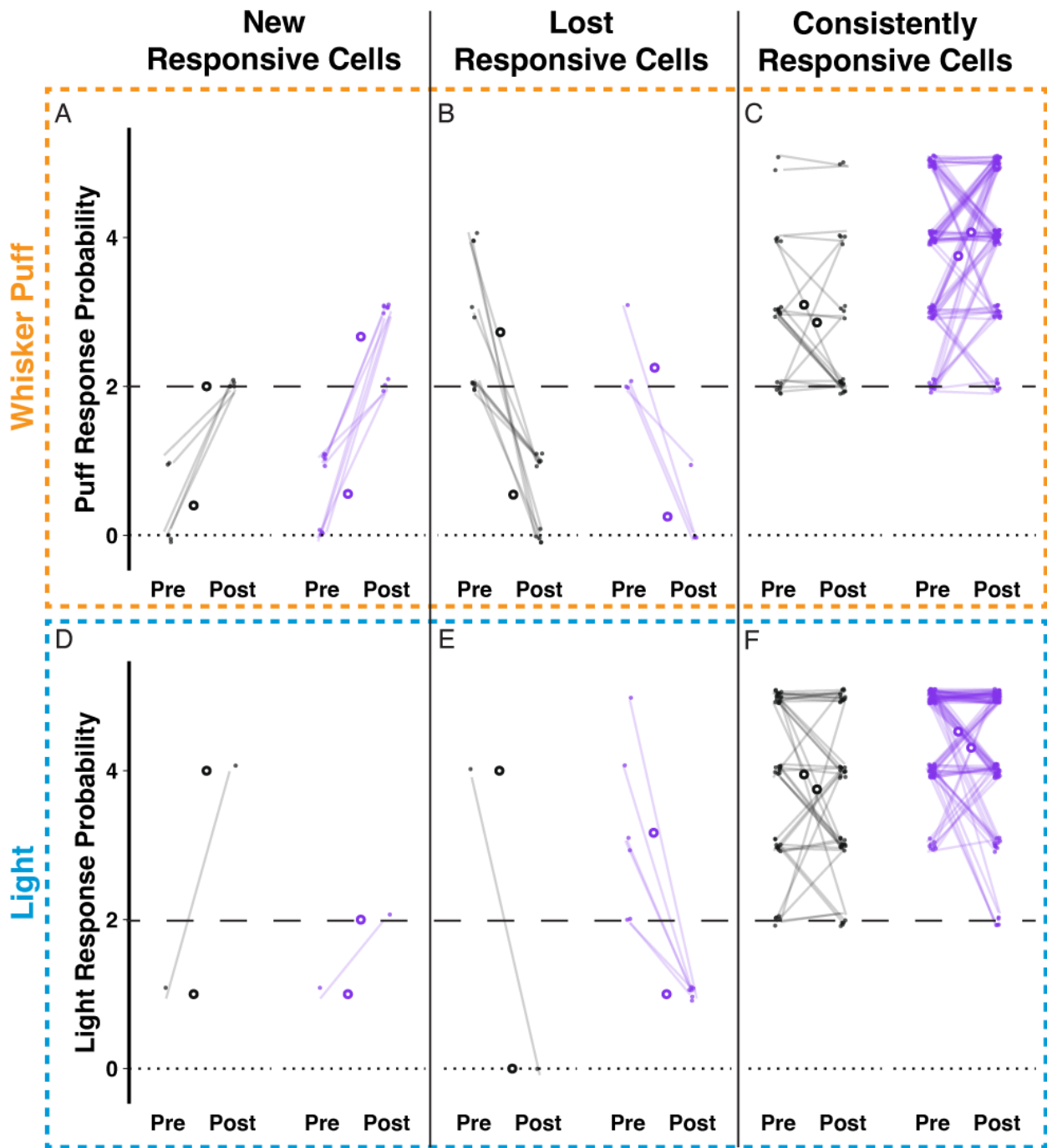
Figure S31. Effects of repeated sensory exposure by animal. (A-D) As in Figure 31A-D, but with cellular data averaged across each animal. Large inset, hollow points indicate median while smaller points depict individual values.
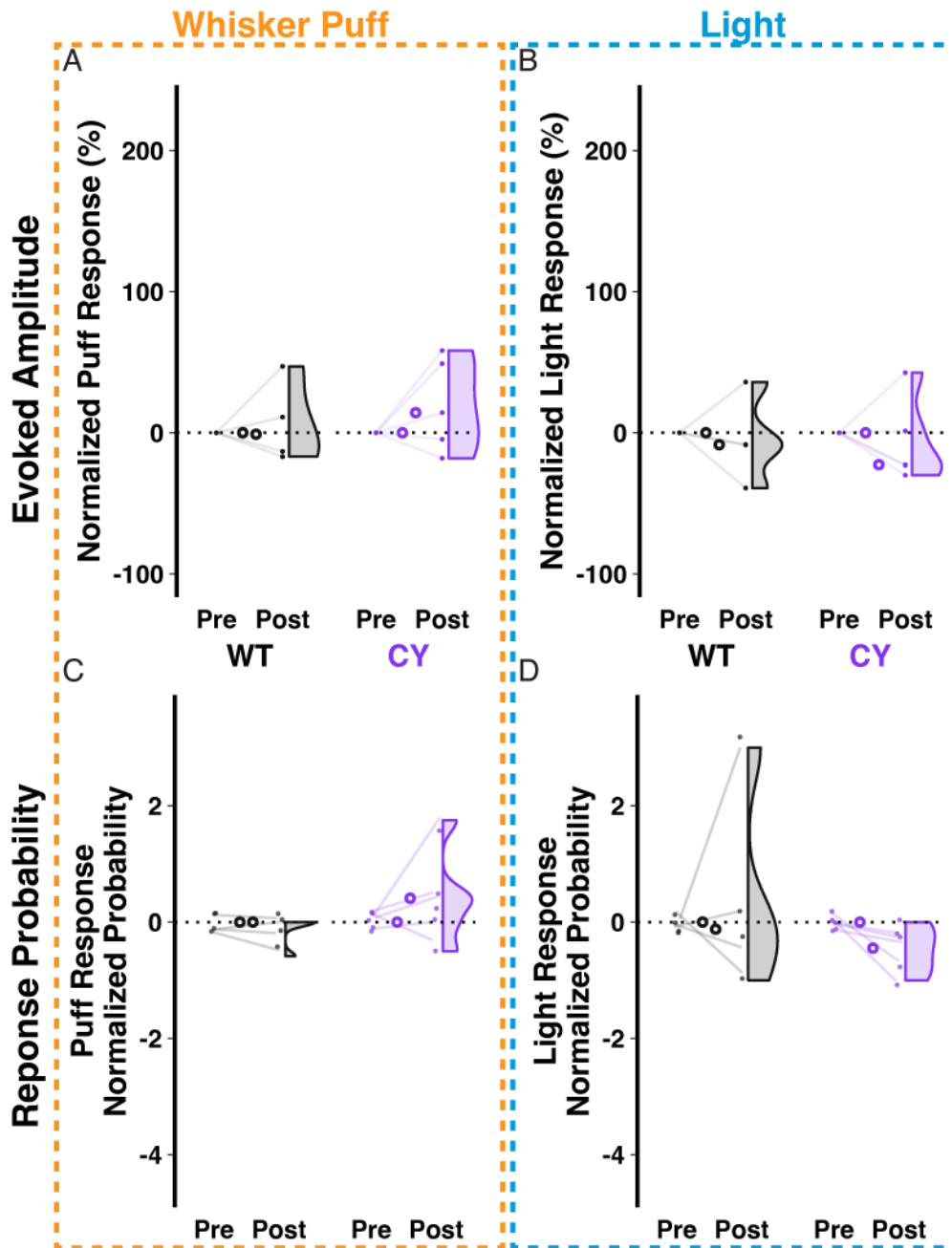
Figure S32. Genotype differences in population responsiveness are supported by changes across distinct types of cellular responsiveness. (A) More unresponsive CYFIPOE cells exhibit at least moderate responsiveness following repeated exposure than WT. Here, cells are defined as responsive if they exhibit more than one Ca^{2+} peak within the response window across 5 trials. This exceeds the ~1/5 chance that ~1Hz spontaneous events may be present during a 250ms response window. **(B)** Fewer responsive CYFIPOE cells exhibit a loss of detectable response

than among WT cells. (**C**) Among cells that are consistently responsive, CYFIPOE cells show an increase in probability of response as compared with a decrease among WT cells. (**D-F**) As in (A-C) for Light stimuli where there is only a moderate effect of decreased responsiveness in the CYFIPOE cell population. For A-D, large inset, hollow points indicate mean ± SEM while smaller points depict individual values.
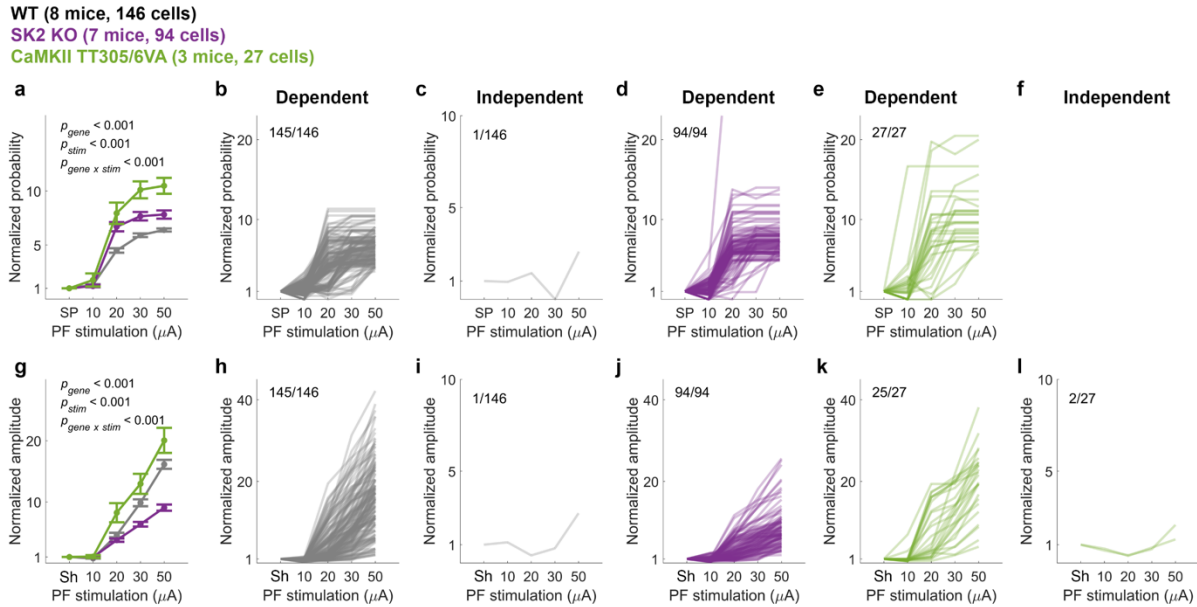
Figure S33. PCs show both linear stimulus intensity-dependent and flat stimulus intensity-independent responses to PF stimulation.

a. Calcium-event probability (mean ± SEM) as depicted in Fig. 33c normalized by the spontaneous values of individual cells. (Two-way ANOVA: $F_{stim}[4,1320] = 328.39$, p <0.001; $F_{gene}[2,1320] = 65.61$, p <0.001; $F_{stim\ x\ gene}[8,1320] = 10.58$, p <0.001, n = 1335).

b-f. Stimulus intensity-dependent (**b, d and e**) and stimulus intensity-independent cells (**c**) categorized according to the correlation coefficient of normalized probability. The labels on top of the plots indicate the number of designated cells out of the total number. The data are derived from the data presented in **a**, but only include the trials that were tested under all four different stimulus conditions.

g. Calcium-event amplitude (mean ± SEM) as depicted in Fig. 33d normalized by the maximum values of individual cells during shuffled 200ms time windows. (Two-way ANOVA: $F_{stim}[4,1320] = 237.35$, p <0.001; $F_{gene}[2,1320] = 53.17$, p <0.001; $F_{stim\ x\ gene}[8, 1320] = 15.43$, p <0.001, n = 1335).

h-l. Stimulus intensity-dependent (**h, j and k**) and stimulus intensity-independent cells (**h, j and l**) categorized according to the correlation coefficient of normalized probability. The labels on top of the plots indicate the number of designated cells out of the total number. The data are derived from the data presented in **f**, but only include the trials that were tested under all four different stimulus conditions.

Only cells that were tested with all four stimulus intensities were included in the categorization, which include wild type (146 cells), SK2 KO (94 cells), CaMKII TT305/6VA (27 cells).

SP, spontaneous calcium events. Sh, shuffled traces.
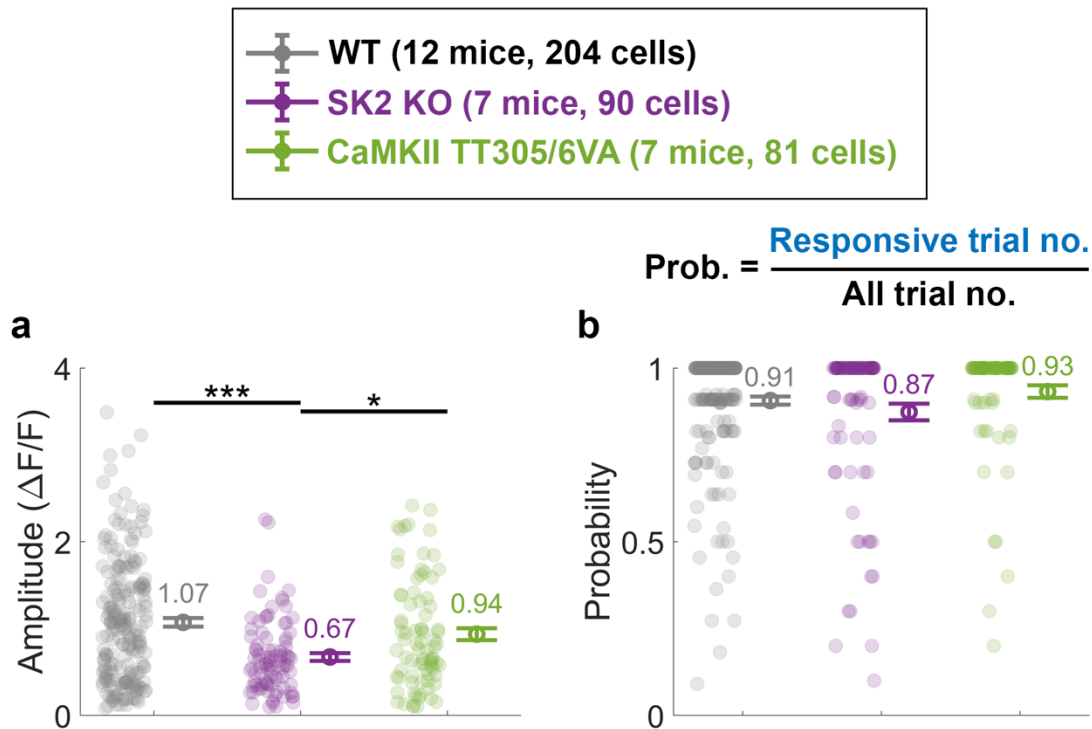
Figure S34. Amplitude and probability of pre-tetanus calcium events in response to PF stimulation.

a. Mean ± SEM of the pre-tetanus amplitudes of calcium transients for responsive trials shown in Fig. 34c-d. (One-way ANOVA: $F_{[2,372]} = 12.61$, $p < 0.001$, $n = 375$).

b. Mean ± SEM of the pre-tetanus probability of detecting a calcium event within the defined time window of 0-200ms. (One-way ANOVA: $F_{[2,372]} = 2.28$, $p = 0.104$, $n = 375$).

Numbers indicate the group mean values. Asterisks denote the significance levels of post hoc comparisons using Tukey's HSD (*, $p < 0.05$; **, $p < 0.01$; ***, $p < 0.001$).
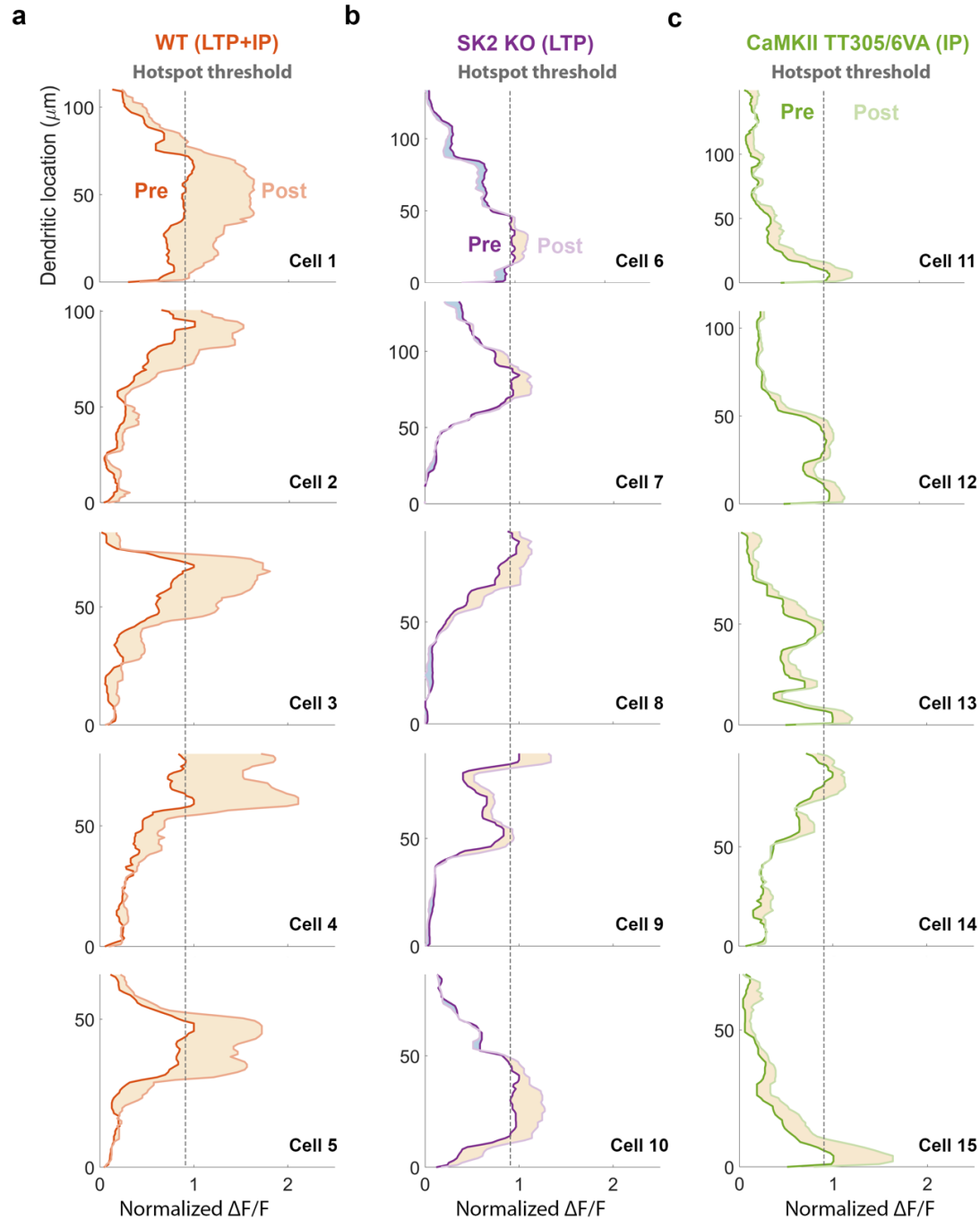
Figure S35. Representative spatial patterns of PF calcium response during pre-tetanus and early post-tetanus periods.

a-c. Representative linescan fluorescence signals of 5 individual PCs per genotype in addition to those shown in Fig. 35e-g. The dark and light traces represent pre- and (early) post-tetanus data, respectively. The dashed lines indicate hotspot area (pixels with >0.9 normalized pre-tetanus ΔF/F). LTP, long-term potentiation. IP, intrinsic plasticity.
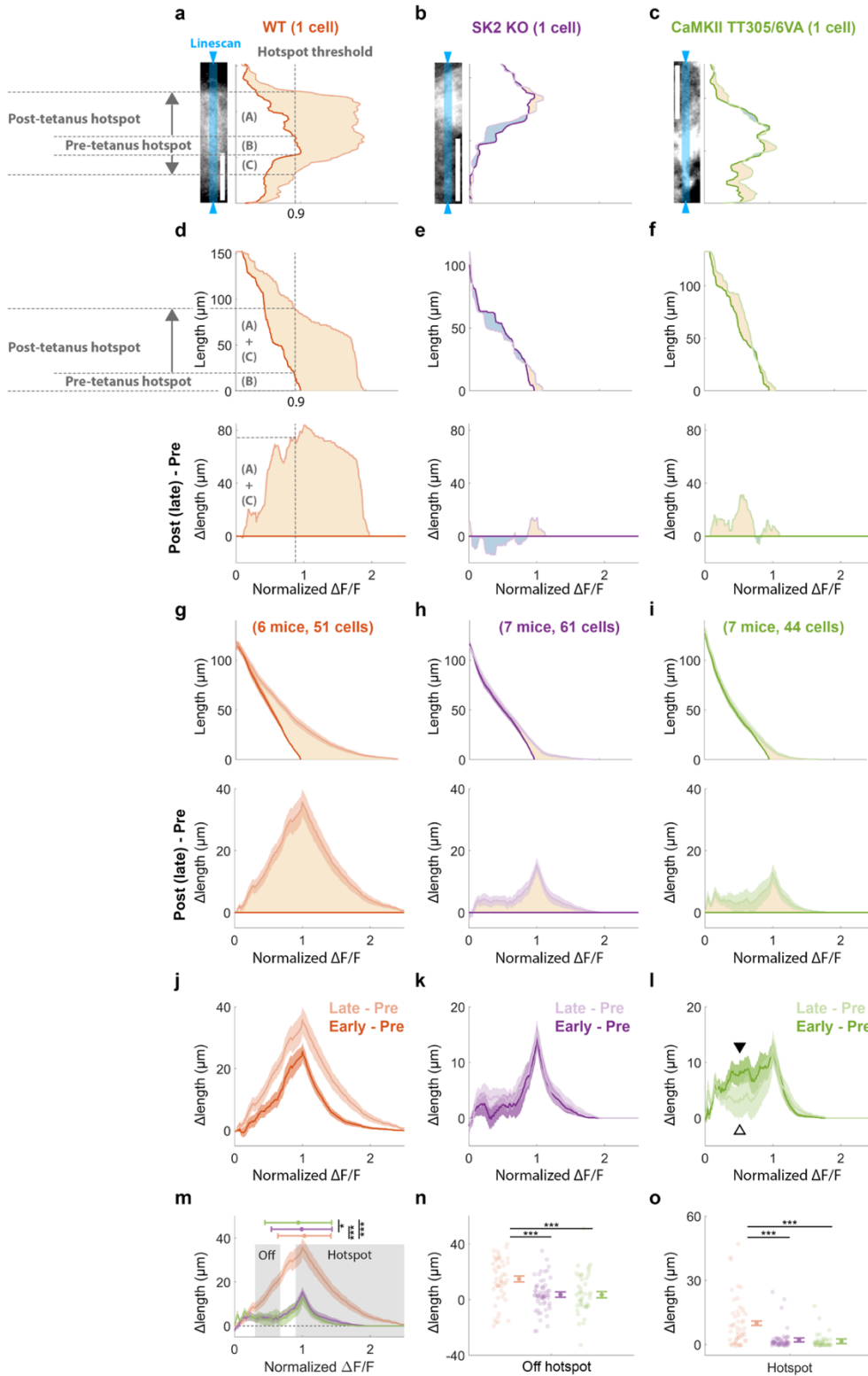
Figure S36. PF calcium spatial patterns are similar across genotypes between early and late post-tetanus periods but show some transience in mutant animals.

a-c. Representative two-photon images of individual PCs from each genotype are shown in the left panels, with corresponding linescan fluorescence signals in the right panels. Blue shaded areas depict the linescan recording site. The dark and light traces represent pre- and (late) post-tetanus data collected from the same cells depicted in Fig. 35e-g. The hotspot area (pixels with >0.9 normalized pre-tetanus ΔF/F) expanded from a length of (B) during the pre-tetanus period to a combined length of (A)+(B)+(C) during the post-tetanus period, thus the (A)+(C) represents Δlengths.

d-f. The top panel displays the cumulative lengths of dendrites as a function of fluorescence level, while the bottom panel displays the corresponding Δlengths of the representative data shown in **a-c.** Cumulative lengths were obtained by summing up the dendritic length exhibiting the given fluorescence level, depicted as the dashed lines in **a** and the top panel of **d**. Δlengths were calculated by subtracting post-tetanus from pre-tetanus cumulative length, as indicated by the dashed line in **d**.

g-i. For all cells from all mice in each group, mean $\pm$ SEM of cumulative lengths (top panel) and Δlengths (bottom panel) as in **d-f**.

j-l. Mean $\pm$ SEM of Δlengths between pre- and early post-tetanus periods, as well as between pre- and late post-tetanus periods, as depicted in Fig. 4k-4m and **g-i**, respectively. The triangles in l indicate a decrease in Δlength from early post-tetanus period (solid triangle) to late post-tetanus period (open triangle).

m. Superimposed genotype Δlengths obtained from the bottom panel of **g-i**. The horizontal bar represents the median $\pm$ median absolute deviation of the distribution. Asterisks denote significance in distribution shift using Dunn & Sidák's approach (*, $p < 0.05$; **, $p < 0.01$; ***, $p < 0.001$) following Kruskal-Wallis test (H[2] = 57.12, $p < 0.001$, n = 3929).

n-o. Mean $\pm$ SEM of Δlengths, calculated from the off-hotspot (**n**) and hotspot (**o**) as grey shaded areas shown in **j**, with individual cell values alongside. (One-way ANOVA: off-hotspot, F[2,153] = 9.77, $p < 0.001$; hotspot, F[2,153] = 21.37, $p < 0.001$, n = 624).

Asterisks denote the significance levels of post hoc comparisons using Tukey's HSD (*, $p < 0.05$; **, $p < 0.01$; ***, $p < 0.001$).
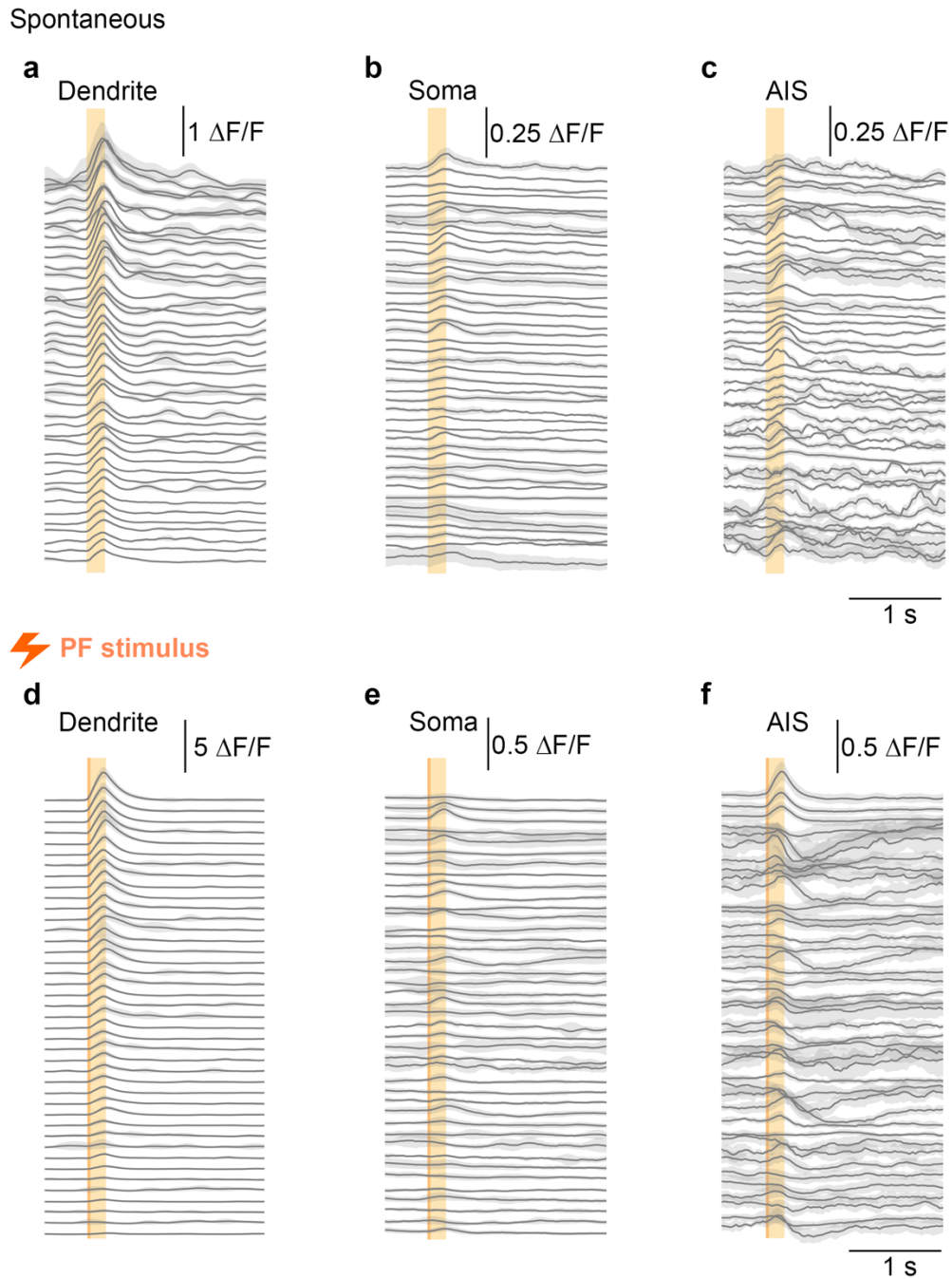
Figure S37. Most individual traces reveal time locked modulation of somatic and AIS calcium despite a saturated signal.

a-c. Spontaneous calcium transients (mean ± SEM) in dendrite (**a**), soma (**b**) and AIS (**c**) for each PC. Cells are sorted based on the amplitude of dendritic signals.

d-f. PF-evoked calcium transients (mean ± SEM) in dendrite (**d**), soma (**e**) and AIS (**f**) for each PC. Cells are sorted based on the amplitude of dendritic signals.
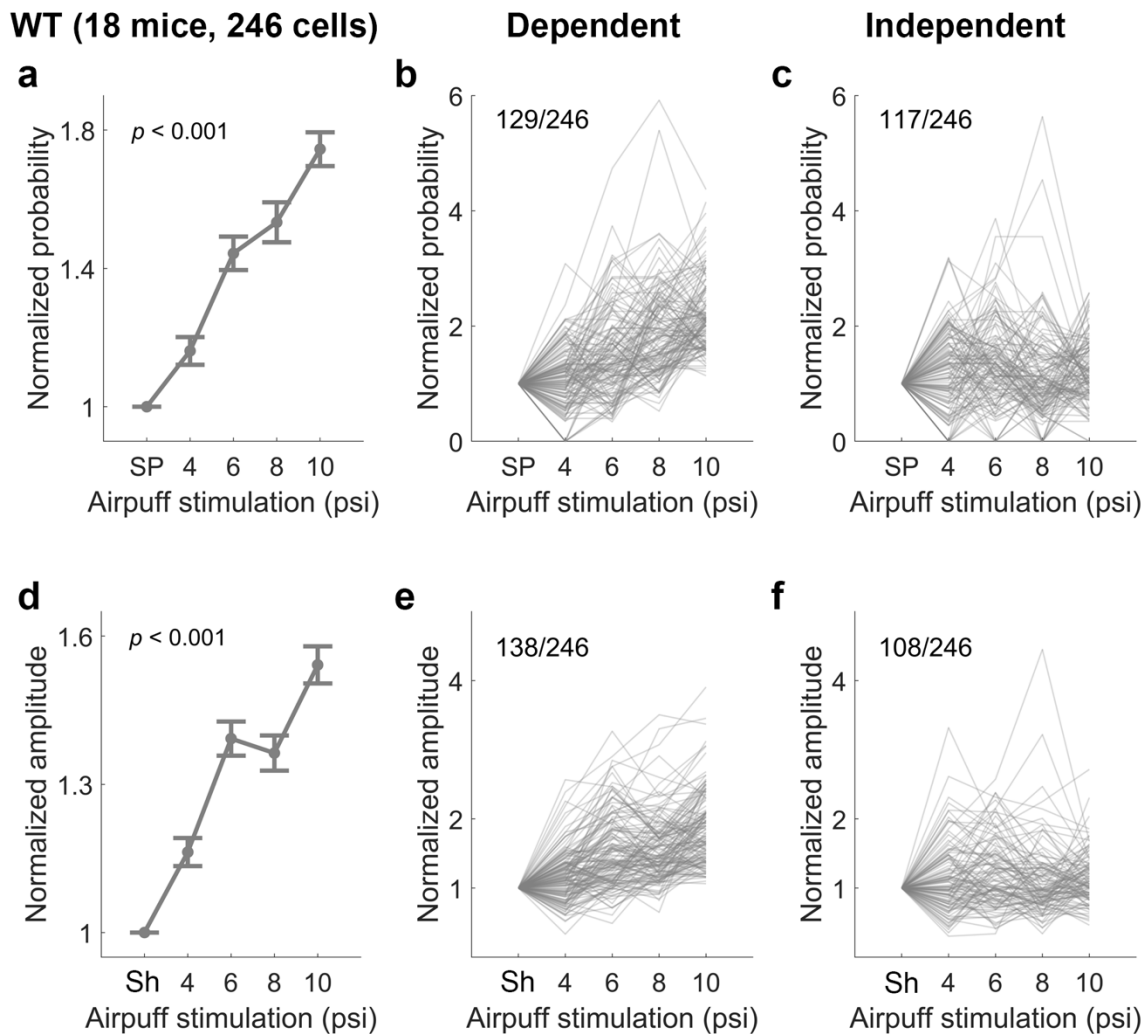
Figure S38. PCs show both linear stimulus intensity-dependent and flat stimulus intensity-independent responses to airpuff stimulation.

a. Calcium-event probability as depicted in Fig. 37d and 37f normalized by the spontaneous values of individual cells. (mean ± SEM). (One-way ANOVA: $F[4,1225] = 45.49$, $p < 0.001$, $n = 1230$).

b-c. Stimulus intensity-dependent (**b**) and stimulus intensity-independent cells (**c**) categorized according to the correlation coefficient of normalized probability. The labels on top of the plots indicate the number of designated cells out of the total number.

d. Calcium-event amplitude as depicted in Fig. 37g normalized by the maximum values of individual cells during shuffled 200ms time windows. (mean ± SEM). (One-way ANOVA: $F[4,1225] = 47.84$, $p < 0.001$, $n = 1230$).

e-f. Stimulus intensity-dependent (**e**) and stimulus intensity-independent cells (**f**) categorized according to the correlation coefficient of normalized probability. The labels on top of the plots indicate the number of designated cells out of the total number.

SP, spontaneous calcium events. Sh, shuffled traces.
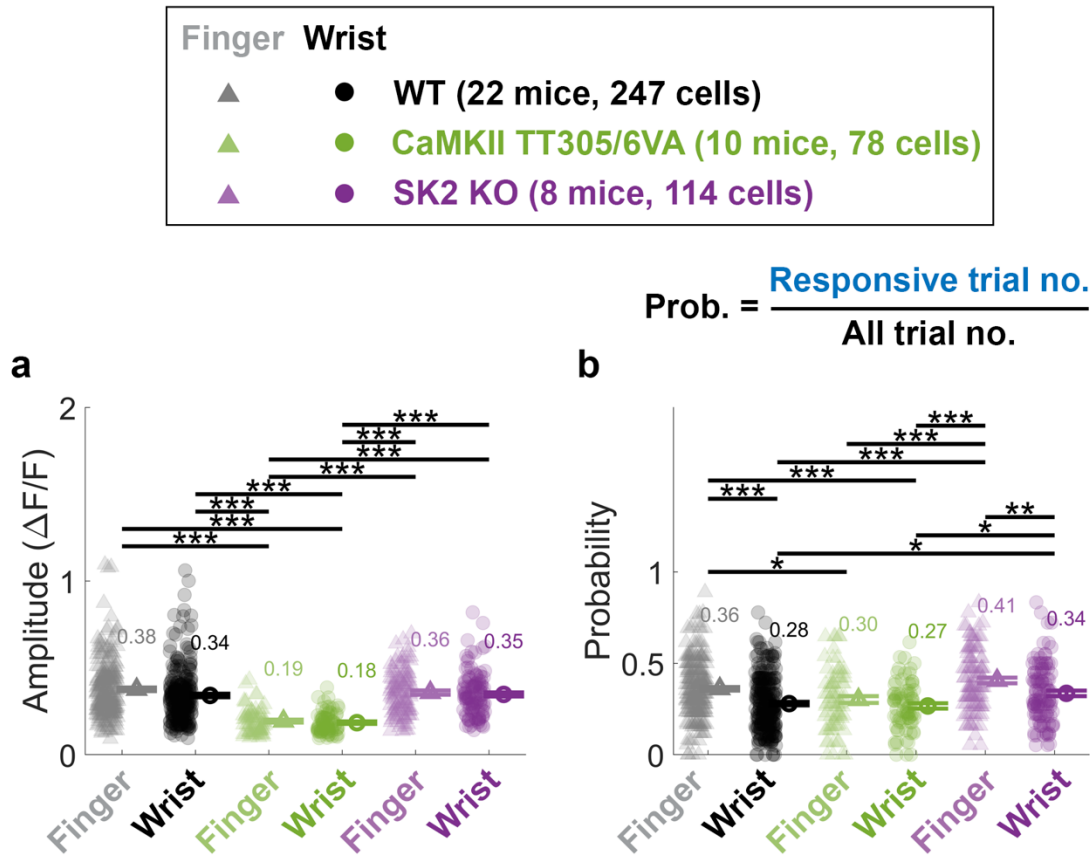
Figure S39. Amplitude and probability of pre-tetanus calcium events in response to airpuff stimulation to finger and wrist locations.

a. Mean ± SEM and individual cell values of the pre-tetanus amplitudes of calcium transients, calculated as the maximum value within the 0-200ms time window of individual trials. (One-way ANOVA: F[5,855] = 37.19, p < 0.001, n = 878).

b. Mean ± SEM and individual cell values of the pre-tetanus probability of detecting a calcium event within the defined time window of 0-200ms. (One-way ANOVA: F[5,872] = 16.07, p < 0.001, n = 878).

Numbers indicate the group mean values. Asterisks denote the significance levels of post hoc comparisons using Tukey's HSD (*, p <0.05; **, p <0.01; ***, p <0.001).
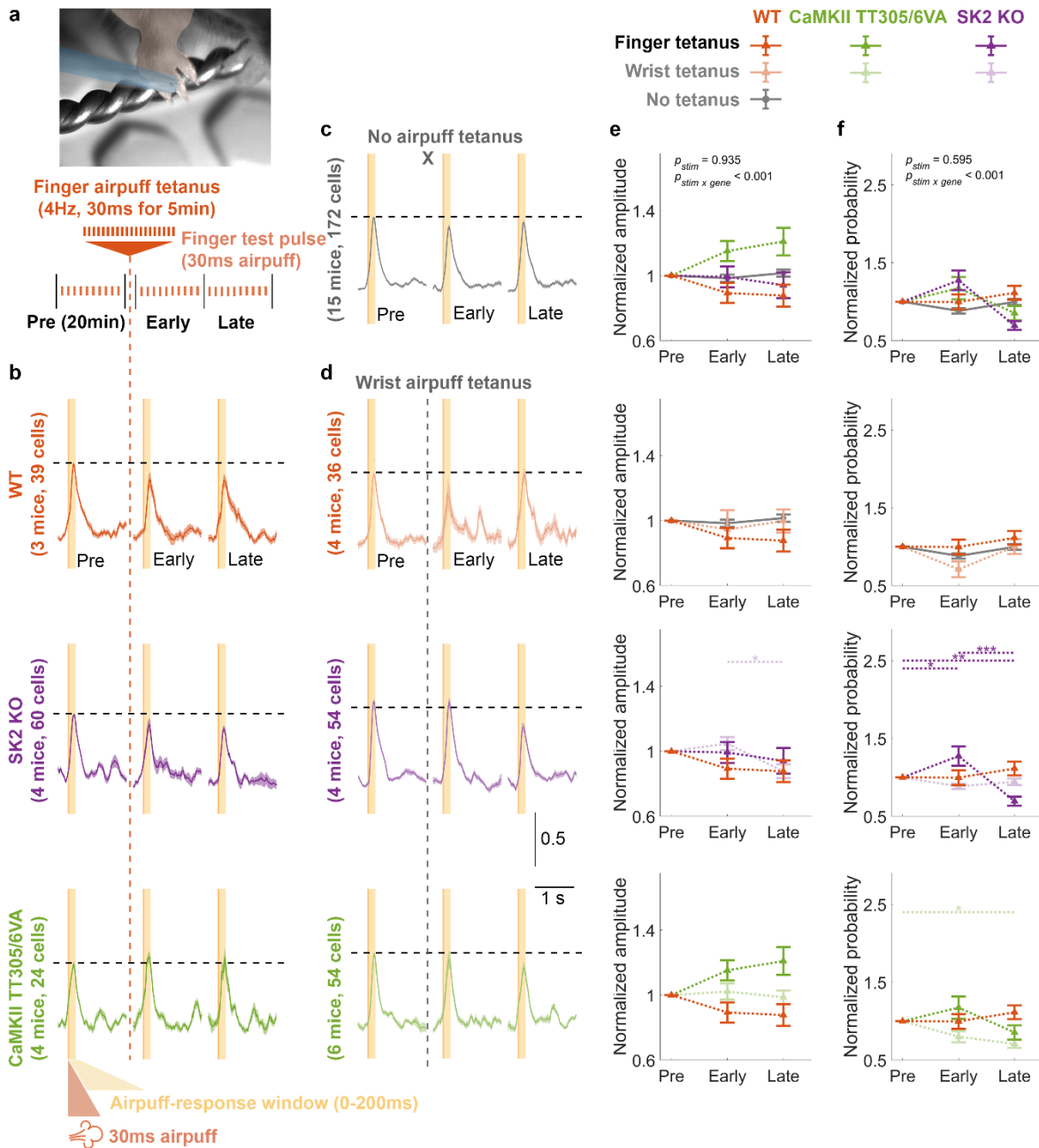
Figure S40. Airpuff finger stimulation does not induce detectable tactile-RF plasticity.

a. Schematic illustration of the experimental protocol. The recording began with a 20min baseline recording consisting of 10-12 trials, followed by a finger airpuff tetanus to potentiate the calcium response. The recording concluded with another 20min early and late post-tetanus recordings, each consisting of 10-12 trials. Post-tetanus trials began immediately (<2min) after cessation of the tetanus.

b. Normalized average calcium signals ± SEM across trials from different genotypes.

c. Normalized average calcium signals ± SEM across trials of the control condition in WTs where no tetanization protocol was applied.

d. Normalized average calcium signals ± SEM across trials from control conditions across genotypes where airpuff tetanization was applied to the wrist and thus was unmatched to the test location (finger). The signals shown in **b-d** are normalized by the average amplitude of pre-tetanus calcium transients (y-axis scale denotes normalized value units). Only trials with detected events within the response window (0-200ms) were included.

e. Mean ± SEM of the normalized calcium-event amplitudes, calculated as the maximum value within the 0-200ms time window of individual trials. The data were normalized by the pre-tetanus amplitude. (Two-way repeated measure ANOVA: $F_{stim}[2,1144] = 0.068$, $p = 0.935$; $F_{stim \, x \, gene}[24,1144] = 4.126$, $p < 0.001$, n = 2067).

f. Mean ± SEM of the normalized probability of detecting a calcium event within the 0-200ms time windows. The data were normalized by the pre-tetanus probability. (Two-way repeated ANOVA: $F_{stim}[2,1356] = 0.520$, $p = 0.595$; $F_{stim \, x \, gene}[24,1356] = 5.274$, $p < 0.001$, n = 2073).

Asterisks denote the significance levels of post hoc comparisons using Tukey's HSD (*, $p < 0.05$; **, $p < 0.01$; ***, $p < 0.001$).
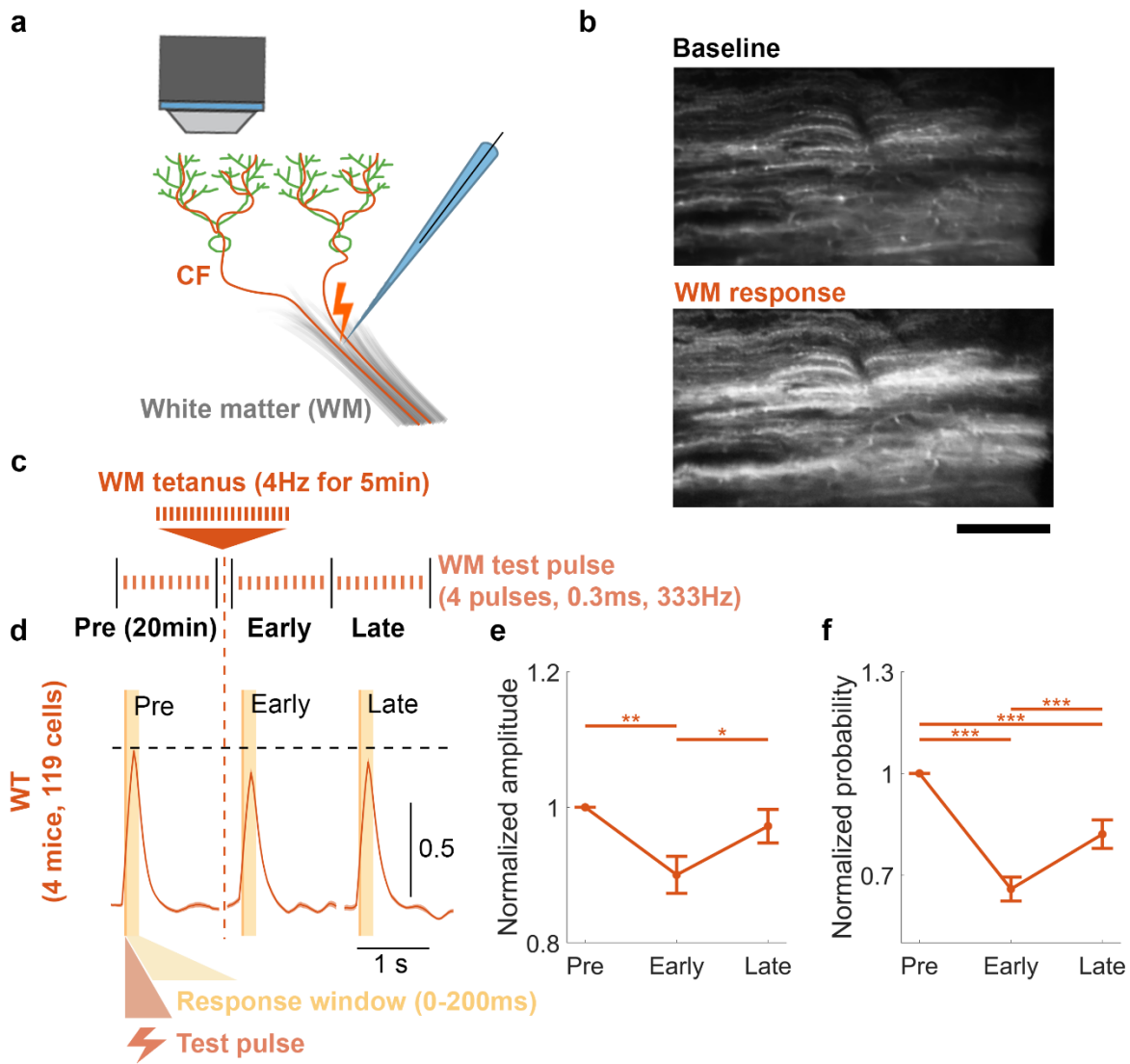
Figure S41. Applying the tactile tetanus protocol directly to upstream white matter tracts that include a strong CF component depresses the response in awake mice.

a. Schematic illustration of the experimental protocol *in vivo*.

b. Two-photon images demonstrating calcium signals in PCs during baseline and with application of the white matter stimulation test pulse. Scale bar is 100μm. Calcium imaging followed the same protocol as for PF-RF experiments (Fig. 32).

c. The recording began with a 20min baseline recording consisting of 10-12 trials, followed by a tetanization using the tactile tetanus protocol of 4Hz for 5min. The recording concluded with early and late post-tetanus recording periods, each consisting of 10-12 trials and lasting 20min. Post-tetanus trials began immediately (<2min) after cessation of the tetanus.

d. Normalized average calcium signals ± SEM for all trials. The signals are normalized by the average amplitude of pre-tetanus calcium transients (y-axis scale denotes normalized value units). Only trials with detected events within the response window (0-200ms) were included.

e. Mean ± SEM of the normalized calcium-event amplitudes, calculated as the maximum value within the 0-200ms time window of individual trials. The data were normalized by the pre-tetanus amplitude. (One-way ANOVA: $F[2,339] = 5.74$, $p = 0.004$, $n = 354$).

f. Mean ± SEM of the normalized probability of detecting a calcium event within the 0-200ms time windows. The data were normalized by the pre-tetanus probability. (One-way ANOVA: $F[2,351] = 28.98$, $p < 0.001$, $n = 357$).

Asterisks denote the significance levels of post hoc comparisons using Tukey's HSD (*, $p < 0.05$; **, $p < 0.01$; ***, $p < 0.001$).
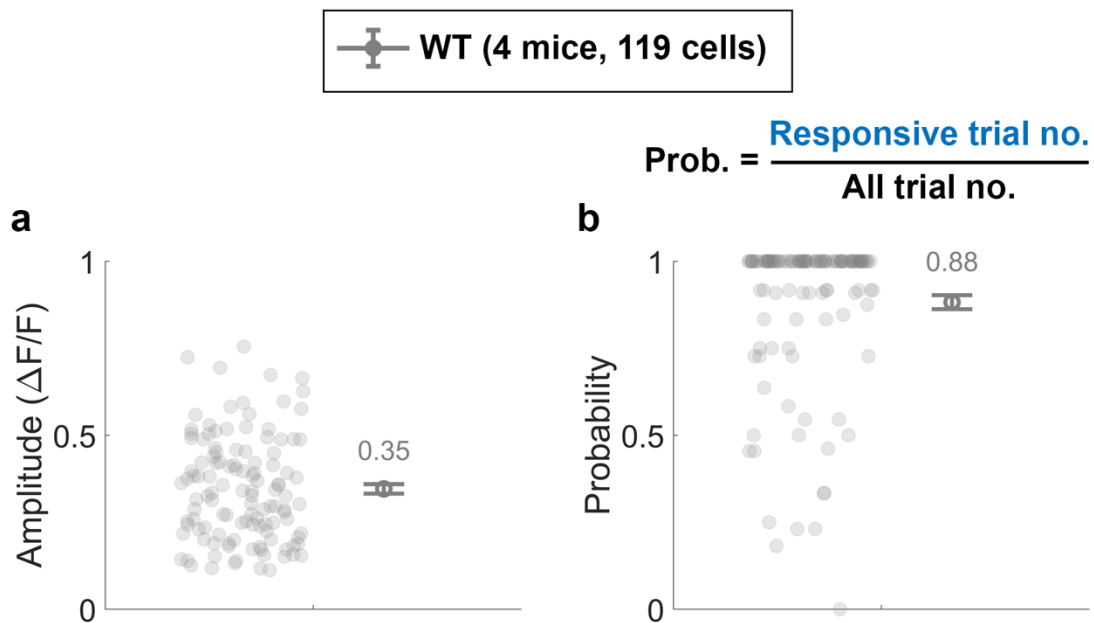
Figure S42. Amplitude and probability of pre-tetanus calcium events in response to white matter stimulation.

a. Mean ± SEM (n = 118) of the pre-tetanus amplitudes of calcium transients for responsive trials.

b. Mean ± SEM (n = 119) of the pre-tetanus probability of detecting a calcium event within the defined time window of 0-200ms.

Numbers indicate the group mean values.

References

Alba, A., Kano, M., Chen, C., Stanton, M. E., Fox, G. D., Herrup, K., Zwingman, T. A., & Tonegawa, S. (1994). Deficient cerebellar long-term depression and impaired motor learning in mGluR1 mutant mice. *Cell*, *79*(2), 377–388. https://doi.org/10.1016/0092-8674(94)90205-4

Albus, J. S. (1971). A theory of cerebellar function. *Mathematical Biosciences*, *10*(1), 25–61. https://doi.org/10.1016/0025-5564(71)90051-4

Anwar, H., Hepburn, I., Nedelescu, H., Chen, W., & De Schutter, E. (2013). Stochastic Calcium Mechanisms Cause Dendritic Calcium Spike Variability. *Journal of Neuroscience*, *33*(40), 15848–15867. https://doi.org/10.1523/JNEUROSCI.1722-13.2013

Anwar, H., Roome, C. J., Nedelescu, H., Chen, W., Kuhn, B., & De Schutter, E. (2014). Dendritic diameters affect the spatial variability of intracellular calcium dynamics in computer models. *Frontiers in Cellular Neuroscience*, *8*. https://doi.org/10.3389/fncel.2014.00168

Apps, R., & Hawkes, R. (2009). Cerebellar cortical organization: A one-map hypothesis. *Nature Reviews Neuroscience*, *10*(9), 670–681. https://doi.org/10.1038/nrn2698

Augustine, G. J., Santamaria, F., & Tanaka, K. (2003). Local Calcium Signaling in Neurons. *Neuron*, *40*(2), 331–346. https://doi.org/10.1016/S0896-6273(03)00639-1

Badura, A., Schonewille, M., Voges, K., Galliano, E., Renier, N., Gao, Z., Witter, L., Hoebeek, F. E., Chédotal, A., & De Zeeuw, C. I. (2013). Climbing Fiber Input Shapes Reciprocity of Purkinje Cell Firing. *Neuron*, *78*(4), 700–713. https://doi.org/10.1016/j.neuron.2013.03.018

Badura, A., Verpeut, J. L., Metzger, J. W., Pereira, T. D., Pisano, T. J., Deverett, B., Bakshinskaya, D. E., & Wang, S. S.-H. (2018). Normal cognitive and social development require posterior cerebellar activity. *eLife*, *7*, e36401. https://doi.org/10.7554/eLife.36401

Baizer, J. S. (2014). Unique Features of the Human Brainstem and Cerebellum. *Frontiers in Human Neuroscience*, *8*. https://doi.org/10.3389/fnhum.2014.00202

Barmack, N. H., Baughman, R. W., & Eckenstein, F. P. (1992). Cholinergic innervation of the cerebellum of rat, rabbit, cat, and monkey as revealed by choline acetyltransferase activity and immunohistochemistry. *Journal of Comparative Neurology*, *317*(3), 233–249. https://doi.org/10.1002/cne.903170303

Beaulieu-Laroche, L., Brown, N. J., Hansen, M., Toloza, E. H. S., Sharma, J., Williams, Z. M., Frosch, M. P., Cosgrove, G. R., Cash, S. S., & Harnett, M. T. (2021). Allometric rules for mammalian cortical layer 5 neuron biophysics. *Nature*, 1–5. https://doi.org/10.1038/s41586-021-04072-3

Beaulieu-Laroche, L., Toloza, E. H. S., van der Goes, M. S., Lafourcade, M., Barnagian, D., Williams, Z. M., Eskandar, E. N., Frosch, M. P., Cash, S. S., & Harnett, M. T. (2018). Enhanced Dendritic Compartmentalization in Human Cortical Neurons. *Cell*, *175*(3), 643-651.e14. https://doi.org/10.1016/j.cell.2018.08.045

Beekhof, G. C., Osório, C., White, J. J., van Zoomeren, S., van der Stok, H., Xiong, B., Nettersheim, I. H., Mak, W. A., Runge, M., Fiocchi, F. R., Boele, H.-J., Hoebeek, F. E., & Schonewille, M. (2021). Differential spatiotemporal development of Purkinje cell populations and cerebellum-dependent sensorimotor behaviors. *eLife*, *10*, e63668. https://doi.org/10.7554/eLife.63668

Belmeguenai, A., Botta, P., Weber, J. T., Carta, M., Ruiter, M. D., Zeeuw, C. I. D., Valenzuela, C. F., & Hansel, C. (2008). Alcohol impairs long-term depression at the cerebellar parallel fiber—Purkinje cell synapse. *Journal of Neurophysiology*. https://doi.org/10.1152/jn.90384.2008

Belmeguenai, A., Hosy, E., Bengtsson, F., Pedroarena, C., Piochon, C., Teuling, E., He, Q., Ohtsuki, G., Jeu, M. T. G. D., Zeeuw, C. I. D., Jörntell, H., & Hansel, C. (2010). Intrinsic plasticity complements LTP in parallel fiber input gain control in cerebellar Purkinje cells. *Journal of Neuroscience*, *30*(41), 13630–13643. https://doi.org/10.1523/JNEUROSCI.3226-10.2010.Intrinsic

Benavides-Piccione, R., Ballesteros-Yáñez, I., DeFelipe, J., & Yuste, R. (2002). Cortical area and species differences in dendritic spine morphology. *Journal of Neurocytology*, *31*(3), 337–346. https://doi.org/10.1023/A:1024134312173

Benavides-Piccione, R., Fernaud-Espinosa, I., Robles, V., Yuste, R., & DeFelipe, J. (2013). Age-Based Comparison of Human Dendritic Spine Structure Using Complete Three-Dimensional Reconstructions. *Cerebral Cortex*, *23*(8), 1798–1810. https://doi.org/10.1093/cercor/bhs154

Benavides-Piccione, R., Regalado-Reyes, M., Fernaud-Espinosa, I., Kastanauskaite, A., Tapia-González, S., León-Espinosa, G., Rojo, C., Insausti, R., Segev, I., & DeFelipe, J. (2020). Differential Structure of Hippocampal CA1 Pyramidal Neurons in the Human and Mouse. *Cerebral Cortex*, *30*(2), 730–752. https://doi.org/10.1093/cercor/bhz122

Bengtsson, F., & Jörntell, H. (2009). Sensory transmission in cerebellar granule cells relies on similarly coded mossy fiber inputs. *Proceedings of the National Academy of Sciences*, *106*(7), 2389–2394. https://doi.org/10.1073/pnas.0808428106

Berry, M., & Bradley, P. M. (1976). The application of network analysis to the study of branching patterns of large dendritic fields. *Brain Research*, *109*(1), 111–132. https://doi.org/10.1016/0006-8993(76)90383-8

Boele, H.-J., Peter, S., Ten Brinke, M. M., Verdonschot, L., IJpelaar, A. C. H., Rizopoulos, D., Gao, Z., Koekkoek, S. K. E., & De Zeeuw, C. I. (2018). Impact of parallel fiber to Purkinje cell long-term depression is unmasked in absence of inhibitory input. *Science Advances*, *4*(10), eaas9426. https://doi.org/10.1126/sciadv.aas9426

Bolton, P. F., Dennis, N. r., Browne, C. e., Thomas, N. s., Veltman, M. w. m., Thompson, R. j., & Jacobs, P. (2001). The phenotypic manifestations of interstitial duplications of proximal 15q with special reference to the autistic spectrum disorders. *American Journal of Medical Genetics*, *105*(8), 675–685. https://doi.org/10.1002/ajmg.1551

Bosman, L. W. J., Koekkoek, S. K. E., Shapiro, J., Rijken, B. F. M., Zandstra, F., Van Der Ende, B., Owens, C. B., Potters, J.-W., De Gruijl, J. R., Ruigrok, T. J. H., & De Zeeuw, C. I. (2010). Encoding of whisker input by cerebellar Purkinje cells. *The Journal of Physiology*, *588*(19), 3757–3783. https://doi.org/10.1113/jphysiol.2010.195180

Bosman, L. W. J., Takechi, H., Hartmann, J., Eilers, J., & Konnerth, A. (2008). Homosynaptic Long-Term Synaptic Potentiation of the "Winner" Climbing Fiber Synapse in Developing Purkinje Cells. *Journal of Neuroscience*, *28*(4), 798–807. https://doi.org/10.1523/JNEUROSCI.4074-07.2008

Bower, J. M. (1997). Chapter 27 Is the cerebellum sensory for motor's sake, or motor for sensory's sake: The view from the whiskers of a rat? In C. I. De Zeeuw, P. Strata, & J. Voogd (Eds.), *Progress in Brain Research* (Vol. 114, pp. 463–496). Elsevier. https://doi.org/10.1016/S0079-6123(08)63381-6

Bower, J. M., & Woolston, D. C. (1983). Congruence of spatial organization of tactile projections to granule cell and Purkinje cell layers of cerebellar hemispheres of the albino rat: Vertical organization of cerebellar cortex. *Journal of Neurophysiology*, *49*(3), 745–766. https://doi.org/10.1152/jn.1983.49.3.745

Bozdagi, O., Sakurai, T., Dorr, N., Pilorge, M., Takahashi, N., & Buxbaum, J. D. (2012). Haploinsufficiency of Cyfip1 Produces Fragile X-Like Phenotypes in Mice. *PLOS ONE*, *7*(8), e42422. https://doi.org/10.1371/journal.pone.0042422

Brandenburg, C., Smith, L. A., Kilander, M. B. C., Bridi, M. S., Lin, Y.-C., Huang, S., & Blatt, G. J. (2021). Parvalbumin subtypes of cerebellar Purkinje cells contribute to differential intrinsic firing properties. *Molecular and Cellular Neuroscience*, *115*, 103650. https://doi.org/10.1016/j.mcn.2021.103650

Brunel, N., Hakim, V., Isope, P., Nadal, J.-P., & Barbour, B. (2004). Optimal Information Storage and the Distribution of Synaptic Weights: Perceptron versus Purkinje Cell. *Neuron*, *43*(5), 745–757. https://doi.org/10.1016/j.neuron.2004.08.023

Buckner, R. L., Krienen, F. M., Castellanos, A., Diaz, J. C., & Yeo, B. T. T. (2011). The organization of the human cerebellum estimated by intrinsic functional connectivity. *Journal of Neurophysiology*, *106*(5), 2322–2345. https://doi.org/10.1152/jn.00339.2011

Burnside, R. D., Pasion, R., Mikhail, F. M., Carroll, A. J., Robin, N. H., Youngs, E. L., Gadi, I. K., Keitges, E., Jaswaney, V. L., Papenhausen, P. R., Potluri, V. R., Risheg, H., Rush, B., Smith, J. L., Schwartz, S., Tepperberg, J. H., & Butler, M. G. (2011). Microdeletion/microduplication of proximal 15q11.2 between BP1 and BP2: A susceptibility region for neurological dysfunction including developmental and language delay. *Human Genetics*, *130*(4), 517–528. https://doi.org/10.1007/s00439-011-0970-4

Busch, S. E., & Hansel, C. (2023). Climbing fiber multi-innervation of mouse Purkinje dendrites with arborization common to human. *Science*, *381*(6656), 420–427. https://doi.org/10.1126/science.adi1024

Busch, S. E., & Hansel, C. (2024). *Non-allometric expansion and enhanced compartmentalization of Purkinje cell dendrites in the human cerebellum* (p. 2024.09.09.612113). bioRxiv. https://doi.org/10.1101/2024.09.09.612113

Busch, S. E., Simmons, D. H., Gama, E., Du, X., Longo, F., Gomez, C. M., Klann, E., & Hansel, C. (2023). Overexpression of the autism candidate gene Cyfip1 pathologically enhances olivo-cerebellar signaling in mice. *Frontiers in Cellular Neuroscience*, *17*. https://www.frontiersin.org/articles/10.3389/fncel.2023.1219270

Butler, M. G., Bittel, D. C., Kibiryeva, N., Talebizadeh, Z., & Thompson, T. (2004). Behavioral Differences Among Subjects With Prader-Willi Syndrome and Type I or Type II Deletion and Maternal Disomy. *Pediatrics*, *113*(3), 565–573. https://doi.org/10.1542/peds.113.3.565

Callaway, J. C., Lasser-Ross, N., & Ross, W. N. (1995). IPSPs strongly inhibit climbing fiber-activated [Ca2+]i increases in the dendrites of cerebellar Purkinje neurons. *Journal of Neuroscience*, *15*(4), 2777–2787. https://doi.org/10.1523/JNEUROSCI.15-04-02777.1995

Canepari, M., & Vogt, K. E. (2008). Dendritic Spike Saturation of Endogenous Calcium Buffer and Induction of Postsynaptic Cerebellar LTP. *PLOS ONE*, *3*(12), e4011. https://doi.org/10.1371/journal.pone.0004011

Carta, M., Mameli, M., & Valenzuela, C. F. (2006). Alcohol Potently Modulates Climbing Fiber→Purkinje Neuron Synapses: Role of Metabotropic Glutamate Receptors. *Journal of Neuroscience*, *26*(7), 1906–1912. https://doi.org/10.1523/JNEUROSCI.4430-05.2006

Cayco-Gajic, N. A., Clopath, C., & Silver, R. A. (2017). Sparse synaptic connectivity is required for decorrelation and pattern separation in feedforward networks. *Nature Communications*, *8*(1), 1116. https://doi.org/10.1038/s41467-017-01109-y

Cerminara, N. L., Lang, E. J., Sillitoe, R. V., & Apps, R. (2015). Redefining the cerebellar cortex as an assembly of non-uniform Purkinje cell microcircuits. *Nature Reviews Neuroscience*, *16*(2), 79–93. https://doi.org/10.1038/nrn3886

Chai, J.-H., Locke, D. P., Greally, J. M., Knoll, J. H. M., Ohta, T., Dunai, J., Yavor, A., Eichler, E. E., & Nicholls, R. D. (2003). Identification of Four Highly Conserved Genes between Breakpoint Hotspots BP1 and BP2 of the Prader-Willi/Angelman Syndromes Deletion Region That Have Undergone Evolutionary Transposition Mediated by Flanking Duplicons. *The American Journal of Human Genetics*, *73*(4), 898–925. https://doi.org/10.1086/378816

Chen, L. Y., Jiang, M., Zhang, B., Gokce, O., & Südhof, T. C. (2017). Conditional Deletion of All Neurexins Defines Diversity of Essential Synaptic Organizer Functions for Neurexins. *Neuron*, *94*(3), 611-625.e4. https://doi.org/10.1016/j.neuron.2017.04.011

Chen, T.-W., Wardill, T. J., Sun, Y., Pulver, S. R., Renninger, S. L., Baohan, A., Schreiter, E. R., Kerr, R. A., Orger, M. B., Jayaraman, V., Looger, L. L., Svoboda, K., & Kim, D. S. (2013). Ultrasensitive fluorescent proteins for imaging neuronal activity. *Nature*, *499*(7458), Article 7458. https://doi.org/10.1038/nature12354

Chen, X. R., Heck, N., Lohof, A. M., Rochefort, C., Morel, M.-P., Wehrlé, R., Doulazmi, M., Marty, S., Cannaya, V., Avci, H. X., Mariani, J., Rondi-Reig, L., Vodjdani, G., Sherrard, R. M., Sotelo, C., & Dusart, I. (2013). Mature Purkinje Cells Require the Retinoic Acid-Related Orphan Receptor-α (RORα) to Maintain Climbing Fiber Mono-Innervation and Other Adult Characteristics. *Journal of Neuroscience*, *33*(22), 9546–9562. https://doi.org/10.1523/JNEUROSCI.2977-12.2013

Cichon, J., Wasilczuk, A. Z., Looger, L. L., Contreras, D., Kelz, M. B., & Proekt, A. (2022). Ketamine triggers a switch in excitatory neuronal activity across neocortex. *Nature Neuroscience*, 1–14. https://doi.org/10.1038/s41593-022-01203-5

Cirtala, G., & De Schutter, E. (2024). Branch-specific clustered parallel fiber input controls dendritic computation in Purkinje cells. *iScience*, 110756. https://doi.org/10.1016/j.isci.2024.110756

Coesmans, M., Weber, J. T., Zeeuw, C. I. D., & Hansel, C. (2004). Bidirectional Parallel Fiber Plasticity in the Cerebellum under Climbing Fiber Control. *Neuron*, *44*(4), 691–700. https://doi.org/10.1016/j.neuron.2004.10.031

Conquet, F., Bashir, Z. I., Davies, C. H., Daniel, H., Ferraguti, F., Bordi, F., Franz-Bacon, K., Reggiani, A., Matarese, V., Condé, F., Collingridge, G. L., & Crépel, F. (1994). Motor deficit and impairment of synaptic plasticity in mice lacking mGluR1. *Nature*, *372*(6503), 237–243. https://doi.org/10.1038/372237a0

Cook, E. H., Lindgren, V., Leventhal, B. L., Courchesne, R., Lincoln, A., Shulman, C., Lord, C., & Courchesne, E. (1997). Autism or atypical autism in maternally but not paternally derived proximal 15q duplication. *American Journal of Human Genetics*, *60*(4), 928–934.

Cook Jr, E. H., & Scherer, S. W. (2008). Copy-number variations associated with neuropsychiatric conditions. *Nature*, *455*(7215), 919–923. https://doi.org/10.1038/nature07458

Cramer, S. W., Gao, W., Chen, G., & Ebner, T. J. (2013). Reevaluation of the Beam and Radial Hypotheses of Parallel Fiber Action in the Cerebellar Cortex. *Journal of Neuroscience*, *33*(28), 11412–11424. https://doi.org/10.1523/JNEUROSCI.0711-13.2013

Crepel, F., & Jaillard, D. (1991). Pairing of pre- and postsynaptic activities in cerebellar Purkinje cells induces long-term changes in synaptic efficacy in vitro. *The Journal of Physiology*, *432*(1), 123–141. https://doi.org/10.1113/jphysiol.1991.sp018380

Davenport, E. C., Szulc, B. R., Drew, J., Taylor, J., Morgan, T., Higgs, N. F., López-Doménech, G., & Kittler, J. T. (2019). Autism and Schizophrenia-Associated CYFIP1 Regulates the Balance of Synaptic Excitation and Inhibition. *Cell Reports*, *26*(8), 2037-2051.e6. https://doi.org/10.1016/j.celrep.2019.01.092

Davie, J. T., Clark, B. A., & Häusser, M. (2008). The Origin of the Complex Spike in Cerebellar Purkinje Cells. *Journal of Neuroscience*, *28*(30), 7599–7609. https://doi.org/10.1523/jneurosci.0559-08.2008

De Schutter, E., & Bower, J. M. (1994). An active membrane model of the cerebellar Purkinje cell. I. Simulation of current clamps in slice. *Journal of Neurophysiology*, *71*(1), 375–400. https://doi.org/10.1152/jn.1994.71.1.375

De Zeeuw, C. I. (2020). Bidirectional learning in upbound and downbound microzones of the cerebellum. *Nature Reviews Neuroscience*, 1–19. https://doi.org/10.1038/s41583-020-00392-x

De Zeeuw, C. I., Hoogenraad, C. C., Koekkoek, S. K. E., Ruigrok, T. J. H., Galjart, N., & Simpson, J. I. (1998). Microcircuitry and function of the inferior olive. *Trends in Neurosciences*, *21*(9), 391–400. https://doi.org/10.1016/S0166-2236(98)01310-1

De Zeeuw, C. I., & Hoogland, T. M. (2015). Reappraisal of Bergmann glial cells as modulators of cerebellar circuit function. *Frontiers in Cellular Neuroscience*, *9*. https://doi.org/10.3389/fncel.2015.00246

Desimone, R. (1996). Neural mechanisms for visual memory and their role in attention. *Proceedings of the National Academy of Sciences*, *93*(24), 13494–13499. https://doi.org/10.1073/pnas.93.24.13494

Devor, A. (2000). Is the cerebellum like cerebellar-like structures? *Brain Research Reviews*, *34*(3), 149–156. https://doi.org/10.1016/S0165-0173(00)00045-X

Du, X., Wang, J., Zhu, H., Rinaldo, L., Lamar, K.-M., Palmenberg, A. C., Hansel, C., & Gomez, C. M. (2013). Second Cistron in CACNA1A Gene Encodes a Transcription Factor Mediating Cerebellar Development and SCA6. *Cell*, *154*(1), 118–133. https://doi.org/10.1016/j.cell.2013.05.059

Du, X., Wei, C., Hejazi Pastor, D. P., Rao, E. R., Li, Y., Grasselli, G., Godfrey, J., Palmenberg, A. C., Andrade, J., Hansel, C., & Gomez, C. M. (2019). α1ACT Is Essential for Survival and Early Cerebellar Programming in a Critical Neonatal Window. *Neuron*, *102*(4), 770-785.e7. https://doi.org/10.1016/j.neuron.2019.02.036

Eccles, J. C., Ito, M., & Szentágothai, J. (1967). *The Cerebellum as a Neuronal Machine*. Springer. https://doi.org/10.1007/978-3-662-13147-3

Eccles, J. C., Llinas, R., & Sasaki, K. (1964). Excitation of Cerebellar Purkinje Cells by the Climbing Fibres. *Nature*, *203*(4942), 245–246. https://doi.org/10.1038/203245a0

Eccles, J. C., Llinás, R., & Sasaki, K. (1966). The excitatory synaptic action of climbing fibres on the Purkinje cells of the cerebellum. *The Journal of Physiology*, *182*(2), 268–296. https://doi.org/10.1113/jphysiol.1966.sp007824

Eccles, J. C., Sabah, N. H., Schmidt, R. F., & Táboříková, H. (1972). Integration by Purkyně cells of mossy and climbing fiber inputs from cutaneous mechanoreceptors. *Experimental Brain Research*, *15*(5), 498–520. https://doi.org/10.1007/BF00236405

Edge, A. L., Marple-Horvat, D. E., & Apps, R. (2003). Lateral cerebellum: Functional localization within crus I and correspondence to cortical zones. *European Journal of Neuroscience*, *18*(6), 1468–1485. https://doi.org/10.1046/j.1460-9568.2003.02873.x

Eilers, J., Augustine, G. J., & Konnerth, A. (1995). Subthreshold synaptic Ca2+ signalling in fine dendrites and spines of cerebellar Purkinje neurons. *Nature*, *373*(6510), 155–158. https://doi.org/10.1038/373155a0

Eilers, J., Takechi, H., Finch, E. A., Augustine, G. J., & Konnerth, A. (1997). Local dendritic Ca2+ signaling induces cerebellar long-term depression. *Learning & Memory*, *4*(1), 159–168. https://doi.org/10.1101/lm.4.1.159

Ekerot, C. F., Garwicz, M., & Schouenborg, J. (1991a). The postsynaptic dorsal column pathway mediates cutaneous nociceptive information to cerebellar climbing fibres in the cat. *The Journal of Physiology*, *441*(1), 275–284. https://doi.org/10.1113/jphysiol.1991.sp018751

Ekerot, C. F., Garwicz, M., & Schouenborg, J. (1991b). Topography and nociceptive receptive fields of climbing fibres projecting to the cerebellar anterior lobe in the cat. *The Journal of Physiology*, *441*(1), 257–274. https://doi.org/10.1113/jphysiol.1991.sp018750

Ekerot, C. F., & Jörntell, H. (2001). Parallel fibre receptive fields of purkinje cells and interneurons are climbing fibre-specific. *European Journal of Neuroscience*, *13*(7), 1303–1310. https://doi.org/10.1046/j.0953-816X.2001.01499.x

Elgersma, Y., Fedorov, N. B., Ikonen, S., Choi, E. S., Elgersma, M., Carvalho, O. M., Giese, K. P., & Silva, A. J. (2002). Inhibitory Autophosphorylation of CaMKII Controls PSD Association, Plasticity, and Learning. *Neuron*, *36*(3), 493–505. https://doi.org/10.1016/S0896-6273(02)01007-3

Errante, L., Tang, D., Gardon, M., Sekerkova, G., Mugnaini, E., & Shaw, G. (1998). The intermediate filament protein peripherin is a marker for cerebellar climbing fibres. *Journal of Neurocytology*, *27*(2), 69–84. https://doi.org/10.1023/A:1006991104595

Fanselow, M. S., & Poulos, A. M. (2005). The Neuroscience of Mammalian Associative Learning. *Annual Review of Psychology*, *56*, 207–234. https://doi.org/10.1146/annurev.psych.56.091103.070213

Farris, S. M. (2011). Are mushroom bodies cerebellum-like structures? *Arthropod Structure & Development*, *40*(4), 368–379. https://doi.org/10.1016/j.asd.2011.02.004

Finch, E. A., & Augustine, G. J. (1998). Local calcium signalling by inositol-1,4,5-trisphosphate in Purkinje cell dendrites. *Nature*, *396*(6713), Article 6713. https://doi.org/10.1038/25541

Fournier, K. A., Hass, C. J., Naik, S. K., Lodha, N., & Cauraugh, J. H. (2010). Motor Coordination in Autism Spectrum Disorders: A Synthesis and Meta-Analysis. *Journal of Autism and Developmental Disorders*, *40*(10), 1227–1240. https://doi.org/10.1007/s10803-010-0981-3

Fricano-Kugler, C., Gordon, A., Shin, G., Gao, K., Nguyen, J., Berg, J., Starks, M., & Geschwind, D. H. (2019). CYFIP1 overexpression increases fear response in mice but does not affect social or repetitive behavioral phenotypes. *Molecular Autism*, *10*(1), 25. https://doi.org/10.1186/s13229-019-0278-0

Friede, R. (1955). Quantitative displacement of the layers within the convolutions of the cerebellar cortex and its biologic importance. *Acta anatomica*, *25*(1), 65–72. https://doi.org/10.1159/000141058

Fujishima, K., Horie, R., Mochizuki, A., & Kengaku, M. (2012). Principles of branch dynamics governing shape characteristics of cerebellar Purkinje cell dendrites. *Development*, *139*(18), 3442–3455. https://doi.org/10.1242/dev.081315

Fujishima, K., Kawabata Galbraith, K., & Kengaku, M. (2018). Dendritic Self-Avoidance and Morphological Development of Cerebellar Purkinje Cells. *The Cerebellum*, *17*(6), 701–708. https://doi.org/10.1007/s12311-018-0984-8

Gaffield, M. A., Bonnan, A., & Christie, J. M. (2019). Conversion of Graded Presynaptic Climbing Fiber Activity into Graded Postsynaptic Ca2+ Signals by Purkinje Cell Dendrites. *Neuron*, *102*, 1–8. https://doi.org/10.1016/j.neuron.2019.03.010

Gaffield, M. A., & Christie, J. M. (2017). Movement Rate Is Encoded and Influenced by Widespread, Coherent Activity of Cerebellar Molecular Layer Interneurons. *Journal of Neuroscience*, *37*(18), 4751–4765. https://doi.org/10.1523/JNEUROSCI.0534-17.2017

Gaffield, M. A., Rowan, M. J. M., Amat, S. B., Hirai, H., & Christie, J. M. (2018). Inhibition gates supralinear Ca2+ signaling in Purkinje cell dendrites during practiced movements. *eLife*, *7*, e36246. https://doi.org/10.7554/eLife.36246

Galliano, E., Potters, J.-W., Elgersma, Y., Wisden, W., Kushner, S. A., Zeeuw, C. I. D., & Hoebeek, F. E. (2013). Synaptic Transmission and Plasticity at Inputs to Murine Cerebellar Purkinje Cells Are Largely Dispensable for Standard Nonmotor Tasks. *Journal of Neuroscience*, *33*(31), 12599–12618. https://doi.org/10.1523/JNEUROSCI.1642-13.2013

Gao, W., Chen, G., Reinert, K. C., & Ebner, T. J. (2006). Cerebellar Cortical Molecular Layer Inhibition Is Organized in Parasagittal Zones. *Journal of Neuroscience*, *26*(32), 8377–8387. https://doi.org/10.1523/JNEUROSCI.2434-06.2006

Gao, Y., Perkins, E. M., Clarkson, Y. L., Tobia, S., Lyndon, A. R., Jackson, M., & Rothstein, J. D. (2011). -III Spectrin Is Critical for Development of Purkinje Cell Dendritic Tree and Spine Morphogenesis. *Journal of Neuroscience*, *31*(46), 16581–16590. https://doi.org/10.1523/JNEUROSCI.3332-11.2011

Gao, Z., van Beugen, B. J., & De Zeeuw, C. I. (2012). Distributed synergistic plasticity and cerebellar learning. *Nature Reviews Neuroscience*, *13*(9), 619–635. https://doi.org/10.1038/nrn3312

Garcia-Garcia, M. G., Kapoor, A., Akinwale, O., Takemaru, L., Kim, T. H., Paton, C., Litwin-Kumar, A., Schnitzer, M. J., Luo, L., & Wagner, M. J. (2024). A cerebellar granule cell-climbing fiber computation to learn to track long time intervals. *Neuron*, *112*(16), 2749-2764.e7. https://doi.org/10.1016/j.neuron.2024.05.019

Gill, D. F., & Hansel, C. (2020). Muscarinic Modulation of SK2-Type K+ Channels Promotes Intrinsic Plasticity in L2/3 Pyramidal Neurons of the Mouse Primary Somatosensory Cortex. *eNeuro*, *7*(2). https://doi.org/10.1523/ENEURO.0453-19.2020

Giovannucci, A., Badura, A., Deverett, B., Najafi, F., Pereira, T. D., Gao, Z., Ozden, I., Kloth, A. D., Pnevmatikakis, E., Paninski, L., De Zeeuw, C. I., Medina, J. F., & Wang, S. S.-H. (2017). Cerebellar granule cells acquire a widespread predictive feedback signal during motor learning. *Nature Neuroscience*, *20*(5), 727–734. https://doi.org/10.1038/nn.4531

Golgi, C. (1874). *Sulla fina anatomia del cervelletto umano* (Vol. 2). Archivio Italiano per le Malattie Nervose.

Grant, S. G. (2012). Synaptopathies: Diseases of the synaptome. *Current Opinion in Neurobiology*, *22*(3), 522–529. https://doi.org/10.1016/j.conb.2012.02.002

Grasselli, G., Boele, H.-J., Titley, H. K., Bradford, N., Beers, L. van, Jay, L., Beekhof, G. C., Busch, S. E., Zeeuw, C. I. D., Schonewille, M., & Hansel, C. (2020). SK2 channels in cerebellar Purkinje cells contribute to excitability modulation in motor-learning–specific memory traces. *PLOS Biology*, *18*(1), e3000596. https://doi.org/10.1371/journal.pbio.3000596

Green, D., Charman, T., Pickles, A., Chandler, S., Loucas, T., Simonoff, E., & Baird, G. (2009). Impairment in movement skills of children with autistic spectrum disorders. *Developmental Medicine & Child Neurology*, *51*(4), 311–316. https://doi.org/10.1111/j.1469-8749.2008.03242.x

Gründemann, J., & Clark, B. A. (2015). Calcium-Activated Potassium Channels at Nodes of Ranvier Secure Axonal Spike Propagation. *Cell Reports*, *12*(11), 1715–1722. https://doi.org/10.1016/j.celrep.2015.08.022

Guo, C., Witter, L., Rudolph, S., Elliott, H. L., Ennis, K. A., & Regehr, W. G. (2016). Purkinje Cells Directly Inhibit Granule Cells in Specialized Regions of the Cerebellar Cortex. *Neuron*, *91*(6), 1330–1341. https://doi.org/10.1016/j.neuron.2016.08.011

Han, K.-S., Chen, C. H., Khan, M. M., Guo, C., & Regehr, W. G. (2020). Climbing fiber synapses rapidly and transiently inhibit neighboring Purkinje cells via ephaptic coupling. *Nature Neuroscience*, 1–11. https://doi.org/10.1038/s41593-020-0701-z

Hansel, C. (2019). Deregulation of synaptic plasticity in autism. *Neuroscience Letters*, *688*, 58–61. https://doi.org/10.1016/j.neulet.2018.02.003

Hansel, C., de Jeu, M., Belmeguenai, A., Houtman, S. H., Buitendijk, G. H. S., Andreev, D., De Zeeuw, C. I., & Elgersma, Y. (2006). αCaMKII Is Essential for Cerebellar LTD and Motor Learning. *Neuron*, *51*(6), 835–843. https://doi.org/10.1016/j.neuron.2006.08.013

Hansel, C., & Disterhoft, J. F. (2020). Why is synaptic plasticity not enough? *Neurobiology of Learning and Memory*, *176*, 107336. https://doi.org/10.1016/j.nlm.2020.107336

Hansel, C., & Linden, D. J. (2000). Long-term depression of the cerebellar climbing fiber-Purkinje neuron synapse. *Neuron*, *26*(2), 473–482. https://doi.org/10.1016/S0896-6273(00)81179-4

Hansel, C., Linden, D. J., & D'Angelo, E. (2001). Beyond parallel fiber LTD: The diversity of synaptic and non-synaptic plasticity in the cerebellum. *Nature Neuroscience*, *4*(5), 467–475. https://doi.org/10.1038/87419

Harris, K. M., & Stevens, J. K. (1988). Dendritic spines of rat cerebellar Purkinje cells: Serial electron microscopy with reference to their biophysical characteristics. *Journal of Neuroscience*, *8*(12), 4455–4469. https://doi.org/10.1523/JNEUROSCI.08-12-04455.1988

Hartell, N. A. (1996). Strong Activation of Parallel Fibers Produces Localized Calcium Transients and a Form of LTD That Spreads to Distant Synapses. *Neuron*, *16*(3), 601–610. https://doi.org/10.1016/S0896-6273(00)80079-3

Hartley, S. L., MacLean Jr, W. E., Butler, M. G., Zarcone, J., & Thompson, T. (2005). Maladaptive behaviors and risk factors among the genetic subtypes of Prader–Willi syndrome. *American Journal of Medical Genetics*, *136A*(2), 140–145. https://doi.org/10.1002/ajmg.a.30771

Hashimoto, K., Ichikawa, R., Kitamura, K., Watanabe, M., & Kano, M. (2009). Translocation of a "Winner" Climbing Fiber to the Purkinje Cell Dendrite and Subsequent Elimination of "Losers" from the Soma in Developing Cerebellum. *Neuron*, *63*(1), 106–118. https://doi.org/10.1016/j.neuron.2009.06.008

Hashimoto, K., & Kano, M. (2003). Functional differentiation of multiple climbing fiber inputs during synapse elimination in the developing cerebellum. *Neuron*, *38*(5), 785–796. https://doi.org/10.1016/S0896-6273(03)00298-8

Heffley, W., & Hull, C. (2019). Classical conditioning drives learned reward prediction signals in climbing fibers across the lateral cerebellum. *eLife*, *8*, e46764. https://doi.org/10.7554/eLife.46764

Henson, R. N. A., & Rugg, M. D. (2003). Neural response suppression, haemodynamic repetition effects, and behavioural priming. *Neuropsychologia*, *41*(3), 263–270. https://doi.org/10.1016/S0028-3932(02)00159-8

Herculano-Houzel, S. (2009). The human brain in numbers: A linearly scaled-up primate brain. *Frontiers in Human Neuroscience*, *3*. https://doi.org/10.3389/neuro.09.031.2009

Herculano-Houzel, S., Avelino-de-Souza, K., Neves, K., Porfírio, J., Messeder, D., Mattos Feijó, L., Maldonado, J., & Manger, P. R. (2014). The elephant brain in numbers. *Frontiers in Neuroanatomy*, *8*. https://www.frontiersin.org/articles/10.3389/fnana.2014.00046

Herzfeld, D. J., Kojima, Y., Soetedjo, R., & Shadmehr, R. (2015). Encoding of action by the Purkinje cells of the cerebellum. *Nature*, *526*(7573), 439–442. https://doi.org/10.1038/nature15693

Hildebrand, M. E., Isope, P., Miyazaki, T., Nakaya, T., Garcia, E., Feltz, A., Schneider, T., Hescheler, J., Kano, M., Sakimura, K., Watanabe, M., Dieudonné, S., & Snutch, T. P. (2009). Functional Coupling between mGluR1 and Cav3.1 T-Type Calcium Channels Contributes to Parallel Fiber-Induced Fast Calcium Signaling within Purkinje Cell Dendritic Spines. *Journal of Neuroscience*, *29*(31), 9668–9682. https://doi.org/10.1523/JNEUROSCI.0362-09.2009

Hillman, D. E., & Chen, S. (1984). Reciprocal relationship between size of postsynaptic densities and their number: Constancy in contact area. *Brain Research*, *295*(2), 325–343. https://doi.org/10.1016/0006-8993(84)90981-8

Hirai, H. (2001). Ca2+-dependent regulation of synaptic δ2 glutamate receptor density in cultured rat Purkinje neurons. *European Journal of Neuroscience*, *14*(1), 73–82. https://doi.org/10.1046/j.0953-816x.2001.01630.x

Hirano, T. (1990). Depression and potentiation of the synaptic transmission between a granule cell and a Purkinje cell in rat cerebellar culture. *Neuroscience Letters*, *119*(2), 141–144. https://doi.org/10.1016/0304-3940(90)90818-T

Hirayama, T., Kadooka, Y., Tarusawa, E., Saitoh, S., Nakayama, H., Hoshino, N., Nakama, S., Fukuishi, T., Kawanishi, Y., Umeshima, H., Tomita, K., Yoshimura, Y., Galjart, N., Hashimoto, K., Ohno, N., & Yagi, T. (2022). CTCF loss induces giant lamellar bodies in Purkinje cell dendrites. *Acta Neuropathologica Communications*, *10*(1), 172. https://doi.org/10.1186/s40478-022-01478-6

Hoang, H., Lang, E. J., Hirata, Y., Tokuda, I. T., Aihara, K., Toyama, K., Kawato, M., & Schweighofer, N. (2020). Electrical coupling controls dimensionality and chaotic firing of inferior olive neurons. *PLOS Computational Biology*, *16*(7), e1008075. https://doi.org/10.1371/journal.pcbi.1008075

Hoge, G. J., Davidson, K. G. V., Yasumura, T., Castillo, P. E., Rash, J. E., & Pereda, A. E. (2010). The extent and strength of electrical coupling between inferior olivary neurons is

heterogeneous. *Journal of Neurophysiology*, *105*(3), 1089–1101. https://doi.org/10.1152/jn.00789.2010

Huang, C.-C., Sugino, K., Shima, Y., Guo, C., Bai, S., Mensh, B. D., Nelson, S. B., & Hantman, A. W. (2013). Convergence of pontine and proprioceptive streams onto multimodal cerebellar granule cells. *eLife*, *2*, e00400. https://doi.org/10.7554/eLife.00400

Ichikawa, R., Hashimoto, K., Miyazaki, T., Uchigashima, M., Yamasaki, M., Aiba, A., Kano, M., & Watanabe, M. (2016). Territories of heterologous inputs onto Purkinje cell dendrites are segregated by mGluR1-dependent parallel fiber synapse elimination. *Proceedings of the National Academy of Sciences*, *113*(8), 2282–2287. https://doi.org/10.1073/pnas.1511513113

Ichise, T., Kano, M., Hashimoto, K., Yanagihara, D., Nakao, K., Shigemoto, R., Katsuki, M., & Aiba, A. (2000). mGluR1 in Cerebellar Purkinje Cells Essential for Long-Term Depression, Synapse Elimination, and Motor Coordination. *Science*, *288*(5472), 1832–1835. https://doi.org/10.1126/science.288.5472.1832

Ing-Esteves, S., Kostadinov, D., Marocha, J., Sing, A. D., Joseph, K. S., Laboulaye, M. A., Sanes, J. R., & Lefebvre, J. L. (2018). Combinatorial Effects of Alpha- and Gamma-Protocadherins on Neuronal Survival and Dendritic Self-Avoidance. *The Journal of Neuroscience*, *38*(11), 2713–2729. https://doi.org/10.1523/JNEUROSCI.3035-17.2018

Ishikawa, T., Shimuta, M., & Häusser, M. (2015). Multimodal sensory integration in single cerebellar granule cells in vivo. *eLife*, *4*, e12916. https://doi.org/10.7554/eLife.12916

Ito, M. (1993). Movement and thought: Identical control mechanisms by the cerebellum. *Trends in Neurosciences*, *16*(11), 448–450. https://doi.org/10.1016/0166-2236(93)90073-U

Ito, M. (2001). Cerebellar Long-Term Depression: Characterization, Signal Transduction, and Functional Roles. *Physiological Reviews*, *81*(3), 1143–1195. https://doi.org/10.1152/physrev.2001.81.3.1143

Ito, M. (2008). Control of mental activities by internal models in the cerebellum. *Nature Reviews Neuroscience*, *9*(4), 304–313. https://doi.org/10.1038/nrn2332

Ito, M., & Kano, M. (1982). Long-lasting depression of parallel fiber-Purkinje cell transmission induced by conjunctive stimulation of parallel fibers and climbing fibers in the cerebellar cortex. *Neuroscience Letters*, *33*(3), 253–258. https://doi.org/10.1016/0304-3940(82)90380-9

Ito, M., Sakurai, M., & Tongroach, P. (1982). Climbing fibre induced depression of both mossy fibre responsiveness and glutamate sensitivity of cerebellar Purkinje cells. *The Journal of Physiology*, *324*(1), 113–134. https://doi.org/10.1113/jphysiol.1982.sp014103

Johnson, B. P., Rinehart, N. J., White, O., Millist, L., & Fielding, J. (2013). Saccade adaptation in autism and Asperger's disorder. *Neuroscience*, *243*, 76–87. https://doi.org/10.1016/j.neuroscience.2013.03.051

Joo, W., Hippenmeyer, S., & Luo, L. (2014). Dendrite morphogenesis depends on relative levels of NT-3/TrkC signaling. *Science*, *346*(6209), 626–629. https://doi.org/10.1126/science.1258996

Jörntell, H., & Ekerot, C.-F. (2002). Reciprocal Bidirectional Plasticity of Parallel Fiber Receptive Fields in Cerebellar Purkinje Cells and Their Afferent Interneurons. *Neuron*, *34*(5), 797–806. https://doi.org/10.1016/S0896-6273(02)00713-4

Jörntell, H., & Ekerot, C.-F. (2003). Receptive field plasticity profoundly alters the cutaneous parallel fiber synaptic input to cerebellar interneurons in vivo. *Journal of Neuroscience*, *23*(29), 9620–9631. https://doi.org/23/29/9620 [pii]

Jörntell, H., & Ekerot, C.-F. (2011). Receptive Field Remodeling Induced by Skin Stimulation in Cerebellar Neurons in vivo. *Frontiers in Neural Circuits*, *5*. https://doi.org/10.3389/fncir.2011.00003

Jörntell, H., & Hansel, C. (2006). Synaptic Memories Upside Down: Bidirectional Plasticity at Cerebellar Parallel Fiber-Purkinje Cell Synapses. *Neuron*, *52*(2), 227–238. https://doi.org/10.1016/j.neuron.2006.09.032

Ju, C., Bosman, L. W. J., Hoogland, T. M., Velauthapillai, A., Murugesan, P., Warnaar, P., van Genderen, R. M., Negrello, M., & De Zeeuw, C. I. (2019). Neurons of the inferior olive respond to broad classes of sensory input while subject to homeostatic control. *Journal of Physiology*, *597*(9), 2483–2514. https://doi.org/10.1113/JP277413

Kaneko, M., Yamaguchi, K., Eiraku, M., Sato, M., Takata, N., Kiyohara, Y., Mishina, M., Hirase, H., Hashikawa, T., & Kengaku, M. (2011). Remodeling of monoplanar purkinje cell dendrites during cerebellar circuit formation. *PLoS ONE*, *6*(5), 1–13. https://doi.org/10.1371/journal.pone.0020108

Kano, M., Hashimoto, K., Kurihara, H., Watanabe, M., Inoue, Y., Aiba, A., & Tonegawa, S. (1997). Persistent multiple climbing fiber innervation of cerebellar purkinje cells in mice lacking mGluR1. *Neuron*, *18*(1), 71–79.

Kano, M., Watanabe, T., Uesaka, N., & Watanabe, M. (2018). Multiple Phases of Climbing Fiber Synapse Elimination in the Developing Cerebellum. *Cerebellum*, *17*(6), 722–734. https://doi.org/10.1007/s12311-018-0964-z

Kapfhammer, J. P. (2004). Cellular and molecular control of dendritic growth and development of cerebellar Purkinje cells. *Progress in Histochemistry and Cytochemistry*, *39*(3), 131–182. https://doi.org/10.1016/j.proghi.2004.07.002

Kato, T., Hirano, A., & Llena, J. F. (1985). A Golgi study of the human Purkinje cell soma and dendrites. *Acta Neuropathologica*, *68*(2), 145–148. https://doi.org/10.1007/BF00688636

Kemp, K. C., Cook, A. J., Redondo, J., Kurian, K. M., Scolding, N. J., & Wilkins, A. (2016). Purkinje cell injury, structural plasticity and fusion in patients with Friedreich's ataxia.

Acta Neuropathologica Communications, *4*(1), 53. https://doi.org/10.1186/s40478-016-0326-3

King, M., Hernandez-Castillo, C. R., Poldrack, R. A., Ivry, R. B., & Diedrichsen, J. (2019). Functional boundaries in the human cerebellum revealed by a multi-domain task battery. *Nature Neuroscience*, *22*(8), 1371–1378. https://doi.org/10.1038/s41593-019-0436-x

Kishimoto, Y., Fujimichi, R., Araishi, K., Kawahara, S., Kano, M., Aiba, A., & Kirino, Y. (2002). mGluR1 in cerebellar Purkinje cells is required for normal association of temporally contiguous stimuli in classical conditioning. *European Journal of Neuroscience*, *16*(12), 2416–2424. https://doi.org/10.1046/j.1460-9568.2002.02407.x

Kitamura, K., & Häusser, M. (2011). Dendritic Calcium Signaling Triggered by Spontaneous and Sensory-Evoked Climbing Fiber Input to Cerebellar Purkinje Cells In Vivo. *Journal of Neuroscience*, *31*(30), 10847–10858. https://doi.org/10.1523/jneurosci.2525-10.2011

Kloth, A. D., Badura, A., Li, A., Cherskov, A., Connolly, S. G., Giovannucci, A., Bangash, M. A., Grasselli, G., Peñagarikano, O., Piochon, C., Tsai, P. T., Geschwind, D. H., Hansel, C., Sahin, M., Takumi, T., Worley, P. F., & Wang, S. S.-H. (2015). Cerebellar associative sensory learning defects in five mouse autism models. *eLife*, *4*, e06085. https://doi.org/10.7554/eLife.06085

Konnerth, A., Dreessen, J., & Augustine, G. J. (1992). Brief dendritic calcium signals initiate long-lasting synaptic depression in cerebellar Purkinje cells. *Proceedings of the National Academy of Sciences*, *89*(15), 7051–7055. https://doi.org/10.1073/pnas.89.15.7051

Kostadinov, D., Beau, M., Pozo, M. B., & Häusser, M. (2019). Predictive and reactive reward signals conveyed by climbing fiber inputs to cerebellar Purkinje cells. *Nature Neuroscience*, *22*(June), 950–962. https://doi.org/10.1038/s41593-019-0381-8

Krienen, F. M., & Buckner, R. L. (2009). Segregated Fronto-Cerebellar Circuits Revealed by Intrinsic Functional Connectivity. *Cerebral Cortex*, *19*(10), 2485–2497. https://doi.org/10.1093/cercor/bhp135

Kuwako, K., & Okano, H. (2018). The LKB1-SIK Pathway Controls Dendrite Self-Avoidance in Purkinje Cells. *Cell Reports*, *24*(11), 2808-2818.e4. https://doi.org/10.1016/j.celrep.2018.08.029

Lackey, E. P., Moreira, L., Norton, A., Hemelt, M. E., Osorno, T., Nguyen, T. M., Macosko, E. Z., Lee, W.-C. A., Hull, C. A., & Regehr, W. G. (2024). Specialized connectivity of molecular layer interneuron subtypes leads to disinhibition and synchronous inhibition of cerebellar Purkinje cells. *Neuron*, *112*(14), 2333–2348. https://doi.org/10.1016/j.neuron.2024.04.010

Lanore, F., Cayco-Gajic, N. A., Gurnani, H., Coyle, D., & Silver, R. A. (2021). Cerebellar granule cell axons support high-dimensional representations. *Nature Neuroscience*, *24*(8), Article 8. https://doi.org/10.1038/s41593-021-00873-x

Larkum, M. E., Zhu, J. J., & Sakmann, B. (2001). Dendritic mechanisms underlying the coupling of the dendritic with the axonal action potential initiation zone of adult rat layer 5 pyramidal neurons. *The Journal of Physiology*, *533*(2), 447–466. https://doi.org/10.1111/j.1469-7793.2001.0447a.x

Larsell, O. (1926). The cerebellum of reptiles: Lizards and snake. *Journal of Comparative Neurology*, *41*(1), 59–94. https://doi.org/10.1002/cne.900410103

LeBel, A., & D'Mello, A. M. (2023). A seat at the (language) table: Incorporating the cerebellum into frameworks for language processing. *Current Opinion in Behavioral Sciences*, *53*, 101310. https://doi.org/10.1016/j.cobeha.2023.101310

LeBel, A., Jain, S., & Huth, A. G. (2021). Voxelwise Encoding Models Show That Cerebellar Language Representations Are Highly Conceptual. *Journal of Neuroscience*, *41*(50), 10341–10355. https://doi.org/10.1523/JNEUROSCI.0118-21.2021

Lee, K. J., Kim, H., Kim, T. S., Park, S.-H., & Rhyu, I. J. (2004). Morphological analysis of spine shapes of Purkinje cell dendrites in the rat cerebellum using high-voltage electron microscopy. *Neuroscience Letters*, *359*(1), 21–24. https://doi.org/10.1016/j.neulet.2004.01.071

Lee, K. J., Kim, H., & Rhyu, I. J. (2005). The roles of dendritic spine shapes in Purkinje cells. *The Cerebellum*, *4*(2), 97–104. https://doi.org/10.1080/14734220510007842

Lefebvre, J. L., Kostadinov, D., Chen, W. V., Maniatis, T., & Sanes, J. R. (2012). Protocadherins mediate dendritic self-avoidance in the mammalian nervous system. *Nature*, *488*(7412), 517–521. https://doi.org/10.1038/nature11305

Lev-Ram, V., Mehta, S. B., Kleinfeld, D., & Tsien, R. Y. (2003). Reversing cerebellar long-term depression. *Proceedings of the National Academy of Sciences*, *100*(26), 15989–15993. https://doi.org/10.1073/pnas.2636935100

Lev-Ram, V., Wong, S. T., Storm, D. R., & Tsien, R. Y. (2002). A new form of cerebellar long-term potentiation is postsynaptic and depends on nitric oxide but not cAMP. *Proceedings of the National Academy of Sciences*, *99*(12), 8389–8393. https://doi.org/10.1073/pnas.122206399

Lin, C.-Y., Louis, E. D., Faust, P. L., Koeppen, A. H., Vonsattel, J.-P. G., & Kuo, S.-H. (2014). Abnormal climbing fibre-Purkinje cell synaptic connections in the essential tremor cerebellum. *Brain*, *137*(12), 3149–3159. https://doi.org/10.1093/brain/awu281

Lin, T.-F., Busch, S. E., & Hansel, C. (2024). Intrinsic and synaptic determinants of receptive field plasticity in Purkinje cells of the mouse cerebellum. *Nature Communications*, *15*(1), 4645. https://doi.org/10.1038/s41467-024-48373-3

Linden, D. J., Dickinson, M. H., Smeyne, M., & Connor, J. A. (1991). A long-term depression of AMPA currents in cultured cerebellar purkinje neurons. *Neuron*, *7*(1), 81–89. https://doi.org/10.1016/0896-6273(91)90076-C

Litwin-Kumar, A., Harris, K. D., Axel, R., Sompolinsky, H., & Abbott, L. F. (2017). Optimal Degrees of Synaptic Connectivity. *Neuron*, *93*(5), 1153-1164.e7. https://doi.org/10.1016/j.neuron.2017.01.030

Liu, Q. A., & Shio, H. (2008). Mitochondrial Morphogenesis, Dendrite Development, and Synapse Formation in Cerebellum Require both Bcl-w and the Glutamate Receptor δ2. *PLOS Genetics*, *4*(6), e1000097. https://doi.org/10.1371/journal.pgen.1000097

Llano, I., Marty, A., Armstrong, C. M., & Konnerth, A. (1991). Synaptic- and agonist-induced excitatory currents of Purkinje cells in rat cerebellar slices. *The Journal of Physiology*, *434*(1), 183–213. https://doi.org/10.1113/jphysiol.1991.sp018465

Llinás, R., & Sugimori, M. (1980). Electrophysiological properties of in vitro Purkinje cell dendrites in mammalian cerebellar slices. *The Journal of Physiology*, *305*(1), 197–213. https://doi.org/10.1113/jphysiol.1980.sp013358

Loschky, S. S., Spano, G. M., Marshall, W., Schroeder, A., Nemec, K. M., Schiereck, S. S., de Vivo, L., Bellesi, M., Banningh, S. W., Tononi, G., & Cirelli, C. (2022). Ultrastructural effects of sleep and wake on the parallel fiber synapses of the cerebellum. *eLife*, *11*, e84199. https://doi.org/10.7554/eLife.84199

Losonczy, A., Makara, J. K., & Magee, J. C. (2008). Compartmentalized dendritic plasticity and input feature storage in neurons. *Nature*, *452*(7186), 436–441. https://doi.org/10.1038/nature06725

Louis, E. D., Lee, M., Babij, R., Ma, K., Cortés, E., Vonsattel, J.-P. G., & Faust, P. L. (2014). Reduced Purkinje cell dendritic arborization and loss of dendritic spines in essential tremor. *Brain*, *137*(12), 3142–3148. https://doi.org/10.1093/brain/awu314

Lu, H., Esquivel, A. V., & Bower, J. M. (2009). 3D electron microscopic reconstruction of segments of rat cerebellar purkinje cell dendrites receiving ascending and parallel fiber granule cell synaptic inputs. *Journal of Comparative Neurology*, *514*(6), 583–594. https://doi.org/10.1002/cne.22041

Lynch, G. (2002). Memory enhancement: The search for mechanism-based drugs. *Nature Neuroscience*, *5*(11), 1035–1038. https://doi.org/10.1038/nn935

Macrì, S., Savriama, Y., Khan, I., & Di-Poï, N. (2019). Comparative analysis of squamate brains unveils multi-level variation in cerebellar architecture associated with locomotor specialization. *Nature Communications*, *10*(1), 5560. https://doi.org/10.1038/s41467-019-13405-w

Maekawa, K., & Simpson, J. I. (1972). Climbing fiber activation of Purkinje cells in the flocculus by impulses transferred through the visual pathway. *Brain Research*, *39*(1), 245–251. https://doi.org/10.1016/0006-8993(72)90800-1

Magielse, N., Heuer, K., Toro, R., Schutter, D. J. L. G., & Valk, S. L. (2023). A Comparative Perspective on the Cerebello-Cerebral System and Its Link to Cognition. *The Cerebellum*, *22*(6), 1293–1307. https://doi.org/10.1007/s12311-022-01495-0

Marin-Padilla, M. (1985). Neurogenesis of the climbing fibers in the human cerebellum: A Golgi study. *Journal of Comparative Neurology*, *235*(1), 82–96. https://doi.org/10.1002/cne.902350107

Markram, H., Rinaldi, T., & Markram, K. (2007). The intense world syndrome—An alternative hypothesis for autism. *Frontiers in Neuroscience*, *1*(1), 77–96. https://doi.org/10.3389/neuro.01.1.1.006.2007

Márquez-Ruiz, J., & Cheron, G. (2012). Sensory Stimulation-Dependent Plasticity in the Cerebellar Cortex of Alert Mice. *PLOS ONE*, *7*(4), e36184. https://doi.org/10.1371/journal.pone.0036184

Marr, D. (1969). A theory of cerebellar cortex. *The Journal of Physiology*, *202*(2), 437–470. https://doi.org/10.1113/jphysiol.1969.sp008820

Maruta, J., Hensbroek, R. A., & Simpson, J. I. (2007). Intraburst and Interburst Signaling by Climbing Fibers. *Journal of Neuroscience*, *27*(42), 11263–11270. https://doi.org/10.1523/JNEUROSCI.2559-07.2007

Masoli, S., Sanchez-Ponce, D., Vrieler, N., Abu-Haya, K., Lerner, V., Shahar, T., Nedelescu, H., Rizza, M. F., Benavides-Piccione, R., DeFelipe, J., Yarom, Y., Munoz, A., & D'Angelo, E. (2024). Human Purkinje cells outperform mouse Purkinje cells in dendritic complexity and computational capacity. *Communications Biology*, *7*(5), Article 1. https://doi.org/10.1038/s42003-023-05689-y

Masoli, S., Solinas, S., & D'Angelo, E. (2015). Action potential processing in a detailed Purkinje cell model reveals a critical role for axonal compartmentalization. *Frontiers in Cellular Neuroscience*, *9*. https://doi.org/10.3389/fncel.2015.00047

Mathews, P. J., Lee, K. H., Peng, Z., Houser, C. R., & Otis, T. S. (2012). Effects of Climbing Fiber Driven Inhibition on Purkinje Neuron Spiking. *Journal of Neuroscience*, *32*(50), 17988–17997. https://doi.org/10.1523/JNEUROSCI.3916-12.2012

Matsuda, K., Miura, E., Miyazaki, T., Kakegawa, W., Emi, K., Narumi, S., Fukazawa, Y., Ito-Ishida, A., Kondo, T., Shigemoto, R., Watanabe, M., & Yuzaki, M. (2010). Cbln1 Is a Ligand for an Orphan Glutamate Receptor δ2, a Bidirectional Synapse Organizer. *Science*, *328*(5976), 363–368. https://doi.org/10.1126/science.1185152

Mavroudis, I. A., Kazis, D., Petridis, F., Chatzikonstantinou, S., Karantali, E., Njau, S. N., Costa, V., Ciobica, A., Trus, C., Balmus, I. M., & Baloyannis, S. J. (2022). Morphological and morphometric changes in the Purkinje cells of patients with essential tremor. *Experimental and Therapeutic Medicine*, *23*(2), 1–8. https://doi.org/10.3892/etm.2021.11090

Mavroudis, I. A., Petrides, F., Manani, M., Chatzinikolaou, F., Ciobică, A. S., Pădurariu, M., Kazis, D., Njau, S. N., Costa, V. G., & Baloyannis, S. J. (2017). Purkinje cells pathology in schizophrenia. A morphometric approach. *Romanian Journal of Morphology and Embryology*, *58*(2), 419–424.

McCormick, D. A., & Thompson, R. F. (1984). Cerebellum: Essential Involvement in the Classically Conditioned Eyelid Response. *Science*, *223*(4633), 296–299. https://doi.org/10.1126/science.6701513

Medina, J. F., Nores, W. L., & Mauk, M. D. (2002). Inhibition of climbing fibres is a signal for the extinction of conditioned eyelid responses. *Nature*, *416*(6878), Article 6878. https://doi.org/10.1038/416330a

Mertens, E. J., Leibner, Y., Pie, J., Galakhova, A. A., Waleboer, F., Meijer, J., Heistek, T. S., Wilbers, R., Heyer, D., Goriounova, N. A., Idema, S., Verhoog, M. B., Kalmbach, B. E., Lee, B. R., Gwinn, R. P., Lein, E. S., Aronica, E., Ting, J., Mansvelder, H. D., … Kock, C. P. J. de. (2024). Morpho-electric diversity of human hippocampal CA1 pyramidal neurons. *Cell Reports*, *43*(4). https://doi.org/10.1016/j.celrep.2024.114100

Midtgaard, J. (1995). Spatial synaptic integration in Purkinje cell dendrites. *The Journal of Physiology*, *89*(1), 23–32. https://doi.org/10.1016/0928-4257(96)80548-1

Midtgaard, J., Lasser-Ross, N., & Ross, W. N. (1993). Spatial distribution of Ca2+ influx in turtle Purkinje cell dendrites in vitro: Role of a transient outward current. *Journal of Neurophysiology*, *70*(6), 2455–2469. https://doi.org/10.1152/jn.1993.70.6.2455

Mittmann, W., Koch, U., & Häusser, M. (2005). Feed-forward inhibition shapes the spike output of cerebellar Purkinje cells. *The Journal of Physiology*, *563*(2), 369–378. https://doi.org/10.1113/jphysiol.2004.075028

Miyakawa, H., Lev-Ram, V., Lasser-Ross, N., & Ross, W. N. (1992). Calcium transients evoked by climbing fiber and parallel fiber synaptic inputs in guinea pig cerebellar Purkinje neurons. *Journal of Neurophysiology*, *68*(4), 1178–1189. https://doi.org/10.1152/jn.1992.68.4.1178

Miyazaki, T., & Watanabe, M. (2011). Development of an anatomical technique for visualizing the mode of climbing fiber innervation in Purkinje cells and its application to mutant mice lacking GluRδ2 and Cav2.1. *Anatomical Science International*, *86*(1), 10–18. https://doi.org/10.1007/s12565-010-0095-1

Mohan, H., Verhoog, M. B., Doreswamy, K. K., Eyal, G., Aardse, R., Lodder, B. N., Goriounova, N. A., Asamoah, B., B. Brakspear, A. B. C., Groot, C., van der Sluis, S., Testa-Silva, G., Obermayer, J., Boudewijns, Z. S. R. M., Narayanan, R. T., Baayen, J. C., Segev, I., Mansvelder, H. D., & de Kock, C. P. J. (2015). Dendritic and Axonal Architecture of Individual Pyramidal Neurons across Layers of Adult Human Neocortex. *Cerebral Cortex (New York, NY)*, *25*(12), 4839–4853. https://doi.org/10.1093/cercor/bhv188

Mosconi, M. W., Luna, B., Kay-Stacey, M., Nowinski, C. V., Rubin, L. H., Scudder, C., Minshew, N., & Sweeney, J. A. (2013). Saccade Adaptation Abnormalities Implicate Dysfunction of Cerebellar-Dependent Learning Mechanisms in Autism Spectrum Disorders (ASD). *PLOS ONE*, *8*(5), e63709. https://doi.org/10.1371/journal.pone.0063709

Mota, B., & Herculano-Houzel, S. (2015). Cortical folding scales universally with surface area and thickness, not number of neurons. *Science*, *349*(6243), 74–77. https://doi.org/10.1126/science.aaa9101

Nabavi, S., Fox, R., Proulx, C. D., Lin, J. Y., Tsien, R. Y., & Malinow, R. (2014). Engineering a memory with LTD and LTP. *Nature*, *511*(7509), 348–352. https://doi.org/10.1038/nature13294

Najafi, F., Giovannucci, A., Wang, S. S.-H., & Medina, J. F. (2014a). Coding of stimulus strength via analog calcium signals in Purkinje cell dendrites of awake mice. *eLife*, *3*, 1–16. https://doi.org/10.7554/elife.03663

Najafi, F., Giovannucci, A., Wang, S. S.-H., & Medina, J. F. (2014b). Sensory-Driven Enhancement of Calcium Signals in Individual Purkinje Cell Dendrites of Awake Mice. *Cell Reports*, *6*(5), 792–798. https://doi.org/10.1016/j.celrep.2014.02.001

Najafi, F., & Medina, J. F. (2013). Beyond "all-or-nothing" climbing fibers: Graded representation of teaching signals in Purkinje cells. *Frontiers in Neural Circuits*, *7*(July), 1–8. https://doi.org/10.3389/fncir.2013.00115

Nakatani, J., Tamada, K., Hatanaka, F., Ise, S., Ohta, H., Inoue, K., Tomonaga, S., Watanabe, Y., Chung, Y. J., Banerjee, R., Iwamoto, K., Kato, T., Okazawa, M., Yamauchi, K., Tanda, K., Takao, K., Miyakawa, T., Bradley, A., & Takumi, T. (2009). Abnormal Behavior in a Chromosome- Engineered Mouse Model for Human 15q11-13 Duplication Seen in Autism. *Cell*, *137*(7), 1235–1246. https://doi.org/10.1016/j.cell.2009.04.024

Nakayama, H., Miyazaki, T., Abe, M., Yamazaki, M., Kawamura, Y., Choo, M., Konno, K., Kawata, S., Uesaka, N., Hashimoto, K., Miyata, M., Sakimura, K., Watanabe, M., & Kano, M. (2024). Direct and indirect pathways for heterosynaptic interaction underlying developmental synapse elimination in the mouse cerebellum. *Communications Biology*, *7*(806), 1–13. https://doi.org/10.1038/s42003-024-06447-4

Napoli, I., Mercaldo, V., Boyl, P. P., Eleuteri, B., Zalfa, F., De Rubeis, S., Di Marino, D., Mohr, E., Massimi, M., Falconi, M., Witke, W., Costa-Mattioli, M., Sonenberg, N., Achsel, T., & Bagni, C. (2008). The Fragile X Syndrome Protein Represses Activity-Dependent Translation through CYFIP1, a New 4E-BP. *Cell*, *134*(6), 1042–1054. https://doi.org/10.1016/j.cell.2008.07.031

Napper, R. M. A., & Harvey, R. J. (1988). Number of parallel fiber synapses on an individual Purkinje cell in the cerebellum of the rat. *Journal of Comparative Neurology*, *274*(2), 168–177. https://doi.org/10.1002/cne.902740204

Nedelescu, H., & Abdelhack, M. (2013). Comparative morphology of dendritic arbors in populations of Purkinje cells in mouse sulcus and apex. *Neural Plasticity*, *948587*. https://doi.org/10.1155/2013/948587

Nedelescu, H., Abdelhack, M., & Pritchard, A. T. (2018). Regional differences in Purkinje cell morphology in the cerebellar vermis of male mice. *Journal of Neuroscience Research*, *96*(9), 1476–1489. https://doi.org/10.1002/jnr.24206

Nettekoven, C., Zhi, D., Shahshahani, L., Pinho, A. L., Saadon-Grosman, N., Buckner, R. L., & Diedrichsen, J. (2024). A hierarchical atlas of the human cerebellum for functional precision mapping. *Nature Communications*, *15*(1), 8376. https://doi.org/10.1038/s41467-024-52371-w

Nguyen, T. M., Thomas, L. A., Rhoades, J. L., Ricchi, I., Yuan, X. C., Sheridan, A., Hildebrand, D. G. C., Funke, J., Regehr, W. G., & Lee, W.-C. A. (2023). Structured cerebellar connectivity supports resilient pattern separation. *Nature*, *613*(7944), Article 7944. https://doi.org/10.1038/s41586-022-05471-w

Nilsson, M. N. P., & Jörntell, H. (2021). Channel current fluctuations conclusively explain neuronal encoding of internal potential into spike trains. *Physical Review E*, *103*(2), 022407. https://doi.org/10.1103/PhysRevE.103.022407

Nishiyama, H., & Linden, D. J. (2004). Differential Maturation of Climbing Fiber Innervation in Cerebellar Vermis. *Journal of Neuroscience*, *24*(16), 3926–3932. https://doi.org/10.1523/jneurosci.5610-03.2004

O'Brien, J., & Unwin, N. (2006). Organization of spines on the dendrites of Purkinje cells. *Proceedings of the National Academy of Sciences*, *103*(5), 1575–1580. https://doi.org/10.1073/pnas.0507884103

Ofer, N., Berger, D. R., Kasthuri, N., Lichtman, J. W., & Yuste, R. (2021). Ultrastructural analysis of dendritic spine necks reveals a continuum of spine morphologies. *Developmental Neurobiology*, *81*(5), 746–757. https://doi.org/10.1002/dneu.22829

Oguro-Ando, A., Rosensweig, C., Herman, E., Nishimura, Y., Werling, D., Bill, B. R., Berg, J. M., Gao, F., Coppola, G., Abrahams, B. S., & Geschwind, D. H. (2015). Increased CYFIP1 dosage alters cellular and dendritic morphology and dysregulates mTOR. *Molecular Psychiatry*, *20*(9), Article 9. https://doi.org/10.1038/mp.2014.124

Ohmae, S., & Medina, J. F. (2015). Climbing fibers encode a temporal-difference prediction error during cerebellar learning in mice. *Nature Neuroscience*, *18*(12), Article 12. https://doi.org/10.1038/nn.4167

Ohtsuki, G. (2020). Modification of Synaptic-Input Clustering by Intrinsic Excitability Plasticity on Cerebellar Purkinje Cell Dendrites. *Journal of Neuroscience*, *40*(2), 267–282. https://doi.org/10.1523/JNEUROSCI.3211-18.2019

Ohtsuki, G., & Hansel, C. (2018). Synaptic Potential and Plasticity of an SK2 Channel Gate Regulate Spike Burst Activity in Cerebellar Purkinje Cells. *iScience*, *1*, 49–54. https://doi.org/10.1016/j.isci.2018.02.001

Ohtsuki, G., & Hirano, T. (2008). Bidirectional plasticity at developing climbing fiber–Purkinje neuron synapses. *European Journal of Neuroscience*, *28*(12), 2393–2400. https://doi.org/10.1111/j.1460-9568.2008.06539.x

Ohtsuki, G., Piochon, C., Adelman, J. P., & Hansel, C. (2012). SK2 channel modulation contributes to compartment-specific dendritic plasticity in cerebellar Purkinje cells. *Neuron*, *75*(1), 108–120. https://doi.org/10.1016/j.neuron.2012.05.025

O'Reilly, J. X., Beckmann, C. F., Tomassini, V., Ramnani, N., & Johansen-Berg, H. (2010). Distinct and Overlapping Functional Zones in the Cerebellum Defined by Resting State Functional Connectivity. *Cerebral Cortex*, *20*(4), 953–965. https://doi.org/10.1093/cercor/bhp157

Oristaglio, J., Hyman West, S., Ghaffari, M., Lech, M. S., Verma, B. R., Harvey, J. A., Welsh, J. P., & Malone, R. P. (2013). Children with autism spectrum disorders show abnormal conditioned response timing on delay, but not trace, eyeblink conditioning. *Neuroscience*, *248*, 708–718. https://doi.org/10.1016/j.neuroscience.2013.06.007

Ouares, K. A., & Canepari, M. (2020). The Origin of Physiological Local mGluR1 Supralinear Ca2+ Signals in Cerebellar Purkinje Neurons. *Journal of Neuroscience*, *40*(9), 1795–1809. https://doi.org/10.1523/JNEUROSCI.2406-19.2020

Ouares, K. A., Filipis, L., Tzilivaki, A., Poirazi, P., & Canepari, M. (2019). Two Distinct Sets of Ca2+ and K+ Channels Are Activated at Different Membrane Potentials by the Climbing Fiber Synaptic Potential in Purkinje Neuron Dendrites. *Journal of Neuroscience*, *39*(11), 1969–1981. https://doi.org/10.1523/JNEUROSCI.2155-18.2018

Pan, M.-K., Li, Y.-S., Wong, S.-B., Ni, C.-L., Wang, Y.-M., Liu, W.-C., Lu, L.-Y., Lee, J.-C., Cortes, E. P., Vonsattel, J.-P. G., Sun, Q., Louis, E. D., Faust, P. L., & Kuo, S.-H. (2020). Cerebellar oscillations driven by synaptic pruning deficits of cerebellar climbing fibers contribute to tremor pathophysiology. *Science Translational Medicine*, *12*(526), eaay1769. https://doi.org/10.1126/scitranslmed.aay1769

Pathania, M., Davenport, E. C., Muir, J., Sheehan, D. F., López-Doménech, G., & Kittler, J. T. (2014). The autism and schizophrenia associated gene CYFIP1 is critical for the maintenance of dendritic complexity and the stabilization of mature spines. *Translational Psychiatry*, *4*(3), Article 3. https://doi.org/10.1038/tp.2014.16

Pätz, C., Brachtendorf, S., & Eilers, J. (2019). Developmental Easing of Short-Term Depression in "Winner" Climbing Fibers. *Frontiers in Cellular Neuroscience*, *13*(May), 1–9. https://doi.org/10.3389/fncel.2019.00183

Person, A. L., & Raman, I. M. (2012). Purkinje neuron synchrony elicits time-locked spiking in the cerebellar nuclei. *Nature*, *481*, Article 7382. https://doi.org/10.1038/nature10732

Pi, J. S., Fakharian, M. A., Hage, P., Sedaghat-Nejad, E., Muller, S. Z., & Shadmehr, R. (2024). The olivary input to the cerebellum dissociates sensory events from movement plans. *Proceedings of the National Academy of Sciences*, *121*(17), e2318849121. https://doi.org/10.1073/pnas.2318849121

Pidoux, L., Le Blanc, P., Levenes, C., & Leblois, A. (2018). A subcortical circuit linking the cerebellum to the basal ganglia engaged in vocal learning. *eLife*, *7*, e32167. https://doi.org/10.7554/eLife.32167

Piochon, C., Irinopoulou, T., Brusciano, D., Bailly, Y., Mariani, J., & Levenes, C. (2007). NMDA Receptor Contribution to the Climbing Fiber Response in the Adult Mouse Purkinje Cell. *Journal of Neuroscience*, *27*(40), 10797–10809. https://doi.org/10.1523/JNEUROSCI.2422-07.2007

Piochon, C., Kano, M., & Hansel, C. (2016). LTD-like molecular pathways in developmental synaptic pruning. *Nature Neuroscience*, *19*(10), 1299–1310. https://doi.org/10.1038/nn.4389.LTD-like

Piochon, C., Kloth, A. D., Grasselli, G., Titley, H. K., Nakayama, H., Hashimoto, K., Wan, V., Simmons, D. H., Eissa, T., Nakatani, J., Cherskov, A., Miyazaki, T., Watanabe, M., Takumi, T., Kano, M., Wang, S. S. H., & Hansel, C. (2014). Cerebellar plasticity and motor learning deficits in a copy-number variation mouse model of autism. *Nature Communications*, *5*, 1–12. https://doi.org/10.1038/ncomms6586

Piochon, C., Levenes, C., Ohtsuki, G., & Hansel, C. (2010). Purkinje Cell NMDA Receptors Assume a Key Role in Synaptic Gain Control in the Mature Cerebellum. *Journal of Neuroscience*, *30*(45), 15330–15335. https://doi.org/10.1523/JNEUROSCI.4344-10.2010

Piochon, C., Titley, H. K., Simmons, D. H., Grasselli, G., Elgersma, Y., & Hansel, C. (2016). Calcium threshold shift enables frequency-independent control of plasticity by an instructive signal. *Proceedings of the National Academy of Sciences*, *113*(46), 13221–13226. https://doi.org/10.1073/pnas.1613897113

Pisano, T. J., Dhanerawala, Z. M., Kislin, M., Bakshinskaya, D., Engel, E. A., Hansen, E. J., Hoag, A. T., Lee, J., Oude, N. L. de, Venkataraju, K. U., Verpeut, J. L., Hoebeek, F. E., Richardson, B. D., Boele, H.-J., & Wang, S. S.-H. (2021). Homologous organization of cerebellar pathways to sensory, motor, and associative forebrain. *Cell Reports*, *36*(12). https://doi.org/10.1016/j.celrep.2021.109721

Popa, L. S., & Ebner, T. J. (2019). Cerebellum, Predictions and Errors. *Frontiers in Cellular Neuroscience*, *12*. https://doi.org/10.3389/fncel.2018.00524

Press, D. A., & Wall, M. J. (2008). Expression of cocaine- and amphetamine-regulated transcript (CART) peptides at climbing fibre-Purkinje cell synapses in the rat vestibular cerebellum. *Neuropeptides*, *42*(1), 39–46. https://doi.org/10.1016/j.npep.2007.11.001

Ramakrishnan, K. B., Voges, K., De Propris, L., De Zeeuw, C. I., & D'Angelo, E. (2016). Tactile Stimulation Evokes Long-Lasting Potentiation of Purkinje Cell Discharge In Vivo. *Frontiers in Cellular Neuroscience*, *10*. https://doi.org/10.3389/fncel.2016.00036

Ramirez, J. E., & Stell, B. M. (2016). Calcium Imaging Reveals Coordinated Simple Spike Pauses in Populations of Cerebellar Purkinje Cells. *Cell Reports*, *17*(12), 3125–3132. https://doi.org/10.1016/j.celrep.2016.11.075

Ramón y Cajal, S. (1917). *Recuerdos de mi vida*.

Ramón y Cajal, S. (with University of Illinois Urbana-Champaign). (1909). *Histologie du système nerveux de l'homme & des vertébrés*. Paris : Maloine. http://archive.org/details/histologiedusyst01ram

Rapp, M., Segev, I., & Yarom, Y. (1994). Physiology, morphology and detailed passive models of guinea-pig cerebellar Purkinje cells. *The Journal of Physiology*, *474*(1), 101–118. https://doi.org/10.1113/jphysiol.1994.sp020006

Reeber, S. L., & Sillitoe, R. V. (2011). Patterned expression of a cocaine- and amphetamine-regulated transcript peptide reveals complex circuit topography in the rodent cerebellar cortex. *Journal of Comparative Neurology*, *519*(9), 1781–1796. https://doi.org/10.1002/cne.22601

Reinert, K. C., Dunbar, R. L., Gao, W., Chen, G., & Ebner, T. J. (2004). Flavoprotein Autofluorescence Imaging of Neuronal Activation in the Cerebellar Cortex In Vivo. *Journal of Neurophysiology*, *92*(1), 199–211. https://doi.org/10.1152/jn.01275.2003

Renzi, M., Farrant, M., & Cull-Candy, S. G. (2007). Climbing-fibre activation of NMDA receptors in Purkinje cells of adult mice. *The Journal of Physiology*, *585*(1), 91–101. https://doi.org/10.1113/jphysiol.2007.141531

Rodriguez, A., Ehlenberger, D., Kelliher, K., Einstein, M., Henderson, S. C., Morrison, J. H., Hof, P. R., & Wearne, S. L. (2003). Automated reconstruction of three-dimensional neuronal morphology from laser scanning microscopy images. *Methods*, *30*(1), 94–105. https://doi.org/10.1016/S1046-2023(03)00011-2

Rogerson, T., Cai, D. J., Frank, A., Sano, Y., Shobe, J., Lopez-Aranda, M. F., & Silva, A. J. (2014). Synaptic tagging during memory allocation. *Nature Reviews Neuroscience*, *15*(3), 157–169. https://doi.org/10.1038/nrn3667

Roggeri, L., Rivieccio, B., Rossi, P., & D'Angelo, E. (2008). Tactile Stimulation Evokes Long-Term Synaptic Plasticity in the Granular Layer of Cerebellum. *Journal of Neuroscience*, *28*(25), 6354–6359. https://doi.org/10.1523/JNEUROSCI.5709-07.2008

Roh, S.-E., Kim, S. H., Ryu, C., Kim, C.-E., Kim, Y. G., Worley, P. F., Kim, S. K., & Kim, S. J. (2020). Direct translation of climbing fiber burst-mediated sensory coding into post-synaptic Purkinje cell dendritic calcium. *eLife*, *9*, e61593. https://doi.org/10.7554/eLife.61593

Romano, V., De Propris, L., Bosman, L. W., Warnaar, P., Ten Brinke, M. M., Lindeman, S., Ju, C., Velauthapillai, A., Spanke, J. K., Middendorp Guerra, E., Hoogland, T. M., Negrello, M., D'Angelo, E., & De Zeeuw, C. I. (2018). Potentiation of cerebellar Purkinje cells facilitates whisker reflex adaptation through increased simple spike activity. *eLife*, *7*, 1–33. https://doi.org/10.7554/eLife.38852

Rondi-Reig, L., Paradis, A.-L., Lefort, J. M., Babayan, B. M., & Tobin, C. (2014). How the cerebellum may monitor sensory information for spatial representation. *Frontiers in Systems Neuroscience*, *8*. https://doi.org/10.3389/fnsys.2014.00205

Roome, C. J., & Kuhn, B. (2014). Chronic cranial window with access port for repeated cellular manipulations, drug application, and electrophysiology. *Frontiers in Cellular Neuroscience*, *8*, 379. https://doi.org/10.3389/fncel.2014.00379

Roome, C. J., & Kuhn, B. (2018). Simultaneous dendritic voltage and calcium imaging and somatic recording from Purkinje neurons in awake mice. *Nature Communications*, *9*(1), 1–14. https://doi.org/10.1038/s41467-018-05900-3

Roome, C. J., & Kuhn, B. (2020). Dendritic coincidence detection in Purkinje neurons of awake mice. *eLife*, *9*, e59619. https://doi.org/10.7554/eLife.59619

Rossi, F., Wiklund, L., Want, J. J. L. van der, & Strata, P. (1991). Reinnervation of cerebellar Purkinje cells by climbing fibres surviving a subtotal lesion of the inferior olive in the adult rat. I. Development of new collateral branches and terminal plexuses. *Journal of Comparative Neurology*, *308*(4), 513–535. https://doi.org/10.1002/cne.903080403

Rowan, M. J. M., Bonnan, A., Zhang, K., Amat, S. B., Kikuchi, C., Taniguchi, H., Augustine, G. J., & Christie, J. M. (2018). Graded Control of Climbing-Fiber-Mediated Plasticity and Learning by Inhibition in the Cerebellum. *Neuron*, *99*(5), 999-1015.e6. https://doi.org/10.1016/j.neuron.2018.07.024

Rudolph, S., Hull, C., & Regehr, W. G. (2015). Active Dendrites and Differential Distribution of Calcium Channels Enable Functional Compartmentalization of Golgi Cells. *Journal of Neuroscience*, *35*(47), 15492–15504. https://doi.org/10.1523/JNEUROSCI.3132-15.2015

Ruela, C., Matos-Lima, L., Sobrinho-Simoes, M. A., & Paula-Barbosa, M. M. (1980). Comparative morphometric study of cerebellar neurons. *Acta Anatomica*, *106*(2), 270–275.

Ryan, T. J., Roy, D. S., Pignatelli, M., Arons, A., & Tonegawa, S. (2015). Engram cells retain memory under retrograde amnesia. *Science Reports*, *348*(6238), 1007–1014.

Saadon-Grosman, N., Angeli, P. A., DiNicola, L. M., & Buckner, R. L. (2022). A third somatomotor representation in the human cerebellum. *Journal of Neurophysiology*, *128*(4), 1051–1073. https://doi.org/10.1152/jn.00165.2022

Sakurai, M. (1987). Synaptic modification of parallel fibre-Purkinje cell transmission in in vitro guinea-pig cerebellar slices. *The Journal of Physiology*, *394*(1), 463–480. https://doi.org/10.1113/jphysiol.1987.sp016881

Sakurai, M. (1990). Calcium is an intracellular mediator of the climbing fiber in induction of cerebellar long-term depression. *Proceedings of the National Academy of Sciences*, *87*(9), 3383–3385. https://doi.org/10.1073/pnas.87.9.3383

Santamaria, F., Wils, S., De Schutter, E., & Augustine, G. J. (2011). The diffusional properties of dendrites depend on the density of dendritic spines. *European Journal of Neuroscience*, *34*(4), 561–568. https://doi.org/10.1111/j.1460-9568.2011.07785.x

Santini, E., Huynh, T. N., Longo, F., Koo, S. Y., Mojica, E., D'Andrea, L., Bagni, C., & Klann, E. (2017). Reducing eIF4E-eIF4G interactions restores the balance between protein synthesis and actin dynamics in fragile X syndrome model mice. *Science Signaling*, *10*(504), eaan0665. https://doi.org/10.1126/scisignal.aan0665

Sawtell, N. B. (2017). Neural Mechanisms for Predicting the Sensory Consequences of Behavior: Insights from Electrosensory Systems. *Annual Review of Physiology*, *79*(1), 381–399. https://doi.org/10.1146/annurev-physiol-021115-105003

Schenck, A., Bardoni, B., Moro, A., Bagni, C., & Mandel, J.-L. (2001). A highly conserved protein family interacting with the fragile X mental retardation protein (FMRP) and displaying selective interactions with FMRP-related proteins FXR1P and FXR2P. *Proceedings of the National Academy of Sciences*, *98*(15), 8844–8849. https://doi.org/10.1073/pnas.151231598

Schmahmann, J. D., & Sherman, J. C. (1998). The cerebellar cognitive affective syndrome. *Brain*, *121*(4), 561–579. https://doi.org/10.1093/brain/121.4.561

Schmahmann, J. D., Weilburg, J. B., & Sherman, J. C. (2007). The neuropsychiatry of the cerebellum—Insights from the clinic. *The Cerebellum*, *6*(3), 254–267. https://doi.org/10.1080/14734220701490995

Schmolesky, M. T., Weber, J. T., De Zeeuw, C. I., & Hansel, C. (2002). The making of a complex spike: Ionic composition and plasticity. *Annals of the New York Academy of Sciences*, *978*, 359–390. https://doi.org/10.1111/j.1749-6632.2002.tb07581.x

Schonewille, M., Belmeguenai, A., Koekkoek, S. K., Houtman, S. H., Boele, H. J., van Beugen, B. J., Gao, Z., Badura, A., Ohtsuki, G., Amerika, W. E., Hosy, E., Hoebeek, F. E., Elgersma, Y., Hansel, C., & De Zeeuw, C. I. (2010). Purkinje Cell-Specific Knockout of the Protein Phosphatase PP2B Impairs Potentiation and Cerebellar Motor Learning. *Neuron*, *67*(4), 618–628. https://doi.org/10.1016/j.neuron.2010.07.009

Schreurs, B. G., Gusev, P. A., Tomsic, D., Alkon, D. L., & Shi, T. (1998). Intracellular Correlates of Acquisition and Long-Term Memory of Classical Conditioning in Purkinje Cell Dendrites in Slices of Rabbit Cerebellar Lobule HVI. *Journal of Neuroscience*, *18*(14), 5498–5507. https://doi.org/10.1523/JNEUROSCI.18-14-05498.1998

Schultz, S. R., Kitamura, K., Post-Uiterweer, A., Krupic, J., & Häusser, M. (2009). Spatial Pattern Coding of Sensory Information by Climbing Fiber-Evoked Calcium Signals in Networks of Neighboring Cerebellar Purkinje Cells. *Journal of Neuroscience*, *29*(25), 8005–8015. https://doi.org/10.1523/JNEUROSCI.4919-08.2009

Schutter, E. D., & Maex, R. (1996). The cerebellum: Cortical processing and theory. *Current Opinion in Neurobiology*, *6*(6), 759–764. https://doi.org/10.1016/S0959-4388(96)80025-0

Sears, L. L., Finn, P. R., & Steinmetz, J. E. (1994). Abnormal classical eye-blink conditioning in autism. *Journal of Autism and Developmental Disorders*, *24*(6), 737–751. https://doi.org/10.1007/BF02172283

Sendhilnathan, N., Goldberg, M. E., & Ipata, A. E. (2022). Mixed Selectivity in the Cerebellar Purkinje-Cell Response during Visuomotor Association Learning. *Journal of Neuroscience*, *42*(18), 3847–3855. https://doi.org/10.1523/JNEUROSCI.1771-21.2022

Shambes, G. M., Beermann, D. H., & Welker, W. (1978). Multiple tactile areas in cerebellar cortex: Another patchy cutaneous projection to granule cell columns in rats. *Brain Research*, *157*(1), 123–128. https://doi.org/10.1016/0006-8993(78)91000-4

Shelton, D. P. (1985). Membrane resistivity estimated for the purkinje neuron by means of a passive computer model. *Neuroscience*, *14*(1), 111–131. https://doi.org/10.1016/0306-4522(85)90168-X

Shibuki, K., & Okada, D. (1992). Cerebellar long-term potentiation under suppressed postsynaptic Ca2+ activity. *NeuroReport*, *3*(3), 231.

Shim, H. G., Jang, D. C., Lee, J., Chung, G., Lee, S., Kim, Y. G., Jeon, D. E., & Kim, S. J. (2017). Long-Term Depression of Intrinsic Excitability Accompanied by Synaptic Depression in Cerebellar Purkinje Cells. *Journal of Neuroscience*, *37*(23), 5659–5669. https://doi.org/10.1523/JNEUROSCI.3464-16.2017

Shimuta, M., Sugihara, I., & Ishikawa, T. (2020). Multiple signals evoked by unisensory stimulation converge onto cerebellar granule and Purkinje cells in mice. *Communications Biology*, *3*(381), Article 1. https://doi.org/10.1038/s42003-020-1110-2

Simmons, D. H., Busch, S. E., Titley, H. K., Grasselli, G., Shih, J., Du, X., Wei, C., Gomez, C. M., Piochon, C., & Hansel, C. (2022). Sensory Over-responsivity and Aberrant Plasticity in Cerebellar Cortex in a Mouse Model of Syndromic Autism. *Biological Psychiatry Global Open Science*, *2*(4), 450–459. https://doi.org/10.1016/j.bpsgos.2021.09.004

Simmons, D. H., Titley, H. K., Hansel, C., & Mason, P. (2020). Behavioral Tests for Mouse Models of Autism: An Argument for the Inclusion of Cerebellum-Controlled Motor Behaviors. *Neuroscience*. https://doi.org/10.1016/j.neuroscience.2020.05.010

Simpson, J. I., Wylie, D., & De Zeeuw, C. (1996). On climbing fiber signals and their consequence(s). *Behavioral and Brain Sciences*, *1996*, 384–398. https://doi.org/10.1017/S0140525X00081991

Sims, R. E., & Hartell, N. A. (2006). Differential Susceptibility to Synaptic Plasticity Reveals a Functional Specialization of Ascending Axon and Parallel Fiber Synapses to Cerebellar Purkinje Cells. *Journal of Neuroscience*, *26*(19), 5153–5159. https://doi.org/10.1523/JNEUROSCI.4121-05.2006

Slemmer, J. E., Haasdijk, E. D., Engel, D. C., Plesnila, N., & Weber, J. T. (2007). Aldolase C-positive cerebellar Purkinje cells are resistant to delayed death after cerebral trauma and AMPA-mediated excitotoxicity. *European Journal of Neuroscience*, *26*(3), 649–656. https://doi.org/10.1111/j.1460-9568.2007.05708.x

Sotelo, C., & Dusart, I. (2009). Intrinsic versus extrinsic determinants during the development of Purkinje cell dendrites. *Neuroscience*, *162*(3), 589–600. https://doi.org/10.1016/j.neuroscience.2008.12.035

Špaček, J., & Hartmann, M. (1983). Three-Dimensional analysis of dendritic spines. *Anatomy and Embryology*, *167*(2), 289–310. https://doi.org/10.1007/BF00298517

Steuber, V., Mittmann, W., Hoebeek, F. E., Silver, R. A., De Zeeuw, C. I., Häusser, M., & De Schutter, E. (2007). Cerebellar LTD and Pattern Recognition by Purkinje Cells. *Neuron*, *54*(1), 121–136. https://doi.org/10.1016/j.neuron.2007.03.015

Stoodley, C. J., D'Mello, A. M., Ellegood, J., Jakkamsetti, V., Liu, P., Nebel, M. B., Gibson, J. M., Kelly, E., Meng, F., Cano, C. A., Pascual, J. M., Mostofsky, S. H., Lerch, J. P., & Tsai, P. T. (2017). Altered cerebellar connectivity in autism and cerebellar-mediated rescue of autism-related behaviors in mice. *Nature Neuroscience*, *20*(12), 1744–1751. https://doi.org/10.1038/s41593-017-0004-1

Stoodley, C. J., & Schmahmann, J. D. (2009). Functional topography in the human cerebellum: A meta-analysis of neuroimaging studies. *NeuroImage*, *44*(2), 489–501. https://doi.org/10.1016/j.neuroimage.2008.08.039

Stoodley, C. J., & Schmahmann, J. D. (2010). Evidence for topographic organization in the cerebellum of motor control versus cognitive and affective processing. *Cortex*, *46*(7), 831–844. https://doi.org/10.1016/j.cortex.2009.11.008

Strata, P., & Rossi, F. (1998). Plasticity of the olivocerebellar pathway. *Trends in Neurosciences*, *21*(9), 407–413. https://doi.org/10.1016/S0166-2236(98)01305-8

Streng, M. L., Popa, L. S., & Ebner, T. J. (2017). Climbing Fibers Control Purkinje Cell Representations of Behavior. *The Journal of Neuroscience*, *37*(8), 1997–2009. https://doi.org/10.1523/jneurosci.3163-16.2017

Südhof, T. C. (2008). Neuroligins and neurexins link synaptic function to cognitive disease. *Nature*, *455*(7215), 903–911. https://doi.org/10.1038/nature07456

Sugihara, I. (2006). Organization and remodeling of the olivocerebellar climbing fiber projection. *The Cerebellum*, *5*(1), 15–22. https://doi.org/10.1080/14734220500527385

Sugihara, I., Wu, H. S., & Shinoda, Y. (1999). Morphology of single olivocerebellar axons labeled with biotinylated dextran amine in the rat. *Journal of Comparative Neurology*, *414*(2), 131–148. https://doi.org/10.1002/(SICI)1096-9861(19991115)414:2<131::AID-CNE1>3.0.CO;2-F

Sugihara, I., Wu, H.-S., & Shinoda, Y. (2001). The Entire Trajectories of Single Olivocerebellar Axons in the Cerebellar Cortex and their Contribution to Cerebellar Compartmentalization. *Journal of Neuroscience*, *21*(19), 7715–7723. https://doi.org/10.1523/JNEUROSCI.21-19-07715.2001

Takechi, H., Eilers, J., & Konnerth, A. (1998). A new class of synaptic response involving calcium release in dendritic spines. *Nature*, *396*(6713), 757–760. https://doi.org/10.1038/25547

Takeo, Y. H., Shuster, S. A., Jiang, L., Hu, M. C., Luginbuhl, D. J., Rülicke, T., Contreras, X., Hippenmeyer, S., Wagner, M. J., Ganguli, S., & Luo, L. (2021). GluD2- and Cbln1-mediated competitive interactions shape the dendritic arbors of cerebellar Purkinje cells. *Neuron*, *109*(4), 629-644.e8. https://doi.org/10.1016/j.neuron.2020.11.028

Tanaka, M. (2015). The Dendritic Differentiation of Purkinje Neurons: Unsolved Mystery in Formation of Unique Dendrites. *The Cerebellum*, *14*(3), 227–230. https://doi.org/10.1007/s12311-014-0585-0

Tempia, F., Miniaci, M. C., Anchisi, D., & Strata, P. (1998). Postsynaptic Current Mediated by Metabotropic Glutamate Receptors in Cerebellar Purkinje Cells. *Journal of Neurophysiology*, *80*(2), 520–528. https://doi.org/10.1152/jn.1998.80.2.520

ten Brinke, M. M., Boele, H.-J., Spanke, J. K., Potters, J.-W., Kornysheva, K., Wulff, P., IJpelaar, A. C. H. G., Koekkoek, S. K. E., & De Zeeuw, C. I. (2015). Evolving Models of Pavlovian Conditioning: Cerebellar Cortical Dynamics in Awake Behaving Mice. *Cell Reports*, *13*(9), 1977–1988. https://doi.org/10.1016/j.celrep.2015.10.057

Thach, W. T. (1967). Somatosensory receptive fields of single units in cat cerebellar cortex. *Journal of Neurophysiology*, *30*(4), 675–696. https://doi.org/10.1152/jn.1967.30.4.675

Thome, C., Kelly, T., Yanez, A., Schultz, C., Engelhardt, M., Cambridge, S. B., Both, M., Draguhn, A., Beck, H., & Egorov, A. V. (2014). Axon-Carrying Dendrites Convey Privileged Synaptic Input in Hippocampal Neurons. *Neuron*, *83*(6), 1418–1430. https://doi.org/10.1016/j.neuron.2014.08.013

Titley, H. K., Brunel, N., & Hansel, C. (2017). Toward a Neurocentric View of Learning. *Neuron*, *95*(1), 19–32. https://doi.org/10.1016/j.neuron.2017.05.021

Titley, H. K., Kislin, M., Simmons, D. H., Wang, S. S. -H., & Hansel, C. (2019). Complex spike clusters and false-positive rejection in a cerebellar supervised learning rule. *The Journal of Physiology*, *597.16*, 4387–4406. https://doi.org/10.1113/JP278502

Titley, H. K., Watkins, G. V., Lin, C., Weiss, C., McCarthy, M., Disterhoft, J. F., & Hansel, C. (2020). Intrinsic Excitability Increase in Cerebellar Purkinje Cells after Delay Eye-Blink Conditioning in Mice. *Journal of Neuroscience*, *40*(10), 2038–2046. https://doi.org/10.1523/JNEUROSCI.2259-19.2019

Triarhou, L. C. (2014). Axons emanating from dendrites: Phylogenetic repercussions with Cajalian hues. *Frontiers in Neuroanatomy*, *8*. https://doi.org/10.3389/fnana.2014.00133

Tsai, P. T. (2016). Autism and cerebellar dysfunction: Evidence from animal models. *Seminars in Fetal and Neonatal Medicine*, *21*(5), 349–355. https://doi.org/10.1016/j.siny.2016.04.009

Tsai, P. T., Hull, C., Chu, Y., Greene-Colozzi, E., Sadowski, A. R., Leech, J. M., Steinberg, J., Crawley, J. N., Regehr, W. G., & Sahin, M. (2012). Autistic-like behaviour and cerebellar dysfunction in Purkinje cell Tsc1 mutant mice. *Nature*, *488*(7413), 647–651. https://doi.org/10.1038/nature11310

Tye, K. M., Miller, E. K., Taschbach, F. H., Benna, M. K., Rigotti, M., & Fusi, S. (2024). Mixed selectivity: Cellular computations for complexity. *Neuron*, *112*(14), 2289–2303. https://doi.org/10.1016/j.neuron.2024.04.017

Uemura, T., Lee, S.-J., Yasumura, M., Takeuchi, T., Yoshida, T., Ra, M., Taguchi, R., Sakimura, K., & Mishina, M. (2010). Trans-Synaptic Interaction of GluRδ2 and Neurexin through Cbln1 Mediates Synapse Formation in the Cerebellum. *Cell*, *141*(6), 1068–1079. https://doi.org/10.1016/j.cell.2010.04.035

van Beugen, B. J., Qiao, X., Simmons, D. H., Zeeuw, C. I. D., & Hansel, C. (2014). Enhanced AMPA receptor function promotes cerebellar long-term depression rather than potentiation. *Learning & Memory*, *21*(12), 662–667. https://doi.org/10.1101/lm.035220.114

van der Zwaag, B., Staal, W. G., Hochstenbach, R., Poot, M., Spierenburg, H. A., de Jonge, M. V., Verbeek, N. E., van 't Slot, R., van Es, M. A., Staal, F. J., Freitag, C. M., Buizer-Voskamp, J. E., Nelen, M. R., van den Berg, L. H., van Amstel, H. K. P., van Engeland, H., & Burbach, J. P. H. (2010). A co-segregating microduplication of chromosome 15q11.2 pinpoints two risk genes for autism spectrum disorder. *American Journal of Medical Genetics Part B: Neuropsychiatric Genetics*, *153B*(4), 960–966. https://doi.org/10.1002/ajmg.b.31055

Van Overwalle, F., D'aes, T., & Mariën, P. (2015). Social cognition and the cerebellum: A meta-analytic connectivity analysis. *Human Brain Mapping*, *36*(12), 5137–5154. https://doi.org/10.1002/hbm.23002

Wagner, M. J., Kim, T. H., Savall, J., Schnitzer, M. J., & Luo, L. (2017). Cerebellar granule cells encode the expectation of reward. *Nature*, *544*(7648), 96–100. https://doi.org/10.1038/nature21726

Wang, D., Buckner, R. L., & Liu, H. (2013). Cerebellar asymmetry and its relation to cerebral asymmetry estimated by intrinsic functional connectivity. *Journal of Neurophysiology*, *109*(1), 46–57. https://doi.org/10.1152/jn.00598.2012

Wang, D., Buckner, R. L., & Liu, H. (2014). Functional Specialization in the Human Brain Estimated By Intrinsic Hemispheric Interaction. *Journal of Neuroscience*, *34*(37), 12341–12352. https://doi.org/10.1523/JNEUROSCI.0787-14.2014

Wang, S. S.-H., Denk, W., & Häusser, M. (2000). Coincidence detection in single dendritic spines mediated by calcium release. *Nature Neuroscience*, *3*(12), 1266–1273. https://doi.org/10.1038/81792

Wang, S. S.-H., Khiroug, L., & Augustine, G. J. (2000). Quantification of spread of cerebellar long-term depression with chemical two-photon uncaging of glutamate. *Proceedings of the National Academy of Sciences*, *97*(15), 8635–8640. https://doi.org/10.1073/pnas.130414597

Wang, S. S.-H., Kloth, A. D., & Badura, A. (2014). The Cerebellum, Sensitive Periods, and Autism. *Neuron*, *83*(3), 518–532. https://doi.org/10.1016/j.neuron.2014.07.016

Wang, X., Chen, G., Gao, W., & Ebner, T. (2009). Long-term potentiation of the responses to parallel fiber stimulation in mouse cerebellar cortex in vivo. *Neuroscience*, *162*(3), 713–722. https://doi.org/10.1016/j.neuroscience.2009.01.071

Weber, J. T., De Zeeuw, C. I., Linden, D. J., & Hansel, C. (2003). Long-term depression of climbing fiber-evoked calcium transients in Purkinje cell dendrites. *Proceedings of the National Academy of Sciences*, *100*(5), 2878–2883. https://doi.org/10.1073/pnas.0536420100

Wilms, C. D., & Häusser, M. (2015). Reading out a spatiotemporal population code by imaging neighbouring parallel fibre axons in vivo. *Nature Communications*, *6*(6464), Article 1. https://doi.org/10.1038/ncomms7464

Wilson, A. M., Schalek, R., Suissa-Peleg, A., Jones, T. R., Knowles-Barley, S., Pfister, H., & Lichtman, J. W. (2019). Developmental Rewiring between Cerebellar Climbing Fibers and Purkinje Cells Begins with Positive Feedback Synapse Addition. *Cell Reports*, *29*(9), 2849-2861.e6. https://doi.org/10.1016/j.celrep.2019.10.081

Witter, L., Rudolph, S., Pressler, R. T., Lahlaf, S. I., & Regehr, W. G. (2016). Purkinje Cell Collaterals Enable Output Signals from the Cerebellar Cortex to Feed Back to Purkinje Cells and Interneurons. *Neuron*, *91*(2), 312–319. https://doi.org/10.1016/j.neuron.2016.05.037

Wu, Y., & Raman, I. M. (2017). Facilitation of mossy fibre-driven spiking in the cerebellar nuclei by the synchrony of inhibition. *Journal of Physiology*, *595*(15), 5245–5264. https://doi.org/10.1113/JP274321

Wu, Y.-C., Louis, E. D., Gionco, J., Pan, M.-K., Faust, P. L., & Kuo, S.-H. (2021). Increased Climbing Fiber Lateral Crossings on Purkinje Cell Dendrites in the Cerebellar Hemisphere in Essential Tremor. *Movement Disorders*, *36*(6), 1440–1445. https://doi.org/10.1002/mds.28502

Wyatt, K. D., Tanapat, P., & Wang, S. S.-H. (2005). Speed limits in the cerebellum: Constraints from myelinated and unmyelinated parallel fibers. *European Journal of Neuroscience*, *21*(8), 2285–2290. https://doi.org/10.1111/j.1460-9568.2005.04053.x

Xu-Friedman, M. A., Harris, K. M., & Regehr, W. G. (2001). Three-Dimensional Comparison of Ultrastructural Characteristics at Depressing and Facilitating Synapses onto Cerebellar Purkinje Cells. *Journal of Neuroscience*, *21*(17), 6666–6672. https://doi.org/10.1523/JNEUROSCI.21-17-06666.2001

Yang, Y., & Lisberger, S. G. (2014). Purkinje-cell plasticity and cerebellar motor learning are graded by complex-spike duration. *Nature*, *510*(7506), 529–532. https://doi.org/10.1038/nature13282

Yiu, A. P., Mercaldo, V., Yan, C., Richards, B., Rashid, A. J., Hsiang, H. L. L., Pressey, J., Mahadevan, V., Tran, M. M., Kushner, S. A., Woodin, M. A., Frankland, P. W., & Josselyn, S. A. (2014). Neurons Are Recruited to a Memory Trace Based on Relative Neuronal Excitability Immediately before Training. *Neuron*, *83*(3), 722–735. https://doi.org/10.1016/j.neuron.2014.07.017

Zack, G. W., Rogers, W. E., & Latt, S. A. (1977). Automatic measurement of sister chromatid exchange frequency. *Journal of Histochemistry & Cytochemistry*, *25*(7), 741–753. https://doi.org/10.1177/25.7.70454

Zang, Y., & De Schutter, E. (2019). Climbing Fibers Provide Graded Error Signals in Cerebellar Learning. *Frontiers in Systems Neuroscience*, *13*. https://doi.org/10.3389/fnsys.2019.00046

Zang, Y., & De Schutter, E. (2021). The Cellular Electrophysiological Properties Underlying Multiplexed Coding in Purkinje Cells. *Journal of Neuroscience*, *41*(9), 1850–1863. https://doi.org/10.1523/JNEUROSCI.1719-20.2020

Zang, Y., Dieudonné, S., & De Schutter, E. (2018). Voltage- and Branch-Specific Climbing Fiber Responses in Purkinje Cells. *Cell Reports*, *24*, 1536–1549. https://doi.org/10.1016/j.celrep.2018.07.011

Zhang, B., Chen, L. Y., Liu, X., Maxeiner, S., Lee, S.-J., Gokce, O., & Südhof, T. C. (2015). Neuroligins Sculpt Cerebellar Purkinje-Cell Circuits by Differential Control of Distinct Classes of Synapses. *Neuron*, *87*(4), 781–796. https://doi.org/10.1016/j.neuron.2015.07.020

Zhou, H., Lin, Z., Voges, K., Ju, C., Gao, Z., Bosman, L. W., Ruigrok, T. J., Hoebeek, F. E., De Zeeuw, C. I., & Schonewille, M. (2014). Cerebellar modules operate at different frequencies. *eLife*, *3*, e02536. https://doi.org/10.7554/eLife.02536

Zobeiri, O. A., & Cullen, K. E. (2022). Distinct representations of body and head motion are dynamically encoded by Purkinje cell populations in the macaque cerebellum. *eLife*, *11*, e75018. https://doi.org/10.7554/eLife.75018

Zoghbi, H. Y. (2003). Postnatal Neurodevelopmental Disorders: Meeting at the Synapse? *Science*, *302*(5646), 826–830. https://doi.org/10.1126/science.1089071

Zoghbi, H. Y., & Bear, M. F. (2012). Synaptic Dysfunction in Neurodevelopmental Disorders Associated with Autism and Intellectual Disabilities. *Cold Spring Harbor Perspectives in Biology*, *4*(3), a009886. https://doi.org/10.1101/cshperspect.a009886